

فعاليات المؤتمر الدولي في الإلكترونيات، الطاقة و القياس

IC²EM'2018



Proceedings of

The International Conference
on Electronics, Energy and Measurement

November 27-28, 2018

IC²EM'2018

© 2018, ISBN 978 9931 9548 04

National Library of Algiers

Laboratory of
INSTRUMENTATION

IC²EM'2018

المؤتمر الدولي في الإلكترونيات، الطاقة و القياس

International Conference on Electronics
Energy and Measurement

November 27-29, 2018, Algiers, ALGERIA



SLC
Enabling communications

RSDT
من أجل بحث علمي مفيد

الجزائر

المكتبة الوطنية الجزائرية
Bibliothèque Nationale d'Algérie

جامعة هواري بومدين
للعلوم والتكنولوجيا
U S T H B

سونلغاز
SONELGAZ

Open Access Proceedings

Copyright © 2018 by the Laboratory of Instrumentation,
Publishing in Open Access, *All Right Reserved*

<https://ic2em-2018.sciencesconf.org/resource/page/id/19>

LINS Laboratory of USTHB

Faculty of Electronics and Computers

Department of Instrumentation and Automatics

PO.Box: 32, Bab-Ezzouar, 16111, Algiers, ALGERIA

URL: <http://www.lins.usthb.dz>

Phone/Fax.: +213 21 207 664



Legal Deposit in the Algerian Library

ISBN: 978 9931 9548 04

Legal Deposit: 11-2018

Designed and Printed in Algeria

Authentication

The content of this documents remains the strict responsibility of theirs authors.

Peer Review Process

All the full-length papers included in the **Proceedings of International Conference on Electronics, Energy and Measurement**, 27-29 November 2018 have been independently peer reviewed by scientists working in the field using EasyChair conference system. Initially, the submitted papers were reviewed by the Scientific Committee, and the review comments were sent to the authors to address the comments in updating their papers. If the work was accepted, the authors were invited to submit full camera-ready papers. The revised papers submitted by the authors were then checked by the Editors and accepted once the papers had satisfied the requirements and standards of the International Conference on Electronics, Energy and Measurement.

Sponsors



Steering Committee

Mohamed Saïdi
Zaïa Alimazighi
Abdelaziz Talha

Amina Ababou
Mokhtar Attari
Samir Boukhenous
Houria Brahim
Merzak Ferroukhi
Saïd Gaoua
Abdelakram Hafid
Abdellah Kouzou
Youcef Remram
Moussa Sardi
Abdellah Skoudarli
Mohamed Tellache
Adel Touchen

Honorary Chair, Houari Boumediene University, Algeria
Honorary Vice-Chair, Houari Boumediene University, Algeria
Conference Chair, Houari Boumediene University, Algeria

Houari Boumediene University, Algeria
Houari Boumediene University, Algeria
Houari Boumediene University, Algeria
Houari Boumediene University, Algeria
Houari Boumediene University, Algeria
Houari Boumediene University, Algeria
University of Djelfa, Algeria
Houari Boumediene University, Algeria
Houari Boumediene University, Algeria
Houari Boumediene University, Algeria
Houari Boumediene University, Algeria
Houari Boumediene University, Algeria

Program Committee

Amina Ababou	Houari Boumediene University, USTHB, Algeria
Noureddine Ababou	Houari Boumediene University, USTHB, Algeria
Mourad Adnane	Ecole Nationale Polytechnique, Algeria
Farid Alilat	Houari Boumediene University, USTHB, Algeria
Soltane Ameur	Mouloud Mammeri University, UMMTO, Algeria
Faycal Amrani	Houari Boumediene University, USTHB, Algeria
Abderrahmane Amrouche	Houari Boumediene University, USTHB, Algeria
Mokhtar Attari	Houari Boumediene University, USTHB, Algeria
Ahmad Taher Azar	Benha University, Benha, Egypt
Viorel Badescu	Polytechnic University of Bucharest, Bulgaria
Said Barkat	Mohamed Boudiaf University, UMBM, Algeria
Lynda Bazi	Houari Boumediene University, USTHB, Algeria
Mohammed Benaissa	University of Sheffield, Sheffield, United Kingdom
Mohamed El Hachemi Benbouzid	University of Brest, Brest, France
Arezki Benfdila	University Mouloud Mammeri Tizi-Ouzou
Khelifa Benmansour	University Yahia Farès, Medea, Algeria
Dalila Beriber	Houari Boumediene University, USTHB, Algeria
El Madjid Berkouk	National Polytechnic School, Algiers, Algeria
Mohamed Seghir Boucherit	National Polytechnic School, Algiers, Algeria
Bachir Boudraa	Houari Boumediene University, USTHB, Algeria
Mounir Bouhedda	University Yahia Farès, Medea, Algeria
Akkila Boukhelifa	Houari Boumediene University, USTHB, Algeria
Samir Boukhenous	Houari Boumediene University, USTHB, Algeria
Abdelmalek Boularas	Ahmed Bin Mohamed Military College, Al Rayyan, Qatar
Ahmed Cheriti	University of Quebec Trois Rivières, Quebec, Canada
Brahim Cherki	Aboubekr Belkaïd University, Tlemcen, Algérie
Youcef Chibani	Houari Boumediene University, USTHB, Algeria
Raghavan Dhanasekaran	Syed Ammal Engineering College, India
Hakim Djelouah	Houari Boumediene University, USTHB, Algeria
Said Drid	Batna University, Batna, Algeria
Hammoudi Escid	Houari Boumediene University, USTHB, Algeria
Leila Falek	Houari Boumediene University, USTHB, Algeria
Said Gaoua	Houari Boumediene University, USTHB, Algeria
Gevork Gharehpetian	Amirkabir University of Technology, Tehran, Iran
Kaci Ghedamsi	Univerity Mira of Bejaia, Bejaia, Algeria
Boualem Haddad	Houari Boumediene University, USTHB, Algeria
Mourad Haddadi	National Polytechnic School, Algiers, Algeria
Ahmed Hafaiifa	University of Djelfa, Djelfa, Algeria
Brahim Haraoubia	Houari Boumediene University, USTHB, Algeria
Samia Harrouni	Houari Boumediene University, USTHB, Algeria
Mohamed Kechouane	Houari Boumediene University, USTHB, Algeria
Malika Kedir	Houari Boumediene University, USTHB, Algeria
Amar Khelif	Houari Boumediene University, USTHB, Algeria
Abdellah Kouzou	University of Djelfa, Djelfa, Algeria
Yazid Krim	Houari Boumediene University, USTHB, Algeria
Youssef Lamhene	Houari Boumediene University, USTHB, Algeria

Cherif Larbes	National Polytechnic School, Algiers, Algeria
Mohand Oulhadj Mahmoudi	National Polytechnic School, Algiers, Algeria
Noureddine Manamanni	University of Reims, Reims, France
Moufid Mansour	Houari Boumediene University, USTHB, Algeria
Abdelouahab Mekhaldi	National Polytechnic School, Algiers, Algeria
Saad Mekhilef	University of Malaya, Kuala Lumpur, Malaysia
Youcef Meslem	Ibn Khaldoun University, Tiaret, Algeria
Nadhir Messai	University of Reims Champagne-Ardenne
Iqbal Messaïf	Houari Boumediene University, USTHB, Algeria
Nacéra Meziane	Houari Boumediene University, USTHB, Algeria
Mohamed Said Nait Said	University of Batna, Batna, Algeria
Rachid Oussaid	Houari Boumediene University, USTHB, Algeria
Nathalie Raveu	Toulouse University, Toulouse, France
Djamila Rekioua	Univerity Mira of Bejaia, Bejaia, Algeria
Youcef Remram	Houari Boumediene University, USTHB, Algeria
Abdellah Skoudarli	Houari Boumediene University, USTHB, Algeria
Abdelaziz Talha	Houari Boumediene University, USTHB, Algeria
Junwu Tao	University of Toulouse, Toulouse, France
Smail Tedjini	Grenoble Institute of Technology, Grenoble, France
Mohamed Tellache	Houari Boumediene University, USTHB, Algeria
Rachida Touhami	Houari Boumediene University, USTHB, Algeria
Mustapha C.E. Yagoub	University of Ottawa, Ottawa, Canada

Message from the Chairman

The *International Conference on Electronics, Energy and Measurement (IC2EM-2018)*, organized by the *Laboratory of Instrumentation* under the supervision of the *University of Science and Technology Houari Boumediene (USTHB)*, will be held at the National Library of Algeria, Algiers on 27 and 29 November, 2018. This event follows previous workshops of the Laboratory of Instrumentation series (JLINS) that held in 2007, 2010 and 2012 respectively.

This edition will aim to bring scientists and engineers from academia, research institutes and industrial establishments to present and discuss the latest results in the field of electronics, instrumentation and measurement, sensors and energy. Thus, IC2EM-2018 will aim to provide answers to the concerns of the industry, innovative ideas and make a state of the art in new technologies of Electronics, Energy and Measurement.

To meet this growing need to master new techniques of Electronics, Energy and Measurement, more than hundred contributions were submitted to IC2EM-2018. The scientific program committee has assumed the difficult task to select high quality papers for preparing a balanced program covering research topics of the conference. In addition to the regular meetings that include the accepted papers, three plenary sessions are proposed by experts of established reputation.

In my capacity as the Chairman of the IC2EM-2018, I wish to address my gratitude to all researchers who kindly answer the call for papers, to all those who have contributed to the preparation of these days, and especially the Editor, the members of the Steering Committee and to the members of the Scientific Committee. Also, many thanks to the DGRSDT, USTHB, Sonelgaz (*Company of Electricity and Gaz*), BNA (*National Library of Algeria*) and SLC for sponsoring the conference.

The main topics of the Conference concern Electronic systems, Energy systems, Instrumentations, Measurement, Telecommunications and applications in various sectors. We hope that the Conference meet the expectations and stimulate the interest of researchers in various laboratories. I wish to express my great pleasure to welcome our guests in the Conference.

Algiers: November 24, 2018

Prof. Abdelaziz TALHA
Chairman of IC2EM-2018



Preface

Preface of the Editor

This volume contains the papers presented at the *International Conference on Electronics, Energy and Measurement (IC2EM-2018)* held on November 27-29, 2018 in Algiers. There were more than hundred submissions. Each submission was reviewed by at least 2 program committee members working principally in the field, and on the average 2.7 program committee members. The steering committee decided to accept 72 papers of high scientific quality and only 54 papers have been presented at the conference and published in this proceedings. The program also includes 3 invited talks.

The past decade has been marked by the emergence of smart technologies in most disciplines. It is due to the increasing demand for new systems and methods of explorations in many aspects of research and engineering from the design of electronic equipment and instruments to complex systems in energy production, biomedical, transport, etc. Smart and intelligent sensors, mobile phones, antennas, computer peripherals, industrial monitoring systems, production of renewable energy, are typical examples of the advanced technology of Electronics, Energy and Measurement.

Many thanks for *EasyChair* that help in the realization of this volume for the diffusion of science through the web by providing an open access online publication service for conference proceedings. It is a very high level automate that manage the whole conference with an intelligence workflow from submitting papers to the preparation of the proceeding through several smart procedures for the review process. My sincerest acknowledgement is also given to *Sciencesconf* of CNRS (*France*) for there helpful in hosting the website of the conference and the possibilities to upload many files.

All my gratitude to all members of the scientific program committee from different countries that assumed a difficult task of reviewing papers and decide on where the acceptance or rejection of the assigned papers. In the end, high quality papers covering research topics of the conference have been selected for this edition of the proceeding.

Algiers: March 19, 2019

Prof. Mokhtar ATTARI
Editor of IC2EM-2018

Table of Contents

Gain improvement of the cascaded single stage distributed amplifier	1
<i>Faycal Amrani, Mohamed Trabelsi and Rachida Touhami</i>	
Design of and Control of Three-phase Vienna Rectifier with PFC for Electrolyzer	6
<i>Faycal Benyamina and Farid Khoucha</i>	
A novel switched series/parallel inverter with asymmetrical sources configuration	13
<i>Mohammed Salim Benmerabet, Talha and Berkouk El Madjid</i>	
CSRR Array Structure For Ceramic Crack Detection	19
<i>Haroune Feddal, Mohamed Tellache and Junwu Tao</i>	
An improved INC-MPPT algorithm based on passivity approach for photovoltaic system .	23
<i>Abdelkader Belboula, Rachid Taleb, Djilali Benyoucef, Fayçal Chabni and Alla Eddine Toubal Maamar</i>	
MPPT Techniques in Stand-alone Photovoltaic System with Batteries	31
<i>Faika Zaouche, Djamila Rekioua, Said Aissou and Seddik Bacha</i>	
Management of the electrochemical storage in Photovoltaic system using the modified Coppetti model	39
<i>Aicha Degla, Madjid Chikh and Achour Mahrane</i>	
Conception of microstrip patch antenna based on SINRD substrate for DSRC application.	46
<i>Narimane Korchi and Rachid Oussaid</i>	
FPGA Hardware Implementation of Image Processing Techniques	52
<i>Marouane Kahlouche, Malika Kedir-Talha, Saliha Ould Slimane and Hadjar Zairi</i>	
Amélioration des performances d'une antenne patch avec Structures Tridimensionnelles à Bande Interdite Electromagnétique	58
<i>Mustapha Hadj Sadok, Youssef Lamhene and Samir Berkani</i>	
An Optimized Hybrid Junction Multi-band Rectifier for Harvesting RF Energy	64
<i>Ali Benayad and Mohamed Tellache</i>	
Theoretical Analysis of Optical Isolator Based on Mode Conversion in Yttrium Iron Garnet Fiber	69
<i>Khadidja Saker, Touraya Bouchemat, Mahieddine Lahoubi and Mohamed Bouchemat</i>	
Generating of high repetition rate pulse train in photonic crystal fibers by induced modulation instability	75
<i>Nedjmeddine Ammar Merabet, Lynda Cherbi-Bazi and Lyes Bahloul</i>	
Joint Angle Measurement Using a Corrected Gyroscope Integration Data	83
<i>Mahdi Zabat, Karim Bensisaid, Amina Ababou and Nouredine Ababou</i>	
Generation and stabilisation of dark solitons in microstructured fiber resonator	92
<i>Hariz Abdel Hafid, Bahloul Lies and Cherbi Lynda</i>	
Low-cost instrumented handrim for manual wheelchair propulsion force analysis	98
<i>Farid Djail, Karim Bensisaid, Kahina Benrekaa, Nouredine Ababou, Amina Ababou and Nadia Saadia</i>	

Electrical Circuit Constants Determination and Voltage Gain Measurement of Unloaded Rosen Type Piezoelectric Transformer Operating in First Mode	107
<i>Faiza Boukazouha, Hamza Barkat, Abderahim Herbadji, Abdesselam Rouabha, Monia Guessoum and Kamel Sedda</i>	
Characterization and verification of ultrasonic equipment: Measurement of the transmitter pulse parameters according to EN 12668-1:2010	112
<i>Hamza Barkat, Abdeslem Rouabha, Abderrahim Herbadji, Rafik Halimi and Ali Badidi Bouda</i>	
Static Platform for Postural Balance Analysis and Recognition	118
<i>Adel Touchen, Mokhtar Attari, Samir Boukhenous and Cherif Zizoua</i>	
Semi empirical models for estimating global solar radiation for inclined surfaces in the north of Algeria _ Algiers	123
<i>Talbi Khaoula and Harrouni Samia</i>	
Foot sole platform for static and dynamic force and pressure analysis	128
<i>Adel Touchen, Mokhtar Attari and Samir Boukhenous</i>	
Finite element analysis of the fundamental anti-symmetric Lamb A0 and Quasi-Lamb qA0 modes for gas sensing applications	132
<i>Laidoudi Farouk, Medjili Fayçal, Bettine Farid and Boubenider Fouad</i>	
Simulation Based Comparative Study of GaAs _{1-x} P _x /GaAs QD for Solar Cell Applications	137
<i>Houcine Guesmi, Abdelkader Aissat, Meriem SAFI, Fethi BENYETTOU and Isabelle Berbezier</i>	
An Efficient Supervision of a Hybrid PV-Battery/Supercapacitor Off-grid System with Diesel Generator for Emergency Standby Power	143
<i>Guichi Amar, Talha Abdelaziz and Berkouk Elmadjid</i>	
Robust Dynamic Surface Control of Interior Permanent Magnet Synchronous Motors	151
<i>Salah Nadji and Samira Benaicha</i>	
Multipurpose Asymmetric Cascaded Inverter	158
<i>Khelil Zaouche, Abdelaziz Talha and El Madjid Berkouk</i>	
Contribution to the Improvement of the Quality of Electrical Energy Produced by Wind Turbine Based on the PMSG Using the Advanced Control Techniques of Multilevel-level Inverter	163
<i>Ihssen Hamzaoui, Farid Bouchafaa and Saida Boukhalfa</i>	
Real-coded genetic algorithm optimization for Harmonic Elimination in Neutral-Point Clamped Multilevel Inverter	169
<i>Nour El Houda Gabour, El Ghalia Boudissa and Mhamed Bounekhla</i>	
Second-Order Sliding Mode Control Scheme with a Non-Linear Phenomena Analysis of a DC-DC Power Converter Dedicated to Distributed Power Systems	176
<i>Amel Hadri Hamida, Adel Ghoggal, Sakina Zerouali and Fatiha Khelili</i>	
Validation of Operating Temperature Models of PV Module for a Grid Connected PV System under Desert Climates of Algeria	183
<i>Rachid Dabou, Farid Bouchafaa, Nordine Sahouane, Abderrezzaq Ziane, Ammar Necaibia, Ahmed Bouraiou, Seyfallah Khelifi and Abdelkarim Rouabhia</i>	

The response of Different Hydrogen liquids to the resonance in a Nanophotonic Structure of an Optical Channel Based on two-dimensional Photonic Crystal Ring Resonator.....	188
<i>Mehdi Ghoumazi and Abdesselam Hocini</i>	
comparison between ANN based MPPT and P&O under fast and slow changing atmospheric conditions and partial shading.....	195
<i>Redouane Abidat and Akila Boukhelifa</i>	
Effect of applied voltage on Electrical Properties and Energy Efficiency of a Ne-Xe Excimer lamp	201
<i>Wafà Benstaali and Ahmde Belasri</i>	
Power Control of a Wind Energy Conversion System Associated with a Battery-based Storage System	207
<i>Karima Boulaam and Akkila Boukhelifa</i>	
Reliable Full-Wave Computation of the Characteristic Impedance of Asymmetrical Finline: Application to the Step Discontinuity.....	215
<i>Abdelhamid Khodja, Mustapha Cherif-Eddine Yagoub, Rachida Touhami and Henri Baudrand</i>	
Metamaterial proprieties exploited in wire antenna design.....	223
<i>Samir Berkani, Youssef Lamhene and Mustapha Hadj Sadok</i>	
WHERE TO BE FROM THE TYPICAL ICG WAVEFORM.....	227
<i>Sara Benouar, Abdel Akram Hafid, Mokhtar Attari, Malika Kedir and Fernando Seoane</i>	
Design of Antenna Array Based on Siw Technology for Satellite Applications.....	233
<i>Abdelkader Zerfaine, Mohamed Tellache and Hichem Mahfoudi</i>	
VEHICLE MOTION PARAMETER ESTIMATION USING CLOSED-FORM SOLUTION BASED ON TIME-FREQUENCY ANALYSIS	237
<i>Hakima Timplt, Adel Belouchrani and Youcef Remram</i>	
Wide range and high linearity CMOS temperature sensor core circuit for RFID applications.	242
<i>Abdelhakim Megueddem and Khaled Bekhouche</i>	
WobbleBox, an adaptive instrument to quantify angles variations during exercises on wobble boards	246
<i>Anwar Benbakhti, Samir Boukhenous and Mokhtar Attari</i>	
Modeling of Thermal Flow Sensor used for Thermal Mass Flowmeter.....	251
<i>Amina Bekraoui</i>	
Sensors Networks for Platform Radiotherapy Services	258
<i>Malika Tighidet, Abdelkrim Allam and Mokhtar Attari</i>	
Photonic Crystal Sensor Arrays Based on Side-Coupled Resonant Cavity Arrays.....	263
<i>Chayma Mosbah, Ahlem Benmerkhi, Mohamed Bouchemat and Touraya Bouchemat</i>	
Vector control of a shunt active power filter based on synchronous reference frame identification method.....	268
<i>Yassine Sadki, Abdellah Kouzou and Ahmed Hafaiifa</i>	

Direct Torque Control - DTC of PMSM Supplied By Photovoltaic Source.....	275
<i>Saida Boukhalfa, Farid Bouchafaa and Ihssen Hamzaoui</i>	
Fuzzy Backstepping Control of Double Star Induction Machine for Driving HEV at Low Speed.....	281
<i>Noureddine Layadi, Ali Djerioui, Samir Zeghlache, Azeddine Houari, Mohamed-Fouad Benkhoris and Fouad Berrabah</i>	
Temperature Effects on the Structure InP/InGaP IBQD for Solar Cell.....	289
<i>Nabila Harchouch, Abdelkader Aissat and Jean Pierre Vilcot</i>	
Exploitation of the XSG in the FPGA Hardware Implementation of a Medical image Signal Processing	297
<i>Saliha Ould Slimane, Fouad Belalem, Malika D Kedir-Talha and Karim Meddah</i>	
Antenna Powered by a Coplanar Waveguide (CPW) For Wi-Fi and WLAN Mobile Phone Applications	305
<i>Belgacem Nassima and Abri Mehadji</i>	
Flattened Chromatic dispersion controllability in nonlinear liquid photonic bandgap fibers	311
<i>Meriem Benlacheheb, Lynda Cherbi-Bazi and Mohamed Lamine Ferhat</i>	
Direct torque control strategies combined with space vector modulation applied to the monitoring of doubly fed induction generator	317
<i>Habib Chaouki Ben Djoudi, Mouloud Guemana and Ahmed Hafaiifa</i>	
Commande Découplée du Système Multi-machines Connectées en Série	323
<i>Taieb Bessaad, Rachid Taleb, M'hamed Helaimi, Abderrahmen Benbouali and Fayçal Chabni</i>	
An Improved Chaos Controller For Genesio-Tesi Chaotic System Based On Sliding Mode .	330
<i>Chibani Abdelilah, Daaou Bachir, Gouichiche Abdelmadjid, Safa Ahmed and Messlem Youcef</i>	

Gain Improvement of the Cascaded Single Stage Distributed Amplifier

Fayçal AMRANI¹, Mohamed TRABELSI² and Rachida TOUHAMI¹

¹ Laboratory of Instrumentation, USTHB, PO.Box. 32, Bab-Ezzouar, Algiers, URL:
<http://www.lins.usthb.dz>, Email: fay_amr@yahoo.fr

² Laboratory LDCCP, Ecole Nationale Polytechnique, 10 Rue des frères Ouadek - Hassan Badi - El harrach - Alger – Algérie, Email: mohamed.trabelsi@enp.edu.dz

ABSTRACT

This article describes a new cascaded single stage distributed amplifier design method, based on the Chebyshev polynomial approximation of the amplifier transducer gain. This method gives an improvement of 6dB in gain and allows having more compact amplifier by eliminating two elements, compared with the conventional cascaded single stage distributed amplifier with a single field effect transistor.

Key Words: distributed amplifiers, bandwidth, Chebyshev polynomial, cascaded single stage, gain, ripple ratio.

1. INTRODUCTION

The distributed amplifier, consisting of a number of cascaded stages (CSSDA), was proposed by J.Y. Liang and C.S. Aitchison [1] (Fig. 1). It is a circuit containing n amplifiers with field effect transistors MESFET (Fig.2), linked to each other, according to the cascade topology, by artificial transmission lines, named for this reason inter-stage lines. Each of these inter-stage lines is constituted by two inductances L_{int} and $L_{int}/2$ and the two capacitors gate-source C_{gs} and drain-source C_{ds} of the transistor (Fig. 2), in addition to another capacitor C connected in parallel to C_{ds} . The first transistor capacitance C_{gs} and two inductances $L/2$ form the input line connecting the generator to the CSSDA first stage, while the capacitance C_{ds} , added to capacitance C , constitute with two other inductances $L/2$ the output line coupling the CSSDA last stage to the load.

All these artificial lines are, therefore, made up of k-constant cells which transmit the signal from DC to the cut-off frequency. This cut-off frequency and the characteristic impedances are depending on the capacitances and inductances [2].

The inter-stage lines and the two input and output lines are terminated respectively by their characteristic impedance Z_{oint} and Z_o . So, these lines are matched and the voltage wave propagated there is a progressive wave. Therefore, the voltage along the lines remains constant even when the frequency varies from DC to the line cutoff frequency. Thus, by applying to the transistor input, this constant voltage V_{gs} will give, via the transistor, a drain-source output current I_{ds} that is also constant, as it is proportional to this voltage $I_{ds} = g_m V_{gs}$ (g_m : the transistor transconductance) (Fig.2). This will result in an available power gain invariable from DC to the cut-off frequency, which gives the CSSDA a low pass character.

Thus, the signal will be amplified, and increases by increasing the number of stages. This number is limited by a maximum value, which essentially depends on the joule losses due to the transistor gate-source and the drain-source resistors (R_{gs} and R_{ds} respectively), not shown in figure 2. We propose another CSSDA that we call Mismatched Cascaded Single Stage Distributed Amplifier (MCSSDA) (Fig. 3), the novelty of this amplifier lies in the fact that the MCSSDA input lines is open. Thus, the first transistor voltage V_{gs} be doubled. This new structure will provide us with a 6 dB gain improvement in low frequency. But, it can generate a variable gain when the frequency

changes, and a bandwidth which may be relatively narrower, because of the input line mismatch. To these two disadvantages, we propose a solution which will be detailed later.

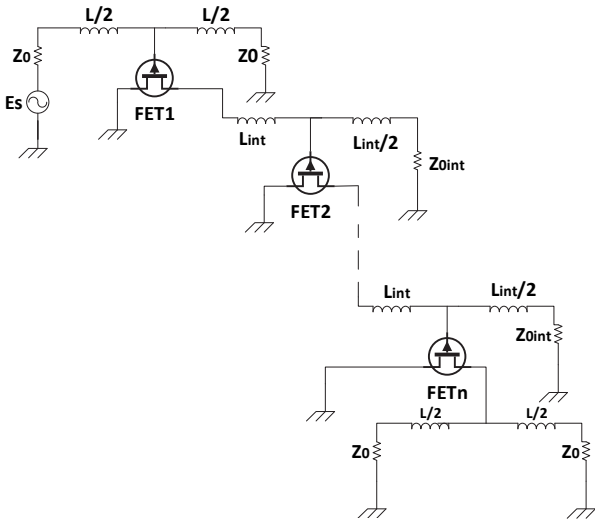


Fig. 1: The CSSDA amplifier.

Thus, the signal will be amplified, and increases by increasing the number of stages. This number is limited by a maximum value, which essentially depends on the joule losses due to the transistor gate-source and the drain-source resistors (R_{gs} and R_{ds} respectively), not shown in figure 2. We propose another CSSDA that we call Mismatched Cascaded Single Stage Distributed Amplifier (MCSSDA) (Fig. 3), the novelty of this amplifier lies in the fact that the MCSSDA input lines is open. Thus, the first transistor voltage V_{gs} be doubled. This new structure will provide us with a 6 dB gain improvement in low frequency. But, it can generate a variable gain when the frequency changes, and a bandwidth which may be relatively narrower, because of the input line mismatch. To these two disadvantages, we propose a solution which will be detailed later.

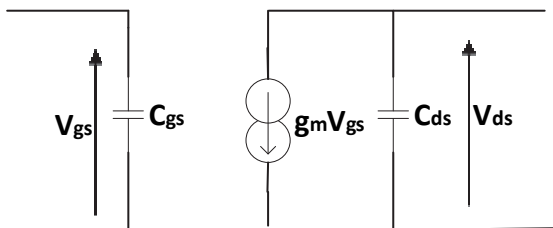


Fig. 2: The simplified unilateral MESFET.

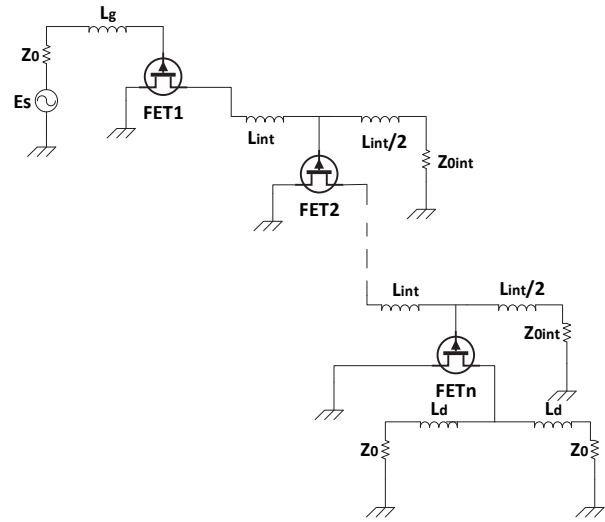


Fig. 3: The MCSSDA amplifier

2. CIRCUIT PRINCIPLE

For n stages CSSDA amplifier, the transducer power gain, in low frequency, is given by [1]:

$$G_{T(CSSDA)} = \frac{Z_0^2 Z_{0int}^{2(n-1)} g_m^{2n}}{4} \quad (1)$$

To calculate the MCSSDA transducer power gain, we must analyse its equivalent circuit given in Fig. 4, where the MESFET transistor is represented by the simple unilateral model (Fig. 2).

C_{gsi} ($i \in [1, n]$) is the transistor grid-source capacitance, and C_{di} ($i \in [1, n-1]$) is the drain-source capacitance to which we added a shunt capacitance C such that $C_{dsi} + C = C_{di} = C_{gsi}$ to have identical inter-stage lines. These lines will therefore have the same characteristic impedance $Z_{0int} = \sqrt{\frac{L_{int}}{C_{gs}}}$.

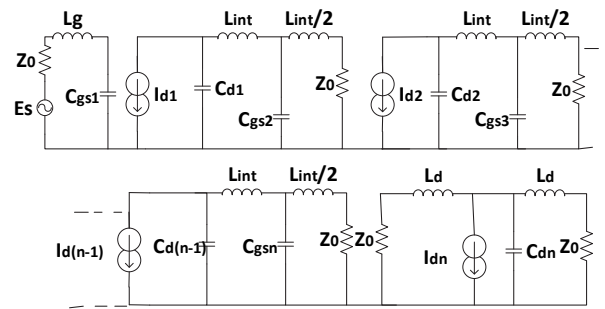


Fig. 4: Equivalent circuit of the MCSSDA

The MCSSDA transducer gain G_T calculation gives:

$$G_{T(MC SSDA)} = \frac{Z_0^2 g_m^{2n} Z_{0int}^{2(n-1)}}{[(1-4x^2)^2 + \alpha_1^2 x^2][(1-x_c^2)^{n-1}]} \quad (2)$$

Or

$$g_{T(MC SSDA)} = \frac{G_{T(MC SSDA)}}{Z_0^2 g_m^{2n} Z_{0int}^{2(n-1)}} = \frac{1}{[(1-4x^2)^2 + \alpha_1^2 x^2][(1-x_c^2)^{n-1}]} \quad (3)$$

Where $x = \frac{\omega}{\omega_{c1}}$ is the normalized pulsation (frequency) with respect to the cutoff frequency of the first stage grid line; $\omega_{c1} = \frac{2}{\sqrt{Lg C_{gs1}}}$, $\alpha_1 = 2 \frac{Z_0}{Z_{c1}}$, with $Z_{c1} = \sqrt{\frac{Lg}{C_{gs1}}}$ the characteristic impedance, at relatively low frequencies, of the k-constant circuits constituting the input grid line. $x_c = \frac{\omega}{\omega_c}$ is the normalized pulsation (frequency) with respect to the cutoff frequency of the interstage lines, $\omega_c = \frac{2}{\sqrt{L_{int} C_{gs}}}$.

At the dc signal, the CSSDA power transducer gain is $\frac{Z_0^2 Z_{0int}^{2(n-1)} g_m^{2n}}{4}$, and that of the MCSSDA is $Z_0^2 g_m^{2n} Z_{0int}^{2(n-1)}$; This shows an improvement of 6dB in the MCSSDA gain compared to the CSSDA.

However, since the amplifier input is mismatched, the input line will be traversed by stationary waves, which generates ripples on the MCSSDA gain curve when the frequency varies.

The question is how to keep the gain $g_{T(MC SSDA)}$ constant over the entire frequency band? The answer is: if the denominator of relation (3) can be approximated by polynomials providing low ripple.

As $(1-x_c^2)^{n-1}$ is almost a constant term over the frequency range of the amplifier, the approximation will be made only on the term $[(1-4x^2)^2 + \alpha_1^2 x^2]$ of the equation (3).

Expanding the denominator, the normalized gain of equation (3) can be rewritten as:

$$g_{T(MC SSDA)} = \frac{1}{[1 + A_2 x^2 + A_4 x^4][(1-x_c^2)^{n-1}]} \quad (4)$$

Where

$$A_2 = \alpha_1^2 - 8$$

$$A_4 = 16$$

The denominator of equation (4) is written like $D = 1 + Q_n(x^2)$, an approximation by a polynomial of degree 4 which is the most appropriate.

To achieve the Chebyshev polynomial approximation, first the denominator of $g_{T(MC SSDA)}$ is written under the form of

$$D = (1 - \varepsilon_1^2) \left[1 + \varepsilon^2 \left(1 + \frac{Q_n(x^2)}{\varepsilon_1^2} \right) \right] \quad (5)$$

Where $\varepsilon = \sqrt{\frac{\varepsilon_1^2}{1 - \varepsilon_1^2}}$ represents the ripple ratio, and then the approximation is carried out by using Chebyshev polynomial $T_n(x)$ of the terms between brackets of the denominator D in the following manner:

$$1 + \varepsilon^2 \left(1 + \frac{Q_n(x^2)}{\varepsilon_1^2} \right) = 1 + \varepsilon^2 T_n^2(x) \quad (6)$$

The adopted form of equation (6) resulted from the fact that the frequency response of the MCSSDA amplifier is a low pass type.

Consequently

$$T_n^2(x) = 1 + \frac{Q_n(x^2)}{\varepsilon_1^2} \quad (7)$$

Since $Q_n(x^2)$ is of degree 4, $T_n(x)$ must be of degree 2 and $T_n^2(x)$ of degree 4:

The approximation of (7) by the Chebyshev polynomial [3] result in the following:

In [4], the approximation by the Chebyshev polynomial was tested efficiently, and as the MCSSDA has the same input as [4], the calculations was made in the same manner, and resulted in the following:

$$\alpha_1 = 2.38 \text{ and } \varepsilon^2 = 0.37 \quad (8)$$

With the values of (8) and by taking $Z_0 = 50\Omega$, the design parameters as a function of the gate capacitance C_{gs1} may be deduced as:

$$L_g = 1764C_{gs1} \quad (9)$$

The results given by equations (8) and (9) are general and thus they can be applied to any field effect transistor. So it is sufficient only to know the value C_{gs} , of the used transistor parameter, to proceed to the design of the amplifier.

3. DESIGN AND SIMULATION

To validate our method, we must naturally confront the results obtained with those given by the simulation software. Moreover, through this confrontation, we must highlight the improvement of the gain that the MCSSDA offers compared to the CSSDA. To accomplish this, the two amplifiers CSSDA and MCSSDA will be designed using a MESFET transistor having $C_{gs}=0.17pF$, $C_{ds} = 0.006pF$ and $g_m = 0.32mS$ as parameters.

Concerning the CSSDA, in order to have characteristic impedance of the drain and gate lines $Z_0 = Z_{0int} = 50\Omega$, a shunt capacitance must be added to the drain capacitances of each transistor such that $C = C_{gs} - C_{ds} = 0.164pF$. The inductances to be added are calculated using the formula $Z_0 = \sqrt{L/C_{gs}}$ so we find $L = 425pH$. For the MCSSDA, the inter-stage lines have an impedance of 50Ω , so the capacities and the inductances to be added have the same values as those of the CSSDA.

It is only the input that must be approximated by the Chebyshev polynomial. After calculation, we find inductors $L_g = 300pH$.

The characteristic impedances, of the CSSDA artificial lines and the MCSSDA inter-stage lines, are frequency-dependent.

The gains simulation results of the two amplifiers CSSDA and MCSSDA are represented by the fig. 5. This figure shows that the MCSSDA offers an improvement of 6 dB in the gain value compared to that of the CSSDA for the same bandwidth.

In addition to the advantage of having an increase of 6 dB in gain, we also have the advantage of maintaining a wide bandwidth despite the mismatch of the input line. The latter advantage comes from the idea of imposing, by a suitable polynomial approximation (Chebyshev) to the gain $G_T(MCSSDA)$, a flat response until the cut-off frequency of the input and output lines.

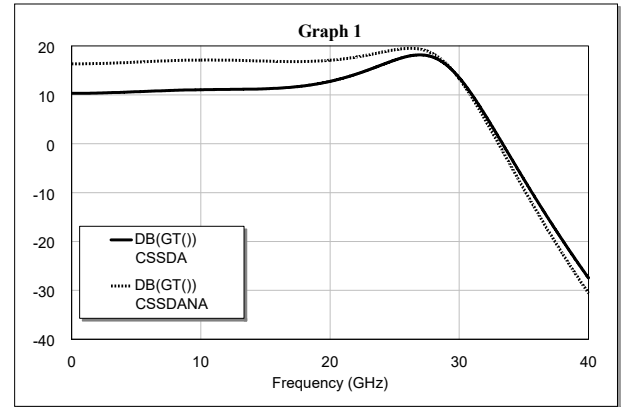


Fig. 5: The gain of four stage CSSDA and MCSSDA amplifiers.

4. CONCLUSION

The advantage of the proposed amplifier is the gain improvement of 6 dB compared to that of the CSSDA amplifier using the field effect transistor. Although the input line is mismatched, the bandwidth of the MCSSDA remains equal to that of the CSSDA whose lines are adapted. In addition, the MCSSDA uses less input components, one resistor and one inductor are eliminated. In addition, the gain of the proposed amplifier can be controlled by the inter-stage lines impedance.

REFERENCES

- [1] Liang. J. Y. and C. S. Aitchison, "Gain Performance of Cascaded Single Stage Distributed Amplifier" *Electronics Letters*, Vol. 31, No. 15, July 1995, pp.1260-1261.
- [2] Thomas T. Y. Wong "Fundamentals of distributed amplification" *Illinois Institute of Technology, Artech house*, 1993.
- [3] Jia-Sheng Hong, M. J. Lancaster "Microstrip Filters for RF/Microwave Applications" *John Wiley & Sons, Inc*, 2001.

- [4] F. Amrani, M. Trabelsi, R. Aksas and M. Azrar
"Bandwidth Improvement of a Single-stage
Distributed Amplifier" *Micro wave Journal*,
Vol.53, No. 5, May 2010. pp. 112-122.

Design and Control of Three-phase Vienna Rectifier with PFC for Electrolyzer

Fayçal BENYAMINA and Farid KHOUCHA

Ecole Militaire Polytechnique, Algiers, Algeria, benyaminafayal27@gmail.com,
fkhoucha04@yahoo.fr

ABSTRACT

Hydrogen production is an interesting alternative of storing energy were the electrolyzers are the essential part of these systems. Electrolyzers produce hydrogen by separating the molecule of water into oxygen (O₂) and hydrogen (H₂), the hydrogen will be used in fuel cells to produce electrical energy. Electrolyzers use rectifiers to convert the grid AC voltage into DC voltage for supplying the electrolyzer cells. Usually these rectifiers are based on diodes and/or thyristors that absorb a non-sinusoidal current, requiring the use of a filtering means to prevent power quality problems and ensure installation protection, which increases the overall cost of the system. Several ways of filtering have been proposed in the literature. This paper aims to use "Vienna rectifier" as an interface to connect electrolyzers to the AC grid, who is a non-regenerative converter that produces sinusoidal currents with low losses due to the reduced number of active switches. The dc voltage applied to the electrolyzer is regulated by using another DC-DC converter, which is selected to be a buck converter for simplicity and maximum efficiency. In this paper a mathematical model for an advanced alkaline electrolyzer has been developed, which is based on a combination of fundamental thermodynamics, heat transfer theory, and empirical electrochemical relationships. The operating principle of the rectifier is given to illustrate the method of power factor correction. Simulation results are given to show the validity of the proposed procedures.

Key Words: Alkaline electrolyzer, Fuel cell, Hydrogen production, Hydrogen storage, Vienna rectifier.

1. NOMENCLATURE

EL	Electrolyzer
FC	Fuel Cell
AC	Alternative Current
DC	Direct Current
THD	Taut Harmonic Distortion
PLL	Phase Looked Loop
PI	Proportional Integral

2. INTRODUCTION

Over the last decades, the depletion of fossil fuels and global climate change have driven the researchers and industrial to find other alternatives in order to produce electricity efficiently and cleanly[1]. There are various ways to produce renewable energy and store that in a remote location. Battery banks can be a solution of energy storage, but they have medium energy density, self-discharge and leakage characteristics [2]-[3]. They are also not suitable for long-term energy storage. Hydrogen has the property of high mass energy density which can be stored for long period without energy loss. This makes hydrogen suitable for energy storage. Moreover, hydrogen is best suited where the conventional fossil fuel is expensive [3]. Hydrogen is often referred to as the energy carrier of the future as it can be used to store intermittent renewable energy. Hydrogen can be produced from electrical power and water by using an electrolyzer who is a device that converts electricity into chemical energy to produces hydrogen through the process of electrolysis [4]. Fuel

cells can be used to return the energy to the grid or to an electric vehicle with no emissions, high efficiency and fast response. Fuel cells also have the capability to supply electricity for unlimited time as long as the required amount of hydrogen is present in the deposit. The electrolyzer requires the use of the rectifier in order to obtain a DC voltage at its terminals. Vienna rectifier has come to eliminate any problem of electromagnetic interference emission (EMI) and it is one of the most popular topologies for three-phase power factor correction due to its good performance and relatively low costs [5]-[6].

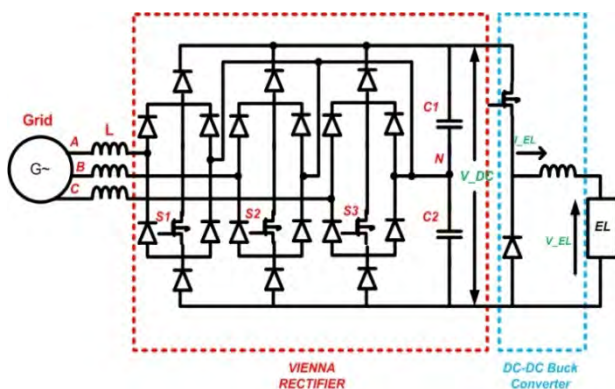


Figure.1: Overall representation of the proposed system.

This manuscript proposes using the Vienna rectifier as an interface to connect electrolyzers to the AC grid. Since the voltage applied to the electrolyzer is smaller than the DC-bus voltage, a DC-DC buck converter is required between the DC-bus and the electrolyzer to regulate the power transmitted to the electrolyzer. This work begins by giving a global modelling of alkaline electrolyzers based on the different laws of thermodynamics, and then Figure. 1 illustrates the proposed electrolysis system based on the Vienna rectifier which absorbs sinusoidal phase currents in phase with the voltage i.e. (unit power factor). Simulation results are given to show the validity of the designed model and the proposed procedures.

3. ALKALINE ELECTROLYZER

The process of electrolysis of water was first performed on May 2, 1800 by two British chemists. It breaks down a molecule of water into a molecule of hydrogen and

half a molecule of oxygen. By using electrical and thermal energy in order to satisfy the energetic demand of the reaction and to guarantee its continuation [7]. A DC current is required to split the water molecule into hydrogen and oxygen. This current should flow between two electrodes (Anode and Cathode) separated by the electrolyte [3]-[8].

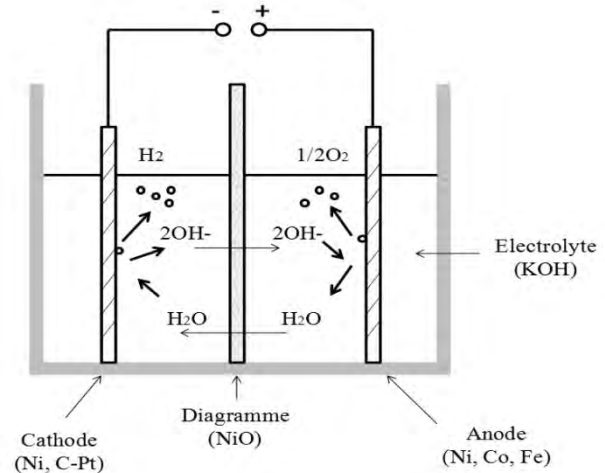
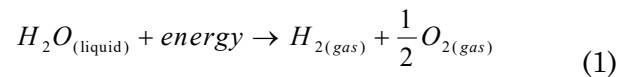


Figure.2: Internal structure of an alkaline electrolyzer.

The general reaction of electrolysis is defined by:



3.1. Technology

The electrolyte used in the conventional alkaline water electrolyzers has traditionally been aqueous potassium hydroxide (KOH). Commercial electrolyzers have several elementary cells, which can be placed in different ways (in series “bipolar” or in parallel “unipolar”) as long as the internal configuration of a cell is unchanged [8]-[7]. One advantage of the bipolar electrolyzer stacks is that they are more compact than unipolar systems. The advantage of the compactness of the bipolar cell design is that it gives shorter current paths in the electrical wires and electrodes. This reduces the losses due to internal Ohmic resistance of the electrolyte, and therefore increases the electrolyzer efficiency.

3.2. Electrochemical Model

The kinetic properties around the electrodes in an electrolyzer cell can be

modeled based on empirical data of different proposed I-V curves. The basic relationship between current and cell voltage in a given temperature is: [8]

$$V = E_{rev} + \frac{I}{A}r + s \log\left(\frac{I}{A}t + 1\right) \quad (2)$$

Where I is the current required for the electrolysis, A is the area of electrodes, r is the parameter related to Ohmic resistance of the electrolyte, s and t are the over voltage coefficients on electrodes and E_{rev} is the reversible voltage.

The total change in enthalpy for splitting water is the enthalpy difference between the products (H_2 and O_2) and the reactants (H_2O). The same applies for the total change in entropy.

$$\begin{cases} \Delta H = \Delta H_{H_2} + 0.5\Delta H_{O_2} - \Delta H_{H_2O} \\ \Delta S = \Delta S_{H_2} + 0.5\Delta S_{O_2} - \Delta S_{H_2O} \end{cases} \quad (3)$$

The changes in enthalpy and entropy induce changes in Gibb's energy and consequently in the E_{rev} . The change in Gibbs energy is expressed by:

$$\Delta G = \Delta H - T \Delta S \quad (4)$$

At standard conditions (25°C and 1 bar) the splitting of water is a non-spontaneous reaction, which means that the change in Gibbs energy is positive. The standard Gibbs energy for water splitting is $\Delta G^\circ = 237 \text{ kJ.mol}^{-1}$. For an electrochemical process operating at constant pressure and temperature the maximum possible useful work (i.e., the reversible work) is equal to the change in Gibbs energy ΔG . Faraday's law relates the electrical energy (emf) needed to split water to the chemical conversion rate in molar quantities. The emf for a reversible electrochemical process, or the reversible cell voltage, is expressed by: [8]

$$E_{rev} = \frac{\Delta G}{zF} \quad (5)$$

Where z is the number of electrons transferred in each reaction, here it is 2, and F is the Faraday constant ($F = 96485 \text{ C.mol}^{-1}$). Reversible voltage is the minimum voltage required for starting the water electrolysis.

In this study the value of reversible voltage is 1.228V per cell [5].

In order to relate the Ohmic resistance parameter r and over voltage coefficient t, the equation (2) can be modified in more detailed way as: [9]

$$V = E_{rev} + \frac{r_1 + r_2 T}{A} I + s \log\left(\frac{t_1 + t_2 / T + t_3 / T^2}{A} I + 1\right) \quad (6)$$

Where T is the electrolyte temperature.

3.3. Hydrogen Production

The Faraday efficiency is defined as the ratio between the actual and theoretical maximum amount of hydrogen produced in the electrolyzer. It will be shown later that one of the parameters that control the hydrogen production is current, so another name of Faraday efficiency is current efficiency. It can be noted that parasitic current increases with the decrement of current density and the increment of temperature resulting the reduction of Faraday efficiency [8]-[6]-[5]. This phenomenon can be expressed as:

$$\eta_F = \frac{\left(\frac{I}{A}\right)^2}{f_1 + \left(\frac{I}{A}\right)^2} * f_2 \quad (7)$$

Where f_1 and f_2 are the parameters related to Faraday efficiency.

According to Faraday's law, the production rate of hydrogen in an electrolyzer cell is directly proportional to the transfer rate of electrons at the electrodes, which in turn is equivalent to the electrical current in the external circuit [9]. Hence, the total hydrogen production rate in an electrolyzer, which consists of several cells connected in series, can be expressed as:

$$n_{H_2} = \eta_F \frac{n_c I}{zF} \quad (8)$$

Where n_c is the number of electrolyzer cells per stack.

The total amount of energy needed in water electrolysis is equivalent to the change in enthalpy ΔH . The standard enthalpy for splitting water is $\Delta H^\circ = 286 \text{ kJ.mol}^{-1}$. The total energy demand ΔH is related to the thermoneutral cell voltage by the expression:

$$V_{in} = \frac{\Delta H}{zF} \quad (9)$$

The energy efficiency can be calculated from the thermoneutral voltage and the cell voltage by the expression:

$$\eta_e = \frac{V_{in}}{V} \quad (10)$$

3.4. Simulation Results

The parameters used in this simulation are taken from [9]. Using equation (6), we can trace the current-voltage characteristic of an electrolysis cell shown in Figure. 3, which shows that, when the temperature increases, the electrical energy necessary to provide the starting point for the reaction of electrolysis is less.

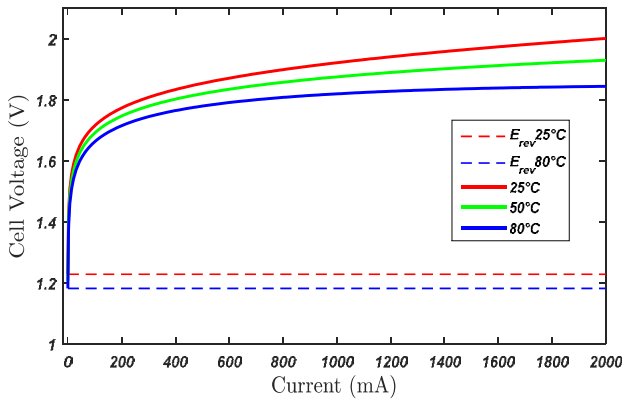


Figure.3: Typical (I-V) curves for an electrolyzer cell at high and low temperatures.

Equation (8) is plotted in Figure. 4, where proportionality is observed between the production of hydrogen and the current flowing through the electrolysis cell.

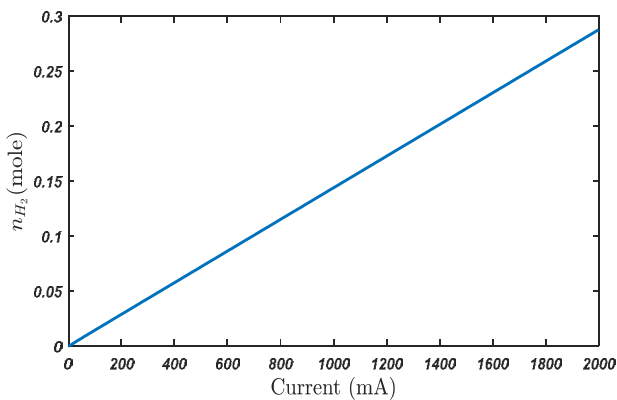


Figure.4: Hydrogen production.

To show that this production depends on Faraday efficiency, Fig. 5 shows that the Faraday efficiency is not equal to the unit,

i.e. the existence of other chemical reactions parasitic with the electrolysis of water.

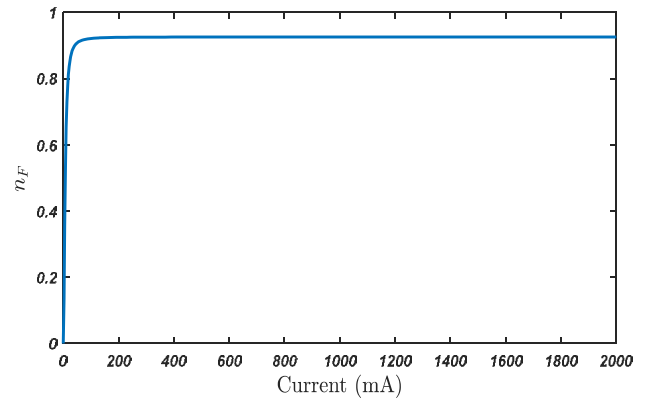


Figure.5: Faraday efficiency.

4. VIENNA RECTIFIER

Rectifiers are needed in electrolyzer systems to transform the grid AC voltage to DC voltage. The output voltage of the fuel cell array varies significantly with the hydrogen supply rate and the pressure. Therefore, a DC-DC converter is also required to control the electrolyzer system[6].

The Vienna Rectifier is an advantageous unidirectional PFC (power factor correction) rectifier with less number of active power switches, sinusoidal input current, and balanced output DC-link voltage, low voltage stress across switches, high switching operation and high efficiency[10]. It consists of 3-switches and 18-diodes with DC-link capacitor at the output. The current flow in the circuit depends on the switching pattern. As shown in Figure. 6a and 6b. For $S_1=0$ (Switch-OFF) current flows through the diodes from phase to neutral when I_A is positive and current flows through the diodes from neutral to phase when I_A is negative. Similarly, for $S_1=1$ (switch-ON) current flows through the switch S_1 from phase to neutral when I_A is positive and current flows the switch S_1 from neutral to phase when I_A is negative as shown in Figure. 6c and 6d. In this way, circuit operation can be expressed for switch S_2 and S_3 i.e. for all three phase voltage and current equations[10]-[11]-[12].

V_{AN} , V_{BN} and V_{CN} are the terminal voltages which can be written as the function of current and state of the switch.

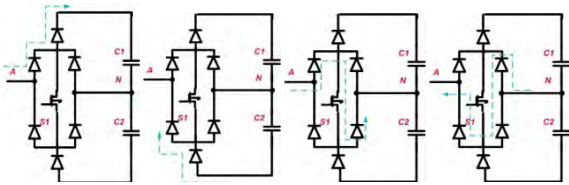


Figure.6: Current Circuit for $S_i=0$ (a & b) and $S_i=1$ (c & d).

$$V_{KN} = \frac{V_{DC}}{2} \text{sgn}(i_K)(1 - S) \quad (11)$$

Where K is A,B and C, 'sgn' is the signum function of $i_{A,B,C}$.

The power factor correction (PFC) control is to force the phase current in the inductances to follow a sinusoidal reference. The current will then be in the form of sawtooth with a sinusoidal carrier. However this form is obtained under a condition on the DC bus expressed in the following equation:[11]

$$3(V_{C,max})_{[0,\pi/3]} p V_{DC} p - 6(V_{B,min})_{[0,\pi/3]} \Leftrightarrow 2.12V_{LL} p V_{DC} p 4.24V_{LL} \quad (12)$$

Where V_{LL} is the effective voltage between phases.

5. CONTROL OF THE ASSOCIATED POWER ELECTRONICS

The proposed system and its control process are given in Figure. 7.

As already described above, the main objective of such system is to produce a precise amount of hydrogen while absorbing a sinusoidal current in phase with the voltage, i.e. (unit power factor).For this, the voltage of the DC bus is regulated by using a PI regulator which provides reference amplitude of the current which will be multiplied by a sinusoidal reference which plays the role of a PLL.

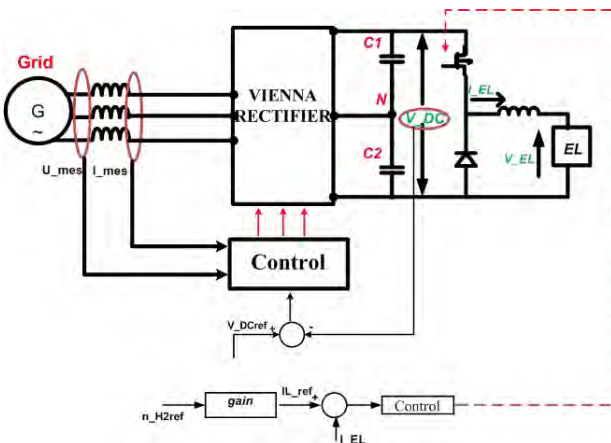


Figure.7: Proposed system.

The products will be compared with the three phase currents to get to a switching table by disrupting the sign of the currents.

The production of hydrogen is controlled by a step-down DC-DC converter, the quantity of hydrogen desired as reference will be multiplied by a factor (equation (8)) in order to obtain a reference current which will be imposed in the inductor by using a hysteresis corrector.

6. SIMULATION RESULTS

Simulations were conducted in order to verify the performance of the system shown in Figure. 7 along with its control strategy. In this simulation the goal is to impose two hydrogen reference values and to see the behaviour of the system with respect to this variation. In the first stage the production is two moles until the moment 0.6 second where it becomes 3 moles, as shown in Figure. 8. The result shows the performance of the hydrogen production operative mode when the hydrogen production reference signal is changed from 2 to 3 moles. As seen in Figure.8 the controller tracks hydrogen production reference signal in a fast and stable manner.

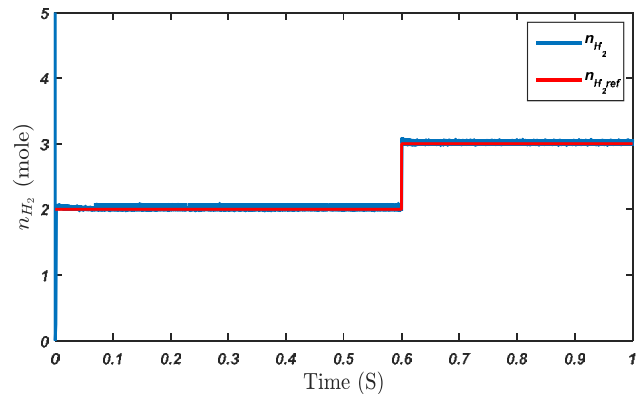


Figure.8: Controlled hydrogen production.

Figure. 9 shows the current flowing in the electrolyzer or it has the same pace as the production of hydrogen, which proves the perfect proportionality between the two parameters.

In Figure. 10 the three phase currents are traced, or they are sinusoidal which validates the control technique designed.

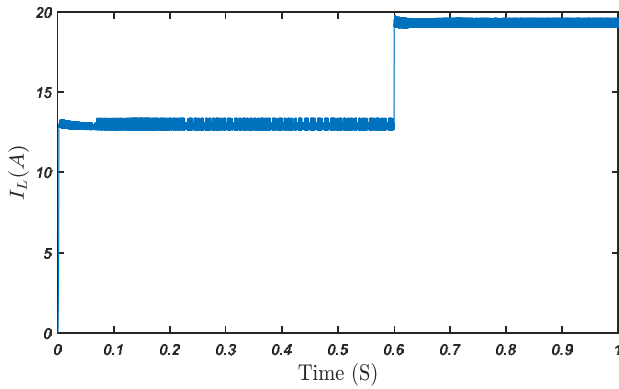


Figure.9: Current flowing in the electrolyzer.

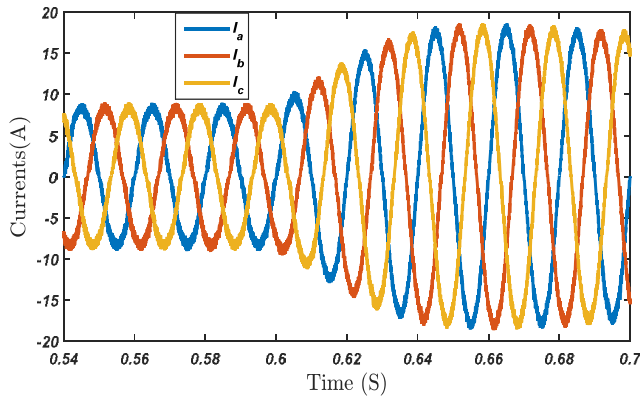


Figure.10: Three phase currents.

Figure. 11 shows the phase A current and voltage waveform when a step change from 2 to 3 moles in the hydrogen production reference signal is applied, the current waveform changes accordingly while remaining in phase with the ac voltage (unity power factor).

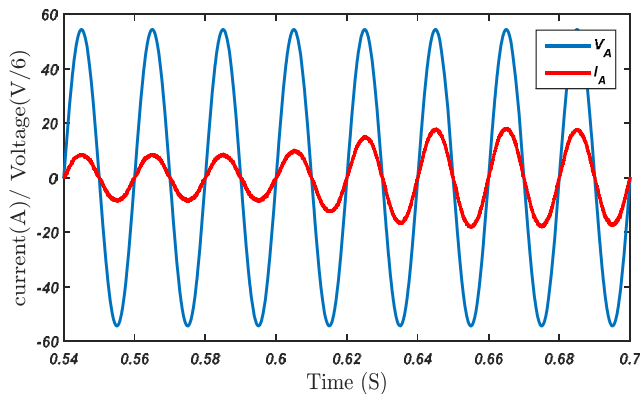


Figure.11: Phase A, voltage and current.

7. CONCLUSION

In this paper, the proposed system is an electrolyzer using Vienna rectifier controlled in “power factor control”. Vienna rectifier circuit minimizes the switching power losses and cost of the conversion unit. It also reduces the THD, input current shaping to sinusoidal, maintains the power factor approximately unity. A mathematical model for an advanced alkaline electrolyzer has been developed based on a combination fundamental thermodynamics. Simulation results corroborate the proper functioning of the proposed new application using the Vienna rectifier for the electrolyzer system.

REFERENCES

- [1] Guilbert, D., S.M. Collura, and A. Scipioni, DC/DC converter topologies for electrolyzers: State-of-the-art and remaining key issues. *International Journal of Hydrogen Energy*, 2017. 42(38): p. 23966-23985.
- [2] Monroy-Morales, J.L., et al. Modeling and control design of a Vienna rectifier based electrolyzer. in 2016 IEEE 7th International Symposium on Power Electronics for Distributed Generation Systems (PEDG).
- [3] Maruf-ul-Karim, M. and M.T. Iqbal. Dynamic modeling and simulation of alkaline type electrolyzers. in *Electrical and Computer Engineering, 2009. CCECE'09. Canadian Conference on. 2009. IEEE.*
- [4] Takahashi, R., et al., Output power smoothing and hydrogen production by using variable speed wind generators. *IEEE Transactions on Industrial Electronics*, 2010. 57(2): p. 485-493.
- [5] Jiang, X., et al. A survey of cascaded multi-level PWM rectifier with VIENNA modules for HVDC system. in *Power Electronics and Application Conference and Exposition (PEAC), 2014 International. 2014. IEEE.*
- [6] Bhumika, S. and J. Shri Harsha, three phase vienna rectifier for wind power generation system. *International Journal of Research in Engineering and Technology*, 2014. 3(3): p. 395-398.
- [7] M. Hammoudi, C. Henao, K. Agbossou, Y. Dubé, M. L. Dombia , New multi-physics approach for modelling and design of alkaline electrolyzers, 2 *International Journal of Hydrogen Energy*, 2012. 37(19): p. 13895-13913.
- [8] Ulleberg, Ø., Modeling of advanced alkaline electrolyzers: a system simulation approach.

- International Journal of Hydrogen Energy, 2003. 28(1): p. 21-33.
- [9] C. Darras, G. Bastien, M. Muselli, P. Poggi, P. Serre-Combe. Techno-economic analysis of PV/H₂ systems. International Journal of Hydrogen Energy, 2015. 40(30): p. 9049-9060.
- [10] D. Reddy, S. Ramasamy, Design of a Three-phase Boost Type Vienna Rectifier for 1kW Wind Energy Conversion System. International Journal of Renewable Energy Research (IJRER), 2017. 7(4): p. 1909-1918.
- [11] Xing Li ; Yao Sun ; Hui Wang ; Mei Su ; Shoudao Huang , A Hybrid Control Scheme for Three-Phase Vienna Rectifiers, IEEE Transactions on Power Electronics, 2018. 33(1): p. 629-640.
- [12] Kanaan, H., Modeling and control design of a Vienna rectifier based electrolyzer, 2016 IEEE 7th International Symposium on Power Electronics for Distributed Generation Systems (PEDG), (DOI: 10.1109/PEDG.2016.7527093).

A novel switched series/parallel inverter with asymmetrical sources configuration

M. S. Benmerabet, A. Talha, and E. M. Berkouk,

Abstract—Switches Series/parallel Sources (SSPS) inverter is a multilevel inverter that was presented in 2009. It was used with a symmetrical sources configuration. It can place the voltage sources in either series or parallel thanks to its unique topology.

In this paper, our aim is to increase the number of levels by reducing the redundancies and to reduce the conduction losses thanks to the existing of parallel paths in the SSPS topology. Therefore, a new modified version of the SSPS inverter is presented compatible with asymmetrical sources configuration. An analysis based on simulations and experimental results of a single phase 31-level inverter are presented.

Index Terms—Asymmetrical source configuration, Multilevel inverters, Switched capacitor, Switched series/parallel inverter.

I. INTRODUCTION

MULTILEVEL inverters are the center of interest of many researchers and industries for the higher output quality in comparison with the conventional PWM inverter that generate high harmonic distortion, especially for the medium and high voltage applications. This interest focuses very often on reducing the overall switching device count, control simplicity and the usage flexibility of the different topologies [1].

As such, Hinago and Koizumi proposed in their 2009 paper a new multilevel inverter topology, based on two parts: a DC/DC converter that allows the rearrangement of the different voltage sources into series or parallel, and a DC/AC converter that generates the full waveform [2]. The new topology called Switched Series/Parallel Sources (SSPS) required the same number of voltage sources as the cascaded H-bridges inverter (CHB). However, it requires a reduced number of power switches and grants greater flexibility for the suggested application, which was for electrical vehicles [1]. However, many multilevel inverter topologies present redundancies, as shown in [3]; using asymmetrical source configurations can reduce the redundancies allowing the inverter to reach a higher number of voltage levels without increasing the number of switches. Even though the proposed topology in [2] can use

First M. S. Benmerabet and A. Talha are with the Laboratory of Instrumentation, USTHB, P.O.Box. 32, Bab-Ezzouar, Algiers, Phone: 213-24217912 (Ext. 804), Fax: 213-21207664, URL: <http://www.lins.usthb.dz>, Email: s.benmerabet@hotmail.com. Second Author is also with the Laboratory of Instrumentation, USTHB, P.O.Box.32, Bab-Ezzouar, Algiers. E. M. Berkouk is with the Laboratory of control and process, ENP, El Harach, Algiers.

ISBN: 978 9931 9548 04/\$00.0 © 2018

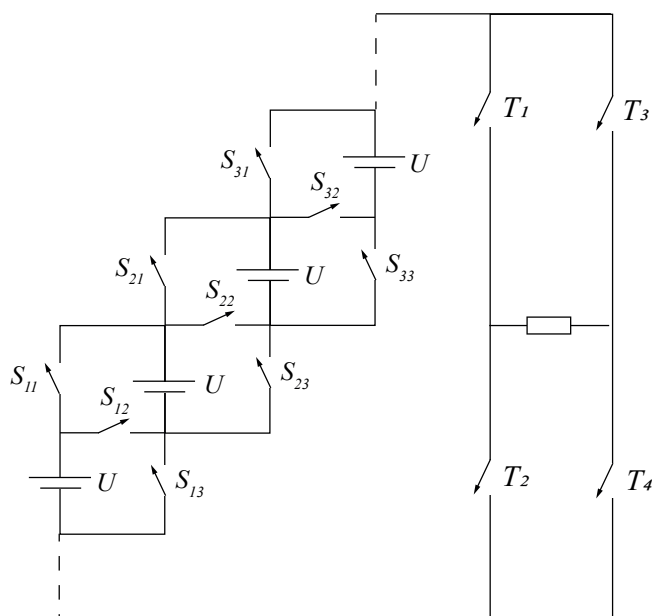


Fig. 1. SSPS topology as presented in [2].

asymmetric power supplies, it was not studied or mentioned in the literature.

When using asymmetrical sources configuration, parallel state in the SSPS inverter become impractical. However, the availability of parallel paths might reduce the conduction losses. In this paper, we propose a modified SSPS inverter, with asymmetric power supplies, and verify its feasibility.

In section II, the proposed topology is described and the modifications for the asymmetrical configuration are introduced. In section III, a case study is presented to prove the induced improvement. In section IV, a comparison with other known topologies is presented. Simulation and experimental results are presented in section IV.

II. DESCRIPTION OF THE PROPOSED TOPOLOGIES

The original SSPS converter is presented in Fig 1. This converter is made of two parts, a number of DC/DC basic units, and a DC/AC converter (H-bridge). The DC/DC basic unit is the level generating part, while the H-bridge allows the voltage inversion and the zero generation part.

A. Basic unit

Fig 2(a) shows the SSPS basic unit. Two states were used in [2], either parallel or series. If S_{x1} and S_{x3} are closed

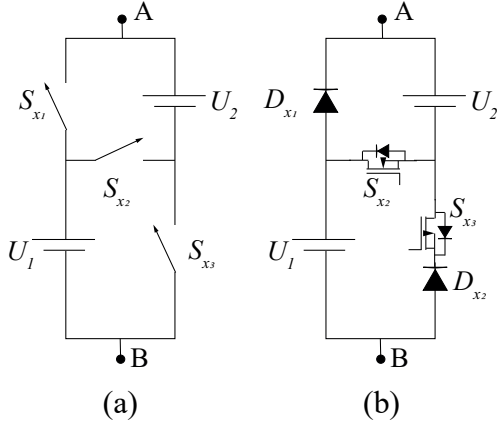


Fig. 2. (a) Ideal basic unit (b) Unidirectional asymmetrical basic unit with U_2 larger than U_1 .

TABLE I
VOLTAGE STRESS ON EACH SWITCH IN THE DIFFERENT STEPS

U_{AB}	$U_{S_{x1}}$	$U_{S_{x2}}$	$U_{S_{x3}}$
U_1	0	$2U_1$	$-U_1$
U_2	U_1	U_1	0
$U_1 + U_2$	$2U_1$	0	U_1

U_1 and U_2 are placed in parallel. if S_{x2} is the one closed they will be in series. The drawback is when U_1 and U_2 have different voltages, where a short circuit could occur. To use this inverter with different sources with different voltages. S_{x1} and S_{x3} should never be closed in the same time. Fig 2(b) shows the proposed basic unit for asymmetrical source configuration, with U_1 voltage being smaller than U_2 . Where the output voltage can be calculated using the following expression :

$$U_{AB} = \neg S_{x2} \neg S_{x3} U_1 + S_{x2} \neg S_{x3} (U_1 + U_2) + \neg S_{x2} S_{x3} U_2 \quad (1)$$

B. Proposed modification over SSPS

Hinago and Koizumi presented a cascaded basic units, while a nested basic units arrangement is proposed in this paper. This modification is proposed to take advantage of the parallel path in the basic units. Thus, the number of switches the current needs to go through to reach the H-bridge is reduced. However, it will increase the voltage stress on those switches, but might reduce the losses related to the involved switches.

Fig 3 shows the nested SSPS general schematic. Fig 4 shows a 31-level single phase inverter proposition. This topology uses binary asymmetrical configuration, where each source voltage magnitude is twice the one below, and thus the voltage magnitude of the different sources is:

$$U_j = (2^{j-1})U_1. \quad (2)$$

With j being the number of the voltage source and is always larger than the number of basic units by one. The inverter output voltage is equal to :

$$U_{inv} = (T_1 T_4 - T_2 T_3) U_{DC} \quad (3)$$

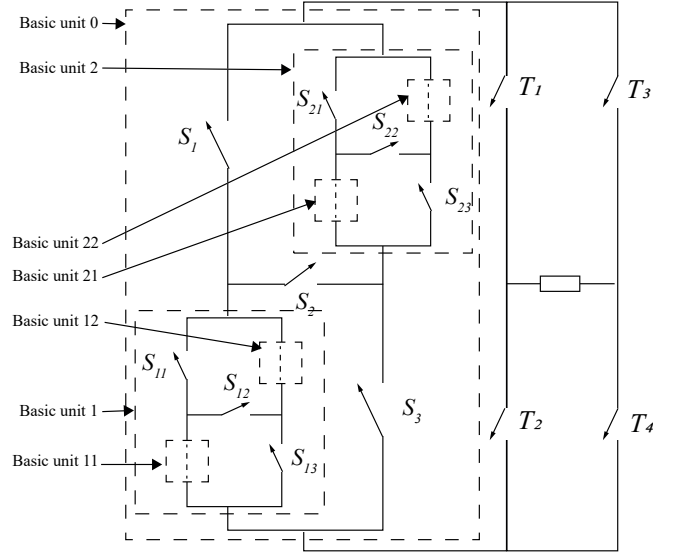


Fig. 3. New arrangement proposition of basic units.

TABLE II
CALCULATION OF THE DIFFERENT PARAMETERS OF THE TWO PROPOSED TOPOLOGY COMPARED WITH THE SYMMETRICAL ONE

	Symmetrical	asymmetrical
Number of steps	$2k + 3$	$2^{k+2} - 1$
Number of switches	$3k + 4$	$2k + 4$
Number of diodes	0	$2k$
Number of sources	$k + 1$	$k + 1$
Maximum voltage	$(k + 1)U_1$	$(2^{k+1} - 1)U_1$
Number of variety	1	k

Using equation 1, the mathematical model can be deduced as follow:

$$U_{DC} = \neg S_2 \neg S_3 U_{BU1} + S_2 \neg S_3 (U_{BU1} + U_{BU2}) + \neg S_2 S_3 U_{BU2} \quad (4)$$

$$U_{BU1} = \neg S_{12} \neg S_{13} U_1 + S_{12} \neg S_{13} (U_1 + U_2) + \neg S_{12} S_{13} U_2 \quad (5)$$

$$U_{BU2} = \neg S_{22} \neg S_{23} U_3 + S_{22} \neg S_{23} (U_3 + U_4) + \neg S_{22} S_{23} U_4 \quad (6)$$

Table II shows the different parameters of the proposed topology in comparison with the original SSPS inverter, with k being the number of basic units.

The general switch states to generate the desired levels is shown in table. III. Note that S_{11}, S_1, S_{21} , are nonexistent in the proposed basic unit and are replaced with diodes, so they should be regarded as the state of the diodes D_{11}, D_1 and D_{21} respectively.

III. NEW ARRANGEMENT IMPROVEMENT

The nested basic unit SSPS inverter is very flexible and the same number of basic units leads to many possible configurations with different possible truth tables. Thus, a case

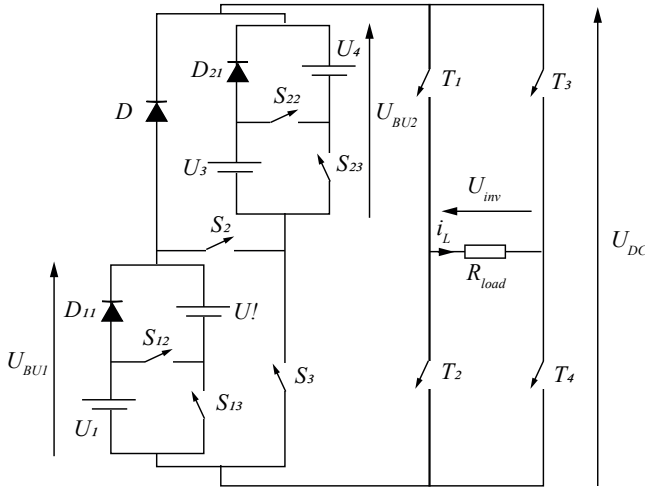


Fig. 4. proposed 31-level inverter topology.

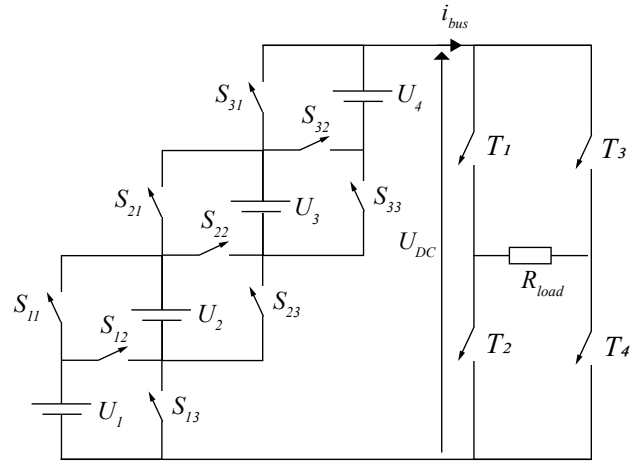
TABLE III
SWITCH STATES FOR THE GENERATION OF DESIRED LEVELS FOR THE TWO PROPOSED TOPOLOGIES

$U_{DC}(U_1)$	On-state switches
1	S_{11}, S_1
2	S_{13}, S_1
3	S_{12}, S_1
4	S_3, S_{21}
5	S_{11}, S_2, S_{21}
6	S_{13}, S_2, S_{21}
7	S_{12}, S_2, S_{21}
8	S_3, S_{23}
9	S_{11}, S_2, S_{23}
10	S_{13}, S_2, S_{23}
11	S_{12}, S_2, S_{23}
12	S_3, S_{22}
13	S_{11}, S_2, S_{22}
14	S_{13}, S_2, S_{22}
15	S_{12}, S_2, S_{22}

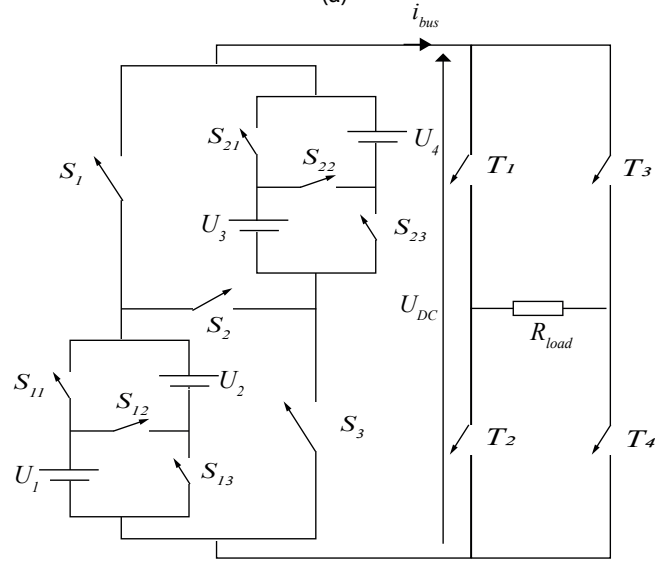
study was chosen to ascertain the reduction in the number of power electronic components in the current path. Table IV shows the truth table of the proposed and the original SSPS topologies with 3 basic unit each(see fig 5). the total number of on-switches is shown in the rightmost column of the table. This result is also illustrated in fig 6. With the number of power electronic components in the current path have been reduced, the conduction losses are expected to be reduced as well.

IV. COMPARISON OF THE PROPOSED TOPOLOGIES WITH OTHERS

The proposed configuration is first compared with the original symmetrical SSPS topology, then with the switched capacitor [4] and other widely used multilevel inverters, such as Cascaded H-Bridges (CHB) [5], Neutral Point Clamped multilevel inverter (NPC) [6], and flying capacitor inverter (FC) [7]. Table. V shows the number of levels obtained for ISBN: 978 9931 9548 04/\$00.0 © 2018



(a)



(b)

Fig. 5. Compared topologies (a) Original disposition (b) Proposed disposition.

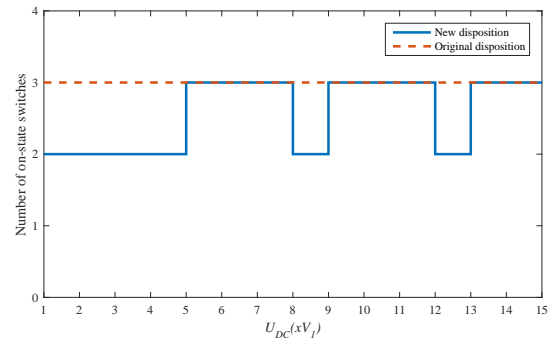


Fig. 6. Number of on-switches in DC/DC side for each voltage step.

each inverter type using nearly similar numbers of switches. It is evident that the proposed topology and configuration is advantageous.

The proposed inverter has an asymmetrical configuration. To make the comparison fairer, similar recently proposed

TABLE IV
COMPARISON OF THE TRUTH TABLE OF THE TWO TOPOLOGIES

Original topology arrangement										
$U_{DC}(U_1)$	S_{32}	S_{33}	S_{31}	S_{22}	S_{23}	S_{21}	S_{12}	S_{13}	S_{11}	Total on-switches
1	0	0	1	0	0	1	0	0	1	3
2	0	0	1	0	0	1	0	1	0	3
3	0	0	1	0	0	1	1	0	0	3
4	0	0	1	0	1	0	0	1	0	3
5	0	0	1	1	0	0	0	0	1	3
6	0	0	1	1	0	0	0	1	0	3
7	0	0	1	1	0	0	1	0	0	3
8	0	1	0	0	1	0	0	1	0	3
9	1	0	0	0	0	1	0	0	1	3
10	1	0	0	0	0	1	0	1	0	3
11	1	0	0	0	0	1	1	0	0	3
12	1	0	0	0	1	0	0	1	0	3
13	1	0	0	1	0	0	0	0	1	3
14	1	0	0	1	0	0	0	1	0	3
15	1	0	0	1	0	0	1	0	0	3
Total on/off	1	2	1	3	6	3	7	14	7	

New topology arrangement										
	S_{32}	S_{33}	S_{31}	S_{22}	S_{23}	S_{21}	S_{12}	S_{13}	S_{11}	Total on-switches
1	0	0	0	0	0	1	0	0	1	2
2	0	0	0	0	0	1	0	1	0	2
3	0	0	0	0	0	1	1	0	0	2
4	0	0	1	0	1	0	0	0	0	2
5	0	0	1	1	0	0	0	0	1	3
6	0	0	1	1	0	0	0	1	0	3
7	0	0	1	1	0	0	1	0	0	3
8	0	1	0	0	1	0	0	0	0	2
9	0	1	0	1	0	0	0	0	1	3
10	0	1	0	1	0	0	0	1	0	3
11	0	1	0	1	0	0	1	0	0	3
12	1	0	0	0	1	0	0	0	0	2
13	1	0	0	1	0	0	0	0	1	3
14	1	0	0	1	0	0	0	1	0	3
15	1	0	0	1	0	0	1	0	0	3
Total on/off	1	2	2	5	6	1	7	8	7	

TABLE V
COMPARISON OF THE FIRST PROPOSED TOPOLOGY WITH SOME SYMMETRICAL INVERTERS

	# of switches	# of sources	# of diodes	# of capacitors	# of levels
proposed topology	10	4	6	0	31
SSPS	10	3	0	0	7
SPSC	10	1	0	2	7
CHB	12	3	0	0	7
NPC	12	1	10	6	7
FC	12	1	0	7	7

topologies are included; the proposed topology is compared with the two hybrid switched capacitor inverter (HSCI) presented in [8], the multilevel inverter with reduced number of power electronic components (MIRC) [9], and the cascaded multilevel inverter using binary units (CMIBU) [10].

Fig 7 shows the required number of MOSFETs or IGBTs to generate N steps; it is clear that the proposed configuration needs fewer switches than the others.

Fig 8 shows the required number of independent DC voltage sources. the proposed topology clearly require more sources. The required number of gate drivers was also calculated and compared; the proposed topology still requires fewer drivers than the others as shown in fig 9.

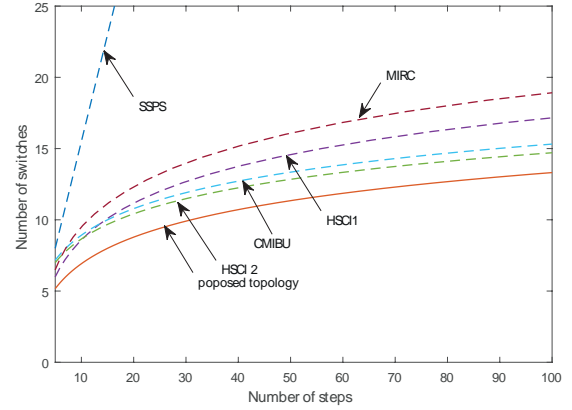


Fig. 7. Comparison of the required number of switches (MOSFETs or IGBTs) to generate N steps.

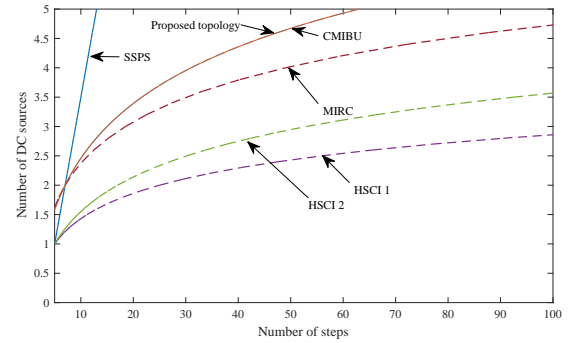


Fig. 8. Comparison of the required number of DC voltage sources to generate N steps.

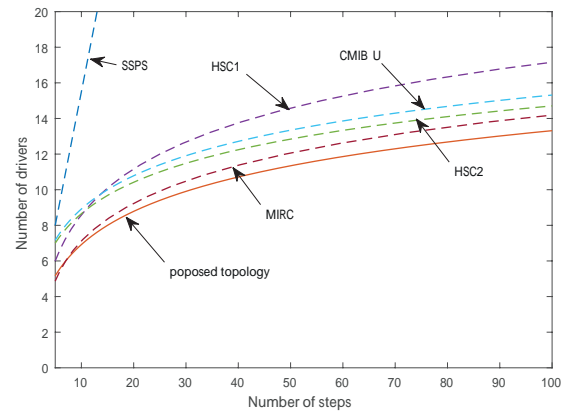


Fig. 9. Comparison of the required number of gate driving circuits to generate N steps.

V. SIMULATION AND EXPERIMENTAL RESULTS

A simulation was done to evaluate the performance of the proposed topology, using Matlab/simulink SimPowerSystem library for a single phase 31-level inverter(Fig 4).

Fig 10 shows the control command signals used and the output voltage of each basic unit. Those control signals were generated using table 3 and a staircase modulation of a

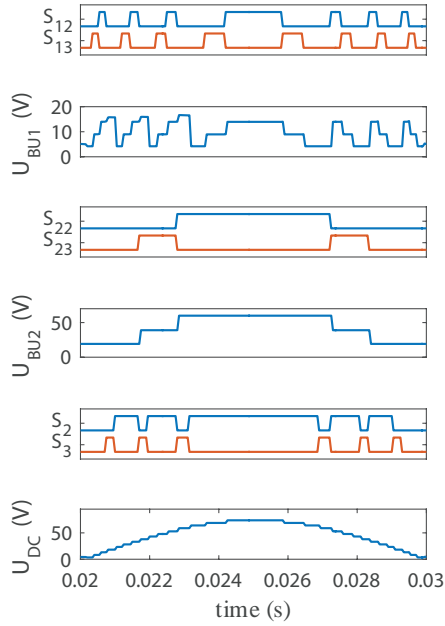


Fig. 10. Level generation command and output signals.

sinusoidal waveform with a frequency equal to 50Hz .

The proposition's results are shown for the applied control signals in fig 10. Where S_{12} and S_{13} are used to generate U_{BU1} . While U_1 and U_2 being respectively equal to 5V and 10V . S_{22} and S_{23} are used to generate U_{BU2} . While U_3 and U_4 being respectively equal to 20V and 40V . S_2 and S_3 are used for U_{DC} , using U_{BU1} and U_{BU2} as voltage sources.

U_{DC} shows an almost perfect positive half wave voltage signal, minus the zero-crossing that is generated using the H-bridge instead. The results also clearly shows that the commutation frequency for both propositions is not high, so using slow switches is possible, hence reducing the overall cost of the inverter.

Fig 11 shows the simulation full output voltage and current wave past the H-bridge with its transition waveform when changing the source voltage and when changing the load. From zero to 0.02s the source voltage rises gradually until it reach it final value. Because of the nonadaptive control used in our application the output voltage change proportionally with the change of the source voltage. Then, at 0.04s , the load impedance was changed, it can be seen that it doesn't disturb the inverter results greatly. Using the simulation, a Fast Fourier Transform (FFT) analysis was performed. Fig 12 shows the FFT spectra of the output voltages of the proposed topology. The proposed topology display low Total Harmonic Distortion (THD) levels: less than 2.99% without using pulse width modulation (PWM) control. Another interesting fact is that no harmonic order magnitude is higher than 1.2% of the fundamental frequency; meaning that a small and cheap filter might be enough to completely remove most harmonics. Experimental prototypes have also been implemented. A photograph of the experimental setup is shown in fig 13.

ISBN: 978 9931 9548 04/\$00.0 © 2018

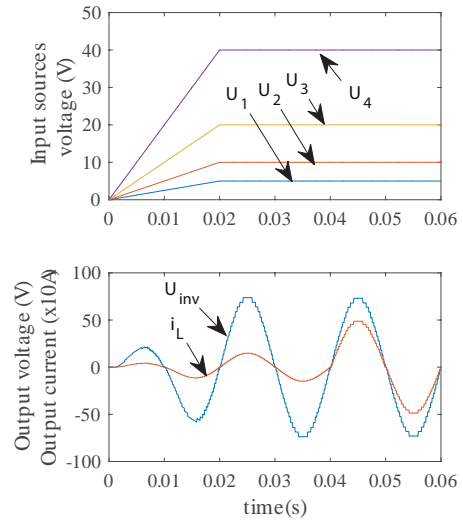


Fig. 11. transition waveform of the output current and voltage while changing the source voltage and changing the load

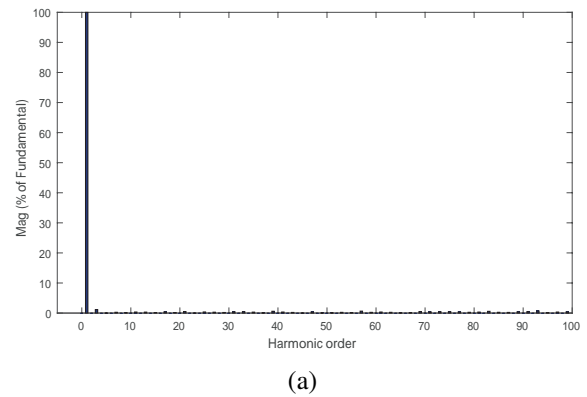


Fig. 12. FFT Spectra of the simulated output voltage of the proposed inverter.

An IRFP260N was used for N-Channel MOSFETs while IRFP9240 was used for the P-Channel MOSFETs. Both have an integrated reverse diode. The other used diodes are MBR40250G. The driving circuits used are TLP250 which have an integrated optocoupler.

To generate the command signals, a C2000 Delphino F28377S LaunchPad development kit by Texas Instruments was used. Note that the used diode and the microcontroller are not mandatory, as there is no need for a Schottky power diode for such a low-frequency switching application such as the one presented in this paper. The microcontroller characteristics are also higher than required. Those choices were made because of availability and for future perspectives.

The voltage magnitudes were 5 , 10 , 20 and 40V . The tests have been done on a resistive load of 100Ω .

The experimental results as captured by the oscilloscope are shown in fig 14 where the output voltage of the different basic units U_{BU1} , U_{BU2} and U_{DC} of the 31-level inverter can be seen. The final output waveform is shown in fig 15. The

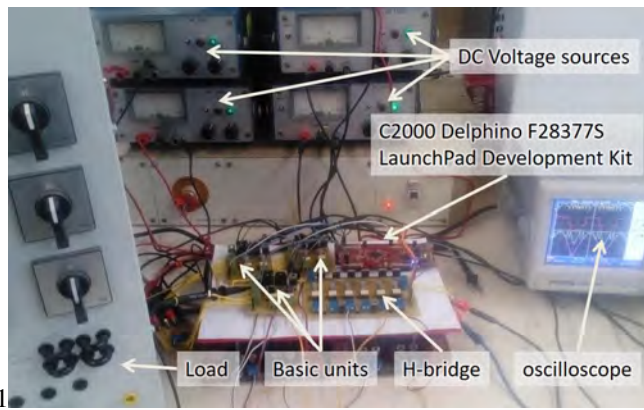


Fig. 13. A photograph of the experimental setup.

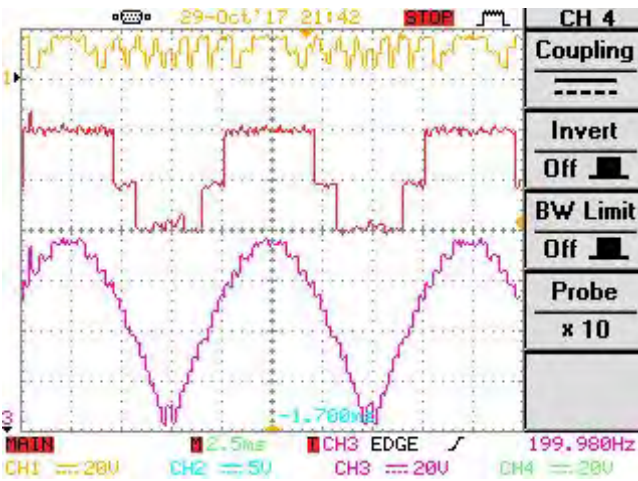


Fig. 14. Output voltages of the 31-level basic unit converters

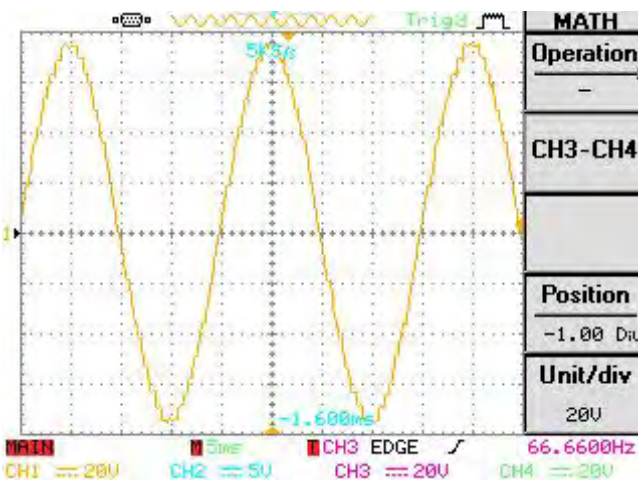


Fig. 15. Output voltages of the 31-level inverter

voltage caliber is set at 20V/div for all signals and the time caliber at 2.5ms/div in fig 14 and 5ms/div in fig 15. It is clear that the experimental results are similar to the simulation, so similar THD analysis results' are expected. Unfortunately, This setup cannot be used for inductive loads, because of the diode placed in the basic units. So using an

inductive load doesn't produce the desired results. Removing all the diodes and replacing them with switches is necessary to adapt the inverter to inductive loads.

VI. CONCLUSION

In this paper, A novel SSPS inverter with asymmetrical sources configuration is presented. The topology reduce the number of power electronic components in the current path as shown in section III. A comparison of three different parameters of the proposed topology with other recently proposed topologies was done and shows good results. The major drawback of the proposed topology is that it's only suitable for active power feeding since its a unidirectional inverter.

REFERENCES

- [1] K. K. Gupta, A. Ranjan, P. Bhatnagar, L. K. Sahu, and S. Jain, "Multilevel inverter topologies with reduced device count: A review," *IEEE Transactions on Power Electronics*, vol. 31, no. 1, pp. 135–151, 2016.
- [2] Y. Hinago and H. Koizumi, "A single-phase multilevel inverter using switched series/parallel dc voltage sources," *IEEE Transactions on Industrial Electronics*, vol. 57, no. 8, pp. 2643–2650, 2010.
- [3] C. Rech and J. R. Pinheiro, "Hybrid multilevel converters: Unified analysis and design considerations," *IEEE Transactions on Industrial Electronics*, vol. 54, no. 2, pp. 1092–1104, 2007.
- [4] Y. Hinago and H. Koizumi, "A switched-capacitor inverter using series/parallel conversion with inductive load," *IEEE Transactions on Industrial Electronics*, vol. 59, no. 2, pp. 878–887, 2012.
- [5] P. W. Hammond, "A new approach to enhance power quality for medium voltage drives," in *Petroleum and Chemical Industry Conference, 1995. Record of Conference Papers., Industry Applications Society 42nd Annual*, pp. 231–235. IEEE, 1995.
- [6] A. Nabae, I. Takahashi, and H. Akagi, "A new neutral-point-clamped pwm inverter," *IEEE Transactions on industry applications*, no. 5, pp. 518–523, 1981.
- [7] T. Meynard and H. Foch, "Multi-level conversion: high voltage choppers and voltage-source inverters," in *Power Electronics Specialists Conference, 1992. PESC'92 Record., 23rd Annual IEEE*, pp. 397–403. IEEE, 1992.
- [8] E. Babaei and S. S. Gowgani, "Hybrid multilevel inverter using switched capacitor units," *IEEE Transactions on Industrial Electronics*, vol. 61, no. 9, pp. 4614–4621, 2014.
- [9] J. Ebrahimi, E. Babaei, and G. B. Gharehpetian, "A new multilevel converter topology with reduced number of power electronic components," *IEEE Transactions on industrial electronics*, vol. 59, no. 2, pp. 655–667, 2012.
- [10] E. Babaei and S. H. Hosseini, "New cascaded multilevel inverter topology with minimum number of switches," *Energy Conversion and Management*, vol. 50, no. 11, pp. 2761–2767, 2009.

CSRR Array Structure for Ceramic Crack Detection

Haroune FEDDAL¹, Mohamed TELLACHE¹ and TAO Junwu²

¹USTHB, LINS Lab, Faculty of Electronics and Computers, PO.Box 32, Bab-Ezzouar, Algiers
hfeddal@usthb.dz, mtellache@usthb.dz

²University of Toulouse, Laboratory of Laplace tao@laplace.univ-tlse.fr

ABSTRACT

In this paper, a new array structure based on double complementary split ring resonator (CSRR) is proposed for crack detection in industrial ceramic (aluminum oxide). The performance of this sensor is explored using ANSYS HFSS simulator. The sensor is first tested when unloaded, then coupled to a flawless ceramic plate. The performance of the CSRR array is verified by varying the geometrical dimensions of the crack and also its position. The resonant frequency of the structure was found to be sensitive to small cracks of different lengths, depths and locations where width can reach 0.1mm. This implies that the designed sensor can detect cracks of different dimensions in any area of the ceramic material. The effectiveness of the sensor is being illustrated in this analysis. Simulated results show the feasibility of detecting cracks using the proposed design.

Key Words: Ceramic inspection, Crack detection, CSRR, Microwaves, Non-destructive test, radiation structure, Resonator.

I. INTRODUCTION

Recently, Microwaves have been broadly used in non-destructive inspection and material characterization in many fields; industry, medicine, aerospace, food industry...etc. They are essential for detecting anomalies and investigating physically the inaccessible objects without affecting those objects' ability to fulfill

their intended functions that might otherwise cause troubling events. The microwave Non-destructive testing technique uses several technologies to determine material properties or to indicate the presence of material discontinuities. The common ones can be summarized into two main categories with their own particular advantages, disadvantages and applications: the first category includes Rectangular waveguides, coaxial probes and horn antennas. The limitation of this technology is the higher frequency range ($\geq 80\text{GHz}$) required in order to get good sensitivity, which will make the system too expensive. While the second technology uses Microstrip structures like Split ring resonators, complementary split ring resonator, patch antenna...etc. due to its small structure, this model works in small frequency ranges. But in order to provide good results the quality factor of this technology must be enhanced.

A Typical example of a material that is receiving extensive attention in recent years and which requires very sensitive nondestructive testing techniques is ceramic. For instance, ceramic is used more and more to make part of internal combustion or gas turbine engine regarding its excellent properties. Yet its poor resistance to crack propagation and lack of stress accommodation due to the absence of plastic deformation makes it very sensitive to crack

initiating defects that cannot be identified or evaluated by common visual observation. Therefore, industrial fabrication of ceramic components requires reliable, flexible and easily implemented NDT (*Non-Destructive Test*) like microwaves. This paper first proposes a new array structure based on CSRR antenna for crack detection in ceramic based-on materials. Then, some results and discussions on the design, showing that this structure presents a better sensitivity to cracks and splits with a smaller frequency, are presented. Finally, a conclusion comparing this design and the ordinary CSRR and SRR is given.

II. DESIGN & STRUCTURE

CSRR are small structures having sub-wavelength resonant frequency. These structure exhibits resonant behavior due to the internal inductance and capacitance present in it[1]. They are achieved by etching out SRR structures from the ground plane of the microstrip line. When a CSRR is coupled with another material, the resonant frequency of the system will be shifted according to the material's characteristics. Regarding this property, a CSRR can be used as a crack detector; any changes in the material characteristics will cause a shift in resonance frequency.

In this work, the proposed structure for crack detection is shown in Fig. 1. It is mainly composed of an fr4 substrate with the dimensions of $a=40\text{mm}$, $b=20\text{mm}$, $c=0.75\text{mm}$, a microstrip line having $w = 1.65\text{mm}$ of copper for sensor excitation as illustrated in Fig.2.(a).

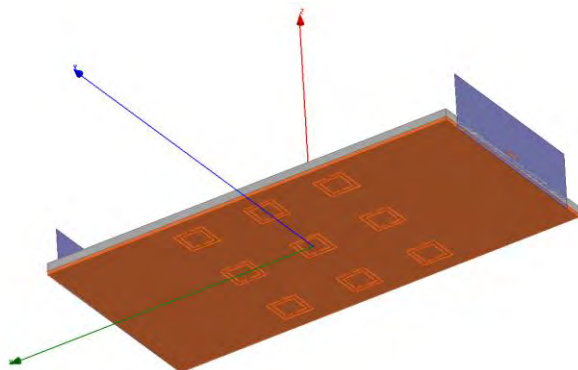


Fig.1. Designed structure for crack detection

The Bottom side consists of a 9 CSRRs array etched on the ground plan. Each CSRR in this

array is composed of two square shaped complementary split ring resonators with $r=3\text{mm}$, $g=0.2\text{mm}$, $s=0.2\text{mm}$, as shown in Fig.2.(b), acting as the sensing element of our crack detection structure.

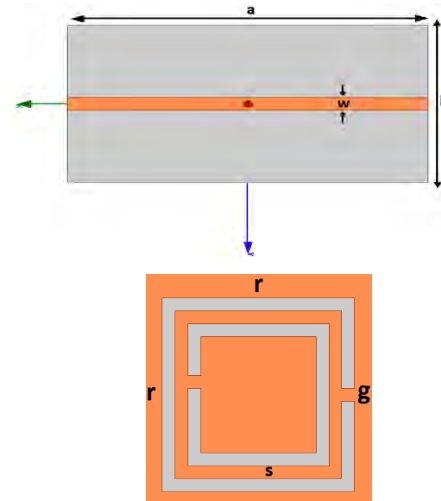


Fig.2. structure dimension (a). structure dimensions (Top view), (b). the CSRR cell.

III. RESULTS AND DISCUSSION

In order to analyze the performance of the designed sensor, a set of tests has been conducted using ANSYS HFSS simulator. The first one consists of testing the sensor without being coupled to any material. The resonant frequency of the transmission coefficient (S_{21}) was found to be 8.685 GHz, as shown in Fig. 3.(a). Then, the same sensing structure was tested with a perfect, 3mm thick, Al_2O_3 ceramic plate. The introduction of this layer caused a significant shift of the original resonant frequency (5.832GHz). Fig. 3.(b) represents the results of this 2nd simulation.

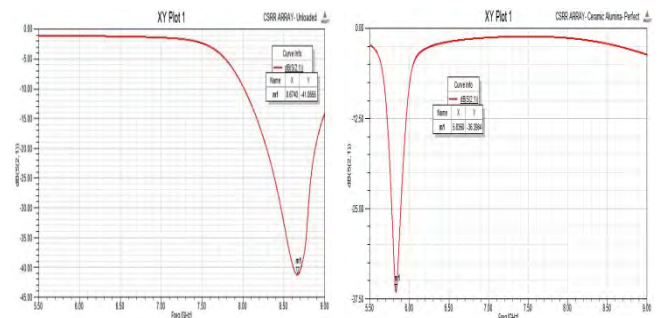


Fig.3. Transmission Coefficient (a). Unloaded sensor, (b). Sensor loaded with perfect Ceramic

Once the designed structure was tested with a flawless ceramic layer, a serie of tests was

realized on the same layer by introducing a narrow rectangular split of 0.3mm width to simulate the material cracks in real life. In these tests, several cases have been considered, where crack length (l), depth (h) and crack position were varied to analyze the performance of the CSRR array. The idea behind these simulations was to test the sensitivity of the designed sensor to cracks of various dimensions and positions.

During the selected tests the cracks parameters were varied keeping one of them constant at one time for reference as will be discussed below.

In this work we have selected (i) a crack with a constant depth of 1.5mm, and varied the length of the crack from 1mm to 2mm, then to 3mm in a single position. (ii) A crack with a fixed length of 1mm and various depths measuring 1.5 mm and 2 mm in a fixed position. (iii) A crack with a fixed length and depth considering different positions.

i. Effect of crack length

In this case an analysis is done by varying the length of crack. The sensitivity of sensor towards cracks of different lengths can be observed here. As a sensor is passed over a defected ceramic plate, a variation in the resonant frequency is observed when crack length of 1mm is considered on the tested surface. When crack length is increased from 1mm to 2 mm then to 3mm, the resonant frequency was shifted further, as shown in Fig.4. This variation shows that the sensor is able to detect cracks of different lengths.

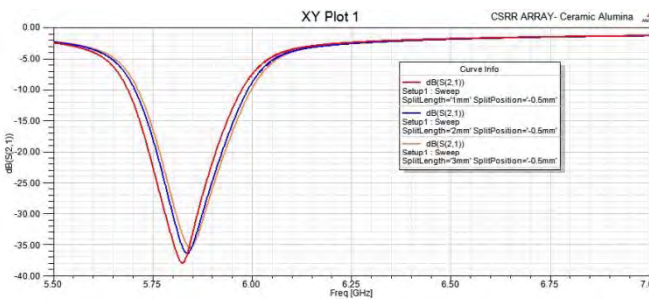


Fig.4. Transmission Coefficient with different crack length

ii. Effect of crack depth

Here we test the performance of the sensor by passing it over a defected ceramic plate having crack depth of 1mm. the resonant frequency experienced a downward shift. Similarly, for the

same crack parameters, while changing the crack depth from 1mm to 1.5mm then to 3mm, a shift in resonance frequency towards lower range is noticed as illustrated in Fig. 5.

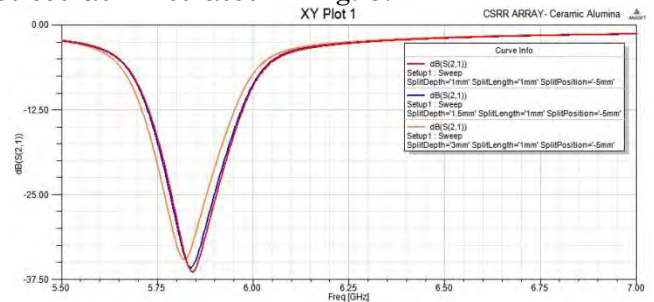


Fig. 5. Transmission Coefficient with different crack depth

iii. Effect of crack position

In this part the performance of sensor is being tested by considering different positions of the same crack. For checking the effectiveness of the sensor three positions are considered, as shown in Fig. 6. The corresponding results illustrating the resonant frequency shift are shown in Fig. 7. In this figure, it can be seen that the location of the crack in the material under test affects the resonant frequency of the sensor and can cause shifts when changed.

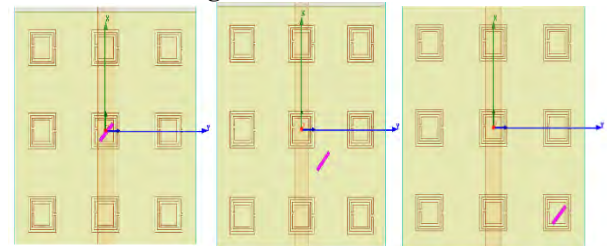


Fig. 6. Test of the structure with different cracks locations

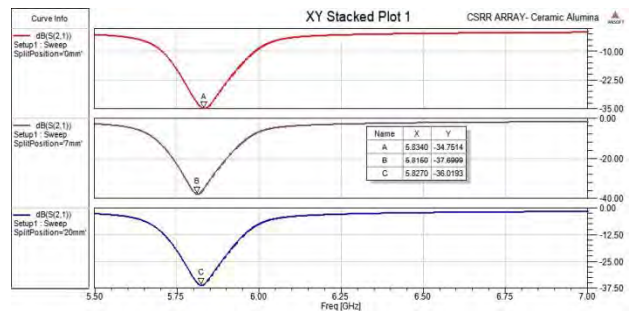


Fig. 7. Transmission Coefficient with different crack locations

Therefore, the obtained results depict that the CSRR based sensor structure can detect cracks of different dimensions with shifts in the resonant frequency. Those shifts result from a disturbance

in the distribution of the electromagnetic field around the resonator caused by the small cracks.

IV. CONCLUSION

In this work, a nine cells CSRR array has been proposed for crack detection. The radiating structure of the designed system basically operates on a frequency range of 5GHz to 8.5GHz. The performance of the sensor was tested and analyzed by varying the geometric dimensions and positions of cracks. It was verified that the proposed design is proficient enough to detect cracks of different depths, lengths and locations by analyzing the shift of the resonant frequency of the resonator in comparison to perfect sample. Unlike single and double CSRR, the proposed array structure provides a better and wide range of sensitivity to internal cracks due to the good quality factor of the equivalent resonator and the wider tested material's surface it covers. These advantages plus the small operating range frequency make this sensor a better and a cheaper candidate for non-destructive inspection in industry.

ACKNOWLEDGMENT

The authors gratefully acknowledge the contributions of M. MAHBOUBI for her work on the original version of this document.

REFERENCES

- [1] Rajni, Amanpreet Kaur, Anupma Marwaha, "Complementary Split Ring Resonator Based Sensor for Crack Detection," *International Journal of Electrical and Computer Engineering (IJECE)*
- [2] Ali M. Albishi, *Graduate Student Member, IEEE*, and Omar M. Ramahi, *Fellow, IEEE*, "Microwaves-Based High Sensitivity Sensors for Crack Detection in Metallic Materials" *IEEE TRANSACTIONS ON MICROWAVE THEORY AND TECHNIQUES*

An Improved INC-MPPT Algorithm Based on Passivity Approach for Photovoltaic System

Abdelkader BELBOULA¹, Rachid TALEB², Djilali BENYOUCEF²,
Fayçal CHABNI² and Alla Eddine TOUBAL MAAMAR²

¹Electrical Engineering Department, USTO-MB University, LDEE Laboratory, Oran, Algeria
Email: aek.belboula@gmail.com

²Electrical Engineering Department, Hassiba Benbouali University, Chlef, Algeria
Laboratoire Génie Electrique et Energies Renouvelables (LGEER)

ABSTRACT

New robust algorithm of Maximum Power Point Tracking (MPPT) for an extraction system solar energy by photovoltaic effect is tackled in this paper. Indeed, the algorithms available today, suffer from non-robustness against climate change as well as system settings. This requires a deep study of the simulation of a robust controller system. Therefore, it is proposed, the Interconnection and Damping Assignment Passivity Based Control (IDA-PBC) application for maximum power point tracking (MPPT), which shows its efficiency and robustness compared to other methods (such as Incremental Conduction), as fast and the decrease against climate perturbations and variations of system parameters.

Key Words: Interconnection and Damping Assignment Passivity-Based Control (IDA-PBC), Maximum Power Point Tracking (MPPT), Solar power system, Robust controller system.

1. INTRODUCTION

Solar power is taking hold since the photovoltaic modules have become very available and acceptable performance. In parallel, the technology of high-power semiconductor components has changed markedly by the introduction of highly efficient power components from the point of view, efficiency, reliability and cost. One of the most important characteristic of photovoltaic modules is that the maximum power available is supplied only to a unique point of operation, called maximum power

point (MPP), located by a known voltage and current [1]-[3].

Furthermore, the position of this point MPP is not fixed but moves according irradiance and temperature of the solar cell module as well as instant use [4]. Despite the relatively expensive cost of this kind of energy, it is required to extract at any time maximum power possible of available photovoltaic modules. This requires a tracking mechanism (tracking) called maximum power point tracking (MPPT) so that maximum power is generated continuously [1]-[3].

Different methods are used for maximum power point tracking. Currently, Incremental Conduction, Perturb and Observe and Ripple Correlation Control are the most frequently discussed and analysed MPPT algorithms in literature [1],[5]. All these maximum power point tracking algorithms are rather slow to respond to the fast-changing weather conditions. Furthermore, most of them can not accurately detect the maximum power point [6].

This paper develop advanced and innovative method combining between both techniques (classical and a non-linear command algorithm IDA-PBC) aimed continuing the maximum power point and improved responses with classical algorithm INC already developed, regardless of the change in climatic conditions (sunshine, temperature, etc.) even in the worst cases. Interconnection and Damping Assignment Passivity-Based Control (IDA-PBC) is a technique that regulates the behavior of nonlinear systems assigning a desired (Port-

Controlled Hamiltonian) structure to the closed-loop [7].

The simulation results showed that the MPPT technique based on passivity (IDA-PBC) present good results and that this controller is powerful and very robust.

This paper is organized as follow, the PV power system and characteristics are discussed in section 2. Section 3 presents the design of the INC MPPT controller. Section 4 presents the Passivity-based control principle. Section 5 presents the design of the proposed IDA-PBC MPPT controller. In section 6, the simulations and result analysis are demonstrated. Also, the comparison analysis between the proposed controller and incremental condition algorithm are provided in this section. In Section 7, we conclude with final remarks.

2. PHOTOVOLTAIC ARRAY MODEL

The model chosen is the "single-exponential" and the characteristic of the selected model is described by the expression (1) where I_{ph} , I_s parameters are function to illumination, the temperature and their respective reference values (I_{ph0} , I_{s0} at 1kW/m^2 , 25°C). This model is known as a single diode because the electrical equivalent circuit diagram of the solar cell comprises a single diode as shown in the figure below (Fig. 1).

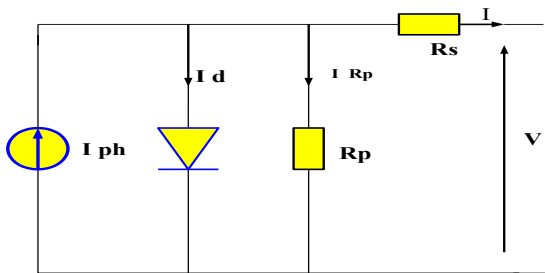


Figure.1: Diagram electrical equivalent of a solar cell (One exponential model).

Where, the current-voltage characteristic is described by the following expression:

$$I = I_{ph} - I_s \left[\exp\left(\frac{q(V + R_s I)}{AKT}\right) - 1 \right] - \frac{V + R_s I}{R_p} \quad (1)$$

I : Current produced by the PV cell;
 V : Voltage delivered by the PV cell;
 I_{ph} : Photo generated current;
 I_s : the diode saturation current;

R_s : serial Resistance;
 R_p : Shunt Resistance;
 q : the electron charge $1.602 \cdot 10^{-19}\text{C}$;
 K : Boltzmann's constant $1.381 \cdot 10^{-23} \text{ J / K}$;
 A : the diode Quality factor, valued between 1 and 2;
 T : the ambient temperature of the cell in $^\circ\text{K}$.

The equation for the current-voltage characteristic (I-V) of a photovoltaic generator of $N_s \times N_p$ cells can be written as follows

$$I_g = N_p I_{ph} - N_p I_s \left[\exp\left(\frac{q\left(V_g + R_s \frac{N_s}{N_p} I_g\right)}{AKTN_s}\right) - 1 \right] - \frac{V_g + R_s \frac{N_s}{N_p} I_g}{\frac{N_s}{N_p} R_p} \quad (2)$$

3. MAXIMUM POWER POINT TRACKING PRINCIPLE (MPPT)

3.1.Principle

The analytical definition of the optimum of a function is the point through which its derivative with respect to a given variable is zero. All algorithms for calculating the maximum power point consulted are based on this principle.

This kind of control is often called "Maximum Power Point Search" or "Maximum Power Point Tracking" (MPPT). The adapter can be achieved using a DC-DC converter so that the power supplied by the photovoltaic generator corresponds to the maximum power (P_{max}) that generates and it can then be transferred directly to load.

Fig. 2 shows a basic chain of elementary solar conversion associated with an MPPT control. To simplify the operating conditions of this command, a DC load is chosen friendly.

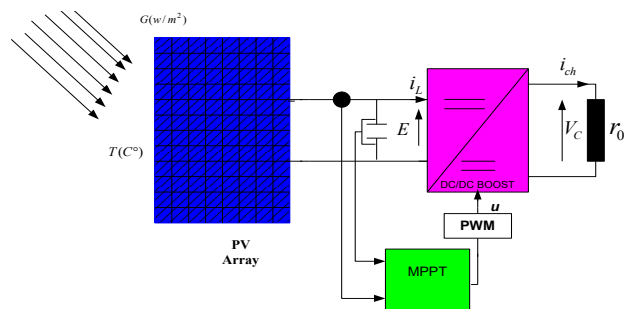


Figure.2: Schematic diagram of the MPPT converter.

3.2. Incremental Conductance (INC)

Algorithm

In the presented mathematical model of solar power plants maximum power point tracking is performed according to INC algorithm [8]. This algorithm is selected because of its simplicity and the ability to detect and track maximum power point keeping the operation point of solar power plants at it [6].

In this algorithm, calculating the derivative of the panel output power; this derivative is zero at maximum power point, positive and negative to the left to right point MPP [9]-[11].

4. PASSIVITY-BASED CONTROL OF PORT CONTROLLED HAMILTONIAN SYSTEM

4.1. Port controlled Hamiltonian (PCH) System

The Hamiltonian systems modeling formalism controlled port allows the representation of a physical system dynamics as an energy exchange network [12], [13].

A Hamiltonian controlled system (PCH) port on \mathfrak{R}^n is defined by an $J(x)$ anti-symmetric structure matrix of dimension $(n \times n)$, $R(x)$ size Diagonal $(n \times n)$, a Hamiltonian function $H(x): \mathfrak{R}^n \rightarrow \mathfrak{R}$, a matrix of dimension entries $(n \times m)$ and the following dynamic equations:

$$\begin{cases} \dot{x} = [J(x) - R(x)] \frac{\partial H}{\partial x}(x) + g(x)u \\ y = g^T(x) \frac{\partial H}{\partial x}(x) \end{cases} \quad (3)$$

where $x \in \mathfrak{R}^n$ State vector of energy variables.

$H(x): \mathfrak{R}^n \rightarrow \mathfrak{R}$ Represents the total energy stored.

$u, y \in \mathfrak{R}^m$ The (input-output) ports variables powers.

u and y are linear variables, their product is a dual power exchanged with the system environment, eg currents and voltages in electrical circuits.

4.2. Interconnection and Damping Assignment Passivity Based Control (IDA-PBC)

The central idea of IDA-PBC is to assign to the closed-loop a desired energy function via the modification of the interconnection and dissipation matrices [14]. The desired target dynamics is a Hamiltonian system of the form:

$$\dot{x} = [J_d(x) - R_d(x)] \frac{\partial H_d}{\partial x}(x) \quad (4)$$

where:

$$H_d(x) = H(x) + H_a(x) \quad (5)$$

$$\frac{\partial H_a}{\partial x}(x) = K(x) \quad (6)$$

J_d and R_d , are the new interconnection matrix and dissipation matrix respectively. $H_d(x)$ is the total storage function with a minimum when $x = x^*$. The problem how to get the control law is transformed into the search for the functions $J_d(x)$, $R_d(x)$ and vector function $K(x)$ satisfying the PDE (Partial Derivative Equation):

$$[J_d(x) - R_d(x)] \frac{\partial H_d}{\partial x}(x) = [J(x) - R(x)] \frac{\partial H}{\partial x} + g(x)u \quad (7)$$

And such that:

-The structure preservation:

$$\begin{cases} J_d(x) = J(x, \beta(x)) + J_a(x) = -[J(x, \beta(x)) + J_a(x)]^T \\ R_d(x) = R(x) + R_a(x) = [R(x) + R_a(x)]^T \end{cases} \quad (8)$$

-Integrability: $K(x)$ is the gradient of a scalar function.

$$\frac{\partial K}{\partial x}(x) = \left[\frac{\partial K}{\partial x}(x) \right]^T \quad (9)$$

-The equilibrium assignment: when $x = x^*$, $K(x)$ to verify in (10):

$$K(x^*) = -\frac{\partial H}{\partial x}(x^*) \quad (10)$$

-Lyapunov Stability:

The Jacobian $K(x)$, at x^* satisfies the relationship:

$$\frac{\partial K}{\partial x}(x^*) \rangle - \frac{\partial^2 H}{\partial x^2}(x^*) \quad (11)$$

Substituting $J_d(x)$, $R_d(x)$, $K(x)$ and $H_a(x)$ into (7), the control can be obtained by solving the PED:

$$\begin{aligned} & [J(x) + J_a(x) - (R(x) + R_a(x))] \cdot K(x) = \\ & [-J_a(x) - R_a(x)] \frac{\partial H}{\partial x}(x) + g(x)u \end{aligned} \quad (12)$$

5. PASSIVITY-BASED CONTROLLER DESIGN

5.1. Interconnection and Damping Assignment Controller (IDA-PBC) for Boost Converter

In this section, we will implement the control law synthesis method based on the passivity of DC-DC boost converter (Fig. 3).

The converter status equations are:

$$\begin{cases} L \frac{di_L}{dt} = E - (1-u)V_C \\ C \frac{dV_C}{dt} = (1-u)i_L - \frac{V_C}{r_0} \end{cases} \quad (13)$$

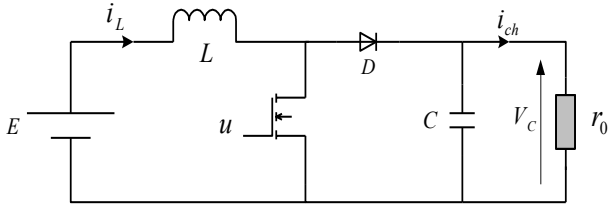


Figure.3: Schematic Boost Converter

We can then write, according to the state variables, the energy stored in a capacitor v_C :

$$v_C = \frac{1}{2C} q_c^2 \quad (14)$$

And the magnetic energy of an inductance T :

$$T = \frac{1}{2L} \Phi_L^2 \quad (15)$$

The Hamiltonian, which represents the total energy of under LC circuit without losses, is then simply:

$$H = \frac{1}{2L} \Phi_L^2 + \frac{1}{2C} q_c^2 \quad (16)$$

Is the state vector: where x_1 is the magnetic flux through the inductor, x_2 is the electric charge in the capacitor.

$$x = \begin{bmatrix} \Phi_L \\ q_C \end{bmatrix} = \begin{bmatrix} Li_L \\ CV_C \end{bmatrix} \quad (17)$$

The Hamiltonian of the system can be written as:

$$H = \frac{1}{2L} \Phi_L^2 + \frac{1}{2C} q_c^2 = \frac{1}{2} x^T Q x \quad (18)$$

with:

$$Q = \begin{bmatrix} \frac{1}{L} & 0 \\ 0 & \frac{1}{C} \end{bmatrix} \quad (19)$$

Thus deriving the Hamiltonian with respect to the state vector, we get:

$$\frac{\partial H(x)}{\partial x} = Qx = \begin{bmatrix} \Phi_L \\ L \\ q_c \\ C \end{bmatrix} = \begin{bmatrix} i_L \\ V_C \end{bmatrix} \quad (20)$$

This leads to model state:

$$\dot{x} = \begin{bmatrix} 0 & 1-u \\ u-1 & -\frac{1}{r_0} \end{bmatrix} \frac{\partial H}{\partial x} + \begin{bmatrix} 1 \\ 0 \end{bmatrix} E \quad (21)$$

This model can be written in the simplified form:

$$\dot{x} = [J - R] \frac{\partial H}{\partial x} + g(x)E \quad (22)$$

where we have the matrices:

$$J = \begin{bmatrix} 0 & u-1 \\ 1-u & 0 \end{bmatrix} \text{ anti-symmetric, } R = \begin{bmatrix} 0 & 0 \\ 0 & \frac{1}{r_0} \end{bmatrix},$$

$$g(x) = \begin{bmatrix} 1 \\ 0 \end{bmatrix}, R_a = \begin{bmatrix} r_a & 0 \\ 0 & -\frac{1}{r_0} \end{bmatrix}, R_d = \begin{bmatrix} r_a & 0 \\ 0 & 0 \end{bmatrix}$$

we have:

$$R_d = R + R_a \text{ with: } \begin{cases} R_d(x) = R(x) + R_a(x) \\ J_d(x) = J(x, u) + J_a(x) \end{cases}$$

The balance points to the desired voltage capacitor items are indicated by $x_d = [x_{1d} \ x_{2d}]^T$.

with: $x_{1d} = LV_d^2 / r_0 E$, $x_{2d} = CV_d$ and $u_d = 1 - \frac{E}{V_d}$.

Pause u is based on independent and x_1 to x_2 : $u = \beta(x_2)$, and $J_a(x) = 0$, Taking:

$$K(x) = [K_1 \ K_2]^T = \frac{\partial H_a}{\partial x} \quad (23)$$

So the desired total energy:

$$(J(\beta(x)) - R_d) \frac{\partial H_a}{\partial x} = R_a \frac{\partial H}{\partial x} + g(x)E \quad (24)$$

This leads to we get the system of equations:

$$\begin{bmatrix} -r_a & u-1 \\ 1-u & 0 \end{bmatrix} \begin{bmatrix} K_1 \\ K_2 \end{bmatrix} = \begin{bmatrix} r_a & 0 \\ 0 & -\frac{1}{r_0} \end{bmatrix} \begin{bmatrix} \frac{1}{L} x_1 \\ \frac{1}{C} x_2 \end{bmatrix} + \begin{bmatrix} 1 \\ 0 \end{bmatrix} E \quad (25)$$

By solving the system of (25) with K_1 and K_2 are unknown which gives :

$$K = \begin{bmatrix} K_1 \\ K_2 \end{bmatrix} = \begin{bmatrix} -\frac{x_2}{r_0 C (1 - \beta(x_2))} \\ \frac{r_a x_2}{r_0 C (1 - \beta(x_2))^2} - \frac{r_a x_1 / L + E}{1 - \beta(x_2)} \end{bmatrix} \quad (26)$$

we have:

$$\frac{\partial K_1(x)}{\partial x_2} = \frac{\partial K_2(x)}{\partial x_1} \quad (27)$$

we find :

$$-\frac{r_a}{L(1-\beta(x_2))} = -\left(\frac{x_2}{r_0 C(1-\beta(x_2))^2} \frac{d\beta(x_2)}{dx_2}\right) - \frac{1}{r_0 C(1-\beta(x_2))} \quad (28)$$

Therefore:

$$\frac{x_2}{1-\beta(x_2)} \frac{d\beta(x_2)}{dx_2} = -\left(1 - \frac{Cr_a r_0}{L}\right) \quad (29)$$

The two variables are separated:

$$\frac{d\beta(x_2)}{1-\beta(x_2)} = -\left(1 - \frac{Cr_a r_0}{L}\right) \frac{dx_2}{x_2} \quad (30)$$

The both terms of equality is integrated:

$$\int \frac{d\beta(x_2)}{1-\beta(x_2)} = -\left(1 - \frac{Cr_a r_0}{L}\right) \int \frac{1}{x_2} dx_2 \quad (31)$$

Defining $\alpha = 1 - (Cr_a r_0)/L$, The controller will be:

$$u = \beta(x_2) = 1 - c_1 x^\alpha \quad (32)$$

where c_1 is constant calculated by the equation:

$$\left. \frac{\partial H_d(x)}{\partial x} \right|_{x=x_2} = \left. \left(\frac{\partial H}{\partial x} + \frac{\partial H_a}{\partial x} \right) \right|_{x=x_2} = 0 \quad (33)$$

result:

$$c_1 = (1 - u_d) / (C V_d)^\alpha \quad (34)$$

This gives a non-linear IDA-PBC control law of the form:

$$u = 1 - (1 - u_d) (x_2 / x_{2d})^\alpha \quad (35)$$

The proposed nonlinear controller ensures the stability and fast response of the system during large disturbances in load and DC-bus voltage [15].

5.2. Design of MPPT Controller Based on Passivity

The control objective is to maximize the power extracted from a solar generating system, In order to combine the MPPT with passivity based control reasonably, considering the operating power point of PV array can be controlled by adjusting of the inverter (Boost) output voltage to tracking a desired V_d by using the IDA-PBC controller design of eq. (35) where the INC algorithm provides the reference voltage V_d for developed the desired power output .

with :

$$V_d = \frac{1}{1-u} V_{MPPT} \quad (36)$$

In summary the block diagram of Passivity-based control for maximum power extraction of photovoltaic system in shown in Fig. 4.

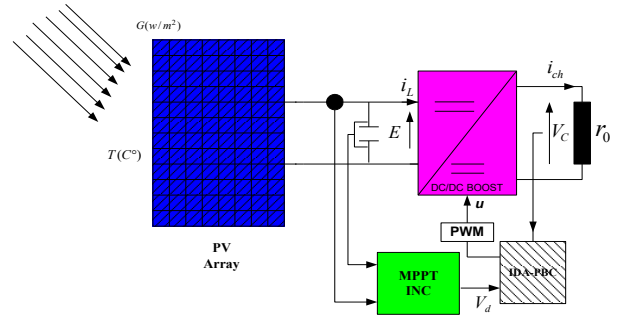


Figure.4:Overall control loop for PV system

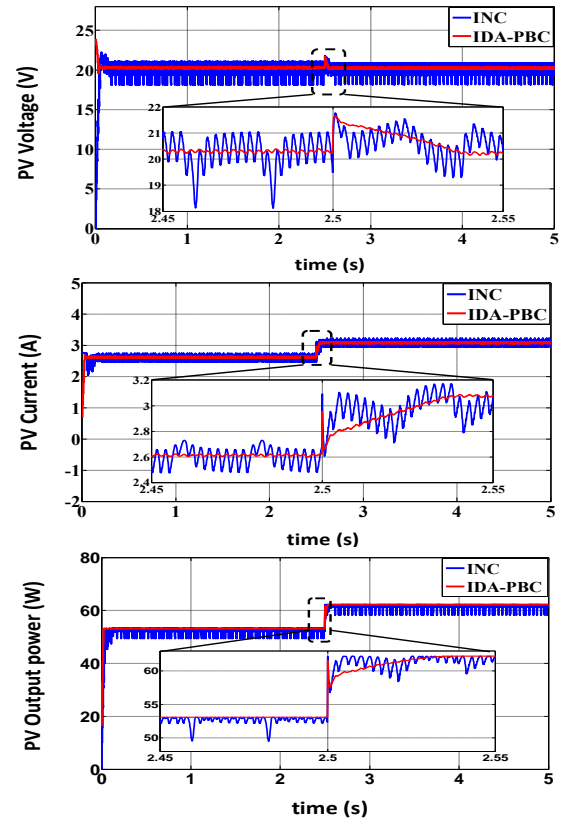
6. SIMULATION RESULTS AND DISCUSSION

6.1. Robustness Study of INC and IDA-PBC Applied for PV System

To validate the algorithm operation INC MPPT and IDA-PBC MPPT, the PVG is performed by introducing variations on the different intervening variables on the operational MPPT. Furthermore, ranks for some variables in $t = 2.5s$, is introduced.

a) Irradiance Change

Assume an increasing in the illumination from 850 to 1000W/m2 to time $t = 2.5s$. The results of the simulation are shown in Fig. 5.



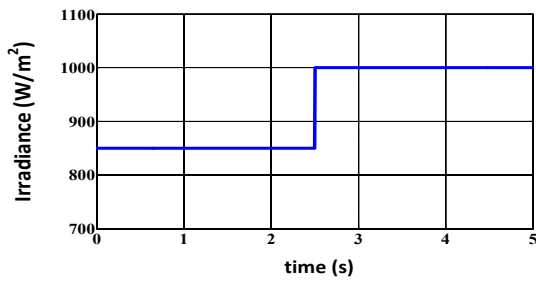


Figure.5: Answers INC MPPT algorithms and IDA-PBC MPPT for a variation of irradiance with a constant temperature and constant load

b) Temperature Variation

Assuming a rise in temperature from 25°C to 40°C at time $t = 2.5s$, the simulation results are shown in Fig. 6.

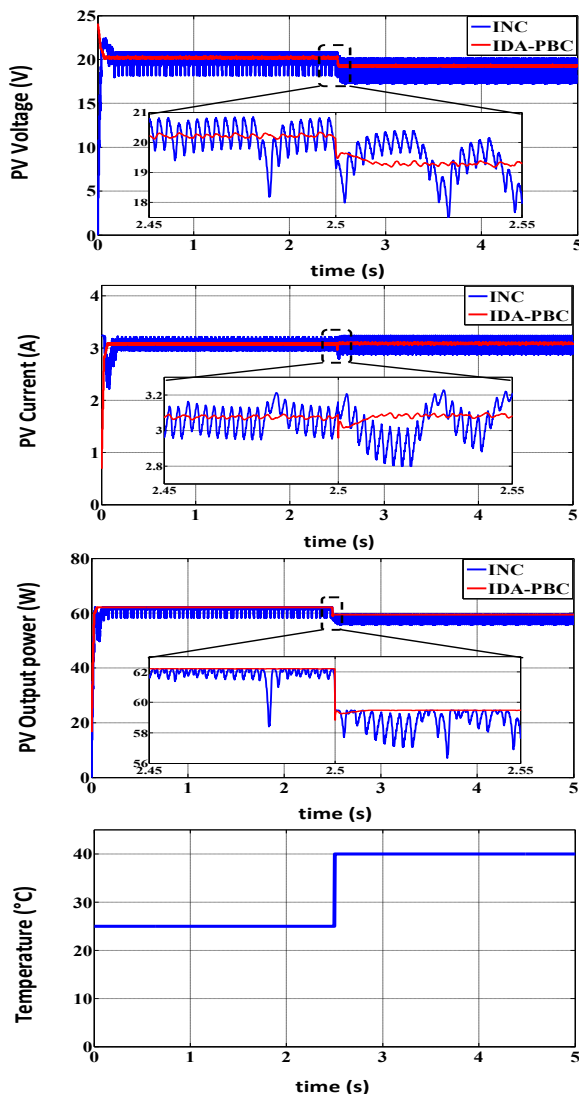


Figure.6: Outcomes INC MPPT algorithms and IDA-PBC MPPT for a temperature increase of 25°C to 40°C at irradiance 1000W/m²

c) Load Variation

Assuming a load increase from 35 to 450hm at time $t = 2.5s$ simulation results are shown in Fig. 7.

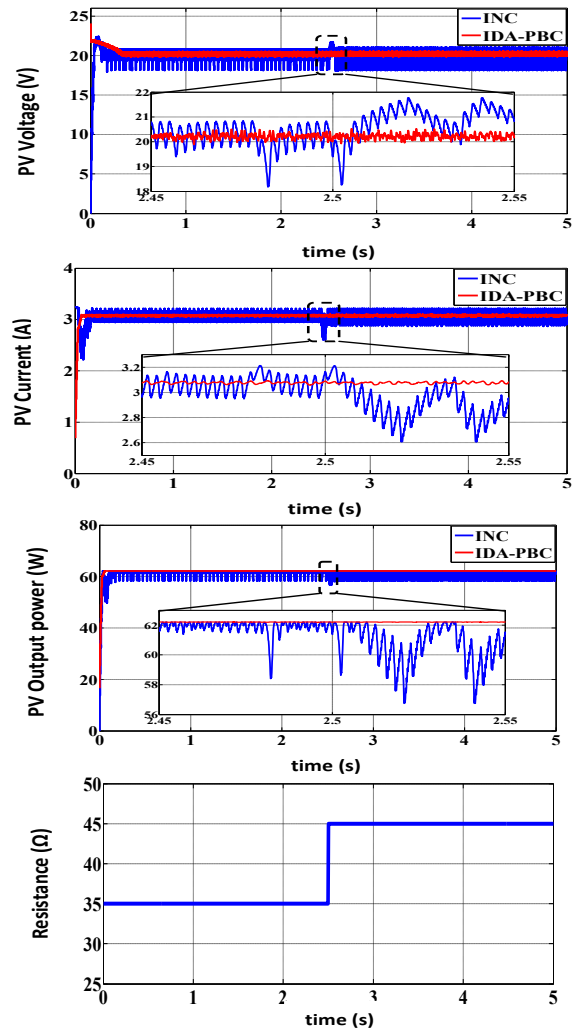
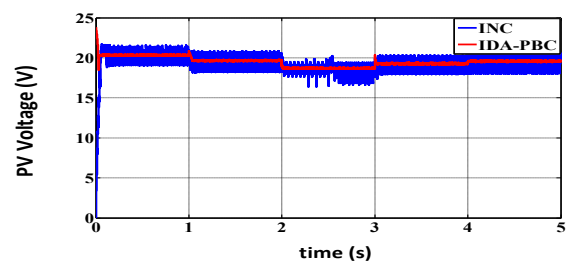


Figure.7: Responses INC and IDA-PBC algorithms for load increase 35 to 450hm with irradiance 1000W/m² and 25° C

d) Irradiance, Temperature And Load Changes

Here, it's exposed both MPPT algorithms to a change in various parameters temperature, solar irradiance and the load at the same time, simulation results are shown in Fig. 8.



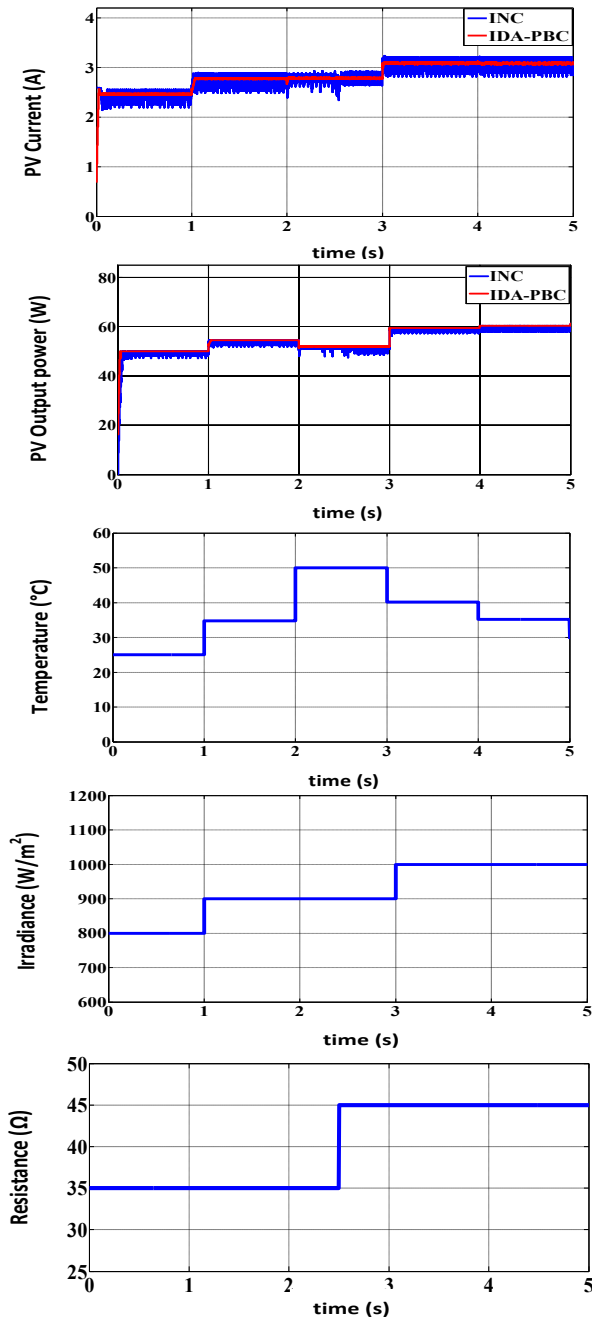


Figure.8:Outcomes of MPPT algorithms INC and IDA-PBC achievement for a parameters variations

6.2. Discussion of the Results

Fig. 5 shows the effect of increasing in power, caused by an increase of the sunlight, which causes a deviation of the maximum power point MPP for both algorithms with increased current and voltage. Once the irradiance stabilizes, the power returns to its steady state with less disruption to IDA-PBC MPPT. This has resulted a very short response time and better dynamic performance with negligible disruption over INC MPPT.

Fig.6 shows that the increase in temperature implies a reduction of the maximum power for both algorithms with voltage reduction, which causes a displacement of the maximum power point .Once the temperature stabilizes, the power returns to its steady state.

It's also noted that in Fig. 7, despite the change in the load, both MPPT algorithms have retained the optimal values of the power of PV generator, and negligible disruption to IDA-PBC MPPT, consequently a good income.

Fig. 8 shows the performance of two algorithms in the case of variation in all weather conditions and load the results of this test show the good pursuit of both algorithms but with speed and higher steadiness and less disruption as of IDA-PBC MPPT controller responses compared to INC MPPT controller.

7. CONCLUSIONS

In this paper, a new MPPT control method was proposed for a stand-alone PV generator system. The MPPT control method was employed with the aim to harvest the maximum power from PV generator power. The control method was presented based on Interconnection and Damping Assignment Passivity Based Control (IDA-PBC), directly creating the control signal for handling the power electronic converter, shows its efficiency and robustness to the other proposed control (INC method) as the speed and lower disturbances against climate change as well as system settings.

REFERENCES

- [1] T. Esmam and P. L. "Chapman, Comparison of Photovoltaic Array Maximum Power Point Tracking Techniques",in *IEEE Transactions on Energy Conversion*, vol 22, no. 2, pp. 439-449, June 2007.
- [2] V. Salas, E. Olias, A. Barrado, A. Lazaro, "Review of the maximum power point tracking algorithms for stand-alone photovoltaic systems", *Solar Energy Materials & Solar Cells* vol 90, pp. 1555-1578, 2006.
- [3] K. Sobaihi, "Etude et réalisation d'un hacheur MPPT à contre réaction de tension", *Mémoire de Magister, ENP, Algérie*, Décembre 2003.

- [4] A. Attou, A. Massoum, M.Chadli, “Comparison study of two tracking methods for photovoltaic systems”, *Rev. Roum. Sci. Techn.–Électrotechn. etÉnerg.*, vol 60, 2, pp. 205–214 (2015).
- [5] A. Dolara, R. Faranda, S. Leva, “Energy Comparison of Seven MPPT Techniques for PV Systems”, *J. Electromagnetic Analysis & Applications*, Vol 3, pp. 152–162, Sept. 2009.
- [6] M. Pikutis, D. Vasarevicius, R. Martavicius , “Maximum Power Point Tracking in Solar Power Plants under Partially Shaded Condition”, *ElektronikairElektrotechnika*, vol 20, no. 4,pp. 49–52, 2014.
- [7] R. Ortega and E. Garcia–Canseco, “Interconnection and Damping Assignment Passivity–Based Control: Towards a Constructive Procedure—Part I”, *43rd IEEE Conference on Decision and Control* pp. 3412–3417, December, 2004.
- [8] H. H. Lee, L. M. Phuong, P. Q. Dzung, N. T. Dan Vu and L. D. Khoa, “The new maximum power point tracking algorithm using ANN-based solar PV systems”, *TENCON 2010 - 2010 IEEE Region 10 Conference, Fukuoka*, pp. 2179-2184, 2010.
- [9] A. Oi, “Design and Simulation of Photovoltaic Water Pumping System”,*Faculty of California Polytechnic State University*, 2005.
- [10] M.A. Ozcelik, A.S. Yilmaz, “Modification of the Incremental Conductance Algorithm in Grid Connected Photovoltaic Systems”, *Rev. Roum. Sci. Techn.–Électrotechn. etÉnerg.*, vol 61, 2, pp. 164–168 (2016).
- [11] B. Bendib, H. Belmili, F.Krim, “A survey of the most used MPPT methods: Conventional and advanced algorithms applied for photovoltaic systems”,in *Renewable and Sustainable Energy Reviews* vol.45, pp.637-648, May 2015.
- [12] M. Miguel Magos rivera, “La modélisation des systèmes dynamiques à topologie variable : une formulation Hamiltonienne à ports paramétrée”, Ph.D. *thesis, University of Claud Bernard–Lyon1*, 2005.
- [13] H. Gonzalez, M.A. Duarte-Mermoud, I. Pelissier, “A novel induction motor control schemeusing IDA-PBC”, *Article, University of Chile, Casilla 412-3*, Santiago,Chile,2008.
- [14] W.Jiuhe; Y.Hongren; X. Shengsheng, “A New Control Strategy of Three Phase Voltage Source PWM Rectifiers”,*Physics Procedia*, Vol 24, pp. 997-1005, 2012.
- [15] J. Zeng, Z. Zhang and W. Qiao, “An interconnection-damping-assignment passivity-based controller for a DC-DC boost converter with a constant power load”, *IEEE Industry Applications Society Annual Meeting, Las Vegas, NV*, pp. 1-7, 2012.

MPPT Techniques in Stand-alone Photovoltaic System with Batteries

Faïka ZAOUCHE¹, Djamila REKIOUA¹, Said AISSOU^{1,2}
and Seddik BACHA²

¹ University of Bejaia, LTII Lab, Faculty of Technology, Bejaia
zaouche.faika@gmail.com, dja_rekioua@yahoo.fr

² University of Tizi ouzou- Algeria
aissou.said@hotmail.fr

³ Univ. Grenoble Alpes, Laboratoire G2Elab, Grenoble, France
seddik.bacha@g2elab.grenoble-inp.fr

ABSTRACT

Stand-alone photovoltaic systems are the most studied systems in renewable energy systems. In this purpose, our work is focused on the study and implementation of photovoltaic system/batteries storage with maximum power point tracking (MPPT) algorithms for the power maximization. Three different algorithms are investigated: Perturb & Observe (P&O), Incremental Conductance (Inc) and Fuzzy Logic Control (FLC).

The implementation is done using dSPACE DS 1104 board and the simulation is made using Matlab/Simulink. To generate the studied system, a power management control (PMC) is applied. This method is simple and makes it possible to determine the various operating processes of the studied system according to the weather conditions. The decisions of criteria required by this method are presented. PMC allows supplying the load in the availability of PV power and protects the batteries against overloads and deep discharges.

Key Words: Batteries, DC-DC power converters, Energy management, Fuzzy control, Maximum power point trackers.

1. INTRODUCTION

Several systems based on the conversion of renewable energies have been developed and presented as sustainable solutions to obtain an inexhaustible energy and respectful of

the environment. Therefore, the hybrid systems are becoming more and more popular. In literature, many MPPT algorithms are used in photovoltaic systems [1-6], such as conventional methods (Perturbation and Observation (P&O), Incremental Conductance (Inc)) and advanced methods (Fuzzy Logic Controller (FLC) or Adaptive Neuro-Fuzzy Inference System (ANFIS)) [4]. The optimization strategies vary according to the different sources and the desired objectives [7]. But in most of these works, only few works has been focused on practice. In Ref [6], authors develop an experimental testing system capable of reproducing environmental conditions for comparing and characterizing two photovoltaic modules in real-time and evaluating MPPT algorithms. They conclude that the developed experimental test rig is a flexible and low-cost system. In this context, in our work a DC/DC boost converter and a measurement card for the voltage and current measurement have been realized. With the global system obtained, we were able to implement three MPPT techniques. Algorithm simulations were done under Matlab/Simulink, will be compiled into code and will be executed on the dSPACE 1104 board for real-time implementation. Then, after comparing the three algorithms in terms of power, the FLC was applied to the power management control (PMC) of the hybrid PV/batteries studied system.

Many articles deal with the energy and power management of photovoltaic systems

[8-17]. Our contribution is based on a simple method which makes it possible to determine the various operating processes of the studied system according to the weather conditions [18-26]. The key decision factors for the power management strategies are the power P_{pv} provided by PV panels and the batteries state of charge (SOC). The use of the management allows producing maximum power from the PV array, protect the batteries against overcharge and deep discharge and satisfy the energy needs.

The goal of this work is the study and the implementation of MPPT algorithms for the photovoltaic power maximization. Three different algorithms are investigated: Perturb & Observe (P&O), Incremental Conductance (Inc) and Fuzzy Logic Control (FLC). A PMC is applied to the studied system. It allows supplying the load in the availability of PV power and protects the batteries against overloads and deep discharges. The implementation is done using dSPACE DS 1104 board and the simulation is made using Matlab/Simulink.

The obtained results are presented to highlight the operability improvement of the proposed power management.

2. MODELING OF THE PROPOSED SYSTEM

The proposed configuration includes a PV generator, two DC/DC converters, a battery bank and an energy management system (Fig.1.).

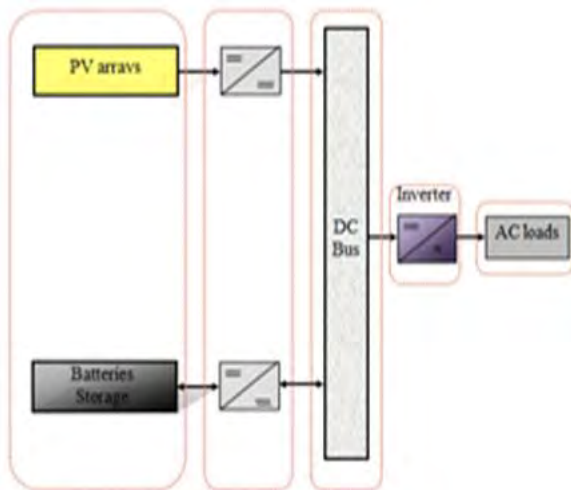


Figure.1: Studied system

2.1. Modeling of photovoltaic panels

Several mathematical models are used to describe the behaviour and the operation of the PV. In this work the following model (Fig 2) is considered [7]. Where: I_{ph} is the light-generated current, I_d is the diode-current, I_{sh} is the shunt-leakage current, R_{sh} is the shunt resistance and is inversely proportional with the leakage current to the ground, I_{pv} is the output-terminal current, R_s is the series resistance which depends on the p-n junction depth, the impurities and the contact resistance and G is the solar irradiance.

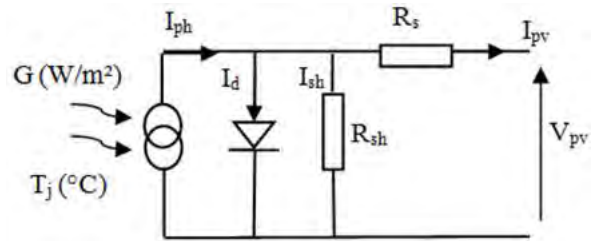


Figure.2: Equivalent circuit of photovoltaic cell

The $I_{pv}(V_{pv})$ characteristic of this model is given by the following equations:

$$I_{pv} = I_{ph} - I_d - I_{Rsh} \quad (1)$$

$$I_{pv} = I_{ph} - I_0 \times \left[\exp\left(\frac{q(V_{pv} + R_s I_{pv})}{A \times N_s \times K \times T_j}\right) - 1 \right] - \frac{V_{pv} + R_s I_{pv}}{R_{sh}} \quad (2)$$

The PV module parameters used in this paper are shown in the Table1.

Table.1 Parameters of the suntechSTPO 80S-12/BB panel

Symbol	Parameters	Values
P_{pv} (W)	Peak power	80
I_{mpp} (A)	Maximum current at maximum power point	4.65
V_{mpp} (V)	Maximum voltage at maximum power point	17.5
I_{sc} (A)	Short circuit current	4.95
V_{oc} (V)	Open circuit voltage	21.9
α_{sc} ($\frac{mA}{^\circ C}$)	Temperature coefficient of short-circuit	3
β_{oc} ($\frac{mV}{^\circ C}$)	Voltage temperature coefficient of open circuit	-150

2.2. Battery modeling

The model used in this paper is shown in the Fig.3. It contains two electrical elements: a voltage source and an internal resistance [10-12].

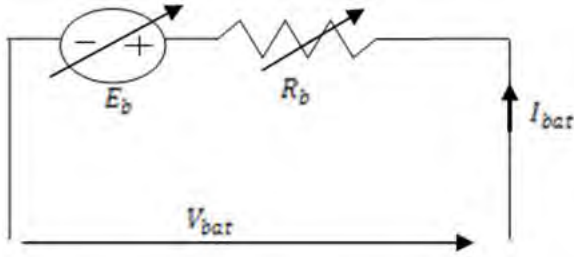


Figure.3: Electrical model of lead acid battery

$$V_{bat} = E_b \pm R_b \times I_{bat} \quad (3)$$

Where: E_b is the voltage source and R_b the internal resistance.

The battery capacity C_{bat} is given by:

$$C_{bat} = C_{10} \times \frac{1.76 \times (1 + 0.005 \times \Delta T)}{1 + 0.67 \times \left(\frac{I_{bat}}{I_{10}}\right)} \times R_b \times I_{bat} \quad (4)$$

Where ΔT the accumulator's heat and C_{10} is the rated capacity (I10).

The battery state of charge can be written as:

$$SOC (\%) = 100 \times \left(1 - \frac{Q}{C_{bat}}\right) \quad (5)$$

$$Q = I_{bat} \times t \quad (6)$$

Where: t is the discharging time.

2.3. DC/DC converter modeling

The electrical DC/DC boost converter model used is shown in Fig. 4. [10].

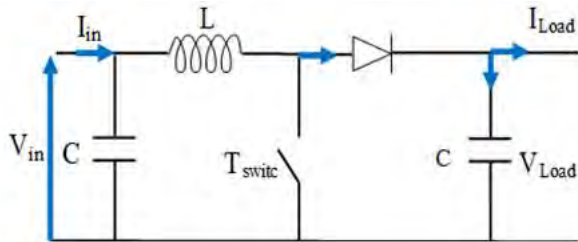


Figure.4: Electrical DC/DC boost converter model

The mathematical model of DC/DC converter is given as follows:

When the switch T_{switch} is on state:

$$V_{in} = L \frac{dI_L}{dt} \quad (7)$$

$$0 = C \frac{dV_{Load}}{dt} + I_{Load} \quad (8)$$

When the switch T_{switch} is off state:

$$V_{in} = L \frac{dI_L}{dt} - V_{Load} \quad (9)$$

$$I_L = C \frac{dV_{Load}}{dt} + I_{Load} \quad (10)$$

In average values, the output voltage is a function of the input voltage and the duty cycle. Its expression is given by the following equation:

$$V_{Load} = V_{in} \left(\frac{1}{1-D}\right) \quad (11)$$

$$I_{Load} = I_L(1-D) \quad (12)$$

Where: D is the duty cycle.

2.4. MPPT control algorithms

2.4. 1. Perturb and Observe (P&O)

The P&O algorithm is one of the most used classical methods for its simplicity and ease of implementation. Its functioning depends on the tracking step size applied to the voltage reference. The flowchart of the P&O algorithm is given in Fig.5. A DC-DC boost converter is used to track the MPPT in order to boost the DC voltage of the PV module. The duty cycle (D) of the switch is obtained using the MPPT controller based on the Perturb & Observe technique.

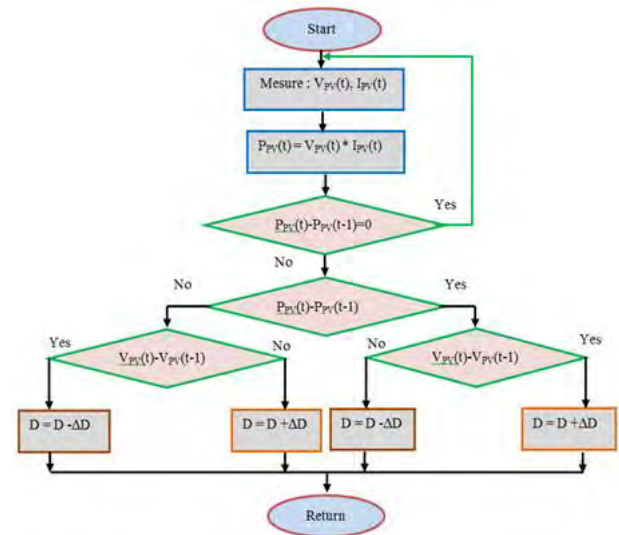


Figure.5: Flowchart of the P&O MPPT

Simulation result for P&O MPPT algorithm is evaluated in the following irradiance profile (Fig.6):

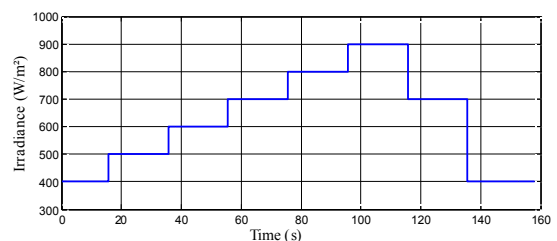


Figure.6: Irradiance profile

2.4. 2. Incremental Conductance (Inc)

In order to find the MPP, this other technique is based on the knowledge of the variation of conductance of the photovoltaic generator and the consequences on the position of the operating point compared with a maximum power point [1-2]. Thus, the conductance (C) of the PV module is defined by the ratio between the current and the voltage of the PV generator as shown below:

$$C = \frac{I_{pv}}{V_{pv}} \quad (13)$$

The elementary variation (increment) of conductance can be defined by:

$$dC = \frac{dI_{pv}}{dV_{pv}} \quad (14)$$

The flowchart of the Inc algorithm is given in Fig.7.

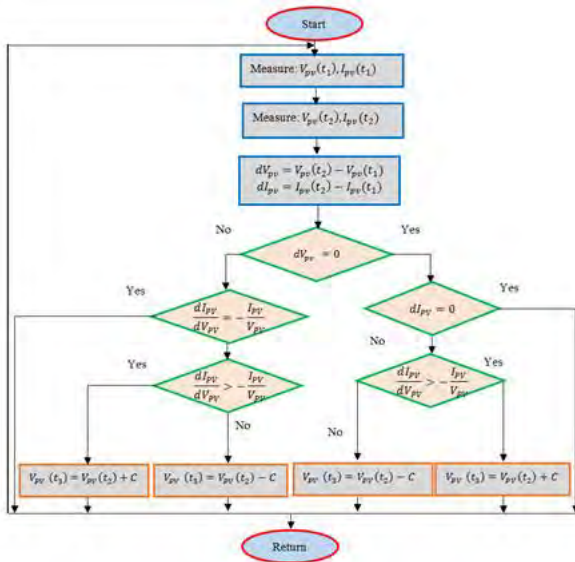


Figure.7: Flowchart of the Inc MPPT

2.4. 3. Fuzzy Logic Control (FLC)

The FLC is mainly composed of three steps which are: fuzzification, inference engine and defuzzification. The system based on MPPT fuzzy logic controller is composed of two inputs that are the error (E) and change in error (CE) as shown in (Fig. 8.). At any given sample instant k, the error and the change in error are calculated by the following relations [1-2]:

$$E(k) = \frac{P(k) - P(k-1)}{V(k) - V(k-1)} \quad (15)$$

$$CE(k) = E(k) - E(k-1) \quad (16)$$

Where: P(k) and V(k) are respectively the power and voltage of the PV generator. The

duty cycle D of a DC/DC converter is the output of the fuzzy logic controller (FLC).

The fuzzification process makes possible to introduce fuzzy sets relative to the desired values to a degree of membership. According to the Fig.8, the defined classes are denoted as: NB: Negative Big, NS: Negative Small, ZE: Zero Environ, PB: Positive Big, and PS: Positive Small.

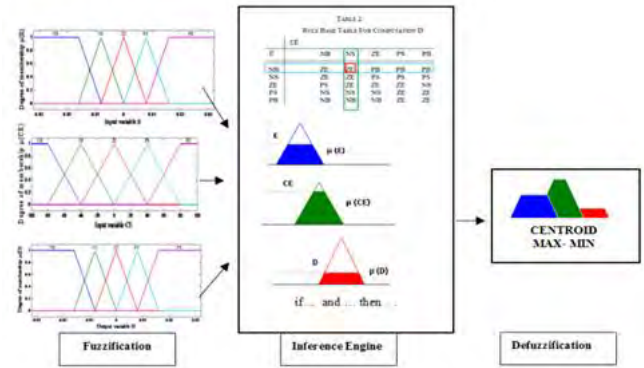


Figure.8 : Membership functions for: (a) input variable E, (b) input variable CE, (c) output variable D.

The duty cycle (D) is the system's output variable that can be found with the relations of center of area (COD). Defuzzification is the last stage of the FLC which is done by the following formula:

$$dD = \frac{\sum_{i=1}^n \mu(D_i) \cdot D_i}{\sum_{i=1}^n \mu(D_i)} \quad (17)$$

2.4. 4. Comparison between P&O, Inc and FLC results

The choice of MPPT technique is important into the system. A comparison between the three techniques (P&O, Inc and FLC) is done in STC conditions. Figure 9 shows that the FLC allows us to obtain a fast and precise response compared to the P&O and Inc. This result allows us to apply the FLC to the studied system.

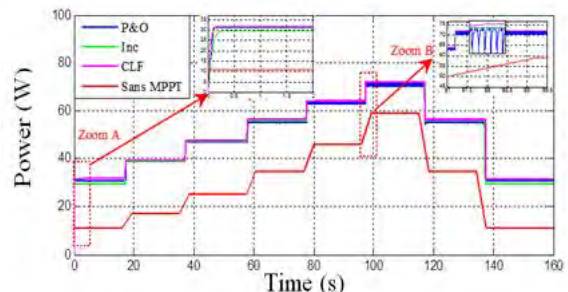


Figure.9: Photovoltaic power waveform of the three methods

2.4.5. Implementation of the three MPPT algorithms

The simulation-based MPPT algorithms made on Matlab/Simulink will be compiled into code and will be executed on the dSPACE 1104 board for real-time implementation (Fig.10). The measurement card (Fig.11) is intended for the voltage and current measurement of the photovoltaic system. These ones are sent to the card for dSPACE treatment, and then a control signal is sent to the DC/DC converter through a drive circuit and an isolation card.

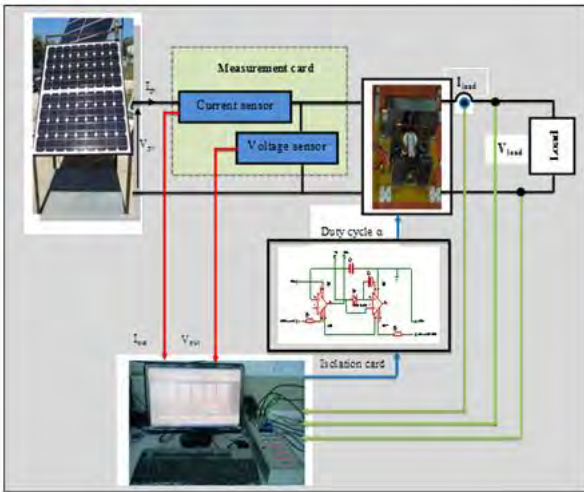


Figure.10: Test bench under dSPACE 1104

As the P&O, the Inc. control presents oscillations at steady-state. However, these oscillations are less important than with the P&O control. Also, the Inc control has a better response to sudden decreasing variations. It is clearly noticed that the FLC control responds with less oscillations compared to the other two classical techniques (P&O, Inc) and with greater power. The measurement card consists of a voltage sensor (LV25-P), a current sensor (LA25-NP), a symmetrical supplying and an isolation card. For sensing the voltage, we use a LV25-P Hall effect sensor which is equivalent to transformer with a primary and a secondary coil. A dSPACE real-time interface is installed on a hardware platform [5, 6]. The simulation and experimental results are introduced and analyzed. The different PV Parameters used in experiments are listed in table 1. The obtained results are represented in Figure 11.

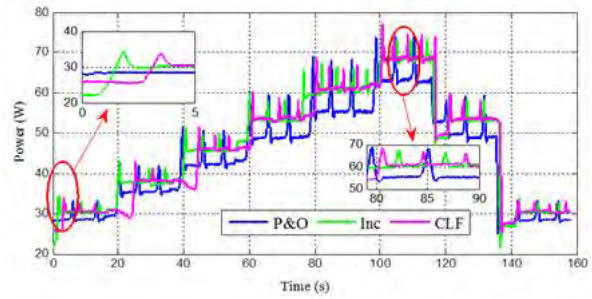


Figure.11: Power profiles of the different MPPT algorithms under variable solar irradiation conditions.

2.5.6. Comparison between simulation and experimental results

A comparison between simulation and experimental results has been made by calculating the error $\epsilon_p(\%)$

$$\epsilon_p(\%) = \left| \frac{P_{exp} - P_{sim}}{P_{exp}} \right| * 100 \quad (19)$$

It is noticed that whatever the solar irradiation, the FLC responds with the smallest error. So, the FLC is the selected MPPT method used in power management control for a system based on batteries.

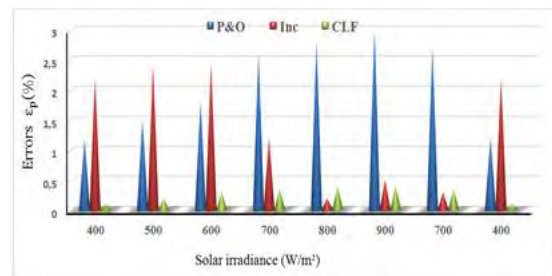


Figure.12: Errors between simulation and experimental results

3. Stand-alone Photovoltaic System with Batteries

This paper aims to optimize the number of PV panels, number of batteries and to minimize the power management control (PMC) of the system by using the MPPT strategy with better results. In our case the FLC strategy has been used and a power management control (PMC) has been applied. The use of the PMC allows a maximum power from the PV generator, protects the batteries against overcharge and depth discharge and satisfies the energy needs [21-26]. The power management shown in Fig.13 depends on the three switches state (K_1 , K_2 and K_3).

The different modes depend on the three switches K_1 , K_2 and K_3 .

Mode 1: In this mode, the power available (P_{av}) at the PV generator ($P_{av} \geq 0$) is quite sufficient to supply the load and charge the batteries.

Mode 2: The power supplied by PV is insufficient ($0 < P_{pv} < P_{load}$); in this case the power of batteries is added to satisfy the power demand. It's the compensation mode.

Mode 3: This mode is operating when no energy provides from the PV generator ($P_{av} < 0$), so, the batteries feed alone the load.

Mode 4: The PV power's is sufficient and batteries are completely charging so the disconnection of the batteries is necessary to protect them.

Mode 5: In this mode, there is no production from the PV generator and the batteries are discharged. The load is disconnected.

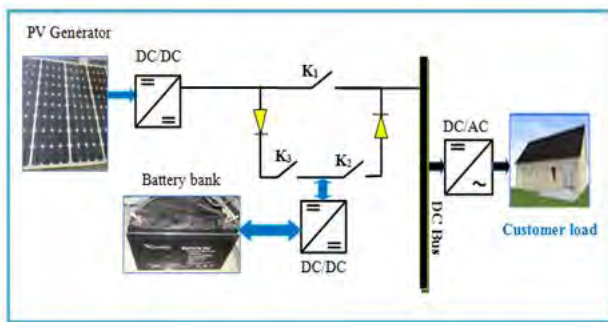


Figure.13: Architecture configuration

The average consumption profile is represented in the figure below (Figure 14): The system operates continuously which implies its effectiveness despite the various conditions introduced (two different days). Also, it is noticed that there is an excess of power on the first day of summer with high irradiation, so it will be interesting to store it in an auxiliary load.

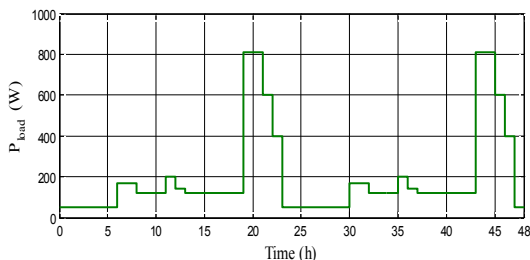


Figure.14: Load profile

Irradiation and the temperature profile are, as follows (Figure 15)

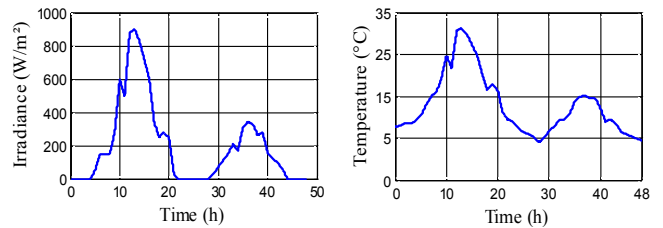


Figure. 15: Temperature and irradiance profile

The different powers are then obtained as (Figure 16):

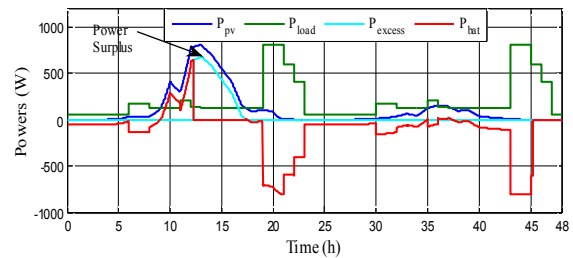


Figure. 16: Photovoltaic, load, surplus and available powers

4. Application to solar / batteries / hydrogen energy system

An application of solar/batteries/hydrogen energy system with PMC has been made (Figure 17).

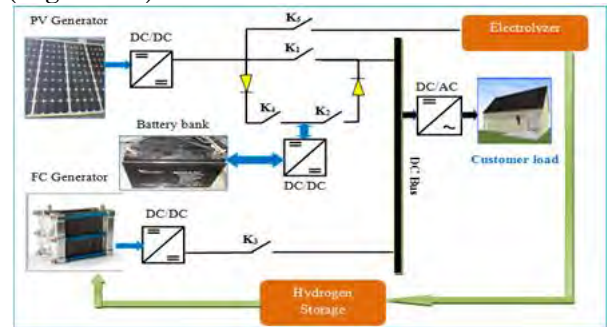


Figure. 17: Solar/batteries/Hydrogen Energy System

The simulation of the PFC was carried out under two days profile, the obtained results for the configurations are as follow (Figure 18).

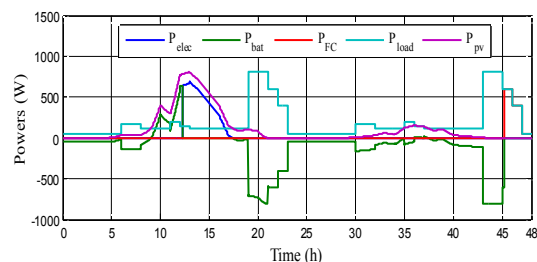


Figure.18: Electrolyzer, battery, fuel cell, load and photovoltaic powers

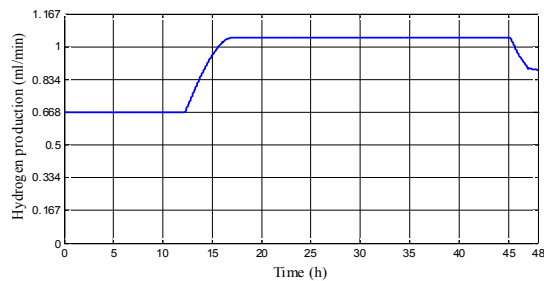


Figure.19: Hydrogen production

Obtained simulation results made under two different days show the effectiveness of the proposed solution.

5. CONCLUSION

The study and the implementation of MPPT algorithms for the photovoltaic power maximization have been presented in this paper. A comparison in terms of power of three different algorithms has been made and the FLC have presented better results in terms of power and in terms of efficiency. It gives a good maximum power operation of the PV array under different conditions such as varying irradiation and temperature. It was then applied to the overall system PV/batteries/hydrogen with power management control. The proposed configuration allows us an optimal operation of the whole system with high performances whatever the meteorological conditions, which shows the effectiveness of this proposed power control.

REFERENCES

- [1] Kamarzaman. NA, Tan. CW, A, Touchen, "A comprehensive review of maximum power point tracking algorithms for photovoltaic systems," *Renewable and Sustainable Energy Reviews*, 2014, 37, 85, 598.
- [2] Elgendy, J-M. A; B. Zhawi and Atkinson, D., "Assessment of Perturb and Observe MPPT Algorithm Implementation Techniques for PV Pumping Applications," *IEEE Transactions on Sustainable Energy*, 2012, 3, 1, 21-33.
- [3] Mohapatra. A, Nayak, B, Das. P, Mohanty. K.B; "A review on MPPT techniques of PV system under partial shading condition," *Renewable and Sustainable Energy Reviews*, 2017, 80, 854-867.
- [4] Attia. H, "Fuzzy Logic Controller Effectiveness Evaluation through Comparative Memberships for Photovoltaic Maximum Power Point Tracking Function," *International Journal of Power Electronics and Drive Systems (IJPEDS)*, 2018, 9, 3.
- [5] Soulatiantork. P, Cristaldi. L, Faifer. M, Laurano. C, Ottoboni. R, Toscani. S, "A tool for performance evaluation of MPPT algorithms for photovoltaic systems," *Measurement*, 2018, 128, 537-544.
- [6] Soulatiantork. P, "Performance comparison of a two PV module experimental setup using a modified MPPT algorithm under real outdoor conditions," *Solar Energy*, 2018, 169, 401-410.
- [7] Rekioua. D, Matagne. E, *Optimization of Photovoltaic Power Systems, Modelization, Simulation and Control*, Edition Springer, 2012.
- [8] Naveen Kumar. R, "Energy Management system for Hybrid RES with Hybrid Cascaded Multilevel inverter," *International Journal of Electrical and Computer Engineering (IJECE)*, 2014, 4(1), 24-30.
- [9] Dursun. E and Kilic. O, "Comparative evaluation of different power management strategies of a stand-alone PV/Wind/PEMFC hybrid power system," *Electrical Power and Energy Systems*, 2012, 34, 81-89.
- [10] Bratcu. A. I.; Munteanu. I, Bacha. S, Raison. B, "Maximum power point tracking of grid-connected photovoltaic arrays by using extremum seeking control," *Journal of Control Engineering and Applied Informatics*, 2008, 10(4), 3-12.
- [11] Singh. S.N.; and Snehlata, "Intelligent home energy management by fuzzyadaptive control model for solar (PV)-grid/dg power system in india, " *International Journal of Power Control Signal and Computation (IJPCSC)*, 2011, 2, 2, 61-66.
- [12] Hajizadeh. A, and Golkar. M. A.; "Intelligent power management strategy of hybrid distributed generation system," *Electrical Power and Energy Systems*, 2007, 29, 783-795.
- [13] Atia. D. M.; Fahmy. F. H.; Ahmed. N. M.; Dorrah. H. T.; "Modeling and Control PV-Wind Hybrid System Based On Fuzzy Logic Control Technique," *TELKOMNIKA*, September 2012, 10, 3, 431-441.
- [14] Rekioua. D, Bensmail. S, Bettar. N, "Development of hybrid photovoltaic-fuel cell system for stand-alone application," *International Journal of Hydrogen Energy*, 2014, 39 (3), 1604-1611.
- [15] Tamalouzt. S, Benyahia. N, Rekioua. T, D. Rekioua, Abdessemed. R, "Performances analysis of WT-DFIG with PV and fuel cell hybrid power sources system associated with hydrogen storage hybrid energy system," *International Journal of Hydrogen Energy*, 2016, 41 (45), 21006-21021.

- [16]Tazerart. F, Mokrani. Z, Rekioua. D, Rekioua. T, "Direct torque control implementation with loss minimization of induction motor for electric vehicles with battery storage," *International Journal of Hydrogen Energy*, 2015, 40(39), 13827-13838.
- [17] Ould Amrouche. S, Rekioua. D, Rekioua. T, Bacha. S, "Overview of energy storage in renewable energy systems, " *International Journal of Hydrogen Energy*, 2016, 41 (45), 20914-20927.
- [18]Mebarki. N, Rekioua. T, Mokrani. Z, Rekioua. D, Bacha. S, "PEM fuel cell/ battery storage system supplying electric vehicle", *International Journal of Hydrogen Energy*, 2016, 41(45), 20993-21005.
- [19]Mokrani. Z, Rekioua. D, Rekioua. T, "Modeling, control and power management of hybrid photovoltaic fuel cells with battery bank supplying electric vehicle", 2014, *International Journal of Hydrogen Energy*, 39 (27) , 15178-15187.
- [20]Rekioua. D, *Energy Management for PV Installations (Book Chapter) Advances in Renewable Energies and Power Technologies* , 2018, 1, 349-369.
- [21]Roumila. Z, Rekioua. D, Rekioua. T, "Energy management based fuzzy logic controller of hybrid system wind/photovoltaic/diesel with storage battery, " *International Journal of Hydrogen Energy*, 2017, 42 (30), 19525-19535.
- [22]Bensmail. S, Rekioua. D, Azzi. H, "Study of hybrid photovoltaic/fuel cell system for stand-alone applications, " *International Journal of Hydrogen Energy*, 2015, 40 (39) , 13820-13826.
- [23]Khiareddine. A, Salah. C.B.; Rekioua. D, Mimouni. M.F.; "Sizing methodology for hybrid photovoltaic/wind/hydrogen/battery integrated to energy management strategy for pumping system, " *Energy*, 2018, 153, 743-762.
- [24]Rahrah. K, Rekioua. D, Rekioua. T, Bacha. S, "Photovoltaic pumping system in Bejaia climate with battery storage, " *International Journal of Hydrogen Energy*, 2015, 40 (39) , 13665-13675.
- [25]Mohammedi. A, Rekioua. D, Mezzai. N, "Experimental study of a PV water pumping system," *Journal of Electrical Systems*, 2013, 9 (2), 212-222.
- [26] Zaouche. F, Rekioua. D, Gaubert. J.P; Mokrani. Z, "Supervision and control strategy for photovoltaic generators with battery storage," *International Journal of Hydrogen Energy*, 2017, 42 (30), 19536-19555.

Management of the electrochemical storage in Photovoltaic system using the modified Coppetti model

Aicha DEGLA¹, Madjid CHIKH² and Achour MAHRANE²

¹USTHB, LINS Lab, Faculty of Electronics and Computers, PO. Box 32, Bab-Ezzouar, Algiers
 degla.aicha@gmail.com

²UDES, Solar Equipment Development Unit, Route Nationale n°11, BP386, Bousmail, 42400, Tipaza,
 Algeria.madjidchikh@yahoo.fr,a_mahrane@yahoo.ca.

ABSTRACT

Battery-based energy storage has generally been promoted as an important tool to support the large-scale integration of renewable energy. Mainly for photovoltaic (PV) applications. Therefore, an accurate battery model is recommended for the PV system given its impact on the overall efficiency of the system. Different battery models have been discussed in the literature. Nevertheless, this paper reviews the modified Coppetti model and presents a simulation under real operating conditions for 04 different charge consumption profile scenarios based on experimental results that were performed on sealed lead/acid batteries. The simulation results were compared with the test data obtained from the battery charging and discharging modes, although several charge consumption profile scenarios led us to approve the accuracy of the parameters of the modified Coppetti model with regard to the battery behaviour.

Key Words: modified Coppetti model; lead acid battery; simulation; PV system; energy management.

NOMENCLATURE

V_{dis}	Battery discharge voltage
I_{dis}	Battery current discharge
K_{bode}	Battery polarisation voltage
V_{bode}	Battery reste voltage
SOC	State of charge
SOC ₀	Initial value of state of charge
C	Battery capacity

P_{1dc}	Empirical parameter
P_{2dc}	Empirical parameter
P_{3dc}	Empirical parameter
P_{4dc}	Empirical parameter
P_{5dc}	Empirical parameter
α_{rdc}	Empirical parameter
V_{boc}	Battery reste voltage
P_{1c}	Empirical parameter
P_{2c}	Empirical parameter
P_{3c}	Empirical parameter
P_{4c}	Empirical parameter
P_{5c}	Empirical parameter
α_{rc}	Empirical parameter
V_g	Battery gassing voltage
A_{gas}	Empirical parameter
B_{gas}	Empirical parameter
α_{gas}	Empirical parameter
A_{fonsc}	Empirical parameter
B_{fonsc}	Empirical parameter
α_{fonsc}	Empirical parameter
V_{ec}	Final battery charging period
$Ah_{restored}$	Ampere-hour restored energy
τ	Time constant
$A_{\tau sc}$	Empirical parameter
$B_{\tau sc}$	Empirical parameter
$C_{\tau sc}$	Empirical parameter
AEP	Application of PV Equipment
EER	Renewable Energy Equipment

1. INTRODUCTION

Lead acid batteries are considered as an important part of the global market for batteries used both for medium and large-scale energy storage, mainly for PV applications [1]. In addition, they are

recognized as the main technological choice because of their low capital cost and high efficiency characteristics [2]. However, even with its wide use in industry, the internal behaviour of lead acid batteries is described by unexpected electrochemical reactions, making its behaviour suddenly complex [3]. Several researchers are reviewing many battery models describing their behaviour [4-5]. However, for PV applications, electrochemical models are more suggested for battery modeling since they describe its internal and external behaviour as chemical reactions occurring inside and the temperature effect, in this paper battery tests were performed allowing us to simulate the sealed lead acid battery voltage according to the modified Coppetti model. The structure of this article is organized as follows: the first part presents the battery modeling using the Coppetti model; in the second part, a simulation in real time conditions of different charge consumption profiles was performed in order to validate the modified Coppetti model in a standalone PV system operating in real conditions.

2. THE EXPERIMENTAL SET UP DESCRIPTION

The experiment test bench was carried out at the laboratory of AEP team in EER division of the UDES / CDER solar equipment development unit located in Bousmail / TIPAZA shown in Figure.1. The practical application was recognized, in order to simulate the battery behaviour through the PV system. Furthermore, this will allow us to simulate the battery voltage evolution under real operating conditions. The experimental test bench consists of, 05 PV array connected in parallel with nominal power of 750 Wp and maximum current of 25A under 24V nominal voltage. Moreover, a battery charge controller which ensures the battery charging, also a depth of discharge controller providing two separate voltages of 12V and 24V at the system output. Two-sealed gelled lead acid batteries CGB Condor manufacturer connected in series the system electrical parameters are listed in table 1. The battery charge/discharge process is accomplished according to a given PV input current profiles. A group of DC lamps with a power of 300W is used to ensure the discharge process

characterized by a voltage output. All the data recorded from data logger system, voltage, current coming from PV array, battery and utility through sensors.

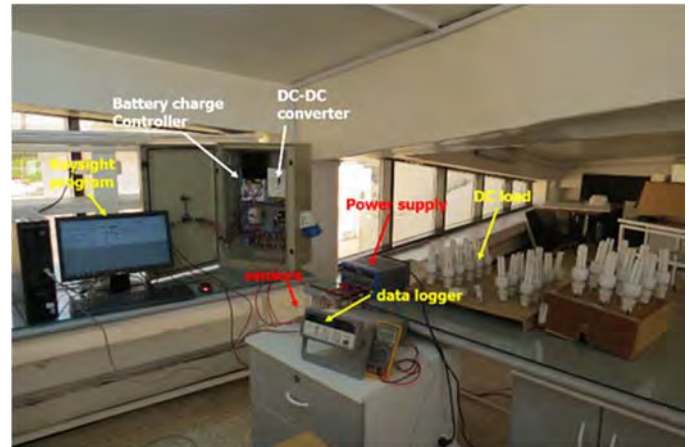


Figure.1: the experimental bench test

Table 1 Electrical parameters of the PV system.

Module Specifications	
Manufacturer	Isofoton
model	IS 150/24
Cell type	monocrystallin
Nominal power P_{max} [W]	150
Open circuit voltage V_{oc} [V]	43,2
Short circuit current I_{sc} [A]	4,45
Voltage at maximum power V_{mpp} [V]	34,6
Current at maximum power I_{mpp} [A]	4,35
Efficiency η_m [%]	11.9
Number of cell	72
Module surface A_m [m ²]	1.45
Battery Specifications	
Manufacturer	condor
model	CGB 12
Capacity [Ah]	250
Nominal voltage [V]	12

3. BATTERY MODELING

In order to estimate and predict the battery behavior under real operating conditions, Coppetti mathematical model is presented in this subsection based on the output voltage expression during charge and discharge process. This battery model was applied particularly to lead-acid batteries.

A Discharge mode

The battery voltage equation is given by the following expression:

$$V_{dis} = (V_{boc} - K_{boc} (1 - SOC(t))) - \frac{|I_{dis}(t)|}{C} \left(\frac{p_{1dc}}{1 + |I_{dis}(t)|^{p_{2dc}}} \right) + \left(\frac{p_{3dc}}{p_{4dc}} + p_{5dc} \right) (1 - \alpha_{rc} \Delta T(t)) \quad (1)$$

$$\Delta T = T - 25 \quad (2)$$

ΔT is the variation of the battery temperature in °C.

This equation is described by two distinct terms: The first one describes the variation of the battery voltage as a function of the state of charge (SOC) and the variation of the electrolyte concentration. The second one defines the variation of this voltage due to its internal resistance [6]. The following relation expresses the expression of SOC for this model:

$$SOC = 1 - \frac{I_{dis} \cdot \Delta t}{C} \quad (3)$$

B Charge mode

Due to the dynamic behavior of the battery during the charging period, Coppetti divided the charging mode into several phases. The boosting charge phase and the floating charge phase. Eq (4) describes the boosting charge phase.

$$V_c = (V_{boc} + K_{boc} (1 - SOC(t))) - \frac{|I_c(t)|}{C} \left(\frac{p_{1c}}{1 + |I_c(t)|^{p_{2c}}} \right) + \left(\frac{p_{3c}}{(1 - SOC(t))^{p_{4c}}} + p_{5c} \right) (1 + \alpha_{rc} \Delta T(t)) \quad (4)$$

The overcharge process is designed as a significant period in the charging mode, which takes into account the gassing mode. The following relation states the gassing voltage V_g for overcharged period:

$$V_g = [A_{gas} - B_{gas} \ln(1 + \frac{I_c}{C})] (1 - \alpha_{gas} \Delta T) \quad (5)$$

The final voltage (V_{ec}) during this phase increases with the charging current and decreases with temperature.

V_{ec} is described by the following equation:

$$V_{ec} = [A_{fonsc} - B_{fonsc} \ln(1 + \frac{I_c}{C})] (1 + \alpha_{fonsc} \Delta T) \quad (6)$$

The gassing progression can be described by the following nonlinear function:

$$V_c = V_g(t) + (V_{ec}(t) - V_g(t)) \cdot [1 - \exp\left(-\frac{A h_{restored} - 0,95 \cdot C}{I(t) \cdot \tau(t)}\right)] \quad (7)$$

Where;

$$\tau(t) = \left[\frac{A_{\tau sc}}{1 + B_{\tau sc} \left(\frac{I}{C}\right)^{c_{\tau sc}}} \right] \quad (8)$$

The SOC first progresses linearly with the charging current until it overtakes 70% of the battery nominal capacity; upon this value, its evolution remains very arduous to be specified [7] due to the dynamic behavior of the battery.

$$SOC = SOC_0 + \frac{I_c \cdot \Delta t}{C} \quad (9)$$

The major issue observed in battery modelling is the accuracy of the model parameters when the battery is working under real operating conditions. The use of original coefficients of the battery manufacturer can introduce significant errors, which depends on working conditions and the battery lifetime. In the present work, the simulation of the modified coppetti model has been expanded and validated according to several

Load consumption profiles scenarios, the modified coppetti model coefficients are reported in table 2.

Table 2 comparison between coppetti model coefficients

Charge mode			Floating mode			Discharge mode		
	<i>Coppetti model</i>	<i>Modified Coppetti model</i>		<i>Coppetti model</i>	<i>Modified Coppetti model</i>		<i>Coppetti model</i>	<i>Modified Coppetti model</i>
$V_{boc}(V)$	24,000	24,080	$A_{gas}(V)$	026,880	030,250	$V_{bodc}(V)$	25,02	25,24
$K_{boc}(V)$	01,920	03,010	$B_{gas}(Vh)$	001,970	-016,570	$K_{bodc}(V)$	01,44	03,40
$P_{1c}(VAh)$	06,000	35,000	$\alpha_{gas}(^{\circ}C^{-1})$	000,002	001,500 10^{-4}	$P_{1dc}(VAh)$	04,00	- 18,06
P_{2c}	00,860	13,890	$A_{Fonsc}(V)$	029,400	018,210 10^{-2}	P_{2dc}	01,30	18,00
$P_{3c}(Vh)$	00,480	- 05,060	$B_{Fonsc}(Vh)$	002,011	-006,010	$P_{3dc}(Vh)$	00,27	- 00,35
P_{4c}	01,200	- 00,640	$\alpha_{Fonsc}(^{\circ}C^{-1})$	000,002	-006,710	P_{4dc}	01,50	02,00
$P_{5c}(Vh)$	00,036	32,410	$A_{\tau sc}(h)$	017,300	077,670	$P_{5dc}(Vh)$	00,02	02,07
				852,000	021,490			
$\alpha_{rc}(^{\circ}C^{-1})$	00,025	- 00,002	$B_{\tau sc}(h)$					
			$C_{\tau sc}$	001,670	467,930			
						$\alpha_{rdc}(^{\circ}C^{-1})$	7 10^{-3}	-00,13

4. RESULTS AND DISCUSSION

In order to test the influence of the updated battery model, selection of 04 scenarios of different load profile consumptions were proposed to simulate the battery behaviour under real operating conditions; table 3 summarizes all these experiments. The purpose of this subsection is to validate the modified Coppetti model under real operating conditions.

Table 3 description of the experiments

Scenarios	(01)	(02)	(03)	(04)
Date of test start	04- 12 2016	18-09 2016	14- 09 2016	06-12 2016

The simulation tests of each scenario were divided into two parts covering both the model validation and the battery behaviour in PV application Comparison between simulation results and real measurements is discussed in the following subsections

We note that during the scenario 1, the evolution of the load consumption follows the solar irradiance evolution as it is shown in Figure.2a

Scenario 2 as illustrated in Figure.2b the evolution of the load consumption profile is inversely proportional to the evolution of the solar irradiance

Scenario 3 as shown in Figure.2c the evolution of the load consumption profile is constant over time

Scenario 4 as it is presented in Figure.2d the evolution of the load consumption profile is random toward the solar irradiance evolution

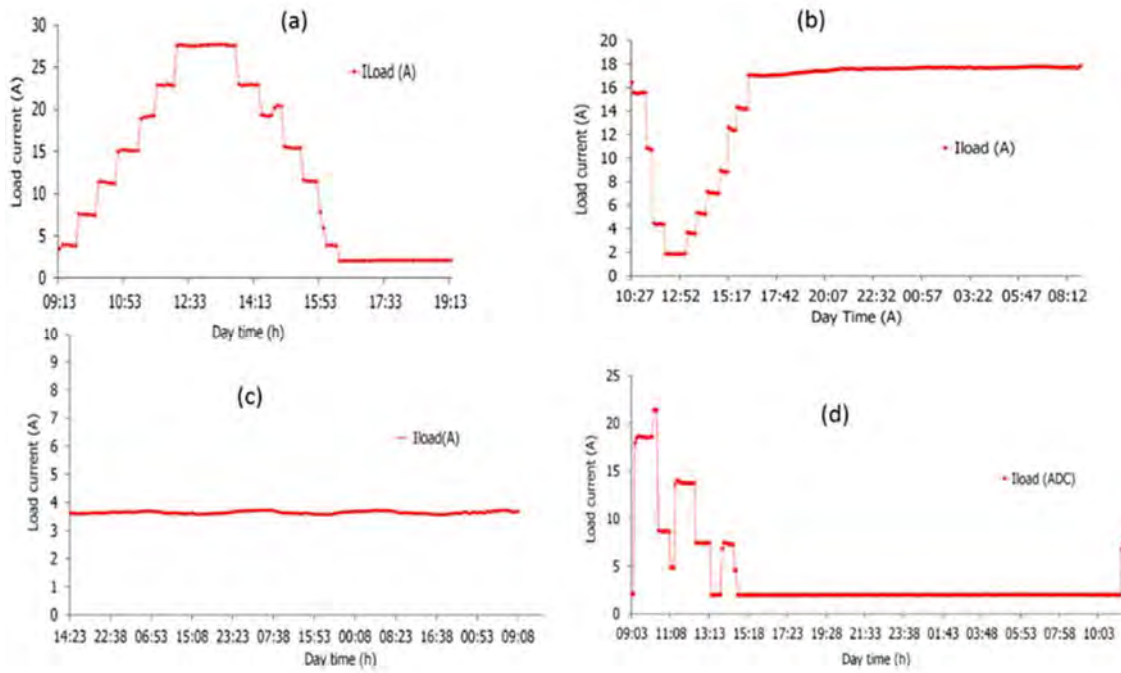


Figure.2: load profile consumption: (a) scenario 1, (b) scenario 2, (c) scenario 3, (d) scenario 4

Figure.3a, figure.4a, figure.5a, and figure.6a show typical operating days of the studied system in which it is reported the daily evolution of the solar irradiance $G(W/m^2)$, the generated current (I_{pv}) and the evolution of the load consumption (I_{load}).

Figure.3b, figure.4b, figure.5b, and figure.6b illustrate the measured battery voltage against the predicted voltage using Coppetti model with new parameters and the original ones; the evolution of SOC is also presented. Scenario 1 as it is presented in Figure.3 we observe that the evolution of the load consumption is proportional to the evolution of the solar irradiance.

Scenario 2 as illustrated in Figure.4 the evolution of the load consumption profile is inversely proportional to the evolution of the solar irradiance we remark that the battery voltage based on new updated coefficients shown in Fig.4b follows the real battery voltage

Scenario 3 as shown in Figure.5 the evolution of the load consumption profile is constant over time we observe that the battery voltage based on new coefficients shown in Figure.5b follows the real battery voltage during charge and discharge process.

Scenario 4 as it is presented in Figure.6 the evolution of the load consumption profile is random toward the solar irradiance evolution we affirm that the battery voltage based on new parameters shown in Figure.6b follows the real battery voltage

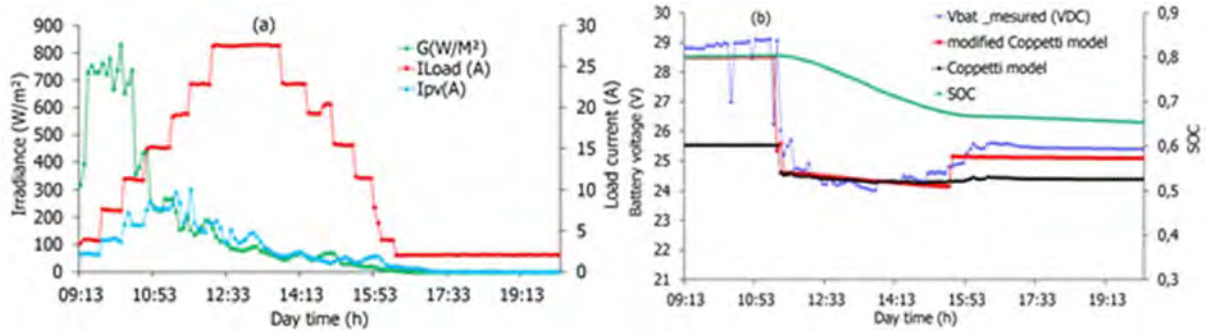


Figure .3: scenario 1(a) solar radiation, load and PV currents evolution (b) Battery voltage evolution of Coppetti model and state of charge.

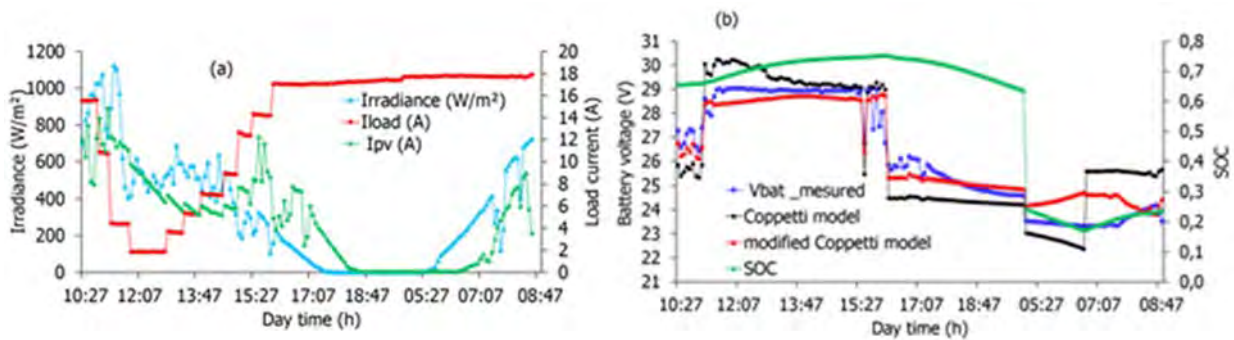


Figure. 4: scenario 2 (a) solar radiation, load and PV currents evolution (b) Battery voltage evolution of Coppetti model and state of charge.

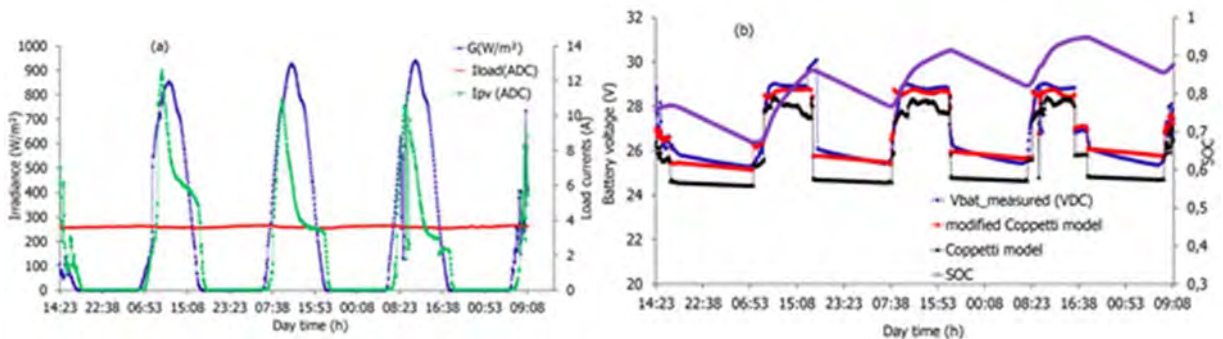


Figure. 5: scenario 3 (a) solar radiation, load and PV currents evolution, (b) Battery voltage evolution of Coppetti model and state of charge.

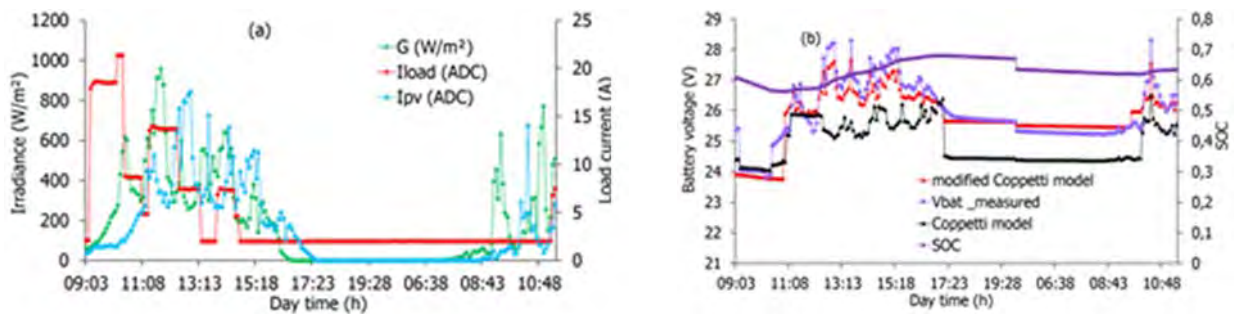


Figure. 6: scenario 4 (a) solar radiation, load and PV currents evolution, (b) Battery voltage evolution of Coppetti model and state of charge.

It should be noted that the Coppetti model based on new coefficients offers better harmony with the measured battery voltage equally for charging and discharging modes. We can confirm this agreement according to results of [9].

5. CONCLUSION

An experimental test of a PV system is performed to acquire a set of data from a sealed gelled lead-acid battery at different scenarios for different given load consumption profiles. The simulation of the modified Coppetti model lead us to confirm that this model reproduce the most accurate behaviour of the battery during charge and discharge mode.

Even though the different variation of the load consumption profiles, however the energy management distribution from the PV array and battery to utility follows efficiently the variation of different consumption profiles.

The Coppetti model accounts for all dynamic characteristics of lead acid battery with different technology and manufacturer if the empirical parameters are appropriately identified.

ACKNOWLEDGEMENTS

This study is sponsored by the laboratory of AEP team, in EER division of the UDES/CDER solar equipment development unit located in Bousmail/Tipaza.

REFERENCES

[1] Jorge-Omar Gil Posada; Anthony J. R. Rennie; S. P.Villar; V. L. Martins. Marinaccio; A. Barnes; C.F. Glover; D.A.Worsley; and P.J .Hall, "Aqueous batteries as grid scale energy storage solutions". *Renewable and sustainable energy review* 2016, 68, 1174-1182.

[2] Abhishek-Malhotra; B. Battke; M. Beuse; A. Stephan; and Tobias S. Schmidt, "Use cases for stationary battery technologies". *A review of the literature and existing projects*, *Renewable and Sustainable Energy Reviews*, 2016, 56,705–721.

[3] Soufiane-Kichou; S. Santiago; G. Letizia, M.L. Llanos and M.C Emilio, "Comparison of two

PV array models for the simulation of PV systems using five different algorithms for the parameters identification". *Renewable Energy journal*, 2016, 99, 270-279.

[4] Mohamed-B.H; Rhouma; A. Gastli; L. B.Brahim; F. Touati; M.Benammar, "A simple method for extracting the parameters of the PV cell single-diode model", *Renewable Energy journal*,2016, 113,885-894.

[5] Ralph-Evins, "A review of computational optimization methods applied to sustainable Building design", *Renewable and Sustainable Energy Reviews* , 2013,22,230-245.

[6] J.B Coppetti; E. Lorenzo and F. Chenlo, ".A general battery model for PV system simulation". *Progress in photovoltaic, research and Applications*, I, 1993, 283-292

[7] J.B Coppetti and F. Chenlo, "Lead/acid batteries for photovoltaic applications. Test results and modelling", *Journal of Power Sources* 1994, 47,109-118.

[8] Kondapalli Siva Prasadet; C.S. Rao and D.N. Rao, ".Application of Hooke & Jeeves Algorithm in Optimizing Fusion Zone Grain Size and Hardness of Pulsed Current Micro Plasma Arc Welded AISI 304L Sheets". *Journal of Minerals and Materials Characterization and Engineering*, 2012, 11, 869-875.

[9] Aicha DEGLA; madjid CHIKH; Aissa CHOUDER; Farid Bouchafaa; Ayoub TAALLAH. "An update Battery Model for Photovoltaic Application based on comparative Analysis and Parameter Identification of Lead acid Battery Models Behaviour", *IET Renewable Power Generation journal*,2018, 12, 4,484 – 493.

Conception of microstrip patch antenna based on SINRD substrate for DSRC application

NARIMANE KORCHI¹, RACHID OUSSAID^{1,2}

¹ USTHB, LINS Lab, Faculty of Electronics and Computers, PO.Box 32, Bab-Ezzouar, Algiers at korchi.narimane@usthb.dz, roussaid@usthb.dz

² ENPEI-BADJI MOKHTAR, Bp 05 Rouiba, Algiers

ABSTRACT

This communication presents a study of a microstrip patch antenna structure based on the substrate integrated non-radiative dielectric (SINRD). The SINRD structure is the air holes used in the substrate. The proposed Antenna is designed at an operating resonant frequency of 5.8GHz to meet Dedicated Short-Range Communication (DSRC) applications. The gain, bandwidth and directivity are analyzed before and after introducing SINRD structure in the microstrip patch antenna. The numerical results obtained from the comparison of three different configurations of SINRD substrate have been analyzed, it is shown that the performance of the patch antenna is enhanced using the SINRD substrate. The simulation has been performed using CST Microwave Studio Suite.

Keywords— Microstrip patch antenna, SINRD, DSRC, Gain, Bandwith, Directivity, Air holes.

I. INTRODUCTION

The DSRC system is a specialized mobile radio communication system for road vehicles. The DSRC is a fundamental technology that combines roads, traffic and vehicles using information and communication technologies [1]. DSRCs are implemented between stationary equipment along the road infrastructure (usually installed on gantries) and on-board equipment. The fixed equipment is connected via a wired network to a control station which centralizes data and ensures the operation of the application. [2]

In the DSRC system, the antenna is the most important part. It essentially ensures the performance of wireless communication systems.

The microstrip patch antennas have been increasingly used in recent years in wide range of application in wireless communication systems and satellite communication systems

due to their great advantages: light weight, low cost, low profile, and conformable. On the other hand, it suffers from some disadvantages as: narrow bandwidth, low gain, excitation of surface waves. Some technique was used to increase the gain and directivity of microstrip antenna in microwave frequency regime, and topologies have been investigated in several researches [3-8].

A solution was proposed in this work is the concepts of substrate integrated circuits (SICs), which was used of a specific air hole pattern that can effectively lower the dielectric constant of a dielectric substrate region of interest, thus creating a wave-guiding dielectric channel in the substrate. This synthesized channel becomes a substrate integrated NRD guide or SINRD.

The substrate integrated nonradiative dielectric (SINRD) waveguide belongs to the family of substrate integrated circuits [9], [10], a promising low-cost high-performance technology for millimeter-wave and terahertz applications. In this technology, the air region of a nonradiative dielectric (NRD) guide is replaced by air holes or a low-dielectric agent on the same substrate, which removes the problem of mechanical support and assembling of the planar substrate that arises in the case of hybrid planar/NRD schemes [11].

In this letter, we propose a new design of realizing high directivity of the patch antenna under CST software working at a frequency of 5.8GHz, inspired by a work already published in literature [12] and in which the author had made the design of a printed antenna resonant to 5.8GHz based on meta-material for DSRC application. We will carry out several simulations of patch antennas based on standard dielectric substrates and then based on SINRD substrates with different configurations of the air holes.

A comparative study will be carried out to demonstrate the performance of the patch antenna according to the substrates used.

II. DESIGN AND ANALYSIS

The microstrip patch antenna is a planar antenna whose radiating element is a generally square conductive surface, separated from a conductive reflector plane (ground plane) by a dielectric sheet called substrate as shown in Fig. 1(a).

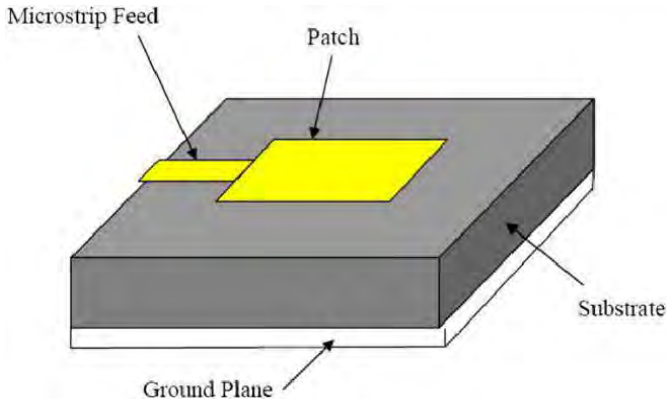


Figure 1a. Patch antenna with rectangular radiation.

In this configuration, upper conducting layer is the source of radiation where electromagnetic energy fringes off the edges of the patch and into the substrate. The lower conducting layer acts as a perfectly reflecting ground plane, bouncing energy back through the substrate and into the free-space. The antenna size mostly depends on the frequency band of operation.

There are several other factors that contribute to deciding the dimension of the antenna and its behavior such as the substrate material used and its thickness [13]. The patch material affects the efficiency of the antenna, while the type of substrate plays a major role in the calculation of the antenna dimensions [14-16].

Topology of the proposed SINRD guide is illustrated in Fig. 1(b). shows the pattern of air holes used to lower dielectric constant of the substrate with geometrical dimensions.

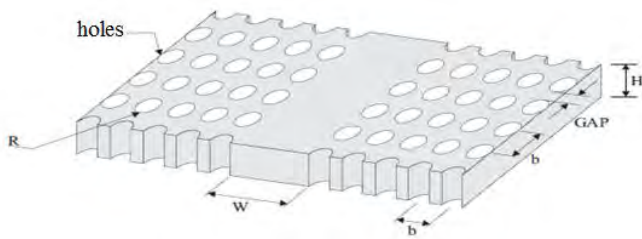


Figure 1b. 3-D view of the hybrid planar/SINRD guide arrangement.

In this equivalent guide, ϵ_r equals to ϵ_{eff} of the air holes patterned region.

This equivalent NRD guide greatly simplifies the design of SINRD circuits. Note that the air hole pattern should not be

subject to the generation of electromagnetic bandgap (EBG) phenomena.

A. Design Microstrip Patch antenna

The parameters of the radiating microstrip patch antenna are calculated with following equations [17].

$$w = \frac{c}{2f_r} \left(\frac{\epsilon_r + 1}{2} \right)^{-1/2} \quad (1)$$

$$L_{eff} = \frac{\lambda_g}{2} = \frac{\lambda_0}{2\sqrt{\epsilon_{eff}}} \quad (2)$$

$$\Delta L = 0.412 h \frac{(\epsilon_{eff} + 0.3) \left(\frac{w}{h} + 0.264 \right)}{(\epsilon_{eff} - 0.258) \left(\frac{w}{h} + 0.8 \right)} \quad (3)$$

Where:

$$\epsilon_{eff} = \frac{\epsilon_r + 1}{2} + \frac{\epsilon_r - 1}{2} \left(1 + 12 \frac{h}{w} \right) \quad (4)$$

With the parameter h is the thickness of substrate, Therefore:

$$L = L_{eff} - 2\Delta L \quad (5)$$

In above equations, W denotes the width of radiating patch, C is the speed of light in vacuum, ϵ_r is the dielectric constant of the host material, L is the length of radiating patch and h is the thickness of substrate. The dimensions of the radiating patch along its length direction extend on two ends by a distance of ΔL and ϵ_{eff} is the effective dielectric constant.

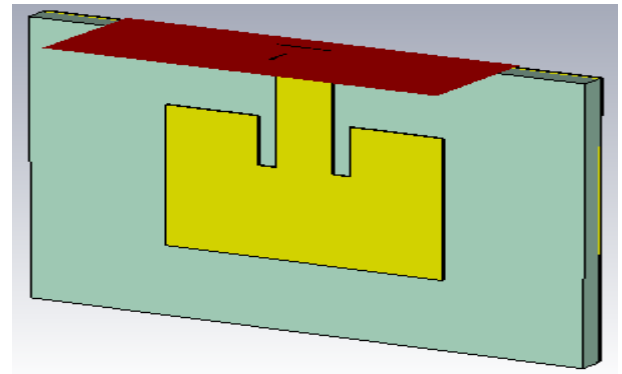


Figure 2. Geometry of patch antenna.

Figure 2 shows the geometrical configuration of the proposed rectangular microstrip patch antenna in CST Microwave Studio. The radiating rectangular patch has the dimensions (15.89 x 11.87mm). The patch was printed on one side of FR4 (loss free) substrate with relative permittivity $\epsilon_r = 4.3$ and at height of 1.6mm from the ground plane.

B. Design air hole pattern

The first step in the design of an SINRD guide is to evaluate for a specific cell lattice with a specific dielectric material.

It is known [18-19] that an appropriate air hole arrangement in a planar dielectric substrate could reduce the effective dielectric constant of the structure. The choice depends on the dielectric profile needed, the layout of the circuit and the, mechanical strength of the substrate [9]. Three possible holes patterns, namely, a square lattice, an equilateral triangular lattice and a star lattice. In each case, the static effective dielectric constant of one cell can approximately be calculated by using [10].

$$\epsilon_{eff} = \frac{\epsilon_r(S_{CELL}-S_{AIR})+S_{AIR}}{S_{CELL}} \quad (6)$$

Where, S_{CELL} is the area of a unit cell of the pattern and S_{AIR} is the area of air holes in the unit cell.

Table I gives the value of ξ_{eff} of each pattern (or lattice) for different holes diameters.

TABLE I. ϵ_{eff} EACH PATTERN

Diameter	Topology		
	Square	Triangular	Star
R=1.75 mm r=0.5mm	2.0422	1.693	1.8579

C. Microstrip patch antenna with SINRD substrate

The design of the patch antennas with SINRD substrate are based on the same model of the waveguide (width of the non-perforated zone, radius of the air holes "R" and the distance between the holes "Gap") integrated in the substrate Dielectric FR-4 for the three arrangements of the SINRD holes.

The choice of the geometry of the SINRD substrate was made according to several criteria:

- R should be as large as possible to improve antenna performance and reduce the losses in the guide.
- Gap must also be as large as possible to allow the mechanical integrity of the guide.
- The diameter of the air holes must be limited to prevent the phenomena of Electromagnetic BandGap (EBG) in the desired frequency band.

The Fig. 3 and 4, 5 shows integration of SINRD structures for the patch antenna with air holes in dielectric square, triangular, star lattice respectively at 5.8 GHz frequency region.

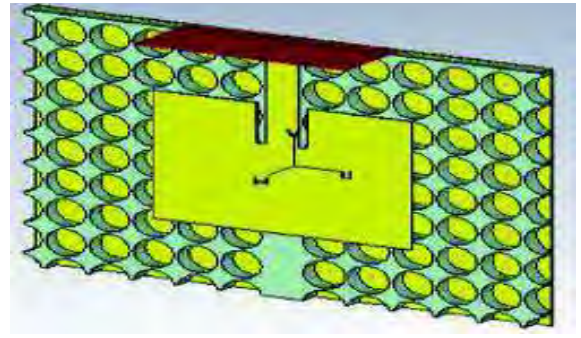


Figure3. Patch antenna with SINRD substrate square lattice.

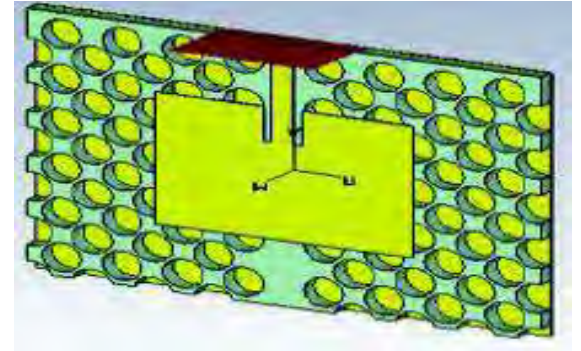


Figure4. Patch antenna with SINRD substrate triangular lattice.

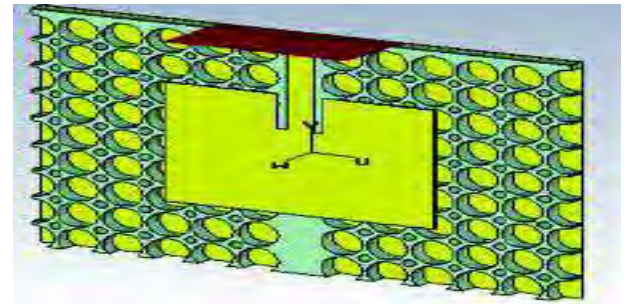


Figure5. Patch antenna with SINRD substrate star lattice.

IV. RESULT SIMULATION AND DISCUSSION

The result simulation was obtained using TIME DOMAIN solver in CST Microwave Studio with accuracy -40dB.

A. Impedance bandwidth

The simulated return loss of microstrip patch antenna is shown in Fig. 6. The S_{11} represents the reflection coefficient at the antenna input. This parameter also allows ensuring the adaptation of the antenna to the resonant frequency. The curve of the modulus of the coefficient of reflection of the antenna structure shows a good adaptation of about -25.104 dB at the resonant frequency of 5.8GHz.

The impedance bandwidth for this antenna is 180,9MHz calculated at -10dB return loss.

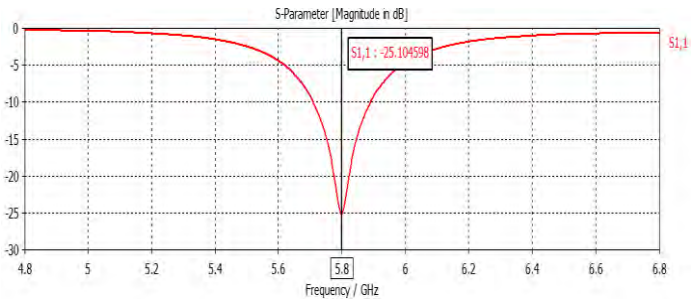


Figure6. Simulation S11 for microstrip patch antenna.

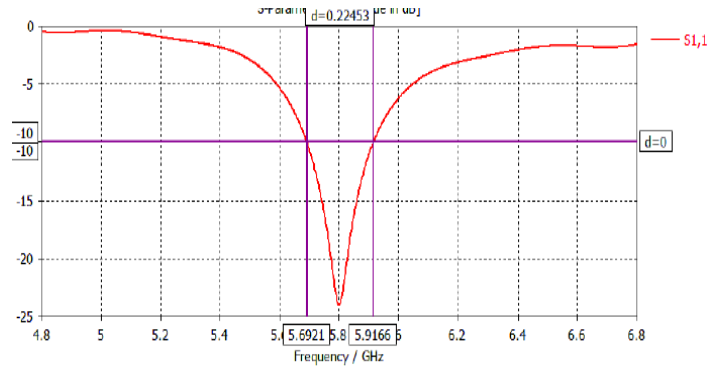


Figure9. Simulation S11 for microstrip patch antenna with SINRD star lattice.

Adaptation of the microstrip patch antenna with SINRD substrate star lattice is done on a bandwidth of 225 MHz around 5.8 GHz, which is wider, compared to that found by the single microstrip patch antenna with a minimum of -24 dB as like represented in Fig. 9.

There is significant improvement in the bandwidth for conventional microstrip patch antenna 180MHz to 231MHz for microstrip patch antenna with SINRD substrate triangular lattice.

B. Radiation pattern

The simulated radiation pattern for the gain and directivity of the microstrip patch antenna and the microstrip patch antenna with SINRD substrate with different structure (square, triangular, star) are indicated in Fig. 10, Fig. 11 and Fig. 12, Fig. 13 respectively at 5.8GHz frequency.

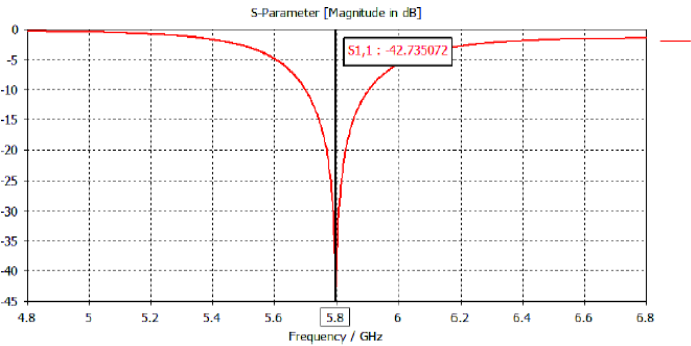


Figure7. Simulation S11 for microstrip patch antenna with SINRD square lattice.

The adaptation of the patch antenna with SINRD substrate square lattice is very satisfactory with a reflection coefficient of less than -10 dB between 5.7 and 5.9 GHz and a minimum of -42.7 dB at 5.8 GHz as shown in Fig. 7. The impedance bandwidth equal to 206 MHz is largely sufficient for our antenna.

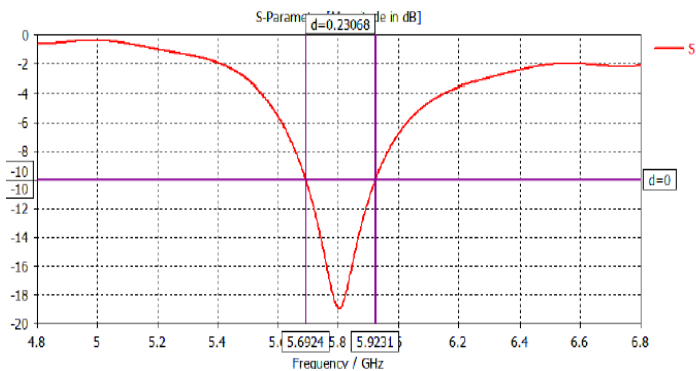


Figure8. Simulation S11 for microstrip patch antenna with SINRD triangular lattice.

The Fig. 8 represent the reelection coefficient of the patch antenna with SINRD substrate triangular lattice, the impedance bandwidth is 231MHz calculated at -10dB.

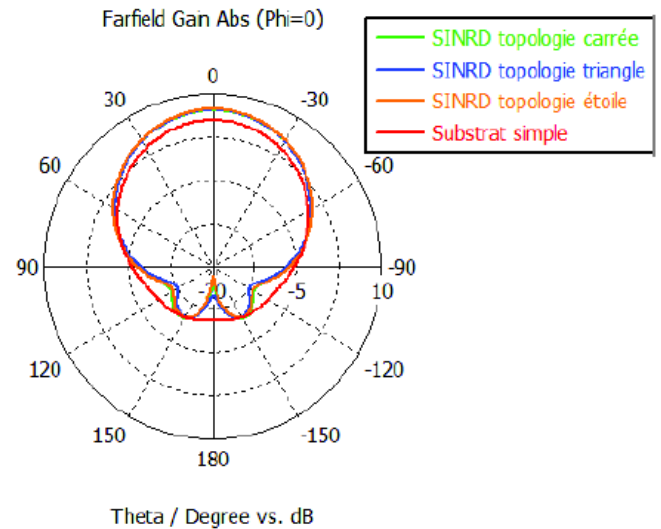


Figure 10. E plane far Radiation pattern of gain for Phi=0° with for microstrip patch antenna with different substrate.

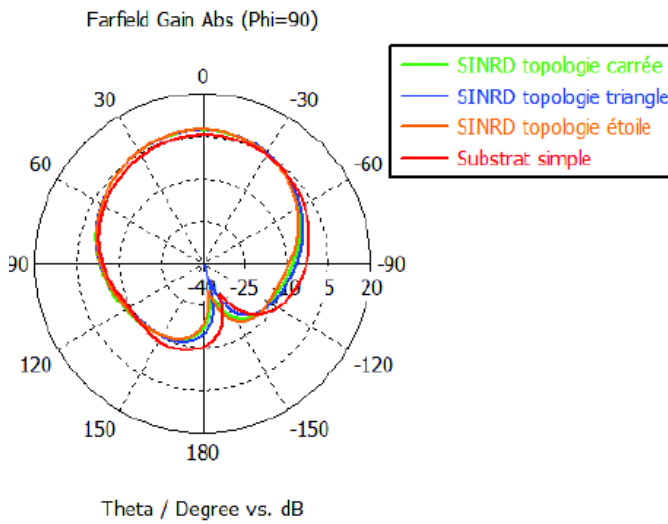


Figure 11. E plane far Radiation pattern of gain for $\Phi=90^\circ$ with for microstrip patch antenna with different substrate.

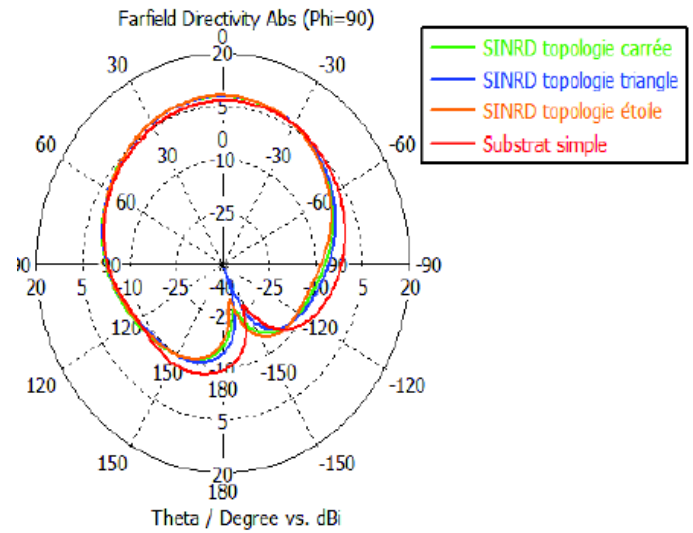


Figure 13. E plane far Radiation pattern of directivity for $\Phi=90^\circ$ with for microstrip patch antenna with different substrate.

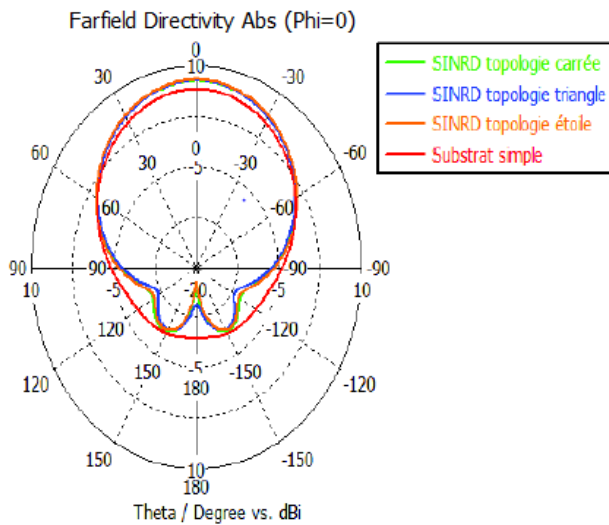


Figure 12. E plane far Radiation pattern of directivity for $\Phi=0^\circ$ with for microstrip patch antenna with different substrate.

The simulation results show that the main lobe direction for the gain and directivity are higher 7.34 dB of patch antenna with star lattice. The Table II summarizes the simulated results obtained with different configurations of microstrip patch antenna.

The electromagnetic wave transmission properties of the microstrip patch antenna show that all of the improvements are due to the SINRD structure substrate.

TABLE II. COMPARAISON TABLE FOR DIFFERENT STRUCTURE OF PATCH ANTENNA

Antennes	Parameter		
	S_{11} (dB)	Gain (dB)	Directivity (dBi)
Simple patch Antenna	-25,10	5.82	6.99
Patch antenna with square lattice	-42,7	7.14	7.8
Patch antenna with triangular lattice	-19	7.24	7.85
Patch antenna with star lattice	-24	7.34	8

By comparing the results obtained, we can observe a good adaptation for the four types of antennas at the desired frequency 5.8 GHz. We observe a minimum for the microstrip patch antenna with SINRD substrate square arrangement is -42.7 dB lower than the simple microstrip patch antenna which is -25.1 dB.

The results obtained by simulation of the microstrip patch antenna with SINRD substrate are approximately similar for the three configurations are very satisfactory compared with the simple microstrip patch antenna.

The diameter of air gap has an effect on the radiation efficiency and gain of the proposed antenna. The maximum directivity is obtained for the patch antenna with substrate SINRD star holes which is 8 dBi.

We also find that the patch antenna SINRD substrate with star arrangement gives better performances compared to those of the square and triangular arrangement.

From the results obtained and from the comparative study of the different configurations with the literature, it seems that the patch antennas conceived based on substrates SINRD gives better results in particular in terms of directivity and gain.

V. CONCLUSION

In this paper, we have simulated four structures of microstrip patch antenna, conventional antenna, patch antenna with SINRD substrate using different arrangement of the air holes, operate at 5.8GHz for DSRC application.

The SINRD substrate is used to reduce the surface wave of the microstrip patch antenna. The gain and directivity was improved using SINRD substrate in the different configurations.

REFERENCES

- [1] Claude CHANET : La route intelligente Centre d'études sur les réseaux, les transports l'urbanisme et les constructions publiques juillet 1998.
- [2] K.J. Button, J. Gifford, J. Petersen : L'TTS aux Etats-Unis et au Japon Dans le domaine du transport : Innovation technologique et société « Public works policy and outcomes in Japan and the USA », October 2001.
- [3] M.T. Islam, M.N. Shakin, High gain microstrip patch antenna , Eur.J.Sci.Res.32 (2)(2009) 187-193.
- [4] T.A. Denidni, N. Hassaine, Q.Rao, Broadband and high gain E-shaped microstrip patch antennas for high-speed wireless networks, Prog. Electrom. Res. C1 (2008) 105-111.
- [5] N. Ghassemi, J. Rashed-Mohassel, M.H. Neshati, S. Tavakoli, A high gain dual stacked aperture coupled microstrip antenna for wide band applications, Prog. Electrom. Res. E9 (2008) 127-135.
- [6] A. Sharma, A. Singh, Design of single pin shorted three-dielectric layered substrate rectangular patch microstrip antenna for communication system, Prog. Electrom. Res. Lett. 2 (2008) 157-1165.
- [7] V.K. Singh, A. Mittal, Design of wide-band microstrip antenna array at millimeter wave frequencies, Int. J. Infrared Millimeter Terahertz Waves 20 (2) (2000) , p, 277-283.
- [8] G. Vetharatnam, B.K. Chung, H.T. Chuah, Design of microstrip patch antenna array for airborne SAR application, J. Electrom. Wave Appl. 19 (12) (2005) ,p, 1687-1701.
- [9] Y. Cassivi and K. Wu, "Substrate integrated NRD (SINRD) guide on high dielectric constant substrate for millimeter wave circuits and systems," *IMS Dig.*, vol. 3, pp. 1639-1642, 2004.
- [10] Y. Cassivi and K. Wu, "Substrate integrated circuits concept applied to the nonradiative dielectric guide," *IEE Proc.-Microw. Antennas Propag.*, vol. 152, pp. 424-433, Dec. 2005.
- [11] Priyanka Mondal and Ke Wu, "A Leaky-Wave Antenna in Substrate Integrated Non-Radiative Dielectric (SINRD) Waveguide", IEEE TRANSACTIONS ON ANTENNAS AND PROPAGATION, VOL. 61, NO. 4, APRIL 2013.
- [12] Minh Thuy Le : Docteur à l'université de Grenoble Thèse de doctorat Contribution à la conception d'un système d'identification et de classification de véhicule par les ondes électromagnétique (may 2013).
- [13] G. Singh, Design considerations for rectangular microstrip patch antenna on electromagnetic crystal substrate at terahertz frequency, Infrared Physics & Technology 53 (2010).p. 17-22.
- [14] Aditi Sharma, G. Singh, D.S. Chauhan, Design Considerations to Improve the Performance of a Rectangular Microstrip Patch Antenna at THz Frequency, in: Proceedings of 33rd International Conference on Infrared, Millimeter and Terahertz Waves, 2008. (IRMMW-THz 2008), 15-19 September 2008, pp. 1-2.
- [15] Aditi Sharma, G. Singh, Rectangular microstrip patch antenna design at THz frequency for communication systems, J. Infrared Millim. THz. Wave 30 (1) (2009) 1-7.
- [16] D.B. Rutledge, D.P. Neikirk, D.P. Kasilingam, Integrated-circuit antennas, Infrared and Millimeter Waves Part II, vol. 10, Academic Press, 1983.
- [17] Constantine A.Balanis, Antenna Theory and Design. John Wiley & Sons, Inc., 1997.
- [18] Wu, K.: „Integration and interconnect techniques of planar and nonplanar structures for microwave and millimeter-wave circuits – current status and future trend“. Asia-Pacific Microw. Conf., Taipei, Dec. 2001, pp. 411-416.
- [19] Wu, K., and Boone, F.: „Guided-wave properties of synthesized nonradiative dielectric waveguide for substrate integrated circuits (SICs)“. IEEE Int. Microw. Symp., Phoenix, June 2001, Vol. 2, pp. 723-726.

FPGA Hardware Implementation of Image Processing technique

M.Kahlouche, M. D. Kedir-Talha, S.Ould Slimane and Zairi Hadjar

USTHB, LINS Lab, Faculty of Electronics and Computers, PO.Box 32, Bab-Ezzouar, Algiers
{kahlouche.marouan, malikakedir, Ouldelhadjsaliha, }@gmail.com, zairi_hadjer@yahoo.fr

ABSTRACT

Our paper describes a hardware implementation of two techniques for processing the image signal, and in particular filtering an image with a median filter and a convolution filter. The implementation is performed directly in VHDL language on the SPARTAN-3E board. We propose the hardware method which offers a parallelism allowing to answer the constraints of execution time and memory space.

Key Words: Hardware implementation, image processing, FPGA, VHDL.

1. INTRODUCTION

FPGA is the programmable logic circuit most commonly used today because of its capabilities, speed and flexibility. Its architecture generally mixes competing hardware and software components in order to respond most effectively to the imposed time constraint.

Moreover, the description of an architecture optimized in code synthesizable VHDL with a hierarchical and modular approach provides a good flexibility to the system [1].

The integration of embedded processing features on an FPGA brings several advantages. There is no fixed architecture implementation and therefore no obligation that the functions are performed by hardware rather than

software. There is therefore a wide range of possible solutions for every application, from the most general to the most specific. The FPGAs provide the very high performance of the hardware but with a simple and fast use by software configuration.

2. HARDWARE REALIZATION

In this part we present the software and hardware implementation of 2 image processing algorithms, the first is the windowing operator, and the second is the convolution operator "under VHDL.

A. Hierarchy of VHDL

Most hardware designers find it convenient to develop a hierarchy before any VHDL development. This is done to facilitate code reuse and to develop a common hierarchy. The use of specific hardware units of arithmetic and memory, has been limited to achieve interchangeability. These algorithms should be easy to use on Xilinx architectures.

B. Window Operator

To implement the first algorithm we need 3 VHDL entities: "_3x3.vhd", "trriage_3x3.vhd" and "counter.vhd" windows. Then we need a single entity "odf_filt_3x3.vhd" to make the grouping of these 3 previous entities and to ensure the proper functioning of the algorithm.

For the "Window Operator" filter to function properly, these three VHDL entities must be instantiated in the algorithm itself. This feature is done by "component, and port

```

entity odf_filt_3x3 is
port (...);
end odf_filt_3x3;

architecture odf_filt_3x3 of odf_filt_3x3 is

component triage_3x3
port (...);
end component triage_3x3;

component fenetre_3x3
port (...);
end component fenetre_3x3;

component counter
port (...);
end component counter;

begin

triage_3x3x : triage_3x3
port map (...);

fenetre_3x3x : fenetre_3x3
port map (...);

counterx : counter
port map (...);

end odf_filt_3x3;

```

Fig. 1. Filter hierarchy odf_filt_3x3.

map" using VHDL [2]. Fig.1 shows the VHDL design structure used for this algorithm.

Generation of the sliding window:

```
«window_3x3.vhd»
```

In order to implement a continuous tracking window system in VHDL, FPGA-specific FIFO units were used for the algorithm using the window generation architecture.

A 3x3 window size was chosen because it was small enough to be easily adapted on FPGA, and is considered large enough and effective for most useful sizes in image processing. With more large window sizes, more FIFOs and flip-flops should be used, which significantly increases the resources of FPGAs used. Fig.2 shows a graphical representation of the FIFO and flip-flop architecture used for this design, and Fig.3, its generation under Xilinx [3] .

Counter Implementation: "counter.vhd"

In order to do this correctly, counters are used to indicate to the algorithm when the boundaries begin.

Since images are two-dimensional data, two counters were needed: one to count rows and one to count columns in the picture [4,5,6]. A VHDL counter has been written to count the pixel motion as well as the data streams in the entity. The VHDL entity that

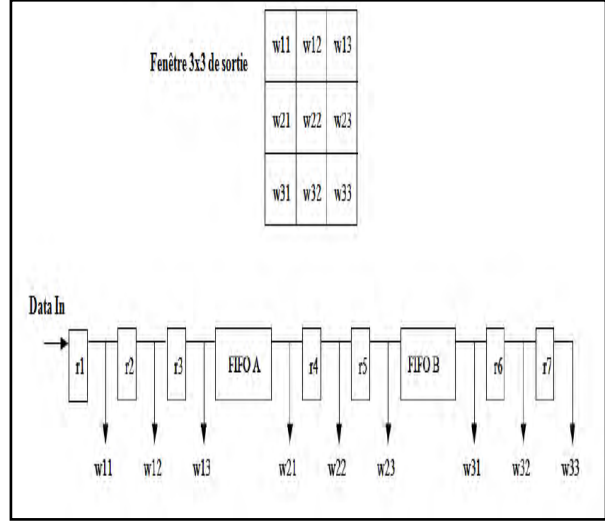


Fig. 2. Architecture of the window generator.

consists in sorting in ascending order the 9 values of the pixel window. It was necessary to find a suitable scheme for sorting these values with all possible probabilities.

This implementation uses registers and comparators for sorting 9 sliding window values of neighborhoods. Each RXY is a register and each CXY is a comparator (Fig. 4). This design is accomplished in VHDL using "if / else".

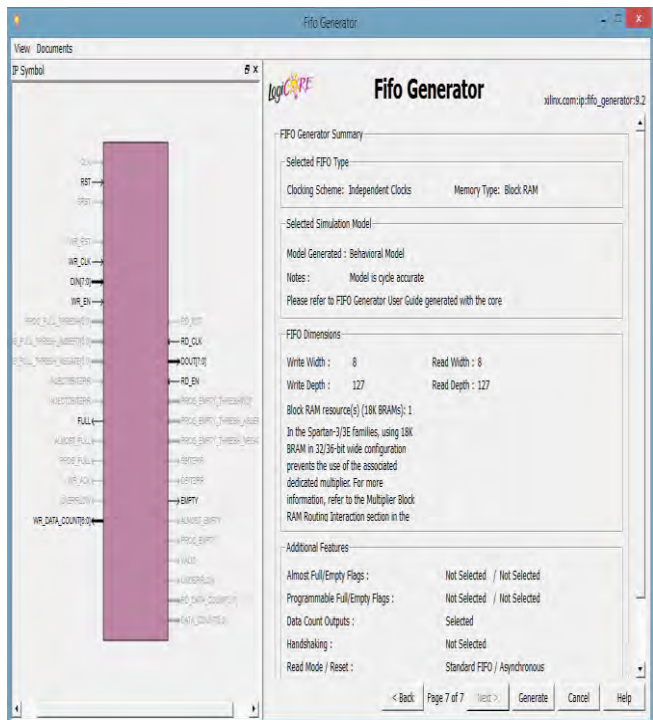


Fig. 3. FIFO entity under Xilinx.

```

if wx1 < wx2 then
  cx1_L <= wx1;
  cx1_H <= wx2;
else
  cx1_L <= wx2;
  cx1_H <= wx1;
endif;

```

Fig. 4. Operation of the comparator.

After that the output list is generated (the 9 values of the 3x3 window processed) with the VHDL sorting_3x3 entity, the algorithm describing the ranking filter functionality, `odf_filt_3x3.vhd`, can operate. At its output, the original pixel value changes according to the specific order of the filter.

C. Convolution Operator

The design of the convolution algorithm in VHDL was a much more difficult problem than the filing filter design. This was due to the use of more complex mathematics. For example, the output filtration filter, just the pixels of a window and at its output it replaces the original pixel by one of them, whereas the convolution algorithm employs adders, multipliers, And dividers to calculate its yield. On FPGA, the use of mathematics tends to slow down execution. Many designers favor techniques that reduce the dependence of the algorithm on complex mathematics. Since the mathematics used in convolution are simple, executing a convolution algorithm was a feasible goal [7, 8].

- *Generation of the Convolution Filter*

Another obstacle in the design of this algorithm concerns the implementation of the possibilities for manipulating negative numbers. In an appropriate convolution algorithm, the mask is composed of negative numbers. The masks in Fig.6 are an example.

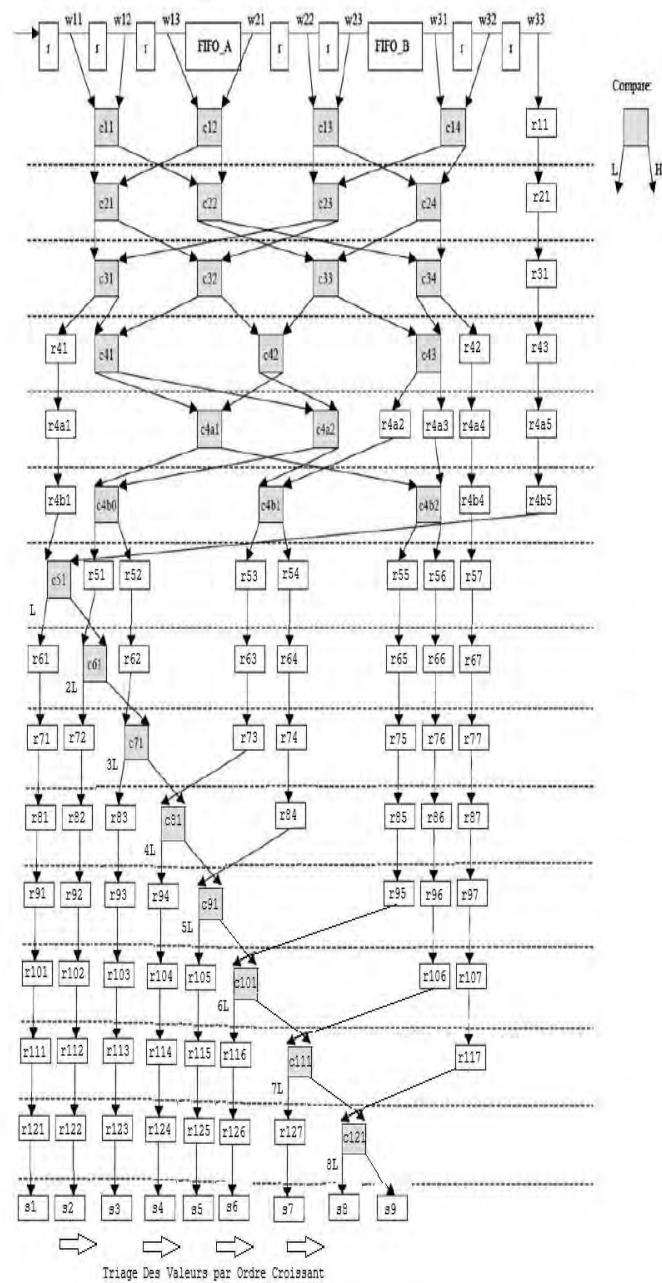


Fig. 5. Operation of the sorting filter.

In fact, the VHDL had to be written to manipulate these numbers using the signed data types.

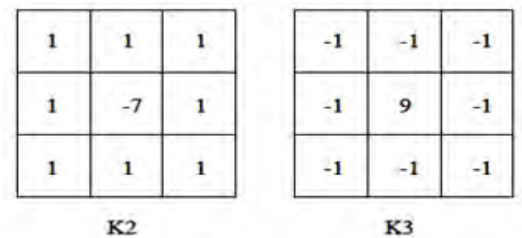


Fig. 6. Example of some masks using negative numbers..

Signed data simply means that a negative number can be interpreted.

The addition and multiplication were instantiated by simply using the "+" and "*" signs in VHDL.

Since an appropriate convolution implies a division by the number of pixels in the window, a certain trick has had to be put in this part of the execution of our algorithm. The hardware dividers on FPGAs are quite large and slow. In addition, they must be attached directly to the FPGA architecture. It was considered necessary to use the shift method instead of the division. Fig.7 shows a graphical representation of the mathematical operations of the convolution filter [9].

The VHDL execution of the convolution operator, called "conv_3x3.vhd", has a hierarchy that is similar to the hierarchy of the "odf_filt_3x3" windowing operator. It contains an instantiation of fenetre_3x3, that is, a counter that allows access to the mobile feature of Pixels window.

A. HDL TEST BENCH PROCESSES

In order to examine the correct functionality of the codes, the VHDL tool provides a device called: simulation. The simulation takes the VHDL code and simulates how it would work in the hardware. In order to do this correctly, the code designer must provide valid inputs to the simulator to produce the expected outputs.

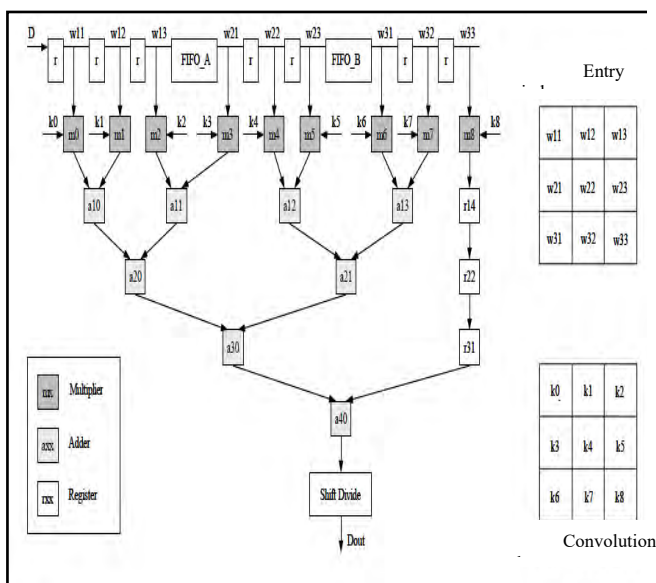


Fig.7. Convolution operation.

```

entity conv_3x3 is
  Port (...);
end conv_3x3;

Architecture conv_3x3 of conv_3x3 is
  Component fenetre_3x3
  Port (...);
  End component fenetre_3x3;

  Component counter
  Port (...);
  end component counter;

Begin
  Fenetre_3x3x : fenetre_3x3
  Port map (...);

  counterx : counter
  Port map (...);

end conv_3x3;

```

Fig. 8. Hierarchy of the filter conv_3x3.

The VHDL algorithm structure is shown in Fig. 8.

An efficient and common method of simulating codes on VHDL is the use of a special type of code called a test bench (VHDL_TEST_BENCH). The test benches effectively surround the VHDL code that the designer wishes to simulate and also provide the stimulus to the entity examined, (Fig.9).

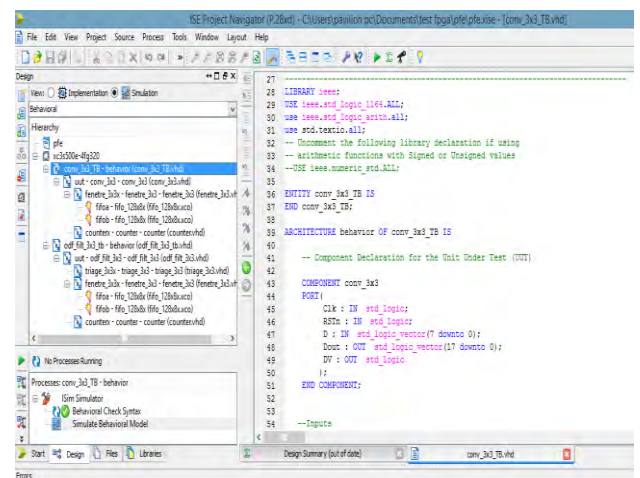


Fig. 9. Hierarchy of the test bench processor.

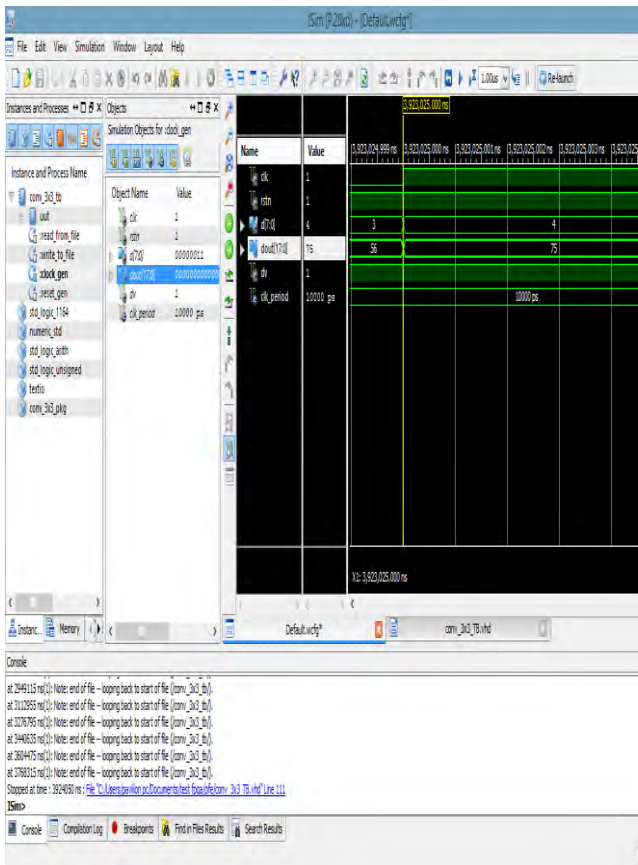


Fig. 10. Simulation of the convolution filter.

If you want to view the processed image, another device must be included in the test bench to allow file writing.

These devices are key to the profitability of the test benches used in the When you want

to process images with a VHDL algorithm, you first create a test bench that can read the folder containing the project, and are quite useful once paired with a program such as MATLAB, which provides effective image representation and viewing capabilities. A test bench for the file "odf_filt_3x3.vhd" and "conv_3x3.vhd", appropriately called "odf_filt_3x3_TB.vhd" and "conv_3x3_TB.vhd".

An example of simulation of the convolution filter is given in Fig.10.

3. TESTS AND RESULTS

Fig. 11 and 12 show comparisons between the VHDL and MATLAB algorithms for the two filters used.

The result of a convolution operation with K1 (left image of Fig. 11) results, after processing on FPGA (VHDL), gives the output (right image) of Fig. 11. It is clear that the information is saved.

The result is greatly improved for a window 4. Figure 12 shows on the left an image after the windowing operation and on the right the result of the VHDL output.

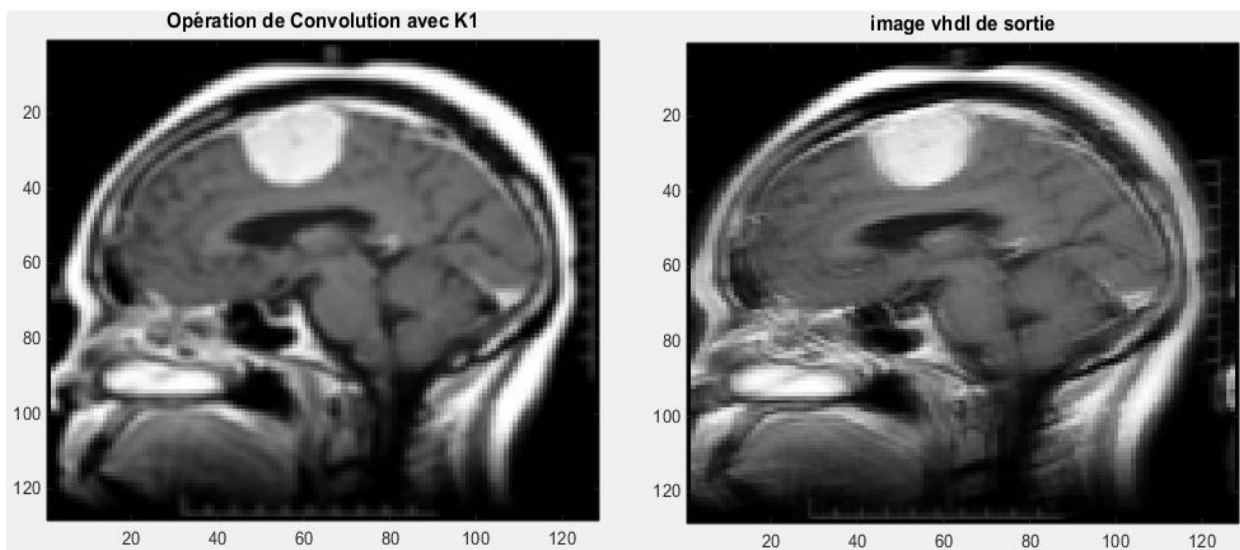


Fig.11. Comparison between the VHDL and MATLAB (left) algorithms of "conv_3x3" with gain = K1(right)

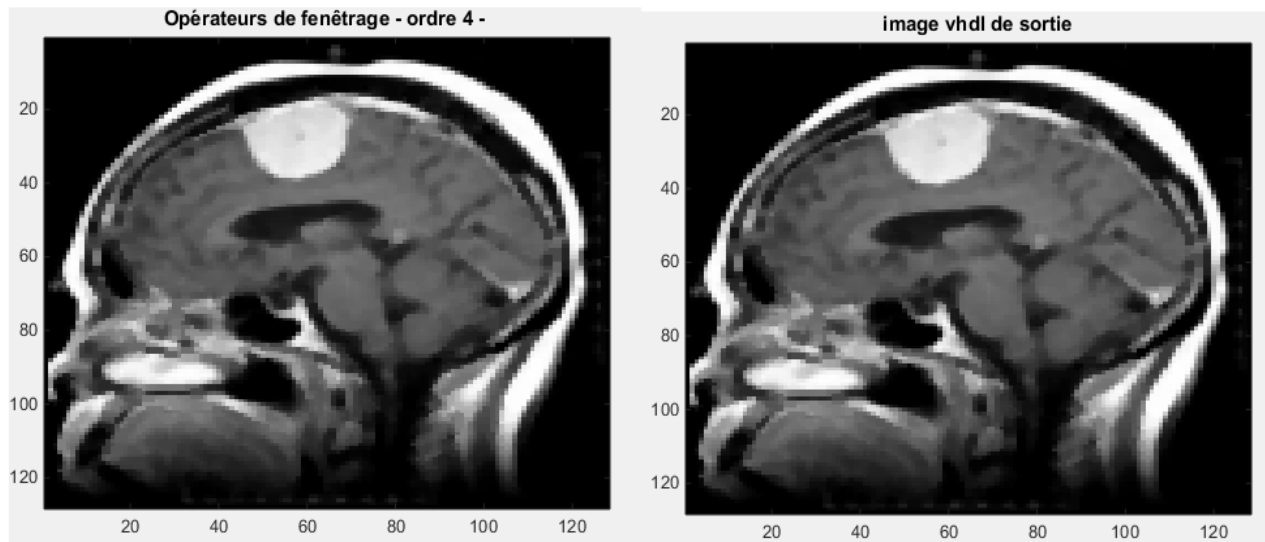


Fig. 12. Comparison of the "odf_filt_3x3" VHDL and MATLAB algorithms with order = 4.(left)Convolution operation with $K1$.(right)

4. CONCLUSION

FPGAs are often used for the prototyping of complex systems (eg SoC), as well as for systems dedicated to signal and image processing.

Hardware description languages such as VHDL or Verilog, usually used for FPGA development, are concurrent in nature. The programming in VHDL implies a good knowledge not only of the algorithm but also of the architecture of the FPGA and of the compiler used.

To better exploit the intrinsic parallelism of the algorithm, it must perform parallel processing tasks to satisfy time constraints.

In our article, we have a design that allows to implement an image signal processing equipment directly in VLDL language.

Spartan 3 to RAM memory compared to the large size of algorithms dedicated to image processing that requires powerful processing.

The goal is to keep the flexibility and flexibility of the process on the one hand and to take advantage of the material resources available in the FPGA.

REFERENCES

- [1] Kaiming He; Jian Sun; Xiaoou Tang "Single Image Haze Removal Using Dark Channel Prior" [IEEE Transactions on Pattern Analysis and Machine Intelligence](#) Vol: 33, Issue: 12, Dec. 2011
- [2] S. Asano, T.Maryama "Performance comparison of fpga, gpu and cpu in image processing" Proceeding Conference IEEE 19th International Conference on Field Programmable Logic and Applications, pp: 126-131, August 2009
- [3] B.Maliatski, O.Yadid-Pecht, "Hardware-driven adaptive kmeans clustering for real-time video imaging", IEEE TCSVT, Vol.15, Issue.1, 2005, pp. 164–166
- [4] T.Saegusa, T.Maruyama, Y.Yamaguchi, "How fast is an FPGA in image processing?", FPL 2008, pp.77-82.
- [5] R.C. Gonzales and R. E. Woods. "Digital Image Processing", Addison-Wesley, 2002.
- [6] Shao L, Yan R, Li X, Liu Y. From Heuristic Optimization to Dictionary Learning: A Review and Comprehensive Comparison of Image Denoising Algorithms. IEEE Transactions on Cybernetics. 2014; 44
- [7] Tan J, Ma Y, Baron D. Compressive Imaging via Approximate Message Passing With Image Denoising" IEEE Trans Signal Process. 2015; 63(8):2085–92.
- [8] Huang Y, Chen X, Zhang J, Zeng D, Zhang D, Ding X. Single-trial ERPs denoising via collaborative filtering on ERPs images. Neurocomputing. 2015.
- [9] 13. Luisier F, Blu T, Unser M. Image Denoising in Mixed Poisson Gaussian Noise. IEEE Trans Image Process. 20(3):696–708. 2011.

Amélioration des Performances d'une Antenne Patch avec Structures Tridimensionnelles à Bande Interdite Electromagnétique

Hadj Sadok Mustapha ¹, Lamhene Youssef ¹ and Berkani Samir ¹

¹USTHB, Laboratoire LINS, Faculté d'électronique et informatique, PO.Box 32, Bab-Ezzouar, Alger. mustaphahadjasadok@gmail.com, lamhene.y@gmail.com, sam-30@live.fr

ABSTRACT

This Dans cet article, nous présentons une antenne patch à deux éléments rayonnants pouvant être utilisée pour les applications sur la bande K. La performance de l'antenne est décrite avec l'intégration d'une structure 3D (3 dimensions) de bande interdite électromagnétique (BIE). Le réseau BIE se compose d'éléments qui sont disposés dans différentes forme placées au-dessus du patch d'antenne Après avoir comparé quelques structures, nous avons retenu celle présentant le gain le plus élevé et la directivité la plus directive possible.

An L'ensemble antenne et structure BIE a été optimisé pour obtenir en définitive une structure rayonnante compacte possédant une adaptation de - 36 dB et un gain réalisé de 16.5 dB à la fréquence de fonctionnement. À 21,6 GHz, l'antenne peut aussi être utilisée pour des services satellites avec des applications en systèmes de communications, télédiffusion, et télédétection ainsi que de nombreux systèmes de radars et radiomètres.

Key Words: Antenne planaire, BIE 3D, métamatériaux.

1. INTRODUCTION

Les antennes micro-ruban sont aujourd'hui très utilisées en raison de leur faible poids et de leur encombrement réduit. Cependant, elles possèdent une bande passante étroite typiquement de quelques pourcents et un gain modéré [1]. Depuis quelques années déjà, il a été montré que l'utilisation des structures BIE permettait d'améliorer les performances d'une antenne. Le succès des demi-matériaux BIE réside

dans le fait que ces matériaux sont associés de manière périodique et possèdent des plages fréquentielles pour lesquelles aucun mode ne peut se propager. Cette périodicité crée artificiellement un filtre spatial et un filtre fréquentiel qui peuvent être très intéressants pour la réalisation d'antenne [2]. L'objectif de ce travail est d'étudier l'apport du BIE sur les performances (gain, adaptation d'impédance, directivité). Différentes structures 3D avec différentes permittivités sont illustrées afin de voir leurs influences notamment sur le gain et la directivité ainsi que sur le coefficient de réflexion S11.

2. ANTENNE PATCH AVEC BIE

2.1. Antenne patch à deux éléments rayonnants :

L'élément rayonnant le plus utilisé est celui de forme rectangulaire Fig. 1, dont l'axe de symétrie passe par le point d'excitation. Ses dimensions sont la largeur w qui doit être inférieure à $\lambda g = \lambda_0/\sqrt{\epsilon_r}$ pour éviter les modes d'ordre supérieur et sa longueur L , légèrement inférieure à la demi-longueur d'onde dans le diélectrique équivalent ϵ_{eff} [3], [4], [5].

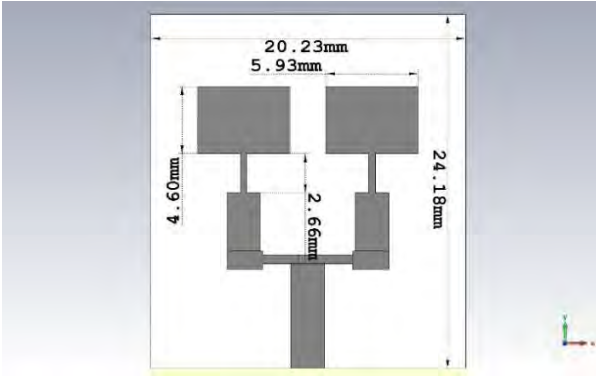


Figure.1: Antenne patch rectangulaire à deux éléments

La technique d'alimentation du patch dans Fig. 1. est discutée dans [5].

La largeur du patch est donné par :

$$w = \frac{1}{2f_r \sqrt{\mu_0 \epsilon_0}} \sqrt{\frac{2}{\epsilon_r + 1}} = \frac{v_0}{2f_r} \sqrt{\frac{2}{\epsilon_r + 1}} \quad (1)$$

Pour $w/h > 1$ la permittivité effective est donnée par la relation suivante :

$$\epsilon_{eff} = \frac{(\epsilon_r + 1)}{2} + \frac{(\epsilon_r - 1)}{2} \left[1 + 12 \frac{w}{h} \right]^{-1/2} \quad (2)$$

L'extension de la longueur du patch est donnée par :

$$\frac{\Delta L_{eff}}{h} = 0.412 \frac{(\epsilon_{eff} + 0.3) \left(\frac{w}{h} + 0.264 \right)}{(\epsilon_{eff} - 0.258) \left(\frac{w}{h} + 0.8 \right)} \quad (3)$$

$$L = \frac{1}{2f_r \sqrt{\mu_0 \epsilon_0 \sqrt{\epsilon_{eff}}}} - 2\Delta L \quad (4)$$

L'impédance caractéristique d'un transformateur quart-d'onde est :

$$Z_T = \sqrt{Z_a + 50} \quad (5)$$

$$Z_a = 90 \frac{\epsilon_r^2}{\epsilon_r - 1} \left(\frac{L}{w} \right)^2 \quad (6)$$

La largeur de la ligne de transition :

$$Z_T = \frac{60}{\sqrt{\epsilon_r}} \ln \left(\frac{8d}{w_t} + \frac{w_t}{4d} \right) \quad (7)$$

La longueur d'un transformateur peut être calculé par :

$$\lambda_T = \frac{\lambda_0}{4\sqrt{\epsilon_{eff}}} \approx \frac{\lambda_0}{4} \quad (8)$$

Pour deux antennes patch, le schéma électrique équivalent qui prend en compte le couplage entre les patches est montré dans Fig. 2. Les éléments qui caractérisent le couplage sont Cc2 et Cc1.

Le modèle que nous proposons est constitué de deux circuits électriques équivalents d'antennes patches. Chaque circuit électrique équivalent d'antennes est constitué d'un circuit RLC en parallèle (une résistance R1, une capacité C1 et une self L1) représente la première antenne, en parallèle avec (une résistance R2, une capacité C2 et une self L2) représente la deuxième antenne, les deux antennes sont identiques ($R1=R2=R$, $C1=C2=C$ et $L1=L2=L$), les éléments qui caractérisent le couplage sont Cc2 disposé horizontalement et Cc1 disposé verticalement [6] [7].

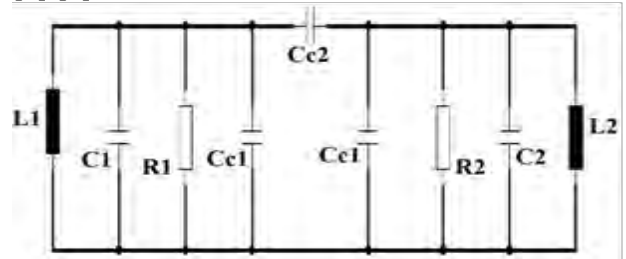


Figure.2: Circuit électrique équivalent de deux patches

2.2. Fonctionnement d'une antenne BIE 3D

Les structures tridimensionnelles, comme leur nom l'indique, sont des structures dont la constante diélectrique est structurée périodiquement dans les trois directions. Cette section résume plusieurs applications typiques de BIE dans la conception d'antennes dans l'espoir de stimuler les discussions et de nouvelles voies de recherche dans ce domaine. On va discuter les caractéristiques d'une antenne patch avec différentes structures BIE (3D) au-dessus sans tenir en compte la bande interdite électromagnétique Fig. 3.

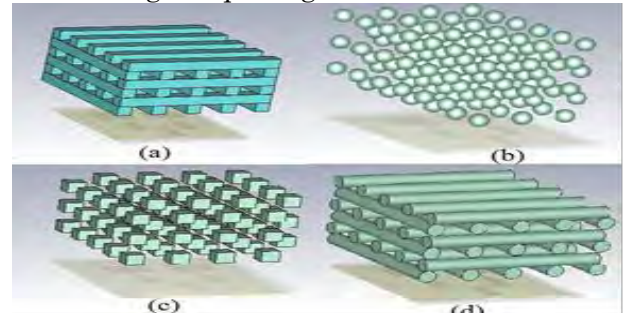


Fig.3: Structures BIE : (a) Tiges, (b) Boules, (c) Cubes et (d) cylindre

Une étude paramétrique a été réalisée pour cette antenne, y compris les structures et les espacements BIE. Le fonctionnement d'une antenne BIE repose sur un mode de structure qui a une fréquence de coupure fixée par la résonance longitudinale entre le plan de masse et le demi-matériau BIE. Cette fréquence de résonance fondamentale qui donne la fréquence de fonctionnement de l'antenne est fonction de la hauteur h du résonateur et du coefficient de réflexion du demi-matériau BIE (ϕ_{SUP} et R_{SUP}) comme cela est montré avec (9) [8]. Ce dernier, influence également le facteur de qualité Q , qui conditionne les performances de la structure. La cavité Fig. 4 a une épaisseur de $\lambda_0/2$ et la structure BIE est constituée de $2n$ couches diélectriques de différentes permittivités et d'épaisseur $\lambda g/4$. Les couches diélectriques sont séparées horizontalement par des couches d'air, également d'épaisseur $\lambda_0/4$. λ est la longueur d'onde pour laquelle l'antenne fonctionne [9].

Le système est totalement caractérisé par les vecteurs de réseau, les constantes diélectriques des formes BIE et du milieu entourant.

$$h = \frac{\lambda}{2} \left(\frac{\phi_{SUP} + \phi_{INF}}{2\pi} \right) \approx \frac{\lambda_0}{2} \quad (9)$$

$$f_0 = \frac{c}{2h} \left(\frac{\phi_{SUP} + \phi_{INF}}{2\pi} \right) \quad (10)$$

$$Q = \frac{\sqrt{R_{SUP}}}{1 - R_{SUP}} \left(\frac{\phi_{SUP} + \phi_{INF}}{2} \right) \quad (11)$$

ϕ_{SUP} et R_{SUP} : respectivement la phase et le module du coefficient de réflexion de l'interface supérieure (demi-matériau BIE).

ϕ_{INF} : la phase de l'interface inférieure (égale à π dans le cas d'un plan de masse métallique).

h : hauteur de la cavité.

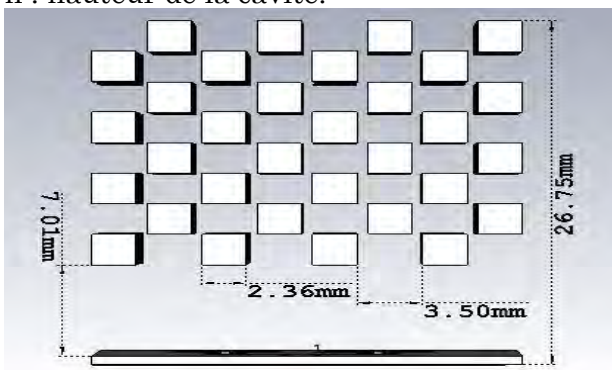
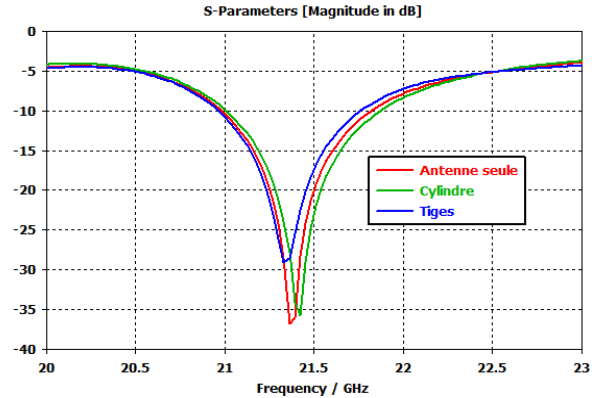


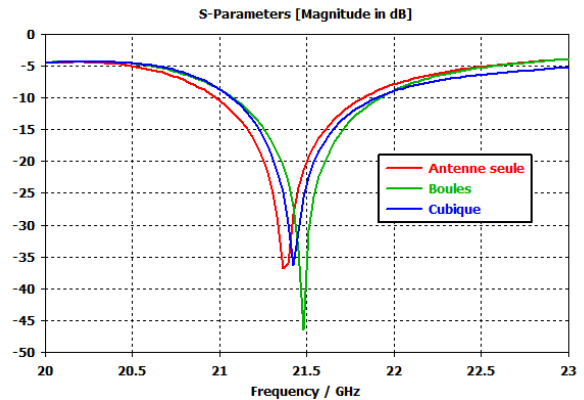
Figure.4: Structure de base d'une antenne BIE 3D

3. SIMULATION ET RESULTATS

Une simulation antennaire a été effectuée à l'aide du logiciel CST Microwave Studio.



(a)



(b)

Figure.5: Comparaison des paramètres S d'une antenne patch avec différentes structures BIE, (a) : (antenne seule, Cylindre et tiges), (b) : (antenne seule, boules et cubes)

Les résultats présentés ci-dessous Fig. 5 sont issus de la simulation. L'antenne seule a une fréquence de résonance = 21.36 GHz et offre un gain de 12.3 dB, une bande passante de largeur 0.84 GHz (20.97-21.82 GHz) où le coefficient de réflexion $S_{11} = -36.8$ dB, l'ajout des structures BIE au-dessus de l'antenne agit sur la fréquence de résonance, on observe le décalage fréquentielle de quelques dizaines de MHz.

La figure 6 révèle la variation du Gain en fonction de la constante diélectrique pour chaque structure BIE, on remarque que le gain des BIE tiges et cylindre diminuent progressivement en augmentons leurs permittivité électrique tandis que le gain des BIE boule augmente de quelques dB. Pour = 10.2, l'intégration de BIE cubique a nettement amélioré les performances de l'antenne et offre un gain de l'ordre de 16.5 dB

à la fréquence de résonance = 21.6 GHz, une largeur de bande de 0.84 GHz où le coefficient de réflexion $S_{11} = -36$ dB.

Sachant qu'en 3D, il y a un nombre infini de géométries possibles. Mais, en particulier on ne s'intéresse pas à celles qui avantagent l'existence d'une bande interdite complète ou quasi-complète.

Normalement, plus grand sera le constante diélectrique, plus grande sera la probabilité que la structure de bandes s'ouvre. Ce fait est dû à la diffusion plus forte de la puissance. Maintenant on peut se demander si chaque géométrie d'une permittivité électrique assez grande aura la même diffusion d'énergie. Pour les structures 2D, c'est presque le cas, à moins que les tiges carré offre une BIE plus large que celle de tiges cylindriques. Mais pour les structures 3D, c'est beaucoup plus difficile, pour deux structures différente (Tiges – Cube) la variation du gain est inversement proportionnelle, ce qui signifie que plus la constante diélectrique du BIE est élevé plus l'espacement d'air entre les formes joue un rôle important sur l'entrelacement des faisceaux.

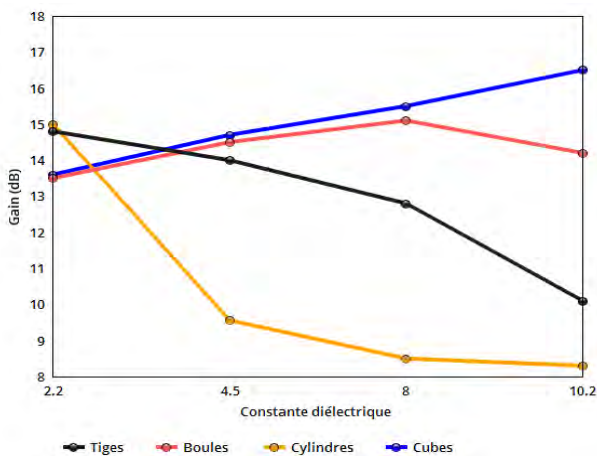


Fig. 6. Comparaison du gain réalisé de l'antenne patch avec différentes structures BIE et constantes diélectrique

Une autre figure Fig. 7. représente la directivité de l'antenne dans le plan E et H, elle est de l'ordre de 16.6 dBi. Les angles φ et θ , connus des coordonnées sphériques (φ représente l'angle avec l'axe X dans le plan XY, θ représente l'angle avec l'axe Z).

Dans les deux plans, la différence entre les deux simulations est faible. Aussi on remarque que dans le plan XZ la directivité est beaucoup plus symétrique autour $\theta = 0$

que dans le plan YZ. Ce fait, on peut expliquer à partir de l'asymétrie dans ce plan causée par l'alimentation, car la ligne micro ruban présente une asymétrie qui génère des modes d'ordres supérieurs produisant un rayonnement de polarisation croisée, pour y remédier à cet état de fait l'alimentation par fente est une solution alternative.

Un couplage électromagnétique est introduit à travers une petite fente réalisée dans le plan de masse qui sépare deux substrats l'un portant l'élément rayonnant et l'autre la ligne micro ruban, cette configuration permet une optimisation indépendante entre la ligne d'alimentation et le patch, facile à modéliser et présente un rayonnement parasite modéré. Cependant, elle est la plus difficile à mettre en œuvre et présente une bande passante étroite.

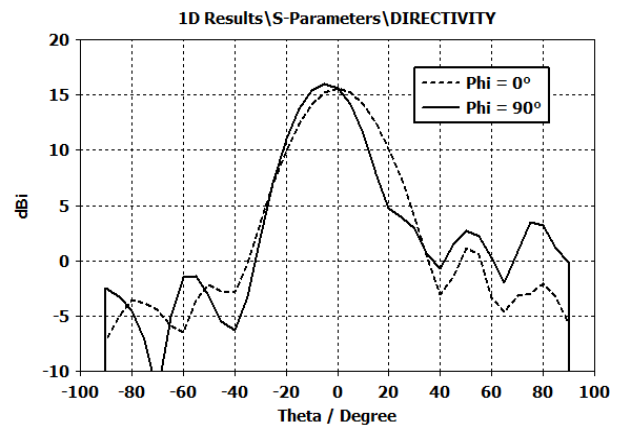


Fig. 7: Diagramme de rayonnement de l'antenne rectangulaire avec BIE cubique.

Le tableau suivant montre l'évolution du gain en fonction de la permittivité électrique pour chaque structure BIE, la variation de la constante diélectrique agit différemment sur le gain et la directivité de chaque structure. Cette augmentation n'aura pas d'effet au-delà de certaine valeur.

Constante dielectric (ϵ_r)	Antenne seule (dB)	Structures BIE (Gain (dB))			
		Tige	Boule	Cylindre	Cube
Arlon Cu 217LX (2,2)	12.3	14.8	13.5	15	13.6
Arlon AR 450 (4,5)		14	14.5	9.56	14.7
ESL 41020-70C (8)		12.8	15.1	8.5	15.5
Rogers RO3210 (10,2)		10.1	14.2	8.3	16.5

Avec les BIE cubique ; la directivité Fig. 8. devient plus étroite. Par conséquent, le gain de augmente d'environ 4.2 dB.

On observe l'apparition des lobes secondaires, mais ils sont assez petits. Aussi au niveau de la directivité, les résultats avec une structure BIE de couches infinies sont peu meilleurs qu'avec des couches BIE fini. Mais il y a seulement une différence de quelques dixièmes de décibels, donc en pratique négligeables.

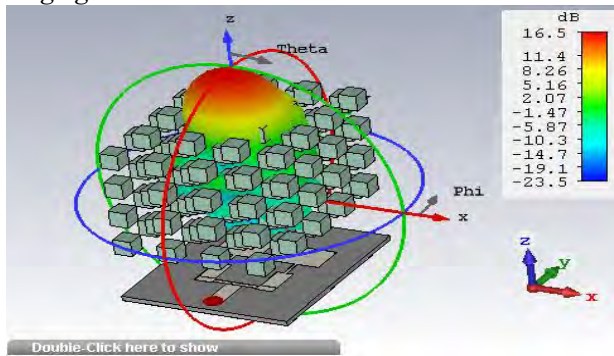


Fig.8 : Diagramme de gain 3D calculé avec CST pour un réseau carré tridimensionnel de 8 couches de forme cubique

Avec quatre couches la réflexion n'est pas trop bonne. Aussi la directivité est moins performante. L'antenne ne peut pas bien se coupler à la cavité construite par le plan métallique et la structure BIE. C'est à cause du fait que quatre couches diélectriques ne sont pas assez pour former un miroir de basse transmission, nécessaire pour obtenir une cavité qui fonctionne comme la cavité Fabry-Pérot. La cavité a de grandes pertes et un bas facteur de qualité. Avec 8 couches la réflexion est encore meilleure qu'avec deux, l'antenne est encore mieux couplée à la cavité. La directivité devient de plus en plus étroite et son gain plus élevé. L'antenne présente un diagramme de rayonnement permettant un rendement optimal de l'ensemble avec des lobes secondaires faibles.

4. CONCLUSION

Les résultats s'avèrent relativement concluants et montrent qu'une antenne patch avec BIE de forme cubique au-dessus a une performance nettement améliorée par rapport à une antenne patch puisque de forte directivité et gain sont constatés.

L'antenne avec BIE occupe un volume réduit de 26.75 mm × 20.23 mm × 24.18 mm. A

partir des résultats, il est observé que le gain maximal obtenu est de 16.5 dB, une directivité de 16.6 dBi, une largeur de bande de 0.84 GHz où l'adaptation est de - 36 dB.

Aussi la structure inverse, des formes d'air dans un milieu diélectrique, est une bonne possibilité à considérer mais la simulation n'a pas donné de bonnes résultats.

L'antenne est d'ordre technologique et se rapporte à la possibilité d'usiner des cubes diélectriques suivant leurs épaisseurs, si possible de manière constante sur des dimensions importantes. La précision à tenir est réellement délicate. La technologie LTCC (Low Temperature Co-fired Ceramic) est une bonne alternative comparée aux technologies planaires classiques, de micro-usinage sur silicium. De plus, les procédés de fabrication de cette technologie multicouches sont maintenant établis. Elle présente d'excellentes précisions de fabrications, des solutions d'intégration 3D et des coûts de fabrication à grande échelle modérés.

REFERENCES

- [1]. Moustapha SALAH TOUBEH "Etude d'antennes BIE planaires de hauteur très inférieure à la longueur d'onde dite : *The ULP EBG Antennas* ". Thèse de doctorat N° 92-2011, ED S2I : Sciences et Ingénierie pour l'Information, faculté de science et technique, université de Limoges, Année : 2011.
- [2]. Eric Arnaud "Contribution à la conception d'antennes B.I.E métalliques à polarisation circulaire alimentées par cornet". Thèse de doctorat N°17-2010, ED N° 521: Sciences et Ingénierie pour l'Information, faculté de science et technique, université de Limoges, Année : 2010.
- [3]. F. Abboud, J.P. Damiano, and A. Papiernik, " *Rectangular microstrip antenna for CAD* ", IEEE Proceedings, Vol.135, Pt H, N°.5, pp. 323-326, October 1988.
- [4]. E. H. Newman, and P.Tylyathan, " *Analysis of microstrip antennas using moment methods*", IEEE Transaction on Antennas and Propagations, Vol. AP-29, N°. 1, pp. 47-53, January 1989.
- [5]. Antennas from Theory to Practice/ Yi. Huang and K. Boyle, John Wiley & sons 2008, ISBN 978-0-470-51028-5.

- [6]. N. I. Dodov1 and P. Z. Petkov, "*The surface waves impact on the coupling effect in microstrip antennas,*" 37th International Conference on Information, Communication and Energy Systems and Technologies, ICEST, Nis, Yugoslavia, pp. 6-7, October 1-4 2002.
- [7]. A. Hafiane, H. Aissat and O. Picon, "*Simple electrical model to calculate patch array antenna S-parameters,*" Electronics Letters Vol. 39, N°. 14, pp. 1031-1033, 10 July 2003.
- [8]. R. SAULEAU, "*Fabry-Perot Resonators*", Encyclopedia of RF and Microwave Engineering, John Wiley & Sons Ed., 2005.
- [9]. R. CHANTALAT. " Optimisation d'un réflecteur spatial à couverture cellulaire par l'utilisation d'une antenne à bande interdite électromagnétique multisources ". Thèse de doctorat n° 36-2003, U.E.R. des Sciences, Université de Limoges, novembre 2003.
-

An Optimized Hybrid Junction Multi-band Rectifier for Harvesting RF Energy

Ali BENAYAD¹ and Mohamed TELLACHE²

¹ USTHB, LINS Lab, Faculty of Electronics and Computers, PO.Box 32, Bab-Ezzouar, Algiers
abenayad@usthb.dz

² USTHB, LINS Lab, Faculty of Electronics and Computers, PO.Box 32, Bab-Ezzouar, Algiers
tellachemoh@yahoo.fr

ABSTRACT

In this paper, we propose a multi-band rectifier design based on hybrid junction technology for harvesting radiofrequency energy. The suggested rectifier is optimized to operate at four popular ambient frequencies GSM-1800GHz, UMTS-2100GHz, WiFi -2.45GHz and 2.6GHz-4G bands. The achieved design was able to function as one to four bandpass filter as a result of optimizing each transmission line of the hybrid junction ring to obtain its own characteristic impedance and electrical length. Beside of reducing 23.6% of the overall size compared to literature, the proposed design simulations satisfy the energy harvesting applications requirements for each signal band, broadband and multi-band ambient energies, where the output voltage across the resistive load will be eight times multiplied due to the four stages voltage doubler.

Key Words: Radiofrequency, Energy harvesting, Optimized hybrid junction, Multi-band, Voltage doubler.

1. INTRODUCTION

The 21st century has seen the speediest technological growth, where researchers over the globe needed to concoct an adaptable and most importantly an innovative solutions to enhance the autonomy of supply systems for low power electronic devices without influencing their embeddability. The issue was raised to the surface for the simple reasons that batteries and customary supply

systems have failed to answer to distant correspondence and incorporated electronic devices necessities under brutal living conditions and in remote and isolated regions. In this context, harvesting ambient RF (Radiofrequency) energy vitality have sparkled as an essential, attractive and above all a creative solution in order to improve and broaden their efficiency which serves out their productivity and makes them less dependent.

The fundamental idea of Rectenna (Rectifying-Antenna) circles around utilizing an antenna to retrieve the surrounding RF power and afterward converting it to valuable DC power by means of its key part, the rectifier. Naturally, so as to expand the measure of the collected RF energy, the utilization of wideband or multi-band antennas is by all accounts the most fitting methodology (see figure 1). However, it would be totally pointless without improving the rectifier's effectiveness.

Several attempts were made to ameliorate the rectifier's efficiency such in branch-line coupler use to accomplish the broadband behavior [1], or the use of hybrid junction, which is utilized as a power divider in order to achieve multi-band function [2]. Although, designing a multi-band and efficient rectifier with a sufficient output voltage that has to be imprinted on a small size layouts is a significant challenge, Nevertheless, the proposed designs in [2] [3] [4] exhibit some disadvantages either on the extent of the rectifier [5] or on the output voltage level.

In our work, a quadri-band rectifier based on the optimized hybrid junction is conceived to work at the GSM-1.8 GHz, UMTS-2.1 GHz, Wi-Fi-2.45 GHz, 4G-2.6 GHz frequencies. The rest of the article is organized as follows. Section 2 is dedicated to detail the ABS's of the proposed quadri-band rectifier based on hybrid junction design. Simulations and results are shown and discussed in section 3. Finally, we end the paper by a conclusion.

2. RECTIFIER DESIGN

The rectifier circuit is designed based on the optimized 180° hybrid junction ring coupler [5]. Generally, the hybrid junction ring comes at an extensive size and a narrow bandwidth and it is usually used for RF signal synthesis, isolation and division [2].

The basic idea of our work was inspired from Li Z and al [5] paper, where each transmission line of the hybrid junction ring will function as a bandpass filter at the chosen operating frequencies. Denoted as E, O1, O2, O3 and O4, the access of the optimized hybrid junction refers to the sum entrance and output ports respectively, where the signal at the sum entrance will be divided and filtered according to the bandwidth of each output branch of the optimized hybrid junction ring. In our work,

we extended the topology of the optimized hybrid ring junction in order to rectify and harvest the most existing four aforementioned ambient frequencies energy that maintain and guarantee an embeddable size of the energy retrieving antenna (1.8GHz-GSM, 2.1GHz-UMTS, 2.45 GHz-WIFI, 2.6GHz-4G), hence, the rectifier's efficiency is increased as same as the harvested output voltage.

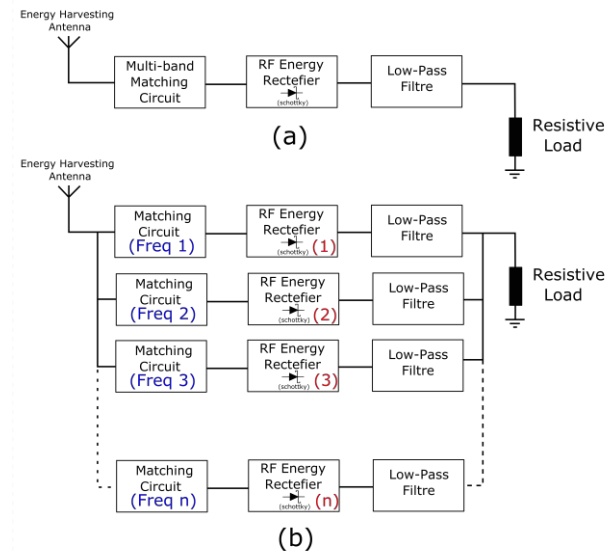


Figure. 1: Multi-band Rectenna topologies: (a) Mono/multi or wide bandpass RF filter with one rectifier antenna, (b) Multi-band Rectenna with separated rectifiers

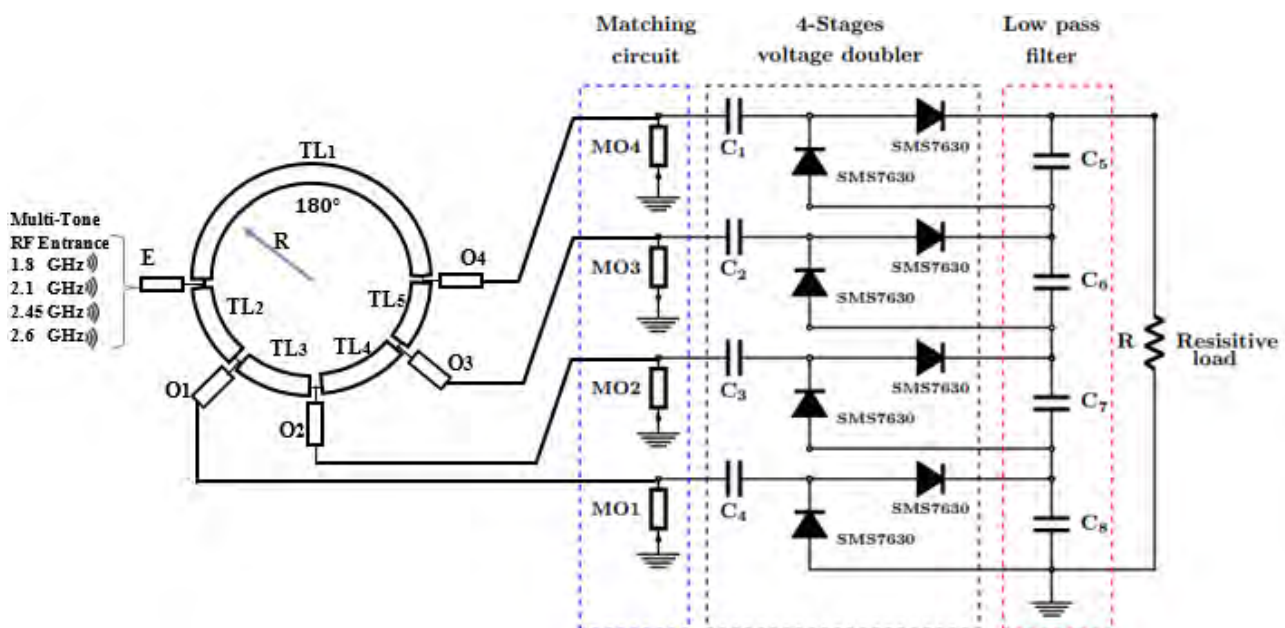


Figure.2: Schematic of the quadri-band optimized hybrid junction ring rectifier

As shown on the schematic depicted in Figure 2, the mixed reaped RF power enters the circuit via the 1st optimized transmission line E (Multi-Tone Signal Entrance) and will be filtered and divided on the four output transmission lines branches O1,O2,O3 and O4 respectively of the optimized hybrid junction each to its corresponding frequency, then we followed the branches by an impedance matching circuit, a Voltage doubler based on HSMS SMS 7630 Schottky diode at each branch and a low pass filter which attempts to block the harmonics, isolate the resistive load from the RF signal and act as a DC filter and finally, a resistive load. The SMS 7630 Schottky diode was chosen because of its fast transit response and its low threshold voltage, which makes it perfect for high frequency application.

The rectifier is designed on an overall dimension of 62.5mmX 55.6mm including the filters and the voltage doublers which is 23.6% smaller than the designs in found in the literature [2] [5].

At the end of each branch of the optimized hybrid junction, a Short-Circuit matching stubs (MO1, MO2, MO3 and MO4 Respectively) are matching the branches each at a specific operating frequency. In order to multiply the harvested DC output voltage, the voltage doublers are stacked together at the same polarity, thus, the output voltage is eight times multiplied across the resistive load.

Since the main objective of our work is mostly to provide an alternative solution to the conventional supplying systems, this by reducing the consumed energy cost for low consuming electronic devices, moreover, diminishing the rectifier's manufacturing cost. For this end, we sought to utilize a popular and low-cost substrate material to concept the desired design on: FR4, with a relative permittivity of 4.3 and 1.58 mm of thickness.

3. SIMULATIONS AND RESULTS

The first steps of followed methodology were to modify and tune the original form of the hybrid junction ring by optimizing the electrical length and the width of each of all its transmission lines, therefore, the final

obtained optimized hybrid ring junction have achieved the filtering and dividing behavior as needed at the four operating frequencies to perform the optimization, we exploited Keysight Advanced Design System 2016 tool, where the primer goals limitations states at the schematic design were set and accomplished while considering the overall size miniaturization aim. The next stage was to match the rectifying circuits with our optimized hybrid junction output branches each at its operating frequency. Once the simulations are completed, a board layout design is built and simulated on Momentum to analyse its compartment and create a lookalike lumped component model that will mimic the examined behaviour and uses it at the Co-simulation to confirm the results. EM Co-simulation has been proved to be an accurate tool that verifies the performance of such schematic designs [6]. The generated lumped model is then transferred to a new schematic area, where we put the final design into evaluation afterwards we compared the final and the primer obtained results.

Table.1 Dimensions of the final layout for the proposed quadri-band rectifier

Transmission Line	Length (mm)	Width (mm)		
E	Le	6.17	We	2.5
TL1	L1	10.5	W1	2.5
TL2	L2	11.5	W2	0.82
TL3	L3	10.6	W3	2.6
TL4	L4	11.25	W4	0.9
TL5	L5	43.5	W5	1.7
O1	Lo1	6.98	Wo1	3.98
O2	Lo2	6.4	Wo2	0.5
O3	Lo3	24.96	Wo3	0.5
O4	Lo4	10.2	Wo4	0.5
MO1	Lm1	8.4	Wm1	2.56
MO2	Lm2	6.8	Wm2	2.51
MO3	Lm3	7	Wm3	2.53
MO4	Lm4	7	Wm4	2.51
Rectifier's T-Line	Lr	8.1	Wr	0.84

Figure 3 illustrates the final design of the quadri-band rectifier's layout. This outcome was generated after fixing the resistive load R value at 4KOhm, the low-pass filter capacitors C5, C6, C7 and C8 each at 10 nF each and the rectifier's capacitors C1, C2, C3 and C4 all at 100 pF each. The final layout's dimensions of the optimized hybrid ring quadri-ban rectifier are mentioned in Table 1.

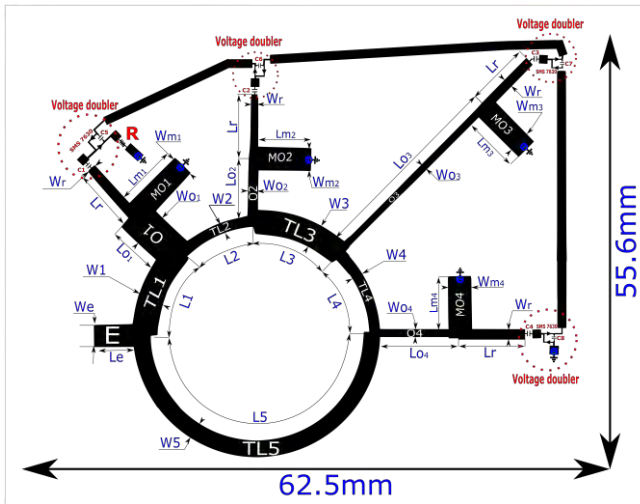


Figure.3: Schematic and dimensions of the final layout of the optimized hybrid junction Quadri-band rectifier

The return loss of the simulated schematic design and the co-simulated layout design are properly matched as portrayed in figure 4. During the simulations, we obtained a return loss S_{11} of -18 dB at 1.8GHz, -21.5 dB at 2.1GHz, -15 dB at 2.45 GHz and -14 dB at 2.6GHz whereas we achieved a -22.5 dB at 1.8GHz, -23.5 dB at 2.1GHz, -12 dB at 2.45 GHz and -13 dB at 2.6GHz for Co-simulations.

In order to verify the validity of the proposed rectifier, we introduced a multi-tone signal of our four operating frequencies at the entrance E with the amplitude of 1V. The rectifier's output voltage over time is shown in the figure 5.

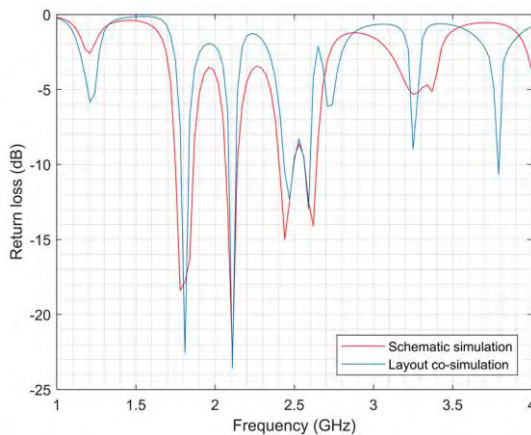


Figure.4: Simulated and Co-simulated return loss of the quadri-band optimized hybrid junction rectifier

In table II we demonstrate the comparative results we obtained for our proposed

optimized junction ring with the works that inspired our research, wherein our work, the proposed rectifier covers four bands on a smaller layout surface and low-cost materials. Compared to the literature, our proposed approach showed a clear improvement to recently suggested architectures, in which, one more frequency band has been explored and rectified which increases the final output voltage.

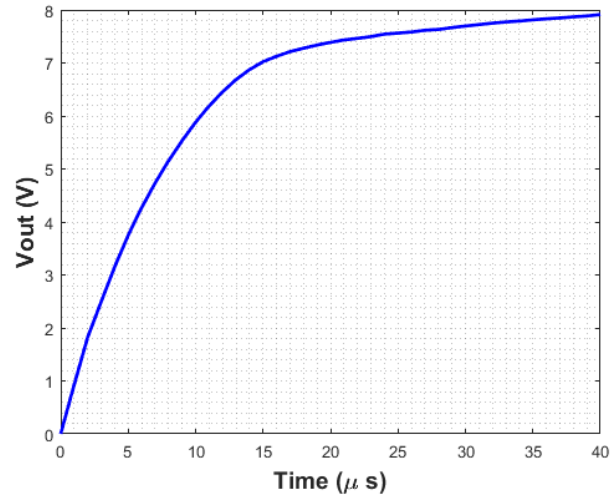


Figure.5: Simulated output voltage across the resistive load in function of time

TABLE.2 COMPARISON WITH PREVIOUS WORKS

Registered Designs	Reg Operating Frequency Bands (GHz)	Overall Size (mm ²)	Output Voltage Multiplication
Sun and al	1.8 & 2.1	144 X55	2
Takhadmit and al	1.8 & 2.45	77 X 98	3
Li Z and al	1.8, 2.1&2.41-2.59	70X65	6
This work	1.8,2.1, 2.45 & 2.6	62.5X 55.6	8

4. CONCLUSION

In this work, we proposed an optimized multi-band hybrid junction RF-DC rectifier. The conceived rectifier has achieved the performance of one to four band-pass filtering by tuning the electrical length and the characteristic impedance of each of its transmission lines. The SMS 7630 Schottky diode was chosen as the main element of the four-stage voltage doubler that was combined

at four stages and matched to the optimized hybrid ring each branch at its specific operating frequency in order to increase the harvested DC voltage.

ACKNOWLEDGEMENTS

The authors would like to thank the Ministère de l'Enseignement Supérieur et de la Recherche Scientifique, Algerian Government.

REFERENCES

- [1] Z.XY, D.ZX and X.Q. "High-efficiency broadband rectifier with wide ranges of input power and output load based on branch-line coupler," *IEEE Trans. Circuits Syst. I Regul Pap.* 2017; 64 (3):731–739.
- [2] Takhedmit. H, Cirio .L, Z .Saddi, Lan Sun Luk JD, O.Picon. "A novel dual-frequency rectifier based on a 180° hybrid junction for RF energy harvesting," 2013 7th European Conference on Antennas and Propagation (EuCAP), Gothenburg, 2013, 2472– 2475.
- [3] Sun.H, Guo. YX, He.M and Zhong.Z. "A dual-band rectenna using broadband yagi antenna array for ambient RF power harvesting," *IEEE Antennas Wirel. Propag. Lett.* 2013; 12:918– 921.
- [4] Jeong.J, Jeong.Y. "A novel dual-band RF energy harvesting circuit with power management unit for low power applications," *Microw. Opt. Technol. Lett.* 2017;59(8):1808–1812.
- [5] Li.Z, Zeng.M, Tan .H-Z. "A multi-band rectifier with modified hybrid junction for RF energy harvesting," *Microw Opt Technol Lett.*2018;60:817–821.
- [6] Kassim.S, Malek.F. "EM/Circuit Co-Simulation: A Highly Accurate Method for Microwave Amplifier Design," *Universal Journal of Computer Science and Engineering Technology* 1 (2), 127-132, Nov. 2010.
- [7] Andrenko AS, Lin.X, Zeng.M. "Outdoor RF spectral survey: A roadmap for ambient RF energy harvesting,". *TENCON 2015– 2015 IEEE Region 10 Conference, Macao, 2015, 1– 4.*
- [8] Pinuela.M, Mitcheson. P.D, and Lucyszyn.O, "Ambient RF energy harvesting in urban and semiurban environments," *IEEE Transactions on Microwave Theory and Techniques*, Vol. 61, No. 7, 2715–2726, May 2013
- [9] Chuang. M.L, and Wu .M.T, "Miniaturized ring coupler using multiple open stubs, *Microwave and Optical Technology Letters*, Vol. 42, No. 5, 379–383, Jul. 2004.
- [10] Wei .MD, Chang .YT, Wang. D, Tseng. CH, Negra.R "Balanced RF rectifier for energy recovery with minimized input impedance variation,". *IEEE Trans. Microw. Theory Tech.* 2017;65(5):1598– 1604.

Theoretical Analysis of Optical Isolator Based on Mode Conversion in Yttrium Iron Garnet Fiber

Khadidja SAKER¹, Touraya BOUCHEMAT¹, Mahieddine LAHOUBI² and Mohamed BOUCHEMAT¹

¹Les Frères Mentouri Constantine University, Department of Electronics, Laboratory L.M.I, Constantine 25017, Algeria, khadidjasak1991@gmail.com, tboumaza2001@yahoo.fr, hm_bouchemat@yahoo.fr

²Badji-Mokhtar Annaba University, Department of Physics, Laboratory L.P.S, Annaba 23000, Algeria, mlahoubi@hotmail.fr

ABSTRACT

In this paper, a kind of magneto-optical (MO) fiber of Yttrium iron garnet $Y_3Fe_5O_{12}$ (YIG) is presented. It is well known that YIG has large Faraday rotation (FR) and high saturation magnetization. Our work aims to study the mode coupling TE-TM, in order to obtain a nonreciprocal effect, which depends on the FR and to determine the MO properties of the proposed structure. The core diameter and gyrotropy are varied to examine their effects on mode conversion TE-TM efficiency, coupling length and FR. To perform the numerical study, the Beam Propagation Method is used. When the gyrotropy parameter is equal to 0.04, the simulation results show an interesting mode conversion efficiency of 91 % with a FR of 2.04×10^4 %/cm. The proposed structure displays attractive MO properties, which make it suitable to the design of optical isolators.

Key Words: Faraday rotation, Gyrotropy, Mode conversion, Optical fiber, YIG.

1. INTRODUCTION

The progress of optical fiber communication systems has encouraged the optical isolators demand. Since, the only existing isolators are enormous and costly. The necessity of low-cost and solid isolators that can be coordinated with other optical devices is required. To satisfy this claim, various optical waveguide isolators scheme have been investigated and classed generally

into two categories: relying on nonreciprocal transverse electric/transverse magnetic (TE/TM) mode conversion and configurations relying on nonreciprocal phase shifts [1]. The integration of such devices on semiconductor platforms has been challenging because of material incompatibilities between semiconductors and magneto-optical (MO) materials that require wafer bonding, and because of the large footprint of isolator designs [2]. MO isolators, which are similar to electrical diode, are incorporated to achieve the nonreciprocity onto photonic platforms and hence, protect light sources [3]. The origin for all non-reciprocal effects is related to the FR [4]. Magnetic garnet films, with large Faraday rotation combined with low optical losses, have been intensively examined in last years. The basis of most experiments is the nonreciprocal TE-TM mode conversion [5]. YIG compound, is a versatile ceramic material. It is known with the following interesting properties: high melting point, large resistivity, high electromagnetic properties [6] and high electric resistivity, high radiation stability, comparatively low magnetization narrowest ferromagnetic line width and consequent low losses. YIG appears as the best magnetic material for high-frequency applications [7] and offers an important FR effect and a good transmittance near infrared region [8]. These interesting properties allow new devices development, which suit various applications in optical devices [9]– [13].

In this paper, a theoretical study of a MO fiber based on of YIG is represented. The

main aim was to realize the TE-TM mode conversion. This technique consists in producing, under the influence of a magnetic field parallel to the direction of propagation, a coupling between the modes TE and TM, which is a way of obtaining a nonreciprocal effect in a guided configuration.

2. THEORETICAL METHOD AND STRUCTURE

We assume that in the absence of external magnetic field, the material is isotropic and the magnetization is directed along the z-axis and parallel with direction of light propagation. The permittivity tensor of magnetic medium $\tilde{\epsilon}$ [14] is given by the following expression:

$$\tilde{\epsilon} = \begin{pmatrix} \epsilon_{xx} & +i\epsilon_{xy} & 0 \\ -i\epsilon_{yx} & \epsilon_{yy} & 0 \\ 0 & 0 & \epsilon_{zz} \end{pmatrix}, \quad (1)$$

where, the non-diagonal terms $\tilde{\epsilon}_{xy} = -\tilde{\epsilon}_{yx}$, correspond to the magnetic gyration, and have a linear dependence with the magnetization. If the attenuation coefficient is equal to 0, so that we have $\tilde{\epsilon}_{xx} = \tilde{\epsilon}_{yy} = \tilde{\epsilon}_{zz} = \tilde{\epsilon}_{material}$ and $\tilde{\epsilon}_{xy} = -\tilde{\epsilon}_{yx} = g$, with g characterizing the gyrotropy parameter. The specific FR parameter θ_F (°/cm) is related to the tensor components of the effective dielectric permittivity as follows [15]:

$$\theta_F = \frac{\pi Re(g)}{n\lambda}, \quad (2)$$

where $Re(g)$, n and λ are real part of the MO permittivity, refractive index and the wavelength, respectively. The variation of the isolation ratio with wavelength can be understood by considering its dependence on the linear birefringence Δ_n and the FR rotation angle θ_F of the material constituting the waveguide. The familiar expression for the maximum mode conversion efficiency R_m is then given by [16]:

$$R_m = \frac{\theta_F^2}{(\theta_F^2 + (\Delta\beta/2)^2)}, \quad (3)$$

where $\Delta\beta$ (°/cm) is the phase mismatch between TE and TM modes: $\Delta\beta = 2\pi\Delta Nm/\lambda$,

where ΔNm is the modal birefringence which is defined by the difference between the TE and TM effective index for mode number m , and λ is the light wavelength [17]. This relation of R_m (%) corresponds to a distance L_C (μm) [18].

$$L_C = \frac{\pi}{\sqrt{4\theta_F^2 + (\Delta\beta)^2}} \quad (4)$$

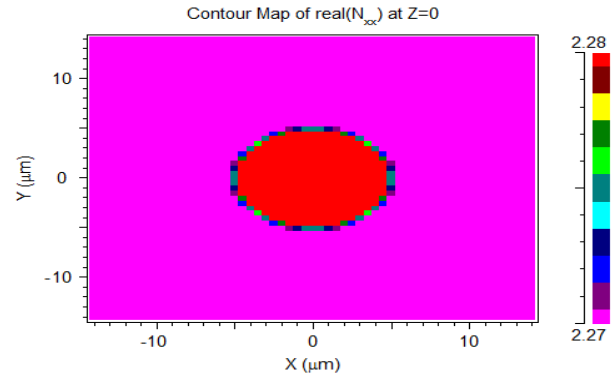
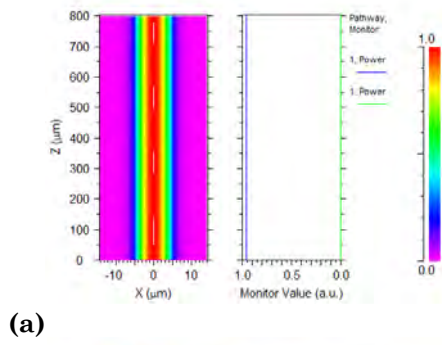


Figure.1: Cross section of the MO PC fiber.

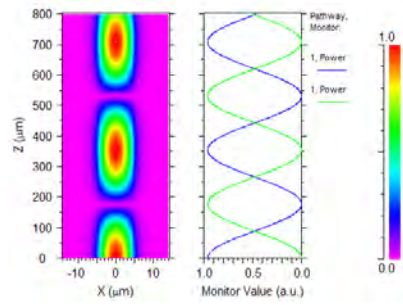
The investigated MO fiber shown in Figure.1, consists of single mode conventional optical fiber of YIG, where the $n_{core} = 2.28$ and $n_{cladding} = 2.27$ with a length equal to $800 \mu m$ and $\lambda = 1.55 \mu m$. To simulate the propagation of a beam in the photonic crystal (PC) fiber and to study the mode conversion, we used the Beam Propagation Method. The finite difference BPM represents the basis of the programming of the computational algorithms adopted by the software that we used along our work, BeamPROP from the company RSoft [19].

3. RESULTS AND DISCUSSION

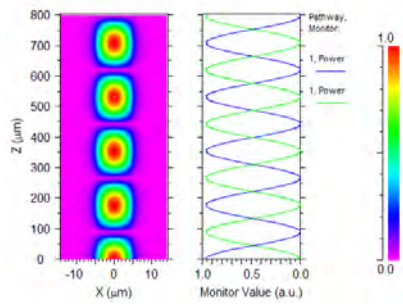
The effect of g on the MO properties of this structure is examined for a core diameter $d = 10 \mu m$ with $g = 0, 0.01, 0.02, 0.03$, and 0.04 are reported on Figure.2, (a), (b), (c), (d), and (e), respectively.



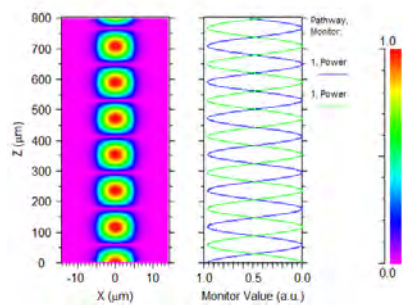
(a)



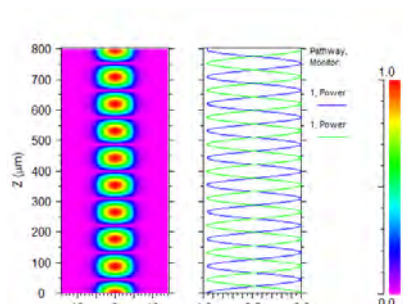
(b)



(c)

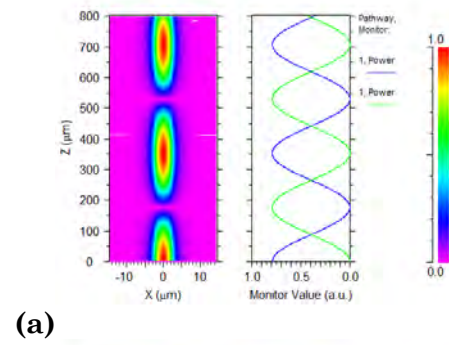


(d)

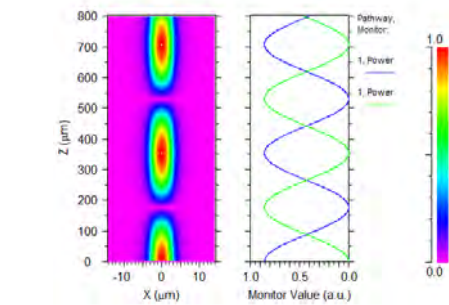


(e)

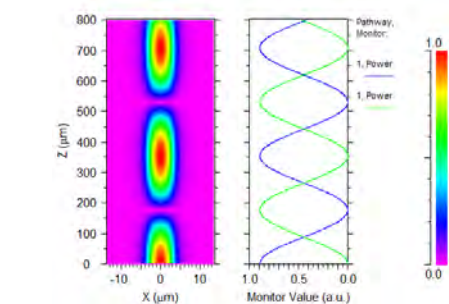
Figure.2: Mode conversion with $d = 10 \mu\text{m}$ for $g = 0$ (a), 0.01 (b), 0.02 (c), 0.03 (d), and 0.04 (e)



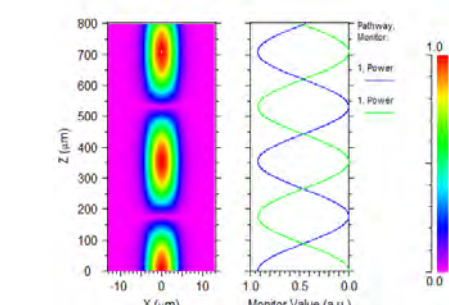
(a)



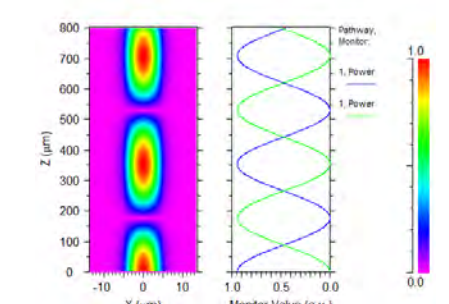
(b)



(c)



(d)



(e)

Figure.3: Mode conversion with $g = 0.01$ for $d = 5$, (a), 6 (b), 7 (c), 8 (d), and $9 \mu\text{m}$ (e)

Figure.2 represents the variation of the mode conversion as a function of the gyrotropy for core diameter $d = 10 \mu\text{m}$. It can be seen that the gyrotropy affects the conversion mode, for $g = 0$, the modes are separated. The existence of this term induces a coupling of modes, which increase proportionally. The modes begin to couple together from $g = 0.01$ and they are strongly coupled as the gyrotropy increase. Figure.3, represents the influence of the core diameter d on the conversion mode efficiency for $g = 0.01$. It can be seen that with the increase of d , the efficiency increase and the mode conversion remains constant.

Further investigation has been undertaken in order to study the influence of both, geometrical and physical parameters on the MO properties of this structure. The variation of the core diameter d in the $5\text{--}10 \mu\text{m}$ range and the gyrotropy g from 0.01 to 0.04 with an increment of 0.005 is displayed in Figure.4. A nonlinear dependence of the mode conversion efficiency with the core diameter is observed. Whereas, at the same time, R_m is inversely proportional to the increase of g , a conversion of 96 % is achieved for $g = 0.01$ and diameter equal to $10 \mu\text{m}$. This value decreases to 91 % for $g = 0.04$. It appears that a rather large diameter is required.

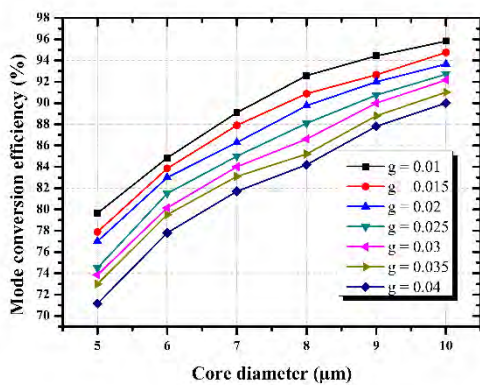


Figure.4: Influence of the core diameter d on the mode conversion efficiency at $\lambda = 1.55 \mu\text{m}$ and various values of the g parameter

Figure.5 shows the coupling length L_c as a function of the gyrotropy g and the core diameter d of the proposed MO fiber. The coupling is inversely proportional to the increase of d , and exhibits an exponential decay with the increasing of g , which means that the coupling is faster when we increase the gyrotropy. For $g = 0.04$, L_c is equal to

$41.22 \mu\text{m}$ and when $g = 0.01$, $L_c = 186.25 \mu\text{m}$, when d decreased L_c is equal to $51.22 \mu\text{m}$ and $228.16 \mu\text{m}$ for $g = 0.04$ and 0.01 , respectively. The constant tensor enables the mode coupling TE-TM in a periodic manner, and the variation of these parameters has a much greater influence on the FR due to the existing relationship between them as shown in Equation (1).

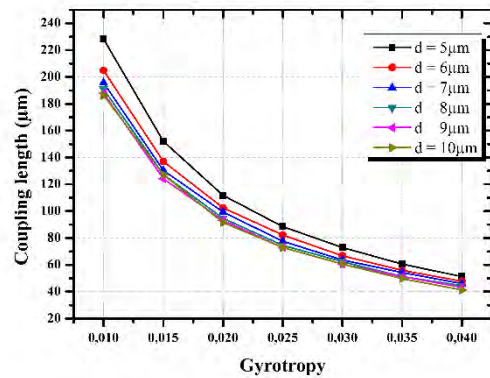


Figure.5: Influence of the gyrotropy parameter g on the coupling length distance at various values of the core diameter d

The variation of FR in function of the core diameter for different gyrotropy values represented in Figure.6 shows linear relation. It increases with the increase of g , for $g = 0.01$, FR reaches a value of $5093.38 \text{ }^\circ/\text{cm}$ and increases to $2.04 \times 10^4 \text{ }^\circ/\text{cm}$ for $g = 0.04$. In addition, the core diameter does not affect its variation. These results show that this structure allows simultaneously an interesting conversion efficiency, thus, decreasing the optical losses at telecommunication wavelength $\lambda = 1.55 \mu\text{m}$ and improving the MO performance, such as increasing FR regarding to those reported in [17], [20].

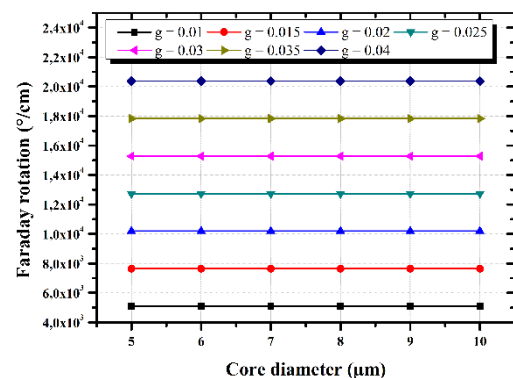


Figure.6: Faraday rotation as a function of the core diameter at different values of the gyrotropy parameter g

CONCLUSION

In summary, we have proposed and demonstrated a novel optical isolator, based on a single-mode gyromagnetic fiber of YIG, using Beamprop software. It was shown that changing the gyrotropy and the core diameter of the fiber affect the MO properties such as mode conversion efficiency and coupling length. In order to minimize the losses in this structure a diameter equal to $10\ \mu\text{m}$ is required. The numerical results show that R_m and L_c are inversely proportional to the increase of gyrotropy. Moreover, changing the gyrotropy values confirmed the relation between Faraday rotation and the TE-TM mode conversion. Therefore, a large Faraday rotation is achievable by optimizing the geometric and MO parameters of the proposed structure. For $g = 0.04$, $R_m = 91\%$, $L_c = 51.22\ \mu\text{m}$ and $\theta_F = 2.04 \times 10^4\ \text{°/cm}$ are obtained. The proposed device shows a significant improvement in conversion efficiency and Faraday rotation, which make this magnetic PC fiber suitable for integrated-optics devices such as isolator.

ACKNOWLEDGEMENTS

This work was supported by MESRS (*Ministère de l'Enseignement Supérieure et de la Recherche Scientifique*) under the supervising of the CNEPRU, www.cnepru-mesrs.dz, project (Grant No. A10N01UN250120130017) of the Laboratory L.M.I., FMCU–Constantine, Algeria and by a joint project with the Laboratory L.P.S. – BMAU, Annaba, Algeria.

REFERENCES

- [1] N. Kono, K. Kakihara, K. Saitoh, and M. Koshihara, "Nonreciprocal microresonators for the miniaturization of optical waveguide isolators," *Opt. express*, Vol. 15, No. 12, pp. 7737-7775, 2007.
- [2] L. Bi, J. Hu, J. Hu, P. Jiang, D. H. Kim, G. F. Dionne, L. C. Kimerling, and C. A. Ross, "On-chip optical isolation in monolithically integrated non-reciprocal optical resonators," *Nat. Photonics*, Vol. 5, No. 12, pp. 758-762, 2011.
- [3] B. J. H. Stadler and T. Mizumoto, "Integrated magneto-optical materials and isolators: A review," *IEEE Photon. J.*, Vol. 6, No. 1, pp. 0600215-15, 2014.
- [4] H. Dötsch, N. Bahlmann, O. Zhuromskyy, M. Hammer, L. WilkensLudger, R. Gerhardt, P. Hertel, and A. F. Popkov, "Applications of magneto-optical waveguides in integrated optics: review," *J. Opt. Soc. Am. B*, Vol. 22, No. 1, pp. 240-251, 2005.
- [5] H. Hemme, H. Dobtsch, and H. Menzler, "Optical isolator based on mode conversion in magnetic garnet films," *Appl. Opt.*, Vol. 26, No. 18, pp. 3811-3817, 1987.
- [6] M. N. Akhtar, A. B. Sulongb, M. A. Khanc, M. Ahmadd, G. Murtazae, M.R. Razab, R. Razaa, M. Saleema, and M. Kashif, "Structural and magnetic properties of yttrium iron garnet (YIG) and yttrium aluminum iron garnet (YAIG) nanoferrites prepared by microemulsion method," *J. Magn. Magn. Mater.*, Vol. 401 pp. 425-431, 2016.
- [7] M. A. Musa, R. S. Azis, N. H. Osman, J. Hassan, and M. M. Dihom, "Structural and magnetic properties of yttrium aluminum iron garnet (YAIG) nanoferrite prepared via auto-combustion sol-gel synthesis," *J. Aust. Ceram. Soc.*, Vol. 54, No. 1, pp. 55-63, 2018.
- [8] T. Boudiar, B. Payet-Gervy, M. F. Blanc-Mignon, J. J. Rousseau, M. Le Berre, and H. Joisten, "Magneto-optical properties of yttrium iron garnet (YIG) thin films elaborated by radio frequency sputtering," *J. Magn. Magn. Mater.*, Vol. 284, No. 1, pp. 77-85, 2004.
- [9] M. N. Deeter, A. H. Rose, and G. W. Day, "Fast, Sensitive Magnetic-Field Sensors Based on the Faraday Effect in YIG," *J. Lightwave Technol.*, Vol. 8, No. 12, pp. 1838-1842, 1990.
- [10] C. He, X. L. Chen, M. H. Lu, X. F. Li, W. W. Wan, X. S. Qian, R. C. Yin, and Y. F. Chen, "Tunable one-way cross-waveguide splitter based on gyromagnetic photonic crystal," *Appl. Phys. Lett.*, Vol. 96, No. 11, pp. 111111-3, 2010.
- [11] L. Zhang, D. Yang, K. Chen, T. Li, and S. Xia, "Design of nonreciprocal waveguide devices based on two-dimensional magneto-optical photonic crystals," *Opt. Laser Technol.*, Vol. 50, No. 38, pp. 195-201, 2013.
- [12] S. K. Mondal and B. J. H. Stadler, "Novel designs for integrating YIG/air photonic crystal slab polarizers with waveguide Faraday rotators," *IEEE Photonics Technology Letters*, Vol. 17, No. 1, pp. 127-129, 2005.
- [13] R. Deghdak, M. Bouchemat, M. Lahoubi, S. Pu, T. Bouchemat, and H. Otmani,

- “Sensitive magnetic field sensor using 2D magnetic photonic crystal slab waveguide based on BIG / GGG structure,” *J. Compu. Electron.*, Vol. 16, No. 2, pp. 392-400, 2017.
- [14] J. Liu, S. Wang, S. Deng, Y. Wang, and J. Zhang, “Polarization research of YIG based two-dimensional Magneto Photonic Crystals,” *Opt. Commun.*, Vol. 402 pp. 319-325, 2017.
- [15] A.K. Zvezdin, and V.A. Kotov, Modern magneto-optics and magneto-optical materials, *IOP Publishing Ltd*, London, 1997.
- [16] R. Wolfe, R. A. Lieberman, V. J. Fratello, R. E. Scotti, and N. Kopylov, “Etch-tuned ridged waveguide magneto-optic isolator,” *Appl. Phys. Lett.*, Vol. 56, No. 5, pp. 426-428, 1990.
- [17] F. Choueikani, F. Royer, S. Douadi, A. Skora, D. Jamon, D. Blanc and A. Siblini, “Low birefringent magneto-optical waveguides fabricated via organic-inorganic sol-gel process,” *Eur. Phys. J. Appl. Phys.*, Vol. 47, pp. 30401-8, 2009.
- [18] H. Otmani, M. Bouchemat, T. Bouchemat, M. Lahoubi, W. Wang, and S. Pu, “Nonreciprocal TE–TM Mode Conversion Based on Photonic Crystal Fiber of Air Holes Filled With Magnetic Fluid Into a Terbium Gallium Garnet Fiber,” *IEEE Trans. Magn.*, Vol. 51, No. 11, pp. 4004604-4, 2015.
- [19] RSoft Photonic Design Software: Photonic Device & Optical Communications System Design. <https://optics.synopsys.com/rsoft>, Licence Rsoft N° 16848079, 2016.
- [20] H. Otmani, M. Bouchemat, T. Bouchemat, M. Lahoubi, S. Pu, and R. Deghdak, “Magneto-optical properties of magnetic photonic crystal fiber of terbium gallium garnet filled with magnetic fluid,” *Photonic Nanostruct. – Fundam. Appl.*, Vol. 22, pp. 24-28, 2016.

Generating of high repetition rate pulse train in photonic crystal fibers by induced modulation instability

Nedjmeddine Ammar MERABET¹, Lynda CHERBI - BAZI¹ and Lyes BAHLOUL¹

¹ USTHB, LINS Lab, Faculty of Electronics and Computers, Bab-Ezzouar, Algiers
merabetnedjmeddine@gmail.com

ABSTRACT

Modulation instability (MI) appears when a continuous light wave breaks under the combined influence of the Kerr effect and dispersive effects to give rise to a pulse train with a well-defined frequency. In this paper, we could exploit the MI to generate a high repetition rate pulse train in photonic crystal fiber length of 180m. Using the linear stability study, we could obtain the expression of the pulses train frequency where we found that the presence of β_3 introduces a phase during the propagation of these pulses and β_4 modifies the repetition rate of the bit stream generated.

Key Words: Optical fiber, Photonic crystal fiber, Modulation instability, High order of dispersion, Optical Kerr effect, Nonlinear Schrödinger equation, Split Step Fourier Method SSFM.

1. INTRODUCTION

For fifteen years, a new generation of fibers has emerged. These fibers with original properties called PCF "Photonic Crystal Fiber". Unlike conventional fibers, they have a micro structuring of the optical cladding, which allows a simpler and more varied control of their guiding properties. This allows reaching new areas of operation as well. PCFs notably have a significant confinement of the light field and lead to clear advances in non-linear optics. Nonlinear

optical phenomena are manifestations of the property of certain materials to acquire under the effect of an intense light field, a polarization dependent in a non-linear way of the amplitude of the electric field. The physical origin of this property comes from the microscopic characteristics of the material namely the nature of the atoms, molecules or the crystalline structure. One of the major non-linear effects in optical fibers is the optical Kerr effect, which is essentially a change in the refractive index dependent on optical power and leads too many side effects, such as Self Phase Modulation (SPM), phase intermodulation (XPM), four-wave mixing (FWM) and Modulation Instability (MI). We will focus on the MI modulation instability process in photonic crystal fibers. This phenomenon is at the basis of many applications such as the generation of pulse trains or the generation of very broad-spectrum signals (supercontinuum), that can be applied in high-resolution medical imaging. In this work, a high rate of pulses train is generated in PCF by using MI and working with the high order of dispersion.

2. THEORY

Modulation instability is a phenomenon likely to occur when a continuous optical wave propagates in the fiber (Fig 1.a. b) [1]. This wave is naturally unstable in the presence of disturbances due to the optical Kerr effect. (Self-phase modulation) as shown

in (Fig 1.c) [2]. For a certain compromise between the fiber parameters (Kerr effect and dispersive effects) and the input power, a disturbance can feel a positive gain and consequently cause a breaking of the wave in the process of ultrashort pulses in the time domain (Fig 1.e). The spectrum of this initially very narrow wave (Fig. 1.d) is then enriched by additional frequency components related to the amplitude modulation of the electric field envelope (Fig 1.f) [3]. In standard fibers, this phenomenon is generally studied in abnormal dispersion regime ($\beta_2 < 0$). But it can also be observed in normal dispersion regime ($\beta_2 > 0$) in the case of PCF fibers when the pumping is carried out close of zero dispersion, in this case the presence of the higher orders of dispersion adds additional degrees of freedom in the phase-tuning condition thus allowing the observation of this phenomenon in the two dispersion regimes. In addition to the phase matching condition, we will see later that the presence of the higher orders of dispersion also makes it possible to reach modulation frequencies of the order of Terahertz, which is impossible to obtain it in fibers standards ($\beta_3 = \beta_4 = 0$). The phase matching condition and the determination of the modulation frequency will be calculated analytically.

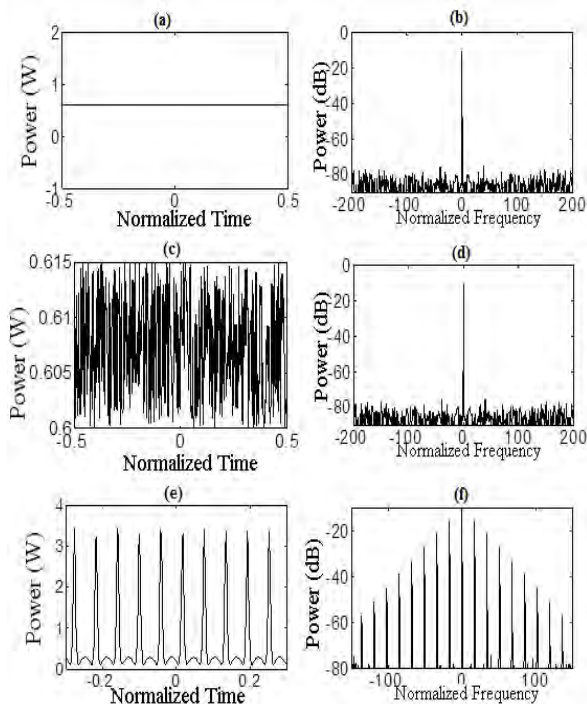


Fig1. Modulation instability phenomenon obtained numerically in standard fiber (a): CW continuous wave. (b): the spectrum of the CW continuous wave. (c): the time course of

disturbed signal. (d): the spectrum of the disturbed signal. (e): the temporal rate of signal at the output. (f): the spectrum at the output.

In order to model the propagation of a wave through an optical fiber we use the nonlinear Schrödinger equation established from the wave equation with the nonlinear polarization of the medium [4]. This equation considers linear and non-linear effects. If we do not take into account the effects of Raman and Brillouin scattering, the nonlinear Schrödinger equation describing the evolution of the envelope A of the electric field in a PCF is writing as follows:

$$\frac{\partial A}{\partial z} = -\frac{\alpha}{2}A - i\frac{\beta_2}{2}\frac{\partial A}{\partial T^2} + \frac{\beta_3}{6}\frac{\partial A}{\partial T^3} + i\frac{\beta_4}{24}\frac{\partial A}{\partial T^4} + i\gamma|A|^2A - i\gamma T_r\frac{\partial |A|^2 A}{\partial T} \quad (1)$$

Where α represents the linear losses, β_2 , β_3 and β_4 are different orders of dispersion. γ is the non-linearity coefficient, T_r is the time relative to the Raman scattering. Finally, T is the reference time that moves at the group speed and is defined by $T = t - \beta_1 z$, with β_1 representing the inverse of the group speed.

• Linear stability study

The linear stability study is an analytical mathematical method generally used in nonlinear systems evolving as a function of time (in our case it is the propagation distance z), these systems are generally described by partial differential equations and are likely to become unstable for some system parameter schemes. This method consists to add analytically, to the stationary solution ($\partial E_s / \partial z = 0$) a small amplitude perturbation, and then linearize the whole system around the amplitude this perturbation, we determine the condition for which this amplitude will feel a positive gain and we will finally be able to deduce the modulation frequency relating to a perturbation whose gain of instability is maximum.

• Linear stability study in the case of standard fibers ($\beta_3 = \beta_4 = 0$)

In this case, only the second order dispersion coefficient is taking into consideration. We work with pulses whose temporal width is greater than 1ps, in this case, the Raman

effect can be neglected, neglecting the linear losses, the nonlinear propagation equation can be written in the following way:

$$\frac{\partial A}{\partial z} = -i\frac{\beta_2}{2}\frac{\partial^2 A}{\partial T^2} + i\gamma|A|^2 A \quad (2)$$

We obtain the expression of the modulation instability gain, which can be considered as the phase agreement condition related to the MI, such that:

$$K = \frac{|\beta_2|\Omega}{2} \sqrt{\Omega^2 - \frac{4\gamma P_0}{\beta_2}} \quad (3)$$

This expression of K allows us to determine the expression of the perturbation frequency whose instability gain is maximum and satisfies the relation $\partial K / \partial \Omega = 0$ is given by:

$$\Omega = \sqrt{\frac{4\gamma P_0}{|\beta_2|}} \quad (4)$$

It is clear from (4) that the modulation instability frequency depends only on the fiber parameters and the input power, and we see that the frequency increases with the increase of the power.

- **Linear stability study in the case of PCFs fibers ($\beta_3 \neq 0, \beta_4 \neq 0$)**

We proceed in the same way as previously and we take into account the higher orders of the dispersion β_3 and β_4 .

By neglecting the losses and the Raman effect, we add to the stationary and homogeneous solution of the system (Es) a perturbation of the form $\delta e^{(Kz - i\Omega t)}$ and then we write a system composed of the envelope of the electric field and its complex conjugated as follows:

$$\begin{cases} E = E_s + \delta e^{Kz - i\Omega t} \\ E^* = E_s^* + \delta^* e^{Kz - i\Omega t} \end{cases} \quad (5)$$

Injecting these solutions into the propagation equation (1), we obtain the following system:

$$\begin{bmatrix} i\frac{\beta_2}{2}\Omega^2 + i\frac{\beta_4}{24}\Omega^4 + 2i\gamma P_0 - K & i\gamma E_s^2 \\ i\gamma E_s^2 & -i\frac{\beta_2}{2}\Omega^2 - i\frac{\beta_4}{24}\Omega^4 - 2i\gamma P_0 - K \end{bmatrix} = \begin{bmatrix} 0 \\ 0 \end{bmatrix} \quad (6)$$

With $a = \delta.e(kz - i\Omega T)$ et $a^* = \delta^*.e(kz - i\Omega T)$

The system admits solutions if the determinant of the matrix is zero. We can thus determine the expression of the instability gain K that is writing as follows:

$$K = i\frac{\beta_3}{6}\Omega^3 \pm \sqrt{-\left(\frac{\beta_2}{2}\Omega^2 + \frac{\beta_4}{24}\Omega^4 + 2\gamma P_0\right)^2 - \gamma^2 P_0^2} \quad (7)$$

We notice from (eq.7) that the presence of the third order of dispersion introduced an imaginary term to the expression of the gain which was purely real+ in its absence, this imaginary part is considered as a phase accumulation all the time along the spread.

Finally, we can obtain the modulation instability frequency:

$$\begin{cases} \Omega^2 = -6\frac{\beta_2}{\beta_4} \\ \Omega^2 = -6\frac{\beta_2}{\beta_4} \left(1 \pm \sqrt{1 - \frac{2}{3}\frac{\gamma P_0 \beta_4}{\beta_2^2}}\right) \end{cases} \quad (8)$$

Equation (8) shows that according to the parameters of the PCF fiber used we can obtain two modes of modulation instability [5]. A regime where we have the simultaneous presence of two unstable frequencies or a regime where a single frequency is obtained in the case where: $1 - \frac{2}{3}\frac{\gamma P_0 \beta_4}{\beta_2^2} = 0$.

3. SIMULATION RESULTS

The Propagation of pulses in standard fiber or PCF in the presence of IM is modeled by the resolution of the nonlinear Schrödinger equation with “Split Step Fourier Method” [4].

- **Modulation instability in the case of a standard fiber ($\beta_3 = \beta_4 = 0$)**

The purpose of this section is to simulate the modulation instability in a standard fiber ($\beta_3 = \beta_4 = 0$). The modulation instability is in this case the result of a balance between the second order dispersion coefficient, the linearity and input power. The parameters used during the simulation are given by the following table [1]:

β_2 [ps ² /km]	Γ [W ⁻¹ .km ⁻¹]	P0 [W]	L [km]
-1.28	1.54	0.6	7

TABLE I : Modulation INSTABILITY SIMULATION parameters for standard fibers

Results of the simulation are illustrated in Fig 2.a and Fig 2.b. Where the first represents

the temporal profile of the modulated wave and the second represents its spectral profile. We can clearly observe that under the effect of modulation instability, the continuous wave breaks to form an ultrashort pulse train whose repetition frequency has been calculated by (4) and is equal to $f = 270.58$ GHz. The spectrum of the originally narrow continuous wave has also been affected since it has been enriched with a large number of new spectral components on both sides of the carrier frequency where the distance between each two components represents the modulation frequency.

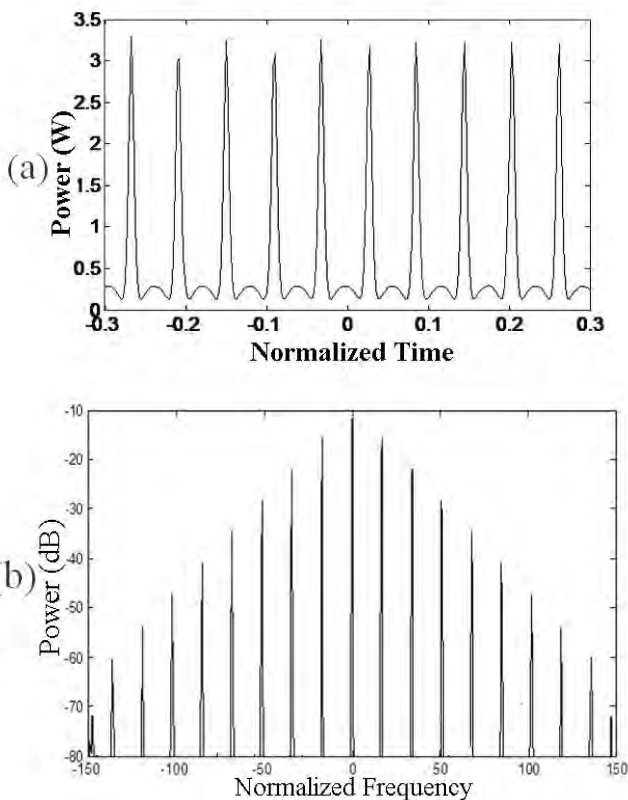


Fig 2. (a) Temporal profile of the pulse train generated by the IM in the absence of the higher orders of dispersion. (b) Spectrum generated by the IM for a length fiber of $L = 7$ Km.

• **Study of Modulation Instability in the case of a photonic crystal fiber**

The influence of fourth-order of dispersion on modulation instability. We will study numerically the impact of using PCF fibers on modulation instability. As a first step, we will only study the influence of the fourth order of dispersion β_4 on the modulation instability in the two dispersion regimes (normal and anomalous). The dispersion of the third order

β_3 will be neglected; this is possible because its presence does not affect the modulation frequency.

• **Result obtained after 6Km of propagation**

We have opted as a first approach to keep the same parameters as for the case of the standard fiber and to introduce in addition the fourth order of dispersion as shown in the following table

β_2 [ps ² /km]	β_4 [ps ⁴ /km]	Γ [W·1.km ⁻¹]	P ₀ [W]	L [km]
-1.28	2.65	1.54	0.6	6

TABLE 2 : the simulation parameters in the presence of the fourth order dispersion coefficient in abnormal dispersion regime.

Fig 2.a and Fig 2.b Show that the modulation instability is observed in the time and frequency domain. We notice that the modulation is better pronounced nevertheless the repetition rate is practically the same compared to the standard fiber case.

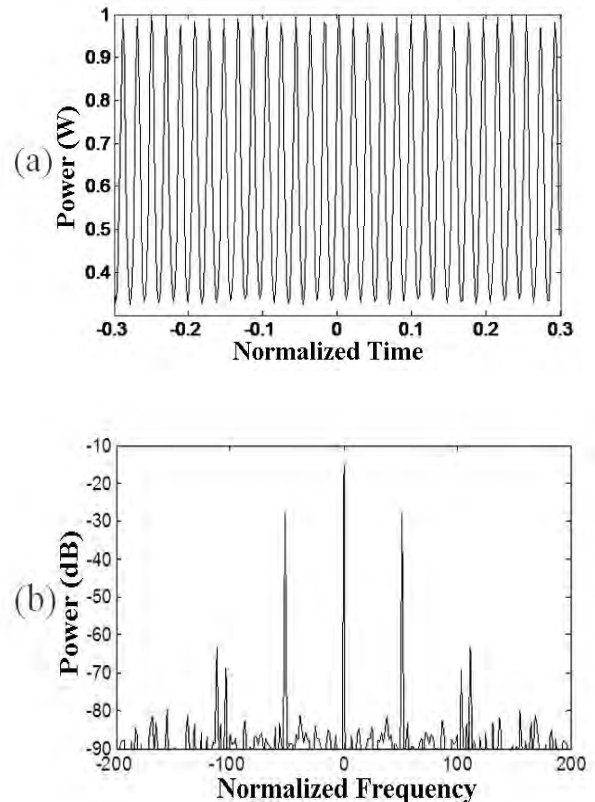


Fig 3. (a) Time profile of the pulse train generated by the IM according to Table 2. (b) Spectrum generated by the IM at the output

of the fiber according to the parameters of Table 2

This result is confirmed by the obtained spectrum (fig3.b) where we notice the appearance in this case also new spectral components. Using (eq.8) the parameters in Table 2 , we deduce the value of the modulation frequency, 263GHz. However, the flexibility of the PCF gives us the possibility of being able to modify even more the parameters of the fiber to try to improve even more this result.

• **Result obtained after 500m of propagation**

In this simulation, we want to reduce the propagation distance for which the modulation instability is obtained. For this, we had to favor the contribution of the non-linear effects compared to the dispersive effects, so we increased the value of the coefficient of nonlinearity and the input power and decreased the value of β_2 and β_4 compared to the previous case as shown in the following table 3 :

β_2 [ps ² /km]	β_4 [ps ⁴ /km]	γ [W ⁻¹ .km ⁻¹]	P0 [W]	L [km]
0.0165	-6.5 .10 ⁻⁵	11.36	0.75	0.500

TABLE 3: simulation parameters in the presence of the fourth order dispersion coefficient in the normal dispersion regime

The first most interesting result in this case is the obtaining of the modulation instability in the normal dispersion regime; this is also due to the presence of β_4 , which gives us an additional degree of freedom compared to the standard fibers. .

We have drawn the temporal profile (Fig.3.a) and the spectral profile (Fig.3.b) of the modulated wave obtained in this parameter regime, we note that in addition to the distance that has decreased, we have been able to increase the value of the modulation frequency which is equal in this case to 9.89 THz. This result is very interesting from a practical point of view but it must nevertheless be emphasized that the

temporal profile of the wave obtained is not very stable and especially the difficulty to design a PCF having a $\beta_2 > 0$ and a $\beta_4 < 0$. This is why during the last simulation we returned to the abnormal dispersion regime.

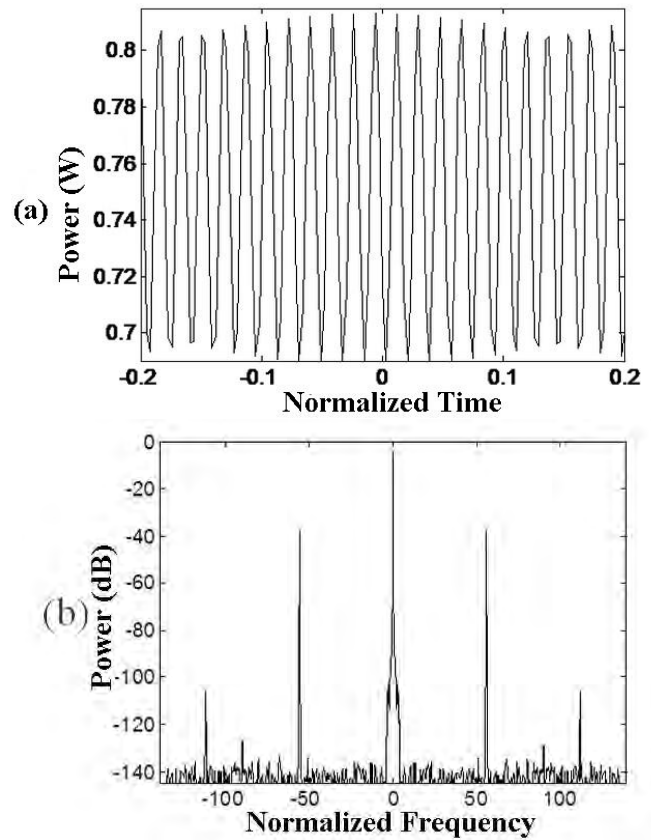


Fig 4. (a) Time profile of the pulse train generated by the IM according to Table III.2. (b) Spectrum generated by the IM at the output of the fiber according to the parameters of Table 3.

• **Result obtained after 180 m of propagation**

We tried in this last part to reduce more the propagation distance; the parameters used are as follows:

β_2 [ps ² /km]	β_4 [ps ⁴ /km]	γ [W ⁻¹ .km ⁻¹]	P0 [W]	L [km]	λ [nm]
-1.176	2,051.10-7	11.36	0.6	0.18	1550

TABLE 4: simulation parameters in the presence of the fourth order dispersion coefficient in anomalous dispersion regime.

Fig.5.a and Fig.5.b give the temporal and spectral profiles of the output signal where

the various parameters given in the Table 4 have been obtained as we shall see in the following by modeling a fiber length of 180m for 600mw input power where the value of the frequency obtained is equal to 542.1 Ghz (using also eq.8). This result can be considered as a good compromise between modulation frequency and propagation distance but it is still expected that it can be further improved.

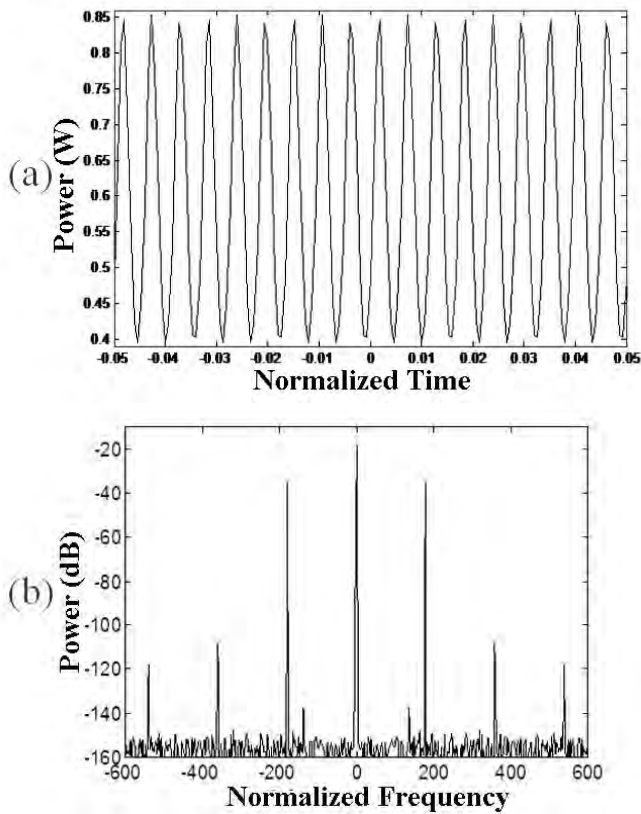


Fig 5. (a) Momentum generated pulse trains in the time domain according to the parameters of Table 4. (b) Spectrum generated by the IM at the output of the fiber according to the parameters of Table 4

- **The influence of the third-order of dispersion on modulation instability**

During all previous simulations, we have neglected the effect of the third order dispersion coefficient (β_3), in order to study the effect of the fourth order dispersion. However, it is also important to understand the behavior of the system in the presence of β_3 . We noticed during the linear stability study in the previous chapter that the presence of β_3 introduced an imaginary part to the expression of the modulation instability gain (7) this imaginary part is

proportional to β_3 and it represents a phase that accumulates the wave as it propagates in the fiber. This phase accumulation induces a time drift with a speed v calculated as follows:

$$v = \frac{\partial \text{Im}(K)}{\partial \Omega} \quad (9)$$

$$v = \frac{\beta_3}{2} \Omega^2 \quad (10)$$

Fig.6.a and Fig.6.b illustrates clearly this drift where we notice that the wave obtained with and without β_3 is shifted, this shift can be an advance or a delay according to the sign of β_3 .

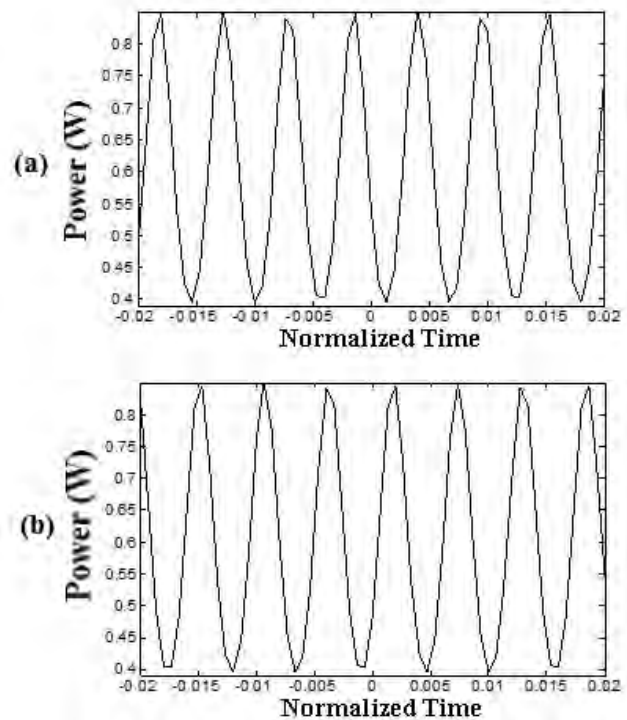


Fig 6. (a) Pulse trains generated by IM in the time domain in the absence of β_3 . (b) Pulse trains generated by IM in the time domain in the presence of β_3 .

4. DESIGN OF PCF

In this part, we have proposed a design of photonic crystal fiber whose parameters ensure the phenomenon of modulation instability. We designed infinitely single mode PCF regardless of the wavelength of work, for this we made an adjustment of its parameters so that the condition $d / \Lambda < 0.406$ is respected. The major advantage of photonic crystal fibers is the extreme confinement of the electromagnetic field due to the strong index difference between the core and the cladding. In order to exploit this advantage we have increased the diameter of the air

holes, the light that tends to spread where the index is larger will be trapped in the core. The predominant disadvantage of micro structured fibers lies in their losses by confinement. The size and arrangement of the constituents of the fiber are the main cause of these losses. In order to limit these and ensure a good confinement of the field in the core, we designed a PCF so that by increasing Λ the ratio d/Λ remains constant, and that the number of rings is quite important.

The choice of the PCF geometry is based on obtaining a low β_2 coefficient in order to introduce the higher order dispersion coefficients β_3 and β_4 . The designed PCF consists of 4 rings, the holes of the first ring have a diameter $d_1 = 0.5\mu\text{m}$ and the other three rings have the same diameters of $d = 0.9\mu\text{m}$, the pitch $\Lambda = 1.618\mu\text{m}$ (Fig .7.a and Fig. 7.b).

The designed PCF is modeled by FEM and adapting a PML layer as bounding conditions [6].

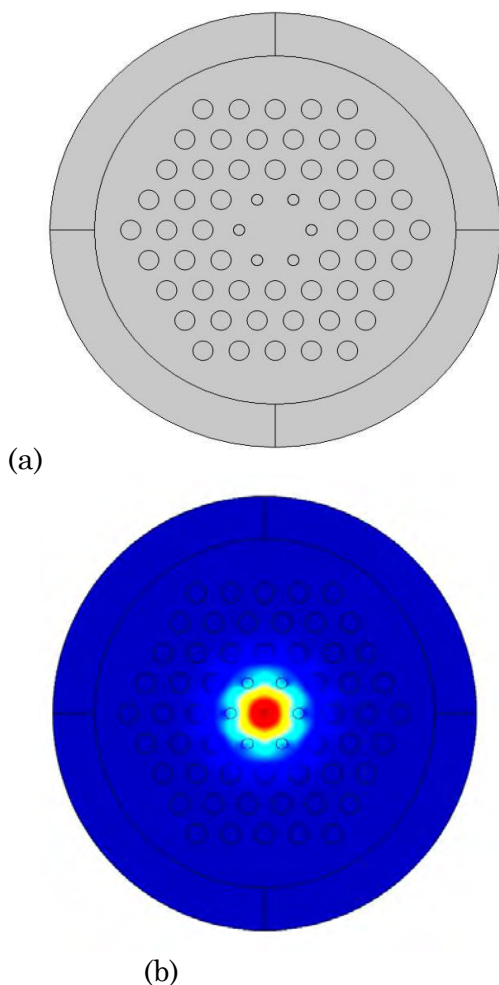


Fig 7. (a). Geometry of the PCF designed. (b). Distribution of the HE 11 mode field in the designed PCF.

5. CONCLUSION

We have studied in this paper the phenomenon of modulation instability in photonic crystals fiber where we could understand and see the consequences of this phenomenon on the propagation of a CW wave. We have studied the higher order effects of dispersion on IM and we have seen that the introduction of β_4 has changed the behavior of the system where we obtained modulation frequencies of the order of THz with a normal dispersion regime. We could also stabilize in the abnormal regime modulated wave from 180m length of fiber. We have tried to see the influence of the third order dispersion on the modulation instability. We noticed that its presence has no influence on the modulation frequency but it produces an additional phase that moves the modulated structure with a speed proportional to β_3 . We have also been able to design a PCF fiber model capable of ensuring modulation instability and generating 542.1 GHz. pulses train in 180 m of fiber.

REFERENCES

1. J.FATOME. Propagation of 160-Gb / s ultra-short pulses in dispersed optical fiber lines. PhD thesis in Physics. University of Burgundy. 2004.
2. Anne Boucon. Instability and supercontinuum generation under near-continuous excitation in highly nonlinear and micro structured optical fibers. PhD thesis in sciences for the engineer. University of Franche-Comté (UFC).
3. S. Pitois. Modulation instability and domain wall solitons in optical fibers. PhD thesis in Physics. University of Burgundy. 2000.
4. Agrawal, G.P. Nonlinear Fiber Optics. The Institute of Optics University of Rochester Rochester, NewYork. 5ème édition. 2013.
5. G.P Agrwal, B.Pal, R . Kumar Varshney, A. B M Rahman: Specialty fibers for terahertz generation and transmission. IEEE Journal of Selected topics in quantum electronics, Vol 22, No 2 . 2016.

6. P. Viale, S.Février, F.Gérome.H.Vilard :Confinement loss compilations in photonic crystal fibres using a novel perfectly matched layer design .Excerpt from proceedings of the COMSOL Multiphysics user's conference , Paris 2005.

Joint Angle Measurement Using a Corrected Gyroscope Integration Data

Mahdi ZABAT, Karim BENSISAID, Amina ABABOU and
Noureddine ABABOU

Laboratory of Instrumentation, University of Science and Technology Houari Boumediene,
Algiers, Algeria.

mzabat@usthb.dz, kbensisaïd@usthb.dz, aababou@usthb.dz and nababou@usthb.dz

ABSTRACT

The purpose of this work was to investigate the accuracy of joint angle measurement method based on virtual sensor approach which leads to good performance when slow motion is considered, but presents some limits on fast motion measurement. In this paper, an inter sensors procedure alignment was applied to a basic wireless sensor body network composed of two nodes. Then, complementary filter was applied using a new corrected gyroscope integration data method. The system has been tested and compared to a four-infrared-camera reference system. The results showed an accuracy improvement of the joint angle measurement when applying complementary filter with corrected gyroscope integration data.

Key Words: Complementary filter; Elbow flexion-extension; Inertial sensors; Sensor nodes; Wireless sensor.

1. INTRODUCTION

A variety of measurement tools are available to clinicians such as goniometers, electro-goniometers [1], systems based on video recordings, and inclinometers [2-4] in order to evaluate the joint range of motion ROM to determine suitable treatments for patient during diagnosis of joint disorder as well as to follow the rehabilitation progress. Goniometry has been widely used due to its portability and low cost, but one limitation of this technique is that it requires the clinician to use both hands, making

stabilization of the extremity more difficult, and thus increasing the risk of error in reading. Modern motion capture (Mocap) systems like infrared video cameras are considered as precise gait analysis tools, but they require a dedicated laboratory and a somewhat complicated using procedure especially for a clinician, in addition to the fact that they are expensive [5]. In the recent past years, researchers investigated the application of inertial sensors in the field of gait analysis by developing new techniques of measurement or new data fusion algorithms [6]. Amasay et al. [7] checked how to best quantify elevation angle exposure of the upper extremity under work condition using accelerometer and found that the RMS angle error was less than 1° and of 3° in static and dynamic conditions, respectively. Others focused on the improvement of inertial sensor measurements by using data fusion algorithms and applying Kalman filter between data acquired from a tri-axial accelerometer [8] and a KPF goniometer. Joint angle measurements based on gyroscope data integration always suffer from drift caused by numerical integration, so the authors in [9-11] proposed methods to get joint angle without integration of the angular velocity. A method based on accelerometer and gyroscope was proposed by Dejnabadi et al. [12] to estimate 2D lower limbs orientation. Their model was based on the joint center of rotation acceleration estimation by virtual sensors (virtual sensors approach) using the rigid body dynamic equation. Their proposed algorithm was tested under dynamic condition and

experiments show good performance for slow motion, but some measurement limitation were related to fast motion and the initial position of sensors on body limbs. They used an alignment procedure based on image processing and photography.

The aim of this paper was to investigate the virtual sensor approach proposed by Dejnabadi et al. [12] by using a 3D alignment procedure based on accelerometric and magnetic sensors data to deduce at slow elbow flexion (or extension) on one hand. On the other hand, we examined a new data fusion method to follow faster joint angle motion.

2. METHODS

2.1. Virtual sensor approach

The virtual sensor VS approach described in [12] is based on the angle θ calculation from the acceleration \vec{a}_O at the center O of a rigid body segment rotating around O, knowing the acceleration at A, as shown in Figure.1.

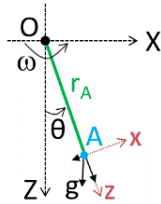


Figure.1: Pendulum rigid body rotating around Y axis

The acceleration measured on a body segment is generally composed of gravitational acceleration, translational acceleration and rotational acceleration. So, based on rigid body dynamic equation, acceleration vector is computed at the joint center point O knowing the acceleration at the point A (r_A being the distance) from O of the rigid body:

$$\vec{a}_O = \vec{a}_A + \vec{\omega}_A \times (\vec{\omega}_A \times r_A) + \dot{\vec{\omega}}_A \times r_A \quad (1)$$

In (1), $\vec{\omega}_A$ and $\dot{\vec{\omega}}_A$ are angular velocity and angular acceleration measured from gyroscope, \vec{a}_O and \vec{a}_A are acceleration at the joint center O and the point A respectively. To identify the joint angle θ_{joint} between the two segments considered as elbow joint model, an accelerometer was placed on each

segment then the VS approach were applied to get the acceleration at the center of rotation O (See Figure.2).

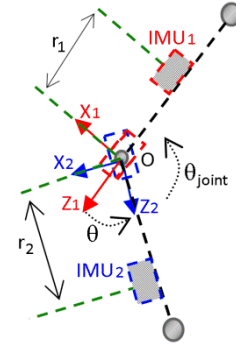


Figure.2: Double pendulum considered as elbow joint model and virtual sensor approach for joint angle measurement

By applying (1), the following equations are obtained:

$$\vec{a}_{O1} = \vec{a}_A + \vec{\omega}_A \times (\vec{\omega}_A \times r_1) + \dot{\vec{\omega}}_A \times r_1 \quad (2)$$

$$\vec{a}_{O2} = \vec{a}_B + \vec{\omega}_B \times (\vec{\omega}_B \times r_2) + \dot{\vec{\omega}}_B \times r_2 \quad (3)$$

Where \vec{a}_{O1} and \vec{a}_{O2} are accelerations at the joint center point O issued from the two virtual sensors placed on it. \vec{a}_A , \vec{a}_B , $\vec{\omega}_A$ and $\vec{\omega}_B$ are physical sensor measurements using accelerometer and gyroscope placed at A and B points. At rest, these accelerations are gravitational, and when the links are in motion, these accelerations are the sum of the gravitational and inertial accelerations [12,13]. As it is the same joint point it should have a unique physical acceleration \vec{a}_{O1} are \vec{a}_{O2} identical; when it is not the case, the difference is due to their different orientations, so

$$\begin{bmatrix} a_{Ox1} \\ a_{Oz1} \end{bmatrix} = \begin{bmatrix} \cos\theta & -\sin\theta \\ \sin\theta & \cos\theta \end{bmatrix} \cdot \begin{bmatrix} a_{Ox2} \\ a_{Oz2} \end{bmatrix} \quad (4)$$

The ulterior step is to calculate the joint angle θ_{joint} between two adjacent segments by resolving (4):

$$\theta = \tan^{-1} \left(\frac{a_{Ox2}a_{Oz1} - a_{Oz2}a_{Ox1}}{a_{Ox1}a_{Ox2} + a_{Oz1}a_{Oz2}} \right) \quad (5)$$

$$\theta_{joint} = \pi - \theta \quad (6)$$

This angle corresponds in our case to the elbow flexion/extension.

2.2. Alignment procedure

In the alignment procedure, one must first align the two local frames SF1 and SF2 of sensors with each other, then align sensors frame with anatomical frame (See Figure.3a). Then, the subject can move freely and joint angles are correctly measured.

2.2.1 Inter sensor 3D alignment

In our procedure, two sensors nodes SN-1 and SN-2 that contain IMU1 and IMU2 respectively were manually placed on the upper limb segments (See Figure.3b). After visually manual alignment of the two local frames SF1 and SF2, some misalignment always persists resulting in negative impact on the measurement accuracy. So, a 3D alignment procedure using accelerometer and magnetometer sensors, and explained here after was applied.

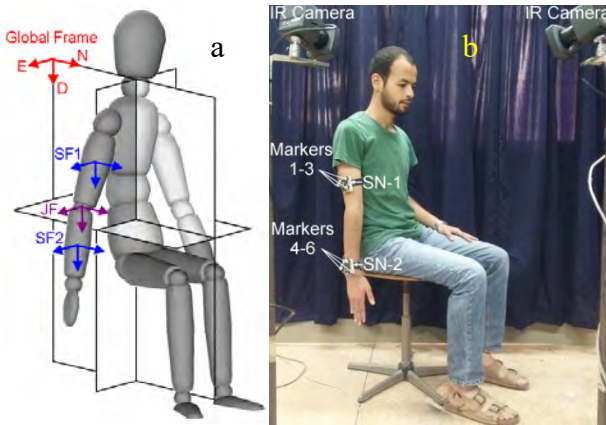


Figure.3: Neutral posture for initial positioning of the two sensors nodes SN-1 and SN-2 on the upper limb. JF is the frame related to the elbow joint.

First, the subject must hold static for few seconds in a neutral posture as illustrated in Figure.3b, to allow collecting data from sensors (accelerometer and magnetometer). The mean value of the two vectors, acceleration \vec{a}_m and magnetic field \vec{b}_m were calculated using equations (7) and (8) where N is the number of samples:

$$\vec{a}_m = \frac{\sum \vec{a}_i}{N} \quad (7)$$

$$\vec{b}_m = \frac{\sum \vec{b}_i}{N} \quad (8)$$

Next, we computed the three normalized vectors which describe the initial orientation of the devices with respect to the global coordinate system (North, East, Down):

$$\vec{A} = \frac{\vec{a}_m}{\|\vec{a}_m\|} \quad (9)$$

$$\vec{H} = \frac{\vec{A} \times \vec{b}_m}{\|\vec{A} \times \vec{b}_m\|} \quad (10)$$

$$\vec{M} = \vec{A} \times \vec{H} \quad (11)$$

So, the initial orientation matrix is expressed by Equation (12) where α , β and γ are the initial orientation angles of sensor frame with respect to global frame, C is for cos and S for sin.

$$R = \begin{bmatrix} C\alpha C\beta & C\alpha S\beta S\gamma - S\alpha C\gamma & C\alpha S\beta C\gamma + S\alpha S\gamma \\ S\alpha C\beta & S\alpha S\beta S\gamma + C\alpha C\gamma & S\alpha S\beta C\gamma - C\alpha S\gamma \\ -S\beta & C\beta S\gamma & C\beta C\gamma \end{bmatrix}$$

$$R = \begin{bmatrix} A_X & H_X & M_X \\ A_Y & H_Y & M_Y \\ A_Z & H_Z & M_Z \end{bmatrix} \quad (12)$$

Any vector measured in sensor frame multiplied with this matrix will transform it from sensor frame to global frame.

2.2.2 Alignment with anatomical frame

In order to measure the elbow joint angle, two sensors nodes were used one on each segment. SN-1 was attached to the arm and SN-2 was attached to the extremity of the forearm and it was visually aligned with the anatomical frame because the radius and ulna provide more reliable support. As SN-2 frame coincides with the anatomical frame [13,14], all measured vectors were expressed in SN-2 frame only for alignment purpose. SN-1 vectors are expressed as

$$\vec{a}_{ri} = R_1^{-1} \cdot (R_2 \cdot \vec{a}_i) \quad (13)$$

$$\vec{\omega}_{ri} = R_1^{-1} \cdot (R_2 \cdot \vec{\omega}_i) \quad (14)$$

where acceleration vector \vec{a}_{ri} and angular velocity $\vec{\omega}_{ri}$ are expressed in SN-2 frame; R_1 and R_2 are initial orientation matrices of sensors 1 and 2; \vec{a}_i and $\vec{\omega}_i$ are vectors which components correspond to sensors measurements. All SN-2 vectors are always expressed in the local frame of the sensor which coincides with the anatomical frame. The vectors \vec{a}_{ri} and $\vec{\omega}_{ri}$ are then used directly in eq. (2), (3), and (5) of the virtual sensor approach.

2.3. Alignment procedure

As joint angles associated with slow movement of the elbow flexion/extension are deduced from accelerometer and gyroscope measurements using the virtual sensor VS approach, and those associated with fast movement were got from gyroscope integration data, a complementary filter CF was applied. However, gyroscope integration data values θ_G need to be first corrected from drift (See Figure.4).

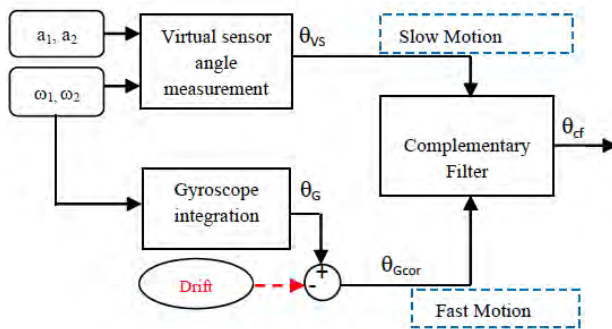


Figure.4: Diagram block of angle measurement system using the complementary filter applied to angles θ_{vs} from virtual sensor approach and θ_{Gcor} from the gyroscope corrected integrated data

The gyroscope integration data values θ_{Gcor} without drift can be expressed by the relation (15) where $\Delta(t)$ corresponds to the drift function.

$$\theta_{Gcor}(t) = \theta_G(t) - \Delta(t) \quad (15)$$

The complementary filter CF fuses the data obtained from the virtual sensor approach and the corrected integrated gyro data by passing the former through a 1st-

order low pass and the latter through a 1st-order high-pass filter, then adding the outputs (See Figure.4) to get the joint angle θ_{cf} expressed by

$$\theta_{cf} = W_{LPF} \cdot \theta_{vs} + (1 - W_{LPF}) \cdot \theta_{Gcor} \quad (16)$$

W_{LPF} is the low-pass characteristic of the CF and $(1 - W_{LPF})$ is the complementary high-pass characteristic of the CF.

3. EXPERIMENTAL

3.1. Measurement system

In order to test the proposed method and to measure the elbow joint angle, a wireless wearable sensor device was developed. It was composed of two wireless emitting nodes SN-1 (or SN-3) and SN-2, each one containing a sensor system and an NRF2401 wireless transmission module.

Each sensor node was attached to one segment and consists of GY_85 sensor module which contains 3-axis digital accelerometer ADXL345 with a resolution of 3.9mg/LSB that enables measurement of inclination changes less than 1.0°, 3-axis gyroscope ITG3200 (sensitivity 14.375LSB/°/s), and 3-axis magnetometer HMC5883 (1° heading angle accuracy). Each node also contains an ATmega328 controller to acquire data from sensors and ensure communication with NRF module. The two emitting nodes share the same reception node which ensures the data transmission to PC (See Figure.5).

Power supply was provided by a rechargeable 3.7V battery. Their response time is less than 6ms.

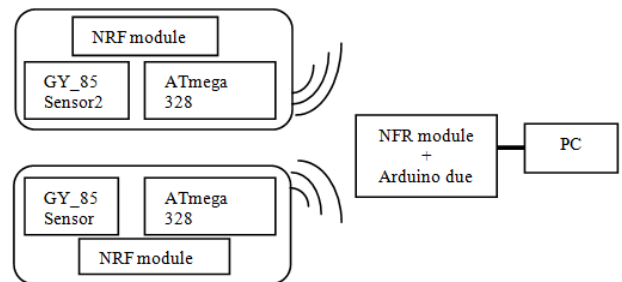


Figure.5: Diagram of the developed sensor device

3.2. Experimental setup for alignment procedure

Before applying the virtual sensor approach to measure angle, the alignment procedure has to be validated. The alignment test was performed in static using a home-made double pendulum with its first joint fixed. The two sensor nodes SN-1 and SN-2 were first aligned then attached on the two parts of the double pendulum with a double-sided tape, as shown in Figure.6. In this configuration, SN-1 and SN-2 measured only gravitational acceleration (9.8 m/s^2) in static.

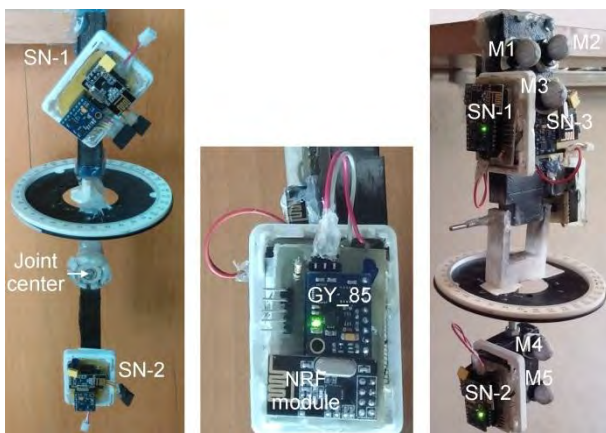


Figure.6: Home-made double pendulum used to test the alignment procedure. SN-1 is rotated by 50° relative to SN-2. Markers M_i are used for simultaneous measurements by Mocap reference system

After applying the alignment procedure in static, both sensors gave the same result. SN-1 was then rotated by 50° relative to SN-2 in the vertical plane; then, the alignment procedure was applied to SN-1 data. The horizontal protractor cannot be used in the alignment procedure validation, but in the measurement of the misalignment between the sensor nodes in the horizontal plane which corresponds to the pronation-supination of the elbow joint when flexed.

3.3. Gyroscope drift detection

The lower part of the double pendulum (considered as elbow joint model) of Figure.6 has been submitted to several free oscillations during approximately 10s. The double pendulum was held in a static position for few seconds between two

successive oscillations, and the angle value obtained from gyro integration data has been acquired versus time. Then, drift error due to gyro data integration was investigated.

3.4. Dynamic measurement of elbow flexion/extension

A seated subject (male, age: 24 years, height: 170 cm, mass: 55 kg) with the two nodes attached to his arm and distal forearm near its wrist (See Figure.7). First, SN-1 was visually aligned with respect to SN-2 and the alignment procedure was applied. Then, the subject was asked to perform several elbow relatively slow flexion/extension fx/ex movement (around $1fx/ex$ per second). A dynamic measurement of its elbow joint flexion/extension was simultaneously performed with the two sensor nodes and a reference Mocap system composed of four Bonita infrared cameras from Vicon. In this experiment, SN-2 frame was taken as reference frame.



Figure.7: Flexion movement performed by the subject

3.5. Effect of misalignment

To study the effect of the misalignment between sensor nodes in the horizontal plane during slow and fast flexion/extension movements, three sensor nodes were placed on the double pendulum as shown in Figure.6.b. SN-1 and SN-3 were attached to the upper part of the double pendulum while SN-2 was placed in the lower part. SN-1 and SN-2 were aligned, but SN-3 was misaligned by 90° with respect to the two others. The joint angles were simultaneously acquired by the reference system and the sensor nodes to investigate the accuracy of the method under same condition tests. Slow and fast motions of the double pendulum have been considered and optical markers ($M1$ to $M6$, $M6$ not visible on Figure.6) were

placed on each side of the pendulum to follow the joint angle by the Mocap system.

4. RESULTS AND DISCUSSION

4.1. Alignment procedure validation

Before application of the alignment procedure on SN-1 node placed on the double pendulum and tilted by 50° relative to the vertical in the vertical plane, SN-1 acceleration was found to be equal to 5.5m/s^2 as illustrated in the associated graph in Figure.8.

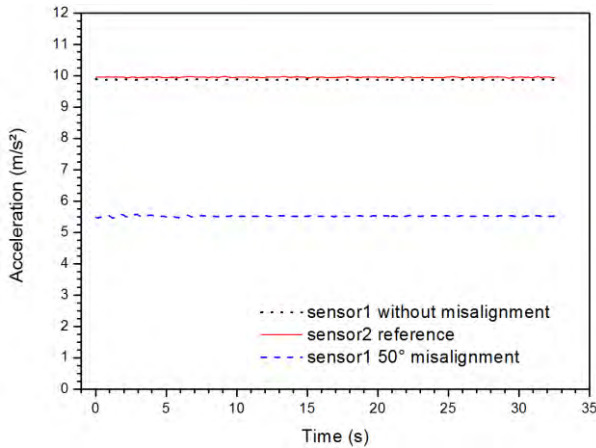


Figure.8: 50° - tilted SN-1 acceleration data versus time before (blue dashed line) and after the alignment procedure (black dots). SN-2 (taken as reference) acceleration data (red solid line) versus time

After the alignment procedure, its acceleration value became the same as that of SN-2, considered as reference. Thus, the alignment procedure application results in the correction of misalignment between the two IMUs of the sensor nodes.

4.2. Gyroscope drift correction

Figure 9 shows the joint angle versus time when the double-pendulum was submitted to several free oscillations separated by static position corresponding to zero-velocity state. The angle values were deduced from gyroscope data integration. The gyro integration signal θ_G with drift illustrated in the graph of Figure.9 shows a baseline that varies with time. One can notice the drift effect of gyroscope data integration on the curve resulting in a base line that can be fitted by a straight line whose equation is expressed by

$$y = -4.353.t \quad (17)$$

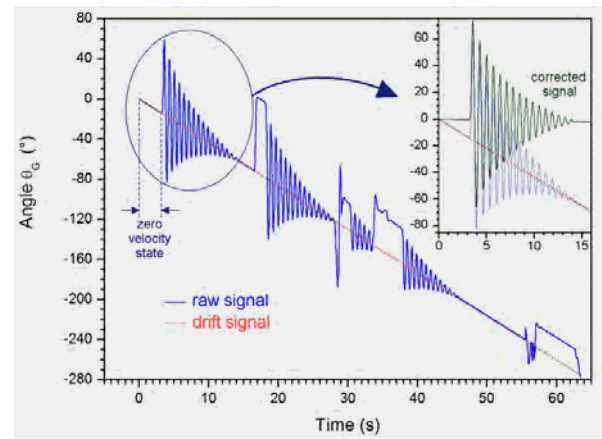


Figure.9: Pendulum angle versus time under several free oscillations separated by static position; the acquisition time was equal to 1 mn. -inset- zoom in of the oscillations during the first 15s

After removing drift effect, the corrected gyroscope integration signal baseline was found to be parallel to time-axis as shown in the inset of Figure.9.

4.3. Dynamic measurement of elbow flexion/extension

Figure.10 represent elbow fx/ex angle performed by the subject of Figure 7 and deduced from the proposed method based (dotted line) simultaneously with the Mocap reference system (solid line). The two curves are almost the same when SN-1 node was visually aligned to SN-2 (0° orientation). The angle difference curve between the two systems (in green on the same graph) shows an error variation with the acceleration associated with the fx/ex or ex/fx movement of the elbow.

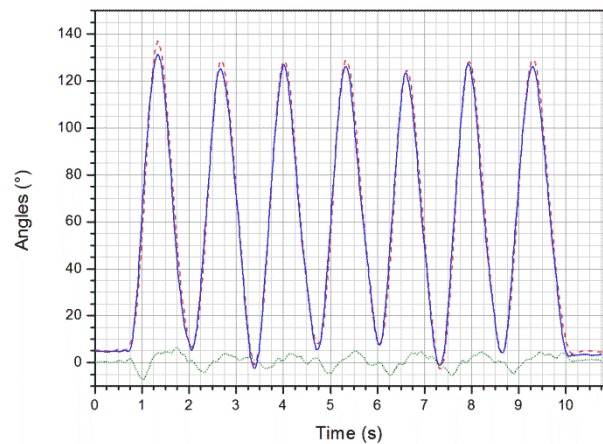


Figure.10: Elbow flexion/extension angle versus time measured simultaneously with proposed method (dashed line) and Mocap reference system (solid line) without misalignment; difference between the two curves (green curve)

The maximal error between the two measures and the mean speed of the fx/ex or ex/fx movements were found to be around 5° and $100^\circ/s$ respectively. The elbow joint having 2ddl, its fx/ex may be accompanied by involuntary pronation /supination. This may cause misalignment of the two sensors attached to the upper limb.

To analyze the sensitivity to this misalignment of the angular measurement, this movement has been performed with the double pendulum first at lower speed, then at higher speed than that of the subject. Figure.11 illustrates the graphs of the double pendulum joint angle θ_{vs} and θ_{cf} obtained by the virtual sensor approach and the proposed complementary filter when sensor nodes are aligned ($\epsilon=0^\circ$) and maximally misaligned ($\epsilon=90^\circ$). In this experiment, the lower arm of the double pendulum moved at $\cong 10^\circ/s$.

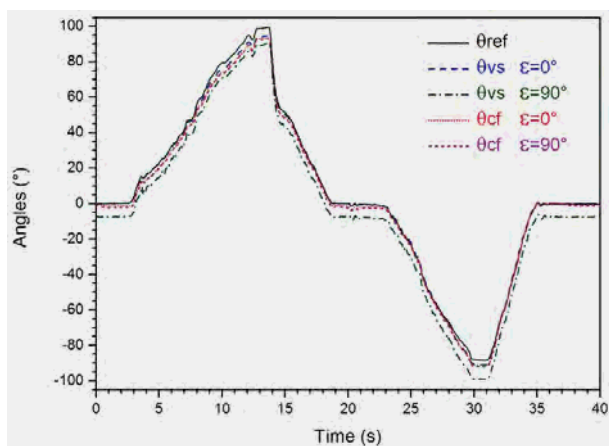


Figure.11: Elbow flexion/extension angle versus time measured simultaneously with proposed method (dashed line), virtual sensor approach (dotted line) and Mocap reference system (solid line) without and with 90° misalignment

Joint angle values have been simultaneously obtained from the reference system θ_{ref} in order to investigate the accuracy of the virtual sensor approach and our proposed method. The error in angle measurements obtained by VS approach and by CF method relative to the reference system is presented in the graph of Figure.12. When sensors are aligned, the VS approach seems to give better results than CF method, but the contrary was found when sensors are misaligned. At this slow motion, the mean angle error in VS approach is lower than that obtained by CF method only when sensors are aligned.

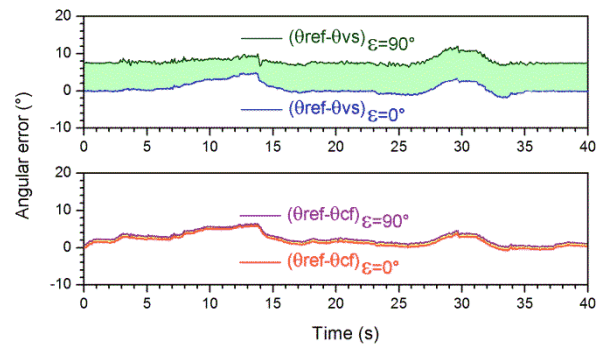


Figure.12: Error measurement of angles obtained from virtual sensor approach and those deduced from complementary filter when the double pendulum joint angle performed a slow motion (around $10^\circ/s$)

For the higher speed study, the lower arm of the double pendulum has been animated with an oscillatory movement at 2Hz leading to an angular speed $\cong 400^\circ/s$. The error in angle measurements obtained by VS approach and by CF method relative to the reference system is presented in Figure.13.

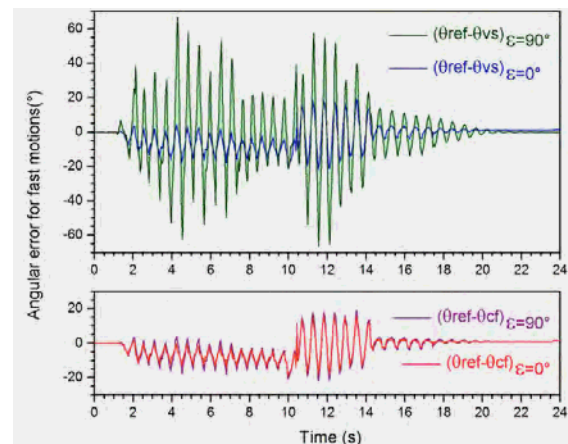


Figure.13: Error measurement of angles obtained from VS approach and those deduced from complementary filter for fast oscillatory motion

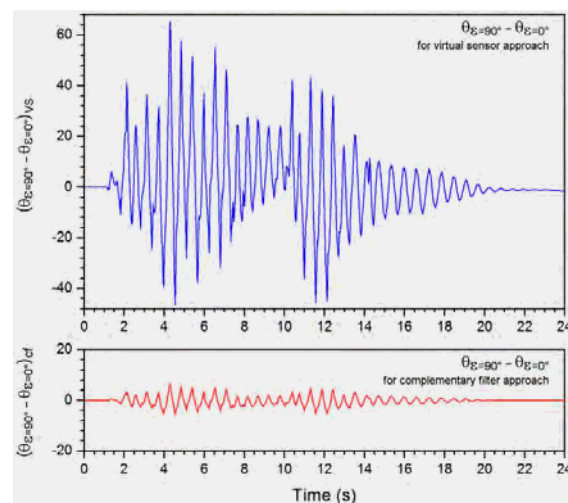


Figure.14: Angle fluctuations due to sensors misalignment when VS approach and CF were considered for fast oscillatory motion

For fast movement, the angular error in CF approach is lower than that obtained by VS method and much less sensitive to misalignment. Figure.14 shows the angle fluctuations due to sensors misalignment obtained from the two methods at fast motion. The fluctuations are more important in VS when sensors are misaligned.

Mean error angle MEA as well as root mean square RMS error deduced from the two methods are presented in Table I for both slow and fast motions. The complementary filter CF results showed an improvement of the angle accuracy when the sensors are misaligned.

TABLE.1 MEA and RMS errors angles obtained by Virtual Sensor approach and complementary filter approach

Virtual sensor approach				
Misalignment(°)	MEA (°) slow motion	MEA (°) fast motion	RMS (°) slow motion	RMS (°) fast motion
$\varepsilon = 0$	0.66	0.29	1.63	3.54
$\varepsilon = 90$	7.97	1.08	8.05	11.07
Complementary filter approach				
Misalignment(°)	MEA (°) slow motion	MEA (°) fast motion	RMS (°) slow motion	RMS (°) fast motion
$\varepsilon = 0$	1.84	2.10	2.50	5.87
$\varepsilon = 90$	2.57	1.96	3.03	6.75

5. CONCLUSION

The elbow flexion/extension angle measurement was performed by using two wireless emitting nodes containing each of them a sensor module and a wireless transmission module. Before the joint angle measurement, the sensors alignment must be achieved. The application of a complementary filter that fused the data obtained from the virtual sensor approach proposed by Dejnabadi et al. and the corrected integrated gyroscope data. This method gave better results than the virtual sensor approach alone and was much less sensitive to sensors misalignment due to muscle contraction or involuntary elbow pronation or supination. The error measurement quantification was performed by using the same sensors in a 1-DOF double-arm pendulum and the results showed an improvement of accuracy in angle measurements at fast motion when the proposed complementary filter was applied. These results may find application in biomechanical analysis of motor skills.

REFERENCES

- [1] Row. P.J, Myles. C.M, Hillmann. S.J and Hazlewood. M.E “Validation of flexible electrogoniometry as a measure of joint kinematics,” *Physiotherapy*, 2001, 87, 479-488.
- [2] Chung. P.Y.M and Ng. G.Y.F, “Comparison between an accelerometer and a three-dimensionnal motion analysis system for the detection of movement,” *Physiotherapy*, 2012, 98, 256–259.
- [3] Luinge. H.J, Veltink. P.H and Batenc. C.T.M “Ambulatory measurement of arm orientation,” *Journal of Biomechanics*, 2007, 40, 78–85.
- [4] Zabat. M, Ouadahi. N, Youyou. A, Ababou. A and Ababou. N “Digital inclinometer for joint angles measurements with a real-time 3D-animation,” *IEEE 12th International Multi-Conference on Systems, Signals & Devices (SSD15)*, Mahdia, Tunisia, pp.1-6, 2015.
- [5] Yazdifar. M, Yazdifar. M. R, Mahmud. J, Esat. I and Chizari. M “Evaluating the Hip Range of Motion using the Goniometer and Video Tracking Methods,” *Proced. Engineering*, 2013, 68, 77 – 82.

- [6] Alonge. F, Cucco. E and D'Ippolito. F “Use of accelerometers and gyros for hip and knee angle estimation,” *IEEE International Conference on Mechatronics and Automation (ICMA)*, Takamatsu, Japan, pp.939-944, 2013.
- [7] Amasay. T, Zodrow. K, Kincl. L, Hess. J and Karduna. A “Validation of tri-axial accelerometer for the calculation of elevation angles,” *Intern. Journ. of Industrial Ergonomics*, 2009, 39, 783-789.
- [8] Tognetti. A, Lorussi. F, Carbonaro. N and de Rossi. D “Wearable Goniometer and Accelerometer Sensory Fusion for Knee Angle Measurement in Daily Life,” *Sensors*, 2015, 15, 28435-28455.
- [9] Cheng. P and Oelmann. B “Joint-Angle Measurement Using Accelerometers and Gyroscopes—A Survey,” *IEEE Trans. Instrumentation and Measurement*, 2010, 59, 404-414.
- [10] Liu. K, Liu. T, Shibata. K and Inoue. Y “Reliability of Measuring Human Segment Three-dimensional Orientation Using Wearable Sensor System,” *IEEE International Conference on Control on Automation (ICCA)*, Christchurch, New Zealand, pp. 1427-1432, 2009.
- [11] Liu. K, Liu. T, Shibata. K and Inoue. Y “Ambulatory Measurement and Analysis of the Lower Limb 3D Posture Using Wearable Sensor System,” *IEEE International Conference on Mechatronics and Automation (ICMA)*, Changchun, China pp. 3065-3069, 2009.
- [12] Dejnabadi. H, Jolles. B. M and Aminian. K “A New Approach to Accurate Measurement of Uniaxial Joint Angles Based on a Combination of Accelerometers and Gyroscopes,” *IEEE Trans. Instrumentation and Measurement*, 2005, 52, 1478 – 1484.
- [13] Alvarez. D, Alvarez. J.C, Gonzalez. R.C and Lopez. M “Upper limb joint angle measurement in occupational health,” *Computer Methods in Biomech. and biomed. Eng.*, 2016, 19, 159-170.
- [14] Wu. G, Van der Helm. F.C.T, Veeger. H.E.J, Makhsous. M et al. “ISB recommendation on definitions of joint coordinate systems of various joints for the reporting of human joint motion-PartII:shoulder, elbow, wrist and hand,” *Journal of Biomechanics*, 2005, 38, 981-992.

Generation and stabilisation of dark solitons in microstructured fiber resonator

Abd El Hafid HARIZ¹, Lies BAHLOUL, Lynda CHERBI and Mustapha TLIDI²

^{*}Laboratoire of Instrumentation, University of Sciences and Technology Houari Boumediene (USTHB), Algeria,

[†]Département de Physique, Faculté des Sciences, Université Libre de Bruxelles (U.L.B.)

Abstract—We consider a photonic crystal fiber resonator, driven by a coherent beam. The threshold for appearance of dark localized structures is estimated analytically and numerically by using a weakly nonlinear analysis in the vicinity of the modulational instability threshold. The nonlinear analysis allows to determine the parameter regime where the transition from supercritical to subcritical modulational instability takes place. This transition determines the threshold associated with the formation of dark cavity solitons. Numerical simulations of the governing model equation are in good agreement with the analytical results.

Index Terms—Non linear optics, microstructured fibers, localized structures.

I. INTRODUCTION

Localized structures (LS's) often called cavity solitons belong to the class of dissipative structures found far from equilibrium. They can be localized in space and consist of bright or dark pulses. Typically, LS's are generated in a sub-critical domain where a uniform solution and a periodic structure coexist. They exhibit a high degree of multistability in a finite range of parameters called a pinning region. Spatial confinement is a universal phenomenon observed in a wide variety of nonlinear systems such as biology, plant ecology, chemistry, fluid mechanics, nonlinear optics and laser physics. The emergence of LS's is a well-documented issue (see latest overviews on this issue [1]–[5]). For broad area optical cavities, LSs were first predicted in [6], [7] and found experimentally in optical bistable systems. They appear when a single homogeneous steady state coexists with periodic structures such as hexagons and stripes [8]. When they are sufficiently separated from each other, bright or dark peaks are independent and randomly distributed in space. However, when the distance between peaks or dips decreases they start to interact via their oscillating, exponentially decaying tails. This interaction then leads to the formation of clusters [9]–[12].

In fiber cavities, the coupling between chromatic dispersion and nonlinearity may be the source of a temporal modulational instability [13]. The theoretical description of all-fiber resonators is well described by the well known Lugiato and Lefever model (LL model, [14]). As in the case of

spatial cavities, LS's are nonlinear bright peaks that have been theoretically predicted [15] and experimentally observed [16] in all fiber cavity driven by a coherent injected signal. This simple and robust device has attracted growing interest in fiber optics due to potential applications for all-optical control of light. All fiber resonators could allow for either the conception of all-optic systems for generation of signals with high repetition rate or to operate as all-optical memories with a bitrate that can reach 25 Gbits/s [16]. Temporal LS's are generated in the pinning range of parameters where the system exhibits a coexistence between two states: the uniform background and the train of pulses of light that emerges from subcritical modulational instability [17]. It has been shown that temporal LSs exhibits a homoclinic snaking type of bifurcation [17].

When all fiber cavities are operating close to the zero dispersion regime, it is necessary to take into account high-order chromatic dispersion effects. These effects may play an important role in the dynamical system of photonic crystal fibers (PCF's) [18]–[20]. PCF's allow a high control of the dispersion curve and permit exploring previously inaccessible parameter regimes [21]–[24]. The inclusion of the fourth order dispersion allows the modulational instability to have a finite domain of existence delimited by two pump power values [25]. Fourth order dispersion has also been predicted to stabilize dark temporal cavity solitons in PCF resonators [17]. Together with this effect, the third order dispersion causes a spontaneous broken reflection symmetry and allows a motion of both periodic and localized structures [26]. The influence of higher order dispersion on the nonlinear dynamical properties of bright temporal LS's in all photonic crystal fiber cavities has been investigated in [27]. Temporal soliton families and resonant radiation near zero group-velocity dispersion have been also reported [28].

II. MEAN FIELD MODEL FOR PHOTONIC CRYSTAL FIBER CAVITIES

We consider an optical system in which a continuous wave (CW) of power S^2 is launched into a single mode photonic

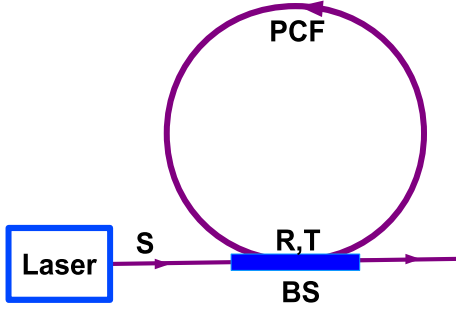


Fig. 1. Schematic setup of PCF cavity. The transmission and the reflexion coefficients of the beam splitter (BS) are denoted by R and T , respectively. The slowly varying envelope of the electric field circulation inside the cavity is represented by E , and S is the injected field amplitude.

crystal fiber resonator by means of a beam splitter, as shown in Fig. 1. The free propagation of light along the fiber is described by a generalized nonlinear Schrödinger equation (NLS) [29] where the propagation constant is expanded to the fourth order of dispersion in Taylor series. The NLS combined with appropriate cavity boundary conditions leads to the model equation [25] :

$$t_r \frac{\partial E(t, \tau)}{\partial t} = (-\alpha - i\delta_0 + i\gamma L |E|^2 - i\beta_2 \frac{L}{2} \frac{\partial^2}{\partial \tau^2} + \beta_3 \frac{L}{6} \frac{\partial^3}{\partial \tau^3} + i\beta_4 \frac{L}{24} \frac{\partial^4}{\partial \tau^4}) E(t, \tau) + \sqrt{T} S, \quad (1)$$

where $E(t, \tau)$ is the slowly varying envelope of the electric field. t_r is the time of one cavity round trip, t is the slow time scale that describes the evolution of the field envelope from one cavity round trip to the other, and τ is the fast time in the reference frame moving with the group velocity of the light, δ_0 is the detuning between the input beam frequency, and the closest cavity resonance. The coefficients $\beta_{2,3,4}$ account for the second, third and fourth order chromatic dispersion, respectively. γ is nonlinear parameter, α represents the linear dissipation and T is the transmission coefficient of the beam splitter. In addition, we have neglected nonlinear phenomena such as two-photon absorption and Raman scattering, since we deal with pulses width larger than 1 ps [17]. The equation (1) is valid when the cavity finesse is high, and when the nonlinear phase shift and losses are much smaller than unity. We furthermore assume that the optical field maintains its polarization as it propagates along the fiber. The Eq. (1) can be further simplified to obtain a generalized Lugiato-Lefever model in an adimensional form [25]

$$\frac{\partial E}{\partial t} = S - (1 + i\Delta)E + i|E|^2 E - iB_2 \frac{\partial^2 E}{\partial \tau^2} + B_3 \frac{\partial^3 E}{\partial \tau^3} + iB_4 \frac{\partial^4 E}{\partial \tau^4}. \quad (2)$$

The link between the adimensional variables and parameters and the physical ones are defined in [25]. The homogeneous steady states (HSS) of Eq. (2) satisfy $S = [1 + i(\Delta - |E_s|^2)]E_s$. We perform a linear stability analysis of the HSS with respect

to finite frequency perturbations of the form $\exp(\lambda t + i\Omega\tau)$, this analysis yields the eigenvalues

$$\lambda = -1 + iB_3\Omega^3 \pm \sqrt{I_s^2 - (-\Delta + 2I_s + B_2\Omega^2 + B_4\Omega^4)^2} \quad (3)$$

where $I_s = |E_s|^2$ corresponds to the uniform intensity background of light.

The system becomes unstable when one of these two eigenvalues becomes zero with a finite frequency. The system exhibits a modulational instability between the first threshold $I_{c1} = 1$, and the second threshold $I_{c2} = [2\kappa + \sqrt{\kappa^2 - 3}]/3$ with $\kappa = B_2^2/(4B_4) + \Delta$. It has been shown in [25], [27] that the fourth-order dispersion limits the region of modulation instability between these two intensity levels. Indeed, when $B_4 = 0$, the second threshold does not exist. We note also frequency degeneracy Ω_l^2 and Ω_u^2 at the first instability threshold where $\Omega_{l,u}^2 = [-B_2 \pm \sqrt{B_2^2 + 4B_4(\Delta - 2)}]/(2B_4)$. At the second threshold I_{c2} , a new critical frequency appears $\Omega^2 = -B_2/2B_4$.

In what follows, we remove the frequency degeneracy for the first threshold by choosing B_2 , B_4 and Δ such as $B_2^2 + 4(\Delta - 2)B_4 = 0$. In this case, the MI zone is limited between two thresholds, the first at $I_{1c} = 1$ and the second will be at $I_{2c} = 5/3$, while the destabilized frequencies in both thresholds will be equal to $\Omega_c^2 = \Omega_l^2 = \Omega_u^2 = -B_2/(2B_4)$.

III. WEAKLY NONLINEAR ANALYSIS

We shall describe the nonlinear evolution of the system in the vicinity of the second instability point $I_{2c} = 5/3$. The small-amplitude inhomogeneous stationary solutions, i.e., solutions that are independent of slow t and fast τ times can be calculated analytically by employing the standard theory [30], [31]. For this purpose, we first decompose the electric field into its real and imaginary parts: $E = x_1 + ix_2$ and introduce the excess variables as $(x_1(t, \tau), x_2(t, \tau)) = (x_{1s}, x_{2s}) - (U(t, \tau), V(t, \tau))$ with x_{1s} and x_{2s} are, respectively, the real and the imaginary parts of the homogeneous solutions independent of t and τ . The homogeneous solutions of Eq. (1) obey to

$$-x_{1s} + S - x_{2s}(x_{1s}^2 + x_{2s}^2 - \Delta) = 0, \quad (4)$$

$$-x_{2s} + x_{1s}(x_{1s}^2 + x_{2s}^2 - \Delta) = 0. \quad (5)$$

Next, we introduce a small parameter $\epsilon \ll 1$ which measures the distance from the critical modulational point. We expand all variables around their critical values at the bifurcation point.

$$S = S_{2c} + \epsilon\mu_1 + \epsilon^2\mu_2 + \dots \quad (6)$$

$$(U, V) = \epsilon(U_0, V_0) + \epsilon^2(U_1, V_1) + \epsilon^3(U_2, V_2) + \dots \quad (7)$$

$$(x_{1s}, x_{2s}) = (a_0, b_0) + \epsilon(a_1, b_1) + \epsilon^2(a_2, b_2) + \dots \quad (8)$$

We expand the time as

$$\frac{\partial}{\partial t} = \frac{\partial}{\partial T_0} + \epsilon \frac{\partial}{\partial T_1} + \epsilon^2 \frac{\partial}{\partial T_2} + \dots \quad (9)$$

At the leading order in ϵ we find that $a_0 = b_0 = \mu_1 = 0$. At this order, near the critical point we can approximate

solutions by a linear superposition of the corresponding critical frequencies Ω_c and Q_c

$$(U_0, V_0) = \left(1, \frac{\rho + 3}{1 - 3\rho}\right) \tilde{W} \exp i(Q_c T_0 + \Omega_c \tau) + c.c. \quad (10)$$

where $c.c.$ denotes the complex conjugate and $\rho = 5/3 - \Delta$. The complex amplitude \tilde{W} associated with the frequency Ω_c does not depend on the time τ , it depends only on the time T_0 . The quantities $a_i, b_i, U_i,$ and V_i can be calculated by inserting (19- 22) into (2, 17, 18) and equating terms with the same powers of ϵ . At order ϵ^2 , the solvability condition imposes that $a_1 = b_1 = \mu_1 = 0$. The application of the solvability condition to the order ϵ^3 brings an amplitude equation for the unstable mode. In terms of the unscaled amplitudes ($W = \epsilon \tilde{W} + \dots$), we obtain

$$\frac{\partial W}{\partial t} = \mu W + (f_r + i f_i) W |W|^2 \quad (11)$$

Where

$$\begin{aligned} \mu &= \frac{S - S_{2c}}{(3\rho + 1)(\rho + 3)S_c} \text{ with } S_{2c} = \sqrt{\frac{5}{3}} \sqrt{1 + \rho^2} \quad (12) \\ f_r &= \frac{ac + bd}{c^2 + d^2} \text{ and } f_i = \frac{bc - ad}{c^2 + d^2} \quad (13) \end{aligned}$$

where the coefficients a, b, c and d are expressed in term of the detuning parameter $\Delta = 5/3 - \rho$. When $f_r(\Delta) < 0$, the modulational instability is subcritical. In this case, it is necessary to retain the fifth order in ϵ , since equation (24) loses its meaning. Thus, if $f_r(\Delta) > 0$, the modulational instability is supercritical, leading to stable small amplitude temporal structures. The parameter regime where the bifurcation is supercritical is plotted in Fig. 2a. The transition from super- to sub-critical modulational instability is explicitly given by $f_r = 0$. This condition corresponds to the threshold of the emergence of temporal cavity solitons that we shall discuss in the next section. The dependence of the threshold as a function of the third order dispersion coefficient and of the detuning parameter is shown in Fig. 2b. Note, however, that the third order dispersion affects the threshold of the modulational instability as well. In the supercritical case where $f_r(\Delta) > 0$, we seek for solutions of Eq. 24 in the form of $W = A \exp(iRt)$. Inserting this ansatz in Eq. 24. The stationary solutions are

$$A_s = 0, \quad A_s = \pm \sqrt{\frac{-\mu}{f_r}} \text{ and } R = \frac{\mu f_i}{f_r} \quad (14)$$

The third order dispersion breaks the symmetry $(\tau, -\tau)$. This breaking symmetry induces a motion of temporal structures and the linear and nonlinear correction to their velocity is

$$v = v_l + v_{nl} \text{ with } v_l = \frac{\partial \lambda_i}{\partial \Omega} \text{ and } v_{nl} = \frac{\partial R}{\partial \Omega} \quad (15)$$

In terms of the dynamical parameters the linear and the nonlinear velocities are

$$v_l = 3B_3 \Omega^2 \text{ and } v_{nl} = \frac{\mu}{f_r} \frac{\partial f_i}{\partial \Omega} \quad (16)$$

The velocity as a function of the third order dispersion coefficient (Eq. 29) is plotted in Fig. 3. The velocity of moving temporal structures calculated through numerical simulations of the model Eq. 2 is in good agreement with the one estimated from the above analysis.

IV. WEAKLY NONLINEAR ANALYSIS

We shall describe the nonlinear evolution of the system in the vicinity of the second instability point $I_{2c} = 5/3$. The small-amplitude inhomogeneous stationary solutions, i.e., solutions that are independent of slow t and fast τ times can be calculated analytically by employing the standard theory [30], [31]. For this purpose, we first decompose the electric field into its real and imaginary parts: $E = x_1 + ix_2$ and introduce the excess variables as $(x_1(t, \tau), x_2(t, \tau)) = (x_{1s}, x_{2s}) - (U(t, \tau), V(t, \tau))$ with x_{1s} and x_{2s} are, respectively, the real and the imaginary parts of the homogeneous solutions independent of t and τ . The homogeneous solutions of Eq. (1) obey to

$$-x_{1s} + S - x_{2s}(x_{1s}^2 + x_{2s}^2 - \Delta) = 0 \quad , \quad (17)$$

$$-x_{2s} + x_{1s}(x_{1s}^2 + x_{2s}^2 - \Delta) = 0 \quad . \quad (18)$$

Next, we introduce a small parameter $\epsilon \ll 1$ which measures the distance from the critical modulational point. We expand all variables around their critical values at the bifurcation point.

$$S = S_{2c} + \epsilon \mu_1 + \epsilon^2 \mu_2 + \dots \quad (19)$$

$$(U, V) = \epsilon(U_0, V_0) + \epsilon^2(U_1, V_1) + \epsilon^3(U_2, V_2) + \dots \quad (20)$$

$$(x_{1s}, x_{2s}) = (a_0, b_0) + \epsilon(a_1, b_1) + \epsilon^2(a_2, b_2) + \dots \quad (21)$$

We expand the time as

$$\frac{\partial}{\partial t} = \frac{\partial}{\partial T_0} + \epsilon \frac{\partial}{\partial T_1} + \epsilon^2 \frac{\partial}{\partial T_2} + \dots \quad (22)$$

At the leading order in ϵ we find that $a_0 = b_0 = \mu_1 = 0$. At this order, near the critical point we can approximate solutions by a linear superposition of the corresponding critical frequencies Ω_c and Q_c

$$(U_0, V_0) = \left(1, \frac{\rho + 3}{1 - 3\rho}\right) \tilde{W} \exp i(Q_c T_0 + \Omega_c \tau) + c.c. \quad (23)$$

where $c.c.$ denotes the complex conjugate and $\rho = 5/3 - \Delta$. The complex amplitude \tilde{W} associated with the frequency Ω_c does not depend on the time τ , it depends only on the time T_0 . The quantities $a_i, b_i, U_i,$ and V_i can be calculated by inserting (19- 22) into (2, 17, 18) and equating terms with the same powers of ϵ . At order ϵ^2 , the solvability condition imposes that $a_1 = b_1 = \mu_1 = 0$. The application of the solvability condition to the order ϵ^3 brings an amplitude equation for the unstable mode. In terms of the unscaled amplitudes ($W = \epsilon \tilde{W} + \dots$), we obtain

$$\frac{\partial W}{\partial t} = \mu W + (f_r + i f_i) W |W|^2 \quad (24)$$

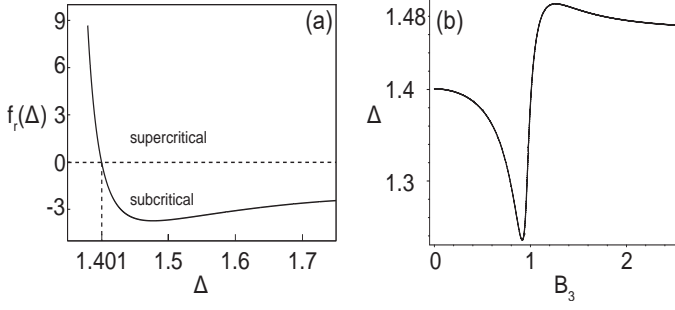


Fig. 2. The threshold associated with the transition from super- to sub-critical modulational instability is plotted (a) as a function of the detuning parameter Δ for $B_3 = 0$; (b) in the plane (B_3, Δ) . Others parameters are $B_4 = 0.5$, and $B_2 = \sqrt{4B_4(2 - \Delta)}$

Where

$$\mu = \frac{S - S_{2c}}{(3\rho + 1)(\rho + 3)S_c} \text{ with } S_{2c} = \sqrt{\frac{5}{3}} \sqrt{1 + \rho^2} \quad (25)$$

$$f_r = \frac{ac + bd}{c^2 + d^2} \text{ and } f_i = \frac{bc - ad}{c^2 + d^2} \quad (26)$$

where the coefficients a , b , c and d are expressed in term of the detuning parameter $\Delta = 5/3 - \rho$. When $f_r(\Delta) < 0$, the modulational instability is subcritical. In this case, it is necessary to retain the fifth order in ϵ , since equation (24) loses its meaning. Thus, if $f_r(\Delta) > 0$, the modulational instability is supercritical, leading to stable small amplitude temporal structures. The parameter regime where the bifurcation is supercritical is plotted in Fig. 2a. The transition from super- to sub-critical modulational instability is explicitly given by $f_r = 0$. This condition corresponds to the threshold of the emergence of temporal cavity solitons that we shall discuss in the next section. The dependence of the threshold as a function of the third order dispersion coefficient and of the detuning parameter is shown in Fig. 2b. Note, however, that the third order dispersion affects the threshold of the modulational instability as well. In the supercritical case where $f_r(\Delta) > 0$, we seek for solutions of Eq. 24 in the form of $W = A \exp(iRt)$. Inserting this ansatz in Eq. 24. The stationary solutions are

$$A_s = 0, \quad A_s = \pm \sqrt{\frac{-\mu}{f_r}} \text{ and } R = \frac{\mu f_i}{f_r} \quad (27)$$

The third order dispersion breaks the symmetry $(\tau, -\tau)$. This breaking symmetry induces a motion of temporal structures and the linear and nonlinear correction to their velocity is

$$v = v_l + v_{nl} \text{ with } v_l = \frac{\partial \lambda_i}{\partial \Omega} \text{ and } v_{nl} = \frac{\partial R}{\partial \Omega} \quad (28)$$

In terms of the dynamical parameters the linear and the nonlinear velocities are

$$v_l = 3B_3\Omega^2 \text{ and } v_{nl} = \frac{\mu}{f_r} \frac{\partial f_i}{\partial \Omega} \quad (29)$$

The velocity as a function of the third order dispersion coefficient (Eq. 29) is plotted in Fig. 3. The velocity of moving

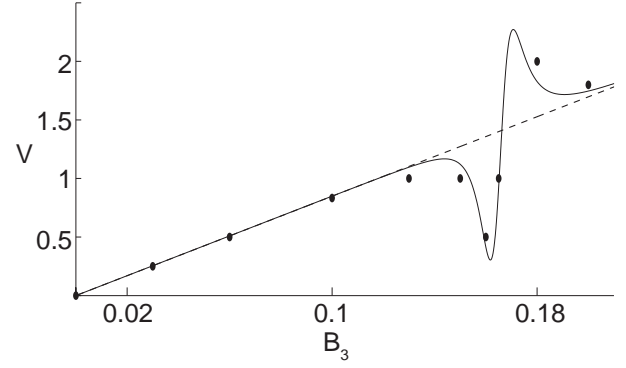


Fig. 3. Linear velocity of the periodic structure and its nonlinear correction with respect to B_3 . Dashed curve denotes the linear velocity. The velocity with its nonlinear correction (Eq. 28) is plotted by a solid line. The velocity obtained from direct numerical simulations of Eq. (2) are indicated by circles. Parameters are $S = 1.4307$, $\epsilon^2 = 0.006$, $\Delta = 1.2$, $B_4 = 0.1$, and $B_2 = -0.5657$.

temporal structures calculated through numerical simulations of the model Eq. 2 is in good agreement with the one estimated from the above analysis.

V. MOVING LOCALIZED STRUCTURES

In this section, we are interested in the situation where the bifurcation towards modulational instability appears sub-critically. In the absence of the third order dispersion, the typical bifurcation diagram is shown in Fig. 4. In the domain, denoted by L , the system exhibits a coexistence between two stable solutions: the homogeneous steady state (uniform background) and the temporal train of periodic pulses that emerges from subcritical modulational instability. Temporal dark cavity solitons, connecting the HSS and a branch of periodic solutions, are found in a well-defined region of parameters called a pinning zone denoted L in Fig. 4. It has been shown that temporal cavity solitons exhibit a homoclinic snaking type of bifurcation [17]. Depending on the initial condition used, a single dip, or multiple ones in the intensity profile can be generated in direct numerical simulations of Eq. 2. Examples of stationary temporal dark cavity solitons involving one to six dips as shown in Fig. 5. They are obtained from the same values of parameters and they are characterized by an oscillating exponentially decaying tails.

Let us now investigate the effect of third order dispersion on the dark cavity solitons. As we have already mentioned, this effect breaks the reflexion symmetry $(\tau \rightarrow -\tau)$ of temporal cavity solitons emerging from subcritical bifurcation point. This symmetry breaking induces a drift of the temporal cavity solitons with a constant velocity. Examples of drifting temporal dark cavity solitons are shown in τ - t maps of the Fig. 6.

VI. CONCLUSIONS

In this paper, we have investigated the weakly nonlinear dynamics of all fiber cavities with both fourth and third order dispersions in the neighborhood of the second modulational

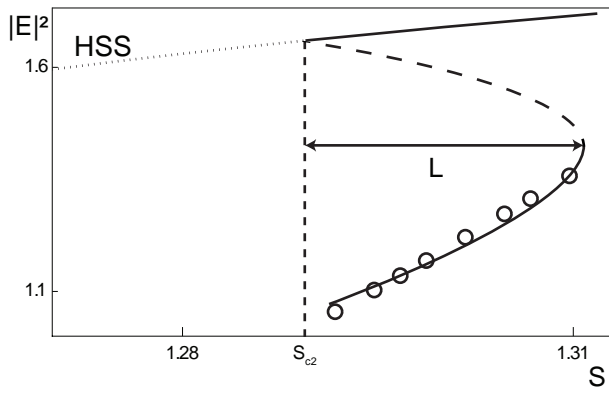


Fig. 4. Bifurcation diagram associated with the temporal train of periodic pulses that emerges from subcritical modulational instability. Parameter are $B_4 = 0.1$, $B_2 = -0.3347$, $B_3 = 0$, $\Delta = 1.72$. The full (dashed) curve indicates stable (unstable) solutions. The open circles represent the numerical values of the minimum intensity of the temporal train of periodic pulses.

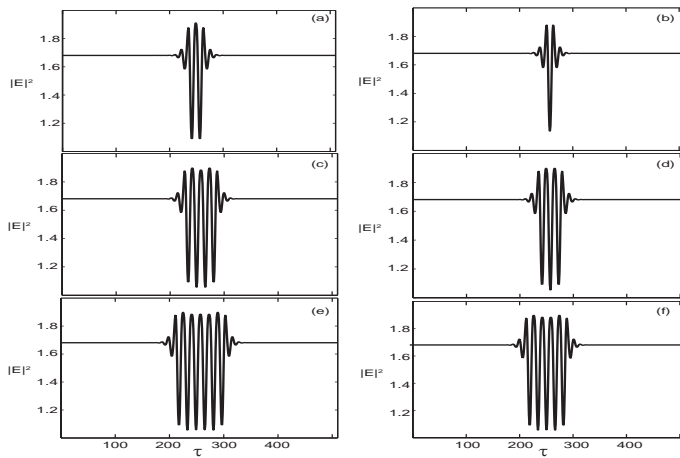


Fig. 5. Stationary temporal dark cavity solitons with up to 6 dips. (a)-(f) corresponding to 1-6 dips or holes in the intensity profiles, respectively. Parameters are the same as figure 3 with $B_3 = 0$

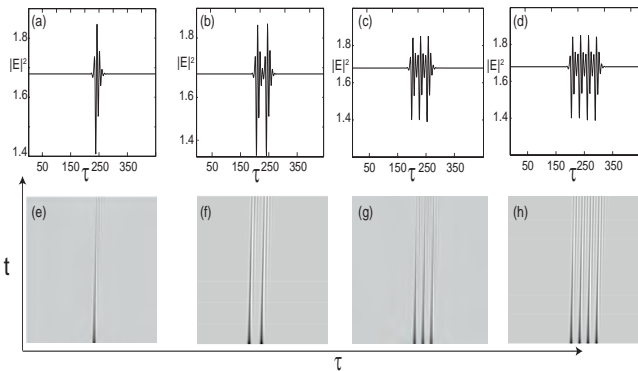


Fig. 6. Moving temporal dark cavity solitons with up to 4 dips. (a)-(d) are the intensity profiles in the PCF cavity at $t = 0$, whereas (e)-(h) are space-time maps in the (t, τ) plane. Parameters are the same as figure 3 with $B_3 = 0.1$

instability point. We have estimated the velocity of moving temporal train of periodic pulses that emerge from supercritical modulational instability point. The drift is a consequence of the third order dispersion that breaks the reflexion symmetry ($\tau \rightarrow -\tau$). When the modulational instability appears subcritically, we found moving temporal dark solitons that can be either isolated or self-organized.

REFERENCES

- [1] H. Leblond, D. Mihalache, Models of few optical cycle solitons beyond the slowly varying envelope approximation, *Physics Reports* 523 (2) (2013) 61 – 126.
- [2] M. Tlidi, K. Staliunas, K. Panajotov, A. G. Vladimirov, M. G. Clerc, Localized structures in dissipative media: from optics to plant ecology, *Philosophical Transactions of the Royal Society of London A: Mathematical, Physical and Engineering Sciences* 372 (2014) 20140101.
- [3] M. Lapine, I. V. Shadrivov, Y. S. Kivshar, Colloquium: Nonlinear metamaterials, *Rev. Mod. Phys.* 86 (2014) 1093–1123. doi:10.1103/RevModPhys.86.1093.
- [4] E. Knobloch, Spatial localization in dissipative systems, *Annual Review of Condensed Matter Physics* 6 (1) (2015) 325–359. arXiv:10.1146/annurev-conmatphys-031214-014514, doi:10.1146/annurev-conmatphys-031214-014514.
- [5] L. Lugiato, F. Prati, M. Brambilla, *Nonlinear Optical Systems*, Cambridge University Press, 2015.
- [6] D. W. McLaughlin, J. V. Moloney, A. C. Newell, Solitary waves as fixed points of infinite-dimensional maps in an optical bistable ring cavity, *Phys. Rev. Lett.* 51 (1983) 75. doi:10.1103/PhysRevLett.51.75.
- [7] N. N. Rosanov, G. V. Khodova, Autosolitons in bistable interferometers, *Optics and Spectroscopy* 65 (1988) 449–450.
- [8] M. Tlidi, P. Mandel, R. Lefever, Localized structures and localized patterns in optical bistability, *Phys. Rev. Lett.* 73 (1994) 640–643. doi:10.1103/PhysRevLett.73.640.
- [9] A. Vladimirov, J. McSloy, D. Skryabin, W. Firth, Two-dimensional clusters of solitary structures in driven optical cavities, *Phys. Rev. E* 65 (2002) 046606. doi:10.1103/PhysRevE.65.046606.
- [10] M. Tlidi, A. G. Vladimirov, P. Mandel, Interaction and stability of periodic and localized structures in optical bistable systems, *Quantum Electronics, IEEE Journal of* 39 (2) (2003) 216–226. doi:10.1109/JQE.2002.807193.
- [11] M. Tlidi, R. Lefever, A. Vladimirov, On vegetation clustering, localized bare soil spots and fairy circles, *Lecture notes in Physics* 751 (2008) 381.
- [12] A. G. Vladimirov, R. Lefever, M. Tlidi, Relative stability of multipole localized patterns of cavity solitons, *Phys. Rev. A* 84 (2011) 043848. doi:10.1103/PhysRevA.84.043848.
- [13] M. Haelterman, S. Trillo, S. Wabnitz, Additive-modulation-instability ring laser in the normal dispersion regime of a fiber, *Opt. Lett.* 17 (1992) 745–747. doi:10.1364/OL.17.000745.
- [14] L. A. Lugiato, R. Lefever, Spatial dissipative structures in passive optical systems, *Phys. Rev. Lett.* 58 (1987) 2209–2211. doi:10.1103/PhysRevLett.58.2209.
- [15] A. J. Scroggie, W. J. Firth, G. S. McDonald, M. Tlidi, R. Lefever, L. A. Lugiato, Pattern formation in a passive kerr cavity, *Chaos, Solitons and Fractals* 4 (8) (1994) 1323. doi:http://dx.doi.org/10.1016/0960-0779(94)90084-1.
- [16] F. Leo, S. Coen, P. Kockaert, S.-P. Gorza, P. Emplit, M. Haelterman, Temporal cavity solitons in one-dimensional kerr media as bits in an all-optical buffer, *Nat Photon* 4 (2010) 471. doi:10.1038/nphoton.2010.120.
- [17] M. Tlidi, L. Gelens, High-order dispersion stabilizes dark dissipative solitons in all-fiber cavities, *Opt. Lett.* 35 (3) (2010) 306–308. doi:10.1364/OL.35.000306.
- [18] S. B. Cavalcanti, J. C. Cressoni, H. R. da Cruz, A. S. Gouveia-Neto, Modulation instability in the region of minimum group-velocity dispersion of single-mode optical fibers via an extended nonlinear schrödinger equation, *Phys. Rev. A* 43 (1991) 6162–6165. doi:10.1103/PhysRevA.43.6162.
- [19] S. Pitois, G. Millot, Experimental observation of a new modulational instability spectral window induced by fourth-order dispersion in a normally dispersive single-mode optical fiber, *Optics Communications* 226 (16) (2003) 415 – 422. doi:http://dx.doi.org/10.1016/j.optcom.2003.09.001.

- [20] J. D. Harvey, R. Leonhardt, S. Coen, G. K. L. Wong, J. Knight, W. J. Wadsworth, P. S. Russell, Scalar modulation instability in the normal dispersion regime by use of a photonic crystal fiber, *Opt. Lett.* 28 (22) (2003) 2225–2227. doi:10.1364/OL.28.002225.
- [21] N. Y. Joly, F. G. Omenetto, A. Efimov, A. J. Taylor, J. C. Knight, P. S. J. Russell, Competition between spectral splitting and raman frequency shift in negative-dispersion slope photonic crystal fiber, *Optics Communications* 248 (13) (2005) 281 – 285. doi:http://dx.doi.org/10.1016/j.optcom.2004.11.091.
- [22] A. V. Yulin, D. V. Skryabin, P. S. J. Russell, Four-wave mixing of linear waves and solitons in fibers with higher-order dispersion, *Opt. Lett.* 29 (20) (2004) 2411–2413. doi:10.1364/OL.29.002411.
- [23] W. J. Wadsworth, N. Joly, J. C. Knight, T. A. Birks, F. Biancalana, P. S. J. Russell, Supercontinuum and four-wave mixing with q-switched pulses in endlessly single-mode photonic crystal fibres, *Opt. Express* 12 (2) (2004) 299–309. doi:10.1364/OPEX.12.000299.
- [24] A. Demircan, U. Bandelow, Supercontinuum generation by the modulation instability, *Optics Communications* 244 (16) (2005) 181 – 185. doi:http://dx.doi.org/10.1016/j.optcom.2004.09.049.
- [25] M. Tlidi, A. Mussot, E. Louvergneaux, G. Kozyreff, A. G. Vladimirov, M. Taki, Control and removal of modulational instabilities in low-dispersion photonic crystal fiber cavities, *Opt. Lett.* 32 (6) (2007) 662–664. doi:10.1364/OL.32.000662.
- [26] M. Tlidi, L. Bahloul, L. Cherbi, A. Hariz, S. Coulibaly, Drift of dark cavity solitons in a photonic-crystal fiber resonator, *Phys. Rev. A* 88 (2013) 035802. doi:10.1103/PhysRevA.88.035802.
- [27] L. Bahloul, L. Cherbi, A. Hariz, M. Tlidi, Temporal localized structures in photonic crystal fibre resonators and their spontaneous symmetry-breaking instability, *Philosophical Transactions of the Royal Society of London A: Mathematical, Physical and Engineering Sciences* 372 (2027). doi:10.1098/rsta.2014.0020.
- [28] C. Milián, D. Skryabin, Soliton families and resonant radiation in a micro-ring resonator near zero group-velocity dispersion, *Opt. Express* 22 (3) (2014) 3732–3739. doi:10.1364/OE.22.003732.
- [29] G. P. Agrawal, *Nonlinear Fiber Optics*, 5th Edition, Academic Press, 2012.
- [30] P. Manneville, *Dissipative Structures and weak turbulence*, Academic Press, 1990.
- [31] M. Tlidi, R. Lefever, P. Mandel, Pattern selection in optical bistability, *Quantum and Semiclassical Optics: Journal of the European Optical Society Part B* 8 (4) (1996) 931.

Low-cost instrumented handrim for manual wheelchair propulsion force analysis

F. Djail¹, K. BenSiSaid¹, K. Benrekaa¹, N. Ababou¹, A. Ababou¹
and N. Saadia²

¹ Laboratory of Instrumentation, University of Science and Technology Houari Boumediene, Algiers, Algeria.

fdjail@usthb, kbensisaid@usthb, kbenrekaa@usthb.dz, nababou@usthb.dz, aababou@usthb.dz

² Laboratory of Robotics, Parallelism & Embedded systems, University of Science and Technology Houari Boumediene, Algiers, Algeria.

nsaadia@usthb.dz

ABSTRACT

Manual wheelchair users have a high risk of injuries on their joints and muscles of upper extremities due to the repetitive motion and their more or less efficient propulsion technique. Therefore, the propulsion technique improvement should decrease the risk of injury. One way of the study of the wheelchair propulsion is the use of an instrumented wheel. Several commercial and non-commercial instrumented wheels used in indoor environment were reported in the literature. In this work, a low-cost instrumented wheel was designed and fabricated for manual wheelchair propulsion force analysis. The prototype consists of a mechanical kit and an electronic embedded system. Outdoor measurements have been performed and the results showed that the propulsion force and the rolling resistance as well as the mechanical power are much more important because of the nature of the ground.

Key Words: Embedded system; Inertial station, Instrumented handrim, Manual wheelchair, Propulsion force.

1. INTRODUCTION

People with disabilities often depend on assistive devices to enable activities of daily living as well as to compete in sport. The wheelchair is fundamental in allowing a paraplegic user to carry out the tasks of daily living. In particular, manual

wheelchair users have a high risk of injuries on their joints and muscles of upper extremities due to the repetitive motion and their more or less efficient propulsion technique [1, 2]. On the other hand, higher risk factors for cardiovascular disease were related to high body mass index values in persons with wheelchair dependent paraplegia after spinal cord injuries [3]. Therefore, the propulsion technique improvement should decrease the risk of injury. The kinematic and kinetic parameters that generally studied are push angle, wheelchair speed, stroke frequency, three-dimensional force and torque, and power output.

The propulsion kinematics and kinetics have been studied in laboratory environment using wheelchair dynamometers [4,5], wheelchair ergometers [6-9], commercial instrumented wheels such as Smartwheel and OptiPush [10-14] or non-commercial instrumented wheels [15, 16]. In Smartwheel, three aluminum beams were mounted 120° apart on the wheel. Linear bearings were used so that force applied directly to the end of a beam toward the hub is transferred to the other two beams. Each beam fits into the point of a pie-shaped wheel section. Each beam was secured at the hub while the pushrim, via its standoffs, was mounted to the outer end of each beam. Each beam was instrumented with one set of full strain gage Wheatstone bridges with its conditioning circuit and dc excitation. An

optical encoder is used to measure the push angle by detecting the position of the reference beam with respect to top dead center [10, 17]. The pushrim force as well as torque components along X, Y and Z axes are obtained from the beams deflection and the wheel angle according to equations described in [17]. As in Smartwheel, three aluminum beams are also mounted 120° apart on the OptiPush wheel. However, the Smartwheel uses instrumented beams with strain gages to measure torques and forces, whereas the OptiPush uses a commercial 6-DOF force-torque sensor at the center, which is attached to the rim through rigid beams. Both wheels come with a software package. A comparison between the results provided by the two wheels when simultaneously mounted on a manual wheelchair has been investigated by Vegter et al. and they found a good agreement between the two instrumented wheels [11]. Wu et al. designed an instrumented wheel using a commercial 6-DOF load cell and a data logger to measure three-dimensional forces and torques during the wheelchair propulsion [18]. Later, Goosey-Tolfrey et al. have developed a force-handrim measuring device composed of eight pairs of strain gages attached to four aluminum beams joining the handrim to the wheel hub. Each pair of strain gages was connected in a half bridge configuration to an associated conditioner to measure push rim forces during racing wheelchair propulsion [19]. More recently, Mallakzadeh and Akbari [16] proposed an instrumented wheel system in which the handrim assembly is attached to a round Plexiglas disc via four L-shaped slotted beams. The assembled hand rim is mounted directly to a commercial 6-DOF load cell without connecting to other parts of the wheel. The other end of the load cell is attached to a round aluminum retainer that is mounted on a wheel hub. The two commercial wheels described above have good performances but are very expensive. They are generally used in an indoor environment and on ergometers or motor-driven treadmills. It is also the case for the non-commercial instrumented wheels.

In this paper, we present a low-cost instrumented wheel prototype to be used in indoor as well as outdoor environments to

measure propulsion force, wheelchair velocity, and wheelchair displacement to assess the mechanical power developed by the user during propulsion.

2. EXPERIMENTAL & METHODS

2.1. Developed prototype

The experimental prototype developed in this work consists of two core components, a mechanical kit and an embedded instrumented device presented in Figure.1. and Figure.2., respectively. The mechanical part is illustrated in Figure.1. The prototype is composed of a wheel, a handrim, four load cells (1), four aluminum beams (2), and two bike accessories: a brake disk (3) and a front hub (4). One end of each load cells is screwed directly to the handrim using the pre-existing threaded holes. Its other end is attached to the brake disk via the extension beam. The initial hub of the chair rear wheel is replaced by the hub (4) of the front wheel of a mountain bike. Once the brake disk is fixed on this hub, the prototype is attached to the wheelchair frame using a suitable bolt. The prototype measures force on the handrim using four 5kg commercially-available aluminum load cells including strain gages already glued and wired together in full-bridge Wheatstone bridge.



Figure.1: Top drawings: assembled handrim prototype inside and front views. Bottom drawings: mechanical used spare parts.

Figure.2. displays the assembly on the wheelchair showing the embedded system

with its constituent modules attached on the rear wheel axle and powered by a 9V battery. The HX711 is a precision 24-bit analog-to-digital converter designed for weighing scales and industrial control applications to interface directly with a bridge sensor. The accuracy of the force measurement is equal to 0.1 % F.S. The BNO055 is a System in Package integrating a triaxial 14-bit accelerometer, a triaxial 16-bit gyroscope with a range of $\pm 2000^\circ/s$, a triaxial geomagnetic sensor and a 32-bit cortex M0+ microcontroller running Bosch Sensortec sensor fusion software, equipped with digital bidirectional I2C and UART interfaces. The HC-05 is a Bluetooth Serial Port Protocol module, designed for transparent wireless serial connection setup, able to use neither receiving nor transmitting data. The Arduino Mega 2560 is a microcontroller board based on the ATmega2560 with 54 digital input/output pins, 16 analog inputs, 4 UARTs, a USB connection, a power jack, an ICSP header, and a reset button.

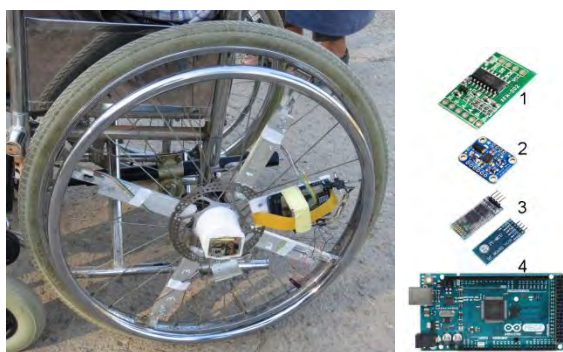


Figure.2: Assembly on the wheelchair showing the embedded system composed essentially of HX711, BNO055, HC-05 and ArduinoMega-2560 modules, respectively indexed from 1 to 4.

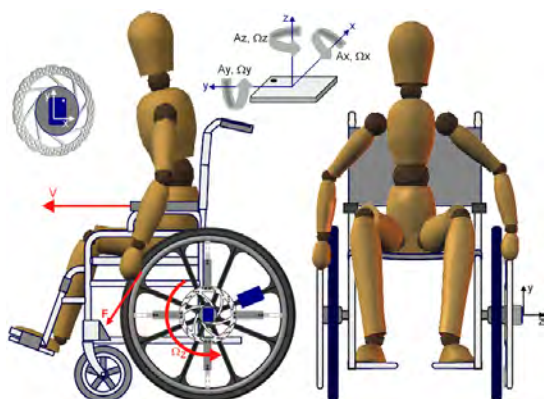


Figure.3: Force, linear and angular velocities during manual propulsion

2.2. Methods

To move the wheelchair, the user must exert on the handrim a push oriented forward. During the push, the user upper limb transmits to the handrim a tri-dimensional force whose three components can be determined from an instrumented wheel similar to those described in the introduction [10-16]. The tangential force component to the handrim that contributes to the displacement of the wheelchair is determined by calculation. During the wheelchair propulsion with our prototype instrumented wheel, the tangential force component is directly measured by the output voltage of the load cells using the calibration curve of the sensor. For the geometry shown in Figure.3., the four load cells are subjected to the same moment of force. The BNO55 module is fixed in the wheel plane as shown in Figure.3. The wheel angular velocity Ω_z expressed in rd/s is measured by the gyro. When the wheelchair moves in a straight line, its linear velocity V is given by (1), where R_{WC} is the rear wheel radius.

$$V = R_{WC} \cdot \Omega_z \quad (1)$$

Figure.4. displays the conventional configuration of the load cell (4a), the force exerted by the hand during propulsion (4b), and the distribution of the forces on the four load cells arranged in the prototype as illustrated in (4c). In the conventional configuration, the load cell is usually anchored at one end and supports a load f at its other end.

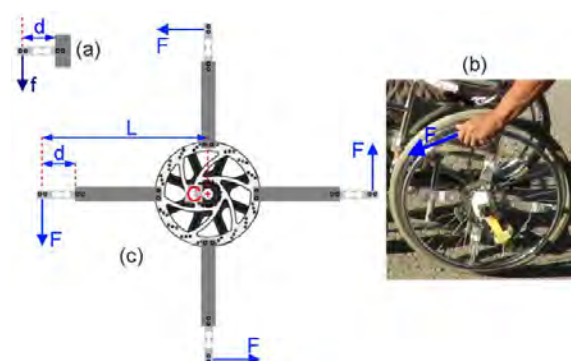


Figure.4: Measurement method of the propulsion force on the instrumented wheel. (a) load cell conventional configuration, (b) tangential force during manual propulsion, (c) Forces applied on the four arms.

The moment of the force f applied to the cell of effective length d is then equal to $f \cdot d$ (See Figure.4a). During propulsion, the handrim causes the sensitive frame torsion resulting in the transfer of the same force F intensity to the four arms via the metallic disk (See Figure.4b). It was observed in a preliminary test on the instrumented wheel that a force F applied tangentially to the handrim gave the same voltage values measured at the output of the four load cells wherever the location of the force point of application on the handrim. In the instrumented wheel, each load cell is centered at one end of the rigid arm which is secured to the rigid brake disc connected to the wheel hub (See Figure.4c). The moment of the force F applied to the handrim with respect to the wheel hub axis C representing a lever of length L is equal to $F \cdot L$. Thus, the force intensity required to rotate the wheel is reduced by a factor d / L . In this work, $d=7\text{cm}$ and $L=28\text{cm}$, so $d/L=0.25$; with 50N load cell, force intensity up to 200N can be applied. Maximal propulsion forces of 180N have been found in the literature.

The typical shape of sensors signals versus time, obtained from a series of preliminary in-door measurements is presented in Figure.5. The evolution of the force versus time in Figure.5a. shows that the cyclic movement is performed in two phases: a push phase during which a force is exerted on the handrim and a recovery phase during which no force is applied. The slight dispersion in peak force intensity F_n , is related to the variability of the measurements generally observed for motor movements performed by the user. The push phase duration is a little shorter than that of the recovery step. As the wheelchair starts the first time, the user applies during the first push cycle a slightly greater force during a little longer time to overcome the initial inertia than for subsequent cycles. Once launched, the wheelchair is submitted to the motor torque exerted by the user and to a resistive torque due to the wheelchair tire rolling resistance. For in-door straight line motion on the horizontal and tiled ground, the wheelchair average speed increases to reach a stationary value as shown in red-dashed lines in Figure.5b.

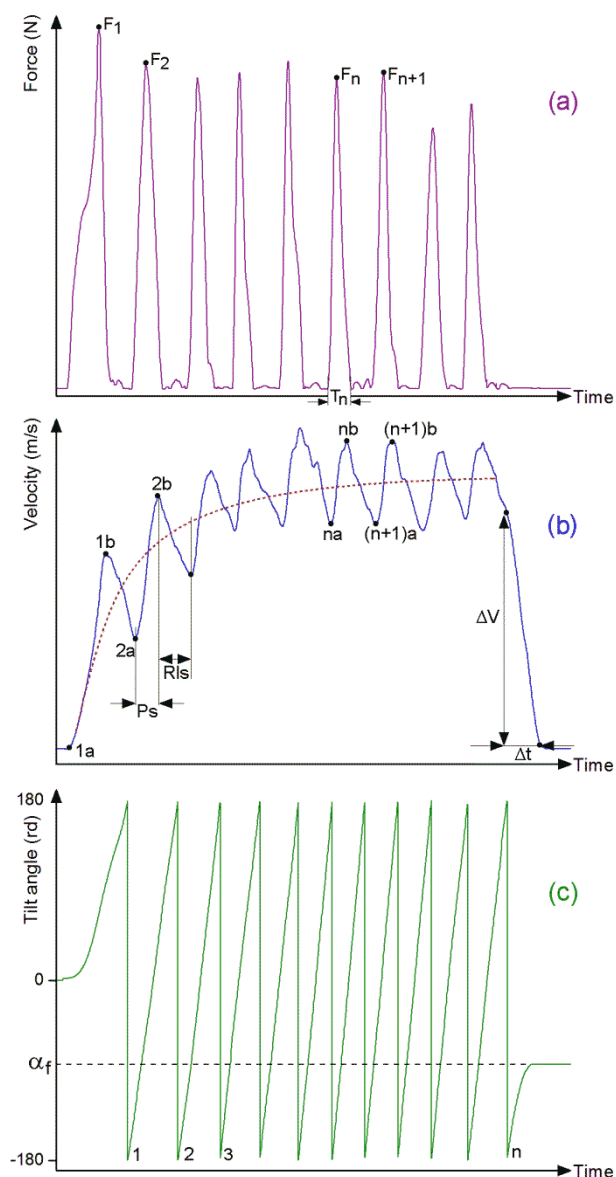


Figure.5: Typical sensors signals during indoor manual wheelchair propulsion

Velocity oscillations (blue solid line in Figure.5b.) reflect the fluctuation of the wheelchair speed during the propulsion. During the push phases (ranges $1a-1b$, $2a-2b$, ... $na-nb$ in Figure.5b), the user exerts a force on the handrim causing an increase of the wheelchair velocity. For the same prefix number n associated to the cycle n , the suffix letters a and b indicate the start and the end of the push, respectively. The time interval between these two moments corresponds to the time duration of the handrim force in the corresponding cycle. At the end of push, the subject releases the handrim and the wheelchair continues to move because of its inertia, but is rapidly slowed down until stop because of the rolling resistance. The velocity $V(t)$ decreases linearly to zero as

shown in the blue solid-line curve of Figure.5b. and the rolling resistance F_R can be deduced from the straight line slope using Equation (2). In this relation, M_T is the mass of user-wheelchair system.

$$F_R = M_T \cdot \Delta V / \Delta t \quad (2)$$

As the manual wheelchair propulsion is a movement in which the user transmits a force F tangential to the handrim to move the wheelchair during a time Δt , the mechanical power P developed during this time is given by

$$P = \frac{W}{\Delta t} = \frac{\int F \cdot dl}{\Delta t} \quad (3)$$

where the work W acting during a time Δt and is expressed by

$$W = \int F \cdot dl \quad (4)$$

In practice, considering a displacement Δl_i during the cycle i , the discrete version of the integral in the relation (4) is the sum, thus

$$W = \sum_{i=1}^n F_i \cdot \Delta l_i \quad (5)$$

Therefore, the wheelchair displacement has to be assessed. The acceleration component A_z issued from the BNO055 module is used to indirectly measure the wheel rotation angle. It reports the angular position over 360° and goes suddenly from 180° to -180° after each complete turn (See Figure.5c.). The displacement Δl_i during push time PS is related to wheel angular displacement $\Delta \alpha$ by

$$\Delta l_i = \Delta \alpha \cdot R_{WC} \quad (6)$$

If α_i and α_f are the initial and final angular position, respectively, after n complete turns of the wheel, the wheelchair linear displacement D_{WC} is expressed as

$$D_{WC} = [\pi - \alpha_i + \alpha_f + (n-1)2\pi] R_{WC} \quad (7)$$

2.3. Experimental conditions

A volunteer non-disabled and unskilled adult man (mass=90kg) sit in a standard manual wheelchair (mass=15kg) with the instrumented wheel mounted on the left side was asked to perform a ride on a straight asphalt road 60m long inside the campus. The road is without obstacle but exhibiting

unevenness less than 1% as well as some bumps. The wheelchair started from zero velocity and the user was asked to propel the wheelchair so as to maintain a speed of a normal walking adult (around 4km/h) and to release the handrim at about ten meters before the arrival line to measure the rolling resistance.

For each load cell static calibration, the rear wheel has been immobilized and several known masses in the range 1-10kg have been hanged at the handrim. For each suspended mass, the output voltage was measured. The procedure has been repeated for the same load cell at different inclinations with respect to the vertical.

3. RESULTS AND DISCUSSION

The calibration curve of one of the four load cells placed on the instrumented wheel exhibits a linear behavior as illustrated in the graph of Figure.6. All the four load cells calibration curves are linear with a discrepancy less than 10%.

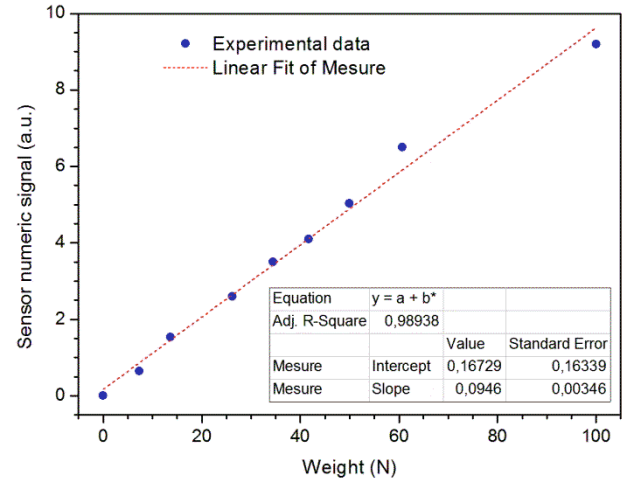


Figure.6: Calibration curve of the load cell.

Energy consumption is an important parameter in an embedded system requiring the use of low-power electronic components. The assessed current consumption by the microcontroller, the load cell conditioner, the BNO055 and the HC-05 circuits were found to be equal to 80mA, 6mA, 12mA and 50mA, respectively. A 9V/1200mAh 6AM6 single-use Lithium battery can provide energy up to 8h. Such a value seems to be sufficient since the user usually needs to know his energy expenditure through the mechanical power calculated during the sessions devoted

to physical exercises. A cheaper option can be considered by using a 9V/600mAh rechargeable Lithium-ion battery the duration is reduced to 6h.

The photograph in Figure.7. shows the manual wheelchair user riding on asphalt road inside the campus with approximately the same speed as that of the man walking slightly front of him. Because of the nature of the road (asphalt, unevenness, bumps), the user found some difficulty in keeping constant the direction of motion of the wheelchair. Going through the bumps slightly slowed down the wheelchair while the little descent in unevenness gave the sensation of a lighter load.



Figure.7: Wheelchair propulsion on straight asphalt road without obstacle with speed of a walking man.

The wheelchair linear position during the outdoor test shown in Figure.7. was obtained using the relation (7). It is represented in Figure.8. as a function of time. When he almost reached the 50m benchmark, the user released the handrim. Unlike the indoor trials where the wheelchair continued to advance over a dozen meters, the wheelchair stopped in the outdoor test just after reaching 50m, about ten meters before the expected arrival line. The slight discrepancy from the linear behavior in the graph of Figure.8. is related to the velocity variation due to the road unevenness. The wheelchair average speed obtained from the distance graph is equal to 1.25m/s and is approximately the same as that of the walker front of him (4.5km/h).

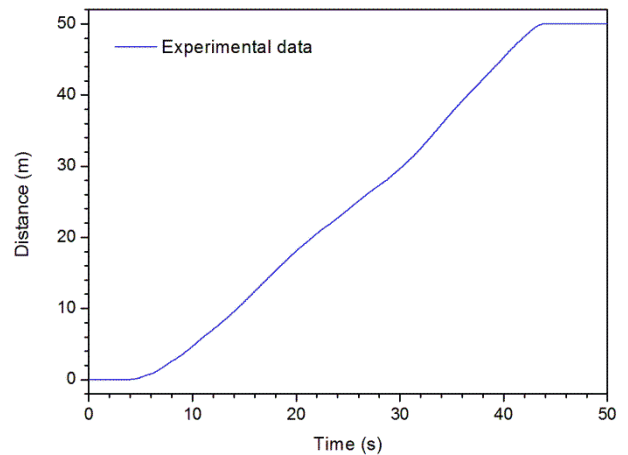


Figure.8: Wheelchair position versus time during outdoor measures of Fig.7.

Figure.9. shows the evolution of the wheelchair velocity during the outdoor test shown in Figure.7. There is a greater fluctuation of the average speed compared to the curve of Figure.5. performed in preliminary indoor tests. This confirms the trends observed in Figure.8. related to the road unevenness. The average speed is equal to 1.27 m/s with a standard deviation of 0.345 m/s. During the eight last cycles, the average speed is raised to 1.50 m/s with a lower standard deviation of 0.10 m/s. It is worth noting that the value of the rolling resistance $FR = 94N$ is almost 20 times greater than in the indoor case. The stroke rate around 1Hz during the outdoor test is close to the values reported in the literature [4, 20].

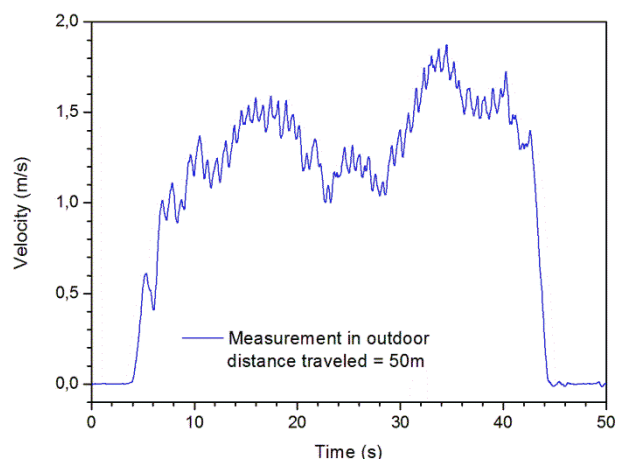


Figure.9: Velocity versus time of the manual wheelchair shown in Fig.7.

The evolution of the pushing force applied to the wheelchair instrumented handrim versus time during the outdoor test is illustrated in Figure.10.

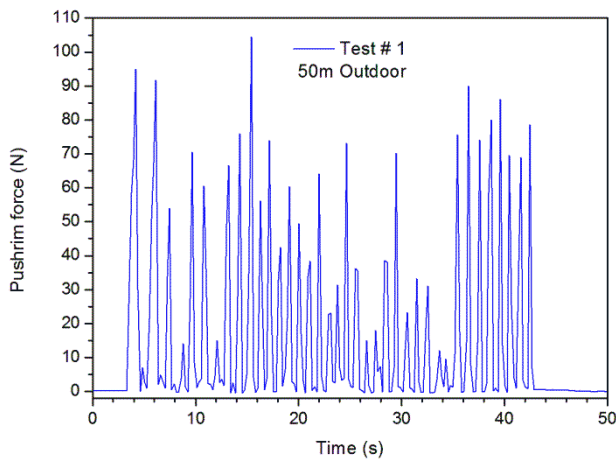


Figure.10: Pushrim force versus time during outdoor trial

There is a greater fluctuation of the force peaks compared to what was observed in the preliminary indoor tests. Values between 15N and 105N are in the range of ergometer data reported by different authors [4, 6, 12, 15], although twice as large values have been reported for wheelchair racers [19].

The average propulsion force is equal to 18N with a standard deviation of 25N. For the last eight pushes, the average force raised to 22N with a standard deviation of 31N.

The force peaks F_{max} as well as the displacement ΔL_i during the push phases are represented on the first two graphs of Figure.11. They were used to estimate the value of the work W_i at each thrust cycle performed during the test. This evolution is represented on the third graph of this figure. The average peak force on the 40s of the test is 54N with a standard deviation of 27N.

For the last 8 push, the average peak force is 78N and its standard deviation equals to 27N. The average displacement during a push cycle is 0.91m with a standard deviation of 0.24m. The average duration of a push cycle is 0.712s with a standard deviation of 0.173s. The mean work per cycle has been found to be equal to 25.7J with a standard deviation equals to 16.3J. The corresponding mean power output P is equal to 35W or 0.38 W/kg with a standard deviation of 19.7W or 0.2W/kg. Such values are compatible with those obtained in literature for indoor measurements [6, 11].

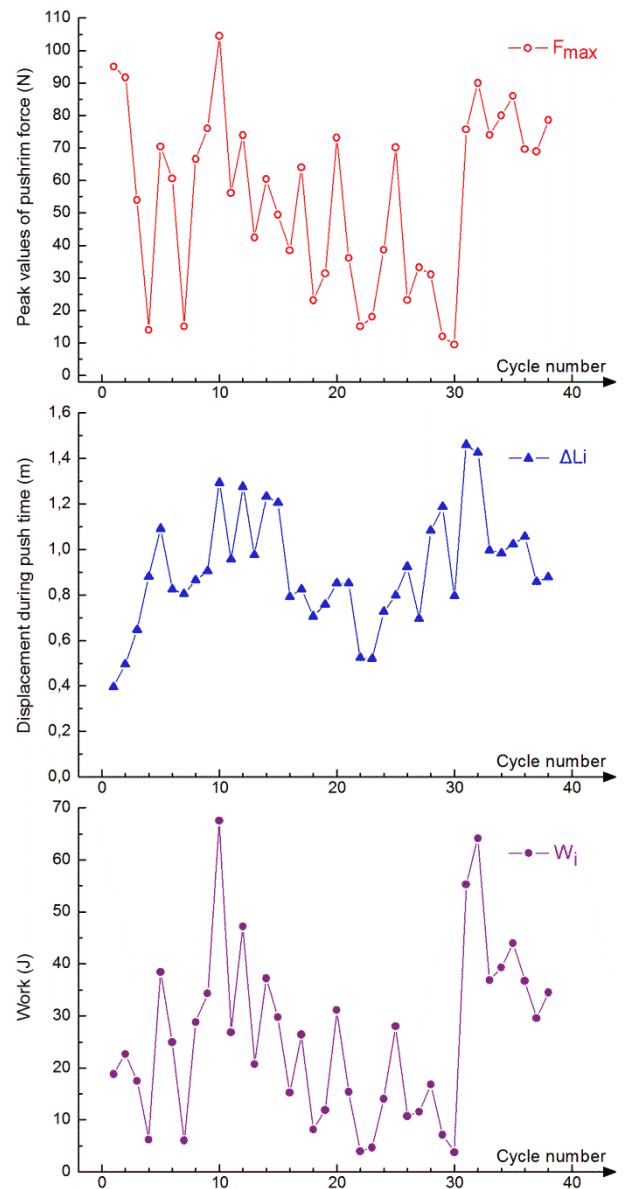


Figure.11: Force peaks, displacement, and work versus push cycle number.

4. CONCLUSION

Instrumented wheels have been developed for kinematics and kinetics analysis in order to improve the manual wheelchair propulsion technique and decrease the risk of injury. Wheelchairs equipped with such wheels are usually used in laboratory environment and on ergometers or motor-driven treadmills. Cost and required equipment associated have limited the use of instrumented wheels to medical or scientific analysis. The home-made device presented in this work is characterized by a low cost and easy implementation. This makes it possible to consider using it on larger scale applications besides the laboratory ones.

The low-cost instrumented wheel presented in this work was designed and fabricated for manual wheelchair propulsion force analysis in the indoor as well as the outdoor environment. Outdoor measurements results showed that the propulsion force and the rolling resistance, as well as the mechanical power developed are much more important due to the nature of the ground. A power output mean value of 0.38W/kg has been developed during wheelchair propulsion on asphalt road which seems to be compatible with the indoor results. As perspective, for general public use, this kind of device could provide data of interest to the user himself, such as the work and power furnished within a time range or during a trip. This type of information associated with energy expenditure could be used to improve the quality of life of manual wheelchair users.

REFERENCES

- [1] Rice. I.M., Pohlig. R.T., Gallagher. J.D. and Boninger. M.L “Handrim Wheelchair Propulsion Training Effect on Overground Propulsion Using Biomechanical Real-time Visual Feedback,” *Archives of Physical Medicine and Rehabil.*, 2013, 9, 256-263.
- [1] Finley. M.A. and Rodgers. M.M “Prevalence and Identification of Shoulder Pathology in Athletic and Nonathletic Wheelchair Users with Shoulder Pain: A Pilot Study,” *Journ. Rehabil. Research & Development*, 2004, 41, 395-402.
- [2] Flank. P., Wahman. K., Levi1. R. and Fahlström. M “Prevalence of Risk Factors for Cardiovascular Disease Stratified by Body Mass Index Categories in Patients with Wheelchair-dependent Paraplegia after Spinal Cord Injury,” *Journ. Rehabil. Med.*, 2012, 44, 440-443.
- [3] Hwang. S., Kim. S., Son. J., and Kim. Y “Manual Wheelchair Propulsion Torque and Power Outputs in Different Skill Groups,” *Journ. Biomech. Sci. and Engineering*, 2012, 7, 349-357.
- [4] Koontz A.M., Worobey L.A., Rice I.M., Collinger J.L. and Boninger M.L “Comparison Between Overground and Dynamometer Manual Wheelchair Propulsion,” *Journ. Applied Biomech.*, 2012, 28, 412-419.
- [5] de Groot. S., Veeger. H.E.J., Hollander. A.P. and van der Woude. L.H.V “Consequence of Feedback-based Learning of an Effective Handrim Wheelchair Force Production on Mechanical Efficiency,” *Clinical Biomechanics*, 2002, 17, 219–226.
- [6] Finley. M.A., Rasch. E.K., Keyser. R.E. and Rodgers. M.M “the Biomechanics of Wheelchair Propulsion in Individuals with and Without Upper-limb Impairment,” *Journ. Rehabil. Research & Development*, 2004, 41, 385–394.
- [7] Kulig. K., Rao. S.S., Mulroy. S.J., Newsam. C.J., Gronley. J.K., Bontrager. E.L. and Perry. J “Shoulder Joint Kinetics During the Push Phase of Wheelchair Propulsion,” *Clinical Orthopaedics and related research*, 1998, 354, 132-143.
- [8] Niesing. R., Eijskoot. F., Kranse. R., den Ouden. A.H. et al. “Computer-controlled Wheelchair Ergometer,” *Medical and Biological Engineering and Computing*, 1990, 28, 329–338.
- [9] Cooper. R.A “SMARTWheel: From concept to clinical practice,” *Prosthetics and Orthotics International*, 2009, 33, 198-209.
- [10] Vegter. R.J.K., Lamoth. C.J., de Groot. S., Veeger. D.H.E. and van der Woude. L.H.V “Variability in Bimanual Wheelchair Propulsion: Consistency of Two Instrumented Wheels during Handrim Wheelchair Propulsion on a Motor Driven Treadmill,” *Journ. NeuroEng. Rehabil.*, 2013, 10, 1-11.
- [11] Lenton. J.P., van der Woude. L.H.V., Fowler. N.E., Nicholson. G., et al. “Handrim Forces and Gross Mechanical Efficiency at Various Frequencies of Wheelchair Propulsion,” *International Journal of Sports Medicine*, 2013, 34,158-164.
- [12] de Groot S., Vegter R.J.K., Vuijk C., van Dijk F. et al. “WHEEL-I: Development of a Wheelchair Propulsion Laboratory for Rehabilitation,” *Journal of Rehabilitation Medicine*, 2014, 46, 493–503.
- [13] Slowik. J.S., Requejo. P.S., Mulroy. S.J. and Neptune. R.R “the Influence of Speed and Grade on Wheelchair Propulsion Hand Pattern,” *Clinical Biomechanics*, 2015, 30, 927-932.
- [14] Limroongreungrat. W., Wang. Y.T., Chang. L.S., Geil M.D. and Johnson J.T. “an Instrumented Wheel System for Measuring 3-D Pushrim Kinetics during Racing Wheelchair Propulsion,” *Research in Sports Medicine: An International Journal*, 2009, 17, 182-194.

- [15]Mallakzadeh. M. and Akbari H “Design and Fabrication of an Instrumented Handrim to Measure the Kinetic and Kinematic Information by the Hand of User for 3D Analysis of Manual Wheelchair Propulsion Dynamics,” *J. of Medical Signals & Sensors*, 2014, 4, 256-266.
- [16]Asato. K.T., Cooper. R.A., Robertson. R.N. and Ster. J.F "SmartWheels: Development and testing of a system for measuring manual wheelchair propulsion dynamics," *IEEE Trans. Biomedical Engineering*, 1993, 40, 1320-1324.
- [17]Wu. H.W., Berglund. L.J., Su. F.C., Yu. B. et al. "an Instrumented Wheel for Kinetic Analysis of Wheelchair Propulsion," *Journal of Biomechanical Engineering*, 1998, 120, 533-535.
- [18]Goosey-Tolfrey. V.L., Fowler. N.E., Campbell. I.G. and Iwnicki. S.D "A kinetic analysis of trained wheelchair racers during two speeds of propulsion," *Medical Engineering & Physics*, 2001, 23, 259-266.
- [19]Vegter. R.J., de Groot. S., Lamoth. C.J., Veeger D.H. and van der Woude L.H.V “Initial skill acquisition of handrim wheelchair propulsion: A new perspective,” *IEEE Trans. on Neural Systems and Rehabilitation Engineering*, 2014, 22, 104-113.

Electrical Circuit Constants Determination and Voltage Gain Measurement of Unloaded Rosen Type Piezoelectric Transformer Operating in First Mode

F. BOUKAZOUHA¹, H. BARKAT², A. HERBADJI², A. ROUABHA², M. GUESSOUM¹, K. SEDDA¹.

¹ Carcterisation and instrumentation laboratory. ² NDT calibration and verification laboratory. Research Center on Industrial Technologies, P.O. Box 64, Cheraga 16014. Algiers, Algeria

¹f.boukazuouha@crti.dz, ²cndlab@crti.dz.

Abstract — In this paper a voltage gain of 155 for an unloaded Rosen type piezoelectric transformer operating at the first mode was successfully measured with a precision of 5%. For this purpose, it was necessary to ensure a good impedance matching along the measuring circuit. Also, using the admittance circles obtained from the measured admittances, the PT equivalent circuit constants were determined experimentally and found matching the calculated ones (model 1D). Precisions less than 10% have been reported.

Index Terms — Acoustic wave, Equivalent circuit, High voltage, Measurements, Piezoelectric transformer, Voltage gain.

I. INTRODUCTION

The demand of miniaturised electronic devices has increased with the rapid rise of portable equipments such as, notebook-type computer and digital camera [1-3]. One interesting solution consists in combining inverse and direct piezoelectric effects to realise piezoelectric transformers (PT), the coupling between primary and secondary is achieved through mechanical vibration at the resonance frequency. Piezoelectric transformers, compared with traditional electromagnetic transformers, provide many merits such as high voltage gain, high power density, high frequency, high efficiency, good isolation, no wires, small size, small weight, low loss, inexpensive and absence of electromagnetic noises.

In this paper, an unloaded Rosen type piezoelectric transformer made of pz26 hard ceramic with dimensions of 25mm×3mm×2mm is studied. Its electrical circuit constants are theoretically and experimentally identified using 1D model and Nyquist diagram method respectively.

II. ROSEN TYPE PIEZOELECTRIC TRANSFORMER

Rosen type PTs have been studied in many papers since they were proposed by Rosen in 1956 [4]. These transformers are made of a long thin bar piezoelectric material. The primary, polarised in the thickness direction, is coupled to the secondary, polarised in the length direction.

When an alternative voltage V_1 is applied between the input electrodes, the transverse mode (31) is created in the material through the electromechanical coupling factor k_{31} (inverse effect). With the transmitting vibration from the primary side, the longitudinal mode (33) induces through the electromechanical coupling factor k_{33} an electrical field in the secondary side (direct effect). A voltage V_2 between the output electrodes is then produced. For the first mode, at the resonance frequency, the external free faces $w \times t$ expand and contract simultaneously and the stress is maximal at the junction (Fig.1).

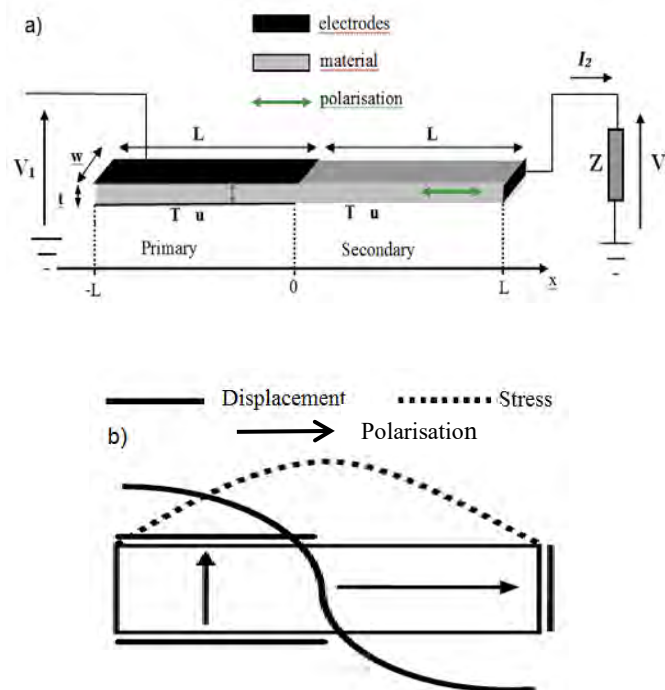


Fig.1. Rosen-type piezoelectric transformer : a) Basic simplified structure. b) half wavelength resonance

The Rosen-type PT discussed in this work is based on a soft-lead titanate zirconate (PZT) ceramic (Pz26, from Ferroperm) with dimensions being $2(\ell \times w \times t) = 25 \times 3 \times 1.5 \text{ mm}^3$. Except the mechanical quality factor Q , Pz26 material constants used for calculation are tabulated in table 1.

TABLE 1
Pz26 MATERIAL CONSTANTS USED FOR CALCULATIONS

	Values
ρ	7700 kg.m^{-3}
s_{11}^E, s_{33}^D	$13 \times 10^{-12}, 11 \times 10^{-12} \text{ m}^2.\text{N}^{-1}$
$\epsilon_{33}^T/\epsilon_0$	1300
d_{31}	$-130 \times 10^{-12} \text{ m.V}^{-1}$
g_{33}	$28 \times 10^{-12} \text{ V.m.N}^{-1}$
k_{31}, k_{33}	-0.33, 0.68
$\ell \times w \times t$	$12.5 \times 5 \times 2 \text{ mm}^3$

A. 1D modeling

Many modeling techniques have been established to analyse the electrical and mechanical behavior of piezoelectric transformers [5-6]. In this paper, we present an analytical model relying only on the one-dimensional assumption : if the thickness and width of the transformer are small compared to the length of the primary and the length of the secondary, by a factor of at least ten, only longitudinal waves along the length of the PT (x axis) can be considered. Then, the differential equation of propagation and equations of piezoelectric can be written as [7] :

For the primary side :

$$\rho \frac{\partial^2 u_1}{\partial t^2} = \frac{\partial T_1}{\partial x_1} \quad (1)$$

$$S_1 = s_{11}^E T_1 + d_{31} E_3 \quad (2)$$

$$D_3 = \epsilon_{33}^T E_3 + d_{31} T_1 \quad (3)$$

And for the secondary side:

$$\rho \frac{\partial^2 u_3}{\partial t^2} = \frac{\partial T_3}{\partial x_3} \quad (4)$$

$$E_3 = \beta_{33}^T D_3 - g_{33} T_3 \quad (5)$$

$$S_3 = s_{33}^D T_3 + g_{33} D_3 \quad (6)$$

Where ρ is the piezoelectric material density. The terms u_i , S_i , T_i , E_i , D_i denote respectively the displacement (change in length, in m), strain (dimensionless), stress (in Pa), electric field strength (in V/m), and electric displacement (in C/m^2), along axis x_i ($i=3$ refers to polarization).

The mechanical and electrical boundary conditions are :

$$T_1(x = -L) = 0 \quad (7)$$

$$T_3(x = L) = 0 \quad (8)$$

$$T_1(x = 0) = T_3(x = 0) \quad (9)$$

$$u_1(x = 0) = u_3(x = 0) \quad (10)$$

$$V_S = Z_L I_S = j \omega t w D_3 \quad (11)$$

The solution of the precedent equations system shows that it is possible to represent the PT by a conventional electrical equivalent circuit near the resonance frequency as shown on figure 2 [8]. Inspired from the Mason circuit [9-10], it is widely used in the literature. It includes a series motional branch RLC. The inductance L and the capacitance C denote inertial and potential mechanical energy respectively, the resistance R takes into account the mechanical losses when the dielectric losses are neglected. N is the ratio of an ideal electromechanical transformer. C_1 and C_2 are the static capacitances of the input and output parts respectively. Since each of these elements is directly related to the size and piezoelectric properties of the pzt6 ceramic.

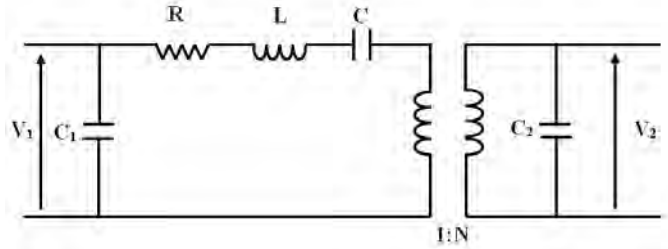


Fig. 2. Conventional electric equivalent circuit of the PT

The unloaded voltage gain V_2/V_1 can be expressed in its symbolic form as [11-14] :

$$V_2/V_1 = \alpha Q \ell / t$$

It is approximately proportional to the ratio of length to thickness, the coupling factors and the mechanical quality factor.

III. EXPERIMENTAL PROCEDURE

A. Admittance measurements

It is possible to determine values of a lumped equivalent circuit (Fig.2) by analysing the complex admittance curves. This method is widely used to characterize piezoelectric resonators. The input admittance Y_1 and the output admittance Y_2 when the secondary side and the primary side are respectively short-circuited have been measured at the first mode.

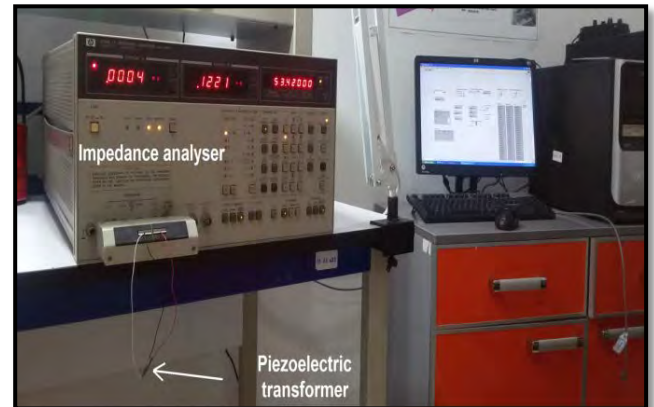


Fig. 3. Admittance measurements

The measurements (conductance G and susceptance B) were performed as a function of frequency using a 4192A LF impedance analyzer (Hewlett-Packard). The PT was excited with a sine wave with amplitude of $1V_{\text{rms}}$ generated by the same impedance analyzer. Data were acquired over a frequency range from 55 to 85 KHz with steps of 10Hz using acquisition software developed in Lab-VIEW (National Instruments Corp., Austin, TX). (Fig.3)

From the admittances modules, the input and output impedance, the resonance frequency and the input and output quality factors Q_1 and Q_2 can be deduced experimentally (bandwidth at -3dB) from the admittance modules. Then, from the admittance circles, the experimental values of the circuit constants (R , L , C , N , C_1 and C_2) can be deduced (fig.4). The comparison between the theoretical values and the experimental ones is shown on table 2.

Except the quality factor Q , experimental results have been compared to theoretical predictions (model 1D) and are found to be globally in good agreement all results are in good adequation. The relative error does not exceed 10%.

For the quality factor Q , the theoretical value (1000) is given before the metallisation of the pz26 ceramic. In fact, it has been verified that the nature (silver, aluminum, ...) and the thickness of the electrode affect considerably this factor [15].

Fig. 4. Input (Y1) and output (Y2) admittance measurements: Module and Nyquist Diagram

TABLE 2 : COMPARISON BETWEEN THEORETICAL AND EXPERIMENTAL ELECTRICAL CHARACTERISTIC OF THE PT

	Experimental values	Theoretical values
Resonance frequency	65.7	66.2
Input impedance (Ω)	103	98
Input quality factor	240	1000
Output impedance (M Ω)	19.24	18.3
Output quality factor	241	1000
C_1 ($\times 10^{-10}$ F)	3.62	3.2
C_2 ($\times 10^{-12}$ F)	5.33	4.94
R (Ω)	10175	11008
L (H)	5.97	6.43
C ($\times 10^{-12}$ F)	0.91	0.99
N	3.76	3.96

B. Unloaded voltage gain measurement

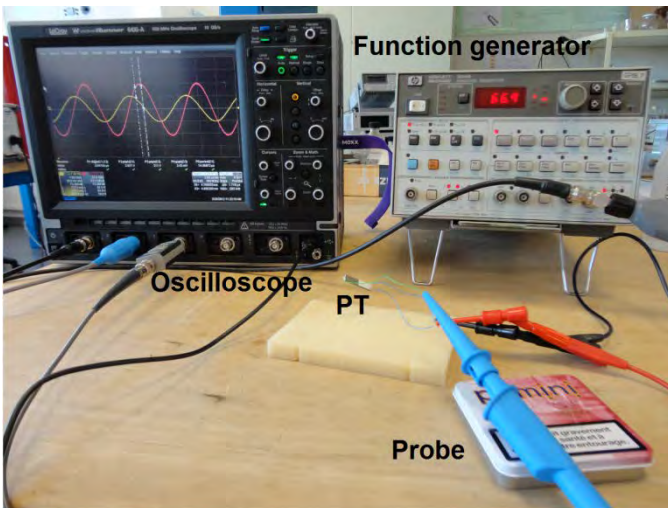


Fig.5. Experimental setup

The transformer was tested under sinusoidal excitation using the experimental set-up shown in figure 5. The transformer was driven using a function generator (HP3314A), a digital oscilloscope (LeCroy 64Xi-A) was used to measure input and output voltages.

According to the input and the output impedance of the transformer, it is necessary to ensure a good impedance adaptation between the generator and the primary side and between the secondary side and the oscilloscope. It was apparent that an even higher impedance diagnostic would be needed to measure the output voltage. In fact, if in the primary side, the generator impedance (from 10 Ω to 10 k Ω) can be settled exactly on the input impedance of the transformer (table 2). In the secondary side, it is difficult to ensure the ideal open circuit condition to measure the unloaded voltage gain of the PT because of the input impedance of the oscilloscope (1M Ω), too low compared to the output impedance of the transformer.

During initial experimentations by using only the oscilloscope, an output voltage of 4.15 at the resonance frequency of 63.1 kHz was measured. Then, by attaching a 1:10 probe, the predictions were moderately improved. (75-64.5 kHz) However, when a 1:100 probe was attached to the oscilloscope, in order to rise its effective impedance the measured value of the output voltage (155) were closer to the theoretical results (183) as it is shown in table 3 and figure 6.

Table 3: Comparison between experimental and theoretical results for voltage gain and resonance frequency

	1D model	Nyquist diagram	Experience (oscilloscope)	Experience (1:10 probe)	Experience (1:100 probe)
Voltage gain	183	155	4.15	75	164
Resonance frequency (kHz)	65.7	71.17	63.1	64.5	66.2

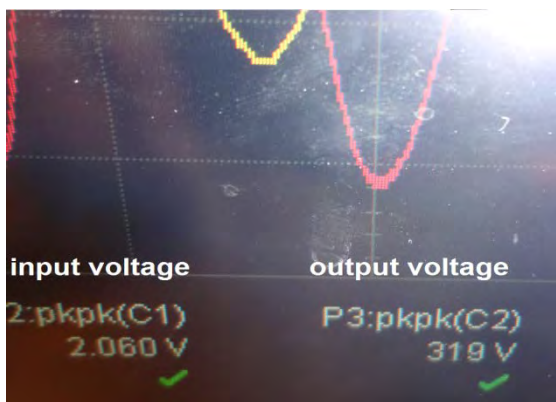
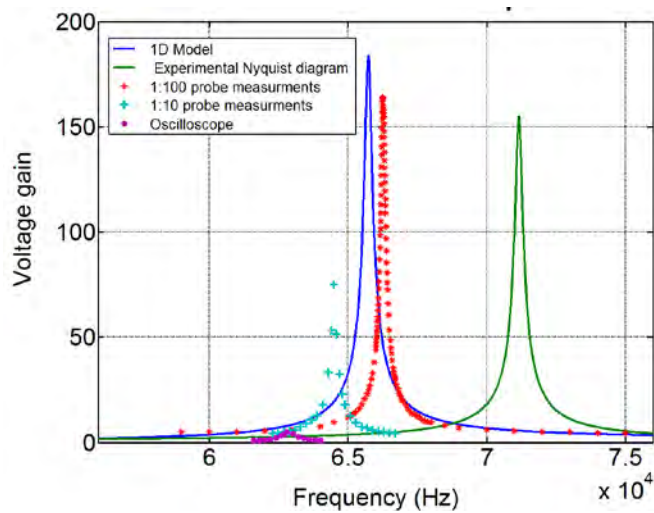


Fig. 6 : Voltage gain for unloaded transformer at the first mode: comparison between theoretical and experimental results

IV- CONCLUSION

In this paper, calculated and experimental characteristics of a Rosen type piezoelectric transformer operating at first mode have been presented. Experimental results have been compared to theoretical predictions (model 1D) and are found to be globally in good agreement despite a few discrepancies.

The major contribution of this work is the measurement of the voltage gain of unloaded transformer with precision. In fact, it has been successfully measured. This requires the control of impedance adaptation along the measurement chain (generator, primary, secondary, and oscilloscope). The piezoelectric transformer equivalent circuit constants were also found with good precisions.

REFERENCES

[1] M. Guo, K. H. Lam, D. M. Lin, S Wang, K W Kwok, Helen L, W Chan, X Z Zhao. A Rosen Type Piezoelectric Transformer Employing Lead Free $K_{0.5}Na_{0.5}NbO_3$ Ceramics. *J Mater Sci.* (2008). P 709-714.
 [2] H. Shin, H. Ahn, Deuk-Young Han. Modeling And Analysis Of Multilayer Piezoelectric Transformer. *Material Chemistry and Physics.*
 [3] O. Ohnishi, H. Kishie, I. Iwamoto, Y. Sasaki, T. Zaitzu, T. Inoue. Piezoelectric Ceramic Transformer Operating in

Thickness Extensional Vibration Mode for Power Supply. *Ultrasonic Symposium IEEE.* (1992). P 483-488.
 [4] C. A. Rosen. *Ceramic Transformers and Filters.* Proceedings of the Electronic Comp. Symp. (1956). P 205-211.
 [5] H. Joo, I. Kim, J. Song, S. Jeong, Minsoo Kim. Piezoelectric Properties of Rosen Type Piezoelectric Transformer Using $0.01Pb(Ni_{1/3}Nb_{2/3})O_3 - 0.08Pb(Mn_{1/3}Nb_{2/3})O_3 - 0.91Pb(Zr_{0.505}Ti_{0.495})O_3$. *Journal of the Korean Physical Society.* Volume 56. (2010). P 374-377.
 [6] E. M. Syed. Analysis and Modeling of Piezoelectric Transformers. Masters of Applied Sciences. Graduate Department of Electrical and Computer Engineering. University of Toronto.
 [7] F. Boukazouha , G. Poulin-Vittrant , L.P. Tran-Huu-Hue , M. Bavencoffe , F. Boubenider , M. Rguiti , M. Lethiecq , A comparison of 1D analytical model and 3D Finite Element Analysis with experiments for a Rosen-type piezoelectric transformer, *Ultrasonics* , Volume 60 , 2015 , pp 41-50
 [8] C. Y. Lin. Design and Analysis of Piezoelectric Transformer Converters. PHD Thesis, Faculty of the Virginia Polytechnic Institute. (1997).
 [9] W.P: *Electromechanical Transducers and Wave Filters.* Van Nostrand, Princeton, New Jersey. (1948).
 [10] G. E. Martin. On the Theory of Segmented Electromechanical System. *The Journal of the Acoustical Society of America*, Vol. 36, No. 2, July 1964
 [11] L Hwang, J Yoo, E Jang, D Oh, Y Jeong, I Ahn, M Cho. Fabrication and Characteristics of PDA LCD Backlight Driving Circuits Using Piezoelectric Transformer. *Sensors and Actuators. A* 115. (2004). P 73-78.
 [12] M.A Smith, J McKittrick, KL Kavanagh. Piezoelectric Ceramic Transformer For Micro Power Supplies. Final report 1996-97 for Micro Project 96-032. Industrial Sponsor. American High Voltage. (1997).
 [13] K. Nakamura , Y Adachi. Piezoelectric Transformer Using Linbo3 Single Crystals. *Electronics And Communications In Japan.* Part 3. Volume 81. N°7. (1998).
 [14] G. Cellucci, S. Pirani, C. Galassi, C. Capiani, B E Watts, E. Melioli, F. Leccabue. The Fabrication and Testing of a Piezoelectric Transformer. *Ferroelectrics.* Volume 228. (1999). P 129-137.
 [15] A. L. Benwell. A High Voltage Piezoelectric Transformer for Active Interrogation. PHD thesis, University of Missouri Columbia, 2009.

Characterization and verification of ultrasonic equipment: Measurement of the transmitter pulse parameters according to EN 12668-1:2010

Hamza BARKAT¹, Abdeslem ROUABHA¹, Abderrahim HERBADJI¹, Rafik HALIMI¹ and Ali BADIDI BOUDA²

Calibration, Analysis and Measurement Workshop, CRTI, Cheraga 16014, Algeria
barkathamza@ymail.com, rouabhaa@gmail.com, her_abderrahim@hotmail.fr and r.halimi@crti.dz
Division of Characterization and Instrumentation, CRTI, Cheraga 16014, Algeria
a.badidi@crti.dz

Abstract — Ultrasonic instruments used by inspection bodies must be periodically verified in order to assess their electrical performances. This requirement can be achieved by subjecting the instrument parameters to a characterization and verification according to the group 2 tests of the EN 12668-1 standard. This paper presents an evaluation of the transmitter pulse parameters for different settings of energy, damping and repetition frequency. Measurement uncertainties were also calculated and a statistical comparison to the manufacturer's technical specification was carried out, taking into account EN 12668-1's maximum permissible errors. A normalized error of 0.59 was achieved for the less fitting settings.

Index Terms — EN 12668-1:2010 standard, measurement uncertainty, normalized error, pulse measurement, ultrasonic instruments.

I. INTRODUCTION

HE use of examination equipments by inspection bodies performing Non-Destructive Testing not only requires a trained and qualified staff, with a satisfactory knowledge of the type and series of the equipment being used, but it also requires the suitable examination equipment, which must be properly maintained and calibrated [1].

The ultrasonic method in Non-Destructive Testing is the most widely used, disregarding the obvious ones of looking, feeling, measuring and weighing [2]. Hence, ultrasonic examination instruments are the most commonly used by inspection bodies.

One way to verify and check on an ultrasonic instrument is to subject it to a characterization and verification according to the group 2 tests of the EN 12668-1:2010 standard, *Non-destructive testing – Characterization and verification of ultrasonic examination equipment. Part 1: Instruments*. The group 2 tests are usually performed by the manufacturer, or his agent, prior to the supply of the ultrasonic instrument; or by a testing laboratory (preferably accredited), at twelve months intervals to verify the performance of the ultrasonic instrument during its lifetime or following a repair [3]. Chapter 9 of EN 12668-1:2010 standard regroups five principal families of tests

to perform on the ultrasonic instrument in order to periodically assess its conformity:

- physical state and external aspects;
- stability;
- transmitter pulse parameters;
- receiver;
- linearity of time-base.

The transmitter is an important part of the ultrasonic instrument. It creates and sends an electrical pulse to the transducer which produces an ultrasonic wave that spreads through the object being inspected and is reflected back to the receiver part of the instrument. The produced ultrasonic wave varies in shape, amplitude and duration depending on the shape and amplitude of the transmitter pulse. Chapter 9.4 of the EN 12668-1:2010 standard describes the procedure to verify four parameters that define the transmitter pulse. Those parameters are:

- pulse voltage;
- pulse rise time;
- pulse duration;
- pulse reverberation.

Using an appropriate set up and depending on different settings of the transmitter pulse (repetition frequency, energy and damping), the four parameters are measured then compared to acceptance criteria quoted in EN 12668-1:2010. Those acceptance criteria are directly linked to the manufacturer's specification of the type and series of the ultrasonic instrument under test.

The present work presents an evaluation of the transmitter pulse parameters according to EN 12668-1:2010 and depending on different pulse settings of the ultrasonic instrument. The values are accompanied with their measurement uncertainties evaluated according to the *Guide to the Expression of Uncertainty in Measurement* [4]. The resulting values are then statistically compared with the manufacturer's specifications for this type of ultrasonic instrument and assessed according to the EN 12668-1:2010 standard acceptance criteria.

II. MATERIALS AND METHODS

The ultrasonic instrument subjected to the pulse transmitter evaluation in this paper is primarily used by our testing laboratory as a certified reference for proficiency testing by comparison with other laboratories. The instrument works in the range of frequency from 0.5 to 20.00 MHz (receiver part). The transmitter pulse has a square shape with a frequency that ranges from 0.1 to 10.00 MHz. Its shape and amplitude depend on three settings to be adjusted on the ultrasonic instrument:

- Repetition frequency (PRF): Values range from 10 Hz to 500 Hz in 10 Hz increments.
- Energy: Pulse voltage values available: 100 V, 200 V, 300 V or 400 V.
- Damping: Pulse damping values available: 50 Ω , 100 Ω , 200 Ω or 400 Ω .

A 50 Ω non reactive resistor is connected across the transmitter output socket. According to the requirements of chapter 9.1 of EN 12668-1:2010, the non reactive resistor must have a tolerance of 1%. The lab ensures that this requirement is fulfilled by periodically verifying the value of the non reactive resistor that must stay within its tolerance.

The pulse signal is visualized with a calibrated TDS 3054 oscilloscope (Tektronix Inc.) which insures that the measured values are metrologically traceable. The AC voltage function of the oscilloscope is calibrated over the 50 mV to 410 V range while the time base function is calibrated over the 2.50 ns to 100 μ s range. The set up for the measurement of the transmitter pulse parameters is shown in Fig. 1.

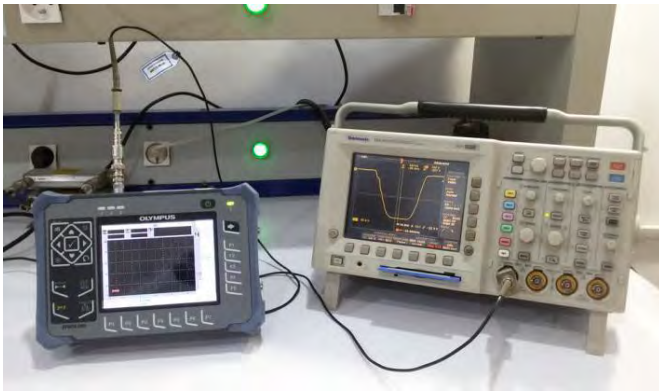


Fig. 1. Set-up for the measurement of the transmitter pulse parameters according to chapter 9.4 of EN 12668-1:2010

The measurement procedure as detailed in chapter 9.4.2.1 of the EN 12668-1:2010 standard begins by setting the PRF, the damping and energy to their maximum values (respectively 500 Hz, 400 Ω and 400 V). Using the oscilloscope, we proceed to measure the transmitter pulse voltage V_{50} , pulse rise time T_r , duration T_d and amplitude of any reverberation that comes after the pulse V_r as shown in Fig. 2 [3]. First step is to adjust time base and amplitude on the oscilloscope such as the pulse signal covers approximately 80% of the screen height and width.

Measurement of V_{50} is carried out by positioning the first V bar cursor at the 0% level of the pulse while the second V bar cursor is positioned at the 100% level of the pulse,

(minimum peak). The value of V_{50} is considered to be the displayed difference of amplitude between the two cursors. The positioning for both cursors is repeated 10 times and a mean value of the transmitter pulse voltage $\overline{V_{50}}$ is obtained.

Measurement of T_r is carried out by positioning the first V bar cursor at the 10% level of the pulse while the second V bar cursor is positioned at the 90% level of the pulse. The value of T_r is considered to be the displayed difference in time between the two cursors. The positioning for both cursors is repeated 10 times and a mean value of the pulse rise time $\overline{T_r}$ is obtained.

Measurement of T_d is carried out by positioning the first V bar cursor at the 10% level on the falling edge while the second V bar cursor is positioned at the 10% on the rising edge of the pulse. The value of T_d is considered to be the displayed difference in time between the two cursors. The positioning for both cursors is repeated 10 times and a mean value of the duration $\overline{T_d}$ is obtained.

Measurement of V_r is carried out by positioning the first V bar cursor at the 0% level of the pulse while the second V bar cursor is positioned at the peak of the ringing after the pulse. The value of V_r is considered to be the displayed difference in amplitude between the two cursors. The positioning for both cursors is repeated 10 times and a mean value of the reverberation amplitude $\overline{V_r}$ is obtained.

Measurements of the four parameters are repeated at each pulse energy adjustment and with minimum damping following the same above procedure. All measurements are performed at a temperature of 23 ± 3 $^{\circ}$ C.

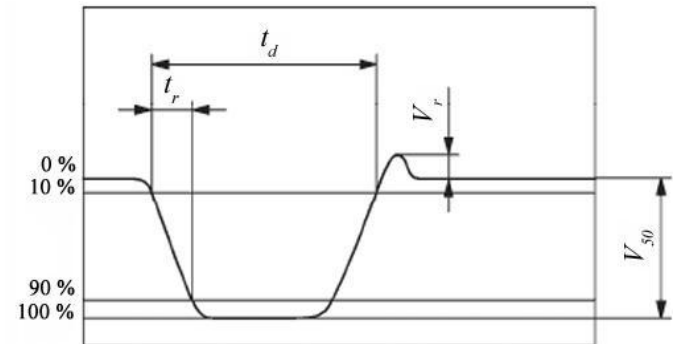


Fig. 2. Transmitter pulse parameters to be measured (square shape) [3]

III. MEASUREMENT UNCERTAINTY (TYPE A AND B)

All parameters are calculated from the pulse signal displayed on the oscilloscope. Hence, a correction of calibration must be added to the mean value for each parameter. This correction is taken from the oscilloscope calibration certificate. Other corrections (drift, resolution, cursors positioning and influence of the ambient temperature) are taken to be zero:

$$\overline{V_{50,C}} = \overline{V_{50}} + C_{cal,Hcur} \quad (1)$$

$$\overline{t_{r,c}} = \overline{t_r} + C_{cal,Vcur} \quad (2)$$

$$\overline{t_{d,c}} = \overline{t_d} + C_{cal,Hcur} \quad (3)$$

$$\overline{V_{r,c}} = \overline{V_r} + C_{cal,Vcur} \quad (4)$$

$C_{cal,Hcur}$ and $C_{cal,vcur}$ are respectively the voltage and time base calibration corrections of the V bar cursors. $\overline{V_{50,C}}$, $\overline{t_{r,c}}$, $\overline{t_{d,c}}$ and $\overline{V_{r,C}}$ are respectively the corrected values of V_{50} , t_r , t_d and V_r .

For each parameter of the pulse transmitter, the Type A uncertainty is evaluated by the experimental standard deviation from 10 repeated measurements.

The principal sources for the Type B uncertainty are the oscilloscope calibration and the positioning of the V Bar cursors (horizontally and vertically). The Type B uncertainty for the oscilloscope calibration is obtained from its calibration certificate using an interpolation method. The drift of the oscilloscope is also taken into account and its uncertainty is estimated by the experimental standard deviation calculated from at the data of at least the last 5 successive calibrations of the oscilloscope.

Resolution and positioning in voltage and time base for the V bar cursors also contribute to the uncertainty budget: Voltage and time base resolutions are assumed to present a rectangular distribution. The Type B uncertainty is then estimated by dividing the cursor voltage resolution and the cursor time base resolution by $2\sqrt{3}$. Whereas, the cursor positioning error, be it vertically or horizontally, introduces a Type B uncertainty estimated from dividing the maximum deviation when positioning the V bar cursors by $2\sqrt{3}$.

Finally, having no indication in the oscilloscope user's manual about the influence of ambient temperature ($23 \pm 3^\circ\text{C}$), its uncertainty component is taken to be negligible. All components of uncertainty were evaluated according to [4]. The expanded uncertainty was reported with a defined coverage factor of $k=2$ (confidence level of 95.45%).

IV. PULSE SIGNAL PARAMETERS ACCORDING TO NF EN 12668-1:2010 MANUFACTURER'S SPECIFICATION

Beside the usual instruction manual accompanying an examination instrument, the ultrasonic instrument evaluated in this paper came with manufacturer's technical specification that defines the performance criteria of this type and series of instrument in accordance with clause 6 of the EN 12668-1:2010 standard [5]. In case of the transmitter, the manufacturer's technical specification contains the measured values of the four pulse parameters, at different settings of PRF, energy and damping with their respective maximum permissible errors (inappropriately called tolerances in [5], according to [6]). This manufacturer's technical specification is essential when performing a characterization and verification of an ultrasonic instrument according to EN 12668-1:2010 standard. This specification can also form part of the instruction manual in other type and series of ultrasonic instruments.

In case of the transmitter pulse voltage and duration, EN 12668-1:2010 chapter 9.4.2.2 defines maximum permissible errors of $\pm 10\%$ of the manufacturer's specification. Rise time should be less than the maximum value quoted in the manufacturer's technical specification. Finally, reverberation

should be less than the maximum value quoted in the manufacturer's technical specification. Finally, reverberation should be less than 4% of the transmitter pulse voltage.

V. ASSESSMENT OF THE TRANSMITTER PULSE PARAMETERS

In order to assess the transmitter part of the ultrasonic instrument in accordance to EN 12668-1:2010, the pulse was defined by the four parameters values $\overline{V_{50,C}}$, $\overline{t_{r,c}}$, $\overline{t_{d,c}}$ and $\overline{V_{r,C}}$, as well as their respective measurement uncertainties, at different settings of PRF, energy and damping. The results were compared with the manufacturer's declared specifications, as well as their defined maximum permissible errors, by calculating the normalized error [7]:

$$E_n = \left| \frac{x_1 - x_2}{\sqrt{U_{x_1}^2 + U_{x_2}^2}} \right| \quad (5)$$

where x_1 represents the corrected value of one measured parameter, x_2 represents the value of the same parameter declared in the manufacturer's specification, and under the same settings as for the measured parameter, U_{x_1} is the expanded uncertainty for the measured parameter, and U_{x_2} represents the defined maximum permissible error from the manufacturer's technical specification, since a manufacturer maximum permissible error is an expanded uncertainty with a confidence level of 100%.

The normalized error is a fine indicator for a testing laboratory performance since it takes into account the uncertainties associated with the measured parameters and reference values [7]. The reference values in case of this study are taken from the manufacturer's specification.

VI. RESULTS AND DISCUSSION

The transmitter pulse parameters (V_{50} , t_r , t_d and V_r) were measured at different settings of PRF, energy and damping as required in chapter 9.4.2.1 of EN 12668-1:2010. The results are presented in Tables I-VIII.

All the measured pulse parameters at different settings can be accepted based on the acceptance criteria defined in chapter 9.4.2.2 of EN 12668-1:2010, because all normalized errors were lower than 1.

The normalized error is mainly affected by the value of the numerator $|x_1 - x_2|$ in (5) which represents the deviation between the value of one measured parameter and the value of the same parameter declared in the manufacturer's specification. For the parameter being evaluated, larger the deviation between x_1 and x_2 will be, greater the normalized error will be, leading to greater chances for not meeting the acceptance criteria according to EN 12668-1:2010, taking into account the manufacturer's technical specification.

Table I. Transmitter pulse parameters values and respective uncertainty values for a pulse frequency of 10 MHz (PRF = 500Hz, Energy = 400V, Damping = 400Ω)

Parameter	Unit	Declared value	Result	Expanded uncertainty	Normalized error
V_{50}	[V]	255.00	258.54	2.60	0.14
T_r	[ns]	11.00	11.99	0.35	0.04
T_d	[ns]	56.54	56.27	1.02	0.05
V_r	[V]	0.84	1.30	0.17	0.04

Table II. Transmitter pulse parameters values and respective uncertainty values for a pulse frequency of 10 MHz (PRF = 500Hz, Energy = 100V, Damping = 400Ω)

Parameter	Unit	Declared value	Result	Expanded uncertainty	Normalized error
V_{50}	[V]	66.50	69.19	0.71	0.40
T_r	[ns]	6.50	6.64	0.10	0.01
T_d	[ns]	63.17	62.05	1.02	0.17
V_r	[V]	0.06	0.40	0.12	0.13

Table III. Transmitter pulse parameters values and respective uncertainty values for a pulse frequency of 10 MHz (PRF = 500Hz, Energy = 400V, Damping = 50Ω)

Parameter	Unit	Declared value	Result	Expanded uncertainty	Normalized error
V_{50}	[V]	255.00	257.54	2.60	0.10
T_r	[ns]	15.20	15.95	0.41	0.03
T_d	[ns]	56.54	56.03	1.02	0.09
V_r	[V]	0.38	1.20	0.12	0.08

Table IV. Transmitter pulse parameters values and respective uncertainty values for a pulse frequency of 10 MHz (PRF = 500Hz, Energy = 100V, Damping = 50Ω)

Parameter	Unit	Declared value	Result	Expanded uncertainty	Normalized error
V_{50}	[V]	66.50	68.76	0.71	0.34
T_r	[ns]	9.72	10.96	0.35	0.05
T_d	[ns]	59.45	58.51	1.02	0.15
V_r	[V]	0.17	0.54	0.16	0.14

Table V. Transmitter pulse parameters values and respective uncertainty values for a pulse frequency of 10 MHz (PRF = 10Hz, Energy = 400V, Damping = 400Ω)

Parameter	Unit	Declared value	Result	Expanded uncertainty	Normalized error
V_{50}	[V]	255.00	258.54	2.60	0.14
T_r	[ns]	11.43	11.04	0.35	0.01
T_d	[ns]	56.54	56.69	1.02	0.03
V_r	[V]	0.31	1.60	0.12	0.13

Table VI. Transmitter pulse parameters values and respective uncertainty values for a pulse frequency of 10 MHz (PRF = 10Hz, Energy = 100V, Damping = 400Ω)

Parameter	Unit	Declared value	Result	Expanded uncertainty	Normalized error
V_{50}	[V]	66.50	70.47	0.72	0.59
T_r	[ns]	6.45	6.54	0.10	0.00
T_d	[ns]	63.17	62.36	1.02	0.13
V_r	[V]	0.27	0.35	0.09	0.03

Table VII. Transmitter pulse parameters values and respective uncertainty values for a pulse frequency of 10 MHz (PRF = 10Hz, Energy = 400V, Damping = 50Ω)

Parameter	Unit	Declared value	Result	Expanded uncertainty	Normalized error
V_{50}	[V]	255.00	256.54	2.60	0.06
T_r	[ns]	15.00	15.69	0.41	0.03
T_d	[ns]	56.54	56.27	1.02	0.05
V_r	[V]	0.51	0.76	0.15	0.02

Table VIII. Transmitter pulse parameters values and respective uncertainty values for a pulse frequency of 10 MHz (PRF = 10Hz, Energy = 100V, Damping = 50Ω)

Parameter	Unit	Declared value	Result	Expanded uncertainty	Normalized error
V_{50}	[V]	66.50	68.37	0.71	0.28
T_r	[ns]	9.73	10.05	0.35	0.01
T_d	[ns]	59.45	58.25	1.02	0.20
V_r	[V]	0.08	0.44	0.15	0.13

For example, considering the transmitter pulse parameter V_{50} , the maximum value of E_n ($E_n = 0.59$) is observed in Table VI for the following settings: PRF= 10Hz, Energy= 100V, Damping = 400Ω (max value of damping and min value of energy). While this value of E_n is considered to be acceptable (lower than 1), it remains above the values of normalized error calculated for the same parameter but for other settings. In contrast, the minimum value of E_n ($E_n = 0.06$) is observed in table VII for the following settings: PRF= 10Hz, Energy= 400V, Damping = 50Ω (min value of damping and max value of energy). The shapes of the transmitter pulse for the results of Tables VI and VII are shown in Fig. 3.

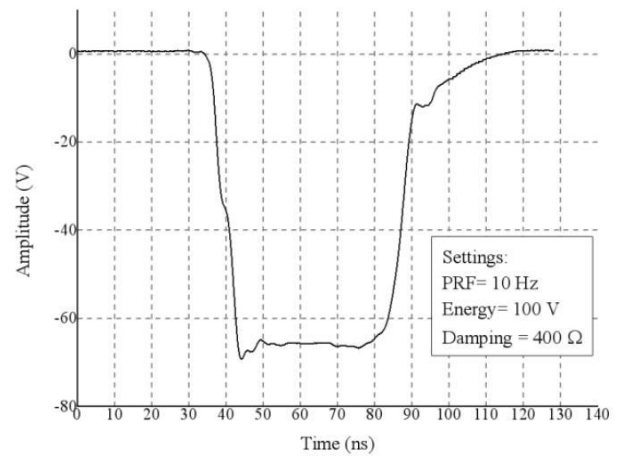
In Fig. 3.a, one can observe that the pulse signal isn't an ideal square shape and the system (instrument + non reactive resistor) oscillates when passing from the high level to the low level before settling down. The system is said to be underdamped.

Considering that EN 12668-1:2010 requires to measure V_{50} at 100% of the signal amplitude as shown in Fig. 2, the negative overshoot observed in Fig. 3.a causes the mean value of V_{50} to be slightly increased than if it was measured at the steady state (after settlement). Therefore, the deviation between x_1 and x_2 is slightly increased as well as the value of E_n calculated in table 6 for the parameter V_{50} . The other pulse parameters (T_r , T_d and V_r) are also affected since they are measured based on the mean value of the pulse voltage ($\overline{V_{50}}$).

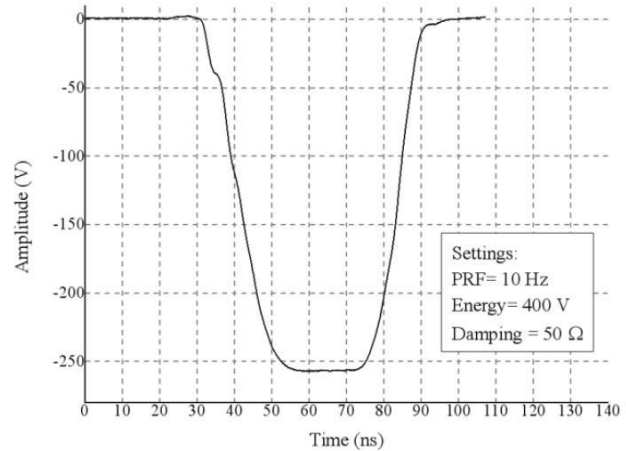
However, in Fig. 3.b, even if the pulse signal isn't an ideal square shape, no oscillation and no negative overshoot are observed when passing from the high level to the low level. 100% of V_{50} is measured at the steady state and the deviation between x_1 and x_2 is reduced ($|x_1 - x_2| = 1.54 V$) compared to the deviation for the settings of Table VI ($|x_1 - x_2| = 3.97 V$). Therefore, the value of E_n is also reduced.

The fact that the system is underdamped is probably related to the adjustment of damping combined with energy, as well as the type and value of the non reactive resistor used for the evaluation of the transmitter pulse parameters. In fact, the damping for an ultrasonic instrument is a resistor in parallel to

the transmitter output which is known to adjust the transmitter pulse shape and to eliminate probe cable reflections [8].



(a)



(b)

Fig. 3. Transmitter pulse shape (a) for the following settings : PRF=10Hz, energy=100V, damping=400Ω and (b) for : PRF=10Hz, energy=400V, damping=100Ω with a pulse frequency of 10 MHz

Adjusting the damping and energy modifies the source impedance Z_S (transmitter output) and when there is a mismatch with the load impedance Z_L (non reactive resistor) it causes the system to be underdamped and overshoots and undershoots (Fig. 3.a) are observed when visualizing the signal on the oscilloscope.

VII. CONCLUSION

Performing inspections by methods of Non-Destructive Testing requires confidence on the behavior of the instruments that are susceptible to drift with time and use, or following a repair. Hence, for an ultrasonic instrument, the values of the electrical parameters can be different from their declared values in a manufacturer's technical specification as seen in the present work. The user of the instrument should periodically verify those parameters.

In this paper, an evaluation of the transmitter pulse parameters of an ultrasonic instrument according to the requirements of the EN 12668-1:2010 standard have been presented. The results and their respective uncertainties were compared to the manufacturer's technical specification and are declared to be acceptable according to the EN 12668-1:2010 standard acceptance criteria.

II. REFERENCES

- [1] *General criteria for the operation of various types of bodies performing inspection*, ISO/IEC 17020:2004, Nov. 2004
- [2] J.Blitz and G. Simpson, *Ultrasonic Methods of Non-destructive Testing*, London, 1996, p. 2.
- [3] *Non destructive testing – Characterization and verification of ultrasonic examination equipment – Part 1 : Instruments*, EN 12668-1:2010, Feb. 2010.
- [4] *Evaluation of measurement data – Guide to the expression of Uncertainty in Measurement (GUM)*, JCGM 100:2008, Sep. 2008
- [5] Olympus NDT, *EN 12668-1:2010 Group 1 EPOCH 600 Specifications*, 920-248B-EN
- [6] *International vocabulary of metrology – Basic and general concepts and associated terms (VIM)*, JCGM 200:2012, 2012
- [7] *Statistical methods for use in proficiency testing by interlaboratory comparisons*, ISO 13528:2015, Aug. 2015
- [8] Rolf Diederichs, *Analog Characteristics of Ultrasonic Flaw Detectors*, NDTnet 19998 May, Vol.3 No.5.
[Online]. Available: <http://www.amdahl.com/doc/products/bsg/intra/infra/html>

Static Platform for Postural Balance Analysis and Recognition

Adel TOUCHEN¹, Mokhtar ATTARI¹, Samir BOUKHENOUS¹
and Chérif ZIZOUA²

¹ USTHB, LINS Lab, Faculty of Electronics and Computers, PO.Box 32, Bab-Ezzouar, Algiers
at.adel.touchen@gmail.com, attari.mo@gmail.com and s.boukhenous@gmail.com

² CERIST, Wireless Sensor Networks and Applications Group, ben Aknoun, Algiers
zizoua.cherif@gmail.com

ABSTRACT

The human balance is one of the most important factors used in the postural analysis. Among all the available technics, usually, the conventional method allows only an approximation analysis of the body balance, and gives a partial factorial study. Nowadays, stabilometry represents a perspective solution for the whole body balance study, analyzing multiple parameters at the same time and making a relationship between them. This letter deals with the design and development of an instrumented static platform. The goal is to acquire the information related to the body posture represented by the movement of the center of gravity (COG) and the center of pressure (COP). A low cost instrumented system built in the form of a platform; its dimensions are (120×80×10cm). The platform is based on two force sensors, Force Sensor Resistor (FSR) and strain gauge. Experimental tests have been carried out on healthy and pathological cases. The results show a typical pathological recognizing and allowed the detection of deficiency type, and the locomotors part responsible for postural deficiencies. Based on the obtained results, we could decide that the developed platform allows to detect both real time COP and COG movement position, in addition to the pathological recognizing..

Key Words: Postural balance, force sensors, center of gravity, center of pressure.

1. INTRODUCTION

Nowadays, having a good posture remains a potential challenge given the life and work conditions that require us to disrupt our posture. Sometimes undergo stresses more than normal affects our health. Balance posture study is an important factor determining the posture organization. So, the balance study is defined by the relative position of body segments and their orientations in space, which represents a particular geometry controlled by neutral's mechanisms. To analyze the human balance, postural system must be studied; the latter is divided into three basic parts illustrated as follows:

- Sensory inputs represented by the external sensors that deliver to the central nervous system our situation in relation to our environment. Also, proprioceptors delivering to our central nervous system information that allow us to know the relative positions of different body segments against each other.
- A processing and integration unit represented by the central nervous system and its pathways.
- An output represented by muscle tone whose role is to maintain the standing despite the gravity, and ensure balance when moving by determining the static support point [1]. Given the daily life conditions, we are all asymmetrical result of our constitution, our habits and lifestyle. Some people counterpoise this situation and have no trouble which is not the same for others.

Indeed, particular circumstances such as working conditions or trauma may decompensate the postural system. In addition, the asynchronous postural sensors, such as a visual or mandibular asymmetry or asymmetry of plantar support, will generate a postural imbalance responsible for its attendant's pathologies. Postural Deficiency Syndrome (PDS) occurs when the body regulation center is not able to achieve a congruent synthesis of information from different sensors [2]. Different methods are used to analyze and detect postural balance deficiencies. Among these, stabilometry method, based on the determination of two important parameters which are: the center of pressure (COP); this corresponds to the center point of the resultant distributed forces applied on floor by entire contact surface foot/ground, and the center of gravity (COG) which is, the point where all the mass is concentrated in the body. Its position is defined and determined from the average positions of segmental mass centers weighted by the mass of the segments [3]. In this context, a static stabilometry platform prototype has been developed, that can determine the center of gravity (COG) and the center of pressure (COP). A relationship between these two parameters was extracted under normal conditions and instabilities. In addition, we propose to study the results in order to classify them according to the type of disease to determine their characteristics [4].

2. PRINCIPAL OF POSTURAL BALANCE ANALYSIS

The postural balance analysis is based on the evaluation of instantaneous COG and COP where the subject is standing on the platform. The analysis may include lateral and anterior/posterior movement of the COG and COP in a time series. For the COG, the system proposed is based on three sensors to measure the ground reaction force. The coordinates of the COG point of ground reactions vectors applications are calculated by the resulting force moments in the yy' and xx' axis [5] (see Figure 1). For the COP, six force sensors (FSR) are placed on a sole distributed on the following pressure map (see Figure 1): left lateral forefoot segment (LA), left medial forefoot segment (LB), left mid foot lateral segment (LC), left medial mid

foot segment (LD), left lateral rear foot segment (LE) and left medial rear foot segment (LF). These six discrete areas contain the majority of force distribution of foot allowing us to draw the pressure line and to calculate the force's moments of each zone. Also the coordinate of the COP according to the following Equations [6]:

$$\begin{aligned} \sum M F / yy' &= 0 \\ 1/3 F_3 - F_2 * L + F_1 * M_G &= 0 \\ x_G = 1/2 (L * F_2 - F_3 / F_1) &= 0 \\ \sum \|F\|_y &= \sum_i y_i F_i \\ \sum M F / xx' &= 0 \\ F_2 + F_3 - 2F_1 * d + F * y_G &= 0 \\ y_G = 1/6 (L\sqrt{3} * 2F_3 - F_2 - (F_3 / F_1)) &= 0 \\ \sum M F / xx' &= 0 \\ \sum \|F\|_x &= \sum_i x_i F_i \end{aligned}$$

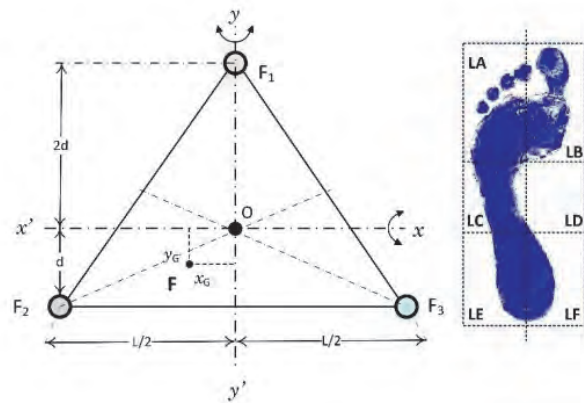


Figure.1: Principal of postural balance analysis

3. PLATFORM & EQUIPMENT

The static platform was designed and developed to embed all sensors and support the heavy body during tests. It is constituted with wood which embeds body sensors in the middle and glass platform fixed on the sensors, may itself bear the weight of the standing individual above. A metallic tube is mounted to the system as a support which ensure the individual's posterior stability during measurements. The platform dimensions are 120×80×10 as shown in Figure 2:

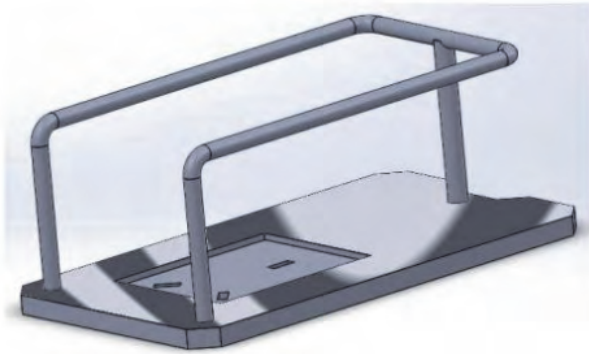


Figure.2: Platform design

The conversion of force information into output signal is provided by sensors based on the resistivity changes depending on the force applied. Two types of sensors are used, the first is a strain gauge mounted on a flexible body where the resistance varies slightly depending on the bending of the body. This sensor is used for acquiring the force related to the COG. For the COP determination, another type of sensor has been used, it is composed of a polymer film changing resistance according to the above support (FSR), and it allows a local measurement of a specific portion with a high resistance variation. The difference between the two sensors and their choice is based on the precision of the strain gauge for determining the COG, and the maneuverability of the FSR installation on a specific foot area without the need of a support [7]. The output of each strain gauge sensor provides a millivolt range voltage from Wheatstone bridge mounted on the sensor body. This tension is pre amplified by an instrumentation amplifier AD622, characterized by its low offset, low noise and high CMRR. Then, conditioned by an offset stage adjustment. As the final phase, the signal passes a 2nd order Butterworth active filter with a 30 Hz cutoff frequency. Regarding the signal from the FSR sensor, it was conditioned and filtered by an operational amplifier stage converting the resistance variation into a voltage signal. All conditioned signals are introduced into a 12-bit ADC microcontroller ARM technology Cortex M3 for digital processing. The data was transmitted to a computer in order to display each sensor output signal and the COG and COP variation.

4. EXPERIMENTAL SETUP

To explore our practical realization, several tests were performed on different individuals either in good posture or with postural deficiencies. As mentioned previously the postural deficiencies can be from interior sensors (proprioceptive) or exo sensors (eyes, ear, skin). Another reason can also unbalance the postural system caused by a bad nerve transmission or a problem in a muscle tone. Based on this hypothesis, firstly, preliminary tests were done on an individual in a good posture to analyze its balance by determining the COP, COG and the relationship between them. In the second part, we performed the same tests on the same individual, but by simulating cases of postural deficiencies by closing the eyes, ear and excitement of his feet by electro stimulator. At the end, we took as pathological cases of scoliosis.

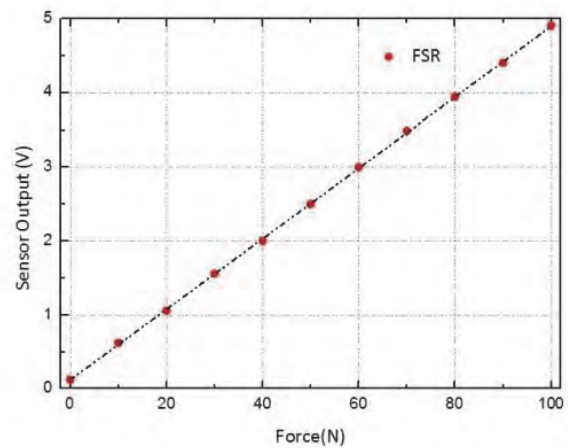


Figure.4: Strain gauge calibration

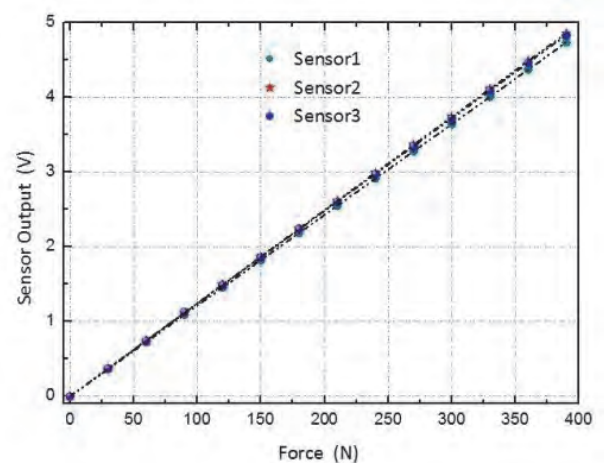


Figure.5: Force Sensor Resistor calibration

5. RESULTS AND DISCUSSION

The two sensors types of the platform were calibrated by using a test bench Lutron FG-5000A equipped with a force indicator. With a maximum force of around 400 N for strain gauge sensor and a maximum force of 100 N for the FSR sensor, experimental data have shown the possibility of applying a linear regression on all extended measurement which procure two-sensor linear characteristics. Figure 6 shows for the healthy case, a good stability is present for COG, oscillating around the equilibrium center. Unlike the latter, instability and a large displacement of the COG is noted for an individual closing his eyes, same thing for an individual closing his ears with low amplitude. Against, instability and a large displacement of the COG is observed also for an stimulated individual's foot, this instability is momentary on shock time, following the foot stimulated direction.

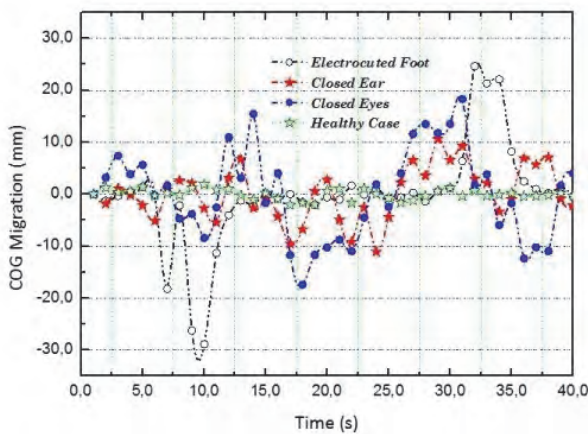


Figure.6: COG migration for pathologic simulation

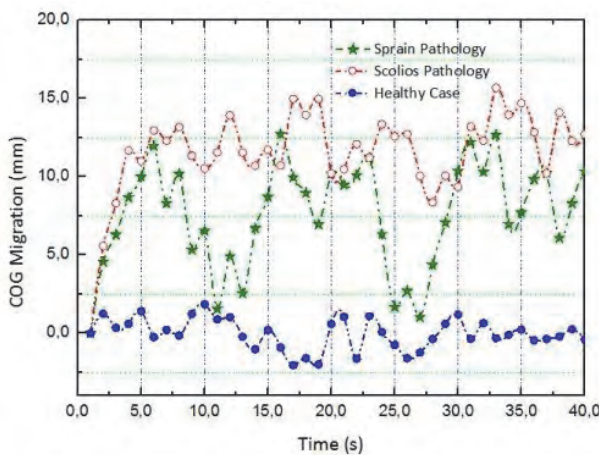


Figure.7: COG migration for real pathology

For the test involving real pathological cases such as scoliosis and a sprained ankle, the same result for the simulation are observed in Figure 7. The only difference is illustrated in the way by which the individual tries to regain its equilibrium position. As the cases with scoliosis, the COG still shifts the center of balance opposed to a person with a sprain which is explained by habit and rehabilitation of individuals with the abnormality unlike a person who is momentary in postural deficiency. Figure 8 shows the pressure line for both posture cases, we observe a pressure line directed to the outside of the foot having low strength at the bottom, this is explained by the type of anomaly that requires the individual to stand up, leaning his foot outward and putting himself on the heel only. Thus, the pressure line follows the path of exerted forces and their direction. However, the calculation of the center of pressure for a healthy case and a case with an anomaly at the front of the foot is used to draw the line of pressure. So, we can extract COP line and illustrate how to restore strengths depending on the zone of the foot.

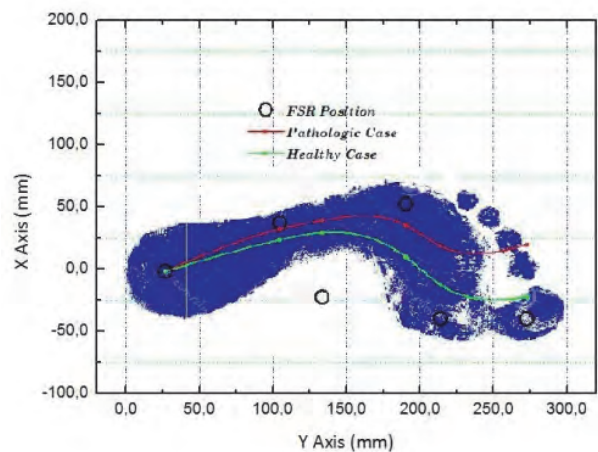


Figure.8: Pressure line and COP migration

5. CONCLUSION

The aim of this work was to develop a platform with simple sensors able to acquire the human force and pressure data. Depending on the obtained results through the tests on healthy and pathological cases, we have studied the stability of an individual observing the migration of centers of gravity and pressure. These results were consistent with the abnormal posture or real

pathological cases. Based on the COP and COG results for the healthy and pathological case, we could localize the body part and the locomotor junction responsible for the deficiency

ACKNOWLEDGEMENTS

This work was supported by the Laboratory of Instrumentation (LINS), and the General Direction of Scientific Research and Development of Technology (DGRSDT).

REFERENCES

[1] Edward D. Lemaire, A. Biswas, and J. Kofman, "Plantar pressure parameters for dynamic gait stability analysis," in *Proc. of 28th International Conference, IEEE-EMBS*, New York City, USA, pp. 4465-4468, Aug. 2006.

[2] J. Fiolka and Z. Kidon, "Center of pressure trajectory segmentation for postural stability analysis," in *Proc. 18th International Conference in Mixed Design of Integrated Circuits and Systems, MIXDES*, Gliwice, Poland, pp. 39-43, June 16-18, 2011.

[3] M. Attari and S. Boukhenous, "A postural stability analysis by using plantar pressure measurements," in *Proc. of 10th International MultiConference on Systems, Signals and Devices, IEEE-SSD'11*, Sousse, Tunisia, March 22-25, 2011.

[4] A. Spaepen, "Opportunities and limitations in the use of force platforms in clinical applications," *International Conference on Clinical Gait Analysis*, Dundee, Scotland, July 1994.

[5] B. J. Benda, P.O. Riley and D.E. Krebs, "Biomechanical Relationship Between Center of Gravity and Center of Pressure During Standing". *IEEE Trans. Rehab. Eng.*, vol. 2, no. 1, pp 3-10, 1994.

[6] R.W. Soutas, K.M. Hillmer, J.C.Hwang and Y. Dhaher, "Role of Ground Reaction Torque and Other Dynamic Measures in Postural Stability". *IEEE Trans. on Eng. Med. and Bio.*, pp 28-31, 1992. 7.

[7] C. Zizoua, M. Raison, S. Boukhenous, M. Attari and S. Achiche "Detecting muscle contractions using strain Gauges" *Electronics Letters*, October 2016 Vol. 52 No. 22 pp. 1836–1838

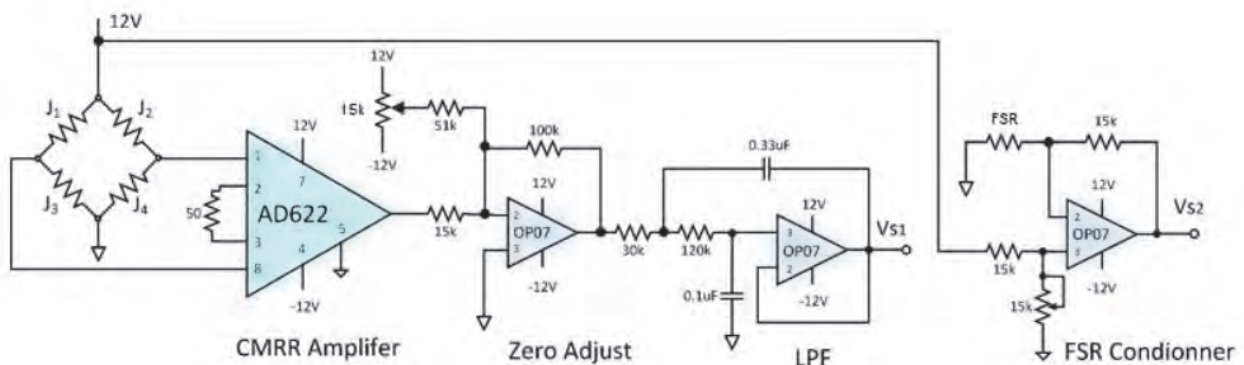


Figure.3: Conditioning circuit

Semi empirical models for estimating global solar radiation for inclined surfaces in the north of Algeria _ Algiers _

Khaoula TALBI¹, Samia HARROUNI²

¹ USTHB, LINS Lab, Faculty of Electronics and Computers, BP. 32 EL Alia, Bab Ezzouar, 16111, Algiers, talbi.kha@gmail.com

ABSTRACT

The present work aims to determine semi empirical models Capderou and Perrin de Brichambaut that will allow us to evaluate the 15 minute global solar radiation on tilted plane for clear and overcast days on the located Algiers city of Algeria and compare with the results measured at the localized site. Statistical indicators used to evaluate the accuracy of the model where the mean bias error (MBE %) and root mean square error (RMSE %). The results show that Capderou model have good estimation results in clear day conditions with RMSE% = 10.93. On overcast days, Perrin de Brichambaut model present the best estimation where MBE % vary from -34 to 4%.

Key words: Global solar radiation; Direct; Diffuse, Capderou; Perrin de Brichambaut, mean bias error (MBE %), root mean square error (RMSE%).

1. INTRODUCTION

The importance of knowing the contribution of solar radiation is vital for adapting and implementing novel solutions for converting solar energy into thermal or electrical energy. For regions where no measured values are available, it is practice to estimate the solar radiation using several models. Although many such models exist, few of them only have been evaluated for short time scales in Algeria locations. Currently,

semi empirical models have been developed to estimate the 15 minute global solar radiation that take into account latitude, longitude, certain climatic parameters, temperature differences or clouds, humidity,..

In this paper, the performance of two models : Capderou [1], and Perrin de Brichambaut [2-4] will be used to estimate 15 minutes of global solar irradiance in Bab ezzouar with different climates.

2. DATA BANK

Geographical characteristics and the tilt value of the studied site are given on the following table:

Table.1 Data Used For Selected Site

Sites	Altitude (°)	Longitude (°)	Latitude (m)	Tilt (°)
Bab ezzouar	36°43'N	3°11'E	12	30

The experimental data used in our study, are global irradiance measured in Bab ezzouar at Algiers located in the north of Algeria. The irradiance data measured with a time step of 15 minutes have been recorded on a tilted surface during the year of 2014 for the considered site.

3. USED MODELS DESCRIPTION

3.1. Capderou model

The total radiation incidence on an unspecified level of orientation is indicated by the sum of two terms as indicated by the relation (1) [1-2]:

$$G = I + D \quad (1)$$

I is the direct radiation on the tilted surface, it is expressed with the equation:

$$I = I_{SC} \exp \left[-T_l \left(0.9 + \frac{9.4}{(0.89)^z} \sin(h) \right)^{-1} \right] \cos(i) \quad (2)$$

where I_{SC} is the extraterrestrial solar constant T_l is the Link turbidity factor [2], z is the altitude in degrees and h the sun height angle (in degrees)

Knowing that for a horizontal plane: $\cos(i) = \sin(h)$ where i is the angle of incidence, equation (2) becomes:

$$I = I_h = I_{SC} \exp \left[-T_l \left(0.9 + \frac{9.4}{(0.89)^z} \sin(h) \right)^{-1} \right] \sin(h) \quad (3)$$

and I_h is the direct radiation on the horizontal surface.

The diffuse radiation D is composed of three parts [1][2]:

$$D = D_1 + D_2 + D_3 \quad (4)$$

D_1 is the diffuse radiation on behalf of the sky expressed by:

$$D_1 = \delta_d \cos(i) + \delta_i \frac{1 + \sin \gamma}{2} + \delta_h \cos(\gamma) \quad (5)$$

with $\gamma = 90 - \beta$ and β is the tilted angle.

D_2 is the diffuse radiation on behalf of the ground or the so called reflected radiation defined by [2]:

$$D_2 = \delta_a \frac{1 - \sin(\gamma)}{2} \quad (6)$$

D_3 is the retro-diffused radiation expressed by the equation:

$$D_3 = \delta_R \frac{1 + \sin(\gamma)}{2} \quad (7)$$

Where:

δ_d : Directional diffuse δ_h : Diffuse horizon's circle

δ_a : Isotropic diffuse soi δ_i : Isotropic diffuse sky

3.2. Perrin de Brichambaut model

The global solar radiation on a tilted surface G presented by Perrin de Brichambaut expressed by [2][3][4]:

$$G = I_n * R_b + D + D_s \quad (8)$$

where I_n is direct normal irradiance, R_b is the inclination factor. D is the scattered or diffuse radiation received on a tilted surface [3] with inclination angle β :

$$D = \left[\frac{1 + \cos(\beta)}{2} \right] * D_h \quad (9)$$

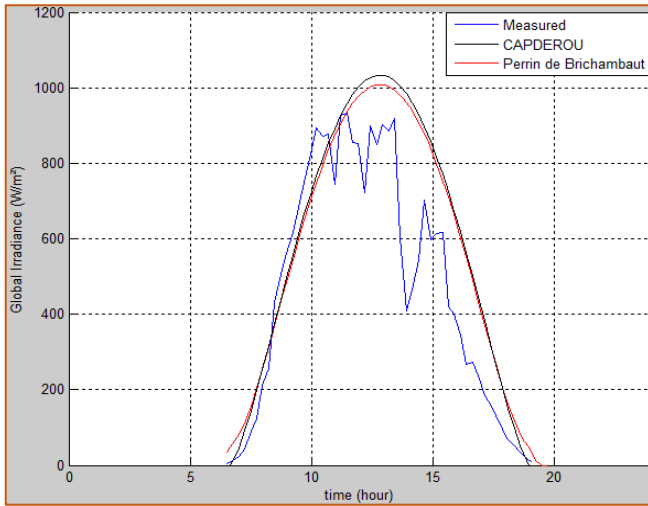
D_h is the diffuse radiation intercepted by a horizontal plane, D_s is the diffuse radiation coming from the soil and received at a horizontal plane; it is expressed by the following formula [4]:

$$D_s = \rho \left[\frac{1 - \cos(\beta)}{2} \right] (I_n * \sin(h) + D_h) \quad (10)$$

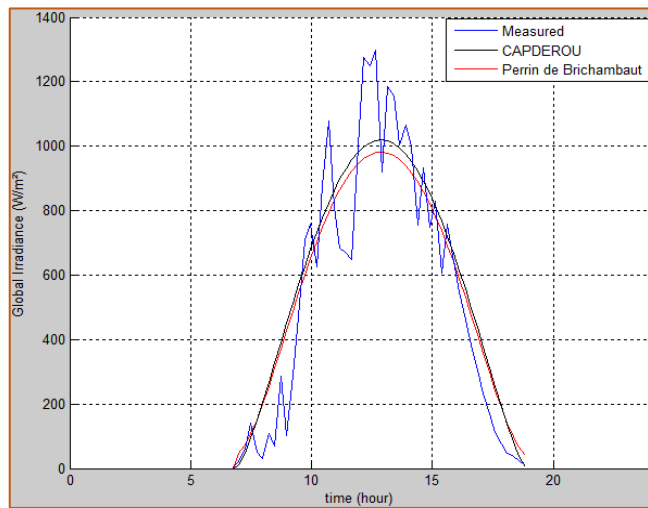
ρ is the Albedo of the soil.

4. RESULTS AND DISCUSSION

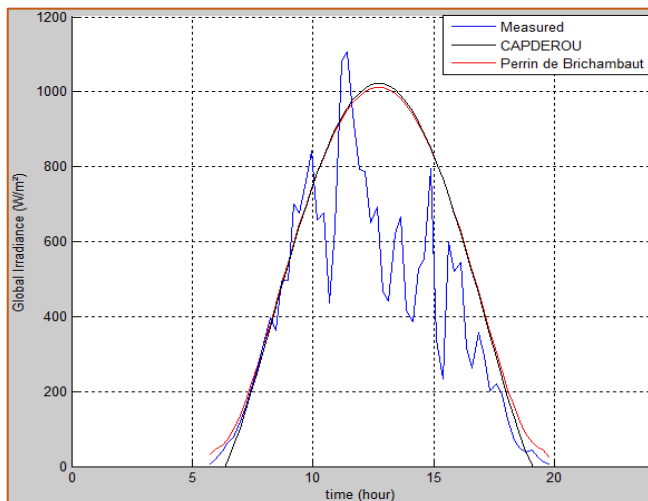
To validate the obtained results we represent in figures 1 and 2 examples of the evolution of solar irradiance measured and estimated by each model versus time for clear and cloudy sky for the studied site. Examples of the 15-minute Matlab simulation results for clear and overcast skies derived using the two described models are shown in Figures 1 and 2:



(A)

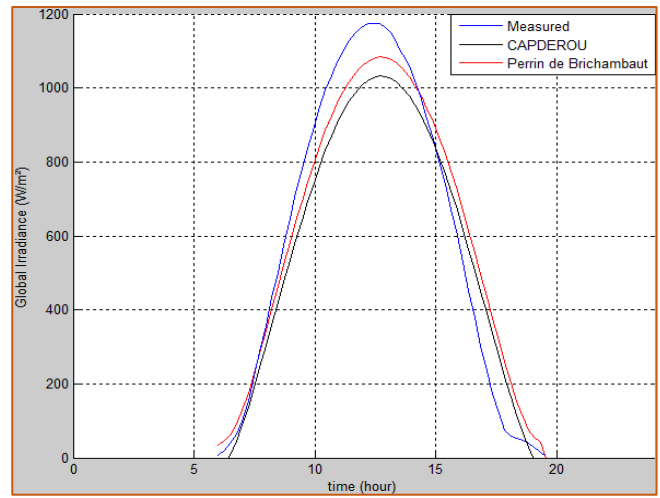


(B)

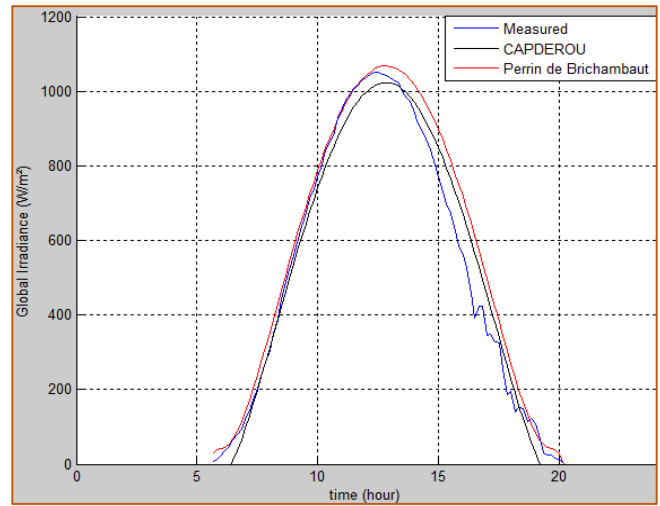


(C)

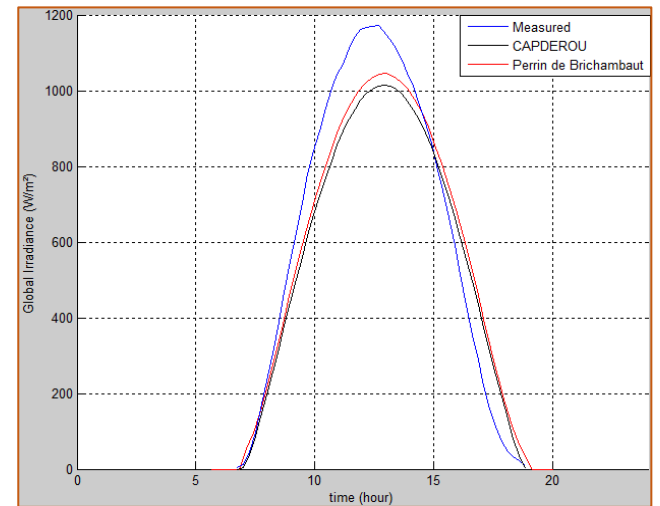
Figure.1: Comparison between measured and computed global solar irradiance by the two models for clear sky days. (A) Day of Mai 06, (B) Day of June 23, (C) Day of March 24.



(A)



(B)



(C)

Figure.2: Comparison between measured and computed global solar irradiance by the two models for overcast days. (A) Day of April 12, (B) Day of March 27, (C) Day of Mai 27.

Figures A, B and C in figure 1 and 2 show that the solar radiations obtained by the two models are in overall in conformity with the measures. We can note that for the site of Bab ezzouar, Capderou model have good estimation results in clear day condition. On overcast days, Perrin de Brichambaut model present the best estimation.

To validate the obtained results, we represent in Table 1 and 2 statistical indicators used to evaluate the accuracy of the two models which are the mean bias error (MBE %) and root mean square error (RMSE%) defined by the following relations:

$$RMSE(\%) = \left(100 * \left(\frac{RMSE}{\sum_{i=1}^n (G_{i,m})} \right) \right) \quad (11)$$

$$MBE(\%) = \left(100 * \left(\frac{MBE}{\sum_{i=1}^n (G_{i,m})} \right) \right) \quad (12)$$

Table.2 Error statistical indicators of the studied models for clear sky days in Bab ezzouar

		RMSE%	MBE%
Mai 06	<i>Capderou</i>	18.0097	6.8728
	<i>Perrin of Brichambaut</i>	16.2773	-1.3913
June 23	<i>Capderou</i>	10.9379	0.0382
	<i>Perrin of Brichambaut</i>	13.8651	-9.3506
March 24	<i>Capderou</i>	18.9217	7.2731
	<i>Perrin of Brichambaut</i>	22.5956	18.3540

The model is more efficient when RMSE and MBE should be closer to zero.

For clear days, the regression analysis shows that the lowest percentage of RMSE and MBE came from the Capderou model values which vary in the intervals [10.9379, 18.9217] and [0.0382, 7.2731] respectively. While the Perrin de Brichambaut model provides the highest RMSE and MBE values.

Table.3 Error statistical indicators of the studied models for overcast days in Bab ezzouar

		RMSE%	MBE%
April 12	<i>Capderou</i>	40.6424	-24.3028
	<i>Perrin of Brichambaut</i>	31.1403	-17.0110
March 27	<i>Capderou</i>	27.4399	-7.7113
	<i>Perrin of Brichambaut</i>	27.2825	4.1632
Mai 27	<i>Capderou</i>	57.6751	-30.9083
	<i>Perrin of Brichambaut</i>	57.1113	-34.4189

As listed in table III, RMSE% and MBE% are considerably higher than on sunny days.

The smallest values of these statistical errors are given by the Perrin of Brichambaut model in this site where RMSE% = 27.2825 and MBE% = 4.1632.

The highest RMSE% and MBE% values are produced by Capderou model which vary in the intervals [27.4399, 57.6751] and [-30.9083, -7.7113] respectively.

5. CONCLUSION

Global solar irradiance data are essential in the solar energy conversion devices. We have estimated 15-minute global solar irradiance at Algiers, with different climates. In this regard, a modeling of the solar radiation by an empirical approach is presented and simulated. The study was carried out for clear and overcast days, prompting our proposal of a "clearness index." This work enabled us to confront measured values and those estimated by the two models; two statistical error indicators were used to compare the models. We found that for clear sky days the best results came from the Capderou model (RMSE=10.9376% and MBE% = 0.0382). For overcast days, we noted that Perrin of Brichambaut model provides the best overall accuracy with the least RMSE for this region.

6. REFERENCES

- Renewable Energy, 'URAER' B.P. 88, Gar Taam, Ghardaïa, Algeria
- [1] M. Capderou, "Atlas solaire de l'Algérie", TOM 1, Vol 1 , "Modèles Théoriques et Expérimentaux", Office des Publication Universitaires. Alger, Aout 1987.
- [2] M.MesriMoukhtari," Introduction au gisement solaire algérien Théorie et applications", Doctorant en Energies Renouvelables, Université Amar Telidji – Laghouat.
- [3] M. Ghodbane, B. Boumeddane, 'Estimating solar radiation according to semi empirical approach of Perrin de Brichambaut: application on several areas with different climate in Algeria', International Journal of Energetica, vol. 1, pp. 20-29, 2016.
- [4] B.M. Tahar, 'Etude théorique et expérimentale des paramètres de fonctionnement d'un capteur solaire plan', University of Biskra, Algiers, 2012.
- [5] M. Mesri-Merad, I. Rougab, A. Cheknane et N.I. Bachari,"Estimation du rayonnement solaire au sol par des modèles semi-empiriques",Département de Génie Electrique, Faculté des Sciences et des Sciences de l'Ingénieur. Université Amar Tilidji, Route de Ghardaïa, Laghouat, Algérie.
- [6] D. S-Koussa, M. Koussa et M. Belhamel," Reconstitution du rayonnement solaire par ciel clair",Centre de Développement des Energies Renouvelables B.P. 62, Route de l'Observatoire, Bouzaréah, Alger
- [7] Benjamin Y. H. Liu, Richard C. Jordan ,” The Long-Term Average Performance of Flat-PlateSolar-Energy Collectors”, Department of Mechanical Engineering, University of Minnesota, Minneapolis, Minnesota, *Vol. 7, No. 2, 1963*
- [8] M. Koussa, A. Malek et M. Haddadi, "Validation de Quelques Modèles de Reconstitution des Eclairments dus au Rayonnement Solaire Direct, Diffus et Global par Ciel Clair", Revue des Energies Renouvelables Vol. 9 N°4 pp. 307 – 332 2006.
- [9] S. Benkaciali and K. Gairaa," Comparative study of two models to estimate solar radiation on an inclined surface", Applied Research Unit on
- [10]RichardE.Bird ,RolandL.Hulstrom ,”Direct insolation models”, solar energy research institute,U.S.department of energy,January 1980.
- [11]Y. El Mghouchi, A. El Bouardi , Z. Choulli, T. Ajzoul ,” Estimate of the Direct, Diffuse and Global SolarRadiations”, ETEE, Faculty of Sciences, AbdelmalekEssaadi University, Tetouan, Morocco International Journal of Science and Research (IJSR) (2012).
- [12]K.Talbi,S.Harrouni,"Modeling of solar radiation received at ground level using semi empirical models for short time scales",8th International Conference on Modelling, Identification and Control (ICMIC-2016)Algiers, Algeria- November 15-17, 2016
- [13]K.Talbi,S.Harrouni," Modeling hourly solar radiation at ground level by semi empirical models in Algeria", International Conference on Artificial Intelligence in Renewable Energetic Systems (IC-AIRES2017), Tipaza,Algeria,July 28,2017.
- [14]http://www.solar-med-atlas.org/solarmed-atlas/socio_economic_policy.htm#s=DZ

Foot sole platform for static and dynamic force and pressure analysis

Adel TOUCHEN, Mokhtar ATTARI and Samir BOUKHENOUS

USTHB, LINS Lab, Faculty of Electronics and Computers, PO.Box 32, Bab-Ezzouar, Algiers
at.adel.touchen@gmail.com, attari.mo@gmail.com and s.boukhenous@gmail.com

ABSTRACT

The posture balance is generally presented by the force distribution in contact with the ground. However, the two feet are the only elements in direct contact with the floor describing a specific force distribution. Each person represents different feet types from the other, based on the geometric form and the angular inclinations in the 3D. This letter deals with the design and the development of an instrumented static and dynamic Force-foot distribution sole. The sensor element designed and developed is a low cost made, composed from a two-copper printed plate (8*8 mm) separated by a polymeric foil. The resistor value of this latter changes with the force applied on it. A matrix of multiple sensors elements are used to acquire the forces applied by the foot on the ground. Regarding the sensors conditioning, a multiplexer algorithm system with a resistance-voltage converter is used for data analysis and acquisition. Experimental tests have been carried out compared to a fully static system showed a high correlation factor ($r = 0.79$). The prototype developed was tested in both static and dynamic mode. The force distribution and the center of pressure migration were the main objectives.

Key Words: foot insole, pressure, force, center of pressure.

1. INTRODUCTION

Even the conditions of daily life, we are all asymmetrical results to our constitution, our habits and our lifestyle. Some persons counterpoise this situation and have no trouble which is not the same for others. Indeed, particular circumstances such as

working conditions or trauma may decompensate the postural system [1]. Balance posture study is an important determinant factor of the posture organization. The balance study is defined by the relative positions of body segments and their orientations in space. This represents a particular geometry controlled by neutral's mechanisms that regulate attitude changes [2]. Both feet are the unique elementary parts of the body which are in direct contact with the ground. The whole forces distributions are concentrated and distributed on four parts (front, middle, rear and lateral). These force distributions give an overall global estimation of the posture. Each foot can represent a lateral part of the posture represented by the center of pressure. And by combining the two data, an estimation of the center of gravity analysis can be deduced [3]. Nowadays, all the techniques used for the forces distributions require very expensive devices, working only in the static and semi dynamic mode. This presents a major obstacle especially for the dynamic analysis of the walking. Multiple systems consisting of hundreds of force sensors are used for the data acquisition. In addition to the complex multiplexing algorithms, these devices are expensive and almost nonefficient for real time analysis [4][5]. In this letter, we propose a development prototype for the forces distributions and the center of pressure migrations analysis. Presenting almost the same characteristics of an industrial system, however, simplicity, low cost, portability and real-time analysis are the major benefits factors. We used a matrix low cost made sensors, printed on a copper plates separated

by polymeric foils. A high speed embedded system based on a hardware multiplexer system and resistancevoltage converters are used for the data acquisition and processing.

2. THE DEVICE

The sensor element used in the global device is a two-copper printed square (8*8 mm) separated by a polymeric foil. The purpose of the copper printed is to conduct the current, also to layout the design of the force sensor. On the other side, the polymeric foil is used for its resistive variation capability in function of the force applied. A total of 150 sensors elements are printed on the same copper plate forming a plantar sole shape. Two identical copper plates are used; on the first one the sensors elements are connected together in column architecture and on the second one, they are joined together in row architecture. The two plantar soles are joined and each copper element is separated from the other by a polymeric foil. The major forces distributions on the foot are concentrated in 4 parts: the front one presented by the 5 fingers, the middle part presented by the cuboid and the 3 cuneiform, the rear part presented by the calcaneus and the lateral part presented by the cuboid [6][7].

3. EXPERIMENTAL SETUP

To detect and measure the resistance change of each sensor element, we used a simple electronic circuit consisting of a foot sole platform for static and dynamic force and pressure analysis non inverter amplifier. This latter assures the resistance voltage conversion with an amplification gain in function of the force applied. The offset is canceled by the amplifier itself trimmed by the user. For a rapid time response and low cost purposes, the number of used conditioners equals to the number of each matrix row. Using an algorithm multiplexing hardware architecture, each matrix element is selected for conditioning separately. By the bias of a decoder, each column is selected sequentially by a microcontroller unit. Whoever, in the same time the multiplexer selects the row. Using only 150 sensors elements with 10 mm separation between them, it's insufficient to get a perspicuous force distribution resolution. So, a software

algorithm was developed to combine the adjacent sensors information for image processing enhancement [8].

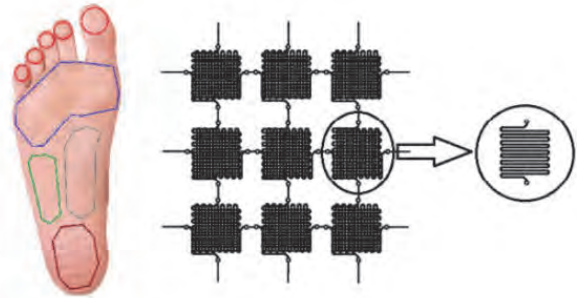


Figure.1: The principal of postural balance analysis

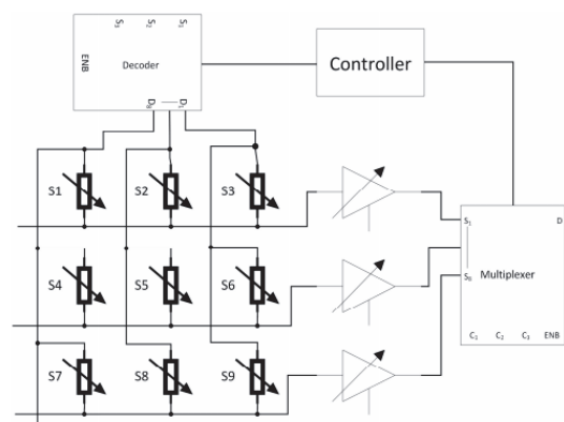


Figure.2: Sensors conditioning system

4. SENSORS CALIBRATION

In order to explore our sensors, multiple experimental tests were made for calibration purposes by applying linear forces. Several repetitive tests were made on both polymeric foil and on each sensor element. The resistances and the voltages variations were measured. A correlation was applied between the sensors elements of each row in order to use them with the same conditioner. The calibration was made by using a test bench Lutron FG-5000A equipped with a force indicator.

Reaching a maximum force around 100 N, experimental data have shown exponential variations for the resistances and the possibility of applying a linear regression on all the extended voltages range measurement. In the same context, and by the same equipment we calibrated a Force sensor resistor (FSR) to use it as a reference.

With high factors ($r=0.83$) for the correlation between the same row sensors and ($r=0.79$) for the correlation between the sensor element and the FSR, the same linear regression for the FSR could be used for all same row sensors. Fig 3. and Fig 4. shows variation graphs of the force as a function of resistance and voltage) [9].

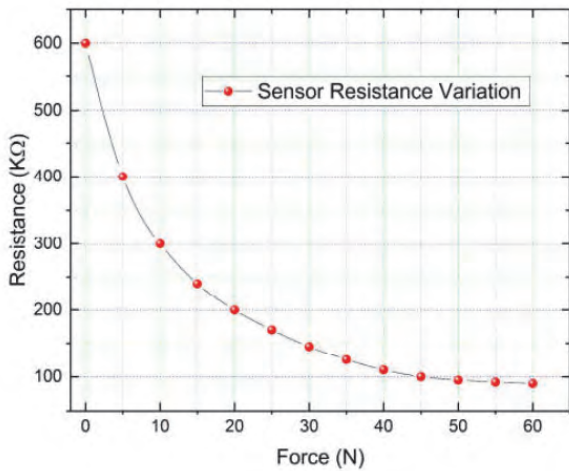


Figure.3: Sensors element calibration (resistance variation)

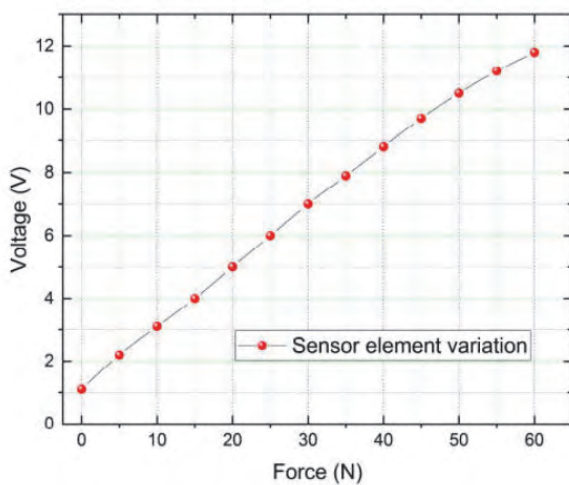


Figure.4: Sensors element calibration (voltage variation)

5. RESULTS AND DISCUSSION

Fig 5. Presents a 3D forces distribution for the entire foot. Since we are interested by a force distribution, the pressure dimension factor is used for measurement. The maximum Pressure values are observed around the great toe, cuboid part and the calcaneus. The pressure in these parts reaches 350 KPa to 500 KPa on the average for a masculine adult. however, for a female adult a maximum of 300 KPa to 400 KPa

is observed. For evaluation purposes, a correlation between our prototype and a static platform was applied and the results showed an acceptable Correlation factor $r = 0.79$.

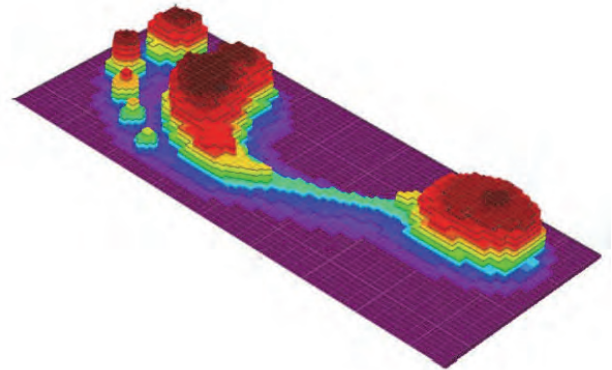


Figure.5: 3D Forces distribution for normal foot

Fig 6. Present the pressure center migration on a walking phase. The sole was placed beneath a shoe and tested on a uniform straight path. The walking is divided to two phases: stance and swing phase. The stance phase starts from the heel strike to the toe off. Whoever, the swing phase starts from the toe off to the heel strike. The COP moves from the rear position (Rear of the calcaneus) to the front position (Front of the great toe) in the stance phase. This migration from the rear to the front position is characterized by a direct leap from the calcaneus to cuboid position since just a light contact is present between them. Contrariwise, the COP is nil on the swing phase since the leg is in the air [10].

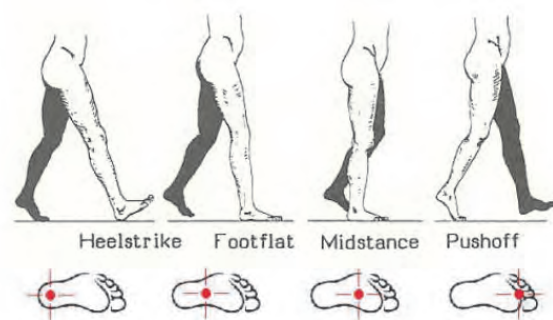


Figure.6: Center of pressure migration in the stance walking phase

In addition to the normal foot, flat and high arch foot were involved in the tests. Fig 7 shows a 3D Forces distributions for the 3 Foot arch types. Concerning the Flat foot, an

additional contact with the ground by the navicular bone was observed. Around 150 KPa of pressure for an adult is present in this area, which moves the COP to the interior side of the foot. Also, a decrease of 100 Kpa was observed on the cuboid part. However, for a high foot, almost no contact with the ground

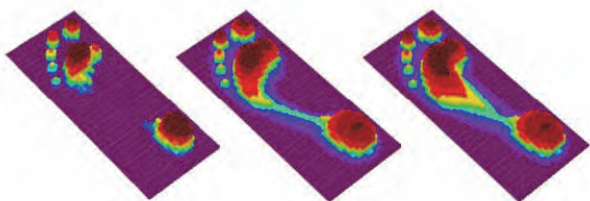


Figure.7: 3D representation of the high arch, normal, and flat foot

6. CONCLUSION

In this letter, the main purpose was the design and the development of a sole able to present the forces distribution of the foot and COP migrations. Using basically low-cost materials for the sensors design and simple processing technics. The prototype evaluation was assessed by a correlation between our results and a static platform results. With a correlation factor ($r = 0.79$), we could confirm that our developed sole sensors could be used for a foot analysis process. The low cost, the portability and the possibility to use it in walking are the main advantages.

ACKNOWLEDGEMENTS

This work was supported by the Laboratory of Instrumentation (LINS), and the General Direction of Scientific Research and Development of Technology (DGRSDT).

REFERENCES

- [1] Rodgers MM. Dynamic foot biomechanics. *J Orthop Sports Phys Ther.* 1995;21:306–316.
- [2] Lawless MW, Reveal GT, Laughlin RT. Foot pressures during gait: a comparison of techniques for reducing pressure points. *Foot Ankle Int.* 2001;22:594–597.
- [3] Eils E, Nolte S, Tewes M, Thorwesten L, Volker K, Rosenbaum D. Modified pressure distribution patterns in walking following reduction of plantar sensation. *J Biomech.* 2002;35:1307–1313.
- [4] Kellis E. Plantar pressure distribution during barefoot standing, walking and landing in preschool boys. *Gait Posture.* 2001;14:92–97
- [5] Rodgers, M. Dynamic biomechanics of the normal foot and ankle during walking and running. *Phys. Ther.* 1988, 68, 1822–1830 [
- [6] Bonato, P. Wearable sensors/systems and their impact on biomedical engineering. *IEEE Eng. Med. Biol. Mag.* 2003, 22, 18–20
- [7] Salpavaara, T.; Verho, J.; Leikkala, J.; Halttunen, J. Wireless Insole Sensor System for Plantar Force Measurements during Sport Events. In Proceedings of IMEKO XIX World Congress on Fundamental and Applied Metrology, Lisbon, Portugal, 6–11 September 2009; pp. 2118–2123 [6] Bonato, P. Wearable sensors/systems and their impact on biomedical engineering. *IEEE Eng. Med. Biol. Mag.* 2003, 22, 18–20
- [8] Saito, M.; Nakajima, K.; Takano, C.; Ohta, Y.; Sugimoto, C.; Ezoe, R.; Sasaki, K.; Hosaka, H.; Ifukube, T.; Ino, S.; Yamashita, K. An in-shoe device to measure plantar pressure during daily human activity. *Med. Eng. Phys.* 2011, 33, 638–645. [6] Bonato, P. Wearable sensors/systems and their impact on biomedical engineering. *IEEE Eng. Med. Biol. Mag.* 2003, 22, 18–20
- [9] Wahab, Y.; Zayegh, A.; Begg, R.K.; Veljanovski, R. Design of MEMS Biomedical Pressure Sensor for Gait Analysis. In *Proceeding of IEEE International Conference on Semiconductor Electronics, 2008 (ICSE)*, Johor Bahru, Malaysia, 25–27 November 2008; pp. 166–169
- [10] R. C. Schafer, Basic Principles of Chiropractic: The Neuroscience Foundations of Clinical Practice, *American Chiropractic Association*, 1984, ISBN : 0960661840, 9780960661848.

Finite element analysis of the fundamental anti-symmetric Lamb A0 and quasi-Lamb qA0 modes for gas sensing applications

Farouk LAIDOUDI^{1,2}, Fayçal MEDJILI², Farid BETTINE², Fouad BOUBENIDER¹

¹ Laboratory of Physics of Materials, USTHB, PO.Box. 32, Bab-Ezzouar, Algiers, Algeria.
f.laidoudi@crti.dz, fboubenider@yahoo.fr

² Research Center in Industrial Technologies CRTI, P.O.Box64 Cheraga 16014, Algiers, Algeria
f.medjili@crti.dz, f.bettine@crti.dz

ABSTRACT

Acoustic waves are used in sensors and actuators, among them Lamb waves propagating in the thickness of thin piezoelectric plates with symmetric S and anti-symmetric A modes are good candidate for signal processing and sensing applications, for gas sensors the fundamental anti-symmetric A0 Lamb and quasi-Lamb modes, propagating in thin film piezoelectric ZnO on SiC substrate with predominant shear vertical displacement profiles, are numerically studied in presence of volatile gases on the top surface of the device, the dispersion curves of phase velocity, the electromechanical coupling coefficient and the effect of gas loading are calculated using finite element approach, high electromechanical coupling and high sensitivity to gas loading were shown by the fundamental anti-symmetric A0 mode. The obtained data are useful for design and micro-fabrication of high sensitivity, high electroacoustic performances gas sensor.

Key Words: Lamb acoustic waves, Finite Element Analysis, Piezoelectric thin films, mechanical characterization, Gas sensor

1. INTRODUCTION

Acoustic waves propagating in thin piezoelectric films on finite or half space substrate have attracted many attentions in the signal processing and sensing fields. Based on the applied boundary conditions, Love, Lamb and Rayleigh waves can propagate in thin piezoelectric plates [1],

Love waves are surface acoustic waves characterized with shear displacement profile, they are suitable for sensing in liquid environment and for viscosity measurement [2]-[3]. Rayleigh waves are also surface acoustic waves with elliptically polarized displacement profile in the in plane of the plate, which makes them more appropriate for gas detection [4]. Lamb waves are acoustic waves propagating in plates with finite thickness, based on the particles motion in respect to the mid plane of the plate, Symmetric S and anti-symmetric (asymmetric) A modes can travel in the bulk of the plate as shown in Fig.1.

Lamb waves have been studied many years to be applied in NDT, in signal processing and in sensing field [5]-[6]-[7], the fundamental symmetric S0 mode have been excited in AlN piezoelectric material for high frequency operating devices [8] and for sensing in liquid environment [9], Higher order Lamb modes have been recently studied for micromechanical resonator and for viscosity measurement [6]-[10].

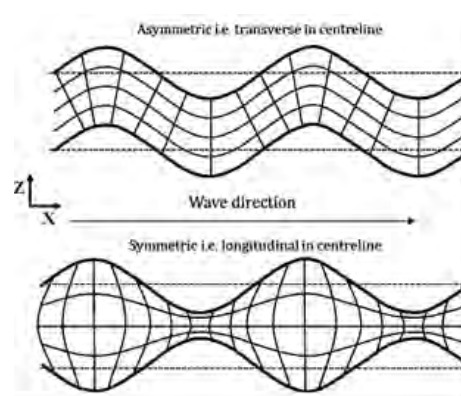


Fig.1 Lamb wave asymmetric and symmetric modes propagating in one layer plate

This paper aims to study theoretically the fundamental Lamb A0 and quasi-Lamb qA0 modes in piezoelectric one layer ZnO and multilayer ZnO/SiC respectively for gas sensing applications, the dispersion curves of phase velocity, the electromechanical coupling factor K^2 and the gravimetric sensitivity to gas loading are calculated by finite element analysis.

2. FINITE ELEMENT FORMULATION

Finite element method is carried out to study the modal vibration of thin piezoelectric plate, the mode shape of the studied plate can be obtained by performing modal analysis in ANSYS APDL environment. The model used in simulation is shown in Fig.2 which is a rectangular plate with a thickness h and a length L , the discretization of the model has been done using 2D coupled field elements PLANE223 suitable for piezoelectric analysis, symmetric boundary conditions are then applied on the left and right sides of the plate, this ensure the vibration of the plate in an integer multiple of wavelength.

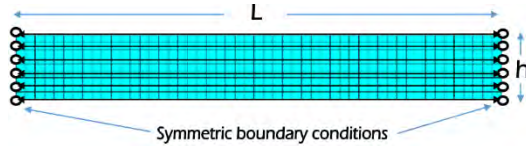


Fig.2 Finite element model used for simulation

The equations of motion for acoustic waves are derivated from the second Newton law for piezoelectric medium [11]:

$$\begin{aligned} \rho \frac{\partial^2 u_j}{\partial t^2} &= C_{ijkl} \frac{\partial^2 u_j}{\partial x_i \partial x_l} + e_{kij} \frac{\partial^2 \phi}{\partial x_i \partial x_k} \\ e_{ikl} \frac{\partial^2 u_k}{\partial x_i \partial x_l} + \epsilon_{ik} \frac{\partial^2 \phi}{\partial x_i \partial x_k} &= 0 \\ i, j, k, l &= 1, 2, 3 \end{aligned}$$

In which C_{ijkl} are mechanical material properties, ρ is the density of the material, e_{ikl} and ϵ_{kl} are the piezoelectric and the dielectric material properties. Φ is the electric potential and $u_{j,k}$ are the particle displacement components.

The resolution of this system is done using finite element analysis, the Sparse direct solver based on Block Lanczos method [12] is

chosen to get the natural frequency f relative to each mode shape of the plate. Based on the symmetry of the shape in respect to the mid-plane of the plate, symmetric and anti-symmetric Lamb modes can be distinguished.

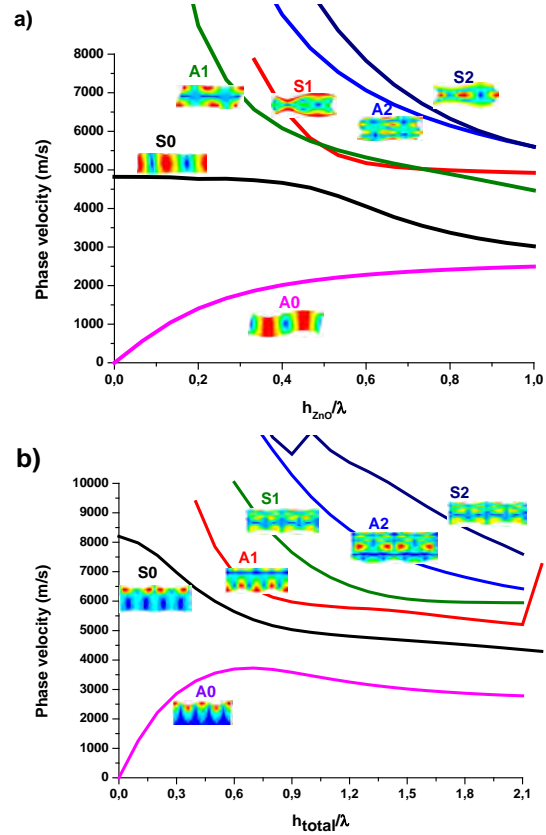


Fig.3 Phase velocity dispersion curves of a) Lamb modes in ZnO and b) quasi-Lamb modes in ZnO/SiC for $h_{ZnO}/h_{SiC} = 0.5$

The phase velocity v of Lamb modes is calculated using the formula $v = f \lambda$, in which λ is the wavelength corresponding to each mode. Fig. 3 shows the phase velocity dispersion curves for the three first fundamental Lamb modes propagating in single and bilayer structure of ZnO and ZnO/SiC respectively, the physical properties of those materials are obtained from[13]-[14].

The dispersion curves of phase velocity allow the choice of the desired mode in its non-dispersive region, this prevent the spread of the acoustic energy of the mode during its traveling in the plate. In electroacoustic devices, the excitation of the mode is carried out by mean of inter digital transducers, however the h_{ZnO}/λ is of interest because it defines the wavelength of the excited mode in respect to the thickness of the piezoelectric layer. Since Lamb waves are bulk waves, the wavelength must be the

same or higher than the thickness of the plate. For high sensitivity and rapid response electroacoustic sensors, it's better to choose the mode with high velocity at the adequate h_{ZnO}/λ value.

Another parameter of high importance in characterization of acoustic sensors and resonators is the electromechanical coupling factor K^2 , which represent the amount of electric energy converted to mechanical energy of the acoustic mode generated by inter-digital transducers IDT's, the different IDT's configurations used in simulation are the same discussed by Jie Zou et al [15]. Fig. 4 shows the electromechanical coupling K^2 of the fundamental anti-symmetric A0 and qA0 modes calculated respectively for one layer of ZnO and double layer of ZnO/SiC.

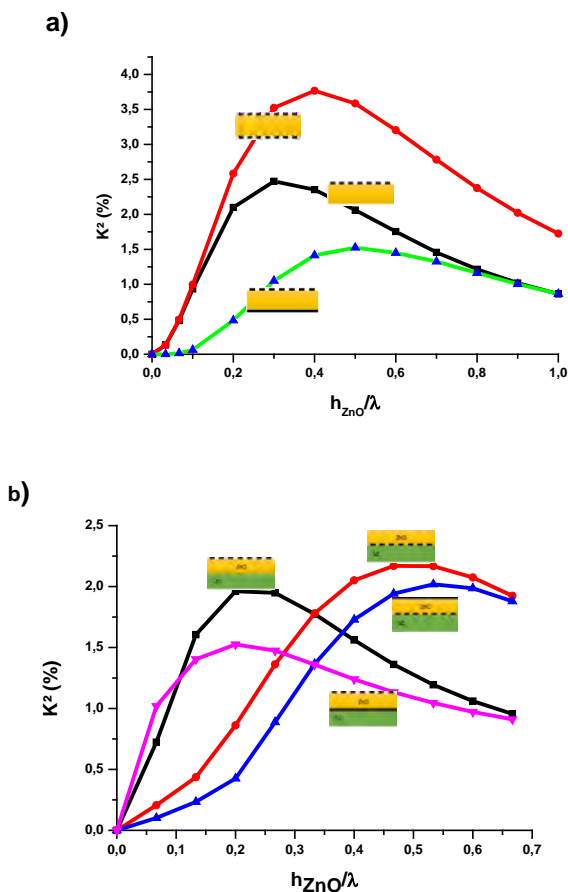


Fig. 4 Electromechanical coupling factor K^2 of Lamb modes for different IDT's configurations and h_{ZnO}/λ values a) A0 mode in single layer ZnO and b) qA0 mode in ZnO/SiC at $h_{SiC}/\lambda = 0.1$.

Fig. 4 shows that for all electrical configurations, the electromechanical coupling factor increases till it reaches a high value then it decreases as h_{ZnO}/λ increases. The higher the K^2 , the higher energy acoustic mode will be generated, in our case, we've

adopted the IDT's on the top of the ZnO layer for both A0 and qA0 modes. For gas sensor, the A0 is generated at $h_{ZnO}/\lambda = 0,3$ which correspond to $K^2 = 2.47\%$ and the qA0 is generated at $h_{ZnO}/\lambda = 0,2$ which correspond to $K^2 = 1.96\%$.

3. APPLICATION OF qA0 MODE FOR GAS SENSING

The A0 and qA0 modes are characterized by a dominant shear vertical displacement, this allow them to be more sensitive to mass loading on the surface of the piezoelectric guiding layer. At high h_{ZnO}/λ values, Lamb modes behave like Rayleigh modes as shown in Fig. 5, this property makes anti-symmetric modes suitable for gas sensing applications.

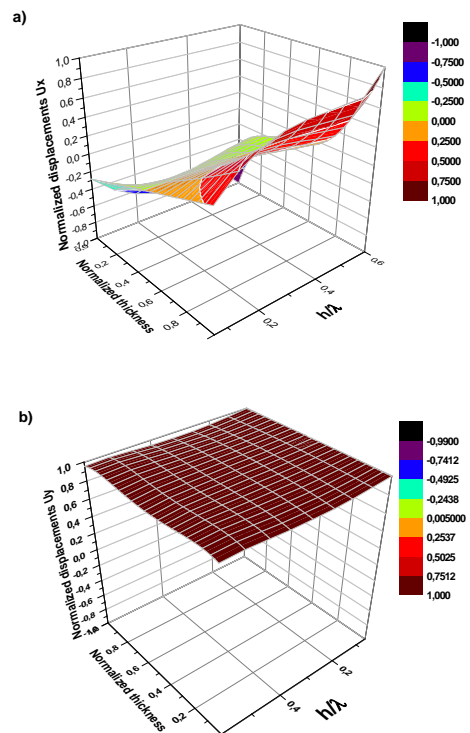


Fig.5. 3D displacement profiles for the fundamental anti-symmetric A0 Lamb mode a) U_x and b) U_z

The anti-symmetric Lamb modes are not well studied for sensing applications, C. Caliendo has used the A0 mode for sensing in liquid environment [16]. The symmetric qS0 and other higher order qL1 and qL2 Lamb modes are used to measure viscosity of liquids [7]. In this paragraph, the fundament anti-symmetric quasi Lamb mode qA0 is exploited to model a gas sensor as shown in Fig. 6.

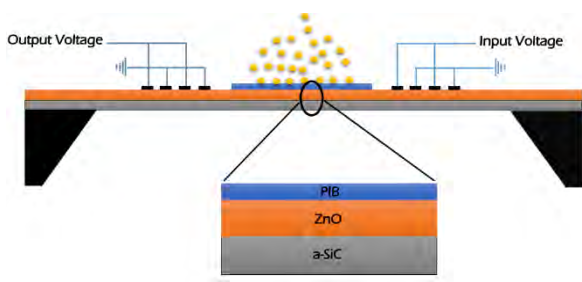


Fig. 6 Model adopted for quasi-Lamb qA0 mode based gas sensor

The model is a thin film of Polyisobutylene PIB of thickness 200 nm deposited on the bilayer of ZnO/SiC, the organic gases to be adsorbed by PIB layer are dichloromethane (CH₂Cl₂), trichloro-methane (CHCl₃), carbontetrachloride (CCl₄), tetrachloroethylene (C₂Cl₄), and trichloroethylene (C₂HCl₃), the density of the PIB layer ρ_{PIB} after absorbing the gases become $\rho = \rho_{PIB} + \Delta\rho$ where $\Delta\rho$ is partial density of the adsorbed gas which is related to the gas concentration, the partial density $\Delta\rho$ and the mechanical properties of PIB are obtained from [17].

The response of the device is based on the shift in modal frequency Δf induced by the change in density of PIB layer due to gas adsorption, this shift is expressed by $\Delta f = f_0 - f_{PIB}$ in which f_0 is the modal frequency with PIB layer in air (before absorbing any gas) and f_{PIB} is the modal frequency after absorbing the gas by PIB layer. Fig. 7 shows the shift in frequency Δf induced by the change, from 100 ppm to 500 ppm, in the concentration of the adsorbed gases.

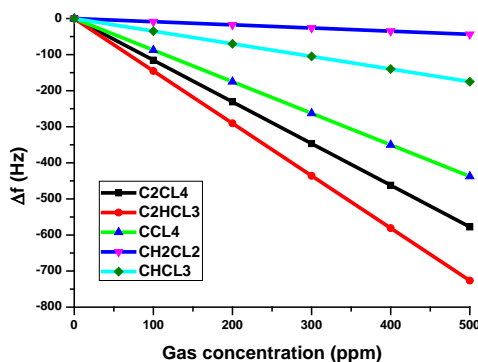


Fig.7 Modal frequency shift for different gas concentrations.

Fig.7 shows that the modal frequency of qA0 mode decreases linearly with the adsorbed gas concentration for different selected gases, it can be also shown that it's possible to sense even a small amounts of gas (100 ppm) which confirm the ability of qA0

Lamb mode for gas sensing. To improve the sensitivity of the device to gas, other simulations must be carried out by changing the delay line, the materials, the electromechanical configurations and the absorbing gas layer.

4. CONCLUSION

The propagation characteristics of acoustic Lamb modes in piezoelectric ZnO single layer and ZnO/SiC multilayered structure is carried out using finite element approach, the phase velocities and the electromechanical coupling factor of the fundamental anti-symmetric modes are presented, the effect of gas loading on the behavior of qA0 Lamb mode sensor is investigated for different gases and concentrations, the analysis has shown an electromechanical coupling factor as high as 3.8% and 2.3% for both A0 and qA0 modes respectively, a high sensitivity of qA0 mode to different concentrations of the selected organic gases, which makes this mode a good candidate for gas sensing. The obtained data are useful for design and fabrication of high performance electroacoustic gas sensor based on the fundamental anti-symmetric Lamb modes.

REFERENCES

1. D. Royer and E. Dieulesaint, *Elastic Waves in Solids I: Free and Guided Propagation*, translated by DP Morgan. Springer-Verlag, New York, 2000.
2. C. Caliendo and M. Hamidullah, "A Theoretical Study of Love Wave Sensors Based on ZnO-Glass Layered Structures for Application to Liquid Environments," *Biosensors*, vol. 6, no 4, pp. 59-72, 2016.
3. C. Caliendo, S. Sait and F. Boubenider, "Love-Mode MEMS Devices for Sensing Applications in Liquids," *Micromachines*, vol. 7, no 1, pp. 15-28, 2016.
4. M. Vanotti, V. Blondeau-Patissier et al, "SAW sensor exploiting palladium layer properties for selective detection of hydrogen," *Eur. Freq. & Time. Forum & IEEE Intl. Freq. Cont. Symp (EFTF/IFC)*, pp. 775-778, 2013.
5. A.V. Ilyashenko and S.V. Kuznetsov, "Theoretical Aspects of Applying Lamb Waves in Nondestructive Testing of Anisotropic Media," *Russ. J. Nondestr. Test.*, vol. 53, no 4, pp. 243-259, 2017.
6. C-M. Llin, Y-Y. Chen, V.V. Felmetzger et al, "AlN/3C-SiC composite plate enabling high-frequency and high-Q micromechanical

- resonators,” *Adv. Mater.*, vol. 24, no 20, pp. 2722-2727, 2012.
7. C. Caliendo, M. Hamidullah and F. Laidoudi, “Amorphous SiC/c-ZnO-Based Quasi-Lamb Mode Sensor for Liquid Environments,” *Sensors*, vol. 17, no 6, pp. 1209-1222, 2017.
 8. C-M. Lin, V. Yantchev, J. Zou et al, “Micromachined one-port aluminum nitride Lamb wave resonators utilizing the lowest-order symmetric mode,” *J. Microelectromech. Syst.*, vol. 23, no 1, pp. 78-91, 2014.
 9. T. Mirea and V. Yantchev, “Influence of liquid properties on the performance of S0-mode Lamb wave sensors: A theoretical analysis,” *Sens. Actuators. B*, vol. 208, pp. 212-219, 2015.
 10. T. Wang, X. Mu, P. Kropelnicki et al, “Viscosity and density decoupling method using a higher order Lamb wave sensor,” *J. Micromech. Microeng.*, vol. 24, no 7, pp. 075002-075012, 2014.
 11. M. Suenaga et al, *Physical Acoustics*, 1st ed., vol. 9 IX. Acad. Press, New York, 1972.
 12. J.H. Klim, C.S. Lee, and S.J. Kim, “High-performance domain wise parallel direct solver for large-scale structural analysis,” *AIAA journal*, vol. 43, no 3, pp. 662-670, 2005.
 13. B.A. Auld, *Acoustic fields and waves in solids*, 1st ed., vol.1. John Wiley & Sons, 1973, pp. 357-382.
 14. T. Kimoto and J.A. Cooper, *Fundamentals of Silicon Carbide Technology: Growth, Characterization, Devices and Applications*, 1st ed., vol.1, John Wiley & Sons, 2014, pp. 30-33.
 15. J. Zou, C-M. Lin, C.S. Lam et al, “Transducer design for AlN Lamb wave resonators,” *J. Appl. Phys.*, vol. 121, no 15, pp. 154502-154515, 2017.
 16. C. Caliendo, “Theoretical investigation of Lamb wave A0 mode in thin SiC/AlN membranes for sensing application in liquid media,” *Sens. Actuators. B*, vol. 179, pp. 287-292, 2013
 17. C. Caliendo and M. Hamidullah, “Zero-group-velocity acoustic waveguides for high-frequency resonators,” *J. Phys. D: Appl. Phys.*, vol. 50, no 47, pp. 474002-474014, 2017.

Simulation Based Comparative Study of GaAs_{1-x}P_x/GaAs Quantum Dot for Solar Cell Applications

Houcine GUESMI¹, Abdelkader AISSAT^{1,2,*}, Meirem SAFI¹,
Fethi BENYETTOU¹, Isabelle BARBEZIER²

¹Faculty of Technology University of Saad Dahlab Blida.1, Blida, Algeria

²Laboratory IM2NP University of Marseille.1, 13397 Aix- Marseille-France

e.mail: sakre23@yahoo.fr

ABSTRACT

With energy conversion efficiencies in continuous growth, quantum dot solar cells (QDSCs) are currently under an increasing interest. Here, we continue through the developing of this kind of cells in order to attain high efficiency QDSCs, modeling the performance. For that, a series of strained GaAsP/GaAs Quantum dots are simulated and optimized to assess the potential of GaAsP for photovoltaic applications. The devices are compared with standard GaAs p-i-n solar cell. Quantum efficiency measurements show the GaAsP devices have a lower energy absorption edge and stronger absorption than the standard GaAs p-i-n solar cell. These measurements also indicate that 40 layers of GaAsP/GaAs QD, provides a relative improvements of 13.41% of efficiency.

Keywords: Quantum Dots; Solar Cell; Quantum Efficiency

1. INTRODUCTION

The development of solar cells led to the discovery of low-dimensional nanostructure to enhanced the conversion efficiency which is one of the most important parameters to optimize for implementing photovoltaic cells on a truly large scale [1], to surmount limit to them of conversion estimated at 30 % by Shockley-Quisser [2,3]. The solar spectrum contains photons with energies ranging from about 0.5 to 3.5 eV. Photons with energies below the semiconductor band gap are not absorbed, while those with energies much larger than the band gap produce hot-carriers and upon cooling down (thermalization) the excess energy get wasted as heat. To reduce the losses of low energy photons, the researchers aims to developed structures that allows us to absorb the maximum photons of the solar spectrum, which

led us to minimize the losses, in this concept we have the intermediate-band solar cell. These cells are designed to provide a large photogenerated current while maintaining a high output voltage. To make this possible, these cells incorporate an energy band that is partially filled with electrons within the forbidden band gap of a semiconductor. Photons with insufficient energy to pump electrons from the valence band to the conduction band can use this intermediate band as a stepping stone to generate an electron-hole pair. Thus, enormous amount of research effort were started due to the potential of IBSCs to replace the traditional devices [4-14]. The development of these cells led to the discovery of low-dimensional nanostructures such as quantum dots (BQs). The energy levels of the confined states in a quantum dot (QD) can be used as an IB[15]. The first solar cells based on this concept were developed in 2004[16]. The maximum efficiency of quantum dot solar cells QDSCs under concentrated sunlight is about 63.1% [17]. The development of these cells passes essentially by the control of materials used in the conception of components. Recently, most laboratories are geared towards finding new materials. Semiconductor III-V presents most of the time a structure of band in direct gap, the maximum of the valence band and the minimum of the conduction band are in the same points of the Brillouin zone, what gives us a high detection efficiency and light emission. The practical relevance of these materials improves the possibility of making a ternary and quaternary substitution of the partial substitution of one of the elements by other one of the same column in the periodic table because of these good physical and optical properties, who helps to create an electronic and optoelectronics devices. But there is a challenge to find a material system with lattice parameter matched to GaAs and lower band gap

to act as QW or QD material. GaAsP is a useful III-V compound for visible light emitting diodes and solar cells. As a solar cell material, GaAsP is one of the leading candidates as a high band gap cell for either monolithic or mechanically stacked cascade cell applications [18, 19] because of its high-quality crystal growth. In this study, structural characteristics of GaAsP/GaAs quantum dot solar cell have been studied and optimized, in goal to show the effect of the number of QDs on the important characteristics of a solar cell: current-voltage J-V, power-voltage P-V, external quantum efficiency EQE and the Photoluminescence. Figure.1 shows structure of GaAsP/GaAs quantum dot solar cell, where four periods of GaAsP/GaAs quantum dot layers are inserted in intrinsic region. Figure.2 shows the diagram energy of GaAsP/GaAs Quantum Dots Solar Cell, where five periods of GaAsP/GaAs Quantum Dots are inserted in the intrinsic region.

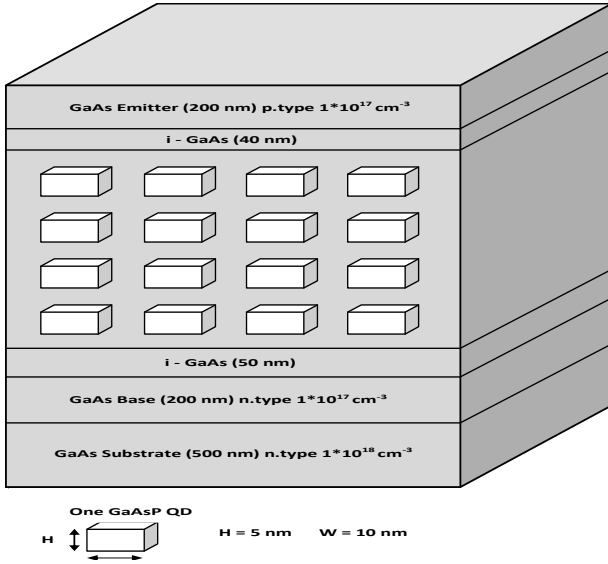


Figure.1: Structure of GaAsP/GaAs quantum dots solar

2. THEORITICAL MODEL

The following section describes the physical models and empirical equations that have been used for this simulation:

The formula for the composition dependent lattice-constant for $\text{GaAs}_{1-x}\text{P}_x$ is found via Vegard's law and the calculated lattice-constant of GaAsP to be:

$$a_{\text{GaAsP}}(x) = xa_{\text{GaP}} + (1-x)a_{\text{GaAs}} \quad (1)$$

The fitted empirical band gap with compositions dependent band bowing :

$$E_g^{\text{GaAsP}} = xE_g^{\text{GaP}} + (1-x)E_g^{\text{GaAs}} - 0.24x(1-x) \quad (2)$$

The EQE of the photogenerated carriers in n/p regions and in the intrinsic region which contains the QD layers is calculated by [20, 21]:

$$EQE(\lambda) = (1 - R(\lambda)) \cdot (1 - \alpha_p l_p - \alpha_n l_n - \alpha_i L) \quad (3)$$

Where $R(\lambda)$ is the surface reflectivity, we have set it to 0.1; $\alpha_{n,p}$ are the absorption coefficients of the n and p-regions and $w_{n,p}$ are their corresponding thicknesses, respectively; α_i is the total intrinsic region absorption and is given by :

$$\alpha_i L = \alpha_B L_B + \alpha_{QD} L_{QD} \quad (4)$$

Where L is the total thickness of the intrinsic region; α_B, QD are the absorption coefficients of the barrier and quantum dot materials and L_B, QD are their thicknesses, respectively.

To calculate the absorption coefficient of the direct band materials constituting the simulated structure, the Urbach equation was used [22]:

$$\alpha(\lambda) = \alpha_0 \sqrt{\frac{1.24}{\lambda} - E_g} \quad (5)$$

Where α_0 is the optical wave energy function constant of a semiconductor.

The optical reciprocity theorem of Rau [23, 24] is used to relate the spectral EL and PL emission ϕ_{EL}, ϕ_{PL} of a solar cell per photon wavelength interval $d\lambda$ into a solid angle $d\Omega$ to its external quantum efficiency (EQE) per photon wavelength interval $d\lambda$ under illumination from the solid angle Ω and it is given by:

$$\Phi_{EL}(\lambda) \cdot d\lambda = \Omega \cdot \Phi_{bb}(\lambda) \cdot EQE(\lambda) \cdot \exp\left(\frac{V}{V_T}\right) \cdot d\lambda \quad (6)$$

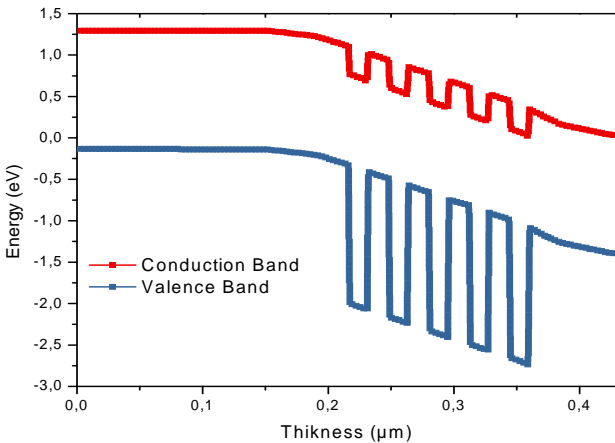


Figure.2 Energy band diagram of GaAsP/GaAs structure.

$$\Phi_{pl}(\lambda) \cdot d\lambda = \Omega \cdot \Phi_{bb}(\lambda) \cdot a(\lambda) \cdot \exp\left(\frac{\mu}{V_T}\right) \cdot d\lambda \quad (7)$$

Where $\varphi_{bb}(\lambda)$ is the black body photon flux per wavelength interval $d\lambda$ and solid angle Ω [25], $a(\lambda)$ is the absorbance and μ is splitting of the quasi-Fermi level, V denotes the junction voltage and V_T the thermal voltage.

3. RESULTS AND DISCUSSION

Along this work, we have choosing a solar spectrum AM1.5 and a temperature of 300 as standard condition. Firstly, we have varied the concentration of phosphor on the alloy $\text{GaAs}_{1-x}\text{P}_x$ on the interval $[0,1]$, in order to have the appropriate percentages of the elements that fit into the component. Then, we studied the variation of the performance parameters of the solar cell with different number of quantum dot layers inserted 10, 20, 30 and 40 respectively. For each simulation, the current-voltage, power-voltage characteristics, External Quantum efficiency EQE curve, and the important characteristic parameters of a solar cell are presented and discussed.

Figure.3 shows the variation of band gap and the variation of strain according to the content of phosphor in $\text{GaAs}_{1-x}\text{P}_x$ alloy. This Figure shows that an increase in GaAsP band gap is accompanied by an decrease in GaAsP Strain, we note a enhancement of 59.15 % of band gap, it was noticed also the low strain between GaAsP and GaAs is about -1.93% with an phosphor content of 0.54. We also note that there is a single Strain (in tension) whatever the Phosphor content. According to this simulation, we fixed the concentration of the phosphor to 54 % which gives us a better strain.

Figure.4 represents the current-voltage $J(V)$ characteristic both of a pin GaAs solar cell and GaAsP/GaAs quantum dots solar cell for a variable number of quantum dot layers inserted: 10, 20, 30 and 40 respectively. In our simulations, the short circuit current increases when more quantum dots are inserted, and open circuit voltage almost stays the same. As a result, the conversion efficiency increases relatively 13.41% when comparing 40-layer quantum dot solar cell with standard solar cell. Beyond this number we notice sudden decrease in efficiency. This is the QD layers number for which we have saturation. Also the enhanced in the short circuit current pulled an increase of the power freed by this structure (Figure 5).

All the characteristic parameters achieved are listed in Table 1.

According to the discussion in the introduction, the most important impact of quantum dots is to allow us to absorb the maximum photons of the solar spectrum, which led us to minimize the losses, which means photons with low energy are successfully absorbed by the solar cell and create photo current.

The maximum wavelength of photons that can be absorbed by a typical standard GaAs solar cell is around 875nm [26]. Figure.6 shows the EQE of a solar cell for 10,20,30 and 40 GaAsP QDs layers inserted into the intrinsic region of a GaAs P-I-N junction. In contrast to the EQE of a pin GaAs solar cell, which drops from 873 nm ($E_g = 1.42$ eV), the QDs solar cell shows an extended spectral response for longer wavelengths due to the absorption of low energy photons by BQs, which means that the photons in this range is effectively absorbed and will contribute to improve the performances of a solar cell.

Table.1 The important parameters of pin solar cell and $\text{GaAs}_{0.46}\text{P}_{0.54}/\text{GaAs}$ QDSC

Number of QD layers	$J_{sc}(\text{mA}/\text{cm}^2)$	$V_{oc}(\text{V})$	FF(%)	$\eta(\%)$
0	21.66	0.75	77.71	12.66
10	18.83	0.905	86.10	14.68
20	19.65	0.906	86.49	15.40
30	20.36	0.907	86.71	16.04
40	21.04	0.907	86.84	16.58

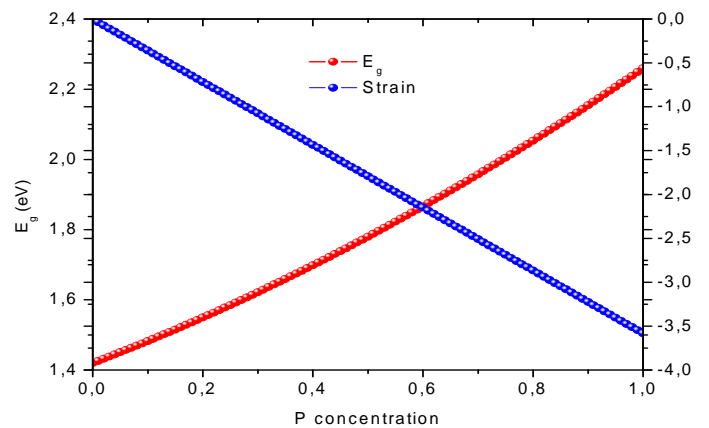


Figure.3. Variation of band gap and the variation of strain according to the concentration of Phosphor

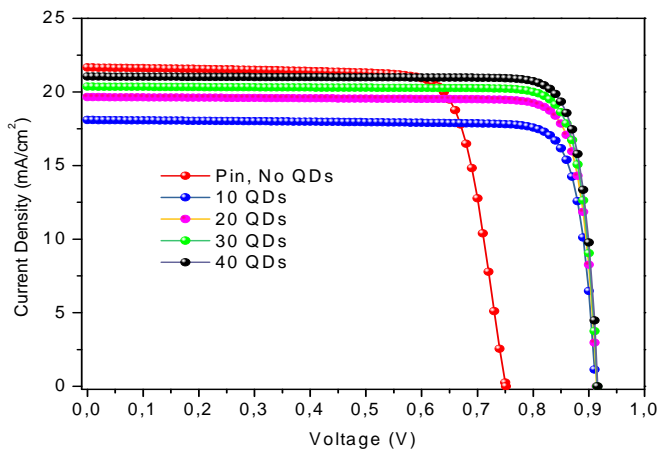


Figure.4: $J(V)$ of pin GaAs solar cell and $\text{GaAs}_{0.46}\text{P}_{0.54}/\text{GaAs}$ QDSC(QD layers= 10, 20, 30 et 40).

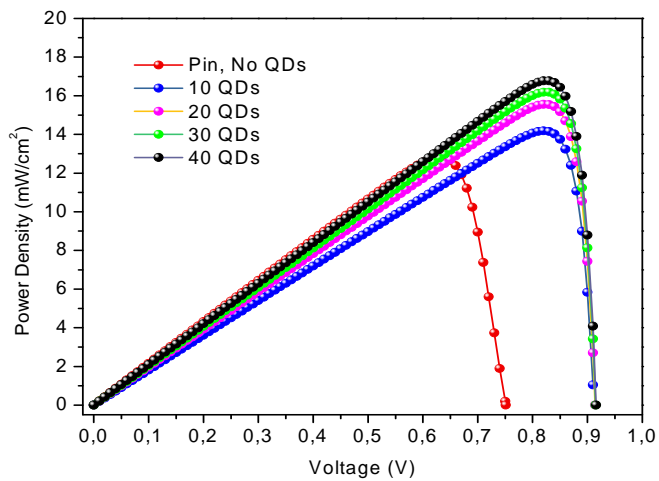


Figure.5: $P(\text{mW}/\text{cm}^2)$ of pin GaAs solar cell and $\text{GaAs}_{0.46}\text{P}_{0.54}/\text{GaAs}$ QDSC (QD layers= 10, 20, 30 et 40).

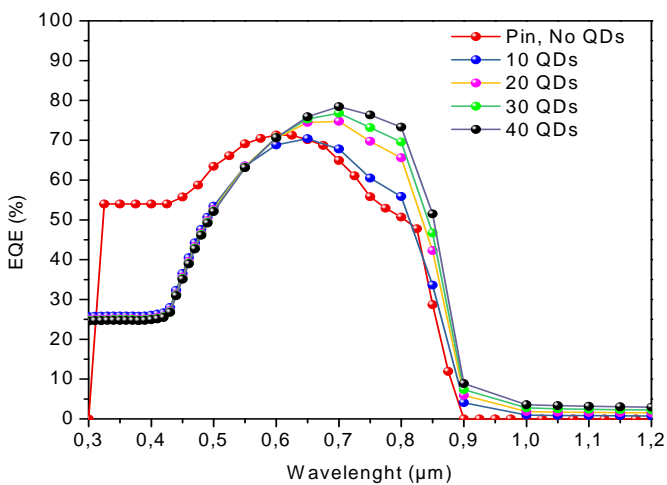


Figure.6: External Quantum Efficiency of pin GaAs solar cell and $\text{GaAs}_{0.46}\text{P}_{0.54}/\text{GaAs}$ QDSC for different number of QD layers.

Figure.7 represents the calculated curve of absorption coefficient both of $p-i-n$ solar cell and $\text{GaAs}_{0.46}\text{P}_{0.54}/\text{GaAs}$ QDSC for 40 layers of QD embedded. It was evident that the $\text{GaAs}_{0.46}\text{P}_{0.54}/\text{GaAs}$ QDSC exploits a wide range of the incident solar spectrum (from 300 to 1200 nm) which was shown in our EQE results. Moreover, the absorption coefficient takes a high values along the interval of wavelengths than $p-i-n$ solar cell. For example at wavelength 600 nm where we can find the maximum intensity of solar spectrum [27], the difference between the absorption coefficient of the two solar cell structures is $\Delta\alpha=3435 \text{ cm}^{-1}$.

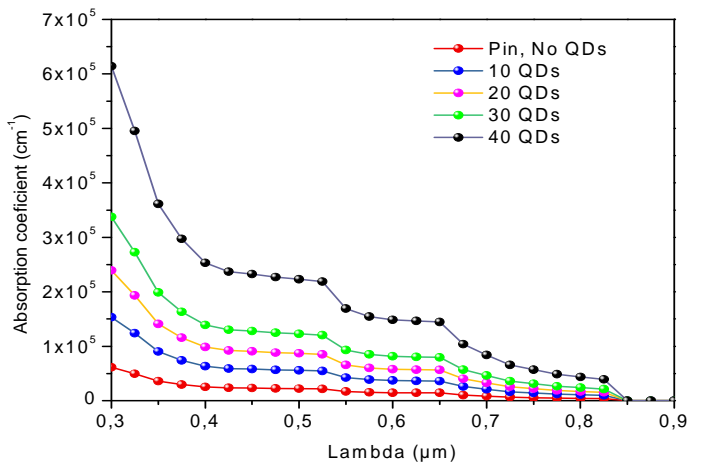


Figure.7: Absorption coefficient of pin GaAs solar cell and $\text{GaAs}_{0.46}\text{P}_{0.54}/\text{GaAs}$ QDSC for 40 QDs layers.

In this part, we have investigated the influence of quantum dots insertion on the optical properties of $\text{GaAs}_{0.46}\text{P}_{0.54}/\text{GaAs}$ QDSC. In this goal, we have examined Photoluminescence PL spectra both of pin GaAs and $\text{GaAs}_{0.46}\text{P}_{0.54}/\text{GaAs}$ QDs solar cell using an external excitation power of about $1 \text{ W}/\text{cm}^2$.

Figure.8 and Figure.9 shows the simulated room temperature RT PL both of $p-i-n$ solar cell and $\text{GaAs}_{0.46}\text{P}_{0.54}/\text{GaAs}$ QDSC for a number of 40 layers inserted in the intrinsic region, respectively. As we can seen in Figure.8, the peak of emission wavelength at room temperature is around 875 nm. Otherwise, whereas the peak around 1200 nm in the $\text{GaAs}_{0.46}\text{P}_{0.54}/\text{GaAs}$ QDSC as we can seen in Figure.9, this peak is usually related to the radiative recombination of carriers in $\text{GaAs}_{0.46}\text{P}_{0.54}\text{QDs}$.

When comparing the PL intensity of $\text{GaAs}_{0.46}\text{P}_{0.54}/\text{GaAs}$ QDSC with 40 QD layers and pin GaAs solar cell, we notice a significant improvement. The enhanced PL signal is mainly due to the fewer non-radiative recombination centers. Moreover, it's clear that the peak

emission of pin GaAs is offset from 875 nm to 850 nm by inserting the GaAs_{0.46}P_{0.54}/GaAs QD layers.

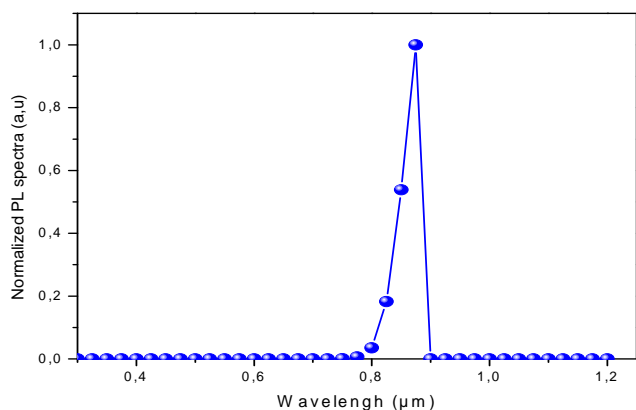


Figure.8: Photoluminescence PL spectra of pin GaAs solar cell at room temperature.

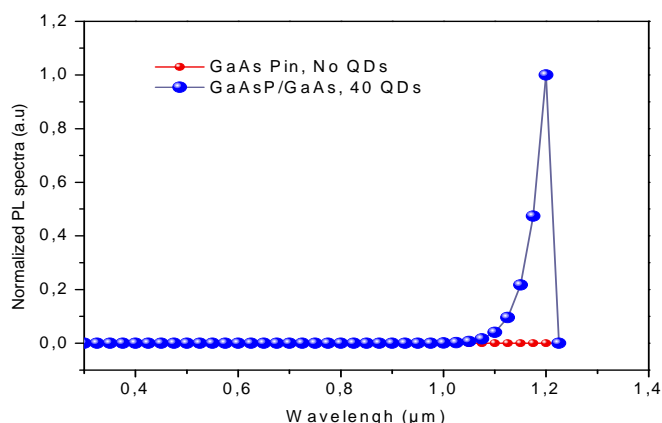


Figure.9: Photoluminescence PL spectra of GaAs_{0.46}P_{0.54}/GaAs QDSC for 40 QDs layers at room temperature.

4. CONCLUSION

The enhancement of solar cells behavior is the main target of our investigation. We have studied a structure based on GaAsP quantum dot solar cell. Firstly, and by using Vegard model to calculate the band gap energy, we find that the band gap of GaAs_{1-x}P_x alloys enhanced by the increasing P concentration with 59.15 %. Otherwise, the low strain between GaAsP and GaAs is about -1.93% with phosphor content of 0.54. Also, under standard condition AM1.5 and a temperature of 300 the effects of the number of the quantum dot is theoretically studied and simulated.

The main target of this study is to determine the optimum value of the number of quantum dots, which give us the optimum value of conversion efficiency. However, for a P content x=54% and for 40, we obtained an optimal short

circuit and efficiency of about 21.04 mA/cm² and 16.58 %, respectively. Moreover, the insertion of 40-layers of GaAs_{0.46}P_{0.54}/GaAs QDs is indeed helpful for solar cells to absorb lower energy photons which have long wavelength from 1060 to 1200nm. Finally, we have examined Photoluminescence PL spectra both of pin GaAs and GaAs_{0.46}P_{0.54}/GaAs QDs solar cell. However, in the one hand the peak of emission wavelength at room temperature is around 875 nm for pin GaAs, in other hand, after the insertion of quantum dots in the intrinsic region, the peak is shifted around 1200 nm.

REFERENCES

- [1] M.A. Green, Third Generation Photovoltaics, Bridge Printery, Sydney, 2001.
- [2] Shockley W and Queisser H, "Detailed Balance Limit of Efficiency of p-n Junction Solar Cells", Journal of Applied Physics 32, 510 (1961).
- [3] M. A. Green, "Third generation photovoltaics: Ultra-high conversion efficiency at low cost, " Prog. Photovolt: Res. Appl., vol. 9, pp. 123-135, 2001.
- [4] P. G.Linares, A. Marti, E. Antolin, C. D. Farmer, I. Ramiro, C. R. Stanley, and A. Luque, 2012 "Voltage recovery in intermediate band solar cells", Solar Energy Materials & Solar Cells 98, pp. 240–244
- [5] Y. Seminovski, P. Palacios, and P. Wahnnon, 2013 "Obtaining an intermediate band photovoltaic material through the Bi insertion in CdTe", Solar Energy Materials & Solar Cells 113, pp. 99–103.
- [6] A. Luque, A. Mellor, I. Ramiro, E. Antolin, I. Tobias, and A. Marti, 2013 "Interband absorption of photons by extended states in intermediate band solar cells", Solar Energy Materials & Solar Cells 113, pp. 138–144
- [7] N. Lopez, L. A. Reichertz, K. M. Yu, K. Campman, and W. Walukiewicz, 2011 "Engineering the Electronic Band Structure for Multiband Solar Cells", PRL 106, 028701.
- [8] W. G. Hu, Y. Harada, T. Inoue, O. Kojima and T. Kita, 2011 "TWO-PHOTONS TRANSITION IN INTERMEDIATE BAND SOLAR CELLS", Photovoltaic Specialists Conference (PVSC), 37th IEEE, pp. 2625-2628.
- [9] J. Lee, S. N. Dahal and C. B. Honsberg, 2011 "Theoretical Analysis for Intermediate Band and Tandem Hybrid Solar Cell

- Materials”, Photovoltaic Specialists Conference (PVSC), 38th IEEE, pp. 68-72.
- [10] A. Lin, J. Phillips, 2011 “Decoupling Spectral Overlap of Intermediate Band Solar Cells using Low-High State Filling”, Photovoltaic Specialists Conference (PVSC), 38th IEEE, pp. 73-77.
- [11] A. S. Lin¹, S. Fu, Y. Zhong, 2012 “A Unified Mathematical Framework for Intermediate Band Solar Cells”, Photovoltaic Specialists Conference (PVSC), 38th IEEE, pp. 78-82.
- [12] P. FazelHamedani, A. Taghinia, F. Yazdi, and Z. M. Artimani, 2012 “Study the Effect of Varying the Thickness of Intermediate Band on the Intermediate Band Solar Cells Efficiency”, Energy Procedia 14, pp. 1496 – 1502.
- [13] Q. Shao and A. A. Balandin, 2007 “Intermediate-band solar cells based on quantum dot supracrystals”, applied physics letters, 91, 163503
- [14] M. Aly and A. Nasr, 2014, “Theoretical Performance of Solar Cell based on Mini-bands Quantum Dots”, J. Appl. Phys., Volume 115, Issue 114311.
- [15] A. M. Aly, 2014, “Progress into power conversion efficiency for solar cells based on nanostructured and realisticspectra”, Journal of Renewable Sustainable Energy, Volume 6, Issue 023118, 2014
- [16] Luque, A. et al. General equivalent circuit for intermediate band devices: Potentials, currents and electroluminescence. J. Appl. Phys. 96, 903–909 (2004).
- [17] Luque A and Martí A, "Increasing the Efficiency of Ideal Solar Cells by Photon Induced Transitions at Intermediate Levels", Phys. Rev. Lett. 78, 5014, June 1997.
- [18] M.W.Wanlass, T.Gessert, M.M.Al-Jassim, J.M.Olson and A.E.Blakeslee, Proc. 18th IEEE Photovoltaic Specialists Conf., 317 (1985).
- [19] R.W.McClelland, B.D.King, J.C.C.Fan, and R.L.Chapman, Proc. 17th IEEE Photovoltaic Specialists Conf., 452 (1984).
- [20] Cabrera, J. C. Rimada, J. P. Connolly, and L. Hernandez. Modelling of GaAsP/InGaAs/GaAs strain-balanced multiple-quantum well solar cells, Applied Physics Letters 2013, 113, p. 024512.
- [21] O. Thériault, Analysis of the external quantum efficiency of quantum dot- enhanced multijunction solar cells, Phd thesis in physics, University of Ottawa 2015.
- [22] H. Reshak, Oleg. V. Parasyuk, H. Kamarudin, I. V. Kityk, Zeyad A. Alahmed, Nasser S. AlZayed, Sushil Auluck, Anatolii O. Fedorchukh and J. Chyský, Experimental and theoretical study of the electronic structure and optical spectral features of PbIn₆Te₁₀, RSC adv 2016, 77.
- [23] U. Rau, “Reciprocity relation between photovoltaic quantum efficiency and electroluminescent emission of solar cells,” *Phys. Rev. B*, vol. 76, pp. 085303-1–085303-8, 2007.
- [24] Daub, “Photolumineszenz von Silizium,” Ph.D. dissertation, Dept.Phys., University of Karlsruhe, Karlsruhe, Germany, 1995.
- [25] M. Planck, *Vorlesungen U” ber Die Theorie Der Wa”rmestrahlung*.Munich, Germany: Johann Ambrosius Barth, 1923.
- [26] C.Bailey, S.Polly, R.Raffaella, et al, "Open-circuit voltage improvement of InAs/GaAs quantum dot solar cells using reduced InAs coverage," IEEE Journal of Photovoltaics, Vol.2, No.3, July 2012, 269-275
- [27] H.Saha and Swapan K.Data, “Enhancement of Performance of Crystalline And Amorphous Silicon Solar Cells through Optical Engineering by Nanostructured Materials”, Springer International Publishing Nov 2013.

An Efficient Supervision of a Hybrid PV-Battery-Supercapacitor Off-grid System with Diesel Generator for Emergency Standby Power

Amar GUICHI^{1,2}, Abdelaziz TALHA¹ and El Madjid BERKOUK³

¹ USTHB, LINS Lab, Faculty of Electronics and Computers, PO.Box 32, Bab-Ezzouar, Algiers
amar.guichi@univ-msila.dz and atalha@usthb.dz

² University of Mohamed Boudiaf, Faculty of Technology, PO.Box 166, M'sila, Algeria

³ ENP, Laboratoire de Commande de Processus, PO.Box 182, El-harrach, Algiers
emberkouk@yahoo.fr

ABSTRACT

Hybrid energy systems are mostly used to overcome the intermittence and the variability of the renewable energy sources. For remote and rural areas with high solar energy potential, the drawbacks of this sources can be defeated by the integration of the appropriate backup sources and storage systems. Therefore, in the present paper, we developed an efficient and an uninterrupted hybrid PV-Battery/Supercapacitor-Diesel generator system for standalone applications, that allows the individuals of this remote areas to generate electricity for self-supply at the lowest cost. The efficiency of the proposed system comes from the adequate used control algorithms, that allow the extraction of the maximum or the intermediate power depends on the loads and battery needs, regulating the AC and DC buses to deliver this power to the loads/battery in the appropriate shape, protecting the battery against the overcharging/deepdischarging, while its cheapest cost returns to take into account the loads' priorities in the power management, this strategy helps to reduce PV generator size. Finally, this system delivers continuous power even in the worst conditions owing to the usage of diesel generator as emergency standby power.

Key Words: Hybrid system, Power management, Off-grid, Intermediate power, diesel generator.

1. INTRODUCTION

The electricity consumption rate increases day by day and becomes a sign of a population's higher living standard and a determinant of their economic growth, especially with the proliferation of the technological devices which require more energy consumption [1]. Therefore, the easiest way to generalize and facilitate its access in the isolated areas, is to promote the use of solar energy, especially for those areas with enormous potential of this energy, as is the case with the vast Sahara in southern Algeria, that has a high potential of an average of 2650 kWh/m²/year [2] accompanied with less population density in a big vast area, that reaches less than 1 inhabitant per km² [3]. It is clear that the both cited factors are a great incentives to develop the solar photovoltaic (PV) sector in this region and all geographic areas with the same conditions. In addition, the PV energy is the most promising energy among the other renewable energies due to its abundance and cleanness. However, the photovoltaic system's dependence on the operating environment has led to the intermittency of its power output, then, in order to overcome this drawback, several works had proposed to combine the PV system with the diesel generator. However, many of the proposed solutions had associated the PV system and the diesel generator with the wind turbine and/or other energy systems, as is the case in

[4], [5], where these solutions cannot be adopted in many regions of weak wind speed. Moreover, the other studies that proposed the PV/Diesel hybrid system [6]–[8], have only focused on the techno-economic feasibility of the system, without modelling and controlling the components of this system, and managing the power flow between them. Hence, in this paper, an efficient control and supervision of a hybrid PV-Battery/Supercapacitor-Diesel Generator system for standalone applications is proposed, it is a low cost and reliable system for remote area power supply, which is strictly sized to supply the prioritized loads and when the battery reaches a low state of charge, the diesel generator starts to supply the loads. Each part of the system has its own control algorithm; the PV generator has been controlled to work in the maximum power mode when the load and the battery are able to receive all the extracted power, whilst it has to work in the intermediate power mode when the extracted power exceeds the demand. The battery/supercapacitor has been controlled to charge and discharge according to its power reference given by the management algorithm; Meanwhile, the amplitude and the frequency of the load voltage have kept regulated by the control of the three phase inverter which is connected between the DC bus and the load. While in the case of the diesel generator, they will be controlled through the control of the synchronous machine and the turbine of the diesel generator (DG) respectively. However, the supervision of the amount of the transferred power between the different parts of the system and its direction will be monitored by the proposed management algorithm, which will take into account the PV extracted power, the battery state of charge (SOC), the loads priorities and their power demand.

2. SYSTEM DESCRIPTION

The proposed system, as shown in Figure 1, is principally composed of a PV generator, a DC/DC converter which is used to track the maximum power point or the limited power point. The converter itself is coupled to a DC bus, where its DC voltage is

controlled by the battery to be maintained at constant value, through the storage of the excess power and the delivering of lack of power. The battery is coupled to the DC bus via a bidirectional buck-boost converter; to meet regular power supply to the AC load, a three phase inverter has been used to convert the DC voltage to an AC voltage with a fixed amplitude and frequency. The DG is directly linked to the AC bus to feed the loads with the adequate voltage. The various used algorithms will be described in the next subsections.

3. MODELING AND CONTROL OF THE PV GENERATOR

The PV generator is composed of series/parallel panels to generate the specified power. The panels are connected in series to form a string. The open circuit voltage of the PV array is the number of this panels multiplied by the open circuit voltage of one panel, while the parallel panels or the strings led to calculate the short circuit current of the PV array. In the literature, the one diode and the double diode models are generally used for modeling the solar cell, nevertheless, the single diode model that is also known by five parameters model is mostly used [9]. The equivalent circuit of the used solar cell's model is depicted in Figure 2.

The following equation gives the relation between the output voltage V_{PV} and the output current I_{PV} for the five parameters model:

$$I_{PV} = I_{irr} - I_0 \left[\exp \left(\frac{V_{PV} + R_s I_{PV}}{V_{therm} n} \right) - 1 \right] - \frac{V_{PV} + R_s I_{PV}}{R_{sh}} \quad (1)$$

Where I_0 is the diode saturation current, V_{therm} ($=kT/q$) is the thermal voltage of the cell, k is the Boltzmann constant ($1.3806503 \times 10^{-23} \text{ J/K}$), T is the temperature of the p-n junction, q is the electron charge ($1.60217646 \times 10^{-19}$) and n ($1 \leq n \leq 1.5$) is the cell ideality factor.

The output of the PV array is directly coupled to the DC/DC boost converter, which leads to track the maximum power point or

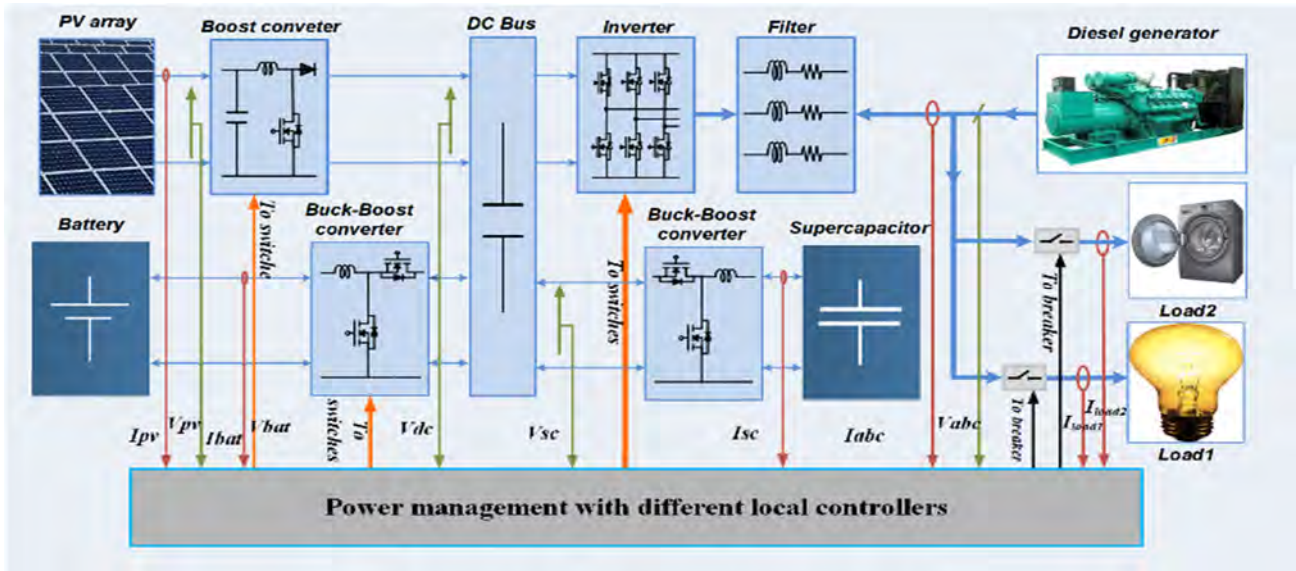


Figure 1. Block diagram of the proposed PV system

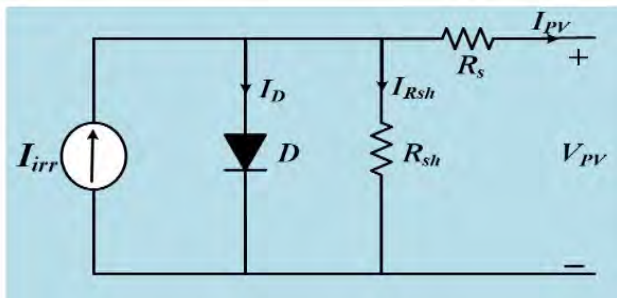


Figure 2. Block diagram of the proposed PV system

the intermediate one depends on the loads and the battery needs. Due to its simplicity of implementation and its good performance, the Perturb and Observe (P&O) algorithm has been applied for harvesting the maximum power. While, a modified P&O was used to track the intermediate power point (IPP). The limited power mode will be applied when the battery is fully charged and the extracted power is greater than the load needs.

4. HYBRID STORAGE SYSTEM TOPOLOGY AND CONTROL

The hybrid storage system (Battery /Supercapacitor) has been chosen for its numerous valuable benefits. It allows to extend the battery's useful life and reduce its size on the one hand. On the other hand, the supercapacitor will respond very quickly to the short-time peak current demand and the battery will deliver the smooth current. Both the storage devices, battery and

supercapacitor, are linked to the DC bus via bidirectional Buck-Boost converter as was shown in Figure 3(a). Which will be used to monitor the stored or the delivered power.

The stored or the delivered power reference P_{str_ref} is given by the power management controller, then it passes through a low pass filter for obtaining the battery and the supercapacitor power references (P_{bat_ref} , P_{sc_ref}) as depicts in Figure 3(b). Figure 3(c) shows a simulation results of hybrid storage system, where the given power reference is P_{str_ref} . The total storage output power is P_{str} , while P_{bat} and P_{sc} represents the output power of the battery and the supercapacitor respectively.

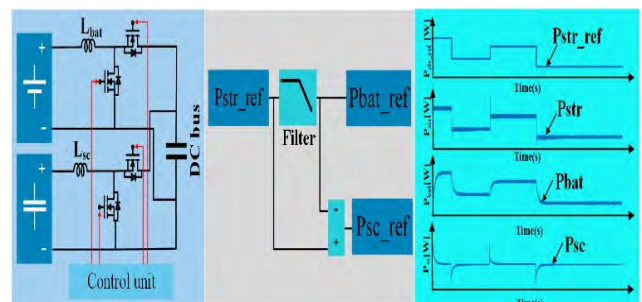


Figure 3. Topology and control of hybrid storage system (a) parallel topology (b) power references (c) stored and delivered power [10]

In addition to its principal role of power storage, the battery has been used also to regulate the DC bus voltage to be maintained at constant value. To do so, the energy management algorithm determines the

power battery reference, taking into account the power of the DC bus. While, a PI controller is used to control the battery current, which is obtained by dividing the power battery reference by its own output voltage. Figure 4 shows the voltage regulation principle, starting by the calculation of the battery current reference I_{bat_ref} till obtaining the switches' (T1, T2) PWM signals.

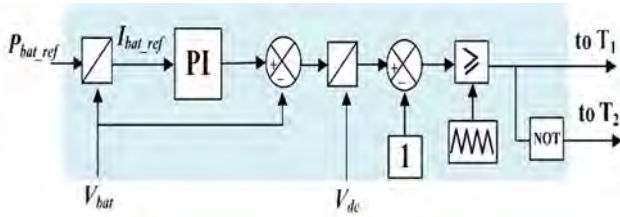


Figure 4. Battery diagram control

5. DIESEL GENERATOR MODELING AND CONTROL

Even though the diesel generator uses a diesel fuel, it is considered as the appropriate emergency power generator owing to the diesel is the cheapest fuel than any other fluids, also, it has a large output range power, from some kW to few MW. Thus, it has been combined with the PV generator and the storage system to give an interruptible renewable power system.

The diesel generator consists of a diesel turbine with a speed regulator coupled to a synchronous generator which has a voltage regulator. It is designed to operate between 80 to 100% of its rating [11].

5.1. Diesel engine model

A simplified model of the diesel engine can be obtained by the identification of static fuel consumption-torque characteristic with a delay time, as presented in Figure 5.

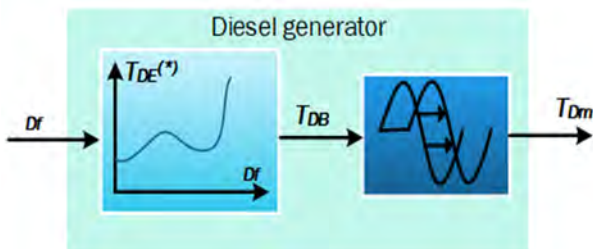


Figure 5. Simplified model of a diesel engine

The diesel engine can be reduced to a system of a first order characterized by a static gain and a time constant. the equation (2) represents the dynamics of the mechanical torque T_{Dm} [12]:

$$T_{Dm}(s) = \frac{K_{Dm}}{1 + sT_{D1}} z(s) e^{-sT_{D2}} \quad (2)$$

Where s denotes the Laplace operator, $z(s)$ is the fuel consumption index, T_{D1} is a time constant expressing the reaction speed limit of the turbine, and the time constant T_{D2} expresses the time for torque to change.

5.2. Speed regulation of the engine

By neglecting the delays due to the measurement and the actuator compared to the time constants T_{D1} and T_{D2} . The rotation speed of the engine ω_{Dm} is regulated by a simple PI regulator (see Figure 6), where the reference speed is the pulsation of the voltages produced by the generator $\omega_{Dm_ref} = 2\pi f$ ($f = 50\text{Hz}$).

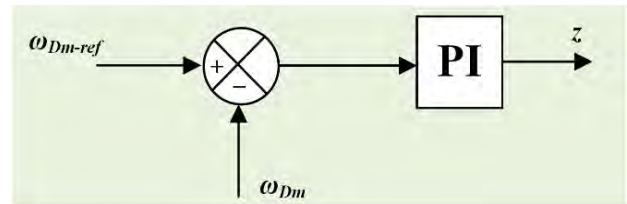


Figure 6. Engine's speed regulation

5.3. Synchronous machine modelling

In this work, the synchronous machine is supposed to be modeled with two dampers, one damper winding for the d-axis and the other for the q-axis. The voltage equations can be written as follows [13]:

$$\begin{cases} V_{abc} = -r_s I_{abc} + \frac{d}{dt} \Psi_{abc} \\ V_f = r_f i_f + \frac{d}{dt} \Phi_f \\ 0 = r_D i_D + \frac{d}{dt} \Phi_D \\ 0 = r_Q i_Q + \frac{d}{dt} \Phi_Q \end{cases} \quad (3)$$

Where:

- V_{abc} , I_{abc} and Ψ_{abc} are the output voltage, the armature current and the stator total flux respectively.

- r_s , r_f , r_D and r_Q are the resistances of the stator, and the dampers respectively.

- i_f , i_D and i_Q are the currents of main field and the two axes dampers respectively.

- Φ_f , Φ_D and Φ_Q are the main total flux and the direct and quadrature axes dampers total flux, while V_f is main field excitation voltage.

5.4. Voltage regulation

The rotor of the synchronous generator is excited by the excitation machine mounted in the rotor itself. The principle of the output voltage regulation is clearly shown in Figure 7. The stator of the excitation machine is supplied by the V_r voltage given by the voltage regulator block.

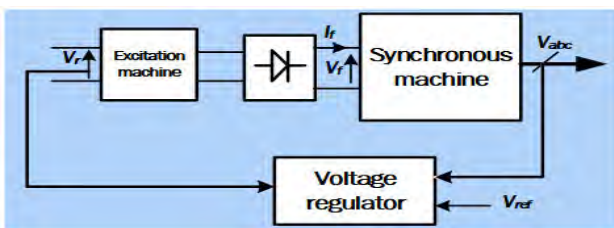


Figure 7. Principle of voltage regulation

6. WHOLE-SYSTEM ENERGY MANAGEMENT

The aim of the energy management strategies is to ensure the supply continuity and to reduce the cost of the hybrid energy production systems. Therefore, the main goal of proposed energy management algorithm (EMA) is to guarantee the continuous load supply despite the solar irradiance fluctuations and to use the DG in the most critical cases only. For this reason, we adopted the prioritized load method, which rely on giving the priorities to the loads, then, when the battery SOC decreases to a certain level previously defined, only the load with the highest priority kept feeding from the battery. Accordingly, the working principle of the EMA depends mainly on the monitoring of the battery SOC to perform the following tasks:

- 1) Protects the battery against the deep discharging and the overcharging, which would extend its useful life.
- 2) Determines the battery used mode, charging or the discharging mode.
- 3) Decided the PV generator working mode, the maximum power or the limited power mode.
- 4) Kept the DC bus voltage at a constant value despite the system perturbations.

- 5) Determines when to switch to the DG and when to return back to the PV system.

From the above discussion, it can be concluded that there are two control levels, the low level which is related to the control of the units of the system, where each unit has its own control algorithm, the operating mode and/or the power reference of the system units are obtained from the higher level mode (power management algorithm). Figure 8 describes how the two levels interact with each other.

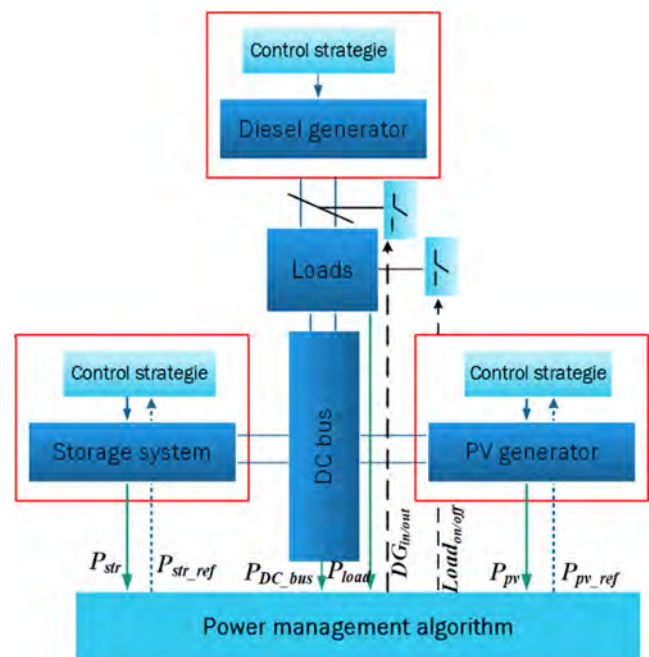


Figure 8. Two control levels interaction

7. SIMULATION RESULTS AND DISCUSSION

The proposed system has been simulated in the MATLAB/Simulink software environment. We have chosen to simulate the system for 24s, which emulate the 24 hours of the day. By doing so, we have been able to test the system under all the possible circumstances. Figure 9 depicts the exemplary day irradiation, where the solar irradiation reaches its maximum in the midday, In the following, the results that were obtained by using this profile will be discussed according to the time intervals that are related to the battery SOC.

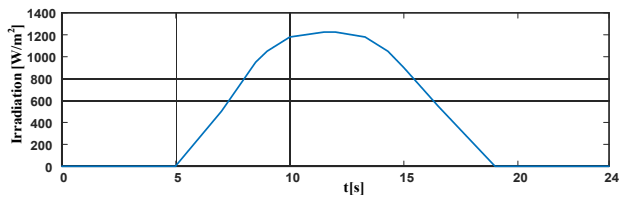


Figure 9. Exemplary day irradiation

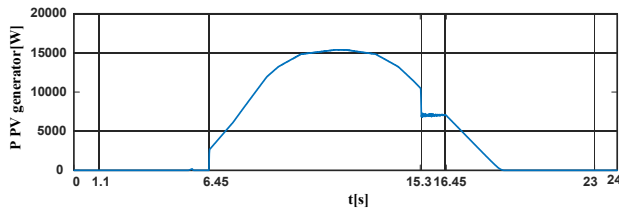


Figure 10. PV generator power

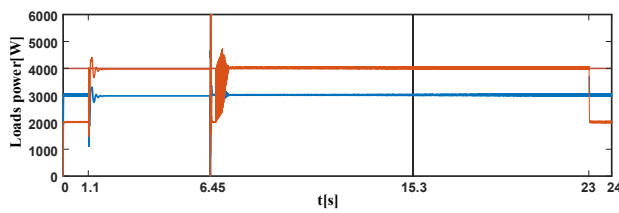


Figure 11. Power consumed by the loads

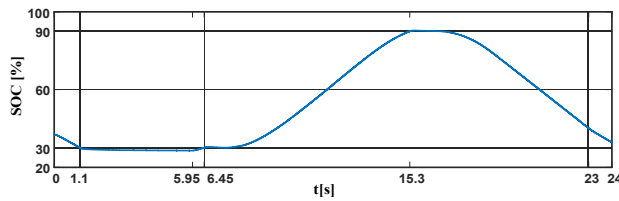


Figure 12. Battery SOC

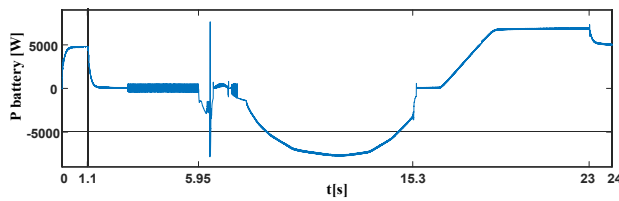


Figure 13. Battery power

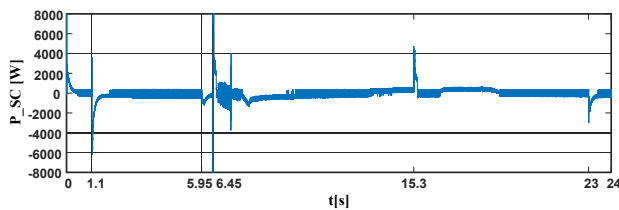


Figure 14. Supercapacitor power

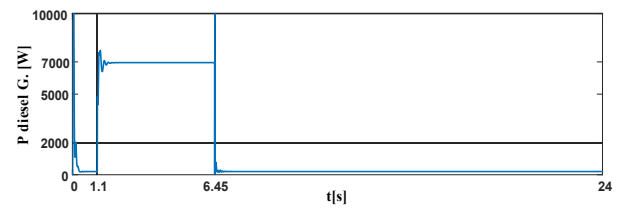


Figure 15. Diesel generator power

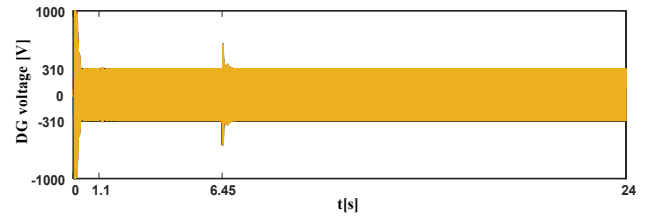


Figure 16. Diesel generator voltage

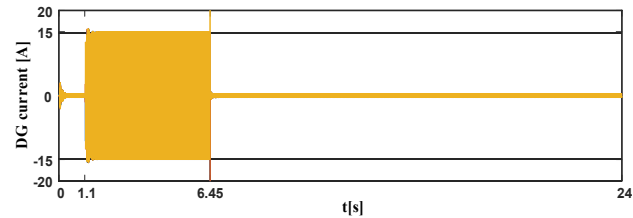


Figure 17. Diesel generator current

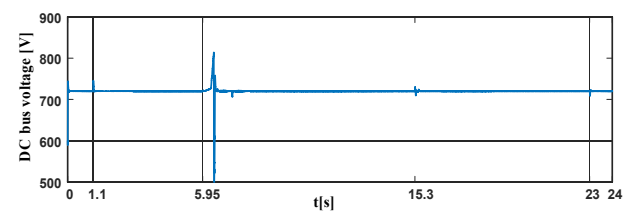


Figure 18. DC bus voltage

From 0s to 1.1s: In this period, it is supposed to be a night time, the PV generator does not generate any power. The SOC is lower than 45%, the supervision algorithm has switch off the lower priority loads, so only the priority loads are powered by the storage system (See Figure 10, 13).

From 1.1s to 6.45s: The SOC is lower than 30%, a level that has been chosen to switch to the diesel generator, then, during this interval, the DG fed both types of loads (with higher and lower priority), its delivered power, their output voltage and current are represented by Figures 15, 16 and 17 respectively.

From 6.45s to 15.3s: During this interval, the PV generator (PVG) has been worked in the MPPT mode, once its power became

higher than the power of the priority load and the SOC exceeded 30%, the loads became fed mainly by the PVG, which was in the beginning slightly helped by the battery. Once the power of the PVG became higher than those consumed by the loads, the battery started charging till 90%, then, more than this level, the supervision algorithm stopped its charging to be protected against overcharging, while the PV system switched to the limited power mode.

From 15.3s to 16.45s: In this interval, the PVG power is greater than the loads demand and the battery has stopped charging, for these reasons, the PVG has switched to the power limitation mode and starts generating the loads consumed power only (See Figures 10, 12-13).

From 16.45s to 23s: In this period, the PVG has returned back to the MPPT mode, but its power remains lower than the power demand, thus, the battery has delivered the lack of power. When the PVG becomes zero, so the loads are fully powered by the storage system (See Figures 10, 12,13).

From 23s to 24s: We can see that when the SOC reached 45%, only the prioritized loads have been powered by the battery once more (See Figures 11,13).

Figure 14 shows how supercapacitor responded to the short-time peak current demand, while the battery delivered the smooth current (see Figure 13). The Figure 18 depicts the DC bus voltage; it can be seen that it has been kept constant despite the different perturbations in the system

8. CONCLUSION

In this study, a low cost hybrid PV-Battery/Supercapacitor Diesel Generator system for standalone applications has been presented. Firstly, its components have been modeled and controlled, the PVG was able to work in the MPPT or in the limitation mode, while the frequency and the amplitude of the output voltage of DG were controlled through the speed of the diesel turbine and the excitation voltage of the synchronous machine respectively. Secondly, a new power

management algorithm has been developed to manage the power flow inside the system. Finally, the whole system has been simulated in the SimPowerSystems environment, the obtained results have confirmed the high efficiency of the proposed management algorithm, which was able to supply the loads according to their priority level and protecting the battery against overcharging and deep-discharging, as well as, resort to the diesel generator at the appropriate time. The results showed also a good complementarity between the supercapacitor and the battery.

REFERENCES

- [1] M. Z. Rahman, M. N. Sajib, M. M. S. H. Rifat, M. Hossam-E-Haider, and M. A. A. Khan, "Forecasting the long term energy demand of Bangladesh using SPSS from 2011-2040," *2016 3rd Int. Conf. Electr. Eng. Inf. Commun. Technol. iCEEiCT 2016*, 2017.
- [2] Z. Bouzid, N. Ghellai, and T. Mezghiche, "Overview of Solar Potential, State of the Art and Future of Photovoltaic Installations in Algeria," *Int. J. Renew. Energy Res.*, vol. 5, no. 2, pp. 427–434, 2015.
- [3] K. Algeria, *Guide to investing in algeria*. 2011.
- [4] M. A. M. Ramli, H. R. E. H. Bouchekara, and A. S. Alghamdi, "Optimal sizing of PV/wind/diesel hybrid microgrid system using multi-objective self-adaptive differential evolution algorithm," *Renew. Energy*, vol. 121, pp. 400–411, 2018.
- [5] A. C. Duman and Ö. Güler, "Techno-economic analysis of off-grid PV/wind/fuel cell hybrid system combinations with a comparison of regularly and seasonally occupied households," *Sustain. Cities Soc.*, vol. 42, pp. 107–126, 2018.
- [6] C. Bastholm and F. Fiedler, "Techno-economic study of the impact of blackouts on the viability of connecting an off-grid PV-diesel hybrid system in Tanzania to the national power grid," *Energy Convers. Manag.*, vol. 171, no. March, pp. 647–658, 2018.
- [7] H. A. Kazem, A. Mohammed, J. Mahdy, and A. Alwaeli, "Techno-economic Evaluation of a Hybrid PV / Diesel Water Pumping System for Different Pumping Heads," *Int. J. Eng. Sci. Emerg. Technol.*, vol. 8, no. July, 2016.
- [8] L. M. Halabi, S. Mekhilef, L. Olatomiwa, and J. Hazelton, "Performance analysis of hybrid PV / diesel / battery system using HOMER: A case study Sabah, Malaysia," *Energy Convers. Manag.*, vol. 144, pp. 322–339, 2017.

- [9] A. Guichi, A. Talha, E. M. Berkouk, S. Mekhilef, and S. Gassab, "A new method for intermediate power point tracking for PV generator under partially shaded conditions in hybrid system," *Sol. Energy*, vol. 170, no. February, pp. 974–987, 2018.
- [10] A. Guichi, A. Talha, E. Berkouk, and N. Sabeur, "Control and energy management of grid-connected pv system with battery-supercapacitor hybrid energy storage," in *IOP Conference Series: Earth and Environmental Science*, 2018, vol. 164, no. 1.
- [11] K. Kusakana and H. J. Vermaak, "Hybrid diesel generator/renewable energy system performance modeling," *Renew. Energy*, vol. 67, pp. 97–102, 2014.
- [12] Tommy Andy Tameghe Theubou, "Modélisation et simulation d'un système de jumelage éolien-diesel alimentant une charge locale," Master thesis, University of Quebec, 2012.
- [13] A. Barakat, S. Tnani, G. Champenois, and E. Mouni, "Analysis of synchronous machine modeling for simulation and industrial applications," *Simul. Model. Pract. Theory*, vol. 18, no. 9, pp. 1382–1396, 2010.

Robust Dynamic Surface Control of Interior Permanent Magnet Synchronous Motors

Salah Nadji¹ and Samira Benaicha²

¹ Electrical Engineering Department university of Setif 1, Setif, Algeria, Email: nadji-salah@univ-setif.dz.

² Engineering Department LSPE laboratory, university of Setif 1, Batna, Algeria, Email: samira_benaicha@yahoo.fr

ABSTRACT

Robust dynamic surface control method of interior permanent magnet synchronous motor (IPMSM) was presented in this paper. The influence of uncertainties such as parameter variations, load disturbances and friction, on the performance of IPMSM was considered. This control method is adapted via the estimation of the unknown load torque and friction effects. A linear extended state observer is devised for this purpose, thus ensuring high closed-loop performance of the motor trajectory tracking task. The concept of virtual command was introduced. There is a weakness in Backstepping method that is a complexity of control law caused by achieving the derivation of the virtual control. Dynamic surface control method solved this problem by calculating the derivative of the virtual control using the first-order low-pass filter. The stability analysis of the controller of IPMSM was achieved by Lyapunov function. Simulation results show that the influence on system performance of uncertainties can be effectively restrained.

Key Words: Backstepping, Dynamic surface control (DSC), Interior permanent magnet synchronous motor (IPMSM), Linear extended state observer (LESO), Lyapunov theorem.

1. NOMENCLATURE

i_d Stator's d-axis current.
 i_q Stator's q-axis current.

v_d Stator's d-axis voltage.
 v_q Stator's q-axis voltage.
 L_d d-axis stator inductance.
 L_q q-axis stator inductance.
 ω Motor speed.
 θ Rotor angular position.
 p Number of pole pairs.
 R Stator resistance.
 ϕ_f Permanent magnet flux.
 J Moment of inertia.
 F Viscous friction coefficient.
 T_L Load torque.
 τ_L Unknown time-varying load torque.

2. INTRODUCTION

Interior permanent magnet synchronous motor (IPMSM) has been attracting more and more attention in high performance electric drive applications since it has certain superiorities such as, high efficiency, high power factor, superior power density, low maintenance cost, large torque to inertia ratio and long life over other kinds of motors such as DC motors and induction motors [1], [2]. However, IPMSM drive systems have the nonlinear dynamics containing parameter uncertainties and unknown external disturbances. In order to meet high performance requirements of IPMSM industrial drive applications, robust or adaptive or other control schemes dealing with parameter uncertainties and unknown

external disturbances have widely been studied thus far [3]-[5].

The Backstepping control is popular in nonlinear system design since the derived system control law and parameters adaptive law are able to make controlled system be global stable and robust. The Backstepping control principle is to simplify controlled system state space to many reduced order subsystems by designing virtual control function and actual control law can be derived through selecting appropriate Lyapunov candidate function. Accordingly, Backstepping is a useful design method for nonlinear system with uncertainties [6], [7]. However, there is a drawback in conventional Backstepping control method called the problem of “explosion of terms” caused by the repeated differentiations of virtual input. To overcome this issue, a dynamic surface control (DSC) method was proposed by introducing a first order filtering of the virtual input at each step of the conventional Backstepping approach [8].

The research on the DSC method has advanced significantly since the late 1990s [9]. DSC is an improved Backstepping control method, whose design process is executed in a step-by-step manner. At each step of design, a feedback controller is designed to guarantee input to-state practical stability of the corresponding subsystem. The primary advantage of DSC is that it can circumvent the problem of “explosion of terms” inherent in the Backstepping design procedure, by introducing a first-order low-pass filter of the synthetic input at each step of the traditional Backstepping approach [10], [11].

This paper proposes a robust angular position tracking controller based on the Backstepping technique complemented with an estimation scheme of the lumped effects related to unknown load torque disturbances, friction forces, and unmodeled dynamics. The approach uses a linear extended state observer (LESO). The information obtained from the LESO observer is adapted to the robust Backstepping tracking controller. This entitles estimating the adverse effects, caused by both internal uncertainties and external disturbances.

The paper is organized as follows: in Section 3, the dynamic model of IPMSM is introduced with some important system properties. This section also introduces the

design of the LESO for the unknown disturbances. In Section 4, the control design law is based on DSC control theory with angular velocity measurement for IPMSM systems is developed. The simulation results are illustrated in Section 5, and some concluding remarks are given in section 6.

3. MATHEMATICAL MODEL

The dynamic model of IPMSM can be described in the well-known d-q frame through the Park transformation [12] as follows:

$$\begin{aligned} \frac{di_d}{dt} &= -\frac{R}{L_d}i_d + p\frac{L_q}{L_d}\omega i_q + \frac{1}{L_d}v_d \\ \frac{di_q}{dt} &= -\frac{R}{L_q}i_q - p\frac{L_d}{L_q}\omega i_d - p\frac{1}{L_q}\phi_f\omega + \frac{1}{L_q}v_q \\ \frac{d\omega}{dt} &= \frac{p}{J}(L_d - L_q)i_d i_q + \frac{P}{J}\phi_f i_q - \frac{1}{J}\underbrace{(T_L + F\omega)}_{\tau_L} \\ \frac{d\theta}{dt} &= \omega \end{aligned} \quad (1)$$

The function τ_L is the unknown time-varying load torque, which includes a viscous friction torque component: $F\omega$.

In Section 3.1, we propose a LESO geared to accurately estimate the time varying load torque input along with the state dependent viscous friction terms.

3.1. LESO for the Unknown Load Torque Estimation

In this section, a LESO is proposed to estimate the load torque signal and the associated friction terms. For this design, the measured quadrature current $u_1 = i_q$ is considered as an input, while the angular velocity is considered as the measured output $y_1 = \omega$. The nominal value of the parameter J is assumed to be known. The estimated value of the load torque parameter is considered to be time varying and unknown, but uniformly absolutely bounded so that existence of solutions for the estimation error dynamics are guaranteed to exist [13]. For the design of the load torque estimator, we consider a natural ultralocal piecewise linear internal model corresponding to a second-order dynamic model of the load torque. The corresponding LESO observer is obtained

within a reduced order observer philosophy via the artificial injection of exact differentials [14]. Therefore, we consider $\tau_1 = \hat{\tau}_L$ and $\tau_2 = \frac{d}{dt} \hat{\tau}_L$, as the observer state variables. Consider then the following LESO load torque estimator:

$$\frac{d\tau_1}{dt} = \frac{d\hat{\tau}_L}{dt} = \tau_2 + k_1(\tau_L - \tau_1) \quad (2)$$

$$\frac{d\tau_2}{dt} = \frac{d^2\hat{\tau}_L}{dt^2} = k_0(\tau_L - \tau_1) \quad (3)$$

Substituting the indirect measurement of the load torque τ_L given by (1) into (2) and (3), we have

$$\dot{\tau}_1 = \tau_2 + k_1 \left(\frac{p}{J}(L_d - L_q)i_d i_q + \frac{P}{J}\phi_f i_q - J\dot{y}_1 - \tau_1 \right)$$

$$\dot{\tau}_2 = k_0 \left(\frac{p}{J}(L_d - L_q)i_d i_q + \frac{P}{J}\phi_f i_q - J\dot{y}_1 - \tau_1 \right)$$

Setting $\psi_1 = \tau_1 + k_1 J y_1$ and $\psi_2 = \tau_2 + k_0 J y_1$, we have

$$\tau_1 = \hat{\tau}_L = \psi_1 - k_1 J y_1$$

$$\frac{d\psi_1}{dt} = -k_1 \psi_1 + \psi_2 + (k_1^2 J - k_0 J) y_1$$

$$+ k_1 \left(\frac{p}{J}(L_d - L_q)i_d i_q + \frac{P}{J}\phi_f i_q \right)$$

$$\tau_2 = \frac{d}{dt} \hat{\tau}_L = \psi_2 - k_0 J y_1$$

$$\frac{d\psi_2}{dt} = -k_0 \psi_1 + k_0 k_1 J y_1 + k_0 \left(\frac{p}{J}(L_d - L_q)i_d i_q + \frac{P}{J}\phi_f i_q \right) \quad (4)$$

The estimated error evolves according to

$$\frac{d^2}{dt^2} e_\tau + k_1 \frac{d}{dt} e_\tau + k_0 e_\tau = \frac{d^2}{dt^2} \tau_L \quad (5)$$

where $e_\tau = \tau_L - \hat{\tau}_L$. Since $\ddot{\tau}_L(t)$ is assumed to be uniformly absolutely bounded, then there exist design coefficients k_1 and k_0 for the observer, such that the estimation errors are uniformly asymptotically convergent to a small neighborhood of the origin of the phase space of the estimation error dynamics. The faster the estimation error dynamics, the smaller the convergence neighborhood of the

origin. The value of the gain parameters is customarily chosen via a term-by-term comparison of (5) with those of a desired, nominal, dominating, second-degree characteristic polynomial

$$p_{d-obs}(s) = (s^2 + 2\xi\omega_n s + \omega_n^2). \quad \text{Therefore,}$$

$$k_1 = 2\xi\omega_n, \quad k_0 = \omega_n^2.$$

4. ROBUST DYNAMIC SURFACE CONTROL OF IPMSM

In this section, we will present a robust DSC for IPMSM based on Backstepping. The control technique is a non-linear Backstepping control having properties of strength. The pursuit of speed takes place with a high yield by the control voltage v_q as long as the current i_d is kept equal to zero. The calculation of Lyapunov function is performed in a recursive way, it is based on the previous system state. A new Control Lyapunov Function (CLF) is constructed by the increase of CLF of the previous step, this procedure calculates allow us to ensure overall system stability. The corresponding block diagram of the proposed scheme of speed tracking design is shown in Figure.1.

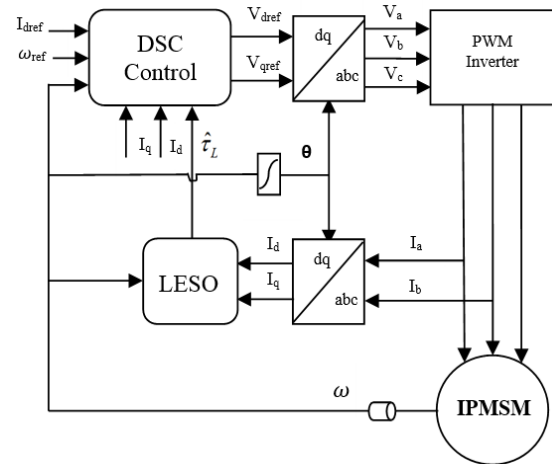


Figure.1: Proposed scheme of speed tracking design.

Step 1: For the reference signal θ_{ref} , we define the tracking error variable as $z_1 = \theta - \theta_{ref}$. The error dynamic system is computed by $\dot{z}_1 = \omega - \omega_{ref}$.

Choose the Lyapunov function as $V_1 = \frac{1}{2} z_1^2$, then the time derivative of V_1 is given by

$$\dot{V}_1 = z_1 \dot{z}_1 = z_1 (\omega - \omega_{ref}) \quad (6)$$

Construct the virtual control law α_1 as

$$\alpha_1 = -k_1 z_1 + \omega_{ref} \quad (7)$$

with $k_1 > 0$ being a positive design control gain. Next, introduce a new state variable α_{1d} . Let α_1 pass through a first-order filter with time constant ε_1 and $\alpha_{1d}(0) = \alpha_1(0)$. The purpose of this filter is to generate α_{1d} and its derivative $\dot{\alpha}_{1d}$ such that $|\alpha_{1d} - \alpha_1|$ is smaller than a given level

$$\varepsilon_1 \dot{\alpha}_{1d} + \alpha_{1d} = \alpha_1, \quad \alpha_{1d}(0) = \alpha_1(0). \quad (8)$$

Define $z_2 = \omega - \alpha_{1d}$.

Step 2: Differentiating z_2 obtains

$$\dot{z}_2 = \frac{p}{J} (L_d - L_q) i_d i_q + \frac{p}{J} \phi_f i_q - \frac{1}{J} \tau_L - \dot{\alpha}_{1d} \quad (9)$$

Now, choose the Lyapunov function candidate as $V_2 = V_1 + \frac{1}{2} z_2^2$. Obviously, time derivative of V_2 can be expressed as

$$\dot{V}_2 = -k_1 z_1^2 + z_2 \left[\frac{p \left[(L_d - L_q) i_d + \phi_f \right]}{J} i_q - \frac{1}{J} \tau_L - \dot{\alpha}_{1d} \right] \quad (10)$$

Then the virtual control α_2 is constructed as

$$\alpha_2 = \frac{J}{p \left[(L_d - L_q) i_d + \phi_f \right]} \left[\frac{1}{J} \tau_L + \dot{\alpha}_{1d} - k_2 z_2 \right] \quad (11)$$

With $k_2 > 0$ being a positive design control gain. Then define a new state variable α_{2d} . Let α_2 pass through a first-order filter with time constant ε_2 to obtain α_{2d} as $\varepsilon_2 \dot{\alpha}_{2d} + \alpha_{2d} = \alpha_2$, $\alpha_{2d}(0) = \alpha_2(0)$. (12) and define $z_3 = i_q - \alpha_{2d}$

Step 3: Differentiating z_3 results in the following equation:

$$\dot{z}_3 = \dot{i}_q - \dot{\alpha}_{2d} = -\frac{R}{L_q} i_q - p \frac{L_d}{L_q} \omega i_d - p \frac{1}{L_q} \phi_f \omega + \frac{1}{L_q} v_q - \dot{\alpha}_{2d}$$

Choose the following Lyapunov function candidate as $V_3 = V_2 + \frac{1}{2} z_3^2$. Furthermore, differentiating V_3 yields

$$\dot{V}_3 = -k_1 z_1^2 - k_2 z_2^2 + z_3 \left[-\frac{R}{L_q} i_q - p \frac{L_d}{L_q} \omega i_d - p \frac{1}{L_q} \phi_f \omega + \frac{1}{L_q} v_q - \dot{\alpha}_{2d} \right] \quad (13)$$

Now, the control input v_q is designed as

$$v_q = L_q \left[\frac{R}{L_q} i_q + p \frac{L_d}{L_q} \omega i_d + p \frac{1}{L_q} \phi_f \omega + \dot{\alpha}_{2d} - k_3 z_3 \right] \quad (14)$$

with $k_3 > 0$ being a design control gain. it is obtained that:

$$\dot{V}_3 = -k_1 z_1^2 - k_2 z_2^2 - k_3 z_3^2 \quad (15)$$

Step 4: At this step, we will construct the control law v_d . To eliminate the reluctance torque, the current reference is fixed to zero, $i_{dref} = 0$, we obtain a similar operation to that of a DC machine separately excited. Define $z_4 = i_d$, differentiating z_4 obtains

$$\dot{z}_4 = -\frac{R}{L_d} i_d + p \frac{L_q}{L_d} \omega i_q + \frac{1}{L_d} v_d \quad (16)$$

Defining the following candidate Lyapunov function as $V_4 = V_3 + \frac{1}{2} z_4^2$. The time derivative is computed as:

$$\dot{V}_4 = -k_1 z_1^2 - k_2 z_2^2 - k_3 z_3^2 + z_4 \left[-\frac{R}{L_d} i_d + p \frac{L_q}{L_d} \omega i_q + \frac{1}{L_d} v_d \right] \quad (17)$$

We design v_d as

$$v_d = L_d \left[\frac{R}{L_d} i_d - p \frac{L_q}{L_d} \omega i_q - k_4 z_4 \right] \quad (18)$$

where $k_4 > 0$ is a positive design control gain, it is obtained that:

$$\dot{V}_4 = -k_1 z_1^2 - k_2 z_2^2 - k_3 z_3^2 - k_4 z_4^2 \quad (19)$$

5. SIMULATION RESULTS

To illustrate the mathematical analysis and to investigate the performance of the proposed robust dynamic surface control of IPMSM, simulations are carried out following the overall block diagram of the control shown in Figure.1. Table 1 gives parameters of the IPMSM which is used in the simulation tests. The simulation has been carried out using Matlab/ Simulink software.

Table.1 The parameters of the IPMSM

ω (rd/s)	R (Ω)	L_d (mH)	L_q (mH)	ϕ_f (wb)	p	J (kg.m ²)	F (N.m/rd/s)
314	6.2	2.502	4.01	0.304	3	0.0036	0.0011

The machine started on the vacuum, then a load torque is applied of 5 N.m at time 0.4s,

and then eliminated where the moment was 0.8s. At time $t = 1.2\text{s}$, the direction of rotation is reversed at 100 rad/s to -100 rad/s. In Figure. 2, it is noted that according to the shape the motor speed follows perfectly its reference which is achieved very rapidly, with a very fast response. The effect of the load perturbation is rapidly disappearing and the electromagnetic torque stabilizes the load torque value.

Figure. 3. (a) shows the estimated load torque. The torque estimation error is detailed by Figure. 3. (b) it is clear that the observer has good performances for this estimation.

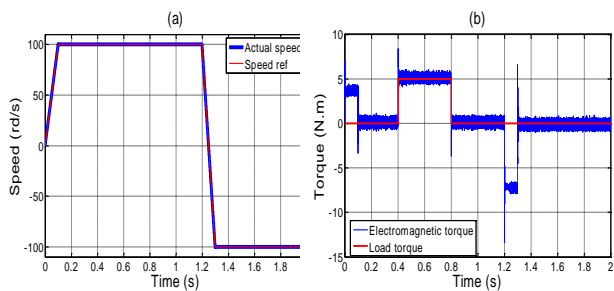


Figure.2: Simulation results: (a) speed rotation, (b) electromagnetic torque and actual load torque.

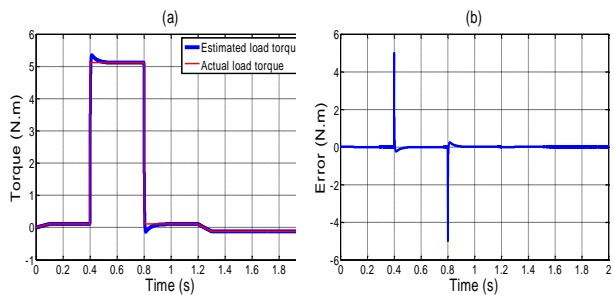


Figure.3: Simulation results: (a) actual load torque and estimated load torque, (b) load torque estimation error.

In Figure. 4. (a) we can note that the response of the two current components i_d and i_q show good decoupling introduced by IPMSM control (The direct axis current i_d is always forced to zero in order to orient all the linkage flux in the d-axis and achieve maximum torque per ampere), as we can see that the current i_q is the couple image. In Figure. 4. (b), the stator current response of the three-phase interior permanent magnet synchronous motor is shown.

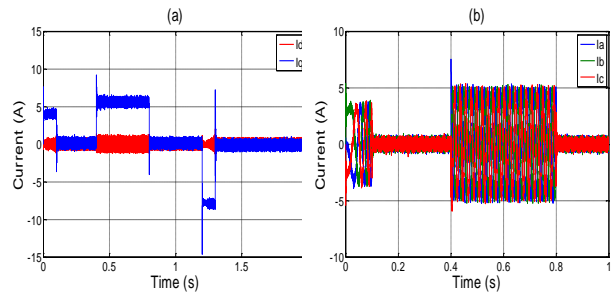


Figure.4: Simulation results: (a) currents i_d and i_q , (b) currents i_a , i_b and i_c

The IPMSM started with a constant acceleration after 0.2s, the speed was maintained to 314 rad/s, while the motor is loaded with a constant torque of 5 N.m at starting. At $t = 1\text{s}$, the speed change form 314 rad/s to 628 rad/s with same constant load torque. Figure. 5. (a) shows the reference and actual speed, we can observe that the actual speed tracks the reference speed very well. By Figure. 5. (b), the electromagnetic torque is given.

The load torque estimation is detailed by Figure. 6. It is clear that the observer has good performance for this estimation. We can see clearly the robustness and the efficiency of the proposed observer in high speed.

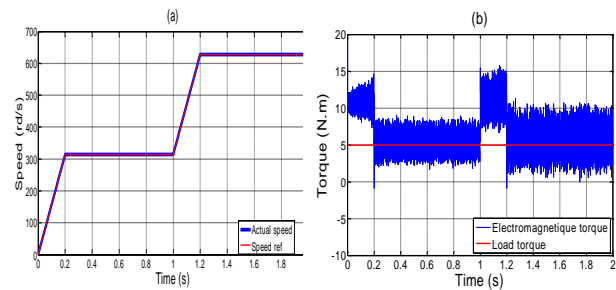


Figure.5: Simulation results: (a) speed rotation, (b) electromagnetic torque and actual load torque.

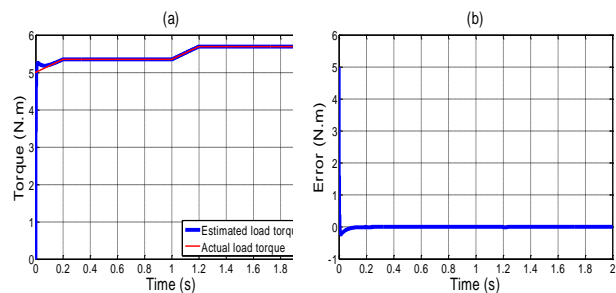


Figure.6: Simulation results: (a) actual load torque and estimated load torque, (b) load torque estimation error.

Figure. 7 shows the speed responses for the backstepping controller for a desired reference signal with constant increments and decrements. Figure. 7. (a) shows the speed tracking responses of Backstepping controller with load torque applied on the IPMSM shaft at starting. In this figure, we note that the motor speed can track the desired reference speed, with very low error, and small overshoot. Figure. 7. (b) shows electromagnetic torque and actual load torque.

Figure. 8. (a) shows the estimated load torque in low speed region. The torque estimation error is detailed by Figure. 8. (b) It can be seen that the proposed observer can estimate the actual load torque accurately.

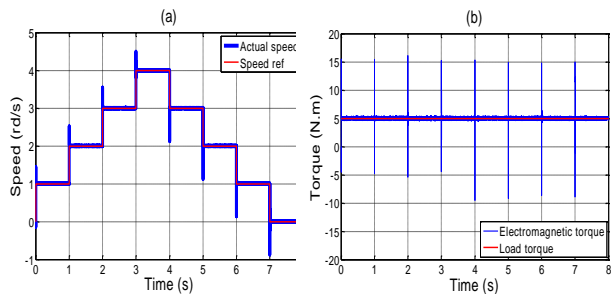


Figure.7: Simulation results: (a) speed rotation, (b) electromagnetic torque and actual load torque.

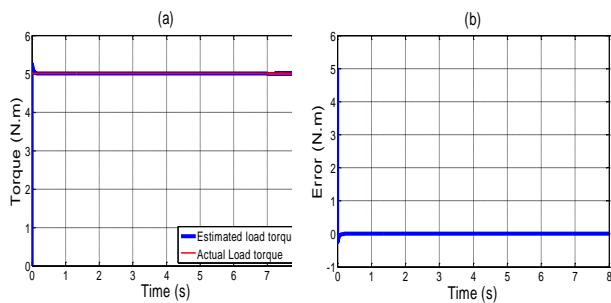


Figure.8: Simulation results: (a) actual load torque and estimated load torque, (b) load torque estimation error.

In Figure. 9, even an error of +50 % on the nominal value of the stator resistance and an error of +30 % on the values of the rotor moment of inertia and viscous friction coefficient it can be seemed that they do not affect the static and dynamic performance of the Backstepping control.

Figure. 10, show the robustness of the observer against parameters variation, it is also shown that the estimated load torque follows the actual load torque with precision.

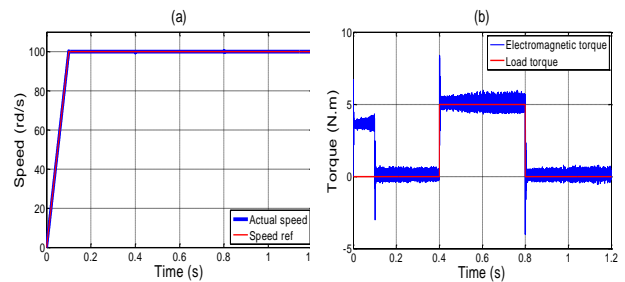


Figure.9: Simulation results: (a) speed rotation, (b) electromagnetic torque and actual load torque.

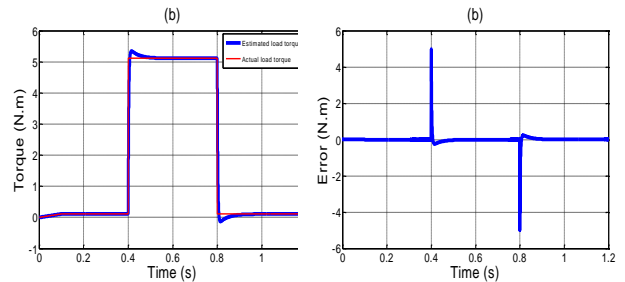


Figure.20: Simulation results: (a) actual load torque and estimated load torque, (b) load torque estimation error.

From the speed tracking simulation result, we can find that the Backstepping controller have good performance.

6. SIMULATION RESULTS

In this paper, we have discussed the design and application of robust dynamic surface control for IPMSM. The controller design is intuitively absorbing and uses first-order low-pass filter to avoid model differentiation, therefore overcoming the problem of “explosion of terms” associated with the traditional Backstepping approach. And then, based on Lyapunov asymptotical stability theory, we have proved that the presented control law can render the closed-loop controlled system asymptotically stabilize at a desired target. Since the feasibility has been considered through the design process, the proposed controller is more applicable to the practical use. Simulation results indicate that the proposed control law is very effective and robust against the uncertainties in system parameters and load disturbances.

ACKNOWLEDGEMENTS

This paper was supported by the Algerian ministry of higher education and scientific research.

REFERENCES

- [1] Qiang. S, Yiting. L and Chao. Jia, "Novel direct torque control method based on asymmetric boundary layer sliding mode control for PMSM," *energies*, vol. 11, 2018.
- [2] Jiang. Q, Liao. M-w and Luo. M-j "Design of permanent magnet synchronous motor speed loop controller based on sliding mode control algorithm." 2018 *IOP Conference Series: Materials Science and Engineering*, 324 012021, 2018.
- [3] Peipei. X, Yongting. D, Zhiqian. W and Hongwen. L, "Speed adaptive sliding mode control with an extended state observer for permanent magnet synchronous motor," *Mathematical Problems in Engineering*, vol. 2018, 13 pages, 2018.
- [4] Mondragon. F. M.; Hernandez-Guzman. V. M., and Resendiz. J. R. "Robust Speed Control of Permanent Magnet Synchronous Motors Using Two-Degrees-of-Freedom Control," *IEEE Transactions on Industrial Electronics*, 2018, 65, 6099-6107.
- [5] Zhanming. Z, Bao. Z and Dapeng. M, "Robust sliding mode control of PMSM based on rapid nonlinear tracking differentiator and disturbance observer," *Sensors*, vol. 18, 2018.
- [6] Jiande. Y, Hui. W, Shoudao. H and Yonghong. L, "Disturbance observer-based Backstepping control of PMSM for the mine traction electric locomotive," *Mathematical Problems in Engineering*, vol. 2018, 2018.
- [7] Rin, G.; Arun, S. M. "Speed control of PMSM using Backstepping method," *International Journal of Engineering Research & Technology*, 2015, 4, 7, 609-612.
- [8] Xiao-Qiang, L.; Dan, W.; Zhu-Mu, F. "Adaptive NN dynamic surface control for a Class of Uncertain non-affine pure-feedback systems with unknown time-delay," *International Journal of Automation and Computing*, 2016, 13, 268-279.
- [9] Swaroop. D.; Hedrick. J. K.; Yip. P. P., and Gerdes. J. C. "Dynamic surface control for a class of nonlinear systems," *IEEE Transactions on Automatic Control*, 2000, 45, 1893-1899.
- [10] Luo. S, "Nonlinear Dynamic Surface Control of Chaos in Permanent Magnet Synchronous Motor Based on the Minimum Weights of RBF Neural Network," *Abstract and Applied Analysis*, vol. 2014, 2014.
- [11] Peng, L.; Jie, C.; Tao, C.; Wang, G. "Adaptive robust dynamic surface control of pure-feedback systems using self-constructing neural networks," *International Journal of Innovative Computing, Information and Control*, 2013, 9, 7, 2839-2860.
- [12] Pillay, P., and Krishnan, R. "Modeling, simulation, and analysis of permanent-magnet motor drives. ii. The brushless dc motor drive," *IEEE Transactions on Industry Applications*, 1989, 25, 274-279.
- [13] Gliklikh. Y. E, "Necessary and sufficient conditions for global-intime existence of solutions of ordinary, stochastic and parabolic differential equations," *Abstr. Appl. Anal.*, vol. 2006, pp. 1-17, 2006.
- [14] Flores, J. L.; Ramirez, H. S., and Cardenas, O. R. "Robust backstepping tracking controller for low-speed PMSM positioning system: design, analysis, and implementation," *IEEE Transactions on Industrial Informatics*, 2015, 11, 1130-1141.

Multipurpose Asymmetric Cascaded Inverter

Khelil ZAOUCHE¹, Abdelaziz TALHA² and El Madjid BERKOUK³

¹Ecole Nationale Supérieure en Informatique, BP 68M - Oued Smar 16270 Algiers, Algeria, k_zaouche@esi.dz

²University of Sciences and Technology Houari Boumediene, BP 32 El-Alia 16111 Bab-Ezzouar, Algiers, Algeria, abtalha@gmail.com

³Polytechnics National School, University of Algiers, Algeria, #10, Hassen Badi Road, El Harrach, BP 182, emberkouk@yahoo.fr

ABSTRACT

This paper presents a photovoltaic grid-connected system based on an Asymmetric Cascaded inverter. A non-linear load is inserted at the point of common coupling.

The purposes of the inverter are as follow: The inverter has to operate the photovoltaic arrays at their maximum powers. All the available photovoltaic power will be extracted and provided to the load. The remaining PV power will be injected to the utility grid. In weak atmospheric conditions, the shortfall will be covered by the grid. The inverter will be set up to produce both active and reactive power. This guaranteed a grid current with a good spectral behaviour and a unity power factor. In order to enhance the system utility factor, a night operating mod is also planned.

Simulations in Matlab/Simulink software are presented to investigate the correctness of the command method.

Key Words: Cascaded Asymmetric H-bridge inverter; harmonics compensation; non-linear load; Photovoltaic.

1. INTRODUCTION

Photovoltaic energy is a promising source of energy with all the qualities required to meet the present and future energy demand. Solar energy is free and abundantly available; this brought a continuous growth in the utilization photovoltaic (PV) for several useful applications.

Because distributed power sources are becoming more and more prevalent, the use

of a multilevel inverter will provide significant advantages due to its fast response and autonomous control. Additionally, multilevel inverter can also control the real and reactive power flow.

Multilevel inverter contains several dc-links which can be used to lessen the effects of modules mismatches in the PV arrays, as well as the shading effect. Cascaded Inverter incorporates several H-bridges with separate dc sources. This requirement makes photovoltaic panels a natural choice for the isolated dc voltage sources needed for the cascade inverter.

In this paper we present an Asymmetric and Cascaded H-bridge (ACHB) inverter feeding a non-linear load. The inverter acts as an interface between a PV arrays and the utility grid.

During the past decade, Cascaded H-bridge topology has been introduced to the photovoltaic field. However most of the presented papers address symmetrically fed inverters [1-8]. This kind of inverter is supposed to operate, most often, under symmetrical conditions. This operating mode occurs when the H-bridge cells transfer an equal amount of power. However, in unequal atmospheric conditions authors in [1-8] reports a dc-link drift problem, which results in a loose of the maximum power point tracking capabilities. An intrinsic instability problem is also reported.

The challenge that comes with the Asymmetric configuration is that the powers handled by the H-bridge cells are intrinsically unequal. This paper presents an efficient solution to deal with this issue.

In [9] we have presented an ACHB PV inverter feeding a non-linear load. In this first approach of our project; the non-linear load is not powered from the grid, at weak atmospheric conditions. Besides, night operations are not allowed. These shortcomings are considered in the present paper.

2. SYSTEM DESCRIPTION AND MODELING

The ACHB PV inverter is shown in Fig.1. The structure is composed of two series connected H-bridges whose dc sides are connected to separate photovoltaic strings. V_{dcj} and I_{pvj} ($j = 1,2$) denote the dc-link voltage and output current of photovoltaic string in the j^{th} H-bridge cell. v_g and i_g denote the grid voltage and current, respectively. C_j is the dc-link capacitor of the j^{th} cell. i_{dcj} is the current entering the j^{th} H-bridge cell. i_s is the inverter output current. i_L and v_L are, respectively, the load current and voltage.

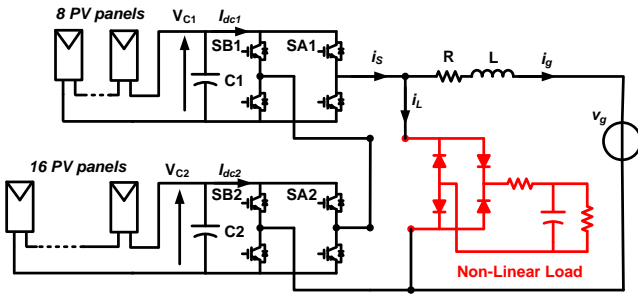


Figure 1: ACHB Photovoltaic Inverter with a non-linear Load

S_{Aj} and S_{Bj} are the switching states of the upper switches of each H-bridges leg.

The system in Fig.1 can be fully modeled by the following equations.

$$\frac{dV_{cj}}{dt} = \frac{1}{C_j} [I_{PV} - (S_{Aj} - S_{Bj})i_s] \quad (1)$$

$$\frac{di_g}{dt} = \frac{1}{L} \left[\sum_{j=1}^2 (S_{Aj} - S_{Bj})V_{cj} - Ri_g - v_g \right] \quad (2)$$

$$i_g = i_s - i_L \quad (3)$$

To describe the electrical behavior of a photovoltaic generator under illumination, a several models were presented in the

literature. One of them is the one diode five parameters model [10].

Considering a photovoltaic string formed by n_s series connected photovoltaic panels; each panel is formed by N_s series connected solar cells. The equivalent electrical circuit of such photovoltaic string may be described by a fictitious components consisting of: photo-generated current source, a single diode, a series parasitic resistance R_s , and a parallel parasitic resistance R_{sh}

R_s and R_{sh} are respectively, the series and the shunt resistances associated to one panel. The mathematical description of this circuit is given by the following equation:

$$I = I_{ph} - I_0 \left[\exp \left(\frac{q \left(\frac{V}{n_s} + I R_s \right)}{N_s n k T} \right) - 1 \right] - \frac{\left(\frac{V}{n_s} + I R_s \right)}{R_{sh}} \quad (4)$$

I stand for the photovoltaic string output current, V stands for the photovoltaic string output voltage, I_{ph} is the photo-generated current, I_0 is the reverse saturation current of the diode, K is the Boltzman constant factor, q is the elementary charge, n is the diode ideality factor. The photo-generated current, I_{ph} , depends on both: the irradiance G , and the temperature T , and is given by:

$$I_{ph} = \frac{G}{G_{STC}} (I_{ph,STC} + \mu_{Isc}(T - T_{STC})) \quad (5)$$

Where $I_{ph,STC}$ is the photo-generated current at the standard test conditions (STC), namely, average solar spectrum at $AM1.5G$, the irradiance is normalized to $1000W/m^2$, and the cell temperature is set to $25^\circ C$.

It is safe to assume that the photo-generated current at standard test conditions, is equals the short circuit current, I_{sc} .

I_{sc} is supplied by the manufacturer.

G_{STC} is the irradiance under standard test condition.

T_{STC} is the cell temperature on the standard test condition.

T is the operating cell temperature

μ_{ISC} is the manufacturer supplied temperature coefficient of short-circuit current.

The diode saturation current, I_0 , is given by:

$$I_0 = I_{0,STC} \left[\frac{T}{T_{STC}} \right]^3 \exp \left(\frac{E_g N_s q}{n k T_{STC}} \left(1 - \frac{T_{STC}}{T} \right) \right) \quad (6)$$

Where $I_{0,STC}$ is the reverse saturation current at standard test conditions. E_g stand for energy band gape.

3. CONTROL STRATEGY

The control system includes an independent Maximum power Point tracker (MPPT) for each PV string, a grid current controller, a dc-link regulators, and, a drift compensation mechanism.

Each independent MPPT algorithm provides the dc-link reference of the corresponding photovoltaic string. The output of the voltage regulator is a DC value corresponding to the magnitude of the inverter output current.

The inverter reference voltage is inferred from the current control loop. This reference voltage is used by the modulation process to generate the ACHB inverter gating signals.

All the regulators in the control loops are tuned to meet the following goals:

1_The inverter has to operate the photovoltaic arrays at their maximum powers. An independent Maximum Power Point Tracking must be achieved.

2_All the available photovoltaic power will be extracted and provided to the load. The remaining PV power will be injected to the utility grid.

3_In weak atmospheric conditions, the shortfall will be covered by the grid.

4_The control strategy is set up to guarantee a grid current with a good spectral behavior and a unity power factor.

5_In night, common photovoltaic systems are disconnected. The System Utilisation Factor (SUF) of such systems is around 30%. In this paper, a night operation mode is planned. The system controls the reactive power. Thus the SUF is enhanced to 100%.

4. RESULTS AND DISCUSSION

To verify the proposed control scheme, the ACHB PV inverter is simulated in three different conditions. First, all PV strings are operated under the same irradiance $S=1000W/m^2$ and temperature $T=25^\circ C$. At $t = 0,5s$ the solar irradiance in the first PV string decreases to $400W/m^2$; and stays the same for the other string. Finally, at $t = 1s$, the irradiance of the first PV string increases to $1000W/m^2$, whereas the irradiance of the second PV string decrease to $400W/m^2$. Fig.2 resumes the changes operated on the irradiance of the two photovoltaic strings.

The two dc-link voltages are shown in Fig.3. At the beginning, the PV strings are operated at the MPP voltage of 173V, and 346V for the first and the second PV string respectively. As the irradiance changes, the first dc-link voltages decrease and track the new MPP voltage 161,9V, while the second PV string is still operated at 346V. At $t = 1s$, changes are made to the irradiance of the two PV strings. Therefore, the first dc-link increases to track the new MPP voltage 173V; when the second dc-link decreases to 323,8V.

The currents of the grid, load, and on the output of the inverter are shown of Figures 4 to 6. Despite the appearance, strongly non-linear, of the load current, the grid current has a perfect sinusoidal shape. The distortion forms are mitigated (compensated) by the inverter. At the third simulation step, the grid current phase is shifted by 180° ; which mean that the grid provides energy to the load, Fig.6.

Fig.7 shows the overall extracted photovoltaic power, plotted together with the load power and the real grid power.

We observe from Fig.7 that the available photovoltaic power is extracted and provided to the load. The remaining PV power will be injected to the utility grid, first and second simulation step.

In the third step, since the PV power is not high enough to satisfy the load demand, the utility grid ensures the supply of the power deficiency. The sign of grid power becomes negative, indicating that the grid provides energy instead of receiving it.

Night operations are also simulated. In this case all the PV strings are disconnected. The system controls the reactive power.

Fig.8 shows the grid current and voltage. The grid current waveform has a sinusoidal shape with power factor close to the unity. The disturbance of the load, at the point of the common coupling, is reduced to the minimum.

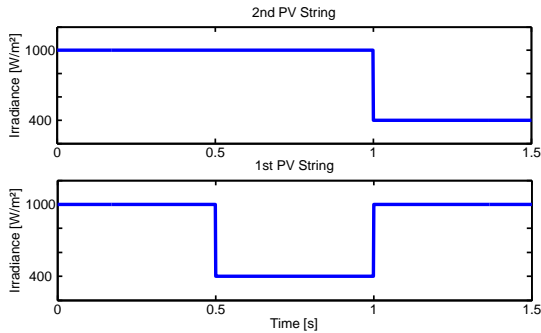


Figure 2: Changes made on the Irradiances

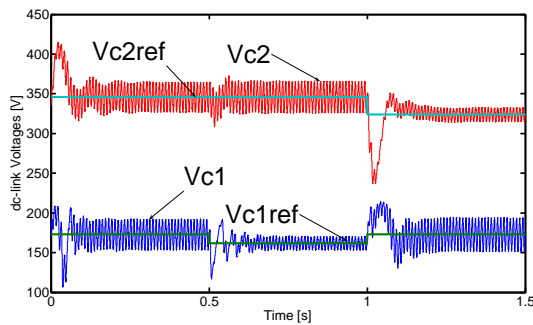


Figure 3: dc-link Voltages

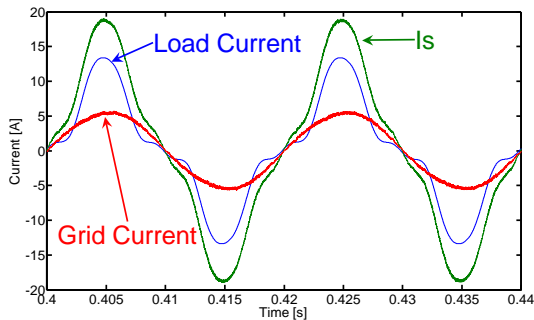


Figure 4 : System Currents behavior at the first simulation step

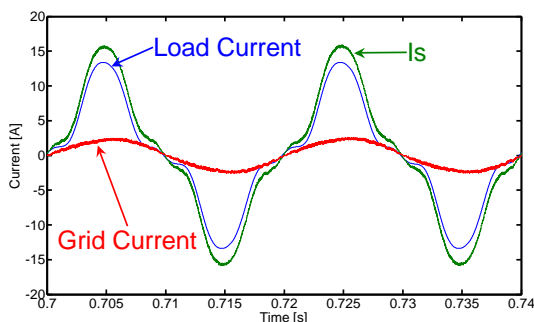


Figure 5 : System Currents behavior at the second simulation step

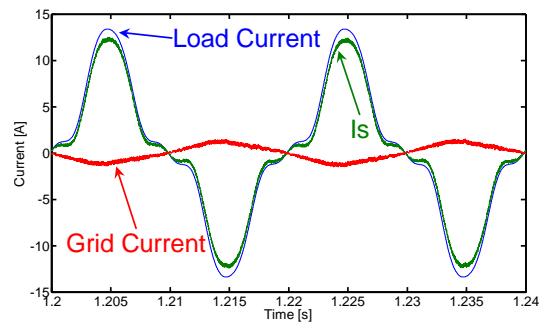


Figure 6 : System Currents behavior at the third simulation step

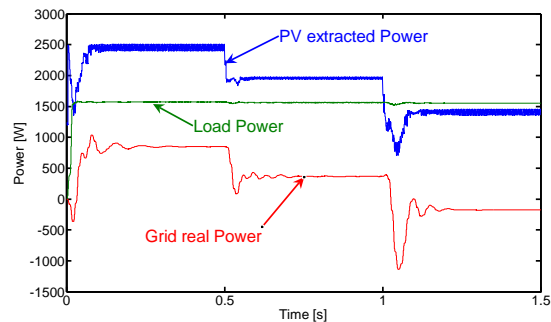


Figure 7 : Powers

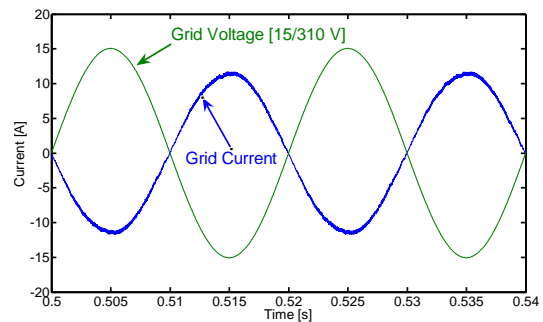


Figure 8 : Grid Current and Voltage

5. CONCLUSION

In this paper, an Asymmetric Cascaded H-bridge inverter for grid-connected photovoltaic system has been presented. Thanks to its fast dynamic response and autonomous control, the ACHB inverter was capable to meet the goals initially set. Hence, a maximum power point tracking is achieved independently for each photovoltaic string. The system operates at a unity power factor, despite the presence of a non-linear load. Finally the System Utilization Factor is enhanced, to reach 100%, by planning a night operation mode.

REFERENCES

- [1] S. Ali Khajehoddin, A. Bakhshai and P. Jain, "A Novel topology and control strategy for maximum power point trackers and multi-string grid-connected PV inverters", *2008 Twenty-Third Annual IEEE Applied Power Electronics Conference and Exposition*, 2008.
Doi: [10.1109/APEC.2008.4522718](https://doi.org/10.1109/APEC.2008.4522718)
- [2] O. Alonso, P. Sanchis, E. Gubia and L. Marroyo, "Cascaded H-bridge multilevel converter for grid connected photovoltaic generators with independent maximum power point tracking of each solar array", *IEEE 34th Annual Conference on Power Electronics Specialist, 2003. PESC '03*.
Doi: [10.1109/PESC.2003.1218146](https://doi.org/10.1109/PESC.2003.1218146)
- [3] B. Xiao, L. Hang, J. Mei, C. Riley, L. Tolbert and B. Ozpineci, "Modular Cascaded H-Bridge Multilevel PV Inverter With Distributed MPPT for Grid-Connected Applications", *IEEE Transactions on Industry Applications*, vol. 51, no. 2, pp. 1722-1731, 2015.
Doi: [10.1109/TIA.2014.2354396](https://doi.org/10.1109/TIA.2014.2354396)
- [4] V. Sridhar and S. Umashankar, "A comprehensive review on CHB MLI based PV inverter and feasibility study of CHB MLI based PV-STATCOM", *Renewable and Sustainable Energy Reviews*, vol. 78, pp. 138-156, 2017.
Doi: [10.1016/j.rser.2017.04.111](https://doi.org/10.1016/j.rser.2017.04.111)
- [5] Y. Yu, G. Konstantinou, C. Townsend and V. Agelidis, "Comparison of zero-sequence injection methods in cascaded H-bridge multilevel converters for large-scale photovoltaic integration", *IET Renewable Power Generation*, vol. 11, no. 5, pp. 603-613, 2017.
Doi: [10.1049/iet-rpg.2016.0621](https://doi.org/10.1049/iet-rpg.2016.0621)
- [6] Chavarria, D. Biel, F. Guinjoan, C. Meza and J. Negroni, "Energy-Balance Control of PV Cascaded Multilevel Grid-Connected Inverters Under Level-Shifted and Phase-Shifted PWMs", *IEEE Transactions on Industrial Electronics*, vol. 60, no. 1, pp. 98-111, 2013.
Doi: [10.1109/tie.2012.2186108](https://doi.org/10.1109/tie.2012.2186108)
- [7] S. Kouro, B. Wu, A. Moya, E. Villanueva, P. Correa and J. Rodriguez, "Control of a cascaded H-bridge multilevel converter for grid connection of photovoltaic systems", *2009 35th Annual Conference of IEEE Industrial Electronics*, 2009.
Doi: [10.1109/IECON.2009.5415332](https://doi.org/10.1109/IECON.2009.5415332)
- [8] E. Villanueva, P. Correa, J. Rodriguez and M. Pacas, "Control of a Single-Phase Cascaded H-Bridge Multilevel Inverter for Grid-Connected Photovoltaic Systems", *IEEE Transactions on Industrial Electronics*, vol. 56, no. 11, pp. 4399-4406, 2009.
Doi: [10.1109/TIE.2009.2029579](https://doi.org/10.1109/TIE.2009.2029579)
- [9] K. Zaouche, A. Talha, and El Madjid Berkouk, "An efficient Asymmetric Cascaded H-bridge inverter for photovoltaic systems", *The 8th International Conference on Modelling, Identification and Control (ICMIC 2016), Algiers, Algeria, 15-17 November 2016*.
DOI: [10.1109/ICMIC.2016.7804117](https://doi.org/10.1109/ICMIC.2016.7804117)
- [10] R. Franco and F. Vieira, "Analytical method for extraction of the single-diode model parameters for photovoltaic panels from datasheet data", *Electronics Letters*, vol. 54, no. 8, pp. 519-521, 2018.
Doi: [10.1049/el.2018.0402](https://doi.org/10.1049/el.2018.0402)

Contribution to the Improvement of the Quality of Electrical Energy Produced by Wind Turbine Based on the PMSG Using the Advanced Control Techniques of Multilevel-level Inverter

I. Hamzaoui, S. Boukhalifa and F. Bouchafaa

Abstract — We present in this paper the modeling and control of a variable speed wind turbine based on the permanent magnet synchronous generator (PMSG) interfaced to the power grid via electronic power converters. We propose two control strategies of the latter, namely the direct control of the torque of the synchronous machine (DTC) applied to the two-level converter on the machine side, and direct power control (DPC) of the network-side converter is considered in this article in three-level, developed by analogy with direct torque control electrical machines and presented in order to mitigate the quality problems of the wave. Indeed, by increasing the level of the converter, it ensures a better control of the vector voltage. The effectiveness of these control strategies is verified by simulation under Matlab / Simulink.

Index Terms — Permanent-magnet synchronous generator (PMSG), Maximum Power Point Tracking (MPPT), Direct torque control (DTC), Direct power control (DPC), Multilevel Inverter.

I. INTRODUCTION

Given the environmental constraints required on the one hand and the increase in the cost of producing electricity on the other, the current trend is oriented towards the exploitation of renewable energy sources like: wind, solar, biomass, geothermal, tidal, hydraulics, ... etc. Among these energy sources, the wind turbine is the most promising in the world in terms of development [1]. Until now, there are two categories of wind turbines: fixed-speed wind turbines directly coupled to the network by the stator and variable-speed wind turbines controlled by the stator or the rotor by means of power electronics converters [2][3].

The wind structure comprising a synchronous generatrix with permanent magnets with a large number of poles, makes variable speed systems more attractive. This type of machine makes it possible to extract a maximum

of energy by reducing the mechanical stresses and this by eliminating the speed multiplier, which improves system reliability and reduces maintenance costs [2]. This article focuses on the choice of a variable speed wind turbine includes the permanent-magnet synchronous generator. This is justified by the interest that research devoted to this type of structures as they are described as the turbines of the future. Indeed the current development in the field of magnetic materials that the major drawback of these structures namely the price of permanent magnets is no longer an obstacle to build gigantic wind turbines with a synchronous machine with permanent magnets [8].

Two predominant control techniques on the current market, including direct control of DTC torque and direct power control DPC of power electronics converters [4,5,6,7]. The wind energy conversion system studied is shown in Fig1. This structure comprises, in addition to the synchronous generator with permanent magnets, converter 1 two-level controlled by the DTC, the continuous bus, converter 2 a three-level controlled by the DPC, the connection to the network via a filter and the transformer.

II. WIND TURBINE MODELING

Power of the wind-turbine is given by:

$$P_t = C_p(\lambda, \beta) P_v = \frac{1}{2} \cdot \rho \cdot \pi \cdot R^2 \cdot C_p(\lambda, \beta) \cdot v^3 \quad (1)$$

The parameter C_p is dimensionless, it expresses the capacity of the wind turbine to extract energy from the wind. This characteristic parameter of the aerogenerator is a function of the specific speed λ and pitch angle β and is called power coefficient.

We define the specific speed λ also called the ratio of the tip speed of pale (Tip-speed-ratio) as the ratio of the peripheral tangential velocity ($\Omega t \cdot R$) on the instantaneous speed of the wind v_{vent} .

$$\lambda = R \frac{\Omega t}{v} \quad (2)$$

R being the radius of the area swept by the pale Ωt and the speed of rotation of the turbine.

The expression of the power coefficient used in this study is given by [9]:

Manuscript received August 08, 2018. This work was supported in part by the MESRS Ministry under Grant J0200220090020. I.Hamzaoui is with the Faculty of Science and Technology University of Khemis Miliana UDBKM, Algeria, Email: hamzaoui_ahssen2000@yahoo.fr. S. Boukhalifa is with the Laboratory of Instrumentation, USTHB, PO.Box. 32, Bab-Ezzouar, Algies, Email: saidaboukhalifa@yahoo.fr. F. Bouchafaa is also with the Laboratory of Instrumentation, USTHB, PO.Box. 32, Bab-Ezzouar, Algies, Phone: 213-24217912 (Ext. 804), Fax: 213-21207664, URL: http://www.lins.usthb.dz, Email: fbouchafa@gmail.com.

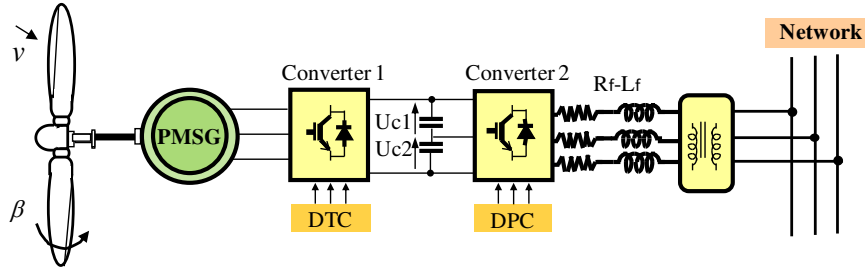


Fig. 1. System structure studied

$$C_p(\lambda, \beta) = (0.5 - 0.00167(\beta - 2)) \sin\left[\frac{\pi(\lambda + 0.1)}{18.5 - 0.3(\beta - 2)}\right] - 0.00184(\lambda - 3)(\beta - 2) \quad (3)$$

The maximum power extraction device (MPPT) must set a reference torque to allow the PMSG to rotate at an adjustable speed to ensure an optimal operating point in terms of power extraction. In this context, the speed ratio of the wind turbine must be maintained at its optimum value ($\lambda = \lambda_{opt}$) (Fig.2) over a certain wind speed range. So, the coefficient power would be maintained at its maximum value ($C_p = C_{p_max}$). The aerodynamic torque is expressed as [10,11]:

$$T_{em-ref} = \frac{1}{2} \frac{\rho \pi R_t^5 C_{p_max}}{\lambda_{opt}^3 G^3} \Omega_{mec}^2 \quad (4)$$

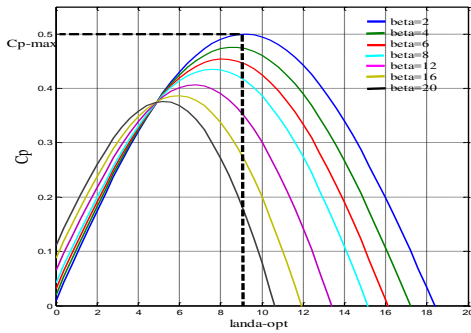


Fig. 2. Power coefficient characteristic for various values of pitch angle

The mechanical transmission between the turbine and the generator can be modeled by the system of equations 5. The lack of speed multiplier is justified by the synchronous machine retaining permanent magnets which has a large number of pairs of poles ($p = 125$) [12].

$$\begin{cases} T_t - T_{em} - f_v \Omega_g = J_t \cdot \frac{d\Omega_g}{dt} \\ \Omega_t = \Omega_g \\ J_t = J_{pales} + J_g + J_{arbre} \end{cases} \quad (5)$$

Where: T_{em} , T_t : Generator and turbine torque, J : total system inertia, f_v is the viscous friction coefficient and Ω_g shows the speed of the rotor. Figure 3 summarizes the

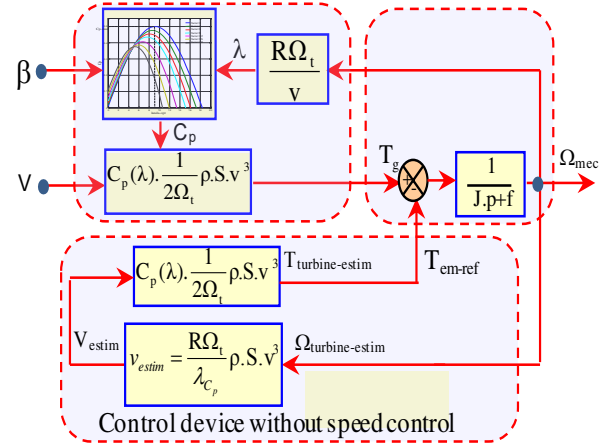


Fig. 3. Block diagram of the MPPT strategy without wind speed measurement

block diagram of the MPPT strategy without measuring the wind speed.

III. PRINCIPLE THE PMSG DTC CONTROL

The DTC control calculates the control quantities of the stator flux and the electromagnetic torque from the stator-related quantities alone. The principle of control is to maintain the stator flux in a fork. The block diagram of the DTC control is shown in Figure 4 [13]. The DTC control of a permanent magnet synchronous machine is based on the direct determination of the sequence of commands applied to the two-level voltage rectifier switches. This strategy is based generally on the use of hysteresis comparators whose role is to control the amplitudes of the stator flux and the electromagnetic torque.

The stator flow and the angle θ_s are calculated from the following equations:

$$\begin{cases} \psi_s = \sqrt{\Psi_{S\alpha}^2 + \Psi_{S\beta}^2} \\ \theta_s = \arctg \frac{\Psi_{S\alpha}}{\Psi_{S\beta}} \end{cases} \quad (6)$$

With:

$$\begin{cases} \Psi_{S\alpha} = \int (v_{S\alpha} - R_S i_{S\alpha}) dt \\ \Psi_{S\beta} = \int (v_{S\beta} - R_S i_{S\beta}) dt \end{cases} \quad (7)$$

The torque can be estimated with:

$$T_{em} = \frac{3}{2} p (\Psi_{S\alpha} i_{S\beta} - \Psi_{S\beta} i_{S\alpha}) \quad (8)$$

The estimated values of the torque and the stator flux are compared with their reference values respectively, the results of the comparison form the inputs of the hysteresis-cycle comparators [4].

The switching table 1 is constructed in the E_ψ , $E_{T_{em}}$ and sector θ position of Ψ_s [4].

TABLE I.
Table switching

E_ψ	$E_{T_{em}}$	θ_1	θ_2	θ_3	θ_4	θ_5	θ_6
1	1	V_2	V_3	V_4	V_5	V_6	V_1
	0	V_7	V_0	V_7	V_0	V_7	V_0
	-1	V_6	V_1	V_2	V_3	V_4	V_5
0	1	V_3	V_4	V_5	V_6	V_1	V_2
	0	V_0	V_7	V_0	V_7	V_0	V_7
	-1	V_5	V_6	V_1	V_2	V_3	V_4

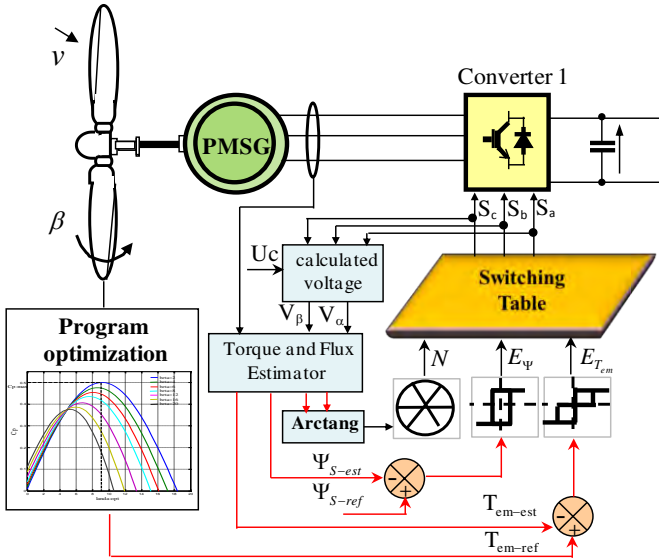


Fig. 4. Basic structure of the control DTC

IV. PRINCIPLE OF THE DPC CONTROL

The overall structure of DPC, using a switching table, applied to the three-level converter 2 is shown in figure 5. It is analogous to direct torque control (DTC) of PMSG. Instead of the torque and the stator flux, it is the active and reactive instantaneous powers that are the controlled quantities. The principle of DPC is to select a sequence of switching commands (S_{a1} , S_{b1} , S_{c1} , S_{a2} , S_{b2} , S_{c2}) semiconductors constituting the Converter 2, from a switching table. Selection is based on digitized errors, S_p et S_q , between the references of active and reactive powers (P^* et q^*) and the actual values (P et q), provided by two hysteresis comparators at two levels, as well as on the angular position of the vector of the tensions $v_{\alpha\beta}$. For the latter, the plane α - β is divided into twelve sectors equal to 30° as shown in the figure 6, where this three-level converter is represented by twenty-seven voltage vectors :

three null vectors and eighteen non-zero vectors [14,15,16,17]:

The calculation of the angular position of the vector of the tensions is defined by the following relation

$$\theta = \text{Arctg}\left(\frac{v_\alpha}{v_\beta}\right) \quad (9)$$

The sector number where the vector of the voltages is located is determined by comparing the angle θ with the limits of each of the twelve sectors which are defined by:

$$(n-2)\frac{\pi}{6} < \text{sect}_n < (n-1)\frac{\pi}{6} \quad n=1,2,\dots,12 \quad (10)$$

The reference of the active power, P^* , is provided by the PI regulator of the DC bus voltage; while that of the reactive power, q^* , is imposed equal to zero for the absorption of sinusoidal currents under a presumed sinusoidal shape source voltage, to ensure operation of the converter with a unit power factor.

The active and reactive powers are estimated using the switching state of the converter, the three-phase line currents, the dc-bus voltage, and the inductance of the reactors. It can be derived as:

$$\hat{P} = L\left(\frac{di_a}{dt}i_a + \frac{di_b}{dt}i_b + \frac{di_c}{dt}i_c\right) + U_{c1}(S_{a1}i_a + S_{b1}i_b + S_{c1}i_c) + U_{c2}(S_{a2}i_a + S_{b2}i_b + S_{c2}i_c) \quad (11)$$

$$\hat{q} = \frac{1}{\sqrt{3}}\left[3L\left(\frac{di_c}{dt}i_c - \frac{di_a}{dt}i_a\right) - U_{c1}(S_{a1}(i_b - i_c) + S_{b1}(i_c - i_a) + S_{c1}(i_a - i_b)) - U_{c2}(S_{a2}(i_b - i_c) + S_{b2}(i_c - i_a) + S_{c2}(i_a - i_b))\right] \quad (12)$$

Reference tracking errors of active and reactive instantaneous powers, introduced in two two-level hysteresis comparators, allow to establish two logical outputs S_p and S_q given by:

$$S_p = \begin{cases} 1 & \text{if } P_{ref} - P_{est} > h_p, \\ 0 & \text{if } -h_p < P_{ref} - P_{est} < h_p, \\ -1 & \text{if } P_{ref} - P_{est} < -h_p \end{cases} \quad (13)$$

$$S_q = \begin{cases} 1 & \text{if } q_{ref} - q_{est} > h_q, \\ 0 & \text{if } -h_q < q_{ref} - q_{est} < h_q, \\ -1 & \text{if } q_{ref} - q_{est} < -h_q \end{cases} \quad (14)$$

Once the logical outputs of the established hysteresis comparators, and following the number of the sector where the vector is located $v_{\alpha\beta}$, the vector of the voltages to be applied to the input of the rectifier is selected from of the conventional switching table as shown in Table 2.

The synthesis of the switching table (Table 2) is based on the signs of derived active and reactive power in each sector, given by the Eq.(15) and (16).

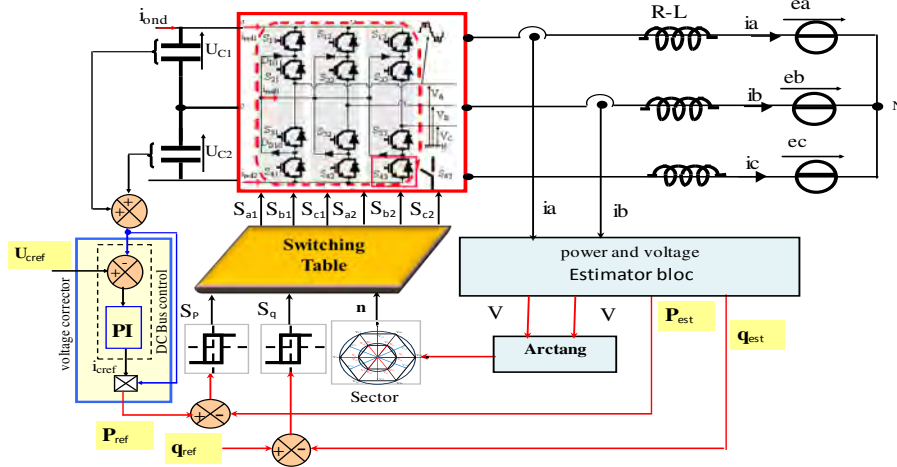


Fig. 5. Basic structure of the DPC control

$$\overline{\Delta P_i} = \frac{\Delta P_i}{L \cdot E \cdot \sqrt{\frac{2}{3}} U_c} = \frac{E}{\sqrt{\frac{2}{3}} U_c} - (\cos(\theta) \cdot \bar{v}_{\alpha i} + \sin(\theta) \cdot \bar{v}_{\beta i}) \quad (14)$$

$$\overline{\Delta q_i} = \frac{\Delta q_i}{\frac{1}{L} E \cdot \sqrt{\frac{2}{3}} U_c} = (\cos(\theta) \cdot \bar{v}_{\beta i} - \sin(\theta) \cdot \bar{v}_{\alpha i}) \quad (15)$$

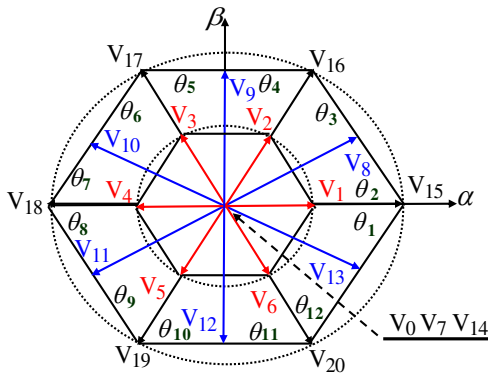


Fig. 6. Sectors and vectors of three-level converter voltages

TABLE II
Table switching

S_p	S_q	θ_1	θ_2	θ_3	θ_4	θ_5	θ_6	θ_7	θ_8	θ_9	θ_{10}	θ_{11}	θ_{12}
1	1	V ₈	V ₁₅	V ₉	V ₁₆	V ₁₀	V ₁₇	V ₁₁	V ₁₈	V ₁₂	V ₁₉	V ₁₃	V ₂₀
	0	V ₁₅	V ₉	V ₁₆	V ₁₀	V ₁₁	V ₁₇	V ₁₂	V ₁₈	V ₁₃	V ₁₉	V ₈	V ₂₀
	-1	V ₅	V ₅	V ₆	V ₆	V ₁	V ₁	V ₂	V ₂	V ₃	V ₃	V ₄	V ₄
0	1	V ₃	V ₃	V ₄	V ₄	V ₅	V ₅	V ₆	V ₆	V ₁	V ₁	V ₂	V ₂
	0	V ₂₅	V ₂₆	V ₂₆	V ₂₁	V ₂₁	V ₂₂	V ₂₂	V ₂₃	V ₂₃	V ₂₄	V ₂₄	V ₂₅
	-1	V ₂₃	V ₂₄	V ₂₄	V ₂₅	V ₂₅	V ₂₆	V ₂₆	V ₂₁	V ₂₁	V ₂₂	V ₂₂	V ₂₃

V. SIMULATION RESULTS

We present, the simulation results of a wind energy conversion chain include a synchronous generator with permanent magnets of 1.5MW illustrated by the figure1. The simulation tests are carried out taking into account the wind profile presented by the figure Fig.7 of average value 10.8 m /s. The reference DC bus voltage equal 2000V. The network is assumed to have infinite power, which allows all production to be injected without constraints. The change of the mechanical speed of the turbine, aerodynamic power and power coefficient are presented in the figures 8,9 and 10 respectively.

Figures 11,12 and 13 illustrate the behavior of the DTC control structure of PMSG. This control system ensures optimization of the extracted power, by maintaining the maximum power coefficient value.

We can find that the torque response and the flux module show good performance. Moreover, during the steady state, we visualize the oscillations of the torque and the flux around their respective setpoint. The amplitude of these oscillations is determined by the hysteresis regulators. The stator flux Φ_s in the complex plane started at point (0,0) and turns in the trigonometric sense to follow a radius circle 2.458 Wb fixed by the setpoint.

The stator currents of the PMSG are sinusoidal but of different frequencies, their amplitudes are related to variations in the speed of rotation of the generator presented by figure 14.

We can see in figure 15 that the voltage bus continuous is not affected by the changes in the rotational speed of the generator. We can conclude that the structure of the chosen conversion chain and the proposed control strategy favor the decoupling between these two quantities. The interest of this decoupling and not to have additional electrical disturbances on the continuous bus that come from the turbine part.

The zoom of the three-phase currents injected into the network are shown in Fig. 16. We see that they are sinusoidal alternating currents with a frequency of 50 Hz. It is in phase opposition to the voltage V_s of the network. This confirms that the wind system only injects active power into the network.

VI. CONCLUSION

In this article we proceeded to the modeling and control of a wind energy conversion chain including a synchronous generator with permanent magnets. We talked about two command techniques, namely the machine-side DTC control used to control the torque and flux through hysteresis comparators and the DPC command applied to the three-level converter on the network side, in order to reduce ripple currents and harmonic content of output voltages. A test of these orders with a suitable wind was carried out on the model of the chain of conversion. Results in line with our expectations were obtained and describe.

REFERENCES

1. M.Boutoubat, L.Mokrani, M. Machmoum, "Control of a wind energy conversion system equipped by a DFIG for active power generation and power quality improvement," *Renew Energy* 2013;50:378e86.
2. M.I.Marei, A.Mohy, A.A.El-Sattar, "An integrated control system for sparse matrix converter interfacing PMSG with the grid," *Journal Electrical Power and Energy Systems* 73 (2015) 340–349.
3. A.Ajami, R.Alizadeh, M. Elmi, "Design and control of a grid tied 6-switch converter for two independent low power wind energy resources based on PMSGs with MPPT capability," *Journal Renewable Energy* 87 (2016) 532-543.
4. A.Moualdia, MO.Mahmoudi, L.Nezli, " DPC and DTC Control of a Wind Speed Based on the Doubly Fed Asynchronous Machine. ,"*Journal of Electrical Engineering JEE*, vol. 12, Edition.2, pp 39-46, 2010.
5. A.Chaoui, J.-P. Gaubert, F. Krim, "Power quality improvement using DPC controlled three-phase shunt active filter,"*Electric Power Systems Research*, Éd. Elsevier, vol. 80, no. 6, pp. 657-666, Jun. 2010.
6. T.Etienne, A.Sergio, C.Ambrish, "Comparative Study of Control Strategies for the Doubly Fed Induction Generator in Wind Energy Conversion Systems," *A DSP-Based Implementation Approach*, IEEE TRANSACTIONS ON SUSTAINABLE ENERGY, VOL. 2, NO. 3, JULY 2011.
7. A.Boulahia, K.Nabti, H.Benalla, "Direct Power Control for AC/DC/AC Converters in Doubly Fed Induction

- Generators Based Wind Turbine," *International Journal of Electrical and Computer Engineering (IJECE)* Vol.2, No.3, June 2012, pp.425-432.
8. Y. Errami, M. Maaroufi, M. Ouassaid , "Modelling and Control Strategy of PMSG Based Variable Speed Wind Energy Conversion System,"978-1-61284-732-0/11/\$26.00 ©2010 IEEE.
9. S.El Aimani, "Modélisation de différentes technologies d'éoliennes intégrées dans un réseau de moyenne tension,"*Thèse de Doctorat*, Ecole Centrale de Lille, France, Décembre 2004.
10. I.Hamzaoui, F.Bouchafaa A.Hadjammar, A.Talha , "Improvement of the performances MPPT system of wind Generation," *Saudi international Electronics, Communications and photonics Conference (CIECPC' 11)*, 23-26 April –2011.
11. I.Hamzaoui, F. Bouchafaa, " Energy optimization for a wind DFIG with flywheel energy storage," 2016; *AIP Conference Proceedings* 1758 (1), 030037.
12. D.Ik,"*Production d'énergie marine: Intégration de la production éolienne offshore dans un bouquet énergétique*," *Thèse de doctorat*, l'Université du Havre, décembre 2014.
13. M.Allagui, O.Hasnaoui,-J.Belhadj, " A 2MW direct drive wind turbine; vector control and direct torque control techniques comparison,"*Journal of Energy in Southern Africa* Vol 25 No 2 May 2014.
14. I.Hamzaoui, F.Bouchafaa, A .Hadjammar, " Investigation of the behavior of a three phase grid connected photovoltaic system to control active and reactive power with DPC," 2011; *Energy Procedia* 6, 493-502.
15. W .Chen, Y .Zou, L .Xu, " Direct power control for neutral-pointclamped three-level PWM rectifier,"*IEEE*; 2008.
16. K.Kulikowskii, A.Sikorski, "Comparison of new DPC methods for two- and three-level AC/DC converters," *Poland: IEEE*;2010.
17. A.Bouafia, F.Krim, JP.Gaubert, "Design and implementation of high performance direct power control of three-phase PWM rectifier via fuzzy and PI controller for output voltage regulation," *Energy Convers Management*.
18. C.Belfedal,S.Moreau,G.Champenois,T.Allaoui,M.Denai, "Comparison of PI and direct power control with SVM of doubly fed induction generator," *J Electr Electron Eng* 2008;8(no.2):633e41.

TABLE III
Wind turbine and PMSG Parameter

Paramètres	Value
Turbine Diameter	D=70.5 m
Number of blades	3
DC bus voltage	2000 V
Nominal power	1.5 MW
Nominal rotor speed	24 tr/min
Number of pole pair	125
Flux of permanent magnets	2.458 Wb
Stator resistance	0.0081 Ω
Inductors with axis d-q	1.2mH

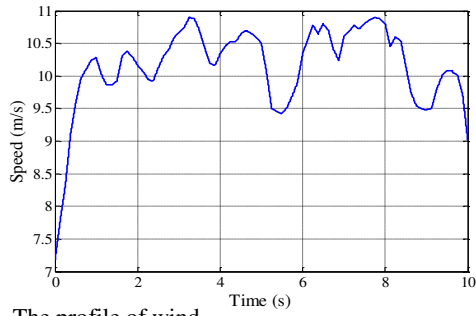


Fig. 7. The profile of wind

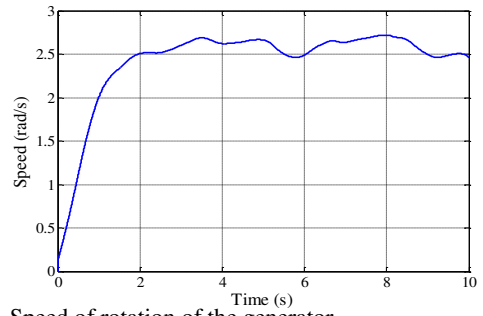


Fig. 8. Speed of rotation of the generator

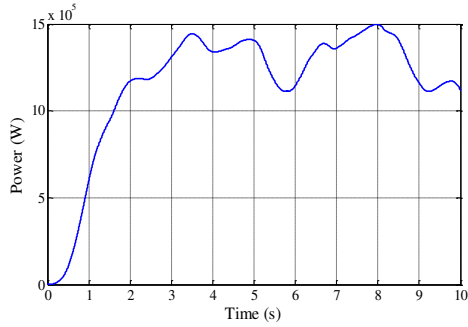


Fig. 9. Aerodynamic power

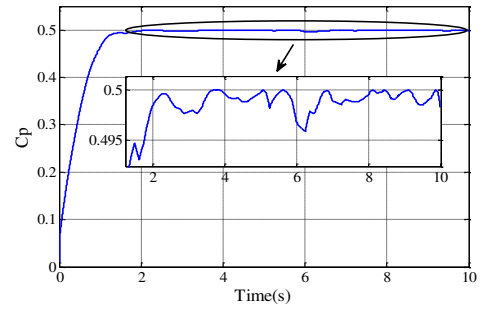


Fig. 10. Power coefficient

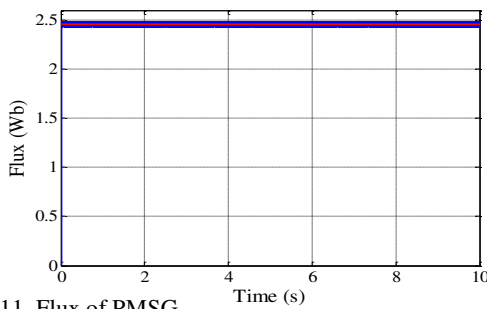


Fig. 11. Flux of PMSG

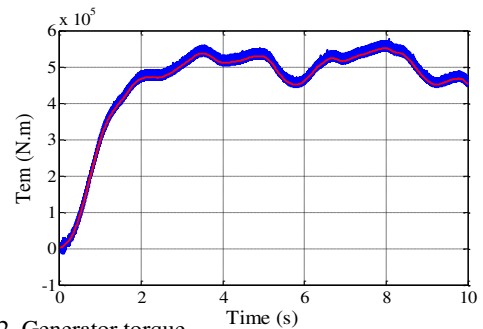


Fig. 12. Generator torque

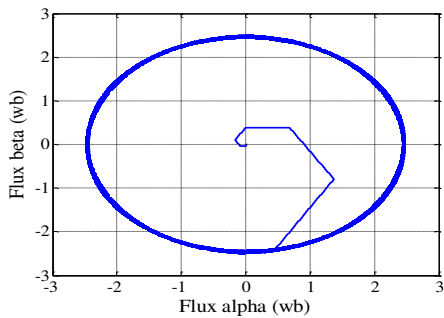


Fig. 13. Trajectory of the stator flux of PMSG

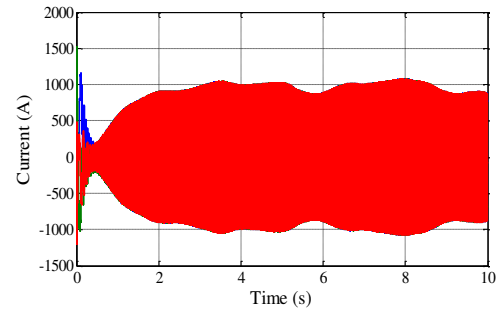


Fig. 14. Stator current of PMSG

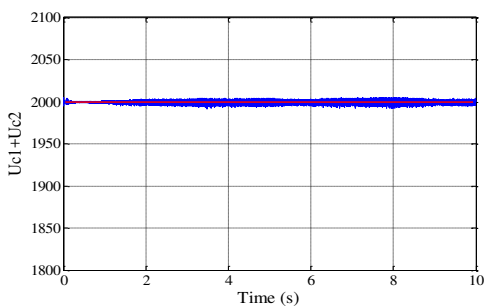


Fig. 15. DC bus voltage

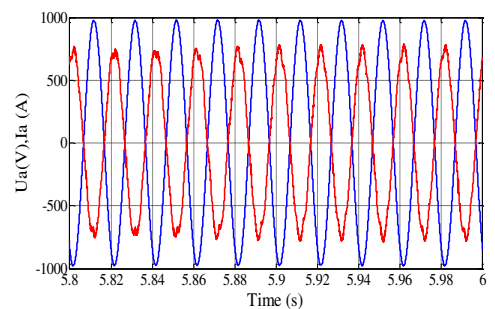


Fig. 16. Zoom voltage and current

Real-coded Genetic Algorithm Optimization for Harmonic Elimination in Neutral-Point Clamped Multilevel Inverter

Nour El Houda GABOUR¹, El Ghalia BOUDISSA¹ and Mhamed BOUNEKHLA¹

¹Laboratoire de Système Electrique et Télécommande Department of Electronics, Saad Dahleb University, Blida, BP 270, route de Soumaa, Blida 09000,
nour_el_houda.gabour@g.enp.edu.dz, boudissaelg@yahoo.fr, bounekhla.mhamed@yahoo.fr

ABSTRACT

In this paper, selective harmonic elimination problem is solved using two different approaches. To reduce THD, Real-coded Genetic algorithm is applied to compute the switching angles of a seven level inverter in order to control the fundamental voltage and simultaneously delete specified low order harmonics. The main disadvantage of the Newton-Raphson conventional method is the starting point choice, which is now diverted into an optimization task. A comparative study is done to highlight the efficiency of both approaches. Neutral-point clamped structure is considered in this work.

Key Words: Genetic Algorithm, Neutral-Point Clamped Multilevel Inverters, Objective Function, Selective Harmonic Elimination, Total Harmonic Distortion.

1. INTRODUCTION

In recent years, use of multilevel inverters has become popular for medium and high power applications. The need for a high power apparatus has been derived from numerous industrial uses [1], [2]. They have found a wide influence in many industrial applications such as renewable energy applications [3], electric vehicles [4], photo-voltaic (PV) systems [5], Battery cells [6], [7], aircraft applications [8], active power filters [9], industrial drives [10], and numerous other fields.

Multilevel inverters have received increased interest over two level inverters from the beginning of their appearance in power electronics [11]—[14] due to high quality output waveform and decreased harmonic distortion in the output waveform without decreasing the inverter power output. Many multilevel converter topologies have been proposed during the last three decades. Most popular structures reported in the literature are cascaded H-bridge inverters [15], diode-clamped inverters [16], and capacitor-clamped inverters [17].

The output waveform generated by multilevel inverter includes an important amount of low order harmonics; an effective method of eliminating these harmonics is the selective harmonic elimination pulse width modulation (SHEPWM) which produces optimum switching angles that lead to minimum switching losses. Related equations are known to be highly transcendental and non-linear. The solution of these transcendental equations can be found by some iterative techniques such as Newton-Raphson Method (NRM). However, this technique has a major disadvantage with finding a proper initial guess that lead to convergence. Furthermore, analytical methods such as NRM will find solutions only for a restricted range of modulation index M ; otherwise, for M without any feasible solution the latter method clashes its limit while facing a continuous range of M . In [18]

and [19], the mathematical Theory of Resultants is used to find all possible solutions to the problem. This is done by converting the transcendental equations into an equivalent set of polynomials. But the complexity of this technique grows with the growing number of levels in MLI's.

For that issue, harmonic elimination problem in multilevel inverters was redrafted into an optimization task and all evolutionary search algorithms [20]-[25] proved themselves efficient to solve the problem. Genetic Algorithm (GA) [26]-[28]; is regarded as stochastic search techniques that mimic the behavior of natural selection and evolution whereas Particle Swarm Optimization (PSO) [29] is inspired from schools of fish or flocks of birds and their coordinated movements to find food while avoiding predators. Various other algorithms were applied; [30] proposed to select optimal switching angles based on Firefly algorithm. In [31], the ant colony optimization for continuous domains (ACOIR) is applied to harmonic elimination problem. [32] proposes a simple graphical approach, if applied to the inverter, eliminates two harmonics and further. In [33], GA and PSO are applied to obtain the switching angles. Then an artificial neural network (ANN) is trained to determine the switching angles. Such algorithms were all applied along with a cost function inspired from the Total Harmonic Distortion formula (THD).

Switching angles determined by NRM faces a deficiency, which is the choice of starting points that can lead to convergence. A solution has been proposed in [34] where GA and PSO are used to choose the starting point of the latter method. Finally, we are confronted to many proposed objective functions, [20], [22], [34] and [35].

In this paper, a comparative study is done between two main proposed objective functions using GA to calculate optimal switching angles in order to control the fundamental voltage and simultaneously delete two low order harmonics. The first objective function is inspired from the general THD formula, and it computes a minimization of this factor. This minimization technique does no longer solve the transcendental non-linear equations as NRM does -when it can- but instead we are having a set of solutions that minimize the global THD for a fixed rang of M. The second objective function has a quadratic

form inspired directly from the set of equations, thus it returns the analytical solution for the range of M where the latter equations are soluble as the NRM method would do. Furthermore, the approach could compute angles even for the range where the transcendental equations do not have any analytical solution, and in this case, angles computed minimize the objective quadratic function rather than solving it.

Furthermore, Particle Swarm Optimization Algorithm is applied in order to confirm the obtained results. Finally, the NRM is diverted, since an evolutionary algorithm used with the right choice of cost function could lead to minimize or ideally solve the transcendental equations related to the selective harmonic elimination-challenging problem.

2. NEUTRAL-POINT CLAMPED MULTILEVEL INVERTER STRUCTURE

A structure of one leg (leg a related to the phase a) of seven-level neutral-point diode clamped converter is depicted in Figure.1. It is worth noticing that the DC input voltage bus E and the capacitor voltages are common to the three legs (leg k, with k=a, b,c). For our study, we assume that total DC voltage E is constant and the voltage Vdc across each of six capacitors (C1, C2, C3, C4, C5 and C6) is likewise constant as $V_{dc} = E/6$. Moreover, the reference point related to output leg voltage is the point n. In Figure.1, S1 to S12 represents switches and D1 to D25 represents clamping diodes. In complementary control mode, Table 1 gives the seven states of the switches S1 to S12 in order to generate seven levels leg voltage Van. [34], [36].

TABLE.1 Switching states related to the seven levels of voltage leg Van.

V_{an}	S ₁	S ₂	S ₃	S ₄	S ₅	S ₆	S ₇	S ₈	S ₉	S ₁₀	S ₁₁	S ₁₂
3V _{dc}	1	1	1	1	1	1	0	0	0	0	0	0
2V _{dc}	1	1	1	1	1	0	1	0	0	0	0	0
V _{dc}	1	1	1	1	0	0	1	1	0	0	0	0
0	1	1	1	0	0	0	1	1	1	0	0	0
-V _{dc}	1	1	0	0	0	0	1	1	1	1	0	0
-2V _{dc}	1	0	0	0	0	0	1	1	1	1	1	0
-3V _{dc}	0	0	0	0	0	0	1	1	1	1	1	1

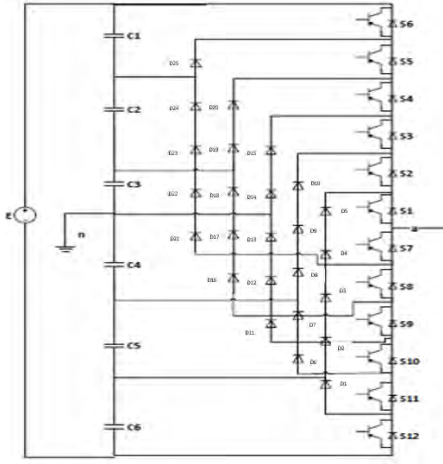


Figure1. One leg structure of seven-level diode clamped converter

3. HARMONIC ELIMINATION PROBLEM

It is well known that the harmonic elimination procedure requires the computation of switching angles allowing the fundamental control and the elimination of undesired low order harmonics.

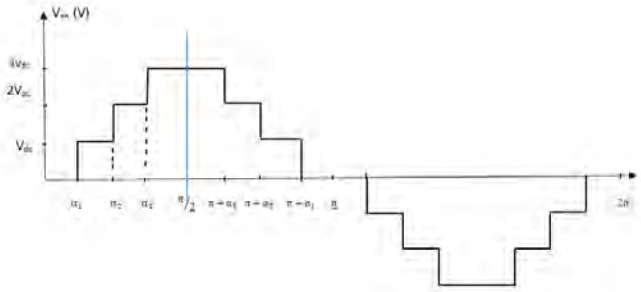


Figure.2 Seven-level output voltage staircase waveform

The symmetric staircase wave of L levels can be depicted with N independent angles given by:

$$N = \begin{cases} (L - 1)/2 & \text{if } L \text{ is odd} \\ (L/2) - 1 & \text{if } L \text{ is even} \end{cases} \quad (1)$$

With these N angles, we can eliminate $(N-1)$ lower order harmonics with fundamental control. The Figure.2 depicts the case of seven levels inverter ($L=7$); it is clear that this wave can be described by using only three independent switching angles ($N=3$) and thus, based on SHE-PWM procedure, two $(N-1)$ low order harmonics can be eliminated. Recalling that output voltage $v(\omega t)$ of pulsation ω can be put under the form:

$$v(\omega t) = \sum_{k=0}^n V_{2*k+1} \sin(2 * k + 1)\omega t \quad (2)$$

Where V_k is the amplitude of the k th harmonic given by:

$$V_k = \frac{4V_{dc}}{\pi k} \sum_{i=1}^S \cos k\alpha_i \quad (3)$$

The amplitude of the fundamental is given for $k=1$:

$$V_1 = \frac{4V_{dc}}{\pi} \sum_{i=1}^S \cos \alpha_i \quad (4)$$

The switching angles can be found by solving the following equations:

$$\begin{cases} \cos \alpha_1 + \cos \alpha_2 + \cos \alpha_3 = \frac{3\pi}{4} M \\ \cos 5\alpha_1 + \cos 5\alpha_2 + \cos 5\alpha_3 = 0 \\ \cos 7\alpha_1 + \cos 7\alpha_2 + \cos 7\alpha_3 = 0 \end{cases} \quad (5)$$

Where, M , i.e. modulation index, is defined as:

$$M = \frac{V_{1max}^*}{(E/2)} \quad (0 \leq M \leq 1) \quad (6)$$

In addition, the switching angles satisfy:

$$0 < \alpha_1 < \alpha_2 < \alpha_3 < \pi/2 \quad (7)$$

The optimal solutions of (5) under the constraints (7) are obtained through the minimization of an objective function.

In this study, we propose to compare two objective functions labelled: THD cost function and Quadratic cost function.

3.1 THD cost function

The minimization technique in this case divert the root of the problem and does no longer solve the transcendental non-linear equations, but instead we are having a set of solutions that minimize the cost function mentioned in (8) which is inspired from the global THD formula.

$$F_{THD}(\alpha_1, \alpha_2, \alpha_3) = \frac{\sqrt{\sum_{k=5,7} V_k^2}}{V_1} \quad (8)$$

3.2 Quadratic cost function

The second cost function presented in (9) is an image of the set of equations that describes the SHEPWM problem.

$$F_{Qua}(\alpha_1, \alpha_2, \alpha_3) = f_1^2 + f_2^2 + f_3^2 \quad (9)$$

Where

$$f_1 = \cos \alpha_1 + \cos \alpha_2 + \cos \alpha_3 - \frac{3\pi}{4} M$$

$$f_2 = \cos 5 \alpha_1 + \cos 5 \alpha_2 + \cos 5 \alpha_3$$

$$f_3 = \cos 7 \alpha_1 + \cos 7 \alpha_2 + \cos 7 \alpha_3$$

4. SELECTIVE HARMONIC ELIMINATION USING GENETIC ALGORITHM

To find the best switching angles for the NPC converter, real-coded GA-based optimization is used to solve the equations set (5) under the cost function (7).

The optimization process starts with a random population composed of a large amount of individuals. Each individual is constituted of the following parameters vector $P = [\alpha_1 \alpha_2 \alpha_3]$ of switching angles. The elements of this vector are called genes. All the values of the genes are taken within a range of permissible solutions. The evaluation of the fitness F is made through an objective function. Then, the individuals are classified from the best to the worst. Being at the top those have an increased chance to be selected for reproduction. The new population is obtained through operators of crossover, mutation, selection and elitism iteratively applied to a set of candidate solution. The generation gap is fixed, meaning the assigned percentage of parent chromosomes that directly turn into the child chromosomes without undergoing the genetic operation crossover and mutation. The elitist model can guarantee not to lose the best individual in the GA optimization. The steps of GAs are illustrated in Figure.3 and are repeated until the convergence criterion is satisfied.

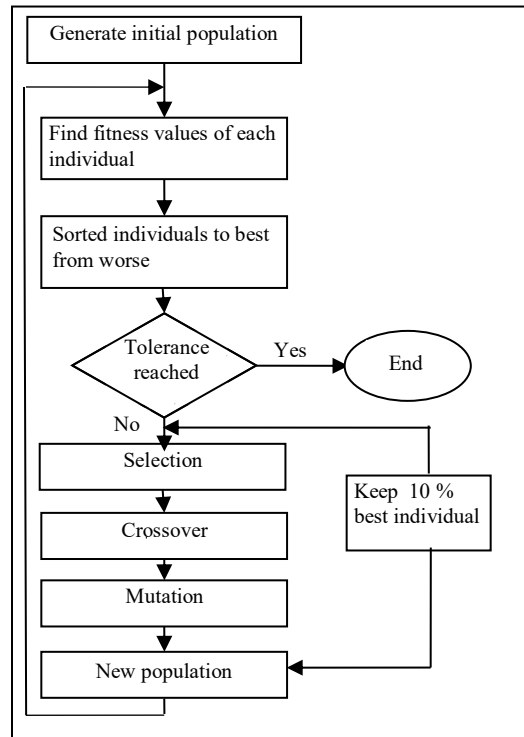


Figure3. Flowchart of Genetic Algorithm

5.SIMULATION AND RESULTS

The simulation is carried out for a seven level neutral-point clamped multilevel inverter in the case where the voltage E is imposed to 660V and thus $V_{dc}=110V$. By using GA, switching angles are determinate in order to control the fundamental and to cancel two low order harmonics: 5th and 7th.

The considered GA is involved with a population of 200 individuals chosen randomly between $[0 \pi/2]$. Beside, GA control vector parameters is taken as: probability of crossover $pc=0.75$, probability of mutation $pm=0.06$ and generation gap is fixed to 10%.

Based on this involved GA and in the case of desired $M= 0.9$ and $M=0.95$, both cost functions are applied. Table II compares the optimal values of switching angles, THDs and calculation times using PSO algorithm and the studied GA. The considered PSO is involved with a population of 200 individuals chosen randomly between $[0 \pi/2]$. Beside, PSO control vector is taken as: the coefficient of inertia of a particle $C1=0.689343$, confidence coefficients that weight the conservative behavior $C2=1.42694$ and $C3=1.42694$. Moreover, the staircase wave of

voltage leg appears in Figure.4, spectrums corresponding to each cost function are depicted in Figure.5, Figure.6 and Figure.7. This procedure has been repeated for the modulation index M varying between [0.1 1] with step=0.0125.

An inspection of the THD cost function spectrum reveals remaining low order harmonics 5th and 7th. Despite they are of negligible amplitude compared to the fundamental one. This technique of minimization does not bring the total suppression of the 5th and 7th harmonic but rather the attenuation of the latter harmonics. For the Quadratic cost function, the resolution of the equations set is successfully carried out for M=0.9 and M=0.95, since the 5th and 7th harmonics are totally suppressed.

Figure.8 depicts THD Variation versus modulation index M for the THD-cost function and highlights the relatively low THD rate for the entire range of M for both evolutionary algorithms. Figure.9 depicts the cost function versus the modulation index M. The Quadratic cost function does the double work of solving the system when a solution exists, or minimizing the latter when a solution does not exist, according to the value of M. Therefore, from Figure.9, the resolution of the set of equations is successfully carried out between M = 0.7 and M=1, since the cost function is nearly zero. These results are not found for the THD cost function since the latter is not concerned with solving the set of equations.

TABLE.2 Solution Angles with involved GA and PSO

Evolutionary Algorithm	Cost function	Modulation Index (M)	α_1 (rad)	α_2 (rad)	α_3 (rad)	THD (%)	Calculation Time (s)
GA	THD	0.9	0.2592	0.4820	0.9888	11.07	33.2031
		0.95	0.2154	0.4258	0.9536	10.13	45.1250
	Quadratic	0.9	0.3056	0.7514	1.1194	19.32	34.1406
		0.95	0.2410	0.6489	1.0806	13.94	38.8750
PSO	THD	0.9	0.2139	0.4301	0.9559	10.09	4.0468
		0.95	0.2116	0.4370	0.9596	9.88	4.0312
	Quadratic	0.9	0.3056	0.7514	1.1194	19.32	2.3437
		0.95	0.2411	0.6491	1.0807	13.94	2.1875

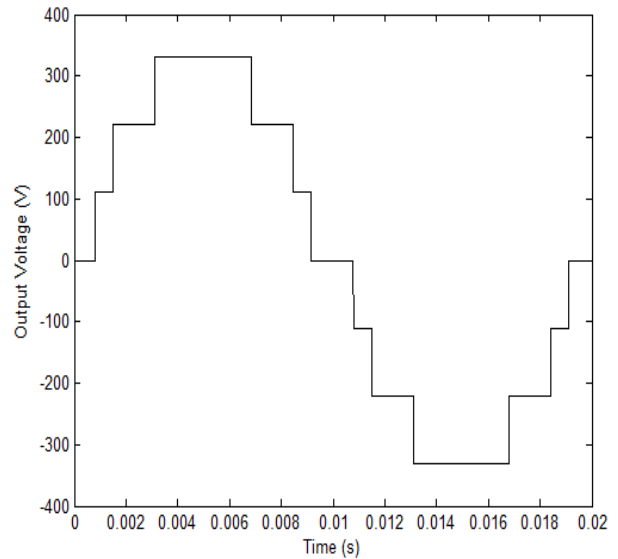


Figure.4 Output voltage of seven-level NPCMI

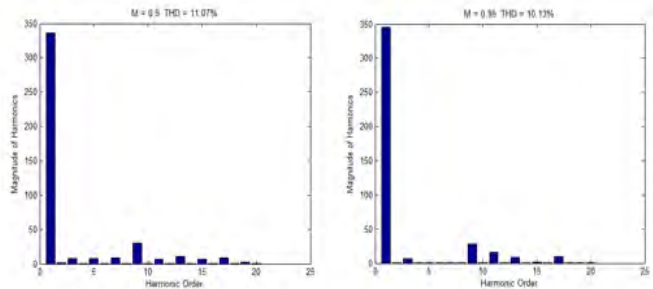


Figure.5 Harmonic Spectra for the THD cost function (GA)

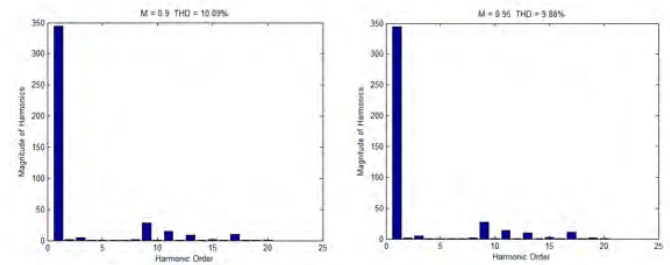


Figure.6 Harmonic Spectra for the THD cost function (PSO)

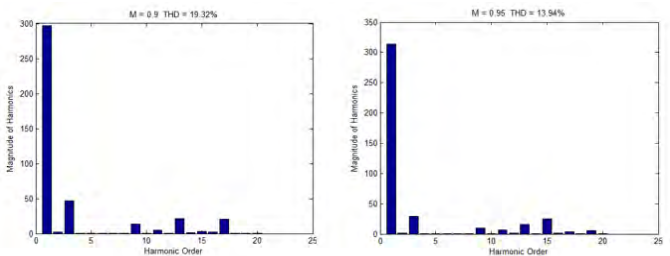


Figure.7 Harmonic Spectra for the Quadratic cost function

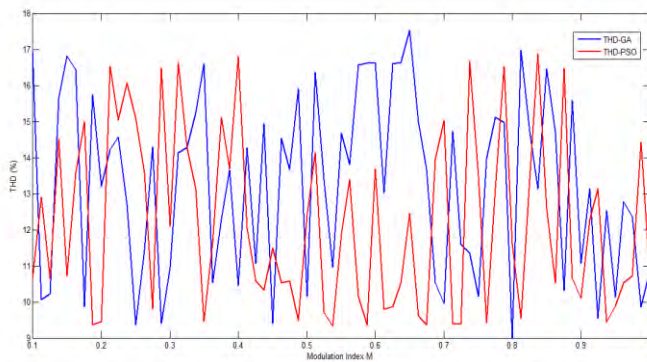


Figure.8 THD versus modulation index M for the THD cost function

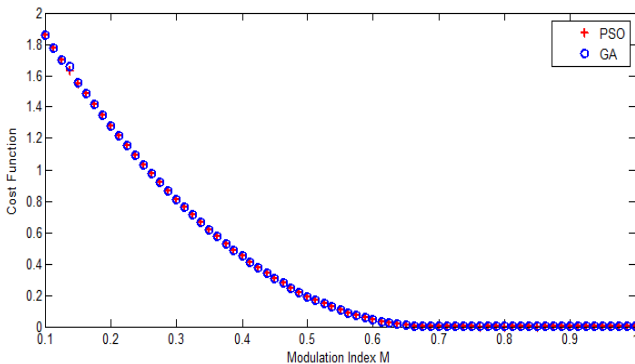


Figure.9 Cost function versus modulation index M

6. CONCLUSION

In this work, GA based minimization is applied to compute the switching angles of a Neutral-Point Clamped Multilevel Inverter. The paper successfully demonstrates the validity of both cost functions to divert the starting point choice of NRM and solve the selective harmonic elimination problem. Furthermore, results show the effectiveness of the Quadratic cost function to solve the set of transcendental non-linear equations for a fixed range of modulation index M. For the THD cost function, the strong point is the relatively low global THD rate for the entire range of M. Comparison is done with the PSO algorithm in order to confirm the latter results.

REFERENCES

[1] N. Rakholiya, R. Garsodiya, A. Virani and H. Sidhpuria, "Multilevel Inverter Topology," IJIRST –International Journal for Innovative Research in Science & Technology | Volume 3 | Issue 11 | April 2017.

[2] R. Shukla and R. Agrawal, "Simulation of Cascade H-Bridge Multilevel Inverter with Equal DC ISBN: 978 9931 9548 04/\$00.0 © 2018

Voltage Source," International Journal of Advanced Research in Electrical, Electronics and Instrumentation Engineering. Vol. 3, Issue 8, August 2014.

- [3] P. Kala and S. Arora, "A comprehensive study of classical and hybrid multilevel inverter topologies for renewable energy applications," Renewable and Sustainable Energy Reviews 76 (2017) 905–931.
- [4] Z. Zheng and K. Wang, "A Hybrid Cascaded Multilevel Converter for Battery Energy Management Applied in Electric Vehicles," IEEE TRANSACTIONS ON POWER ELECTRONICS, VOL. 29, NO. 7, JULY 2014
- [5] B. Xiao and L. M. Tolbert, "Single-phase cascaded H-bridge multilevel inverter with nonactive power compensation for grid-connected photovoltaic generators », in Energy Conversion Congress and Exposition (ECCE), 2011 IEEE, 2011, p. 2733–2737.
- [6] T. Halder, "A smart solar power cultivation using the flyback converter & multi-level inverter », in Power Electronics (IICPE), 2016 7th India International Conference on, 2016, p. 1–6.
- [7] J. Kim, J. Shin, C. Chun, and B. H. Cho, "Stable Configuration of a Li-Ion Series Battery Pack Based on a Screening Process for Improved Voltage/SOC Balancing », IEEE Transactions on Power Electronics, vol. 27, no 1, p. 411 424, janv. 2012.
- [8] J. John and J. Jose, "A three phase step up multilevel inverter for aircraft applications », in Electrical, Electronics, and Optimization Techniques (ICEEOT), International Conference on, 2016, p. 405–408.
- [9] A. Varschavsky, J. Dixon, M. Rotella, and L. Morán, "Cascaded Nine-Level Inverter for Hybrid-Series Active Power Filter, Using Industrial Controller », IEEE Transactions on Industrial Electronics, vol. 57, no 8, p. 2761 2767, août 2010.
- [10] M. Veenstra and A. Rufer, "Control of a Hybrid Asymmetric Multilevel Inverter for Competitive Medium-Voltage Industrial Drives », IEEE Transactions on Industry Applications, vol. 41, no 2, p. 655 664, mars 2005.
- [11] J. Rodriguez, Jih-Sheng Lai, and Fang Zheng Peng, "Multilevel inverters: a survey of topologies, controls, and applications », IEEE Transactions on Industrial Electronics, vol. 49, no 4, p. 724 738, août 2002.
- [12] M. Devi and A. U. Ahmad, "Review of Multilevel Inverters-Topologies, Control Techniques and Reduction of Leakage Current in Cascaded Multilevel Inverter ».
- [13] J.-S. Lai and F. Z. Peng, "Multilevel converters-a new breed of power converters », IEEE Transactions on industry applications, vol. 32, no 3, p. 509–517, 1996.

- [14] M. Sandhu and T. Thakur, « Multilevel inverters: literature survey-topologies control techniques & applications of renewable energy sources-grid integration », *Int. Journal of Engineering Research and Applications*, vol. 4, no 3, p. 644–652, 2014.
- [15] M. Malinowski, K. Gopakumar, J. Rodriguez, and M. A. Pérez, « A Survey on Cascaded Multilevel Inverters », *IEEE Transactions on Industrial Electronics*, vol. 57, no 7, p. 2197–2206, juill. 2010.
- [16] A. Nabae, I. Takahashi and H. Akagi, « A New Neutral-Point-Clamped PWM Inverter », *IEEE Trans. Ind. Appl.*, vol. IA.17, n°. 5, pp. 518–523 Sept./Oct/ 1981.
- [17] T. A. Meynard and H. Foch, « Multi-Level Choppers for High Voltage Applications », *EPE Journal*, vol. 2, no 1, p. 45–50, janv. 1992.
- [18] J. N. Chiasson, L. M. Tolbert, K. J. McKenzie, and Zhong Du, « Control of a multilevel converter using resultant theory », *IEEE Transactions on Control Systems Technology*, vol. 11, no 3, p. 345–354, mai 2003.
- [19] J. N. Chiasson, L. M. Tolbert, K. J. McKenzie, and Z. Du, « A Complete Solution to the Harmonic Elimination Problem », *IEEE Transactions on Power Electronics*, vol. 19, no 2, p. 491–499, mars 2004.
- [20] D. Kumar, S. Pattnaik, and V. Singh, « Genetic algorithm based approach for optimization of conducting angles in cascaded multilevel inverter », *IJERA*, vol. 2, no 3, p. 2389–2395, 2012.
- [21] S. Barkat, E. M. Berkouk, and M. S. Boucherit, « Particle swarm optimization for harmonic elimination in multilevel inverters », *Electrical Engineering*, vol. 91, no 4–5, p. 221–228, déc. 2009.
- [22] A. K. Kaviani, S. H. Fathi, N. Farokhnia, and A. J. Ardakani, « PSO, an effective tool for harmonics elimination and optimization in multi-level inverters », in *Industrial Electronics and Applications*, 2009. ICIEA 2009. 4th IEEE Conference on, 2009, p. 2902–2907.
- [23] M. H. Etesami, N. Farokhnia, and S. H. Fathi, « Colonial Competitive Algorithm Development toward Harmonic Minimization in Multilevel Inverters », *IEEE Transactions on Industrial Informatics*, p. 1–11, 2015.
- [24] M. A. Memon, S. Mekhilef, and M. Mubin, « Selective harmonic elimination in multilevel inverter using hybrid APSO algorithm », *IET Power Electronics*, vol. 11, no 10, p. 1673–1680, août 2018.
- [25] M. A. Memon, S. Mekhilef, M. Mubin, and M. Aamir, « Selective harmonic elimination in inverters using bio-inspired intelligent algorithms for renewable energy conversion applications: A review », *Renewable and Sustainable Energy Reviews*, vol. 82, p. 2235–2253, févr. 2018.
- [26] J.H. Holland, « Adaptation in natural and artificial systems », *Ann Arbor, MI: Univ. Mich. Press*, 1975.
- [27] A. D.E. Goldberg, « Genetic Algorithms in search, optimization and machine learning », Reading, MA: Addison-Wesley, 1989.
- [28] Baker, J.E. "Adaptive selection methods for genetic algorithm," In *Proc. First Int Conf. on Genetic Algorithms and their Applications*. Hillsdale, NJ: Lawrence Erlbaum, pp. 101–111, 1985.
- [29] J. Kennedy and R. Eberhart, « Particle Swarm Optimization » *IEEE 0-7803-2768-3/95*, 1995.
- [30] N. Karthik and R. Arul, « Harmonic elimination in cascade multilevel inverters using Firefly algorithm », in *Circuit, Power and Computing Technologies (ICCPCT)*, 2014 International Conference on, 2014, p. 838–843.
- [31] M. Babaei and H. Rastegar, « Selective harmonic elimination PWM using ant colony optimization », in *Electrical Engineering (ICEE)*, 2017 Iranian Conference on, 2017, p. 1054–1059.
- [32] C. Buccella, M. G. Cimatoroni, H. Latafat, G. Graditi, and R. Yang, « Selective harmonic elimination in a seven level cascaded multilevel inverter based on graphical analysis », in *Industrial Electronics Society, IECON 2016-42nd Annual Conference of the IEEE*, 2016, p. 2563–2568.
- [33] H. R. Mohammadi and A. Akhavan, « A new adaptive selective harmonic elimination method for cascaded multilevel inverters using evolutionary methods », in *Industrial Electronics (ISIE)*, 2014 IEEE 23rd International Symposium on, 2014, p. 1484–1489.
- [34] S. Barkati, L. Baghli, E. M. Berkouk, and M.-S. Boucherit, « Harmonic elimination in diode-clamped multilevel inverter using evolutionary algorithms », *Electric Power Systems Research*, vol. 78, no 10, p. 1736–1746, oct. 2008.
- [35] V. G. Agelidis, A. Balouktsis, and I. Balouktsis, « On Applying a Minimization Technique to the Harmonic Elimination PWM Control: The Bipolar Waveform », *IEEE Power Electronics Letters*, vol. 2, no 2, p. 41–44, juin 2004.
- [36] P. Sanoop and V. Chellappan, « Seven Level Inverter Topologies: A Comparative Study », *IJIREICE*, Vol. 3, Special Issue 1, February 2016.

Second-Order Sliding Mode Control Scheme with a Non-Linear Phenomena Analysis of a DC-DC Power Converter Dedicated to Distributed Power Systems

Amel HADRI-HAMIDA¹, Adel GHOGGAL², Sakina ZEROUALI¹ and
 Fatiha KHELILI¹

¹LMSE Laboratory, Electrical Engineering Department, Biskra University, Algeria,
 am_hadri@yahoo.fr, sakina_z@yahoo.fr, fkhelili@gmail.com

²LGEB Laboratory, Electrical Engineering Department, Biskra University, Algeria,
 ghoetudes@yahoo.fr

ABSTRACT

This paper presents a theoretical stability analysis of a DC-DC power converter dedicated to distributed power systems to explore the non-linear phenomena in this converter. The input-output feedback linearization approach is based on the exact cancellation of the nonlinearity, for this reason, this technique is not efficient, because system parameters can vary.

First a nonlinear system modelling is derived by using power balance of the input and output. Then, a nonlinear control scheme was implemented to regulate the output voltage and to eliminate the high current ripples for the proposed converter. Simulation results are obtained using Matlab. It shows how the nonlinear law provides an efficient control design both for parameters variation sensitivity and regulation in order to improve the dynamic of the system. A detailed bifurcation analysis is undertaken.

Key Words: Bifurcations, Non-linear phenomena, Power converters, Parameters variation sensitivity, Second-order sliding mode control.

1. NOMENCLATURE

V_e	Input voltage	V_C	Capacitor voltage
T_r	Controlled switch	i_L	Inductor current
D	Diode	V_{rc}	Voltage drop across rc
I_s	Load current	V_s	Output voltage

L	Inductor	α	Duty ratio
C	Capacitor	T	Switching cycle
R	Load resistance	F	Switching frequency
r_L	Equivalent series resistance of L	r_c	Equivalent series resistance of C
S	Sliding surface	T_R	Control law
V_{ref}	Reference voltage	i_{ref}	Reference current
K	Positive constant	λ	Positive constant
T_{Req}	Equivalent control	T_{Rn}	Stabilizing control
H_v	Sensor gain for V_s	H_i	Sensor gain for i_L
v	Control law	σ	Sliding function
k	Entire number	r	Degree of S

2. INTRODUCTION

One of the requirements for the next generation of power supplies for distributed power systems (DPS) is to achieve high power density with high efficiency [1]. In the traditional front-end converter based on the two-stage approach for high-power three phase DPS, the DC-link voltage coming from the power factor correction (PFC) stage penalizes the second-stage DC-DC converter [2]. This DC-DC converter not only has to meet the characteristics demanded by the load, but also must process energy with high

efficiency, high reliability, high power density and low cost [3].

In its simplest terms, the operation of a DC-DC converter can be described as an orderly repetition of a fixed sequence of circuit topologies. The conversion function of the converter is determined by the constituent topologies and the order in which they are repeated. Such toggling between circuit topologies is achieved by placing switches at suitable positions and turning them on and off in such a way that the required topological sequence is produced [4].

Clearly, the absence of a fixed circuit configuration poses a serious problem to the analysis and modelling of DC-DC converters. The major difficulty lies in the fact that the manner in which the system operates is highly nonlinear [5] – [8]. To date, most analytic techniques of modelling and analysis of DC-DC converters implement different degrees of approximation and varying levels of restrictions in order to fit them into the framework of conventional linear system theory where there is a large body of standard theory for the analysis and design of linear feedback systems[9] – [11]. In general, modelling techniques can be continuous, discrete or combination of continuous and discrete models.

In most of the above investigations, sampled-data models or maps of the converters have been derived, and the bifurcation structures have been investigated with the discrete models.

Bifurcation denotes for a change in the number of candidate operating conditions of a nonlinear system when a parameter is quasi-statically varied [12]. The complex behaviour associated with bifurcations can be understood through bifurcation analysis [13] – [16]. Then, sliding mode control (SMC) technology is adopted to suppress the input disturbance and reduce the effects from the load variation. In [17] an improved SMC method for a modular multi-level high-voltage DC converter is presented. It can solve the chattering problem that exists in conventional SMC on-line. The hysteresis modulation SMC is designed in [18] for the inherently variable structure of the negative-output elementary boost converter by using a state-space average based model. In [19], the problem of driving stability for a

hybrid vehicle is discussed. Comparing these works with our work, the contribution of this paper is to apply a second-order SMC (SOSMC) to a power DC-DC converter.

In order to eliminate the bifurcations and steady state error, an SMC control is introduced to the exact feedback control law. The goal of the first order SMC is to force the state trajectories to move along the sliding manifold. In the SOSMC, the purpose is to move the states along the switching surface and to keep its order successive time derivatives by using a suitable discontinuous control action. In the SOSMC, the time derivative of the control input would be designed to act on the second order derivatives of the sliding variable [20]. Hence, the time derivative of the control would be used as the control input. The new control would be designed as a discontinuous signal, but its integral would be continuous for the eliminating of the high frequency chattering. It is shown via simulation results that the SOSMC has high performance both in the transient and steady state operations. A good control of the output voltage is obtained.

3. SYSTEM MODEL DEVELOPMENT

A power circuit of a high frequency Buck DC-DC converter is introduced in figure 1. From the detailed analysis of the PWM Buck converter presented in [21], we deduce the following large-signal continuous-time system:

$$\left\{ \begin{array}{l} \dot{x} = \left(\begin{array}{cc} -\frac{1}{L} \left(r_L + \frac{r_C \times R}{r_C + R} \right) & \frac{1}{L} \left(\frac{R}{r_C + R} \right) \\ \frac{R}{C \times (r_C + R)} & -\frac{1}{C \times (r_C + R)} \end{array} \right) x + \begin{bmatrix} 1 \\ L \\ 0 \end{bmatrix} \overline{V}_e \alpha \\ + \left(\begin{array}{cc} -\frac{1}{L} \left(r_L + \frac{r_C \times R}{r_C + R} \right) & -\frac{1}{L} \left(\frac{R}{r_C + R} \right) \\ \frac{R}{C \times (r_C + R)} & -\frac{1}{C \times (r_C + R)} \end{array} \right) x + \begin{bmatrix} 0 \\ 0 \\ 0 \end{bmatrix} \overline{V}_e (1-\alpha) \\ \overline{V}_s = \left(\begin{array}{cc} \frac{r_C \times R}{r_C + R} & \frac{R}{r_C + R} \\ \frac{r_C \times R}{r_C + R} & \frac{R}{r_C + R} \end{array} \right) \alpha + \left(\begin{array}{cc} \frac{r_C \times R}{r_C + R} & \frac{R}{r_C + R} \\ \frac{r_C \times R}{r_C + R} & \frac{R}{r_C + R} \end{array} \right) (1-\alpha) \end{array} \right. \quad (1)$$

where $x = [i_L, V_C]^t$.

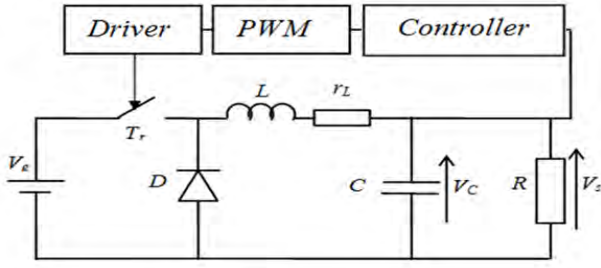


Figure.1: A high frequency Buck DC-DC converter.

4. DESIGN OF THE FEEDBACK CONTROL

4.1. SMC controller

The goal is to select a control method capable of improving the efficiency of the converter, and being less effected by component variation which is the main objective in this work. The bloc scheme in figure 2 gives the configuration of the DC-DC Buck converter with the SMC law. The analysis of this controller is presented in the appendix.

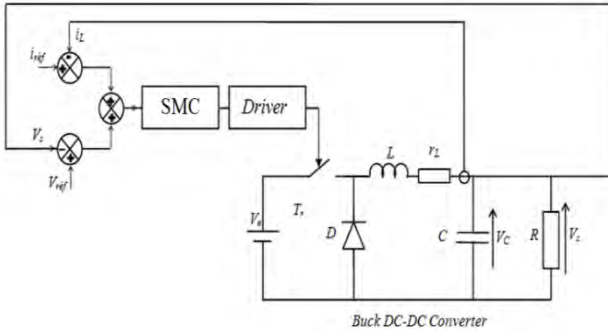


Figure.2: Closed-loop DC-DC Buck converter with SMC.

4.2. Second order sliding mode controller

The objective of the synthesis of a second order sliding mode control is to force the trajectories of the system (16) to move in a finished time on the whole sliding surfaces with a defined order r by:

$$S^r = \left\{ x \in R^n \mid S = \dot{S} = \dots = S^{r-1} = 0 \right\} \quad (2)$$

The r^{th} order derivative of $S(x)$ satisfies the following equation:

$$S^r(x) = EE(x) + QQ T_R \quad (3)$$

where the matrices $EE(x)$ and $QQ(x)$, are the derivatives of the smooth functions in (23). The r^{th} order sliding mode control of system (16) with respect to the sliding variable $S(x)$ can be expressed as [22]:

$$\begin{cases} \dot{z}_i = z_{i+1} \\ \dot{z}_r = EE(x) + QQ(x)T_R \end{cases} \quad (4)$$

where $1 \leq i \leq r - 1$, and $[z_1 \ z_2 \ \dots \ z_r]^t = [S(x) \ \dot{S}(x) \ \dots \ S^{r-1}(x)]^t$. By taking the first order time derivative of (23), we obtain:

$$\begin{aligned} \ddot{S} &= \dot{E}(x) + \dot{Q} T_R + Q \dot{T}_R \\ &= EE(x, T_R) + Q \dot{T}_R \end{aligned} \quad (5)$$

where

$$\begin{aligned} EE &= \left(\frac{H_i}{LC} - \frac{H_i r_L^2}{L^2} + \frac{H_v r_L}{LC} \right) i_L + \left(\frac{H_v}{LC} - \frac{H_i r_L}{L^2} \right) V_C \\ &- \frac{H_i}{LC} I_s + \left(\left(\frac{H_i r_L}{L^2} - \frac{H_v}{LC} \right) V_e \right) T_R \end{aligned}$$

Finally, the new control law is given by:

$$T_R = -Q^{-1} EE(x, T_R) \quad (6)$$

Now, with z as the state variable, and from [23], the r^{th} order sliding mode control for system (16) can be written as:

$$\begin{cases} \dot{z}_i = z_{i+1} + \Delta f_i(z, t) \\ \dot{z}_r = EE_n(z) + QQ_n(z)T_R + \Delta f_r(z, t) \end{cases} \quad (7)$$

where $\Delta f(z, t) = \Delta EE(z) + \Delta QQ(z)T_R$, which are the uncertain parts of the matrices $EE(z)$ and $QQ(z)$, and $EE_n(z)$, $QQ_n(z)$ are the nominal parts of matrices $EE(z)$ and $QQ(z)$ respectively. Assuming $y_1 = S(z)$ and $y_2 = \dot{S}(z)$, the system dynamics can be written as [24]

$$\begin{cases} \dot{y}_1 = y_2 \\ \dot{y}_2 = \Phi(z, T_R) + \Psi(z) \end{cases} \quad (8)$$

where $\Phi(z, T_R) = EE_n(z) + QQ_n(z)T_R + \Delta f(z, t)$, $v =$

T_R and $\Psi(z) = QQ_n(z)$. Thus, the new control input of the system (8) to be determined becomes v . The sliding function for system (8) is considered as:

$$\sigma = y_2 + K y_1 \quad (9)$$

The derivative of (9) is obtained as:

$$\dot{\sigma} = \dot{y}_2 + K \dot{y}_1 \quad (10)$$

Now, we consider the sliding surface suggested by [23]

$$S(z) = z_n - z_n(0) \quad (11)$$

where $z_n(0)$ is the initial condition of the system. The time derivative of (11) is:

$$\dot{S}(z) = \dot{z}_n = EE_n(z) + QQ_n(z)T_R + \Delta f(z, t) \quad (12)$$

and consequently:

$$\ddot{S}(z) = \dot{EE}_n(z) + \dot{QQ}_n(z)T_R + \dot{QQ}_n(z)T_R + \dot{\Delta f}(z, t) \quad (13)$$

from equations (10), (12), and (13) we can obtain:

$$\begin{aligned} \dot{\sigma} &= \dot{EE}_n(z) + \dot{QQ}_n(z)T_R + \dot{QQ}_n(z)T_R + \dot{\Delta f}(z, t) \\ &+ K(\dot{EE}_n(z) + \dot{QQ}_n(z)T_R + \dot{\Delta f}(z, t)) \\ &= \Phi(z, T_R) + \Psi(z)v + K \begin{pmatrix} \dot{z} \\ \sigma \end{pmatrix} \end{aligned} \quad (14)$$

The new control law becomes:

$$v = -\Psi^{-1}(z) \left\{ \Phi(z, T_R) + K \begin{pmatrix} \dot{z} \\ \sigma \end{pmatrix} - \dot{\sigma} \right\} \quad (15)$$

5. SIMULATION RESULTS

Figure 3 shows the steady-state waveforms of the closed-loop system with $V_e = 23, 26,$ and $40V$, respectively. The two-dimensional projections of the phase portraits on the $iL-VC$ plane corresponding to these three cases are also shown. They demonstrate clearly the period-1, period-2, and chaotic orbits. The power spectrum density for each of these cases is also shown. The power spectrum of the response in the chaotic region is wide band, unlike that of the period-one solution, which is

characterized by a fundamental at the switching frequency and its higher harmonics. Thus, the higher the controller gain and hence the higher the loop gain, the more likely the instability will occur on the fast scale.

The SOSMC is verified by detailed using MATLAB. A PWM DC-DC model is developed to simulate a switch-on and change load transient conditions, with the control scheme in figure 2.

From figure 4 (a), we show that the SMC controller ensures finite time convergence of the system states. However, the high frequency chattering is always present. In figure 4 (b), the undesired chattering in the current and voltage signal was removed. The dynamic performance of the designed AHOSMC controller is found to be satisfactory compared to that obtained with the conventional SMC.

6. CONCLUSION

In this paper a nonlinear model was derived for a high frequency Buck DC-DC converter. The nonlinear model was used to study the stability of this converter. Bifurcation diagrams were generated to study the total behavior of the system as one of its parameters varies.

Next, to improve the performances of our system, we have introduced a sliding mode controller. The results show that the SMC control has fast dynamic response to external disturbances. This technique of control can reduce and sometimes eliminate the effect of load and component variation (bifurcations).

Moreover, a robust model reference SOSMC is designed. The advantage of the SOSMC is translated by the reduction of chattering. The proposed control scheme gives satisfactory simulation results.

It is shown through simulation results that the SOSMC can reduce the internal oscillations, and the performance of the high frequency Buck DC-DC converter based on SOSMC scheme is better than the ones based on classical SMC scheme.

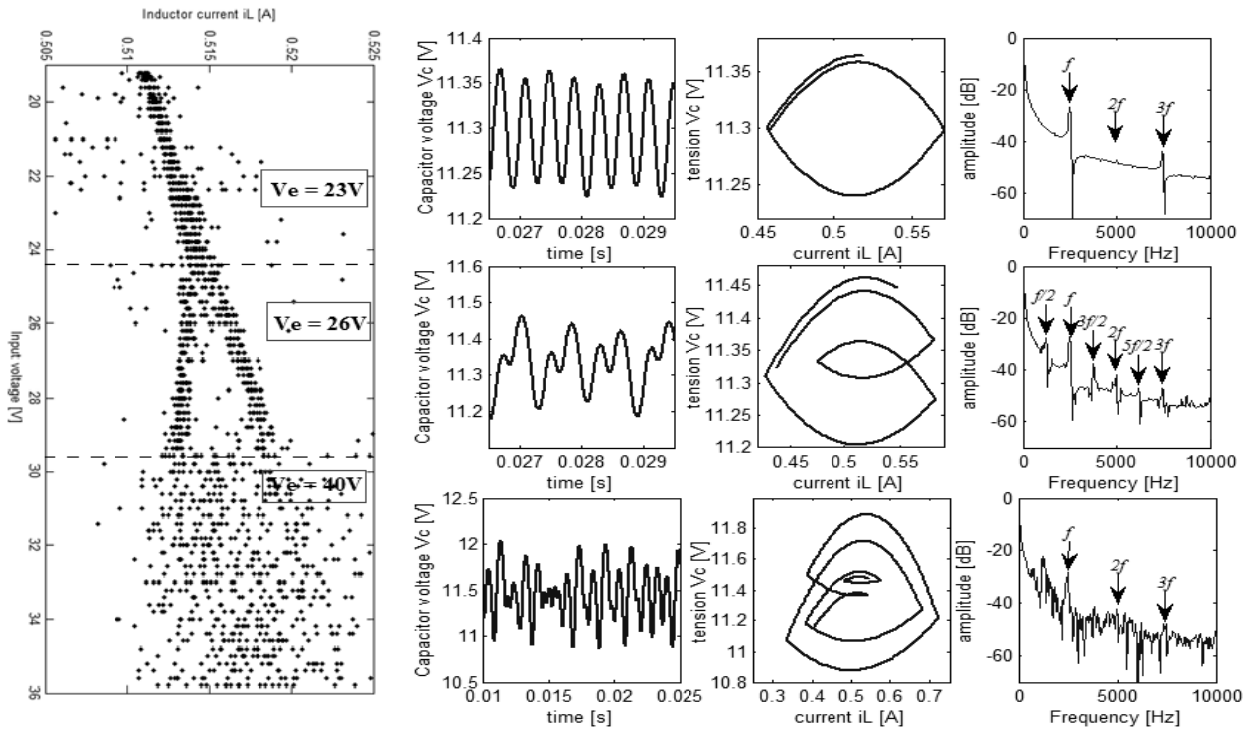


Fig. 3 (1 - 3). Bifurcation diagram, long time history, state plane and power spectral density of the capacitor voltage.

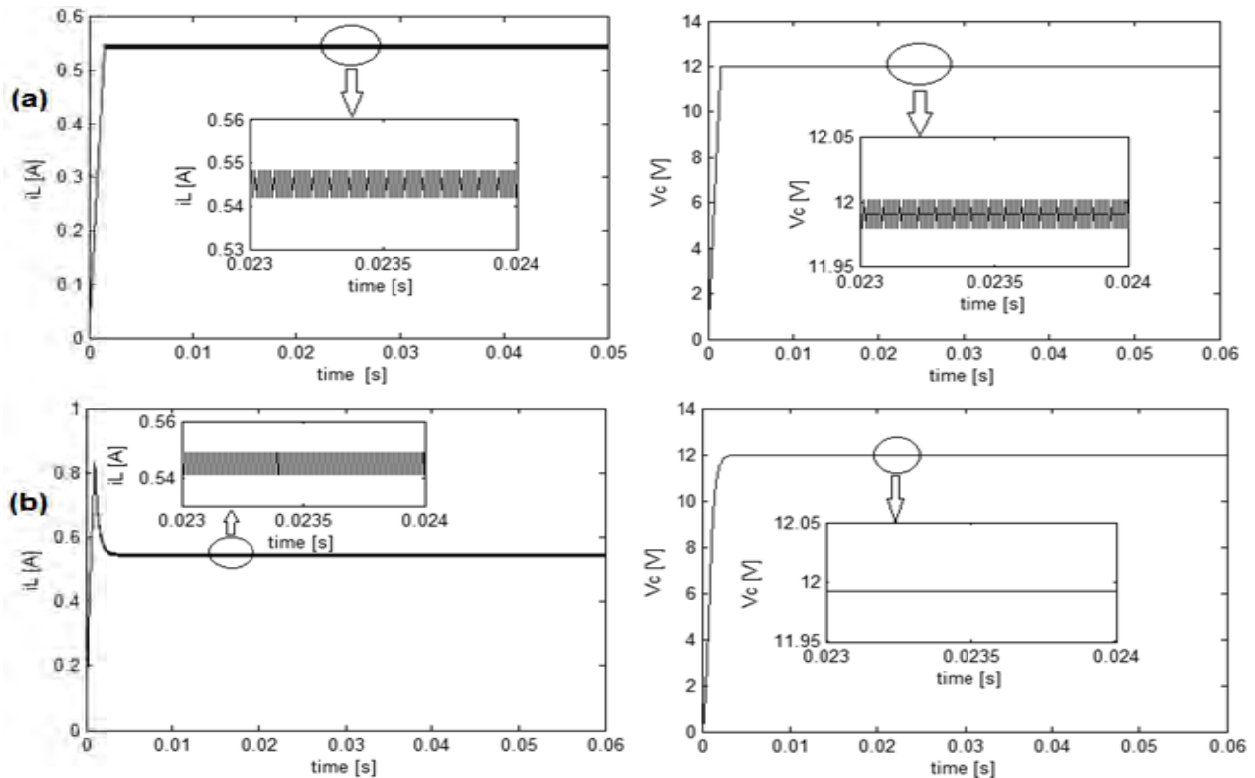


Fig. 4. - Inductor current i_L and capacitor voltage V_C , (a) with SMC, (b) with SOSMC.

7. APPENDIX

We have introduced firstly the SMC controller. In SMC, the trajectory of the system is constrained to move or slide along

a predetermined hyper plane in the state space. Such mode is completely robust and independent of parametric variations and disturbances [25, 26]. By eliminating the parasitic effect of the capacitor ($r_C = 0$), The

system is described by the following state-space equations [24]:

$$\begin{cases} \dot{x} = F(x) + G(x, V_e) T_R \\ y = S(x) \end{cases} \quad (16)$$

where the matrices F and G are given by:

$$F(x) = \begin{bmatrix} -\frac{r_L}{L} i_L - \frac{1}{L} V_C \\ \frac{1}{C} i_L - \frac{1}{RC} V_C \end{bmatrix}, \quad G(x, V_e) = \begin{bmatrix} \frac{V_e}{L} \\ 0 \end{bmatrix} \quad (17)$$

and S(x) is the measured output function known as the sliding variable. The general form of S(x) is given as follows [25]:

$$S(x) = \left(\frac{d}{dt} + \lambda_x \right)^{r-1} e(x) \quad (18)$$

It is the first convergence condition which permits dynamic system to converge towards the sliding surfaces. It is a question of formulating a positive scalar function $V(x) > 0$ for the system states variables which are defined by the following Lyapunov function [27]:

$$V(x) = \frac{1}{2} S(x)^T S(x) \quad (19)$$

$$\dot{V}(x) < 0 \Rightarrow S(x)^T \dot{S}(x) < 0 \quad (20)$$

Now, we define

$$T_R(t) = \frac{1}{2} (1 + \text{sign}(S)) = T_{Req}(t) + T_{Rn}(t) \quad (21)$$

where $TReq(t)$ and $TRn(t)$ represent the equivalent control [25] and the nonlinear switching control and:

$$\text{sign}(S) = \begin{cases} 1 & S(x) > 0 \\ -1 & S(x) < 0 \end{cases}$$

The sliding surfaces are given by the following expression:

$$S = e(V_s) + e(i_L) = V_{ref} - H_v V_s + i_{ref} - H_i i_L \quad (22)$$

and consequently, their derivatives are given by:

$$\dot{S} = E(x) + Q T_R \quad (23)$$

where $x = [i_L \quad V_C]^T$, $Q = -\frac{H_i}{L} V_e$ and

$$E = \left(\frac{H_i r_L}{L} - \frac{H_v}{C} \right) i_L + \frac{H_i}{L} V_C + \frac{H_v}{C} I_s \cdot$$

Finally, the control law is given by:

$$T_R = -Q^{-1} E(x) + K \text{sign}(S) \quad (24)$$

TABLE. I. Parameters of the Buck DC-DC converter [28]

Input voltage (V)	15 ÷ 50
Switching frequency (Hz)	2.5 * 10 ³
Inductance (H)	20 * 10 ⁻³
Output capacitor (µF)	47
r_L (Ω)	0.022
r_C (Ω)	0.022
Load resistance (Ω)	12 ÷ 35

ACKNOWLEDGMENT

This work was supported by MESRS (*Ministère de l'Enseignement Supérieure et de la Recherche Scientifique*) under the supervising of the CNEPRU, www.cnepru-mesrs.dz.

REFERENCES

- [1] Allag, A. Hadri Hamida, S. M. Mimoune, S. Zerouali and M. Féliachi, "Power Loss Analysis In High Frequency Quasi Resonant DC Link Power Conversion For Induction Heating Application", AMSE Journals, vol. 79, no. 2, pp. 73-84, France, Mai, 2006.
- [2] Hadri-Hamida, A. Allag, et all., "Adaptive Nonlinear Control of a Passively Clamped Two Switch Quasi Resonant DC Link Converter", International Journal of Applied Electromagnetic and Mechanics, vol. 25, no. 1-4, pp.537-542, ISEM, IOS Press, 2007.
- [3] Hadri-Hamida, A. Allag, et all., "A Nonlinear Adaptive Backstepping Approach Applied to a Three Phase PWM AC-DC Converter Feeding Induction Heating", ELSEVIER Journals, CNSNS, vol. 14, no. 4, pp. 1515-1525, 2009.
- [4] K. Tse and K. M. Adams, "Quasi-Linear Modeling and Control of DC/DC converters", IEEE Trans. in PE, vol. 7, no. 2, Apr. 1992, pp. 315-323.
- [5] Middlebrook, R. D. and Cuk, S., "A general unified approach to modelling switching converter power stages", IEEE PE Specialists Conference, pp. 521-550, 1977.
- [6] H. Nayfeh and B. Balachandran, Applied Nonlinear Dynamics. New York: Wiley, 1995.
- [7] Middlebrook, R. D. and Cuk, S., "A general unified approach to modelling switching dc

- to dc converters in discontinuous conduction mode”, IEEE PE Specialists Conference, pp. 36-57, 1977.
- [8] Lee, F. C., Modeling, analysis, and design of PWM converter, Virginia Power Electronic Center Publications Series, vol. 2, Blacksburg, Virginia, 1990.
- [9] Alfayyumi, M., Nayfeh, A. H., et al., 1999, “Input filter interactions in dc-dc switching regulators”, IEEE Power Electronic Specialists Conference, pp. 926-932.
- [10] Mazumder, S. K., Nayfeh, A. H., et al., “Theoretical and experimental investigation of the fast- and slow-scale instabilities of a dc-dc converter”, IEEE Transactions on Power Electronics, 2001, vol. 16, no. 2, pp. 201-216.
- [11] S. Maity, D. Tripathy, et al., “Bifurcation Analysis of PWM-1 Voltage- Mode-Controlled Buck Converter Using the Exact Discrete Model”, IEEE Transactions on Circuits and Systems, 2007, vol. 54, no. 5, pp. 1120-1130.
- [12] E. H. Abed, H. O. Wang, and A. Tesi, Control of bifurcations and chaos, The Control Handbook (W. S. Levine, ed.), CRC Press & IEEE Press, Boca Raton, FL, 1995, pp. 951-966.
- [13] S. Wiggins: Introduction to applied nonlinear dynamical systems and chaos. Springer-Verlag, New York, 1990.
- [14] S. Wiggins, “Global Bifurcations and Chaos”, Springer-Verlag, 1988.
- [15] H. O. Wang, D. S. Chen and L. G. Bushnell, “Dynamic Feedback Control of Bifurcations”, in Proc. IEEE Decision and Control Conf., 2000, pp. 1619–1624.
- [16] K. Tse, “Flip Bifurcation and Chaos in Three-State Boost Switching Regulators”, IEEE Transactions on Circuits and Systems, 1994, vol. 41, no. 1, pp. 16-23.
- [17] Shuang Li , Zhixin Wang & Guoqiang Wang (2013) Proportional-integral-differential Neural Network Based Sliding-mode Controller for Modular Multi-level High-voltage DC Converter of Offshore Wind Power, Electric Power Components and Systems, 41:4, 427-446, DOI: 10.1080/15325008.2012.749553.
- [18] K. Ramash Kumar & S. Jeevananthan (2012) Analysis, Design, and Implementation of Hysteresis Modulation Sliding-mode Controller for Negative-output Elementary Boost Converter, Electric Power Components and Systems, 40:3, 292-311, DOI: 10.1080/15325008.2011.631085.
- [19] Madhulika Das, Chitrlekha Mahanta, "Optimal second order sliding mode control for nonlinear uncertain systems", ISA Transactions, Volume 53, Issue 4, July 2014, Pages 1191-1198.
- [20] V. I. Utkin, K. K. D. Young. Methods for constructing discontinuity planes in multidimensional variable structure systems. Automatic Remote Control, 1978, 39: 1466 – 1470.
- [21] Hadri-Hamida, A. Ghoggal, and S. Zerouali, “Bifurcation analysis of a Buck DC–DC converter applied to distributed power systems”, International Journal of System Assurance Engineering and Management, SPRINGER Journals, Sweden, vol. 5, no. 3, pp. 307-312, 2014.
- [22] Mohamed Benbouzid, Brice Beltran, Yassine Amirat, Gang Yao, Jingang Han, Hervé Mangel, "Second-order sliding mode control for DFIG-based wind turbines fault ride-through capability enhancement", ISA Transactions, Volume 53, Issue 3, May 2014, Pages 827-833.
- [23] Hadri Hamida, “Higher-Order Sliding Mode Control Scheme with an Adaptation Law for Uncertain Power DC–DC Converters”, Journal of Control, Automation and Electrical Systems, Springer Journals, vol. 26, no. 2, pp. 125-133, April 2015.
- [24] S. Mondal, C. Mahanta, “Adaptive integral higher order sliding mode controller for uncertain system”, Journal of Control Theory Appl. CAS and Springer-Verlag Berlin Heidelberg, vol. 11 (1) pp. 61–68, 2013.
- [25] Utkin V. I., "sliding mode in control and optimization", Springer –Verlag, Berlin, 1992.
- [26] Zhankui Song, Kaibiao Sun, "Adaptive backstepping sliding mode control with fuzzy monitoring strategy for a kind of mechanical system", ISA Transactions, Volume 53, Issue 1, January 2014, Pages 125-133.
- [27] V. Utkin, J. Guldner, and J. X. Shi, Sliding Mode Control in Electromechanica Systems. London, U.K.: Taylor and Francis, 1999.
- [28] Hadri Hamida, “ Contribution à l'analyse et à la commande des convertisseurs DC-DC parallèles à PWM ”, PhD Thesis, University of Biskra, Algeria, April, 2011.

Validation of Operating Temperature Models of PV Module for a Grid Connected PV System under Desert Climates of Algeria

Rachid DABOU¹, Farid BOUCHAFAA², Nordine SAHOUANE¹,
Abderrezzaq ZIANE¹, Ammar NECAIBIA¹, Ahmed BOURAIYOU¹, Seyfallah
KHLIFI¹ and Abdelkarim ROUABHIA¹

¹ Unité de Recherche en Energies Renouvelables en Milieu Saharien, URERMS,
Centre de Développement des Energies Renouvelables, CDER, 01000, Adrar, Algeria,
dabourachid@gmail.com and dabourachid@urerms.dz

² USTHB, LINS Lab, Faculty of Electronics and Computers, PO.Box 32, Bab-Ezzouar, Algiers
at.adel.touchen@gmail.com, attari.mo@gmail.com c s.boukhenous@gmail.com

ABSTRACT

The objective of this study is to find a valid simulation model of the operating temperature of the mono-Si PV modules installed in areas with a hot desert climate such as Adrar, this temperature influences the efficiency of the PV conversion, and that depends on ambient temperature, solar irradiation and wind speed. The choice of the thermal model potentially influences the results of the simulation and the modeling of the PV performance. In this analysis, we adjusted and assessed four thermal models already existing in the literature to the measurements made in this region. The measured data of weather, power output (DC et AC) and PV module temperature are collected from the monitoring system of 1.75 kWp PV plant installed and connected to the local electrical network. The resulting model providing the best fit to the measured data with RMSE of 2.46% and R^2 of 0.973. This model can be used for the prediction of the temperature of the PV module, and as a valid model in the simulation software with different types of climate. This contribution aims to provide validated thermal models for simulation and prediction better adapted to local conditions in Adrar.

Key Words: Hot desert climate, operating temperature, PV module, Simulation and prediction, validation.

1. INTRODUCTION

The operation performance of a PV station is influenced by several factors, and especially the conversion efficiency of the PV module, which can be affected by different PV technology [1], by different tilt angle of PV array [2], by accumulation of dust on the photovoltaic panels [3], by partial shading on PV module [4], and by variation of meteorological conditions [5]. but the factor which has important influence on the efficiency is PV module temperature, in this reason, the many work of research are interested to develop the thermal model to estimate the PV module temperature [6], which are based on the explicit and implicit correlations between the PV module temperature and the weather parameters [7].

This paper presents the evaluation and the validation of operating PV temperature models found in the literature, based on weather and module temperature data monitoring of grid connected PV station, which installed in region with a hot desert climate such as Saharian of Algeria (Adrar). The selection of thermal model is based on best fit to the measured data with the comparison of the fit coefficients (R^2 , RMSE).

2. METHODS AND MATERIALS

Details of location, PV system and monitoring tools

The 1.75 kWp grid-connected PV systems mounted on the roof of unit research in renewable energy in southwest of Algeria (Adrar). This region is characterized by low humidity rate, high solar insolation potential and high ambient temperature in the summer, which is classified as hot desert climate BWh according to climate classification of Köppen [8]. The PV station comprises a PV array of 1.75 kWp, which is composed of 10 SHARP (NT-R5E3E) mono-crystalline silicon PV modules connected in series (see Fig. 1), this PV array feed the FRONIUS IG 15 PV inverter. The details of PV module and array are shown in Table I.



Fig. 1. The 1.75 kW of PV array installed in the roof of URERMS, Adrar.

TABLE I.
PV modules and array specifications

PV module/array	Specification
Type	Mono-crystalline silicon
Module efficiency	13.5%
Maximum power (P_{max})	175 W
Maximum power voltage (V_{pm})	35.4 V
Maximum power current (I_{pm})	4.95 A
Open circuit voltage (V_{oc})	44.4 V
Short circuit current (I_{sc})	5.4 A
Output power tolerance	-5% / +10%
Maximum system voltage (V_{dc})	1000 V
Temperature coefficient of P_{max}	-0.485 %/C°
Module area	1.3 m ²
No. of modules	10
NOCT	47.5 C°

Fig. 2 show the PV inverter, electric meters, DC and AC sensors of voltage and current and breakers installed in electrical cabinet. Table II presents the technical characteristics of the FRONIUS IG inverter.



Fig. 2. View of PV Inverter, conditioning circuits, electric meters and circuit breakers

TABLE II.
Fronius IG 15 inverter specifications

Inverter	Specification
Maximum dc power	2000 W
Maximum dc voltage	500 V
PV – voltage range at MPPT	150 – 400 V
Maximum dc current	10.75 A
Maximum ac power	1500 W
Nominal ac power	1300 W
Nominal ac voltage	230 V / 50 Hz
Nominal ac current	5.7 A
Maximum Efficiency	94.2%
Euro-efficiency	91.4%
Admissible ambient temperature	-20 – 50 C°

The data measurements are recorded on 1 min intervals and collected from the monitoring system over a two-year period, starting from 2014. The measurements of in-plan solar irradiance, module temperature, outputs DC\AC voltage and current are performed by the Fluke Hydra 2635A data logger, and the weather station New Energy Algeria (NEAL) is utilized for the measurement of ambient temperature, wind speed, global horizontal irradiance, diffuse horizontal irradiance and direct normal irradiance, which stored with intervals of 1 min. On the left of Fig. 3, presents the pyranometer sensor mounted in-plan of PV array, and right of Fig. 3, shows the module temperature sensor installed on back of PV array.

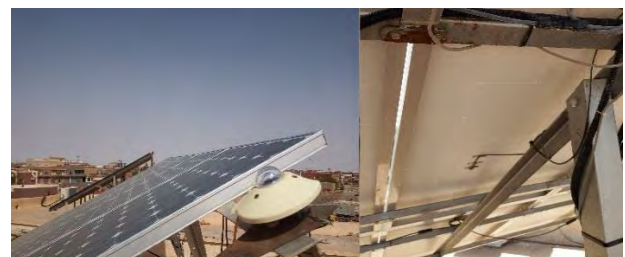


Fig. 3. View of pyranometer, module and ambient temperature sensors disposed on PV array.

Methodology

Several works of research interested to the study and modeling of PV solar module operating temperature [9] [10] [11] [7] because it is one of the key factors that affect its conversion efficiency and it is strongly affected by the surrounding conditions, so we have validated thermal modeling quads to the data collected by the module temperature sensor. The mathematical models developed in this work were obtained from the models existing in literature and adjust to the experimental data of the temperature of the PV module. The equation used for each mathematical model was chosen from among several possibilities available in the "Origin Lab" software that best corresponds to the experimental data.

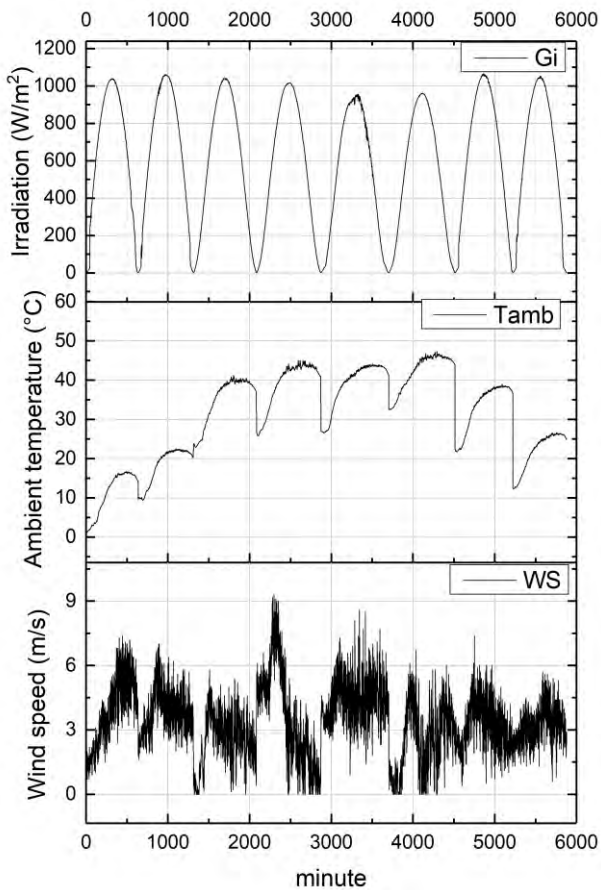


Fig. 4. Evolution of the climatic parameters during the PV station operation over the eight days with clear sky.

The coefficients of these thermal models are determined experimentally by using linear regression, we used the measured data of eight days with clear sky and without defects, including two days of each season of the year 2015 which are indicated on the Table III and the evolution of the climatic parameters of these days is presented in Fig.

4. These data are used to simulate the healthy operation of the PV system.

TABLE III.
Selected days with clear sky and without defects to simulate the case of the functioning of pv system

Season	Winter	Spring	Summer	Fall
Days	01/01/2015 14/02/2015	20/04/2015 04/05/2015	30/06/2015 27/07/20015	05/10/2015 12/11/2015

The input parameters of the PV module thermal model are GI radiation, Tam ambient temperature, and WS wind speed. The mathematical model function, the reference of the corresponding original works, and the linear adjustment coefficients (R^2 , RMSE) are listed in Table IV. The thermal model providing the lower root mean square errors (RMSE) and higher coefficient of determination (R^2) is selected for the final model validation.

TABLE IV.
PV module temperature models to validate

Model	Mathematical function	Reference
Tm11	$T_{am}+a*GI+b*WS+c$	[11]
Tm12	$a*T_{am}+b*GI*(c+\exp(d.-e*WS))$	[12]
Tm13	$a*T_{am}+b*GI-c*WS-d$	[13]
Tm14	$a*T_{am}+(b+c*T_{am}+d*GI*(1-nc))/(e+f*WS)$	[9]

3. RESULTS AND DISCUSSIONS

The thermal models are however modified for a better correlation to the measurements, the determined coefficients of the thermal models and the fit coefficients (R^2 , RMSE) are listed in Table V. The fit curves of the thermal models Tmxx to the measured temperature Tm.mes of PV module are presented in Fig. 5. In model Tm14 function, the PV conversion efficiency (nc) is used.

TABLE V.
Validate determination of the coefficients of thermal model for pv module

MODEL	MATHEMATICAL FUNCTION	R^2	RMSE
TM11	$1,017*[0,023*GI+T_{AM}-1,46*WS+1,88]-1,441$	0.961	2.99%
TM12	$1.034*[T_{AM}+GI*(0.003+\exp(-3.7-0.09*WS))-2.5]-1.473$	0.973	2.47%
TM13	$1.022*[1.04*T_{AM}+0.021*GI-0.9*WS-6*0.135]-0.856$	0.969	2.65%
TM14	$1,017*[T_{AM}-3+(1,3*T_{AM}+GI*(1-0,135))/(35+1,7*WS)]-1,336$	0.973	2.46%

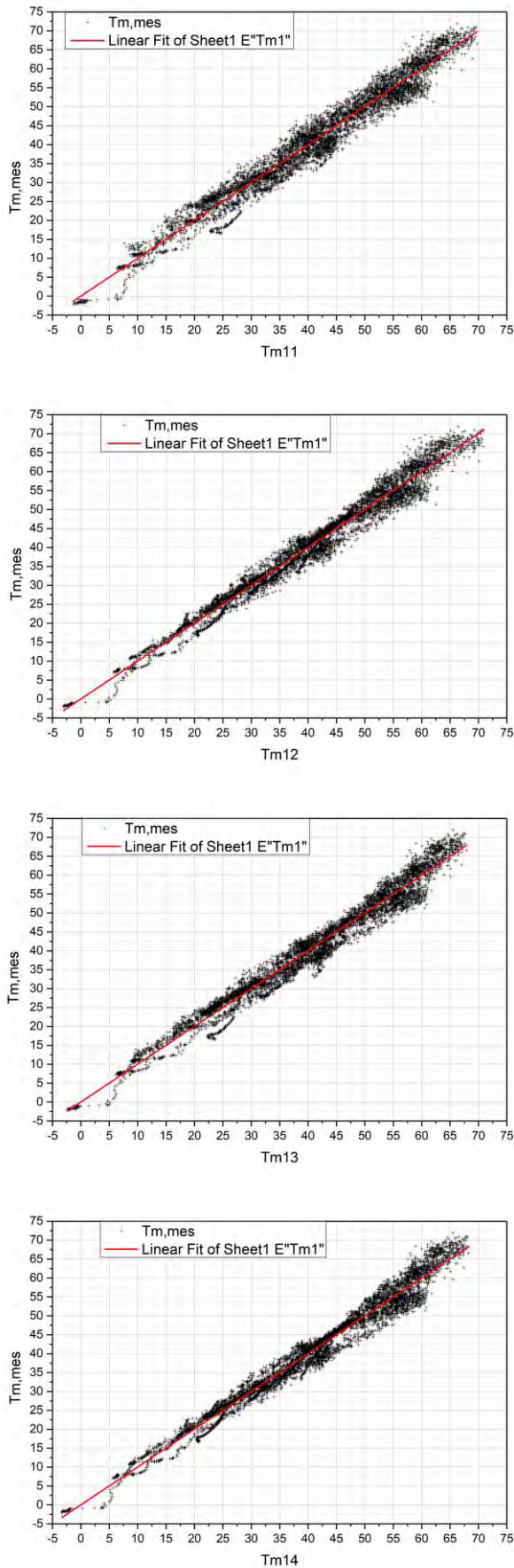


Fig. 5. Measured temperature $T_{m,mes}$ of PV module and fit curves of the thermal models T_{mxx} .

The comparison between the thermal models is based on R^2 and RMSE. The T_{m14} model is based on the Schott model, provides the highest R^2 and the lowest RMSE. The fit of T_{m12} model based on the "Sandia" model also gives a better fit in terms of R^2 and RMSE compared to T_{m11} and T_{m13} which are based on the Risser and Duffie models respectively. From the data presented in Table 8, the R^2 and RMSE values for the four models are better than those already found by [9].

The evolution curves of the temperature models T_{mxx} with respect to the measured temperature $T_{m,mes}$ are presented in Fig. 6. The four thermal models of T_{mxx} used for the prediction of the temperature of the PV module have a good correlation with the measured data, and that can be used as a valid model in the simulation software. The objective of this analysis is to offer validated thermal models for photovoltaic modules deployed in the Adrar region.

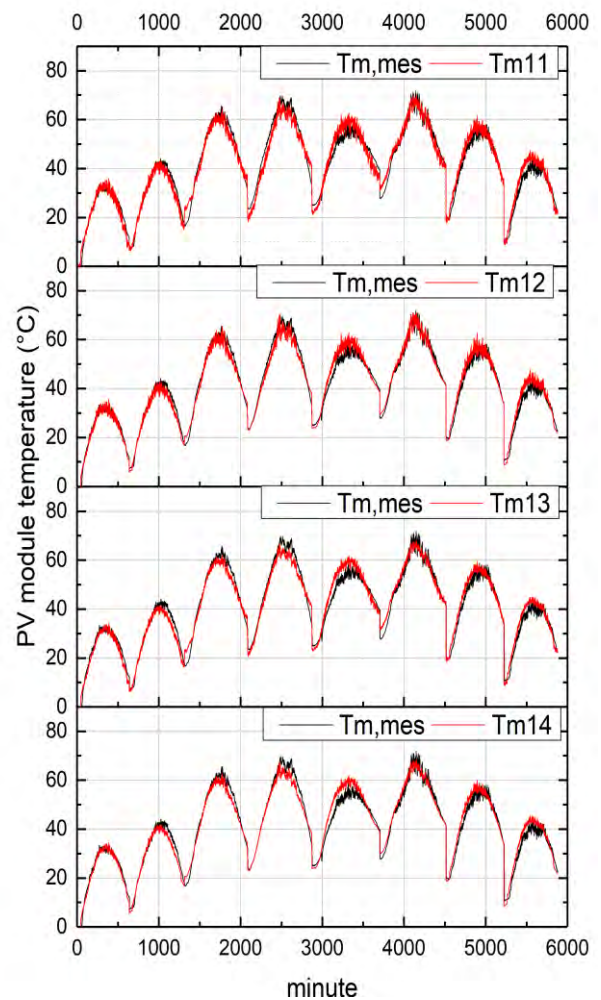


Fig. 6. Curves of the temperature models T_{mxx} compared to the measured temperature of PV module.

4. CONCLUSION

The PV module temperature is key factor, which has big influence on the efficiency of the PV conversion, In this work, we were interested to find a valid model of the operating temperature of mono-Si PV module for a grid connected PV station, which installed in hot desert climate region such as south west of Algeria (Adrar), we used the four thermal models found in the literature to estimate temperature of PV module, the ambient temperature, the incident irradiance and the wind speed are input variable for these thermal models. The selected thermal model is based on the comparison of the fit coefficients (R^2 , RMSE). The Tm14 model was chosen, which is based on the Schott model, gave a lower RMSE of 2.46% and higher R^2 of 0.973. The obtained model can be used in the simulation and prediction software of the operating temperature of the PV module.

REFERENCES

- [1] S. Edalati, M. Ameri, and M. Iranmanesh, "Comparative performance investigation of mono- and poly-crystalline silicon photovoltaic modules for use in grid-connected photovoltaic systems in dry climates," *Appl. Energy*, vol. 160, pp. 255–265, 2015.
- [2] E. M. Saber, S. E. Lee, S. Manthapuri, W. Yi, and C. Deb, "PV (photovoltaics) performance evaluation and simulation-based energy yield prediction for tropical buildings," *Energy*, vol. 71, pp. 588–595, 2014.
- [3] Z. Abderrezzaq, M. Mohammed, N. Ammar, S. Nordine, D. Rachid, and B. Ahmed, "Impact of dust accumulation on PV panel performance in the Saharan region," in *18th international conference on Sciences and Techniques of Automatic control & computer engineering - STA'2017*, 2017, pp. 471–475.
- [4] R. Dabou, N. Sahouane, A. Neçaibia, M. Mostefaoui, F. Bouchafaa, A. Rouabhia, A. Ziane, and A. Bouraiou, "Impact of partial shading and PV array power on the performance of grid connected PV station," in *18th international conference on Sciences and Techniques of Automatic control & computer engineering*, 2017, pp. 476–481.
- [5] R. Dabou, F. Bouchafaa, A. Hadj Arab, A. Bouraiou, M. D. Draou, A. Neçaibia, M. Mostefaoui, "Monitoring and performance analysis of grid connected photovoltaic under different climatic conditions in south Algeria," *Energy Convers. Manag.*, vol. 130, pp. 200–206, 2016.
- [6] I. Santiago, D. Trillo-Montero, I. . Moreno-Garcia, V. Pallarés-López, and J. J. L.-R. Universidad, "Modeling of photovoltaic cell temperature losses: A review and a practice case in South Spain," *Renew. Sustain. Energy Rev.*, vol. 90, pp. 70–89, 2018.
- [7] E. Skoplaki and J. A. Palyvos, "Operating temperature of photovoltaic modules: A survey of pertinent correlations," *Renew. Energy*, vol. 34, pp. 23–29, 2009.
- [8] "Climat Adrar (Algérie)." [Online]. Available: [https://fr.wikipedia.org/wiki/Adrar_\(Algérie\)#Climat](https://fr.wikipedia.org/wiki/Adrar_(Algérie)#Climat). [Accessed: 16-Aug-2017].
- [9] A. Tuomiranta, P. Marpu, S. Munawwar, and H. Ghedira, "Validation of thermal models for photovoltaic cells under hot desert climates," *Energy Procedia*, vol. 57, pp. 136–143, 2014.
- [10] C. Y. Huang, H. J. Chen, C. C. Chan, C. P. Chou, and C. M. Chiang, "Thermal Model Based Power-Generated Prediction by Using Meteorological Data in BIPV System," in *Energy Procedia*, 2011, vol. 12, pp. 531–537.
- [11] R. Rawat, S. C. Kaushik, and R. Lamba, "A review on modeling, design methodology and size optimization of photovoltaic based water pumping, standalone and grid connected system," *Renew. Sustain. Energy Rev.*, vol. 57, pp. 1506–1519, 2016.
- [12] D. L. King, W. E. Boyson, and J. A. Kratochvil, "Photovoltaic array performance model," 2004.
- [13] G. Tamizhmani, L. Ji, Y. Tang, L. Petacci, and C. Osterwald, "PHOTOVOLTAIC MODULE THERMAL/WIND PERFORMANCE: Long-Term Monitoring and Model Development For Energy Rating," in *NCPV and Solar Program Review Meeting*, 2003, pp. 936–939.

The Response of Different Hydrogen Liquids to the Resonance in a Nanophotonic Structure of an Optical Channel Based on Two-dimensional Photonic Crystal Ring Resonator

Mehdi GHOUMAZI¹, Abdesselam HOCINI²

^{1,2}Laboratory of Signal Analysis and Systems, Department of Electronics, Faculty Of Technology, Mohamed Boudiaf University of M'Sila, Bp.166, Route Ichbilia, M'sila 28000, Algeria.

mghoumazi@gmail.com, hocini74@yahoo.fr

¹Research Unit in Optics and Photonics (UROP-Sétif), Advanced Technologies Development Center (CDTA), Cité 20 Aout 1956 Baba Hassen, Algiers, Algeria

mghoumazi@gmail.com

ABSTRACT

In this work, we proposed a new structure of an optical channel on 2D photonic ring resonator. We studied three kinds of hydrogen liquids at resonance, such Hydrogen (H₂), Hydrogen cyanide (HCN) and Hydrogen disulfide (H₂S). The structure is composed of dielectric rods immersed in air. Also, we presented as numerical results of the band gap (TE & TM) by using plane wave expansion method (PWE). The electric field distribution of the each hydrogen liquids at the resonance, the meshing structure, the repartition of the refractive index and the total energy density (TED) are extracted by using the finite element method (FEM) with the help of COMSOL software. At different wavelength, we had different resonance and this due to refractive index of hydrogen liquids used of H₂, HCN and H₂S: 1.1096, 1.26136 and 1.460 respectively. Only the radius (r) of the rods and the lattice constant (a) are fixed at 205.625nm and 0.875 μ m respectively.

Key Words: Hydrogen liquids, Photonic crystals, Ring resonators.

1. INTRODUCTION

Hydrogen is the most plentiful element in the universe [1] and promising sustainable, secure, and clean alternative energy carrier as the environmental pollution and depletion of fossil fuels become more and more serious [2]. Hydrogen is an energy carrier that has the following properties: similar to electricity [3,4], flexible and scalable, high energy capacity [5], and can be used in fuel cell form green hydrogen to produce energy and heat cleanly and efficiently in a wide range of power generation and transportation in portable and stationary applications [5].

Currently, in order to be able to produce hydrogen, the solution is to steam-reform fossil fuels such as coal and natural gas [6]. In return, the main disadvantage of its fossil fuels is global warming, environmental pollution and because of the latter, it is necessary to produce hydrogen from renewable sources such as biomass (agricultural wastes, municipal wastes, algae etc.), biogas, renewable energy (wind and solar etc.), nuclear energy [1].

This paper aims to use hydrogen in the form of three form liquids which are H₂, HCN and H₂S for detection in the field of

optics and photonics and more particularly in photonic crystal-based structures.

Since 1987, a new study and research has been created for optical and physical researchers in photonic crystals [7]. Photonic crystals have a special wavelength (frequency) range in which the propagation of optical waves inside these artificial structures is forbidden. This special range is called photonic band gap (PBG) [8, 9]. Basis of photonic crystals based on internal change in refractive index to more or less within a crystal [10]. Due to the remarkable importance of the PBG, many applications of photonic crystals depend on their PBG's properties [11, 12].

By creating unrighteousness (point line) in a periodic structure different optical devices based on PCs can be developed, they include, optical filters [13], optical converters [14], optical switches [15], optical waveguides [16], ring resonators [17], optical power dividers [18] optical sensors [19]. We created a ring shape inside the photonic crystals.

Over the last decades, a group of researchers such David, Abrishamian, Mehdizadeh et al, studied the effect of several parameters such as refractive index of dielectric rods and so on...which are important parameters for tuning the filter [7]. In our work, we will study three hydrogen liquids of H₂, HCN and H₂S with refractive index of 1.1096, 1.26136 and 1.460 respectively in 2D photonic crystal ring resonator by using finite element method (FEM).

2. DESIGN AND PROEDURE

Two numerical methods are used to extract the photonic band gap (PBG), the electric field distribution at resonance and the total energy density for different hydrogen liquids (H₂, HCN and H₂S) by using plane wave expansion method (PWE), finite element method (FEM) and designed by COMSOL software. In this work, we have used a ring resonator with two waveguides to design an optical filter; one guide is horizontal bus, created by removing a complete row of dielectric rods in the Γ -M direction and the second is perpendicular

output waveguide created by removing some rods in the M-X direction figure.3.



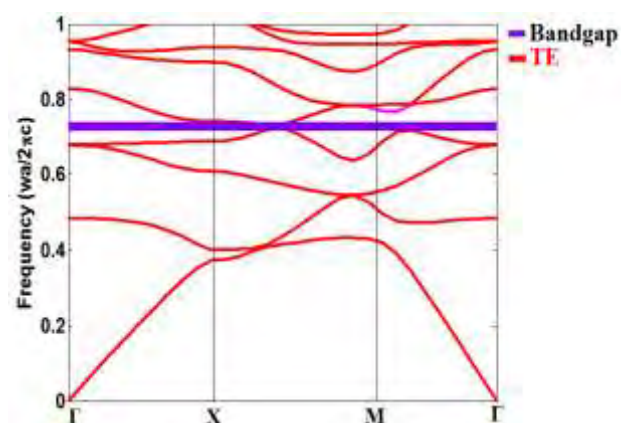
Figure.1: Hydrogen, hydrogen cyanide and hydrogen sulfide

The structure is a two dimensional photonic crystal composed of 31X24 square lattice of dielectric rods immersed in air. The refractive index of the rods is taken to be 3.46 and for the air background is 1 with lattice constant $a=0.875\mu\text{m}$. The radius of rods of perfect PC (with no defects) is $r=0.235a$.

By solving Maxwell's Equations, we studied electromagnetic wave propagation in a photonic crystal structure where following form for magnetic field is given by [12, 20]:

$$\nabla \times \left(\frac{1}{\epsilon(\vec{r})} \nabla \times H(\vec{r}) \right) = \left(\frac{\omega}{c} \right)^2 H(\vec{r}) \quad (1)$$

c is the speed of light in vacuum, ω is the angular frequency, and $\epsilon(\vec{r})$ is the relative permittivity of material. (xy) plane represent the light propagation of the square lattice structure. The PBGs of the Phc with aforementioned values is depicted in figure.2. In the next part of work, the simulations are adapted to our structure of an optical channel drop filter based on 2D photonic crystal ring resonator.



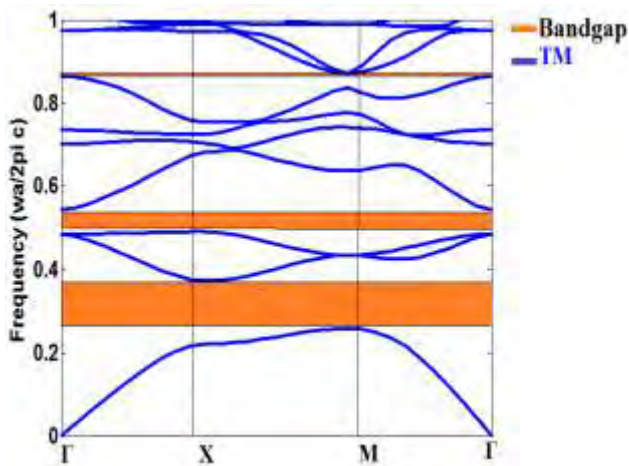


Figure.2: The band structure of TE & TM for the proposed structure

Figure.2, displays four PBGs, one for TE mode (purple zone) and three for TM mode (brown zone). The TE PBGs range ' a/λ ' goes for the largest TM PBG from 0.2582 to 0.3731 and the medium PBG from 0.4898 to 0.5446 and the smallest PBG from 0.8363 to 0.8718. The TE PBGs have one range ' a/λ ' that goes from 0.7241 to 0.7322. We took the largest PBG in TM mode which is large enough for covering the sufficient wavelengths for optical communication applications. In order to have maximum compatibility with optical communication ranges, we took $a = 875\text{nm}$ where the study will be in $2345\text{nm} < \lambda < 3388\text{nm}$ range in TM mode.

As explained above, to realize the proposed filter in a fundamental platform, we removed a complete row of dielectric rods in the Γ -M direction, and some rods in the M-X direction we created the bus waveguide and the output waveguide respectively. Next step is creating resonant ring between bus waveguide and the output waveguide, first we removed from a 9X9 array of dielectric rods at the appropriate place some rods for creating a ring shape. This shape is created by 16-fold quasi crystal which is quasi-periodic structure and composed of one central air pore as core rod. The radius of the ring form is the same as the radius of all other rods in the initial Pc structure. The final schematic diagram of the proposed filter is depicted in Figure.2.

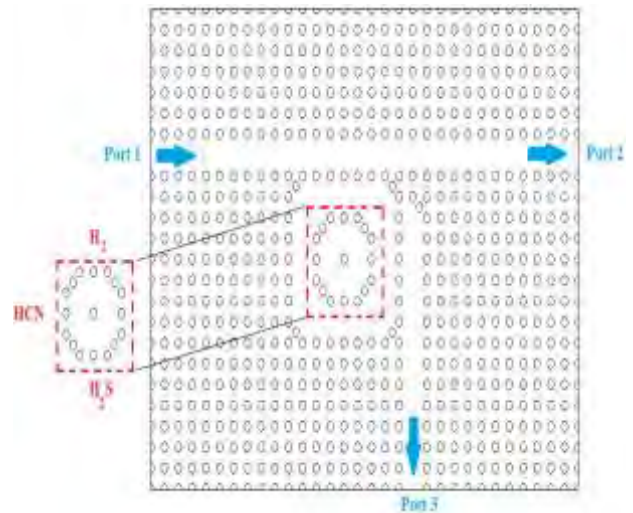


Figure. 3: The final sketch of our structure

From our design structure, we have got three ports: The port of entry: port (1), the output waveguide: port (2) and also called forward transmission terminal and the port (3) of waveguide is denoted as forward dropping (see Figure.3).

The path that takes the optical waves in the structure is from the entrance of the port (1) to the output of the port (2), but it turns out that for a desired wavelength the optical wavelengths drop to drop waveguide through the resonant ring and travel toward port (3).

The frame shape surrounding the ring has the same radius and refractive index as the initial structure. Also, the refractive index of the ring inside the resonator has been changed for different hydrogen liquids such as H_2 , HCN and H_2S . The refractive index rods changed are labelled with red circle as shown in figure.3.

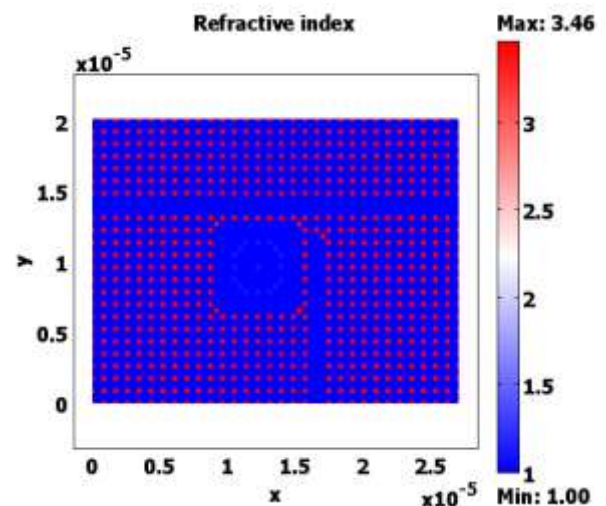


Figure. 4: The distribution of the refractive index in the proposed structure

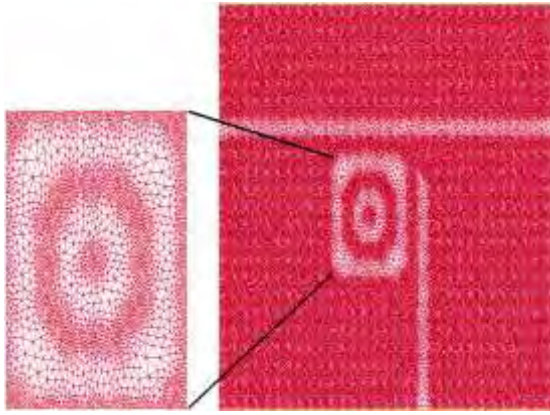


Figure. 5: The proposed structure with mesh

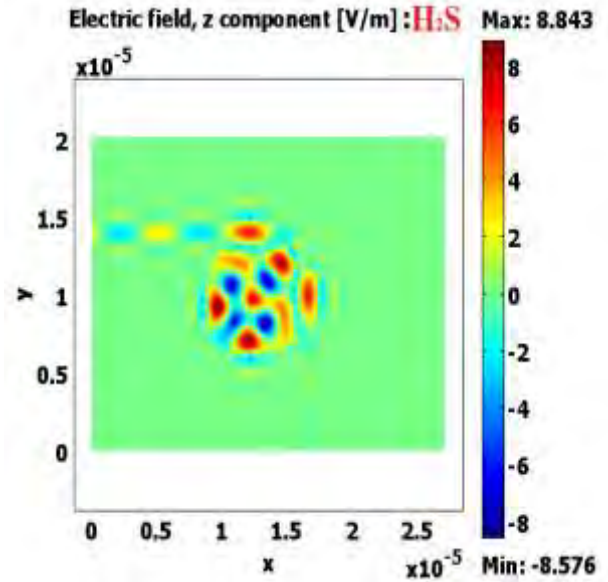
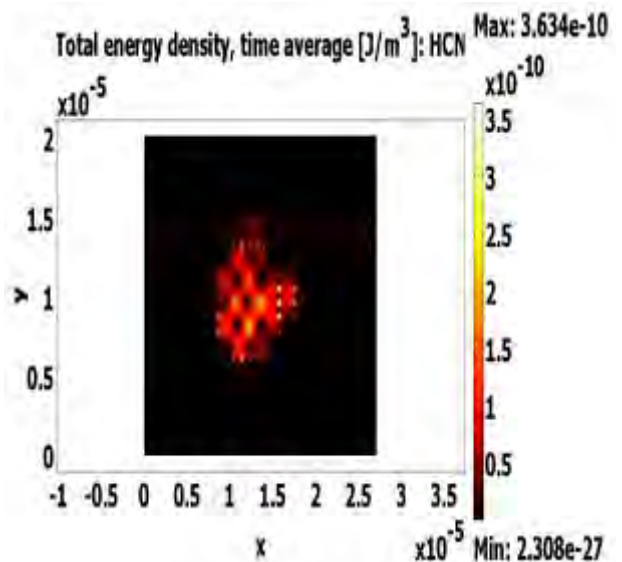
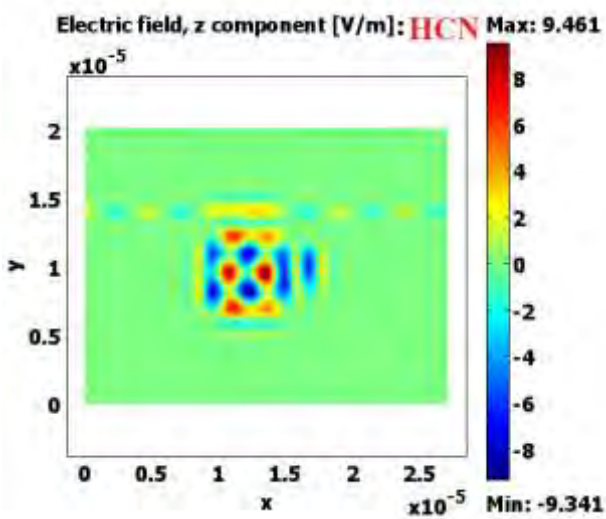
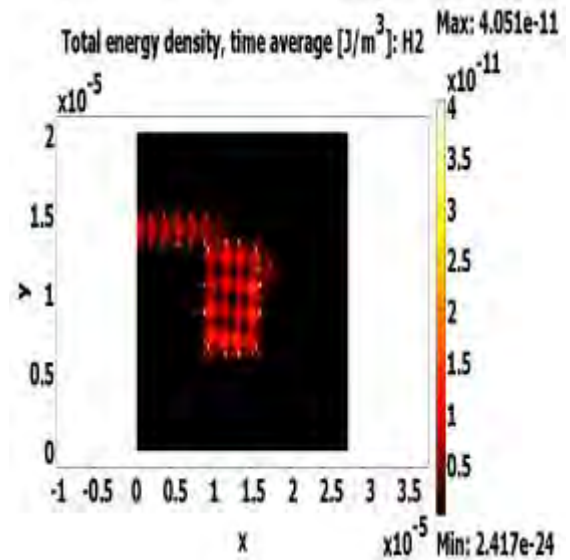
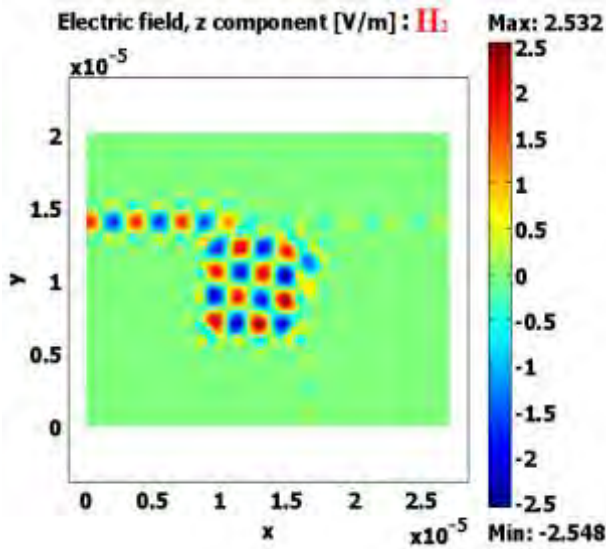


Figure.6 : The field distribution for different refractive index of: H₂, HCN, and H₂S at different resonance wavelengths.



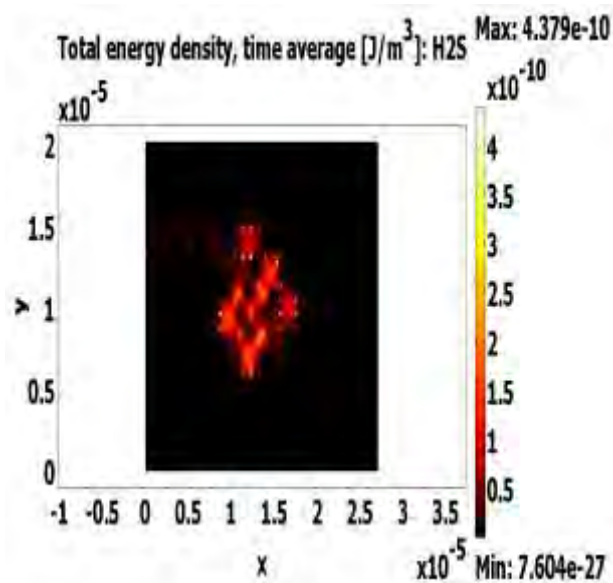


Figure7: Total Energy Density for different refractive index of: H₂, HCN, and H₂S at different resonance wavelengths.

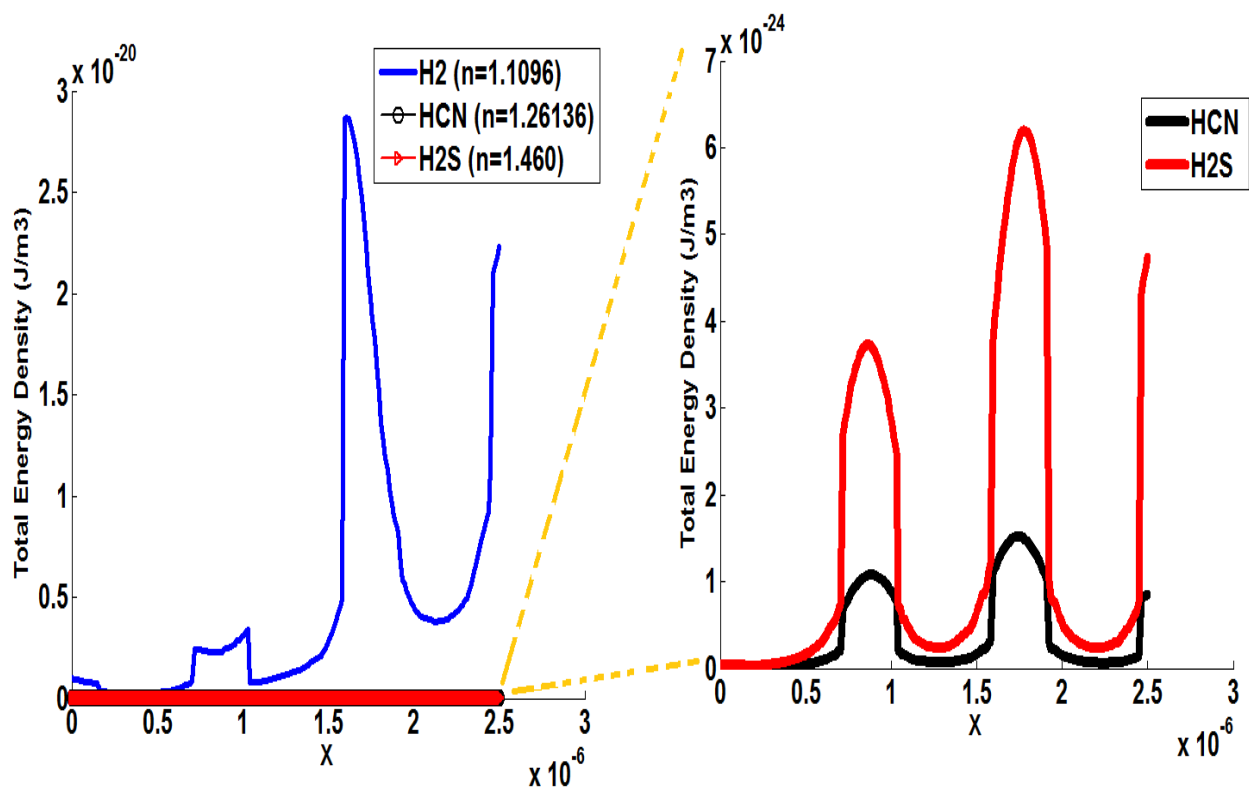


Figure. 8: Total Energy Density for different refractive index of: Hydrogen (H₂), Hydrogen Cyanide (HCN) and Hydrogen sulfide (H₂S)

3. SIMULAION AND RESULTS

We were able to extract our numerical results thanks to the finite element method which is the basis of COMSOL software [21].

In this study, we show the distribution of the refractive index in the whole of structure. Then, the electric field distribution and the total energy density for different refractive index of hydrogen liquid such as: Hydrogen (H₂), Hydrogen Cyanide (HCN), and Hydrogen sulfide (H₂S) at different resonance wavelengths. Besides, the total Energy density versus line cross section for H₂, HCN and H₂S and finally, by displaying the total energy density versus the refractive index of: H₂, HCN and H₂S. This whole study is in a two-dimensional square lattice structure based on photonic crystals and the plane of propagation of the electromagnetic wave is (xz).

Figure. 4 shows the distribution of the refractive index along the structure for different materials used in this study such as, Air with its index of 1 and silicon of 3.46 as well as the three hydrogen liquids such as

H₂, HCN and H₂S with indices of 1.109, 1.26136 and 1.460 respectively. In addition, Figure. 5 gives us an overview of the mesh of the proposed structure.

Figure.6 and Figure.7 show the propagation of the electric field and the total energy density for different hydrogen liquids (H₂, HCN and H₂S) at the resonant wavelengths which are 2441.2nm, 2688.6nm and 2783.78nm, respectively.

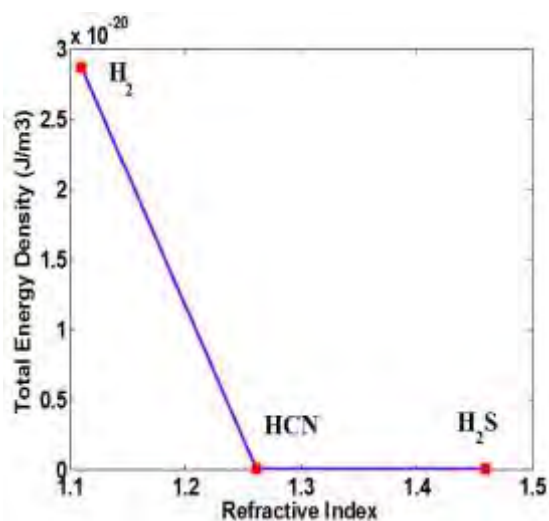


Figure. 9: The Total Energy Density versus refractive index of: H₂, HCN and H₂S

From figure.8, it can be seen that the total energy density reaches its maximum for hydrogen (H₂) at 2.87×10^{-20} (J/m³) with a refractive index of 1.1096 as well as for hydrogen cyanide (HCN), and Hydrogen sulfide (H₂S) their maximum is 1.52×10^{-24} , 1.74×10^{-24} for a refractive index of 1.26136, 1.460 respectively. Also, we can see that there is a strong energy shift of 104 J / m^3 between hydrogen (H₂) and the two other hydrogen's which are closer to each other, which means that the total energy density of Hydrogen is more important than HCN and H₂S. So, the last figure.9 summarizes our work by noting that liquid hydrogen is more present in terms of energy density for a low refractive index compared to hydrogen cyanide (HCN) and hydrogen sulfide (H₂S).

4. CONCLUSION

First, we proposed a channel drop filter (CDF) based on a photonic crystal ring resonator. Using the PWE plane wave expansion method, we were able to extract the band diagram for the TE and TM mode using MATLAB. COMSOL software has been used to simulate the propagation of the signal at different resonance wavelengths for the three liquids hydrogen's (H₂, HCN and H₂S). In addition, we have succeeded in presenting the distribution of the refractive index along the structure with the mesh that suits it. Also, a representation of the total energy density for different refractive indices of hydrogen liquids such as: hydrogen (H₂), hydrogen cyanide (HCN) and hydrogen sulfide (H₂S). And finally, as summary we depicted the total energy density versus the refractive index of liquids hydrogen in order to show the utility and influence of the refractive index parameter 'n' on each material uses and that can infect the resonance wavelength. The three hydrogen materials are used in liquid phase on nano-photonic structures as sensors for applications in the fields of astronautic, industry, environment and health.

ACKNOWLEDGEMENTS

The present work was supported by the Ministry of Higher Education and Scientific Research of Algeria

REFERENCES

- [1] Jinling Wu, Yanan Yin, Jialong Wong, "Hydrogen-based membrane biofilm reactors for nitrate removal from water and wastwaeter", international journal of hydrogen energy 43(2018)1-5.
- [2] Ping Liu, Jing Li, Yalin Lu, Bin Xiang," Facile synthesis of NiS₂ nanowires and its efficient ectrocatalytic performance for hydrogen evolution reaction", international journal of hydrogen energy 43(2018)72-77.
- [3] Ayegul Abusoglu, Sinan Demir, Ozahi Emrah ," Energy and economic analyses of models developed for sustainable hydrogen production from biogas-based electricity and sewage sludge," international journal of hydrogen energy xxx (2016) I-IO; <https://doi.org/10.1016/j.ijhydene.2016.05.105>.

- [4] Christos M. Kalamaras and Angelos M. Efstathiou, "Hydrogen production technologies: current state and future developments," *Conference papers in energy*. Vol 2013, Article ID 690627, 9 pages; 2013. <https://doi.org/10.1155/2013/690627>.
- [5] Alves HJ, et al., "Overview of hydrogen production technologies from biogas and the applications in fuel cells". *International Journal of Hydrogen Energy* (2010); <https://dx.doi.org/10.1016/j.ijhydene.2013.02.057>.
- [6] Montenegro Camacho YS et al., Development of a robust and efficient biogas processor for hydrogen production. Part1: Modelling and simulation, *international journal of hydrogenenergy*(2017),<https://dx.doi.org/10.1016/j.ijhydene.2017.07.147>.
- [7] Farhad Mehdizadeh, Hamed Alipour-Banaei and Somaye Serajmohamadi;" Channel- drop filter based on a photonic crystal ring resonator"; *IOP Publishing. J.opt.15* (2013) 075401(7pp).Doi:10.088/20408978/15/7/075401.
- [8] Hamed. Alipour-Banaei, Farhad Mehdizadeh, and Behnaz Amini, "All optical communications Filter based on photonic crystal Structure". *International journal of Future Computer and Communication*, Vol.4, NO, October 2015. Doi: 10.18178/ijfcc.2015.4.5.414.
- [9] A. Harhouz and A. Hocini, Design of high-sensitive biosensor based on cavity waveguides coupling in 2D photonic crystal. *Journal of Electromagnetic Waves Applications* 29 659–667 (2015). <http://dx.doi.org/10.1080/09205071.2015.1012597>.
- [10] Abolfazl Abbaspour, Hamed Alipour Banaei, Alireza Andalib, "The new Method for Optical Channel Drop Filter with High Quality Factor Based on Triangular Photonic Crystal Design", *Journal of Artificial Intelligence in Electrical Engineering*, Vol. 2, No.6 August 2013.
- [11] Skoda K., *Optical properties of photonic crystals*. Berlin: Springer; 2001.
- [12] Joannopoulos, J.D., S.G. Johnson, J.N. Winn, et al. "Photonic Crystals: Molding the Flow of Light". Princeton, NJ: Princeton University Press; 2008.
- [13] Seifouri,M., Fallahi, V., Olyae S., "Ultra-high-Q optical filter based on photonic crystal ring resonator", *Photon Netw. Commun.*2, 1-6. (2017).
- [14] Mehdizadeh Farhad, Soroosh Mohammad, Alipour-Banaei Hamed and Farshidi Ebrahim, "A Novel Proposal for All Optical Analog-to-Digital Converter Based on Photonic Crystal Structures", *IEEE Photonics Journal*, Vol.9, No.2 (2017) 4700311.
- [15] Serajmohammadi, H. Alipour-Banaei and F. Mehdizadeh, "All optical decoder switch based on photonic crystal ring resonators", *Optical and Quantum Electronics*, 47 (2015) 1109-1115. <http://dx.doi.org/10.1007/s11082-014-9967-2>.
- [16] N. Janrao, R. Zafar and V. Janyani, "Improved design of photonic crystal waveguides with elliptical holes for enhanced slow light performance", *Optical engineering*, 51 (2012) 064001-1-064001-7.
- [17] S. Arafa, M. Bouchemat, T. Bouchemat, A. Benmerkhi,A. Hocini, Infiltrated photonic crystal cavity as a highly sensitive platform for glucose concentration detection, *Opt. Commun.* 384 (2017) 93–100.
- [18] N.Mesri and H. Alipour-Banaei, "An optical power divider based on twodimensional photonic crystal structure", *Journal of Optical Communications*, 38 (2017) 129-132.
- [19] Olyae and A. Mohebzadeh-Bahabady, "Designing a novel photonic crystal nanoring resonator for biosensor application", *Optical and Quantum Electronics*, 47 (2015) 1881-1888.
- [20] Hocini Abdesselam, Harhouz Ahlam, Modeling and analysis of the temperature sensitivity in two dimensional photonic crystal microcavity. *Journal of Nanophotonics*. Vol .10(1) 016007– 016010 (2016).
- [21] COMSOL Multiphysics, 2005. www.comsol.com

Comparison Between ANN Based MPPT and P&O Under Fast and Slow Changing Atmospheric Conditions and Partial Shading

ABIDAT Redouane and BOUKHELIFA Akkila

Abstract — This paper presents a maximum power point tracking (MPPT) technique, based on an artificial neural network (ANN) with irradiation and temperature as inputs. Compared to the perturbation and observation (P&O) method for slow and rapid variations in solar radiation, and under partial shading conditions. Bias a system compound of a Photovoltaic (PV) module and DC-DC Buck-Boost converter. the system is simulated using Matlab Simulink and Simpower and the results presented shows the effectiveness of ANN method under slow and fast changing of insolation conditions. Also shows the failure of the two MPPT techniques under non-uniform shading conditions.

Index Terms — Artificial neural network (ANN), P&O, MPPT, partial shading, local maximum power point, global maximum power point.

I. INTRODUCTION

Solar energy converted to electricity bias photovoltaic systems has a negligible running cost. On the otherside, a high installation cost [1]. Photovoltaics (PV) are the most suitable economically for the energy need in the future in urban and rural areas, where the electrical network is remote [2].

On the other hand, PV energy has a big problem of reduction in power production. Due to many factors, the most significant ones are the intermittence of the irradiation, MPP, mismatch and shadowing [1]. These losses reverberate on the amount and quality of electricity produced. To reduce these effects on the efficiency of PV systems, studies proposed many maximum power point tracking (MPPT) techniques forcing the PV module to work at its MPP, therefore, extracting the maximum power that could be produced by the PV module.

We can distinguish MPPTs by their complexity, precision, speed, technology, cost and popularity [3]. In the absence of shading effects, tracking the MPP is insured by the MPPT, the swiftness of the MPPT in fast changing insolation conditions is relative to the technique in use.

First Author is with the Laboratory of Electrical and Industrial Systems, USTHB, PO.Box. 32, Bab-Ezzouar, Algiers, Phone: 213-212017669, URL: <http://www.lsei.usthb.dz>, Email: redouane.abidat@outlook.fr. Second Author is with the Laboratory of Instrumentation, USTHB, PO.Box. 32, Bab-Ezzouar, Algiers, Phone: 213-24217912 (Ext. 804), Fax: 213-21207664, URL: <http://www.lins.usthb.dz>, Email: boukhelifa.a@gmail.com.

In the presence of partial shading most of these techniques fail to track the global maximum power point (GMPP), owing to the presence of multiple peaks, by getting trapped in a local peak (LMPP) instead of the GMPP. Pushing the PV module to work abroad its maximum power.

MPPTs are classified into three types according to the technique in use, indirect: current/voltage-based methods, Look-up tables method, curve fitting method... Direct: Perturb & Observe, Incremental Conductance, Particle Swarm Optimization (PSO) based method... Artificial Intelligence (AI) based methods: Artificial Neural Network (ANN), fuzzy logic, Fibonacci Line Search (FLS), Genetic algorithms... [4].

P&O is the most renowned method. This algorithm is based on perturbing the control variable, and by collecting the output power and comparing it with the previous one, it decides in which way is going to be the next perturbation. In this way this technique reaches the MPP and continues to oscillate around it. However, P&O owns some drawbacks considering oscillations when reaching MPP and when insolation rapidly changes [3]. On the other side, MPPTs based on AI have attracted considerable attention of researchers due to the flexibility and robustness of the solution, taking example of artificial neural network. The idea of artificial neural network was developed in 1943, by Warren S. McCulloch and Walter H.Pitts, [5]. Inspired by the behavior of nervous activity (biological neural networks) submitting to the law of all-or-none. So, the neural events and relations among them can be treated by propositional logic. In the past 20 years, ANN was applied to develop software applications for different fields, to build predictive models of the process from routinely collected multidimensional database [6].

Various MPPT techniques based on ANN are found in literature, using different aproachs, like predicting the open circuit voltage [7], generating the duty cycle by measuring irradiation and temperature using the capacity of training [8], or by measuring the voltage and the current of PV module output to get the GMPP for a vehicle application [9].

This paper addresses a comparison between P&O algorithm and ANN based MPPT method, that provides the reference voltage from inputs insolation and temperature. Generating via a Buck-Boost converter,

under uniform insolation with fast and slow variation conditions, and under partial shading conditions. Matlab is used to simulate the system and the results are discussed in the end of the paper.

II. MODELLING SOLAR CELL

A PV cell is basically a diode that behaves as a current source when exposed to light. This current is produced by collecting and transporting the free charge carriers generated during the absorption of light. We can assemble cells in series and/or in parallel to get a module with desired current and voltage [1].

The standard five parameters model or single diode model [10], presented by the equivalent circuit in Fig.1, is the commonly used model.

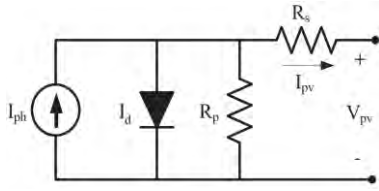


Fig. 1. Equivalent circuit of the single diode model

From this equivalent circuit, the equation of the output current is deduced and given by the equations (1) and (2);

$$I_{PV} = I_{Ph} - I_D - I_P \quad (1)$$

$$I_{PV} = I_{Ph} - I_d \left[\exp \left\{ \frac{V_{PV} - I_{PV} R_S}{V_T} \right\} - 1 \right] - \frac{V_{PV} - I_{PV} R_S}{R_P} \quad (2)$$

where, I_{Ph} is photo-generated current. I_d , reverse saturation current of the cell. $V_T = nKT/q$, thermal voltage. R_S , series resistance. R_P , parallel resistance. Are the five parameters representing I-V characteristic of the single diode model.

$$I_{Ph} = \{ I_{Ph,ref} [1 + \alpha (T - T_{ref})] \} \frac{G}{G_{ref}} \quad (3)$$

with $I_{Ph,ref} = I_{Sc,ref}$

$$I_d = I_{d,ref} \left(\frac{T}{T_{ref}} \right)^{\frac{3}{n}} \exp \left[E_g \left(\frac{1}{T_{ref}} - \frac{1}{T} \right) \right] \quad (4)$$

Where, $I_{Ph,ref}$, is photo-generated current at STC. α , current temperature coefficient. T and T_{ref} are operating temperature and STC temperature respectively. G and G_{ref} , operating irradiation and STC irradiation respectively. $I_{d,ref}$, reverse saturation current of the cell at STC. E_g , gap energy.

When a module is under partial shading conditions, the shaded cells deliver less current than the illuminated ones, and forced to operate in reverse bias to compensate the difference as presented in Fig.2. So, it leads to a power dissipation by heat and hence hotspot occurs and leads to cell destruction [16]. That is why bypass diodes are connected in anti-parallel with a string of few cell to isolate them when shaded, and prevent the hotspot effect

from destructing the cell.

The phenomenon manifesting in the partial shading conditions called the reverse breakdown voltage, in the absence of bypass diodes, is not taken into consideration in the previous model. Adding the extension term from the Bishop's model to introduce diode breakdown at high negative voltages [17]. So, equation (2) becomes,

$$I_{PV} = I_{Ph} - I_d \left[\exp \left\{ \frac{V_{PV} - I_{PV} R_S}{V_T} \right\} - 1 \right] - \frac{V_{PV} - I_{PV} R_S}{R_P} - \alpha \frac{V_{PV} - I_{PV} R_S}{R_P} \left(1 - \frac{V_{PV} - I_{PV} R_S}{V_{Br}} \right) \quad (5)$$

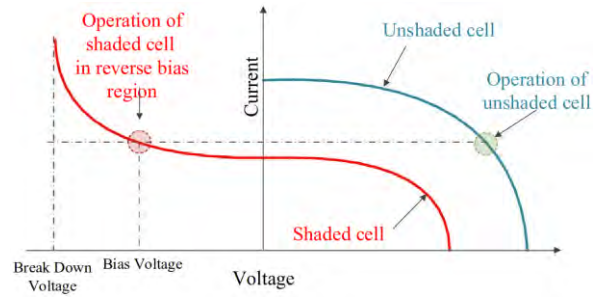


Fig. 2. I-V characteristic of module under partial shading

V_{Br} is breakdown voltage.

Other works presented more accurate models presented by adding a second diode representing the recombination of charge carriers in the semiconductor [11, 14]. Or even three diodes to consider more effects was proposed in [15].

III. P&O

P&O algorithm, presented by the organigramme in Fig.3, operates by periodically incrementing or decrementing voltage of PV. By increasing (decreasing) the operating voltage, power increases (decreases) when operating on the left side of MPP, and decreases (increases) when operating on the right side. According to comparison between the operating power point and the previous one, the algorithm keeps or changes the direction of the perturbation as explained in TABLE I. This process is repeated until the MPP is reached when the condition $dP/dV = 0$ is accomplished [18]. This slope can be calculated by the consecutive output current and voltage expressed as follow.

$$\frac{dP}{dV} (n) = \frac{P(n) - P(n-1)}{V(n) - V(n-1)} \quad (6)$$

The major problem of P&O algorithm is keeping oscillating around the MPP when reached. A solution is to reduce the step size of perturbation to minimize the oscillations. However, it leads to slowing down the algorithm when there is a variation of insolation to reach the new MPP.

TABLE I.
Summary of P&O algorithm.

Perturbation	Power variation	Next perturbation
Positive	Positive	Positive
Positive	Negative	Negative
Negative	Positive	Negative
Negative	Negative	Positive

The major problem of P&O algorithm is keeping oscillating around the MPP when reached. A solution is to reduce the step size of perturbation to minimize the oscillations. However, it leads to slowing down the algorithm when there is a variation of insolation to reach the new MPP.

The other big problem is under fast changing of the incoming irradiance, distorting the algorithm to go in the opposite direction of the MPP. To rectify this problem, after every respective two steps in the same direction a change in direction is applied. So, if the algorithm is blinded by sudden atmospheric variations, failure is spotted. This operation called three points comparison, will correct its direction [19], [20].

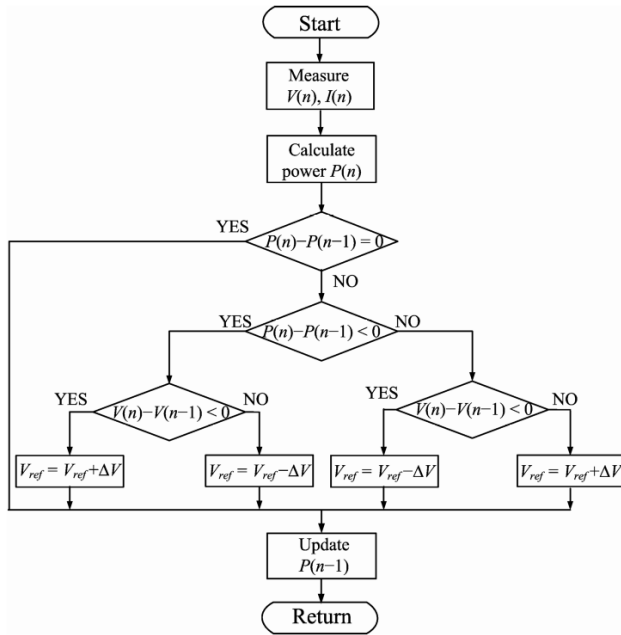


Fig. 3. Flow diagram of P&O algorithm

IV. ANN

ANN is a computational model imitating the biological neural network. A neuron is processing mechanism that weights the inputs then elaborate the sum using activation function (AF), then forward the result to next neurons. The model of common neurons is presented by the following relationship [3], [9],

$$z = \sum_{m=1}^M \omega_m x_m + \alpha \quad (7)$$

Where z is the argument of AF, $x_1 \dots x_M$ are the M

incoming signals, $\omega_1 \dots \omega_M$ are related synopsis weights

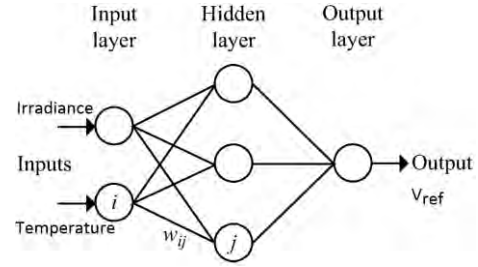


Fig. 4. Diagram of Neural Network architecture

For this paper, the ANN based MPPT method is based on a feed-forward backpropagation Levenberg-Marquardt algorithm. Compound of three layers, the first constituted of two inputs, irradiance and temperature. The second is a hidden layer of twenty neurons using tangent sigmoid as activation function to produce hidden layer outputs. The third is the output layer with a linear activation function to provide reference voltage as output of the network, as resumed in Fig.4. This network architecture came down by trial and error, since there is no rule to designate a precise architecture [18], [21], [22].

The network training procedure is based on a range of irradiance between 50-1000 W/m² with a step of 50 W/m², and temperature 0°-90°C with a step of 10°C. During training the weights are adjusted by the back-propagation learning rules to minimize MSE (mean square error) function. After training, network should correctly estimate outputs even from inputs not presented in training data set.

V. ANALYSIS AND DISCUSSION OF SIMULATION RESULTS

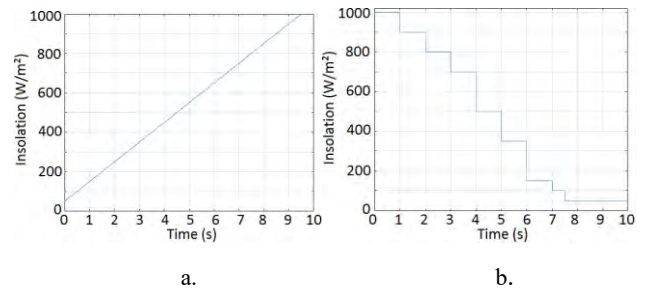


Fig. 5. Variation insolation profiles a. slow variation b. fast variation

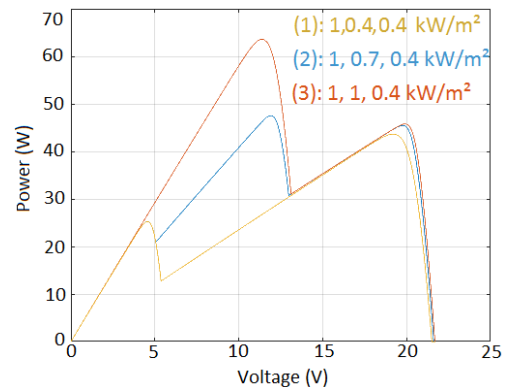


Fig. 7. P&O characteristics for (a). Slow changing condition

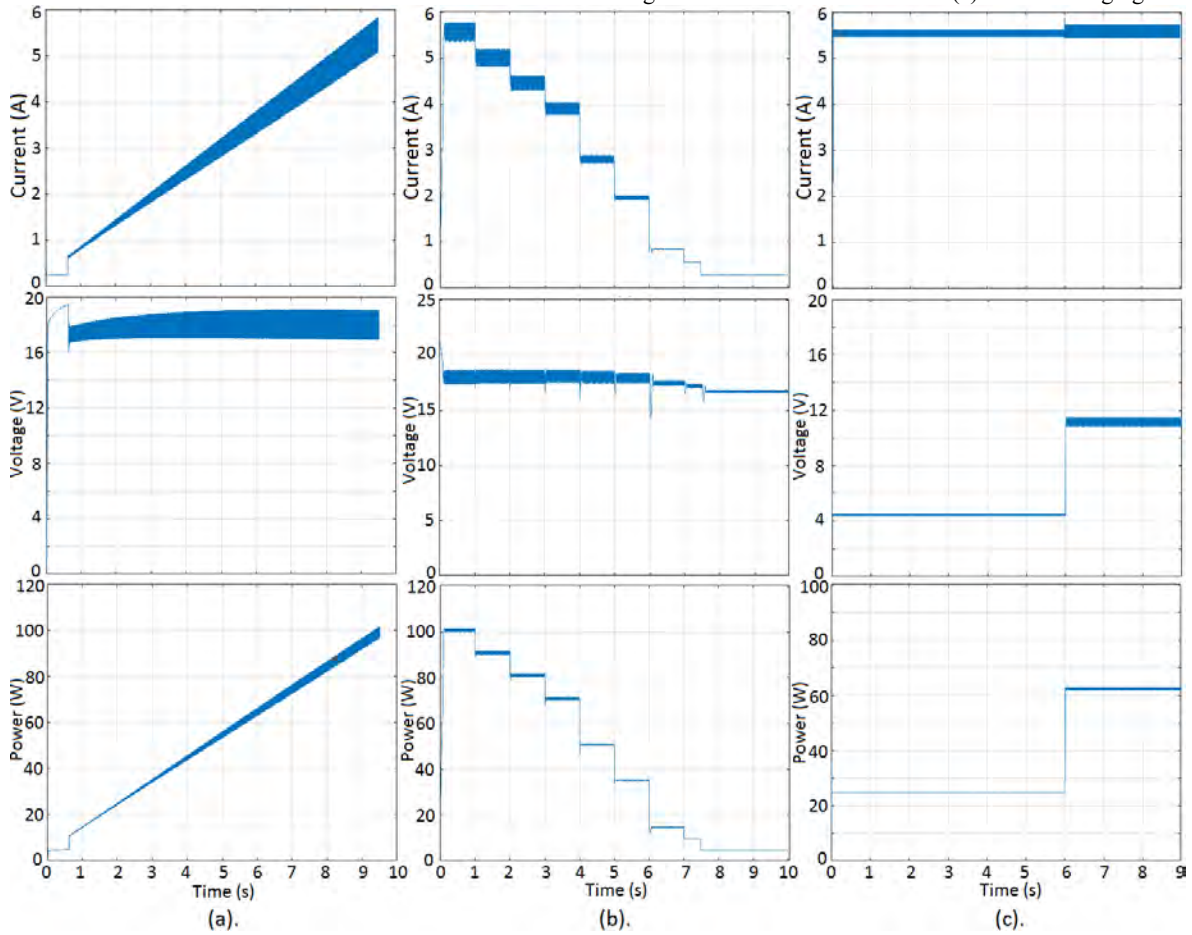


Fig. 6. Partial shading condition

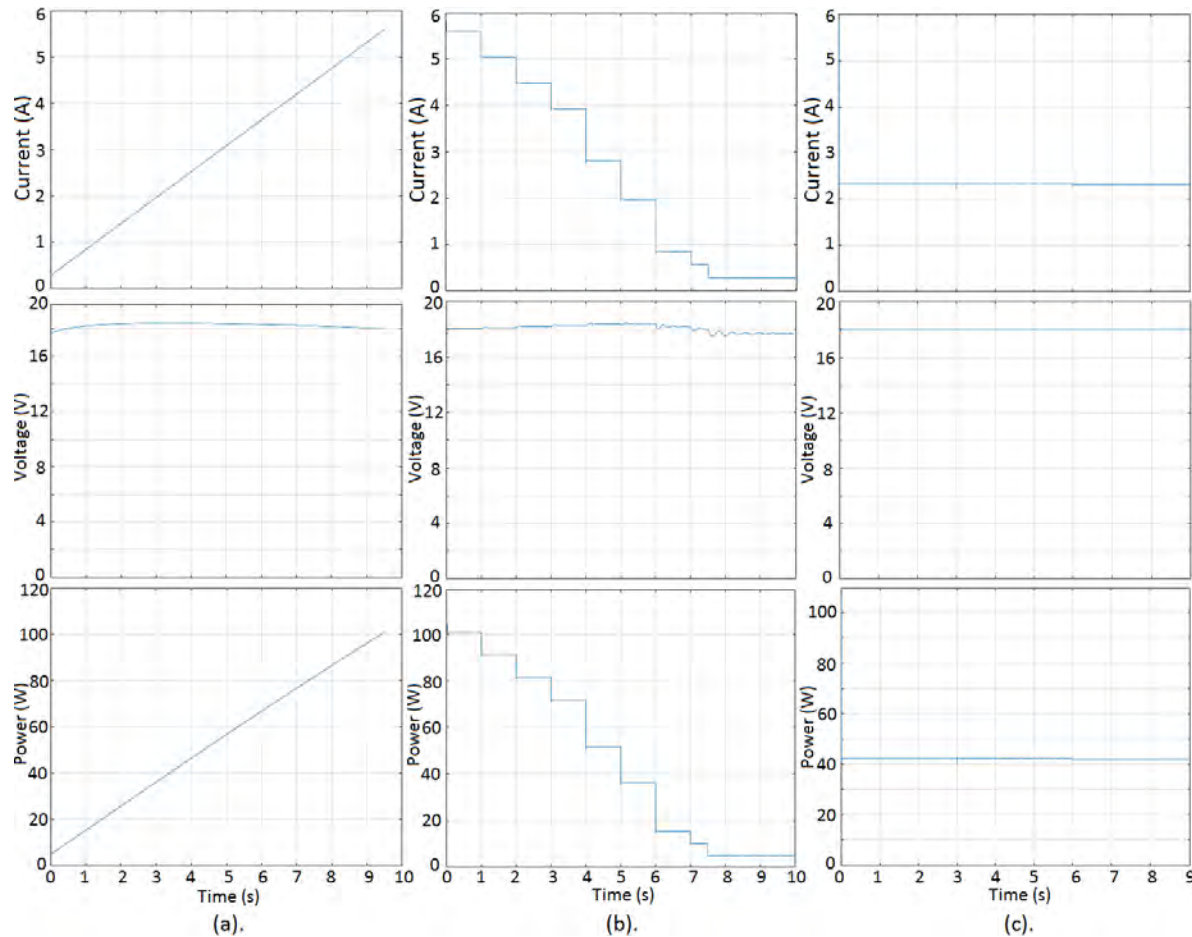
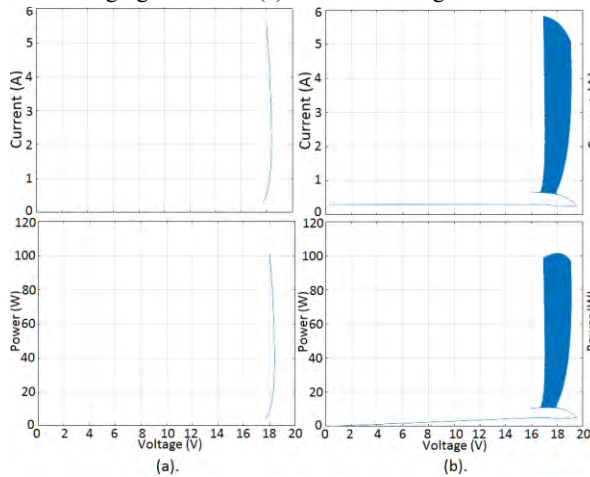


Fig.8. ANN characteristics for (a). Slow changing condition

(b). Fast changing condition (c). Partial shading condition Fast



(b). changing condition (c). Partial shading condition

Fig.9. Voltage-current and Voltage-Power curves for slow changing condition (a). ANN (b). P&O and fast changing condition (c). ANN (d). P&O

For the simulation, the PV module chosen produces $100W_C$ under STC conditions with $V_{MPP} = 18.0V$ and $I_{MPP}=5.61A$, $V_{OC}= 21.7V$ and $I_{SC}= 5.9A$.

To simulate the system, three insolation profiles characterizing three frequent types of irradiation variations are applied.

A. Slow changing insolation

To simulate the system under slow irradiation condition, the signal presented in Fig.5.a. is applied to module input with constant temperature equal to $25^{\circ}C$. The response of the module is presented in Fig.7.(a) for the P&O method, and Fig.8.(a) for ANN method. As seen, P&O algorithm follows the insolation variation presenting oscillations which increases with the increasing of irradiation Fig9.(b). ANN method follows the insolation with no oscillations Fig9.(a).

B. Fast changing insolation

The fast variation in irradiation is presented in the Fig.5.b. P&O algorithm follows the irradiation profile with a small delay in presence of oscillations observed in Fig9.(d). Regarding ANN method, which instantly pursue the changing in insolation Fig9.(c).

C. Partial shading condition

The profile used to simulate the non-uniform shading patterns are presented in Fig.6. By applying for different group cells, different irradiation. the present module composed of 36 cells, and a bypass diode for a group of 12 cells,

- The first pattern; $1000 (W/m^2)$ for the first 12 cells, $400(W/m^2)$ for the rest, 2 peaks appear on the voltage-power curve. P&O algorithm is trapped at the first local peak as seen in Fig.7.(c) producing power corresponding to the lowest

peak with the presence of oscillation as seen in

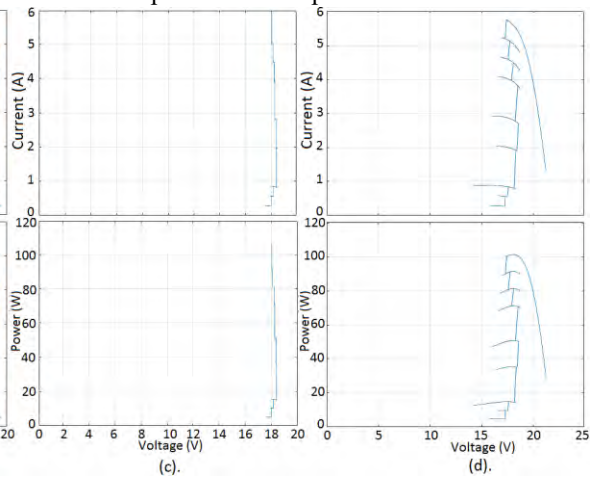


Fig.7.(c). As for ANN method, the operating point is near the global MPP. Fig.8.(c).

- Second pattern; $1000 (W/m^2)$ for the first 12 cells. $700 (W/m^2)$ for the second 12 cells and $400 (W/m^2)$ for the last 12 cells, which means that 3 peaks appear in the Voltage-power curve. P&O still trapped at the same peak Fig.7.(c) and ANN still working at the same point Fig.8.(c), which is far from the global MPP but producing more power than P&O.
- Last pattern; $400 (W/m^2)$ for the first 12 cells. $1000 (W/m^2)$ for the rest, in this case only 2 peaks appear in the Voltage-Power curve. P&O, because of the absence of the peak were the algorithm worked in the previous states, the algorithm leaps to the next peak which, in this case, is the GMPP Fig.7.(c). We notice a small variation in power produced by ANN method Fig.8.(c)

VI. CONCLUSION

From results of simulation presented in this paper, the inference is that P&O algorithm is slower than the ANN based MPPT under fast changing conditions. Also has high oscillations contrary to ANN under fast and slow irradiation conditions, which pose power losses. It leads to settle that ANN based MPPT is better than P&O method for these scenarios. The algorithm follows instantly the uniform variations and performs at the exact MPP, proving its effectiveness. However, under partial shading conditions P&O is always trapped at the first peak encountered, local or global. In other hand, ANN method operates at the reference voltage corresponding to the irradiation measured. Most of time it is not even a peak. So, ANN method based on insolation and temperature as inputs is not effective under non-uniform conditions.

REFERENCES

1. R. Ramabrabha. "Maximum energy extraction from solar energy array under partial shaded conditions," PhD Thesis, Faculty of Electrical Engineering ANNA University, India, 2011.

2. M. Q. Huynh. "Optimisation de la production de l'électricité renouvelable pour site isolé," D. Thesis, University of Reims Champagne-Ardenne, France.
3. R. Khanaki, M. A. M. Radzi and M. Hamiruce Marhaban. "Comparison of ANN and P&O MPPT methods for PV application under changing solar irradiance," IEEE Conference on Clean Energy and Technology, pp. 287–292, Japan, 2013.
4. A. Dadge, N. Djongyang and J. Domra Kana. "Maximum power point tracking methods for photovoltaic systems operating under partially shaded or rapidly variable insolation conditions: a review paper," International Journal of Sustainable Engineering, pp. 1–16, Feb. 2016.
5. W. S. McCulloch and W. H. Pitts. "A logical calculus of the ideas immanent in nervous activity," Bulletin of mathematical biophysics, Vol. 5, pp. 115–133, 1943.
6. K. Rajesh. "Development of artificial neural network model to estimate global solar radiation and energy performance analysis of an institutional building," PhD Thesis, Shoolini University of Biotechnology and Management Sciences, India, 2014.
7. T. Hyama. "Identification of optimal operating point for PV modules using neural network for real time maximum power point tracking control," IEEE Transactions on Energy Conversion, Vol. 10, pp. 360–367, Jun. 1995.
8. A. B. G. Bahgat, N. H. Helwa, G. E. Ahmad and E. T. El Shenawy. "Maximum power point tracking controller for PV systems using neural networks," Renewable Energy, Vol. 30, pp. 1257–1268, 2005.
9. S. A. Rizzo and G. Scelba. "ANN based MPPT method for rapidly variable shading conditions," Applied Energy, Vol. 145, pp. 124–132, 2015.
10. J. A. Duffie and W. A. Beckman. Solar engineering for thermal process. John Wiley Sons, 3rd edition, 2006.
11. J. A. Gow and C. D. Manning. "Development of photovoltaic array model for use in power-electronics simulation studies," IEEE Proceedings - Electric Power Applications, Vol. 146, No. 2, pp. 193–200, 1999.
12. J. Hyvarinen and J. Karela. "New analysis method for crystalline silicon cells," Proceedings of 3rd world conference on photovoltaic energy conversion, Vol. 2, pp. 1521–1524, 2003.
13. V. Quaschnig and R. Hanitsch. "Numerical simulation of current-voltage characteristics of photovoltaic systems with shaded solar cells," Solar energy, Vol. 56, No. 6, pp. 513–520, 1996.
14. K. Ishaque, Z. Salam, H. Tahri and Syafaruddin. "modeling and simulation of photovoltaic (PV) system during partial shading based on a two-diode model," In Simulation modelling practice and theory, Vol. 19, pp. 1613–1626, 2011.
15. K. Nishioka, N. Sakitani Y. Uraoka and T. Fuyuki. "Analysis of multi crystalline silicon solar cells by modified 3-diodes equivalent circuit model taking leakage current through periphery into consideration," Solar energy materials and solar cells, Vol. 91, No. 13, pp. 1222–1227, 2007.
16. N. H. B. Prasad Koirala, B. Sahan and N. Henze. "Study on mpp mismatch losses in photovoltaic applications," 24th European Photovoltaic Solar Energy Conference and Exhibition, 2009.
17. J. W. Bishop. "Computer simulation of the effects of electrical mismatches in photovoltaic cell interconnection circuit," Solar cells, Vol. 25, pp. 73–89, 1988.
18. T. Esran and P.L. Chapman. "Comparison of photovoltaic array maximum power point tracking techniques," IEEE Transactions on Energy Conversion, Vol. 22, No.2, pp. 439–449, 2007.
19. J. A. Jiang, T. L. Huang, Y. T. Hsiao and C. H. Chen. "Maximum power tracking for photovoltaic systems," Tamkang Journal of Science and Engineering, Vol. 8, No. 2, pp. 147–153, 2005.
20. Y. Hsiao and C. Chen. "Maximum power tracking for photovoltaic power system," 37th IAS annual meeting, Industry applications conference, Vol. 02, pp. 1035–1040, USA, Dec. 2002.
21. N. Khaldi, H. Mahmoudi, M. Zazi and Y. Barradi. "Implementation of a MPPT neural controller for photovoltaic systems on FPGA circuit," Wseas Transactions on Power Systems, Vol. 9, pp. 471–478, 2014.
22. K. Punitha, D. Devaraj and S. Sakthivel. "Artificial neural network based modified incremental conductance algorithm for maximum power point tracking in photovoltaic system under partial shading conditions," Energy, Vol. 62, pp. 330–340, 2013.

Effect of applied voltage on Electrical Properties and Energy Efficiency of a Ne-Xe Excimer lamp

Wafâ BENSTAALI^{1,2} and Ahmed BELASRI²

¹ UMAB, Faculty of Sciences and Technology ,B.P.227, Route de Belhacel, 27000, Mostaganem, wafabenstaali7@yahoo.fr

² USTO, Laboratoire de Physique des Plasmas, Matériaux Conducteurs et leurs Applications LPPMCA, El Mnaouar, BP 1505, Bir El Djir 31000, Oran.

ABSTRACT

Excimer lamps are actually one of the principal ultraviolet (UV) sources. This environmentally friendly technology has different applications; however, they still need many improvements like the UV efficiency and the luminous efficacy. Different ways are possible. One of these ways is to improve the part of the input energy deposited by electrons into xenon excitation, which can increase the U.V production and then the visible light production

In this paper we present a study of a dielectric barrier discharge filled with a neon- xenon10% gas mixture at excimer lamp conditions. We use a one dimensional particle in cell with Monte Carlo simulation (PIC-MCC) to investigate the effect of the applied voltage on the discharge xenon excitation efficiency. The results show the variation of energy deposited on different reactions as excitation and ionization for different voltage values. The discharge is more efficient to excite xenon atoms at higher voltage. However an increase of voltage induces the increase of the part of energy deposited on the other collision. The electrons lost on walls become more important

Key Words: Dielectric Barrier discharge, efficiency, excitation, Xenon, lamps.

1. INTRODUCTION

In recent decades, VUV and UV light sources became more attractive because of their different applications like plasma display panels [1] and excimer lamps. In both of these sources, a Dielectric Barrier Discharge (DBD) can be produced, where two electrodes are covered by one or two dielectrics. The space between them is filled with different mixtures. One of the possible gases which can be used are based on excimer molecules as Xe₂^{*}, Kr₂^{*}, KrBr^{*}, XeCl^{*}...etc. In these discharges, under the effect of an applied voltage, the atoms are excited to upper levels. Then, they emit UV radiations which will be converted by phosphors to visible light.

In this work, we are interested on Excimer lamps which represent one of the most environmentally friendly technologies because of the absence of mercury. This is why different applications are possible for them, as light source, photochemistry, water treatment, microelectronics, microbiology, medicine (skin treatment), and photo regulation of plants by UV radiation.

Excimer lamps have many advantages; Narrow band emissions in the UV and VUV regions, high photons energy, long lifetime, and high flexibility in geometry. However, they still need many improvements. Different simulation [2-5] and experimental [6-7] works have been done to understand these sources and optimize their properties.

Among the principal properties which need improvement, luminous efficiency is the most important one [8]. There are different ways to increase this property as discharge waveforms (different waveforms and pulse frequencies), lamp geometry (cylindrical, plane), and gas mixture (different gases are studied as Xe, Kr, He, KrBr). In many of these research works, the aim of scientists is to provide progress to this technology in order to replace mercury lamps which are harmful to health.

We are interested, in our work, to study the energy deposited into excitation which contribute to lamp's UV efficiency. We present, in this paper, a dielectric barrier discharge filled with xenon-neon mixture. A one dimensional particle in cell model is used; it is described in section 2. The results obtained from our model are presented in section 3.

2. PHYSICAL MODEL

In this paper, a one dimensional Particle In Cell with Monte Carlo Collisions (PIC-MCC) model was used [9]. The particle in cell model consists of charged particles moving about due to forces of their own and applied fields [1]. The physics comes from two parts, the fields produced by the particles and the motion produced by forces.

The charged particles trajectories are obtained by integrating the following equations at each time step:

$$m \frac{d\vec{V}}{dt} = \vec{F} = q\vec{E} \quad (1)$$

$$\frac{dX}{dt} = V \quad (2)$$

where m is the particle mass, V the velocity, X the position, F the applied force and E is the electric field.

The electric field is obtained from Poisson's equation:

$$\nabla^2 \Phi = -\frac{\rho}{\epsilon_0} \quad (3)$$

where Φ is the electric potential, ρ is the charged density, and ϵ_0 is the permittivity

The Newton-Lorentz equations described above are discretized using the leapfrog scheme. In finite-difference form, we obtain the following equations:

$$m \frac{V_i^{t+1/2} - V_i^{t-1/2}}{\Delta t} = F_i^t = q \cdot E_i^t \quad (4)$$

$$\frac{X_i^{t+1} - X_i^t}{\Delta t} = V_i^{t+1/2} \quad (5)$$

$$\Phi_{j+1} - 2\Phi_j + \Phi_{j-1} = -\frac{(\Delta x)^2}{\epsilon_0} \cdot \rho_j \quad (6)$$

where, X_i , V_i , F_i , and E_i are position, velocity, force, and electric field at the particle position. Φ_j is the potential at grid point j , Δx , is the distance between grid points.

The electric field at grid point j is deduced from the potential:

$$E_j = \frac{\Phi_{j-1} - \Phi_{j+1}}{2 \cdot \Delta x} \quad (7)$$

The electric field at each position is calculated as follows (Weighting grid to Particles):

$$E_i = E(X_i) = \left(\frac{x_{j+1} - X_i}{\Delta x} \right) \cdot E_j + \left(\frac{X_i - x_j}{\Delta x} \right) \cdot E_{j+1} \quad (8)$$

where E_j and E_{j+1} are electric fields at j and $j+1$ respectively, x_j and x_{j+1} are the positions of adjacent cells, X_i is the particle position. Δx is the space between two neighbor cells.

A Monte Carlo collisions method is used to study particles collisions. When we consider the collision dynamics, a number of electron-neutral collision events are possible, including elastic scattering, excitation and ionization.

The energy deposited into these different collision processes can be then calculated. For the case of the ionization collision, the part of the energy given into the process is calculated by the relation:

$$\Delta \epsilon = \epsilon_2 + \epsilon_{iz}, \quad (9)$$

where $\Delta\varepsilon$ is the energy given into the process, ε_2 is the energy of electron produced by ionization and ε_{iz} is the ionization threshold.

For an excitation collision, the incident electron loses the excitation threshold energy and $\Delta\varepsilon$ is given as follows:

$$\Delta\varepsilon = \varepsilon_{exc} \quad (10)$$

where ε_{exc} is the excitation threshold.

3. RESULTS AND DISCUSSIONS

In this section, a single discharge for a planar dielectric barrier discharge filled with xenon-neon mixture for lamp's conditions. The gas mixture is 10% xenon in neon. The gap length d is 3 mm, the total gas pressure p is 400 Torr, and the equivalent capacity of dielectric layers is 230 pF/cm². The gas temperature is supposed to be constant and equal to 300°K. The neon secondary emission coefficient is 0.25.

3.1. Electrical and energy characteristics of a single discharge

We have studied, at first, the electrical and energetic properties of a single discharge at an applied voltage of 1.1kV. The current density, the voltage on gas domain, V_g , and the voltage on dielectrics, V_d , are then represented on Figure. 1, for a Xe10-Xe mixture with the parameters cited previously.

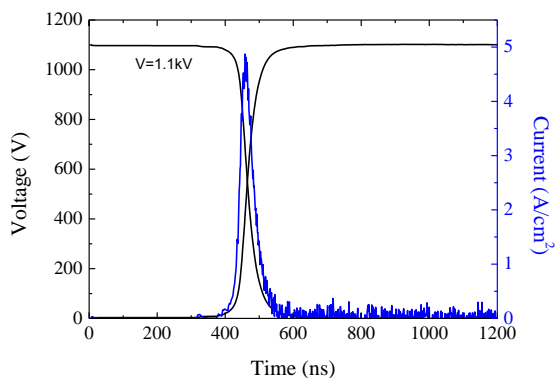


Figure.1. Temporal variation of gas and dielectric voltages, and current density for a mixture of Xe10-Ne, the applied voltage is 1.1KV.

It is observed that after approximately 400 ns, the dielectric voltage starts to increase until it reaches a value of 1.1kV.

This is due to the charges migration toward dielectrics. At this time, the voltage decreases at discharge gap. This corresponds to the duration of a pulse discharge. It is also seen that, at the beginning of the discharge the current density increases until it reaches a value of 5 A/cm². After this moment, it decreases. The discharge duration is less than 100 ns.

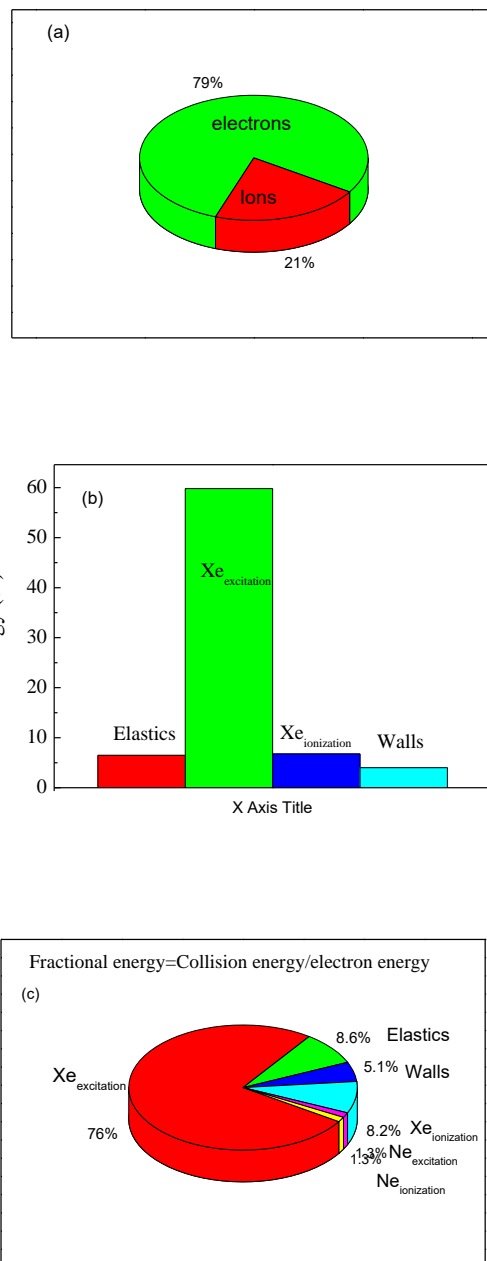


Figure.2. Diagrams of energy balance of a single discharge for a mixture of Xe10-Ne, the applied voltage is 1.1KV. (a) energies deposited by space charges, (b) energies by electrons in different collisions, and (c) partial fractional energy by electrons in different collisions.

We were also interested by the fractional energy deposited on different collisions. The total fractional energy is calculated as the ratio between the energy deposited in collision and the total energy dissipated in the discharge. The partial fractional energy is calculated as the ratio between the energy deposited in collision and the energy dissipated by electrons in the discharge

Figure.2(a) shows the energy used by space charges. Figure.2 (b) represents the energy deposited by electrons in different collisions. Figure.2 (c) represents the partial fractional energy deposited by electrons in different collisions. The discharge efficiency is defined as:

$$\rho = \frac{\text{Energy deposited into Xe excitation}}{\text{Input energy}} \quad (11)$$

It is noted that Most of total energy deposited in discharge is used by electrons; about 80% of input energy, when only 20% is dissipated by ions. The results show also that the major part of electron energy; 76%, contributes to xenon excitation. This allows to important discharge efficiency; about 59% of the total energy is used to excite xenon atoms. The other reactions use less than 10% of the input energy.

3.2. Effect of the applied voltage on excimer lamp discharge characteristics

As it was suggested, it is important to optimize the excimer lamp performances by increasing the part of the input energy deposited by electrons into xenon excitation. For this reason, we present in the second part of our paper, the effect of the applied voltage on electrical and energy properties of this discharge.

Figure.3 represents the variation of peak value of current density for different applied voltage values; 900 V, 1000V, 1100V and 1200V. It is observed that, at 900V, the discharge current peak is quite low; in order to 3A/cm². It increases with the applied voltage until it reaches a value of about 7 A/cm² for 1.2 kV

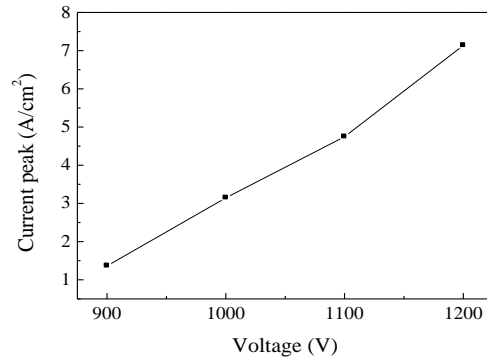


Fig.3. Variation of current peak with applied voltage for Xe10-Ne mixture.

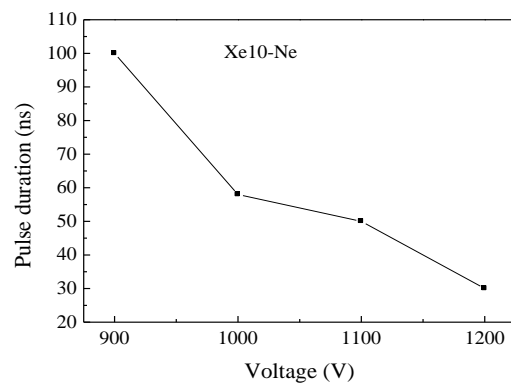


Figure.4. Variation of pulse duration with applied voltage for Xe10-Ne mixture

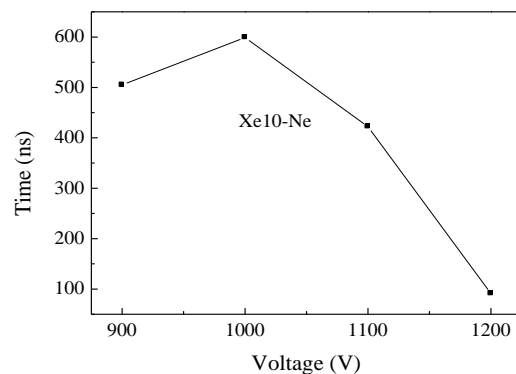


Figure.5. Variation of discharge beginning time with applied voltage for Xe10-Ne mixture

We also calculate the pulse duration as the width of the pulse at half of the peak current. Figure.4 shows that the current pulse duration reduces at higher voltage. It is also noted that the discharge takes less time to start when the voltage increases, as it is shown on Figure.5.

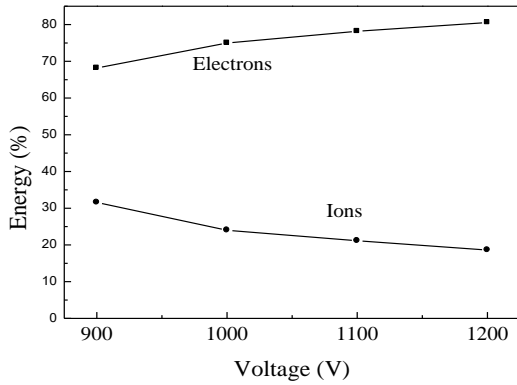


Figure.6. Variation of energy deposited by charges with applied voltage.

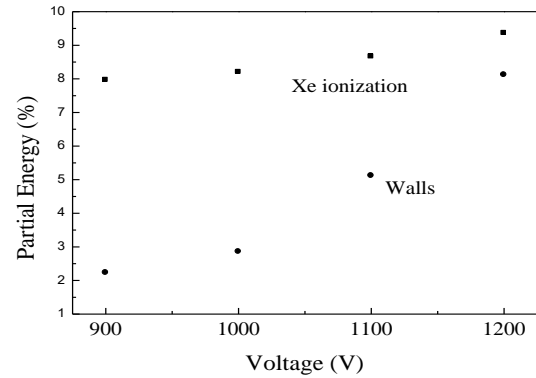


Figure.8. Variation of partial fractional energy deposited in xenon ionization and on walls with applied voltage.

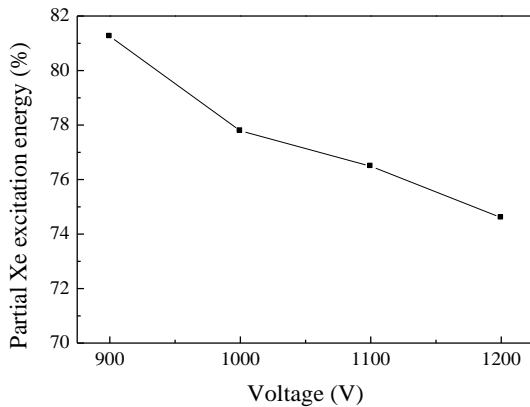


Figure.7. Variation of partial fractional energy deposited in xenon excitation with applied voltage.

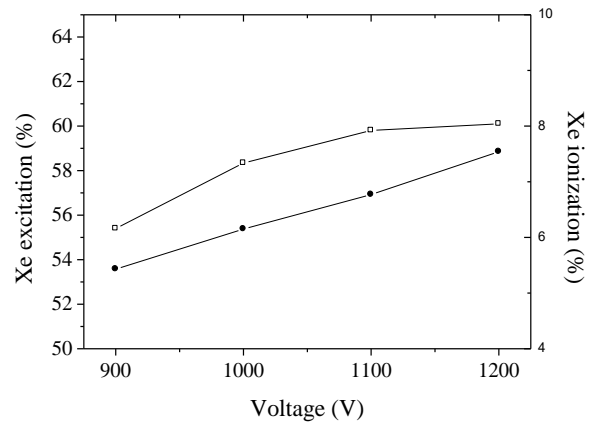


Figure.9. Variation of total fractional energy deposited in xenon excitation and ionization.

Figure.6 represents the effect of the applied voltage on the energy deposited by charges. It is noted that electrons use more energy at higher voltages when energy dissipated by ions is less important; Electrons used 68% of the discharge energy at 900 V, and reach 80% of the total energy at 1.2KV.

Then we studied how it is distributed by electrons. On Figure.7, It was found that, for our conditions, the part of xenon excitation from the electron energy decreases from 82% to 74% when the applied voltage increases from 900V to 1.2KV

This means that, at higher voltage, electrons have sufficient energy to ionize xenon atoms (see Figure.8). The energy deposited in this collision is of about 9.3% at 1.2KV. This is not the only reason; it is also seen that more electrons are lost because they keep away discharge domain towards dielectrics. An increase of about 6% is then observed. However, this does not prevent a better performance. In fact, Figure.9 shows an increase of the total fractional part used in xenon excitation by 5 % when the applied voltage increases from 900V to 1.2KV. It is equal to about 60% at 1.2KV. It is also observed an increase of 2% of the energy deposited in xenon ionization for the same conditions.

CONCLUSION

In this work we used a one dimensional particle in Cell with Monte Carlo collisions (PIC/MCC) to investigate the effect of the applied voltage on fractional energies used by charges species in a dielectric Barrier Discharge at lamp conditions.

The results show that despite, electrons lost less energy to excite xenon atom at higher voltage, the discharge is more efficient to excite xenon atoms (total fractional energy). At an applied voltage of 1.2 kV, the energy used by electrons is about 80%, the total xenon excitation energy reaches a value of 60%.

However an increase of voltage induces the increase of the part of energy deposited on the other collision. The electrons lost on walls become more important. We must be careful to make a balance between high xenon excitation and lost energies. An applied voltage of 1.1 kV, is the optimum condition for an efficient excimer lamp discharge at Xe10-Ne.

REFERENCES

- [1] T. Callegari, R. Ganter, and J. P. Boeuf, "Diagnostics and modeling of a macroscopic plasma display panel cell," *J. Appl. Phys.*, vol. 88, no. 7, pp. 3905–3913, Oct. 2000.
- [2] R. J. Carman and R. P. Mildren, "Computer modeling of a short-pulse excited dielectric barrier discharge Xenon excimer lamp ($\lambda \sim 172$ nm)," *J. Phys. D, Appl. Phys*, vol. 36, pp. 19–33, 2003.
- [3] R. J. Carman, N.T. Goldberg, S.C. Hansen, N.Gore, and D.M. Kane, "Performance Enhancement of a Dielectric Barrier Discharge Vacuum-Ultraviolet Photon Source Using Short-Pulsed Electrical Excitation" *IEEE Trans. Plasma Sci.* Vol.46, 90, 2018.
- [4] L.T.Doanh, S.Bhosle, G.Zissis, and H.Piquet, "Estimation of the Light Output Power and Efficiency of a XeCl Dielectric Barrier Discharge Exciplex Lamp Using One-Dimensional Drift-Diffusion Model for Various Voltage Waveforms" *IEEE Trans. Plasma Sci.*, vol. 49, pp.331-340, 2018.
- [5] A Benmoussa, A Belasri, Z Harrache « Numerical investigation of gas heating in Dielectric Barrier Discharge in Ne-Xe excilamp", *Current Applied Physics*, vol. 17 (4), pp.479-483, 2017.
- [6] Q.Han, R.An, W.Xu, G.Lister, and S. Zhang, "Radiation characteristics of coaxial KrBr* excilamps based on a dielectric barrier discharge", *J. Phys. D: Appl. Phys.*vol. 46, 505203 (10pp), 2013.
- [7] A.Shuaibov1, R.Gritzak, "Optical characteristics of UV–VUV lamps on the electronic-vibrational transitions of the hydroxyl radical pumped by a nanosecond capacitive discharge", *High Volt.*, Vol. 2 Iss. 2., pp. 78-81, 2017
- [8] Sz Beleznai, G Mihajlik, I Maros, L Bal'azs and P Richter, "High frequency excitation waveform for efficient operation of a xenon excimer dielectric barrier discharge lamp" *J. Phys. D: Appl. Phys.* **43**, 015203, 2010
- [9] W. Benstâali and Belasri," Discharge Efficiency Improvement in PDP Cell via a 1-D PIC/MCC Method" , *IEEE Trans. Plasma Sci.* **39** 1460, 2011.

Power Control of a Wind Energy Conversion System Associated with a Battery-based Storage System

Karima BOULAAM¹ and Akkila BOUKHELIFA²

¹ Department of Electrical Engineering and Industrial Computing, ENST, Algiers, Algeria, kboulaam@yahoo.fr

² Faculty of Electronics and Computers, USTHB, Bab-Ezzouar, Algiers, Algeria, aboukhelifadz@yahoo.fr

ABSTRACT

In this paper, a grid-connected wind energy conversion system (WECS) associated with a battery-based energy storage system (ESS) is studied. The purpose is to filter wind power fluctuations in order to satisfy the grid power requirement. The main idea is the development of an appropriate supervisory algorithm for the storage system to manage its power flow. The proposed WECS configuration is based on a doubly fed induction generator (DFIG), whose the rotor grid connection is ensured by three-level converters. The wind generator is controlled so that the output power is maximized by adjusting the rotational speed. The control of the battery-assisted wind turbine system is developed and a supervisory algorithm is proposed to control the battery bank taking into account both the grid demand and the generated wind power. The whole system performances are analyzed through simulation and a comparative study is made to show the main role of the battery storage system to smooth the wind power delivered to the grid.

Key Words: Battery storage, DFIG, Power storage management, three-level converter, wind power.

1. INTRODUCTION

Among different renewable energy generators, wind generator is technically and economically the most developed one,

expanding globally at a rate of 20–30% annually over the last decade [1-3].

Due to the intermittent behavior of the wind speed generally unpredictable, the generated power from the wind turbine fluctuates causing frequency variation and voltage flicker inside the electrical grid. Therefore, high penetration of wind power can introduce technical challenges and issues [4-6]. Hence, the wind-caused power variations have to be erased in order to smooth the produced power delivered to the grid.

Various power smoothing methods for WECS have been proposed in the literature. In [6], authors reviewed and discussed different approaches and showed that “energy storage based power smoothing method” is more effective compared with “without energy storage based power smoothing method” which presents lower costs.

Different energy storage systems (ESSs) have been used by authors for power smoothing of wind energy conversion systems (WECSs) such as batteries, flywheels, super capacitors, fuel cells with electrolyzer and hydrogen storage tank, compressed air storage, superconducting magnetic energy storages, etc [6- 8]. These ESSs are considered to be an effective solution to balance the generation and demand, supporting the renewable energy deficit when necessary and storing the primary energy excess when possible.

The use of batteries for wind turbines power smoothing has been largely found in literature [9-14]. In these works, the trends of authors varied in different ways. In [9], a rule based control strategy has been proposed in the aim to extend the BESS life of a wind farm considering the SOC and depth of discharge limitations. A similar control algorithm has been adopted in [10] and applied to a BESS associated to a WECS based on a doubly fed induction generator (DFIG). In [11], authors developed a state-machine based supervisory control system where different states have been considered according to the battery SOC in the aim to perform a suitable energy management of the two sources. For the objective of maximizing battery life, reducing maintenance costs and increasing the efficiency of the energy storage system, [12] proposed a control strategy based on multi-branch battery-bank configuration using switches to connect just the necessary number of branches according to the required power from the control system. In [13], an optimization-based control strategy for the power management of a wind farm has been proposed where the objective was to minimize the error between the power delivered by the wind farm with battery storage and the power demand from an operator, while extending battery life.

In the above-mentioned works, two-level voltage source converters have been used for the wind generator grid connection. Yet, with the increase of WECS capacity; this conventional converters tend to be replaced gradually with multilevel converters, which permit to reduce at once voltage stress on the switching devices, output voltage harmonic distortion and switching frequency [15-17].

In this paper, a grid-connected DFIG-based wind energy conversion system combined with a battery-based energy storage system is studied. The proposed configuration use three-level converters for the rotor side generator grid connection. A management algorithm is developed to control the power flow between the battery storage system, the wind generator and the grid, so that to smooth the output power generated by the wind conversion system, while ensuring good energy availability.

Firstly, the system modeling is presented in section 2. Then, the control scheme of the whole system is described in section 3; it includes the stator active and reactive powers control, the rotational speed control for maximum power point tracking (MPPT), the DC-bus regulation and the control of the battery storage system. A supervisory control algorithm is then developed in section 4, which is responsible for determining the reference power must be generated by/stored in the ESS. Finally, the proposed models and control strategies are tested by simulation under Matlab/Simulink software. The obtained results show the ability of the wind conversion system combined with battery ESS to achieve the desired objectives.

2. MODELING OF THE WIND CONVERSION SYSTEM

The structure of the considered system is represented in Fig. 1. The system consists of a wind turbine coupled to a doubly fed induction generator (DFIG) through a gear box. The stator winding is directly connected to the grid. The rotor winding is connected to the grid via two three-level PWM bidirectional power converters linked by a two capacitors DC-bus. The rotor power flows to/from the grid according to whether the generator operates in hyper or hypo synchronous mode respectively. A battery energy storage system (battery-ESS) is connected to the DC-bus through a DC/DC PWM bidirectional power converter. This latter allows the charge and discharge of the storage unit according to an appropriate power management algorithm.

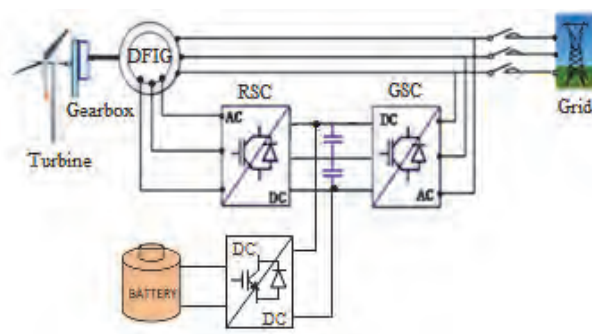


Figure.1: 30 Battery ESS associated with a DFIG-based wind conversion system

2.1. Modeling of the Wind Turbine

The aerodynamic power developed by a wind turbine is given by the expression (1) [18-21].

$$P_{aer} = \frac{1}{2} \cdot C_p(\lambda, \beta) \cdot \rho \cdot \pi \cdot R^2 \cdot v^3 \quad (1)$$

Where ρ is the air density; R is rotor radius, v is the wind speed and C_p is the power coefficient. This latter can be represented by various approximation expressions. In this paper, C_p is expressed by (2) [21].

$$C_p = (0,5 - 0,00167\beta') \cdot \sin\left(\frac{\pi(\lambda + 0,1)}{18,5 - 0,3\beta'}\right) - 0,00184\beta'(\lambda - 3) \quad (2)$$

$$\text{With: } \beta' = \beta - 2 \quad \text{and} \quad \lambda = \frac{R \cdot \Omega_{turb}}{v} \quad (3)$$

Where β is the blade pitch angle; λ is the tip-speed ratio and Ω_{turb} is the turbine rotor speed.

2.2. The Generator (DFIG) and its Converters

A simplified generator's dynamic model has been used [18]. It adopts the oriented-flux strategy defined in the synchronous reference frame (d - q) fixed to the stator flux:

$$\begin{cases} V_{sd} = 0 \\ V_{sq} = V_s = \omega_s \Phi_s \end{cases} \quad (4)$$

$$\begin{cases} V_{rd} = R_r I_{rd} + \sigma L_r \frac{d}{dt} I_{rd} - s \omega_s \sigma L_r I_{rq} \\ V_{rq} = R_r I_{rq} + \sigma L_r \frac{d}{dt} I_{rq} + s \omega_s \sigma L_r I_{rd} + s \frac{M}{L_s} V_s \end{cases} \quad (5)$$

$$\begin{cases} P_s = -V_s \frac{M}{L_s} I_{rq} \\ Q_s = -V_s \frac{M}{L_s} I_{rd} + \frac{V_s^2}{\omega_s L_s} \end{cases} \quad (6)$$

Where s (r) is stator (rotor) index, V (I) is voltage (current), Φ_s is stator flux, P (Q) is active (reactive) power, R is a resistance, L (M) is an inductance (mutual inductance), ω (ω_s) is angular speed (synchronous speed), s is the slip and σ is the leakage coefficient ($\sigma = 1 - M^2 / L_s L_r$).

The generator rotor is fed by two PWM three-level bidirectional converters, namely rotor side converter RSC and grid side converter GSC, linked by a two capacitors DC-bus (Figure.1).

The structure of the three-level NPC (Neutral Point Clamped) inverter is presented in [15, 16].

2.3. The battery and its converter

The storage system uses lead-acid batteries. This type of batteries is the most used since it presents low self discharge, cost effectiveness, high specific power and good temperature performance [7, 14]. Among different models found in literature [10, 22], we have adopted the model adopted in [22].

The battery bank is connected to the DC-bus by means of a two-quadrant DC/DC PWM converter (bidirectional chopper) (Figure.1). This latter adapts the voltage levels and ensures the battery power flow

3. CONTROL SCHEME OF THE CONVERSION SYSTEM

The proposed control scheme of the chain is represented in Figure.2. The rotor-side converter (RSC) controls the stator powers via the rotor voltages. The grid-side converter (GSC) controls the DC-bus voltage and the line currents flowing out between the converter and the grid. The generator speed is regulated in order to extract the maximum of power from the wind. The DC/DC converter controls the battery power flow through the DC-bus so that the battery supply or absorb the difference between grid power requirement and the fluctuating wind power.

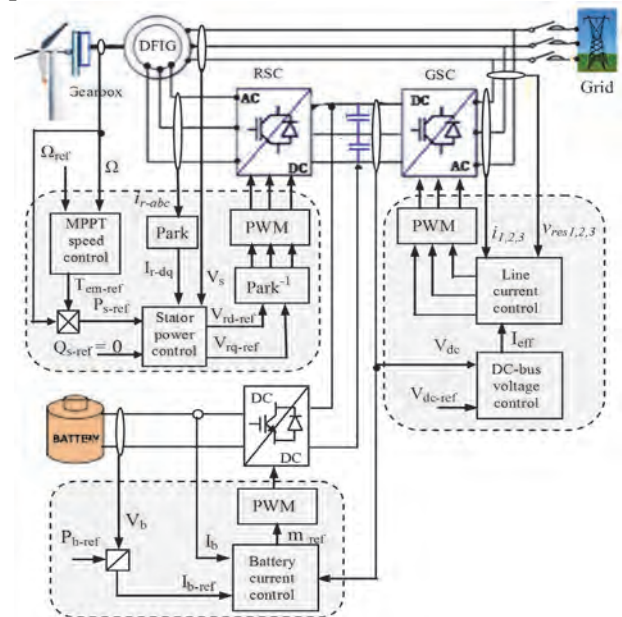


Figure.2: Wind-battery conversion system control scheme

3.1. Generator control

According to equation (6), we can easily see that stator active and reactive powers P_s and Q_s can be controlled independently by the rotor current d, q components I_{rq} and I_{rd} respectively. This control is made via rotor voltage components V_{rq} and V_{rd} (5).

The block diagram of generator powers control based on field oriented strategy is show in Figure.3.

The desired reference value of active power P_{s-ref} corresponds to the maximum power point based on rotational speed control, and the desired reference value of reactive power Q_{s-ref} is set equal to zero in order to operate at unitary power factor.

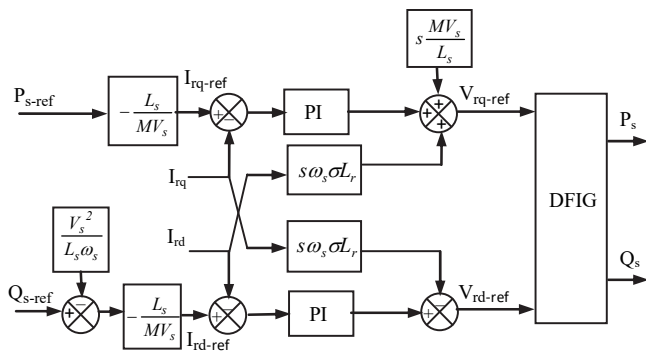


Figure.3: Generator stator powers control scheme

3.2. Grid side converter control

The objective of GSC control is to keep the DC-bus voltage constant regardless of the rotor power flow direction. The control algorithm contains an inner loop regulating line currents and an outer loop regulating DC-bus voltage [16].

3.3. Battery control algorithm

An appropriate control algorithm of the DC/DC power converter (Figure.4) allows the battery to adjust the power it transits, to a reference value (P_{b-ref}) determined by the supervisory control system.

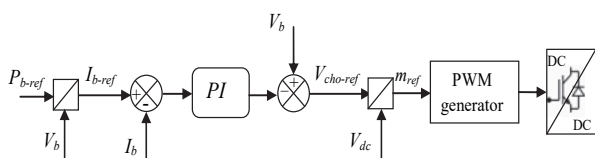


Figure.4: Control scheme of the battery storage system

3. SUPERVISORY CONTROL SYSTEM

The supervisory control system permits to determine the value of the reference power must be generated by/stored in the battery (P_{b-ref}) taking into account at the same time the power demanded by the grid, the available wind power and the state of charge (SOC) of the battery.

The battery power reference P_{b-ref} is deducted as follows:

The difference ΔP between the grid power requirement P_{g-ref} and the fluctuating wind power P_w is first estimated; then, according to the battery SOC, P_{b-ref} is set to ΔP or to zero.

For efficiency and security reasons, the battery bank SOC is limited from 30% to 70% of the total capacity.

In order to achieve the suitable operation of the battery-assisted wind conversion system, we consider the following scenarios for the battery operating:

- If the SOC is within the two thresholds, it is the normal operating mode, the battery absorbs power difference ΔP if this amount is positive (charging mode) or generates it if it is negative (discharging mode).

- If the SOC reaches its maximum limit, only the discharge process is allowed. This discharge process is valid only if power difference ΔP is negative, i.e. the wind power is less than the grid demand, otherwise the reference P_{b-ref} is set to zero.

- If the SOC reaches its minimum limit, only the charge process is allowed. This charge process is valid only if the power difference ΔP is positive, i.e. the wind power is greater than the power demand, otherwise the reference P_{b-ref} is set to zero.

Finally, the power delivered to the grid is calculated as follows:

$$P_g = P_w + P_b \quad (7)$$

With:

$$\begin{cases} P_w = P_s + P_r \\ P_r = -s \cdot P_s \end{cases} \quad (8)$$

Where P_w is the wind generator power, P_s is the generator's stator active power, P_r the generator's rotor active power and s is the slip.

The flow diagram of the proposed supervisory control system is depicted in Figure.5.

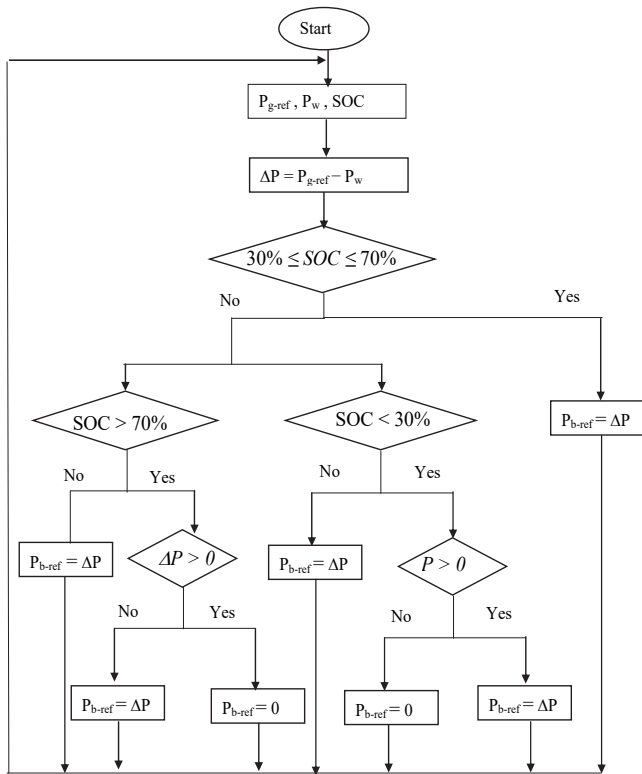


Figure.5: Flow diagram of the supervisory control system

4. SIMULATION AND RESULTS

The proposed models and the developed control algorithms have been tested on a 1.5 MW rated power variable wind energy conversion system. The simulation is carried out using Matlab/Simulink software. The wind turbine and generator parameters are given in Table.1 and Table.2 respectively.

Table.1 Wind Turbine Parameters

Rated power (MW)	ρ (kg/m^3)	R (m)	G	J ($kg.m^2$)	f (N.m/s)
1.5	1.225	0.5	90	1000	0.0024

Table.2 Generator Parameters

Rated power (MW)	p	U _s (V)	R _r (Ω)	L _s (H)	L _r (H)	M (H)
1.5	2	690	0.021	0.0137	0.0136	0.0135

The wind profile used in this simulation is depicted in Figure.6, and simulation results are presented from Figure.7 to Figure.16. They show the performances of the wind conversion system towards the proposed control algorithms and a comparison has been made in both cases without and with the battery storage system.

We start by the generator (DFIG) performances which are globally satisfactory. Figure.7 shows that the generator speed follows its reference successfully with rapid response. So, we can say that the speed controller has a good behavior.

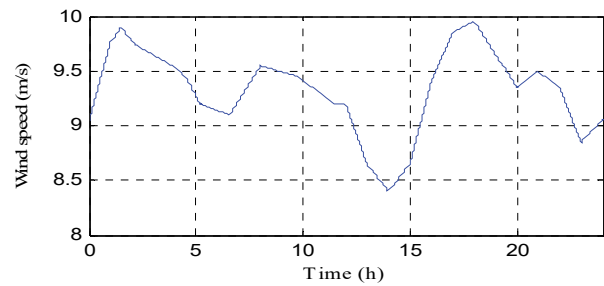


Figure.6: Wind profile

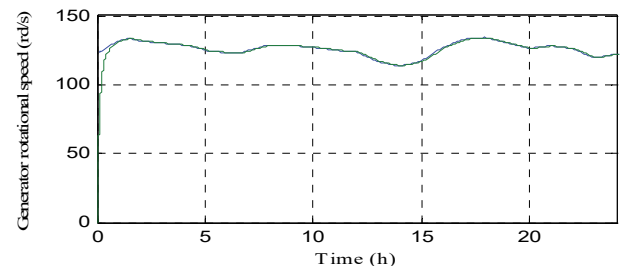


Figure.7: Actual and reference generator speed

Stator's active and reactive powers are represented in Figure.8 and Figure.9 respectively. It can be observed that the active power oscillates around its reference, which means that the generated power is maximum. Concerning the reactive power, it oscillates also around its reference which has been set equal to zero to guarantee a unit power factor operation in the stator side. The evolution of the stator powers shows that the oriented stator field technique has successfully permitted their independent control.

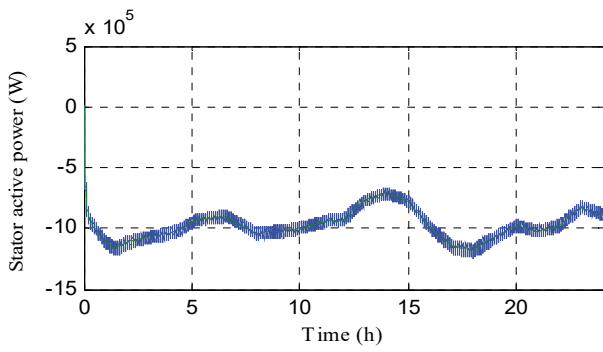


Figure.8: Actual and reference stator active power

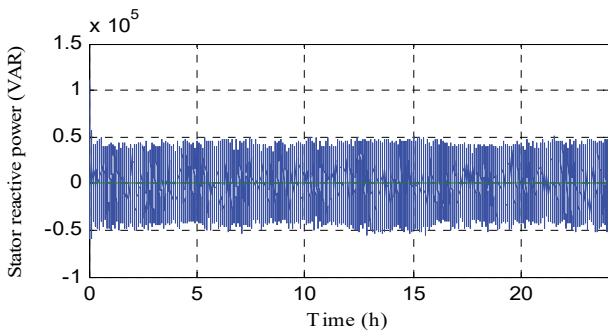


Figure.9: Actual and reference stator reactive power

Figure.10 and Figure.11 show the power sent to the grid in both cases: without storage and with storage respectively. Before integrating the battery bank, the power sent to the grid corresponded to the wind generated power which either exceeded or was less than grid demand set to 750 kW.

After having introduced the battery bank, the power sent to the grid has become smooth (Figure.11).

The battery power is reported in Figure.12. This figure shows that when the wind generated power is more than the power demanded by the grid, battery power is positive which corresponds to the charging mode; and when the wind generated power is less than the grid required power, battery power is negative which corresponds to the discharging mode.

The battery operating modes appear clearly in the variations of the state of charge (Figure.13). The battery current is reported in Figure.14. We can see that it follows the reference imposed by the supervisory system which means that the current controller parameters have been properly chosen.

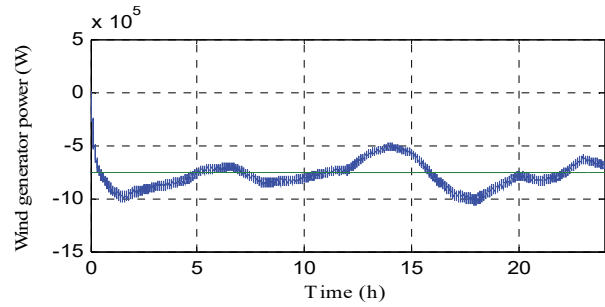


Figure.10: Power sent to the grid without storage

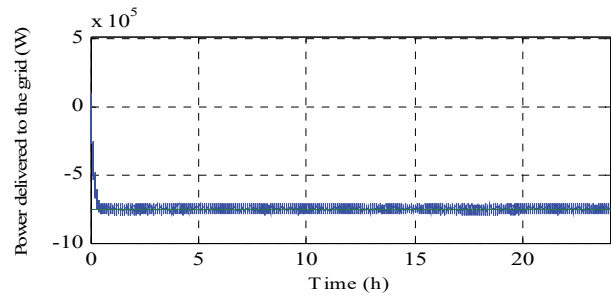


Figure.11: Power sent to the grid with storage

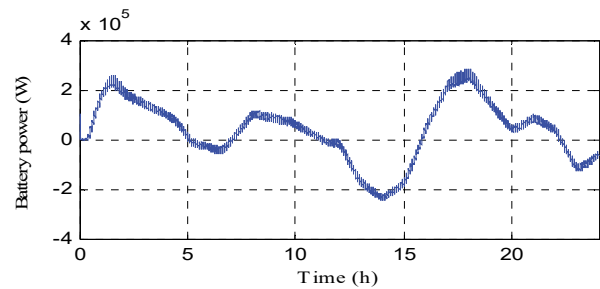


Figure.12: Battery power evolution

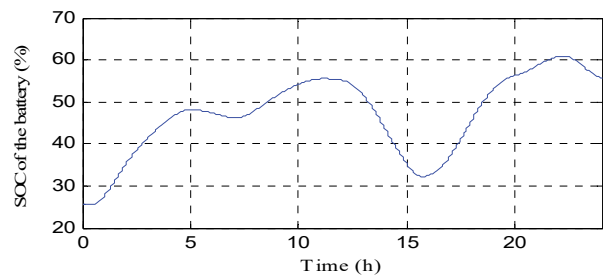


Figure.13: Battery SOC evolution

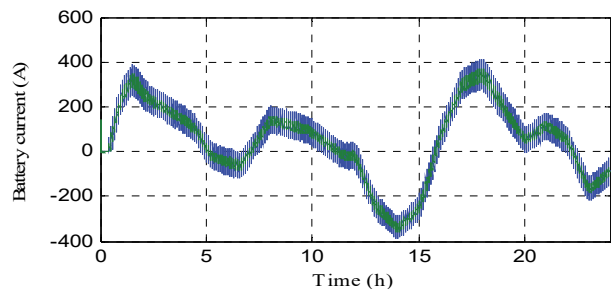


Figure.14: Actual and reference battery current

Figure.15 and Figure.16 show that DC-bus voltage is well regulated around its reference (1400 V) with few overshoots during the transients. We notice that DC-bus voltage has not been affected after the introduction of the storage system.

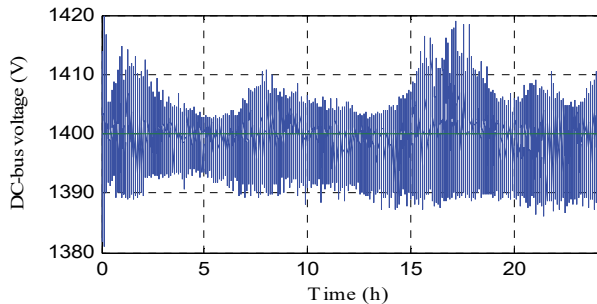


Figure.15: DC-bus voltage without storage system

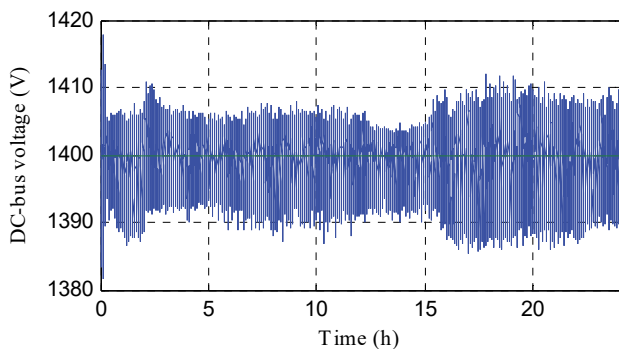


Figure.16: DC-bus voltage with storage system

5. CONCLUSION

In this paper, a power control scheme for a battery-assisted wind energy conversion system has been developed. The wind generator is connected to the grid through a back to back three-level converter. The main part of the proposed control scheme is the supervisory algorithm, necessary for the power management of the battery bank to operate in the appropriate mode. The aim was to satisfy the grid power requirement by smoothing the wind generated power. Besides, active and reactive powers of the wind generator have been independently controlled in order to optimize its operating.

Simulation results have shown satisfactory behavior of the whole system, so the battery bank has been able to smooth the wind generated power so that it corresponds to the grid's requirement without affecting static and dynamic performances of the wind generator.

REFERENCES

- [1] Cheng, M. and Zhu, Y., "The state of the art of wind energy conversion systems and technologies: A review," *Energy Conversion and Management*, vol. 88, Dec. 2014, pp. 332-347.
- [2] Hossain, M.M. and Ali, M.H., "Future research directions for the wind turbine generator system," *Renewable and Sustainable Energy Reviews*, vol. 49, Sep. 2015, pp. 481-489.
- [3] Kaldellis, J.K. and Zafirakis, D., "The wind energy revolution: A short review of a long history," *Renewable Energy*, vol. 36, iss. 7, Jul. 2011, pp. 1887-1901.
- [4] Georgilakis, P.S., "Technical challenges associated with the integration of wind power into power systems," *Renewable and Sustainable Energy Reviews*, vol. 12, iss. 3, Apr. 2008, pp. 852-863.
- [5] Fernández, R.D.; Mantz, R.J. and Battaiotto, P.E., "Impact of wind farms on a power system. An eigenvalue analysis approach," *Renewable Energy*, vol. 32, iss. 10, Aug. 2007, pp. 1676-1688.
- [6] Howlader, A.M.; Urasaki, N.; Yona, A.; Senjyu, T.; and Saber, A.Y., "A review of output power smoothing methods for wind energy conversion systems," *Renewable and Sustainable Energy Reviews*, vol. 26, Oct. 2013, pp. 135-146.
- [7] Díaz-González, F.; Sumper, A.; Gomis-Bellmunt, O.; and Villafáfila-Robles, R., "A review of energy storage technologies for wind power applications," *Renewable and Sustainable Energy Reviews*, vol. 16, iss. 4, May 2012, pp. 2154-2171.
- [8] Rabiee, A.; Khorramdel, H.; and Aghaei, J., "A review of energy storage systems in microgrids with wind turbines," *Renewable and Sustainable Energy Reviews*, vol. 18, Feb. 2013, pp. 316-326.
- [9] Teleke, S.; Baran, M.E.; Bhattacharya, S., and Huang, A., "Validation of battery energy storage control for wind farm dispatching," presented at the *IEEE Power and Energy Society General Meeting*, Providence, RI, USA, 2010.
- [10] Shaltout, A. and Gamal, H., "Power coordination of grid-connected wind turbine doubly fed induction generator augmented with battery storage," presented at the *IEEE International Conference on Smart Energy Grid Engineering (SEGE)*, Oshawa, ON, Canada, 2013.

- [11] Sarrias, R. L.; Fernández, M.; García, C., and Jurado, F., "Supervisory control system for DFIG wind turbine with energy storage system based on battery," *2011 International Conference on Power Engineering, Energy and Electrical Drives*, Málaga, Spain, 2011.
- [12] Babazadeh, H.; Gao, W., and Duncan, K., "A new control scheme in a battery energy storage system for wind turbine generators," *2012 IEEE Power and Energy Society General Meeting*, San Diego, CA, USA, 2012.
- [13] Borhan, H.; Rotea, M.A., and Viassolo, D., "Optimization-based power management of a wind farm with battery storage," *Wind Energy*, vol. 16, iss. 8, Nov. 2013, pp. 1197-1211.
- [14] Subburaj, A.S.; Kondur, P.; Bayne, S.B.; Giesselmann, M.G., and Harral, M.A., "Analysis and review of grid connected battery in wind applications," *2014 Sixth Annual IEEE Green Technologies Conference*, Corpus Christi, TX, USA, 2014.
- [15] Abbes, M., Belhadj, J., and Ben Abdelghani Bennani, A., "Design and control of a direct drive wind turbine equipped with multilevel converters," *Renewable Energy*, vol. 35, iss. 5, May 2010, pp. 936-945.
- [16] Chibani, R.; Berkouk, E, and Boucherit, M., "Input DC voltages of three-level neutral point clamped voltage source inverter balancing using a new kind of clamping bridge," *International Journal of Computer and Electrical Engineering*, vol. 2, no. 5, Oct. 2010, pp. 879-886.
- [17] Calle, A. and al., "Three-level three-phase neutral-point-clamped back-to-back converter applied to a wind emulator," *13th European Conference on Power Electronics and Applications (EPE'09)*, Barcelona, Spain, 2009.
- [18] Boulaam, K.; Boukhelifa, A., and Janajreh, I., "A non-Linear Control of Power Wind Turbine Based on Doubly Fed Induction Generator," *1st International Conference & Exhibition on the Applications of Information Technology to Renewable Energy Processes and Systems (IT-DREPS)*, Amman, Jordan, 2013.
- [19] Boutoubat, M.M.; Mokrani, L., and Machmoum, M., "Control of a wind energy conversion system equipped by a DFIG for active power generation and power quality improvement," *Renewable Energy*, vol. 50, Feb. 2013, pp. 378-386.
- [20] Taraft, S.; Rekioua, D.; Aouzellag, D., and Bacha, S., "A proposed strategy for power optimization of a wind energy conversion system connected to the grid," *Energy Conversion and Management*, vol. 101, Sep. 2015, pp. 489-502.
- [21] El Aimani, S., "Modélisation de différentes technologies d'éoliennes intégrées dans un réseau de moyenne tension," *Thèse de Doctorat*, Lille 2004.
- [22] Wichert, B., "Control of photovoltaic-diesel hybrid energy systems," *Ph.D. Dissertation*, Curtin University of Technology, 2000.

Reliable Full-Wave Computation of the Characteristic Impedance of Asymmetrical Finline: Application to the Step Discontinuity

Abdelhamid KHODJA¹, Mustapha Cherif-Eddine YAGOUB², Rachida TOUHAMI¹ and Henri BAUDRAND³

¹USTHB, Instrumentation Laboratory, Fac. Electronics & Informatics, Algiers, Algeria
akhodja@usthb.dz and rachida.touhami@gmail.com

²EECS, University of Ottawa, 800 King Edward, Ottawa, KIN 6N5, Canada
myagoub@uottawa.ca

³ENSEEIH, 2 rue Charles Camichel, Toulouse, France
henri.baudrand@yahoo.fr

ABSTRACT

This paper investigates the computation of the characteristic impedance of asymmetrical isotropic unilateral finlines. Applying the full-wave integral modal technique along with the most widely-used impedance definition, allowed characterizing asymmetrical step discontinuities in enclosed finline cavities. Enhanced numerical solutions were obtained by selecting appropriate choice of trial functions through the Galerkin's method.

Key Words: Admittance operator, hybrid mode, scattering matrix, trial functions

1. INTRODUCTION

Finline structures have been widely explored to design various microwave and millimeter-wave integrated circuits [1-3] most of them dealing with symmetric structures with respect to the E-plane of the shielding. However, the asymmetrical case is still an interesting option to consider with regard to a flexibility improvement of metallic waveguides as well as an increase of the degree of integration, leading to a significant extension of the panel of applications [1]. This asymmetrical case can be obtained by varying the position of the slot between the two zero-thickness conducting strips inserted in the waveguide propagating a hybrid mode as shown in Fig.1. To this end, modal integral technique combined with the formalism of

mathematical operators has already been used to compute the phase constants, guided wavelengths, or effective permittivities as well as cutoff frequencies of such waveguiding structures [4-5]. Among structures largely exploited in Monolithic Microwave Integrated Circuit (MMIC) design, finline step discontinuities have been commonly used as impedance transformers. Theoretical approaches of such junction discontinuities have been indeed described [6], but quite few works have been reported on the characterization of asymmetric finline discontinuities.

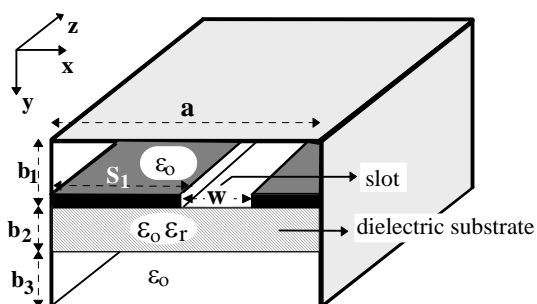


Figure.1: Perspective view of asymmetrical finline structure

The aim of this paper is to determine the characteristic impedance of asymmetrical unilateral finlines printed on isotropic dielectric substrates, mainly because this parameter is indeed a key element to characterize such structures. In fact, from this parameter, it would be possible to

characterize an asymmetrical finline discontinuity by determining its scattering matrix at the junction discontinuity.

The retained integral modal technique is based on the Galerkin's method, which involves an adequate choice of trial functions defined in the slot. Applying this full-wave technique results in a homogeneous system of algebraic equations from which the phase constants of dominant and higher order modes can be obtained. Then, the tangential electric fields in the slot between the metallic strips can be determined. In fact, knowing these fields allows computing all the components of the electromagnetic (EM) fields in all the metallic waveguide structure. Consequently, the total EM power propagating in this asymmetrical finline can be deduced. Thus, for a given width "w" of the slot, the characteristic impedance of the finline can be computed, by using a predefined power-voltage relationship [7-8], once the voltage known in the slot.

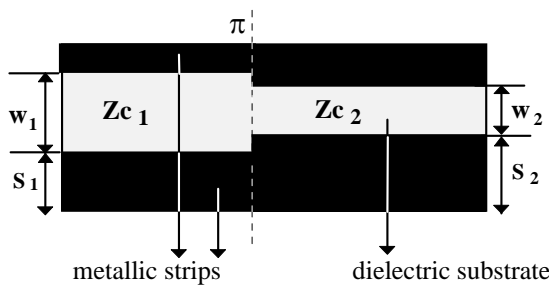


Figure.2: Longitudinal cross section of step discontinuity in asymmetrical unilateral finline technology

From that, we can deduce the magnitude of the S-parameters at the junction discontinuity, since

$$|S_{11}| = |S_{22}| = \left| \frac{Z_{C2} - Z_{C1}}{Z_{C2} + Z_{C1}} \right| \text{ and } |S_{21}| = |S_{12}| = \sqrt{1 - |S_{11}|^2}.$$

In this case, the considered structures are matched and lossless. Here, Z_{C1} and Z_{C2} state for the characteristic impedances of the two finlines of respective slot widths w_1 and w_2 , and connected to each other at the π junction (Fig. 2). These two conducting strips allow the propagation of EM waves in hybrid mode. Therefore, none of the two longitudinal components of the EM field can be neglected. The dispersive nature of the propagation is expressed by the frequency dependence of the characteristic impedance

of the finline, highlighting the existence of a dominant mode with a non-zero cutoff frequency F_c , leading to a numerical determination of this parameter. Thus, the operating frequency F (with $F > F_c$) can be set before starting the calculation of the dispersion parameters of the considered finline.

2. THEORETICAL APPROACH

The proposed technique uses the formalism of mathematical operators to easily resolve the boundary conditions in the interface due to the deposit of metallic strips. Indeed, such formalism permits to determine the admittance operator \hat{Y} to which the Galerkin's method is applied. In fact, this operator constitutes the key issue in the development of this technique [9-10]. For this case, we assumed a fictitious propagation in the oy-transverse direction of the considered finline instead of the real oz-longitudinal direction. Then, we considered the transverse section of the structure as a set of cascaded lines terminated by short-circuited loads, noted "sc" (Fig.3).

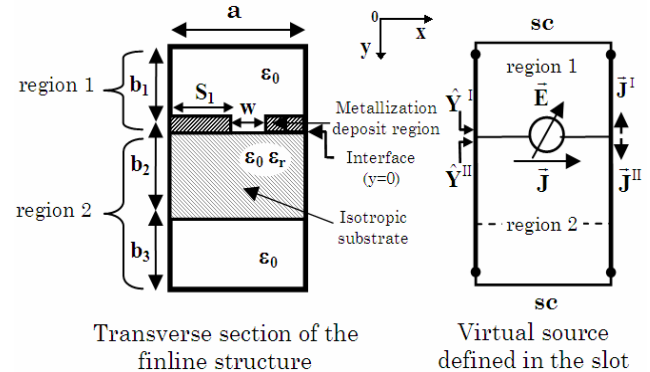


Figure.3: Equivalent circuit of the finline structure

The equivalent circuit of the transverse section of a finline with negligible thickness includes the presence of a non-zero virtual adjustable source represented by the transverse electric field \vec{E} in the slot [11]. Here, the admittance operators \hat{Y}^I and \hat{Y}^{II} for region 1 and 2, respectively, are viewed in the air-dielectric interface. The Kirchoff's law allows writing:

$$\vec{J} = \vec{J}^I + \vec{J}^{II} \quad (1)$$

with

$$\vec{J}^I = \hat{Y}^I \vec{E} \quad \text{and} \quad \vec{J}^{II} = \hat{Y}^{II} \vec{E} \quad (2)$$

leading to:

$$\vec{J} = (\hat{Y}^I + \hat{Y}^II) \vec{E} = \hat{Y} \vec{E} \quad (3)$$

with

$$\begin{cases} \vec{E} = \vec{0} & \text{on the metal} \\ \vec{J} = \hat{Y} \vec{E} = \vec{0} & \text{in the slot} \end{cases} \quad (4)$$

$$(5)$$

The matrix representation of the \hat{Y} operator should be determined to obtain the dispersion matrix via the Galerkin's technique. This requires the involvement of a complete set of orthogonal basis functions ($\{f_n\}_{n=0,N}$), which expressions are given in [4], and also the use of the mode admittances at the interface y_n^I and y_n^{II} of region 1 and 2, respectively, where N states for the number of modes.

The admittance operator is determined such as:

$$\hat{Y} = \sum_{n=0}^N \left[\langle f_n | (y_n^I + y_n^{II}) | f_n \rangle \right]^{e+h} = \sum_{n=0}^N \left[\langle f_n | y_n | f_n \rangle \right]^{e+h} \quad (6)$$

where "e" and "h" state respectively for the TM_n and TE_n modes along the transverse direction (Oy). Here, the expression of the mode admittance (y_n) is detailed in [4]. $|f_n\rangle\langle f_n|$ represents the projection operator on the basis vectors $\{f_n\}_{n=0,N}$, while " $\langle |$ " and " $| \rangle$ " represent the "bra" and "ket" operators, respectively. Note that the product of vector "bra" ($\langle f_n |$) with vector "ket" ($| f_m \rangle$) represents the inner product of these two quantities deduced from the integral calculation through the integration domain ID [10] such as:

$$\langle f_n, f_m \rangle = \int_{ID} \bar{f}_n^+(x) \bar{f}_m(x) dx. \quad (7)$$

with "+" stating for the transpose conjugate.

The unknown electric field is expressed on the base of trial functions (Φ_{px} and Φ_{qz}) expressed in the slot and pondered by weighting coefficients e_{px} and e_{qz} such as:

$$E_x = \sum_{p=1}^K e_{px} \Phi_{px} \quad \text{and} \quad E_z = \sum_{q=1}^K e_{qz} \Phi_{qz} \quad (8)$$

with K the number of trial functions per component along the Ox and Oz directions.

The application of the Galerkin's procedure to the admittance operator requires the projection of the terms of (5) with trial functions, leading to a homogeneous system of algebraic equations.

This system constitutes the dispersion matrix, which elements are composed of mode admittances and inner products of basis functions with trial functions [4]. Setting its determinant to zero allows evaluating the propagation constant (β) of dominant and higher order modes of the finline. The resolution of this homogeneous system allows computing the required e_{px} and e_{qz} weighting coefficients of trial functions and thus, the electric field \vec{E} in the slot. We can also express the transverse electric field at the interface ($y=0$) by using basis functions such as:

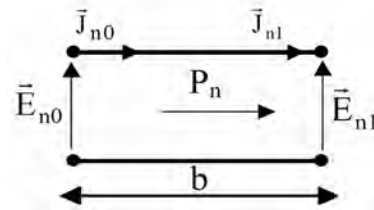
$$|\vec{E}\rangle = \sum_{n=0}^N a_n |f_n\rangle \Rightarrow \begin{bmatrix} E_x(x) \\ E_z(x) \end{bmatrix} = \sum_{n=0}^N a_n \begin{bmatrix} f_{nx}(x) \\ f_{nz}(x) \end{bmatrix} \quad (9)$$

The coefficients $a_{n(n=0,\infty)}$ represent the components of the transverse field \vec{E} in the base of modes such as:

$$a_n^{(e+h)} = \left[\sum_{p=1}^{Kx} e_{px} \langle f_{nx}, \Phi_{px} \rangle + \sum_{q=1}^{Kz} e_{qz} \langle f_{nz}, \Phi_{qz} \rangle \right]^{(e+h)} \quad (10)$$

where "e+h" refers to the TM_y and TE_y modes. By comparison with the telegraphist's equations, we can determine the chain matrix linking the input and output parameters (\vec{E}_n and \vec{J}_n) of any guide such as [4]:

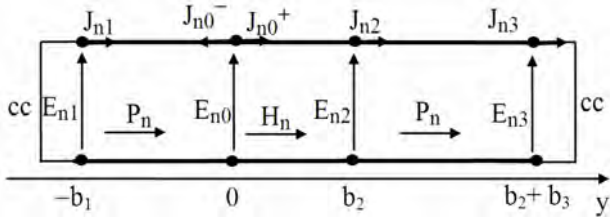
$$\begin{bmatrix} \vec{E}_{n0} \\ \vec{J}_{n0} \end{bmatrix} = \begin{bmatrix} ch(p_n b) & Z_n sh(p_n b) \\ Y_n sh(p_n b) & ch(p_n b) \end{bmatrix} \begin{bmatrix} \vec{E}_{n1} \\ \vec{J}_{n1} \end{bmatrix} \quad (11)$$



Knowing that P_n states for the propagation constant relative to the mode n , and Y_n (or Z_n) represents the admittance (or the impedance) of mode for an infinite guide.

The equivalent circuit of the finline, with regard to the Oy fictitious propagation direction, results in:

$$\begin{cases} P_n^2 = \left(\frac{n\pi}{a}\right)^2 + \beta^2 - \beta_0^2 \\ H_n^2 = \left(\frac{n\pi}{a}\right)^2 + \beta^2 - \beta_0^2 \epsilon_r \\ \beta_0^2 = \omega^2 \mu_0 \epsilon_0 \end{cases} \quad (12)$$



From (11) we can determine the expressions of the transverse EM fields in the three media.

Medium 1: $(-b_1 \leq y \leq 0)$

$$\begin{bmatrix} \bar{E}_n(x,y) \\ \bar{J}_n(x,y) \end{bmatrix} = \begin{bmatrix} ch(-P_{n1}y) & Z_{n1} sh(-P_{n1}y) \\ Y_{n1} sh(-P_{n1}y) & ch(-P_{n1}y) \end{bmatrix} \begin{bmatrix} \bar{E}_{n0} \\ -\bar{J}_{n0^-} \end{bmatrix} \quad (13)$$

Medium 2: $(0 \leq y \leq b_2)$

$$\begin{bmatrix} \bar{E}_n(x,y) \\ \bar{J}_n(x,y) \end{bmatrix} = \begin{bmatrix} ch(P_{n2}y) & -Z_{n2} sh(P_{n2}y) \\ -Y_{n2} sh(P_{n2}y) & ch(P_{n2}y) \end{bmatrix} \begin{bmatrix} \bar{E}_{n0} \\ \bar{J}_{n0^+} \end{bmatrix} \quad (14)$$

Medium 3: $(b_2 \leq y \leq b_2+b_3)$

$$\begin{bmatrix} \bar{E}_n(x,y) \\ \bar{J}_n(x,y) \end{bmatrix} = \begin{bmatrix} ch(P_{n3}(y-b_2)) & -Z_{n3} sh(P_{n3}(y-b_2)) \\ -Y_{n3} sh(P_{n3}(y-b_2)) & ch(P_{n3}(y-b_2)) \end{bmatrix} \begin{bmatrix} \bar{E}_{n0} \\ \bar{J}_{n0^+} \end{bmatrix} \quad (15)$$

with:

$$\bar{E}_n(x,y) = \begin{bmatrix} E_{nx}(x,y) \\ E_{nz}(x,y) \end{bmatrix} \text{ and } \bar{J}_n(x,y) = \begin{bmatrix} J_{nx}(x,y) \\ J_{nz}(x,y) \end{bmatrix}$$

Thus, we can write at $y=0$:

$$\bar{J}_{n0} = \bar{J}_n(x,0) = \begin{bmatrix} J_{nx}(x,0) \\ J_{nz}(x,0) \end{bmatrix}$$

and

$$\bar{E}_{n0} = \bar{E}_n(x,0^-) = \bar{E}_n(x,0^+) = \bar{E}_n(x,0) = \begin{bmatrix} E_{nx}(x,0) \\ E_{nz}(x,0) \end{bmatrix}$$

knowing that:

$$\begin{cases} \text{at } y = 0^- : \bar{J}_{n0}^- = \bar{J}_n(x,0^-) = Y_n^I \bar{E}_n(x,0) \\ \text{at } y = 0^+ : \bar{J}_{n0}^+ = \bar{J}_n(x,0^+) = Y_n^{II} \bar{E}_n(x,0) \end{cases} \quad (16)$$

From the above, with the contribution of all modes, the expressions of the EM fields can be deduced in the three media:

$$\bar{E}(x,y) = \sum_{n=0}^N \bar{E}_n(x,y), \quad \bar{J}(x,y) = \sum_{n=0}^N \bar{J}_n(x,y) \quad (17)$$

where $\vec{H} = \vec{n} \wedge \vec{J} \Rightarrow \begin{bmatrix} H_x \\ H_z \end{bmatrix} = \vec{n} \times \begin{bmatrix} J_x \\ J_z \end{bmatrix} \Rightarrow$

$$\begin{cases} H_x(x,y) = J_z(x,y) \\ H_z(x,y) = -J_x(x,y) \end{cases} \quad (18)$$

To summarize, all the transverse components of the EM fields in the different media can be expressed as function of the transverse electrical fields $\bar{E}_{nx}(x,0)$ and $\bar{E}_{nz}(x,0)$ at the discontinuity plane between the two conducting strips, with:

$$\begin{cases} E_x(x,0)^{e,h} = \sum_{n=0}^N E_{nx}(x,0)^{e,h} = \sum_{n=0}^N (a_n f_{nx})^{e,h} \\ E_z(x,0)^{e,h} = \sum_{n=0}^N E_{nz}(x,0)^{e,h} = \sum_{n=0}^N (a_n f_{nz})^{e,h} \end{cases} \quad (19)$$

Here the symbol "e,h" states for TM_y or TE_y mode.

Note that for a TE_y mode, $(E_y)^h = 0$, whereas for a TM_y mode, $(H_y)^e = 0$.

Furthermore, the Maxwell's equations allow expressing the longitudinal fields (relatively to Oy) in function of the transverse fields [4]. In fact, we have $\vec{\nabla} \times \vec{E} = -j\omega\mu\vec{H}$ and $\vec{\nabla} \times \vec{H} = j\omega\epsilon\vec{E}$ which can be rewritten as:

$$\begin{matrix} (a) \\ (b) \\ (c) \\ (d) \\ (e) \\ (f) \end{matrix} \begin{bmatrix} j\omega\epsilon & 0 & 0 & 0 & -j\beta & -\partial_y \\ 0 & j\omega\epsilon & 0 & j\beta & 0 & \partial_x \\ 0 & 0 & j\omega\epsilon & \partial_y & -\partial_x & 0 \\ 0 & j\beta & \partial_y & j\omega\mu & 0 & 0 \\ -j\beta & 0 & -\partial_x & 0 & j\omega\mu & 0 \\ -\partial_y & \partial_x & 0 & 0 & 0 & j\omega\mu \end{bmatrix} \begin{bmatrix} E_x \\ E_y \\ E_z \\ H_x \\ H_y \\ H_z \end{bmatrix} = 0 \quad (20)$$

Equation (20a) gives H_y in function of E_x and H_z while (20d) shows E_y as function of H_y and E_z .

The next step is to determine the power carried by the EM wave through the transverse plane (xoy) perpendicular to the direction of real propagation (oz). This power is equal to [2]:

$$P = \frac{1}{2} \Re e \langle E | J \rangle \quad (21)$$

By decomposing the scalar product $\langle E | J \rangle$ on the transverse components (xoy) in the three media, we get:

$$\langle E | J \rangle = \sum_{i=1}^3 \left[\langle E_x | J_x \rangle^{(e+h)} + \langle E_y | J_y \rangle^{(e+h)} \right] \quad (22)$$

where "i" refers to the medium 1, 2 or 3. Therefore, for the direction of real propagation (oz), we have:

$$\vec{J} = \vec{H} \wedge \vec{n} \Rightarrow \begin{cases} J_x(x,y) = H_y(x,y) \\ J_y(x,y) = -H_x(x,y) \end{cases} \quad (23)$$

Note that $H_y = 0$ for a TM mode (i.e., $(J_x)^e = 0$) and $E_y = 0$ for a TE mode (i.e., $(E_y)^h = 0$).

On the other side, the circulation of the electrical field between the two conducting strips allows expressing the potential V as [4]:

$$V = - \int_{-w/2}^{w/2} E_x(x,0) dx = - \sum_{n=0}^N \int_{-w/2}^{w/2} E_{nx}(x,0)^{(e+h)} dx$$

leading to the characteristic impedance [4]:

$$Z_C = \frac{V^2}{2P} \quad (24)$$

Finally, the magnitude of the S-parameters of the step discontinuity between two matched and lossless finlines of different slot widths (figure 2), can be obtained:

$$|S_{11}| = |S_{22}| = \left| \frac{Z_{C2} - Z_{C1}}{Z_{C2} + Z_{C1}} \right| \quad \text{and} \quad |S_{21}| = |S_{12}| = \sqrt{1 - |S_{11}|^2} \quad (25)$$

with $Z_{C2} = Z_c(w_2)$ and $Z_{C1} = Z_c(w_1)$.

3. NUMERICAL RESULTS

To efficiently analyze the dispersive behavior of the characteristic impedance (Z_c) of such asymmetrical finlines with regard to the physical and electrical parameters, sinusoidal trial functions taken into account edge effects were selected [4-5]. Moreover, to reach convergence, a sufficient number of trial functions ($K \leq 6$) and modes ($N \leq 2500$) have been taken according to the widths of both conducting strips and slot. We first studied the effect of lateral metallic strip width S_1 on Z_c while varying the normalized slot width (w/a) or the frequency of asymmetrical finline embedded in a WR-28 metallic rectangular waveguide. From Fig. 4, we can deduce that the asymmetric structure constitutes an additional advantage with regard to the symmetrical case, because this Z_c can be controlled not only by varying the width of the slot (w) but also by varying the width of the lateral strip (S_1).

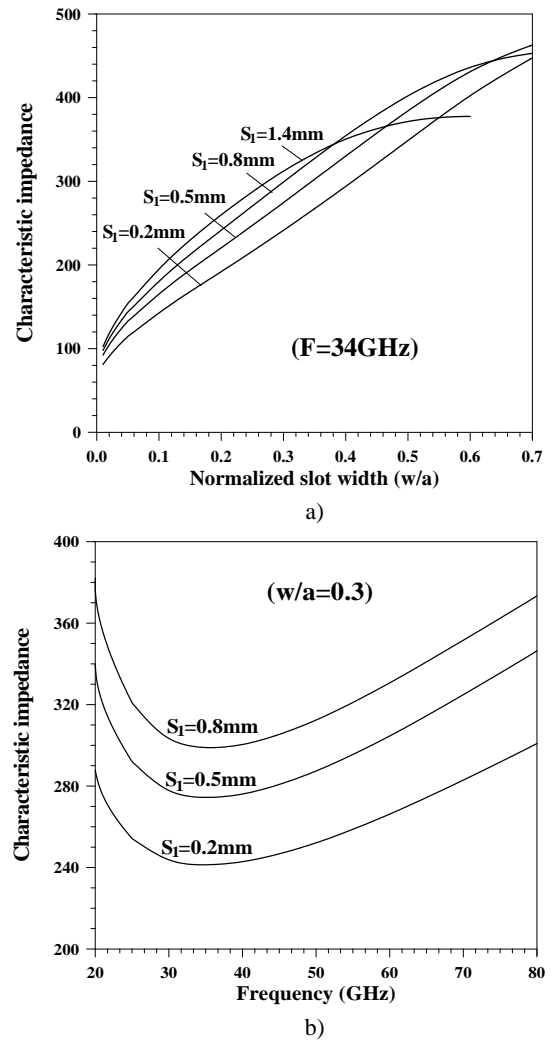


Figure 4: Effects of lateral metallic strip width on Z_c with $a=b_1=3.556\text{mm}$, $b_2=0.254\text{mm}$, $b_3=3.302\text{mm}$, $\epsilon_r=2.22$. (a) Variation of Z_c versus normalized slot width (w/a), (b) Variation of Z_c versus frequency (F)

Moreover, from fig.4-a, the range of variation of Z_c is more important when S_1 is smaller. However, Fig.4-b describes the same shape of the Z_c curves versus frequency for different values of S_1 .

The evolution of Z_c versus the lateral metallic strip width S_1 is plotted in the Fig. 5, which shows an increase followed by a decrease of Z_c versus the width S_1 , specially for the low dielectric constant ($\epsilon_r=2.2$), since the variation of Z_c is more important when the constant dielectric is lower. However, this structure becomes symmetrical for $S_1=1.2446\text{mm}$.

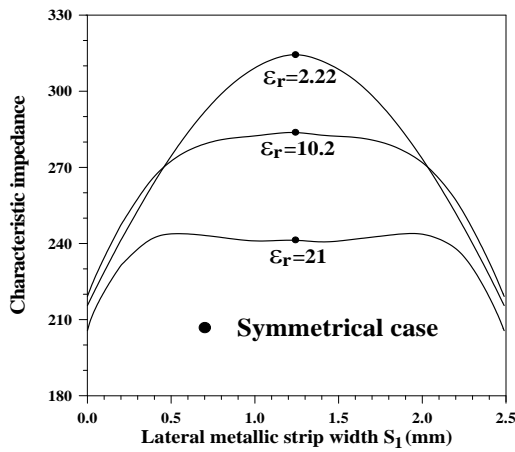


Figure.5: Variation of Z_c versus lateral metallic strip width with regard to the dielectric constant of substrate with $a=3.556\text{mm}$, $w/a=0.3$, $b_1=b_3=3.429\text{mm}$, $b_2=0.254\text{mm}$, $F=34\text{GHz}$

To verify the reliability and accuracy of this modal technique used to compute Z_c , we compared our results with those published in [1] and [12]. Figure 6 computes the impedance characteristic of asymmetrical finline embedded in a WR-28 metallic box.

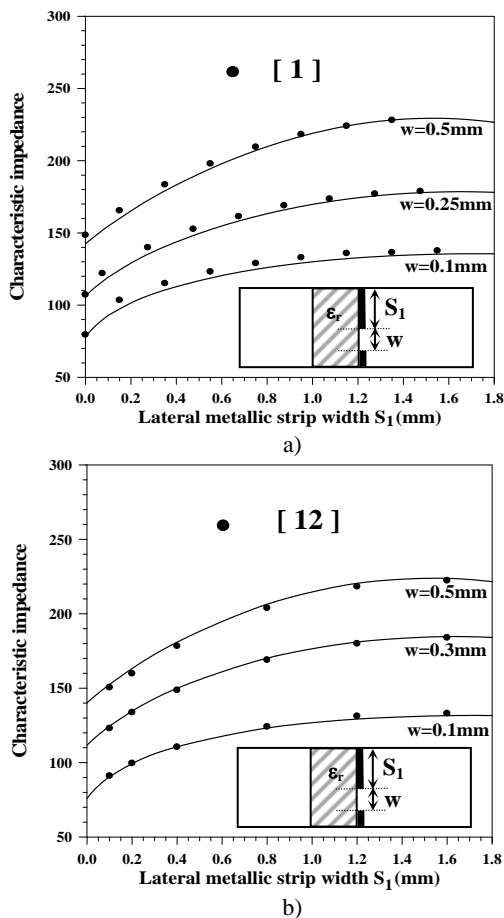


Figure.6: Evolution of Z_c of the asymmetrical finline versus S_1 (a) $a=3.556\text{mm}$, $b_1=b_3=3.4935\text{mm}$, $b_2=0.125\text{mm}$, $\epsilon_r=2.2$, $F=33\text{GHz}$, (b) $a=b_1=3.556\text{mm}$, $b_2=0.254\text{mm}$, $b_3=3.302\text{mm}$, $\epsilon_r=2.22$, $F=34\text{GHz}$

From this figure, we show an increase of Z_c versus S_1 , which becomes less important while reaching stability for three selected widths of the slot. In addition, for $w=0.5\text{mm}$, this Z_c tends to decrease from $S_1=1.4\text{mm}$.

A good agreement was obtained between our results and those published in [1] and in [12], with an average relative error less than 3.25 % and 0.9% respectively.

The next step involved the computation of Z_c of an asymmetrical single finline consisting of a single lateral metallic strip deposited on a dielectric substrate ($\epsilon_r=2.22$) embedded inside a WR-28 waveguide.

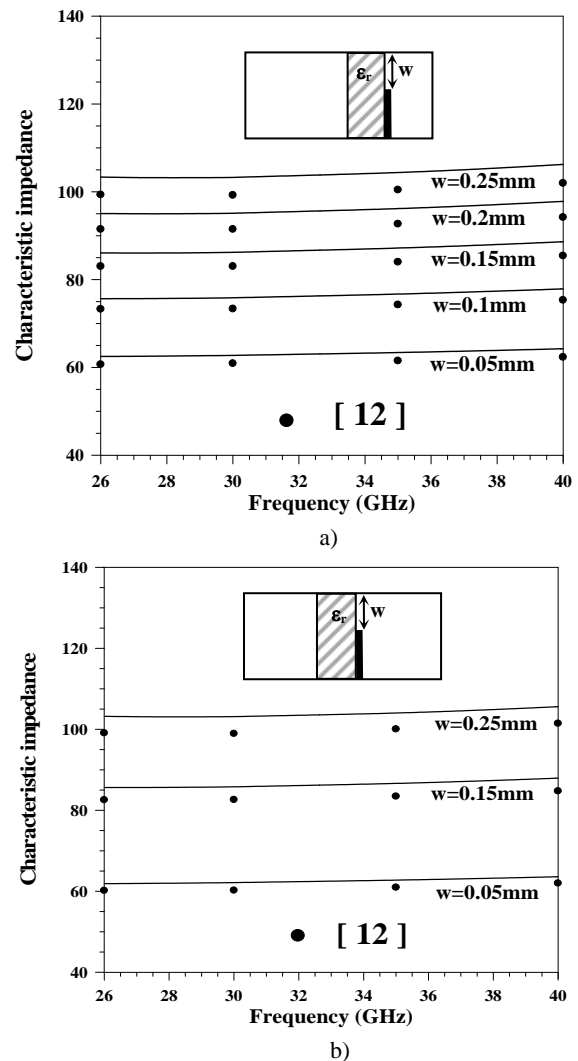


Figure.7: Evolution of Z_c of asymmetrical single finline versus frequency with $a=3.556\text{mm}$, $b_2=0.254\text{mm}$, $S_1=0\text{mm}$ and $\epsilon_r=2.22$. (a) $b_1=1.778\text{mm}$, $b_3=5.08\text{mm}$, (b) $b_1=3.556\text{mm}$, $b_3=3.302\text{mm}$

Fig. 7 shows the frequency variation of Z_c with a quasi-stability of the values for two different positions of substrate while several widths of the slot being selected. The results

were obtained with an average error of 3.6% compared to those in [12].

From that, the scattering matrix related to the asymmetrical step discontinuity embedded in a WR-28 rectangular metallic box and built from two asymmetrical finlines of different slot widths. Figure 6 shows the variations of the magnitude of the S-parameters versus the w_2/a ratio for different widths of the lateral metallic strip (S_1) by assuming $S_2=S_1$ (see Fig. 2) and considering two different dielectric constants of substrate.

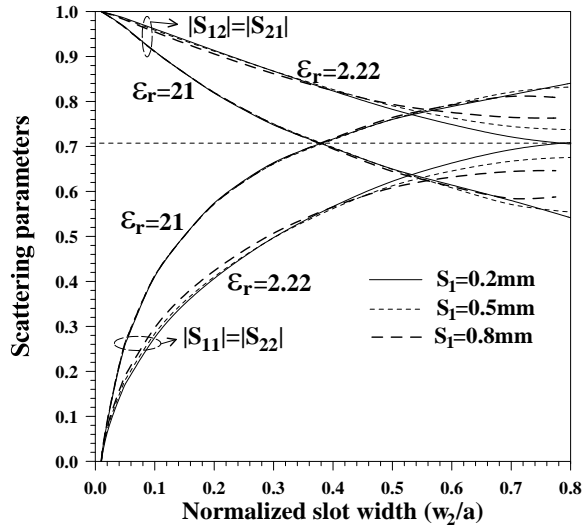


Figure.8: Scattering parameters versus w_2/a with $a=3.556\text{mm}$, $b_1=b_3=3.429\text{mm}$, $b_2=0.254\text{mm}$, $w_1/a=0.01$, $F=34\text{GHz}$

We practically got the same overlapping points corresponding to the equidistribution of the incident and reflected powers (i.e., $|S_{11}|=|S_{22}|=|S_{12}|=|S_{21}|=0.707$).

Indeed, the obtained curves show an increase of $|S_{11}|$ and $|S_{22}|$ and a decrease of $|S_{12}|$ and $|S_{21}|$ versus w_2/a and ϵ_r . However, we observe a weak influence of the lateral strip width S_1 on the scattering parameters when the slot of the second access of this discontinuity is sufficiently narrow ($w_2/a < 0.4$). On the other hand, this influence is more important for wider slot ($w_2/a > 0.6$).

Figure 9 illustrates the frequency behavior of the scattering parameters of the above asymmetrical step discontinuity inserted into a WR-28 metallic waveguide when several widths of the lateral strip S_1 are selected. In this case, we set $w_2/a=0.4$ to study the influence of S_1 on these parameters.

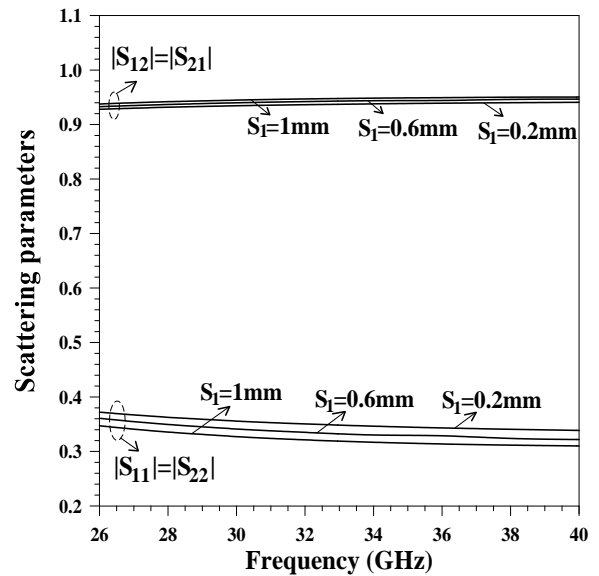


Figure.9: Scattering parameter versus frequency with $a=3.556\text{mm}$, $b_1=b_3=3.429\text{mm}$, $b_2=0.254\text{mm}$, $w_1/a=0.1$, $w_2/a=0.4$, $\epsilon_r=2.22$

We notice a very small variation of the S-parameters over frequency as well as a weak influence of S_1 on the transmission coefficients compared to the reflection ones, since the curves of $|S_{12}|$ and $|S_{21}|$ obtained from the different widths S_1 tend towards the same values, while $|S_{11}|$ and $|S_{22}|$ decrease when S_1 increases.

4. CONCLUSION

In this paper, an efficient integral modal technique based on the mathematical operators has been proposed to efficiently compute the Zc for asymmetrical finlines. It successfully uses the Galerkin's procedure with appropriate trial functions that take into account the edge metallic effects. Good agreement was found while comparing the obtained simulated results to published data. This allows to properly characterize the asymmetrical finline step discontinuity with regard to different physical and electrical parameters.

REFERENCES

- [1] L. P. Schmidt, T. Itoh, and H. Hofmann, "Characteristics of unilateral fin-line structures with arbitrarily located slots," *IEEE Trans. Microwave Theory Tech.*, vol. 29, n°4, pp. 352-355, Apr. 1981.
- [2] A. Sharma and W. J. R. Hoefer, "Empirical expressions for fin-line design", *IEEE Trans. Microwave Theory Tech.*, vol. 31, n°4, pp. 350-356, Apr. 1983.

- [3] R. Vahldieck, "Accurate hybrid-mode analysis of various finline configurations including multilayered dielectrics, finite metallization thickness, and substrate holding grooves", *IEEE Trans. Microwave Theory Tech.*, vol. 32, n°11, pp. 1454-1460, Nov. 1984.
- [4] A. Khodja, "Contribution à la modélisation des circuits planaires multicouches symétriques/asymétriques par une méthode intégrale dans le domaine modal", *Ph.D Thesis*, USTHB, Algeria, Oct. 2017.
- [5] A. Khodja, M.C.E. Yagoub, and R. Touhami, "Full-wave modal integral method for robust modeling of symmetrical/asymmetrical finlines structures embedded in multilayered dielectric substrates", 1st Int. Conf. Electronic Engineering and Renewable Energy, Saidia, Morocco, Apr. 2018.
- [6] H.Y. Yang and N.G. Alexopoulos, "Characterization of the finline step discontinuity on anisotropic substrates", *IEEE Trans. Microwave Theory Tech.*, vol. 35, n°11, pp. 956-963, Nov. 1987.
- [7] J.R. Brews, "Characteristic impedance of microstrip lines", *IEEE Trans. Microwave Theory Tech.*, vol. 35, n°1, pp 30-34, Jan. 1987.
- [8] G. Cano, F. Medina, and M. Horno, "Characteristic impedances of microstrip and finline with uniaxial or biaxial anisotropic substrates", *Electron. Lett*, vol. 24, n° 19, pp. 1211-1212, Sept. 1988.
- [9] A. Khodja, D. Abbou, M.C.E. Yagoub, R. Touhami and H. Baudrand, "Novel dispersive modal approach for fast analysis of asymmetric coplanar structures on isotropic/anisotropic substrates", *the Journal of Electromagnetic Wave and Applications, Francis and Taylor*, Vol 28, n° 12, pp. 1522-1540, July 2014.
- [10] H. Baudrand and D. Bajon, "Equivalent circuit representation for integral formulations of electromagnetic problems", *Intern. Journal of Num. Modelling: Electronic Networks, Devices and Fields*, Wiley, vol. 15, n°1, pp. 23-57, Jan/Feb.2002.
- [11] H. Baudrand, H. Aubert, D. Bajon and F. Bouzidi, "Equivalent network representation of boundary conditions involving generalized trial quantities, *Annales des Telecom.*, vol. 52, n°5-6, pp. 285-292, May/June 1997.
- [12] B. Bhat and S.K. Koul, "*Analysis, Design and Application of Finline*", Norwood: Artech House, USA, 1987.

Metamaterial proprieties exploited in wire antenna design

BERKANI Samir¹, LAMHENE Youssef¹, HADJ-SADOK Mustapha¹

¹ USTHB, LINS Lab, Faculty of Electronics and Computers, PO.Box 32, Bab-Ezzouar, Algiers
sam-30@live.fr, lamhene.y@gmail.com, mustaphahadjsadok@gmail.com

ABSTRACT

In this paper, HIS (High Impedance Surface) proprieties are exploited, in order to verify the HIS application utility; we have used a metamaterial as a ground, to that end, a wire antenna is considered above 2D metamaterial structure using digital capacitance with resonant rings. The structure is investigated by simulation and compared at the frequency 12 GHz, the metamaterials proprieties are successfully verified around the resonant frequency.

Key words

Wire antenna, EBG structures, metamaterials, digital capacitance, negative index materials.

I. INTRODUCTION

The antennas manufacture requires a big precision in realization because the dimensions of these circuits are of the same order of magnitude as the wave length.

Considering the imprecision factors due to the manufacture constraint, surface waves will be engendered; consequently, antenna performance will be influenced. Special materials are used to block surface waves known as metamaterials, they enhance significantly the antenna performance and characterized by simultaneously negative values of the permeability and the permittivity [1], they don't exist in natural state.

Interesting proprieties [2] of metamaterials consist in stopping surface waves to propagate along the surface which is known as EBG (Electromagnetic Band Gap) and there is no phase delay to be introduced to the progressive wave. The structure chosen is 2D metamaterial using digital capacitance, it uses the inductance resulting from the current flowing through the via and capacities which constitute the elementary metamaterial circuit [3].

II. SIMPLE DIPOLE ANTENNA RESPONSE

Fig. 1 shows the radiation pattern of dipole antenna in free space. In horizontal plane (1.B), when viewed from above, the pattern exhibits two lobes which represent the omnidirectional characteristic of the dipole antenna (bidirectional radiation).

When a dipole antenna is installed close to the earth's surface, the pattern radiation is attenuated because of the reflection from the surface and also the surface of earth is lossy [6].

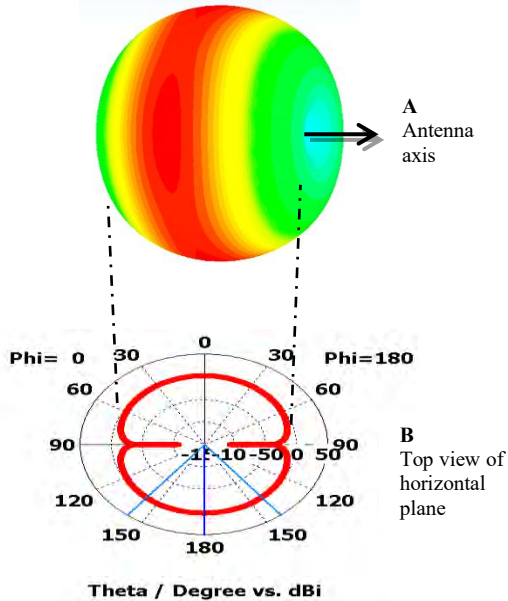


Fig. 1. Idealized dipole radiation pattern.

In the ideal case, the gain of the dipole antenna does not exceed 3 dB as shown on fig. 2.

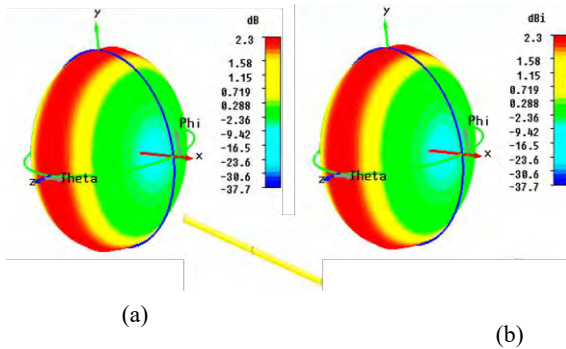


Fig. 2. dipole radiation diagram at 12 GHz : (a) Gain ; (b) directivity.

III. MODELS AND DIMENSIONS

A. Dipole above a perfect electric conductor (PEC)

In order to investigate the performance of the dipole antenna, it will be installed close to different surfaces. Each structure will be also optimized in order to seek the best results. The most simple is a ground plane placed under the dipole antenna (27.5X27.5 mm) of distance $h_{\text{distance}} = 1.925$ mm functions as reflector as shown on fig. 3.

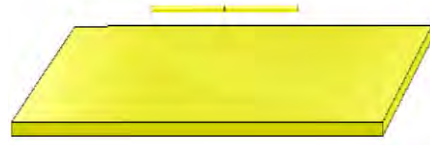


Fig. 3. Dipole antenna above a reflector.

B. Dipole antenna above 2D structure substrate with digital capacitance and rings.

The second model is the dipole antenna placed above substrate of distance $h_{\text{dip}} = 0.02\lambda$, permittivity $\epsilon_r = 2.2$ and thickness $h = 1.25$ mm, composed of several patches of width $w_{\text{patch}} = 0.084\lambda$, seven digits digital capacitances of parameters $w_{\text{digit}} = 0.0084\lambda$ and rings with parameters $r_{\text{ring}} = 0.08\lambda$ [4], $a = 0.007\lambda$, space between rings $g = 0.02\lambda$ and via hole of ray $r = 0.005\lambda$.

We have considered $L_{\text{digit}} = \lambda/4$, dipole length $L = 0.41\lambda$ for the frequency 12 GHz (red graph on fig.7) and $L_{\text{digit}} = \lambda/5$, dipole length $L = 0.42\lambda$ for the frequency 11.772 GHz (green graph on fig.7).

Figure 5 illustrates the model and the digital capacitance (fig. 4) can be calculated by the following formula [5]:

$$C \left(\frac{\text{pF}}{\mu\text{m}} \right) = (\epsilon_r + 1)l[(N - 3)A_1 + A_2] \quad (1)$$

such as:

$$A_1 = 4.409 \tanh [0.55(h/W)^{0.45}]10^{-6} \quad (2.a)$$

$$A_2 = 9.92 \tanh [0.52(h/W)^{0.5}]10^{-6} \quad (2.b)$$

And $W = S = S'$, N number of digits.

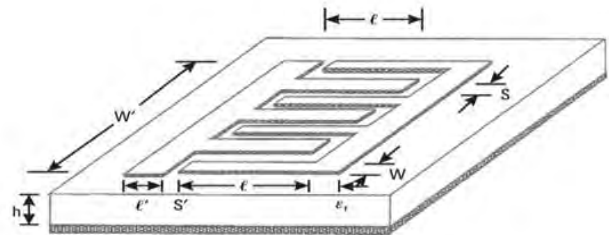


Fig. 4. Seven digits digital capacitance.

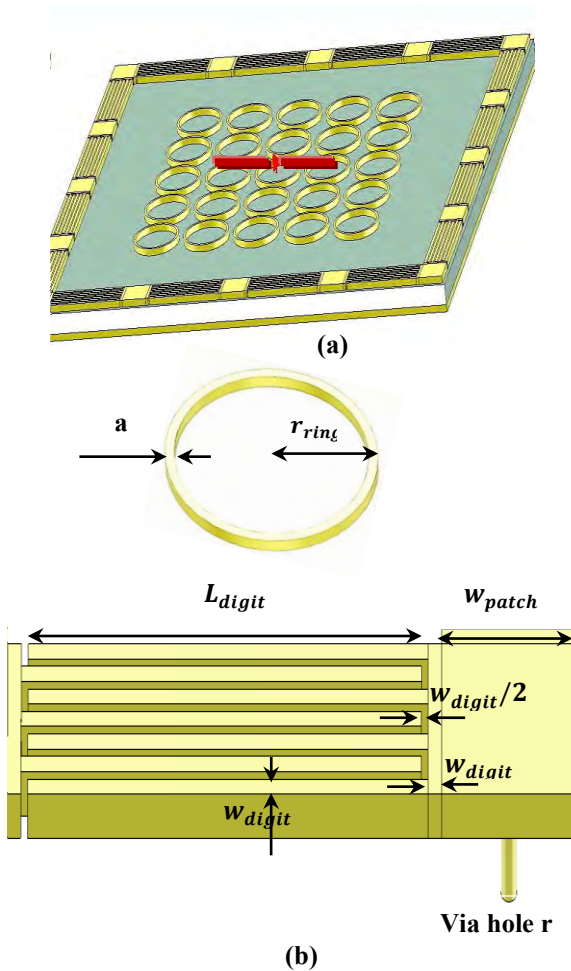


Fig. 5. 2D structure with digital capacitance and rings: (a) Structure; (b) parameters.

IV. RESULTS

The return loss of the first model as shown on the fig. 6 doesn't satisfy the minimum attenuation, it can't be used as ground.

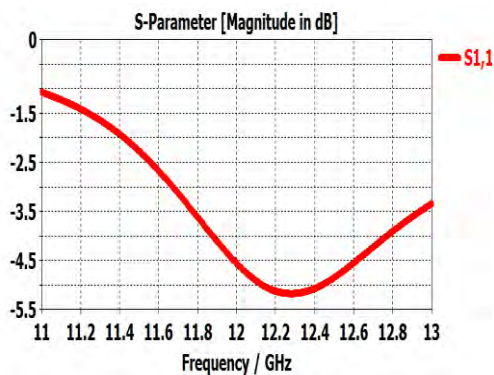


Fig. 6. S_{11} vs. freq:dipole above PEC ground.

Figure 7 shows the graph of reflection coefficient dipole antenna 2D structure with digital capacitance and rings; we have more reflection at 12 GHz and also around the resonant frequency: -30 dB at 12 GHz and -45 dB at 11.772 GHz.

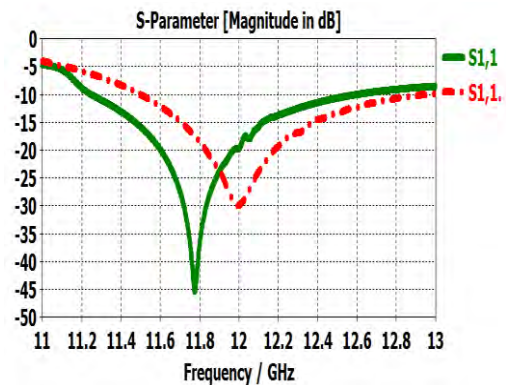


Fig. 7. Dipole+2D structure with digital capacitance and rings: return loss for 12 GHz operating frequency and around.

Furthermore, the gain is important, more than 9 dB compared to the gain of simple dipole at 12 GHz as shown on fig. 2 and fig. 8.

As for the directivity, we obtain 59.4 deg. At 12 GHz and 56 deg. around the resonant frequency as shown on the fig. 9 but the simple dipole antenna is omnidirectional as shown on fig. 1.

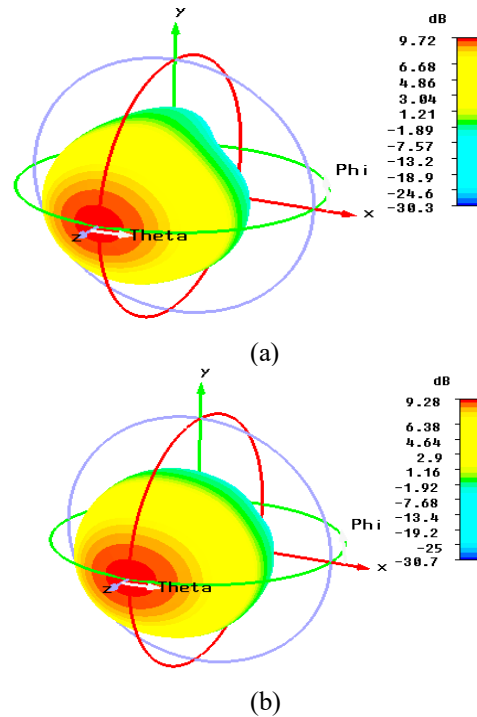


Fig. 8. Dipole+2D structure with digital capacitance and rings: (a) gain at 11.772 GHz; (b) gain at 12 GHz.

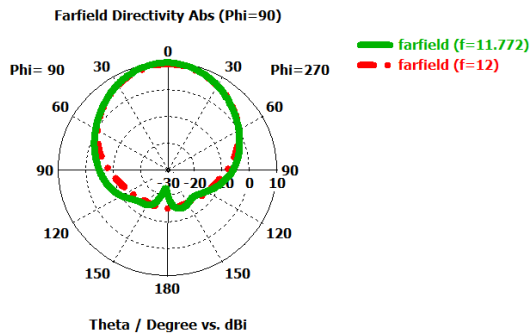


Fig. 9. Dipole+2D structure with digital capacitance and rings: directivity.

The metamaterial structure studied has exploited HIS properties to enhance dipole performance.

V. CONCLUSION

A metamaterial structure has been simulated and compared to the simple dipole antenna prove the application utility of metamaterials and verify their properties, the structure has successfully enhanced performance of the dipole, whereas the simple dipole is an omnidirectional antenna, the antenna considered in this article become directive with a much higher gain: close to 10 dB compared to the gain of 2 dB simple dipole antenna, this structure have successfully contributed to block surface waves.

We have used the digital capacitance because it allows a greater capacity value than the gap capacitance used in classical mushroom structure.

The results are obtained by using a specialized software based on one of the popular computational methods for microwave problems: FDTD (Finite-Difference Time-Domain method), CST is one of tools specialized in microwave design and simulation in 3D.

VI. REFERENCES

- [1] V. G. Veselago, *The Electronics of Substances with Simultaneously Negative Values of ϵ and μ* , P. N. Lebedev Physics Institute, Academy of Science, USSR, January-February 1968.
- [2] Ben A. Munk, *Metamaterials Critique and Alternatives*, Professor of Electrical Engineering, Emeritus The Ohio State University, ed. Wiley.
- [3] C. Caloz, T. Itoh, *Electromagnetic Metamaterials: Transmission Line Theory and Microwave Applications The Engineering approach*, Ecole Polytechnique de Montréal, University of California at Los Angeles, Ed. wiley 2006.
- [4] I. Tomeo-Reyes, E. Rajo-Iglesias, *Comparative Study on Different HIS As Ground Planes and its Application to Low Profile Wire Antennas Design*, University Carlos III of Madrid, Spain, 2011.
- [5] Inder Bahl, *Lumped Elements for RF and Microwave Circuits*, Ed Artech House, inc., 2003.
- [6] Joseph J. Carr, *Practical Antenna Handbook*, Ed. McGraw-Hill, 2001.



Samir Berkani is a PhD student in Telecommunication and microwave at the FEI (Faculté d'Electronique et d'Informatique) and LINS Laboratory (Laboratoire d'Instrumentation), USTHB (Université des Sciences et Technologies Houari Boumediene), he received the diploma of electronics engineer from Saad Dahlab University Blida, Algeria, Faculty of communications, in 1998, and Magister in rayonnement and microwave in USTHB, FEI, Bab ezzouar Algeria, in 2013. He is working actually on metamaterials applied in antennas design interesting in enhancing gain and directivity, under the supervision of Dr. Y. Lamhene.



Youssef Lamhene received bachelor's degree then master's degree in Electronic, Electrotechnic and Automatic (EEA), in 1978 and 1980 from Lille University in France, and later on, in the same place, the DEA diploma in 1982 and the third cycle Doctorate diploma in Biotechnology domain in 1984. He is also, since 2009, state Doctor of the Houari Boumediene university of sciences and technology. He teaches graduate level courses in applied electronic, microwave and antenna theory at the sciences and technology university of Algiers. His research interests are in the area of electromagnetic simulations of microwave and millimeter-wave passive components.



Hadj Sadok Mustapha is a PhD student in Electronique Instrumentation and Optronique systems at the FEI (Faculty of Electronics and data processing), in 2014 he received the master's degree from USTHB (University of Science and Technology Houari Boumediene), Algeria, He is working actually on metamaterials applied in antennas design interesting in enhancing gain and directivity, at LINS (Instrumentation Laboratory), under the supervision of Dr. Y. Lamhene.

Where To Be From The Typical ICG Waveform

Sara BENOUAR¹, Abdelakram HAFID¹, Mokhtar ATTARI¹,
Malika KEDIR-TALHA¹ and Fernando SEOANE²

¹ USTHB, LINS Lab, Faculty of Electronics and Computers, PO.Box 32, Bab-Ezzouar, Algiers
sara_benouar-hafid@outlook.com, hafidakram@hotmail.com, attari.mo@gmail.com,
malikakedir@gmail.com

² Swedish School of Textiles, University of Borås, 50190, Borås, Sweden. The Dept. for Clinical Science, Intervention and Technology, Karolinska Institutet, 14186 Stockholm, Sweden and the Dept. Biomedical Engineering, Karolinska University Hospital, 14186 Stockholm, Sweden.
fernando.seoane@ki.se

ABSTRACT

The ICG characteristic points are crucial for the calculation of hemodynamic parameters. However, in opposite of the relatively constant morphology of the PQRST waves in electrocardiography. The waveform morphology of the ABEXYOZ complex of the ICG is far from stationary, which yields to difficulties in the automated detection of characteristic ICG points. This study evaluates ICG recordings obtained from 4 volunteers. The results indicate that there are atypical ABEXYOZ complex in addition to the known typical complex. These atypical waveforms increase the difficulty of ICG signal analysis. To accurately and automatically detect the characteristic ICG points, and as a perspective of a future work, the targeted waveform must be known. In a purpose of classifying the atypical waveform into several types of the ABEXYOZ complex. This waveform types should be identified before the analysis of the dZ/dt ICG signal.

Key Words:

Bioimpedance, Impedance cardiography, ICG, Z-RPI, Characteristic ICG points, ECG, Biomedical Instrumentation.

1. INTRODUCTION

Impedance cardiography (ICG) was presented as a non-invasive method to measure the mechanical function of the heart, in the 1940s [1]. Few years after, [2] the commercial version of the impedance cardiogram was developed with the support of the National Aeronautics and Space Administration, NASA. A derivative of the ICG signal, dZ/dt was introduced (Fig.1) to accurately detect ejection time [3, 4]. They showed that the maximum point of the first derivative, dZ/dt_{max} (noted also; C or E), has a direct relationship with the rate of the ejection of ventricular blood [5]. Other characteristic point, is the B point, which is the crossing point with the baseline of the dZ/dt signal [4] (opening of the aortic valve). This point was changed to a 15% response of the dZ/dt waveform from the baseline to avoid interference as presented in [5]. A research previously presented in [6] have used the characteristic points of the dZ/dt signal as a simultaneous reference for phonocardiogram events, evoking that the dZ/dt signal can yield to a direct characterization of the systolic and diastolic time intervals.

Theses characteristic points are crucial for the calculation of time intervals and hemodynamic parameters of the ICG signal [7]. Such as left ventricular ejection time (LVET), which is a principal element to calculate the stroke volume (SV) and cardiac output (CO) [8]. LVET is the B to X point period in the dZ/dt signal. Another time

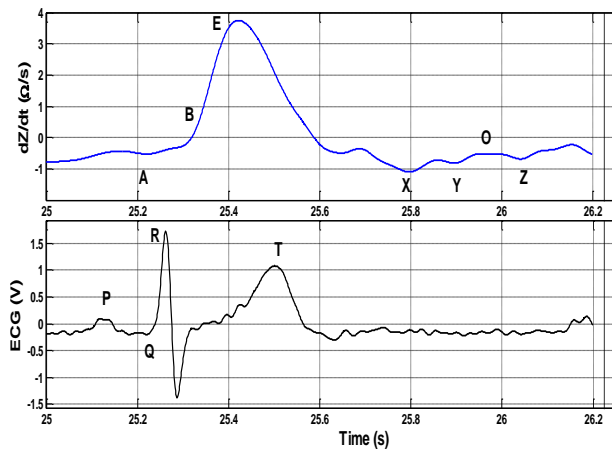


Fig. 1: Typical model of dZ/dt waveform recorded simultaneously with an ECG signal. Each signal is marked by characteristics points.

interval is the isovolumic relaxation time (IVRT). It is the X to O point period, which measures the diastolic function and activity of the ventricular relaxation [9].

Nevertheless, a straightforward and reliable automated detection of these time intervals is often problematic [7], [10-12]. Both the B and X points are difficult to detect, and one of the principal cause is due to two primary factors: (1) Physiological events of the heart where the time between the opening and closure of the aortic valves varies from person to another [13]; (2) The morphology of the dZ/dt waveform is changing considerably in clinical testing. Similar relevant problems are also present in the other characteristic points of the ABEXYOZ complex [7].

From the beginning, authors have raised concerns about changes in the ΔZ ICG waveform [14] proposing that the observed variabilities in the morphology of the ΔZ waveforms was principally caused by the changes in the placement of the electrodes. Recently other authors have studied the phenomena further on the dZ/dt signal with 4D FEM simulations [15, 16] and echocardiographic explorations [17] targeting the influence of lung perfusion, erythrocyte orientation and cardiac pumping on the dZ/dt waveform in addition to aortic volume expansion.

To decrease artifacts and changes in the ABEXYOZ complexes, ensemble averaging method is the method of choice in ICG analysis [18, 19]. The method is applied over time windows, typically greater than 60 s

[20]. In spite of that, averaging ABEXYOZ complexes may discard information about certain important points and lead to approximate results, especially when differences between shapes of cycles are important.

In this work, we are interested in the detecting morphology changes in dZ/dt waveforms from ICG recordings obtained from 4 healthy young male volunteers. The ICG recordings were analyzed to categorize the ABEXYOZ complexes into typical and atypical waveforms cases. Where according to the typical model (Fig.1) of the dZ/dt waveform all complexes that has at least one missed characteristic point are considered as atypical complex. The existence of an important percentage of atypical waveform of the ABEXYOZ complexes may provide a novel view of the ICG signal. Thus, with more optimization and enabling a future analysis of those atypical complexes to improve the detection of characteristic points.

2. METHOD

A. ICG RECORDING AND MEASUREMENT PROTOCOL

The sets were recorded at the laboratory for Medical Textile-Electronics at the University of Borås, Sweden. At two different times with two different groups of volunteers and two different recorders of continuous thoracic bioimpedance. These sets were established to expand the study, to enlarge the data acquired and to show that for different sets we have a similar behavior of the ICG complex.

One of the set of ICG signals was obtained in 2013 with the recorder Respimon device (Medical Electronics Lab, Chalmers University of Technology, Sweden) [21, 22]. The second set were obtained in 2017 with the use of Z-RPI recorder fully described elsewhere [23]. The two recorders record ECG signal simultaneously with the ICG signal. In both cases, the recordings were performed on 4 healthy young male volunteers. Once the participants signed an informed consent form according to the ethical approval 274-11 granted by the Regional Committee for Ethical Vetting of Gothenburg.

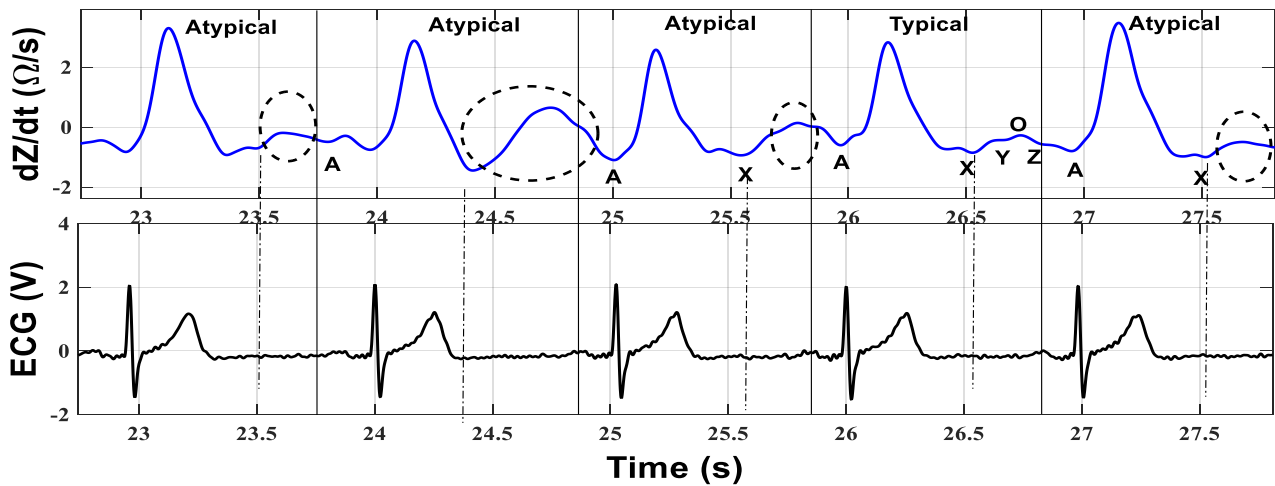


Fig. 2: Five consecutive ABEXYOZ complexes including atypical and typical waveforms.

To maintain a certain equivalence between the two ICG recording systems, the measurement protocol used for the Z-RPI device was adjusted to the measurement protocol executed in [21, 22], using a neck to chest electrode configuration [4]. For that, in each group, the measurements were performed in the seated position and during rest conditions, using gel Ag/AgCl electrodes. In addition, the analyses of recordings were 60s windows. To avoid respiration artifacts, the breathing was kept shallow, 10 cycles/min, during the recording.

B. ANALYSIS AND VISUALIZATION

All the ICG and ECG data were pre-processed offline on MATLAB™. The heart rate was calculated from the ECG signal by detecting the R-peaks and applying the Pan-Tompkins algorithm [24]. The first derivative of the ICG signal (dZ/dt) was obtained from the derivation of the ΔZ and after smoothing with a low-pass filter. Thus, the dZ/dt signals were analyzed first by displaying the processed ECG and ICG signals and then evaluating the PQRST and the ABEXYOZ complexes. The ABEXYOZ complexes were triggered by the R peaks of the ECG. Thus, the ABEXYOZ complexes were classified into two cases (Typical or Atypical) according to the known typical ICG waveform model given in Fig.1. Where all complexes that has at least one characteristic point missed are considered as atypical complexes. This categorization enabled the calculation of the percentage of the ABEXYOZ complex cases in both group. The percentage of each characteristic ICG point in each group was also calculated.

3. RESULTS

Different Atypical waveforms were identified for the ABEXYOZ complex in the dZ/dt signal. Figure 2 presents a 5s recording of a dZ/dt signal with the corresponding ECG as an example. Five consecutive ABEXYOZ complexes showing the presence of atypical waveforms and one typical complex.

The pie chart in Fig.3 indicates the distribution of the two cases of ABEXYOZ complexes observed in both groups.

Table I indicates the percentage of atypical and typical ABEXYOZ waveform in each volunteer, for both group. The average heart rate (mean \pm sd) for each volunteer was also presented.

According to the absence of characteristic ICG points, Table II presents the percentage of absence for each characteristic point observed in the recordings per volunteer.

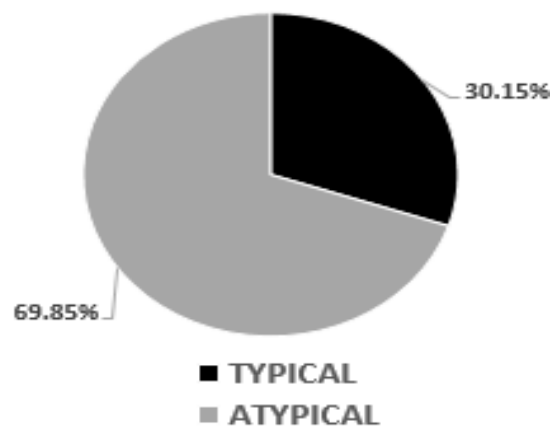


Fig. 3: Distribution of the two cases of ABEXYOZ complexes. In grey the percentage of atypical complexes and in black typical complexes.

TABLE I:
Percentage Of The Abexyoz Complexes Cases Contained In Each Recording Per Volunteer, With Average Heart-Rate (Mean \pm Sd), For Group 1 And 2.

Waveform type & HR	Typical (%)	Atypical (%)	HR(bpm)
Group 1-V1	72.3	27.7	55 \pm 5
Group 1-V2	11.3	88.7	60 \pm 3
Group 2-V1	29.4	70.6	75 \pm 5
Group 2-V2	07.6	92.4	66 \pm 7

TABLE II:
Percentage Of Missing Points Of Each Characteristic Point In Each Volunteer For Both Groups.

	A, B, E (%)	X (%)	Y, O, Z (%)
Group 1-V1	21.3	23.4	25.6
Group 1-V2	07.6	73.6	68.0
Group 2-V1	14.1	62.9	46.2
Group 2-V2	07.7	81.6	80.0

The absence of characteristic points is reported in 3 different groups: (1) A, B and E. (2) X. (3) Y, O and Z. Because given the shape of the visualized ICG complexes, the frequency of presence/absence of characteristic points were noticed common between some of the complexes.

Figure 4 summarizes the total percentage of missing points per group, demonstrating a similar behavior outcome between groups but with difference in percentage ranges.

4. DISCUSSION

For this work, two different sets of ICG recordings were used. They were recorded at two different times with two different groups of volunteers using two different ICG devices. In both groups, the same measurement protocol was used for each subject where the arrangement of electrodes was performed as by Kubicek [4].

These measurement sets enrich the study because at the same time they are equivalent; the measurement sets present similar behaviour despite being collected from different volunteers also completely independent years a part.

This work reports the existence of several ICG complex waveforms different than the ICG waveform and widely reported a typical.

Atypical waveforms are defined when at least one of the characteristic points is missing. The typical waveforms are identical to the model presented previously in fig.1, where we have the presence of all the ICG characteristic points. The average percentage of atypical complexes in group 1 and group2 respectively are 58.2% and 81.5%.

Percentage of missing points of each characteristic point in each volunteer for both groups present similar behaviour but we notice higher percentage of missing point in group 2 then it is in group 1. That is expected since we have higher percentage of atypical waveform in group 2 then group 1 as presented above in table I.

The average heart rate for group 1 is 57 bpm and for group 2 is 71 bpm, slightly different ranges, where we notice that higher average Heart rate are also for the group 2 that have higher atypical complexes. But at the same time we notice that in group 1 we have also for volunteer 2 a higher atypical percentage (88.7%) even if the heart rate is less than the heart rate of V 1 of group 2 that have less atypical percentage (70.6%). Thus, more work must be done on this point to see the amount of atypical waveform dependence with the influence of the heart rate or the changes of volunteers or other parameters. In each group the volunteers were completely different, this is to be expected because specific physiological and cardio-dynamic events change between individuals [13].

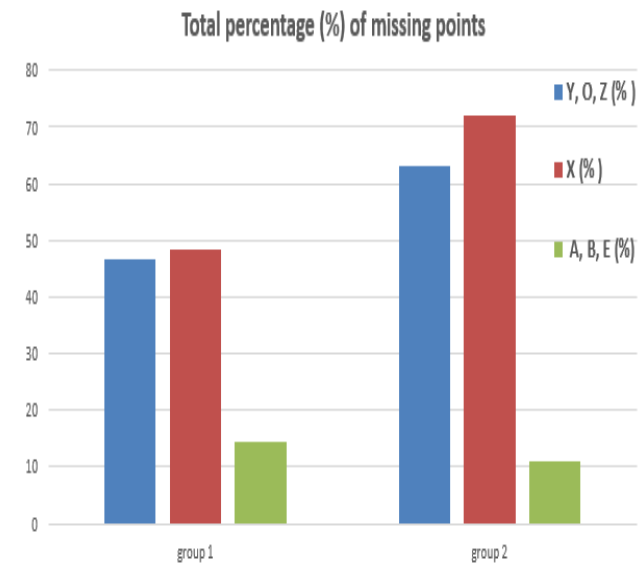


Fig.4: Total percentage (%) of missing points in both groups.

Variation in the ABEXYOZ complex between volunteers has been also previously observed and reported [25].

Among all the analyzed ABEXYOZ complexes, the X point varies the most, with the lowest minimum after the E wave. Such variation of the X point has been observed [17] and studied previously [15, 16]. The authors in [15, 16] studied the physiological sources that might contribute to build the ICG signals: ΔZ and dZ/dt . While confirming that the main contribution of the ICG signal is produced by aortic expansion, the authors also showed that the contribution from lung perfusion and erythrocyte orientation cannot be neglected.

In our study, the typical X point were the most common missed point, and despite the importance of the detection of the X point to the calculation of time intervals and hemodynamic parameters such as ventricular LVET, SV and CO, which require the detection of both X and B. this problematic cannot be neglected. The most missed points also were the Y, O and Z that have the same behavior in presence or appearance. Those points are used to calculate the IVRT and FT time intervals that require the accurate detection of X-O and Y-Z, respectively. These last two parameters are important for the diagnosis of diastolic functions of the heart and cardiac malformations. The less common missed point were the A, B and E points, we have used the equation that relate the R peak of the ECG to the E peak of the ICG [11] for the calculation of the B point, thus, if we have no E point automatically we will not be able to detect the B points. And it was less ABEXYOZ complexes that have not a clear E peak. The point A were almost present except in some complexes and it is expected since we have healthy volunteers.

The current evaluated recording suggests that it is possible to estimate all the hemodynamic parameters of interest (ET, SV, CO, IVRT, FT) in only 30.15% of cases. Additionally, no parameters can be accurately determined, due to the missing X and YOZ points in the atypical complexes. Where, the ET, SV and CO can be estimated only in 7.67 % of the atypical complexes. The

IVRT cannot be estimated and FT can be estimated in 10.25% in the typical complexes.

5. CONCLUSION

In this work, a new ICG complexes have been identified and noted as atypical. All of the atypical complexes are clearly different from the ABEXYOZ complex typically reported in scientific literature.

If we use as reference the typical ICG complex, we have at least one missing characteristic point. It is only possible to clearly identify the ICG characteristic points previously defined in the literature in only one of the cases. In the other case which is the atypical, very few ICG characteristic points can be detected, and in the rest, no characteristic ICG points can be detected. As the presence of atypical ICG complex is considerable and consequent, the targeted waveform must be known and refer to the atypical ICG complex in addition to the typical ones. Both of ABEXYOZ complex types should be identified before the analysis of the dZ/dt signal.

Thus, to calculate the hemodynamics parameters, it is important to accurately detect ICG characteristic points, and it might be helpful to identify which ABEXYOZ complexes types are present in the dZ/dt signal. More investigations are subject of another paper to analyses more details on the atypical complexes into several classes for automated classification. Thus, to bring novel ICG analysis method for more robustness and accuracy of the ICG characteristic points detection. And knowing the atypical models, will yield to this perspective.

ACKNOWLEDGMENT

The authors would like to thank the research group textile and wearable sensing for p-health solutions, at university of borås. This work was supported by the MESRS (Ministère de l'Enseignement Supérieure et de la Recherche Scientifique).

REFERENCES

- [1] J. Nyboer, "Bagno, s., Barnett, A, Halsey, RH Radiocardiograms: Electrical Impedance Changes of the Heart in Relation to Electrocardiograms and Heart Sounds," J. Clin. nves., 19, vol. 963, 1940.

- [2] W. Kubicek, D. Witsoe, R. Patterson, M. Mosharrata, J. Karnegis, and A. From, "Development and evaluation of an impedance cardiographic system to measure cardiac output and development of an oxygen consumption rate computing system utilizing a quadrupole mass spectrometer," National Aeronautics and Space Administration, NASA-CR-92220.(Also N68-32973.), 1967.
- [3] W. R. Patterson and J. Shewchun, "Alternate approach to the resolution of tunneling current structure by differentiation," *Review of Scientific Instruments*, vol. 35, pp. 1704-1707, 1964.
- [4] J. Karnegis, W. Kubicek, R. Mattson, R. Patterson, and D. Witsoe, "Development and evaluation of an impedance cardiac output system," 1966.
- [5] W. Kubicek, R. Patterson, and D. Witsoe, "Impedance cardiography as a noninvasive method of monitoring cardiac function and other parameters of the cardiovascular system," *Annals of the New York Academy of Sciences*, vol. 170, pp. 724-732, 1970.
- [6] Z. Lababidi, D. Ehmke, R. E. Durnin, P. E. Leaverton, and R. M. Lauer, "The first derivative thoracic impedance cardiogram," *Circulation*, vol. 41, pp. 651-658, 1970.
- [7] M. T. Allen, J. Fahrenberg, R. M. Kelsey, W. R. Livallo, and L. J. Doornen, "Methodological guidelines for impedance cardiography," *Psychophysiology*, vol. 27, pp. 1-23, 1990.
- [8] D. Bernstein and H. J. Lemmens, "Stroke volume equation for impedance cardiography," *Medical and Biological Engineering and Computing*, vol. 43, pp. 443-450, 2005.
- [9] R. L. Summers, W. C. Shoemaker, W. F. Peacock, D. S. Ander, and T. G. Coleman, "Bench to bedside: electrophysiologic and clinical principles of noninvasive hemodynamic monitoring using impedance cardiography," *Academic emergency medicine*, vol. 10, pp. 669-680, 2003.
- [10] A. P. DeMarzo and R. M. Lang, "A new algorithm for improved detection of aortic valve opening by impedance cardiography," in *Computers in Cardiology*, 1996, 1996, pp. 373-376.
- [11] D. L. Lozano, G. Norman, D. Knox, B. L. Wood, B. D. Miller, C. F. Emery, et al., "Where to B in dZ/dt ," *Psychophysiology*, vol. 44, pp. 113-119, 2007.
- [12] J. H. Meijer, S. Boesveldt, E. Elbertse, and H. Berendse, "Method to measure autonomic control of cardiac function using time interval parameters from impedance cardiography," *Physiological measurement*, vol. 29, p. S383, 2008.
- [13] M. Handke, C. Jahnke, G. Heinrichs, J. Schlegel, C. Vos, D. Schmitt, et al., "New three-dimensional echocardiographic system using digital radiofrequency data—visualization and quantitative analysis of aortic valve dynamics with high resolution," *Circulation*, vol. 107, pp. 2876-2879, 2003.
- [14] K. Sakamoto, K. Muto, H. Kanai, and M. Iizuka, "Problems of impedance cardiography," *Medical and Biological Engineering and Computing*, vol. 17, pp. 697-709, 1979.
- [15] M. Ulbrich, J. Mühlsteff, S. Leonhardt, and M. Walter, "Influence of physiological sources on the impedance cardiogram analyzed using 4D FEM simulations," *Physiological measurement*, vol. 35, p. 1451, 2014.
- [16] M. Ulbrich, J. Mühlsteff, P. Paluchowski, and S. Leonhardt, "Erythrocyte orientation and lung conductivity analysis with a high temporal resolution FEM model for bioimpedance measurements," *Lecture Notes on Impedance Spectroscopy: Measurement, Modeling and Applications*, vol. 3, p. 71, 2012.
- [17] P. Carvalho, R. P. Paiva, J. Henriques, M. Antunes, I. Quintal, and J. Muehlsteff, "Robust Characteristic Points for ICG-Definition and Comparative Analysis," in *BIOSIGNALS*, 2011, pp. 161-168.
- [18] Y. Miyamoto, M. Takahashi, T. Tamura, T. Nakamura, T. Hiura, and M. Mikami, "Continuous determination of cardiac output during exercise by the use of impedance plethysmography," *Medical and Biological Engineering and Computing*, vol. 19, pp. 638-644, 1981.
- [19] H. Riese, P. F. Groot, M. van den Berg, N. H. Kupper, E. H. Magnee, E. J. Rohaan, et al., "Large-scale ensemble averaging of ambulatory impedance cardiograms," *Behavior Research Methods*, vol. 35, pp. 467-477, 2003.
- [20] G. Cybulski, "Ambulatory impedance cardiography," in *Ambulatory Impedance Cardiography*, ed: Springer, 2011, pp. 39-56.
- [21] J. C. M. Ruiz, M. Rempfler, F. Seoane, and K. Lindcrantz, "Textrode-enabled transthoracic electrical bioimpedance measurements—towards wearable applications of impedance cardiography," *Journal of Electrical Bioimpedance*, vol. 4, pp. 45-50, 2013.
- [22] M. REMPFLER, "On the Feasibility of Textrodes for Impedance Cardiography," Bachelor thesis Biomedical engineering University of Borås, SWEDEN, 2011.
- [23] A. Hafid, S. Benouar, M. Kedir-Talha, F. Abtahi, M. Attari, and F. Seoane, "Full Impedance Cardiography measurement device using Raspberry PI3 and System-on-Chip biomedical Instrumentation Solutions," *IEEE Journal of Biomedical and Health Informatics*, 2017.
- [24] J. Pan and W. J. Tompkins, "A real-time QRS detection algorithm," *IEEE transactions on biomedical engineering*, pp. 230-236, 1985.
- [25] S. Thomas, "Impedance cardiography using the Sramek-Bernstein method: accuracy and variability at rest and during exercise," *British journal of clinical pharmacology*, vol. 34, p. 467, 1992.

Design of Antenna Array based on SIW Technology for Satellite Applications

Abdelkader ZERFAINE, Mohamed TELLACHE and Hichem MAHFOUDI
USTHB, LINS Lab, Faculty of Electronics and Computers, PO.Box 32, Bab-Ezzouar, Algiers
zerfaine.aek@gmail.com, mtellache@usthb.dz and hmahfoudi@usthb.dz

ABSTRACT

In this paper, an Antenna Array design using substrate integrated waveguide technology (SIW) is presented to operate in Ku-band Satellite applications [12, 18] GHz. The whole antenna and feeding system are designed on a single substrate to overcome the drawbacks associated with conventional metallic waveguide antennas. The radiation on these antennas is insured by etching longitudinal slots on the top metallic surface. The simulated antenna radiation parameters give good results in terms of S11 bandwidth, gain and radiation pattern, and then we simulated two antenna arrays consisting of two and four elements.

Key Words: Antenna array, substrate integrated waveguide (SIW), via holes, Ku-band, power divider.

1. INTRODUCTION

In recent years, the development of the telecommunications sector has led to the realization of increasingly compact and efficient equipment, operating at increasingly higher frequencies. The practical implementation of these devices is very expensive, since weight and volume are crucial parameters. Satellite telecommunications systems require compact, low-cost antennas with high gain, low loss, and high efficiency [1].

The network association of several printed radiating elements allows the production of radiation patterns of variable shapes and directions, by acting on the following parameters: the configuration and arrangement of the antenna array, amplitude and phase of the power supply,

characteristics of the elementary source and a judicious choice of these parameters makes it possible to synthesize diagrams of complex forms, which can answer particular requirements.

In order to achieve an antenna network that meets these requirements, we have chosen the Substrate Integrated Waveguide SIW because it allows the properties of guided propagation to be used to transform a substrate into a waveguide. And it doesn't only take advantages from this last technic, but it also combines those of planar technology [2-3]. Therefore, it represents a very promising solution for the development of circuits and components that operate in the ku band.

2. ANTENNA DESIGN

The design of single antenna based on the technology of SIW consists to put two rows of periodic metallic posts in the substrate, to realize bilateral edge walls like a rectangular waveguide [4-5]. Figure 1 shows the physical parameters that are important for designing the SIW structure with d the diameter of the metal vias, P unit intervals between vias and p is the separation between via rows (centre to centre). The equivalent width between conventional rectangular waveguide and waveguide based on SIW can be approximated by these empirical equation as follows [6].

$$W_{\text{SIW}} = a + \left(\frac{d^2}{0.95p} \right) \quad (1)$$

$$P \leq 2d \quad (2)$$

$$d < \lambda_g / 5 \quad (3)$$

With λ_g the electrical wave length of the guide.

The SIW can only support the TE_{0n} modes propagation, with $n=1,2,3,\dots$ while the TM modes cannot be guided due to the gaps between metal vias, and to the resemblance between SIW and rectangular waveguide. The fundamental mode in SIW structure is similar to the TE_{10} mode of a rectangular waveguide.

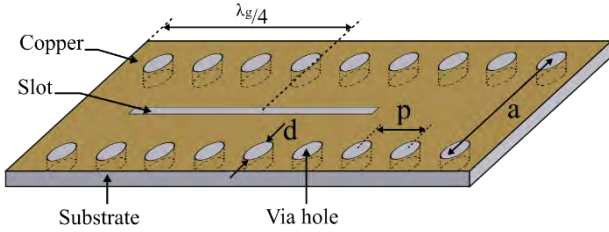


Fig. 1. Geometry of a SIW antenna

The design of resonant longitudinal slots is positioned on the opposite side of the waveguide at an interval of half a guided wavelength. The distance from the end of the guide to the middle of the last slot is $\lambda_g/4$. The approximate slot length is determined by following expression [7].

$$L_s = \frac{\lambda_0}{\sqrt{2(1 + \epsilon_r)}} \quad (4)$$

A. Transition Feeding

The feeding line-to-SIW transition is shown in Fig. 2. The taper line is utilized to realize the impedance matching between SIW and 50 Ohm microstrip line [8]. A tapered line has the following parameters [9]: the width of the feed line w_0 , the width W_T and the length L_T .

$$W_T = 0.4(W_{SIW} - d) \quad (5)$$

$$\frac{\lambda}{2} \leq L_T \leq \lambda \quad (6)$$

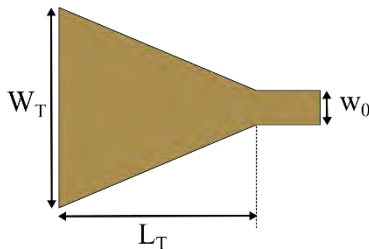


Fig. 2. Microstrip-to-SIW transition

3. RESULTS AND DISCUSSION

The antenna array element has been designed to resonate at 16 GHz in the ku band [12, 18] GHz. the rectangular waveguide in this frequency band has the following dimensions $a = 15.85$ mm and $b = 7.9$ mm (WR_{62}). Its cut-off frequency is around 9.49 GHz and from this one we get the equivalent waveguide width a . Then the design parameters are determined (Table 1). The SIW single element is designed in one substrate where we used the Arlon AD320 with a relative permittivity $\epsilon_r = 3.2$, thickness $h = 0.782$ mm and loss tangent of $\delta = 0.0038$. The structure has been simulated using the EM commercial software CST Microwave Studio, which is based on Finite Integral Technique (FIT) method.

TABLE I
Dimensions of antenna array element

Parameters	Value (mm)
Vias diameter	$d = 1.66$
Space between the vias	$p = 3.33$
Space between the two rows	$a = 10$
Feed line width 50 Ω	$W_0 = 1.88$
Feed line length 50 Ω	$L_{lin} = 10$
Taper width	$W_T = 4$
Taper length	$L_T = 3.8$
Slot length	$L_S = 6.5$

A. Reflection Coefficient

According to Fig. 3, the S_{11} of SIW slot antenna array is less than -10 dB over the whole band [15.85, 16.14] GHz, and at the resonance frequency of 16 GHz we have an adaptation of -45 dB.

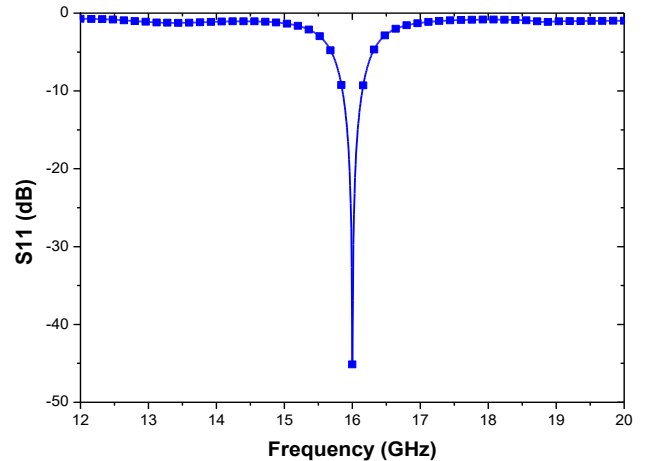


Fig.3. Simulated reflection coefficient S_{11} of one element vs frequency

B. Radiation Pattern

Fig. 4 shows two radiation patterns of the proposed antenna at 16 GHz; it presents directive radiation pattern. It is shown more properly in the 3D radiation pattern of polar gain in Fig. 5.

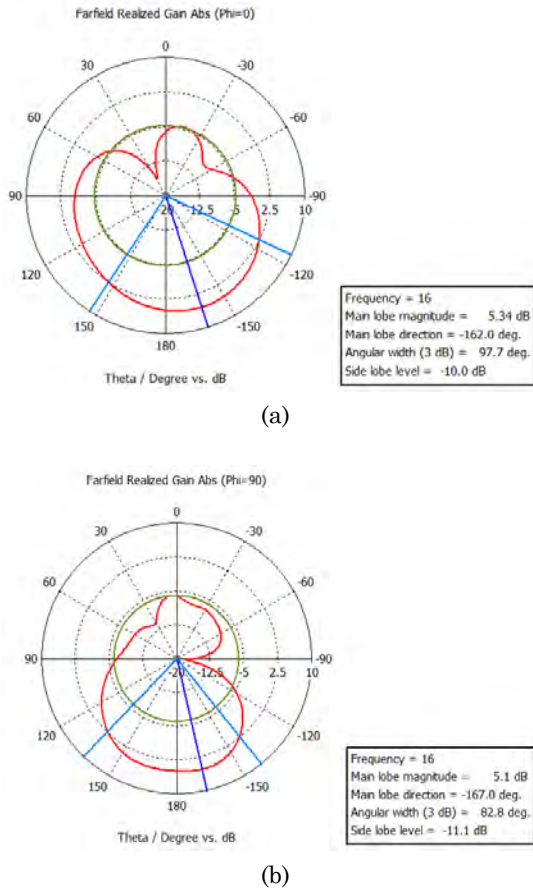


Fig.4. Simulated radiation patterns at 16 GHz: (a) $\Phi = 0^\circ$, (b) $\Phi = 90^\circ$

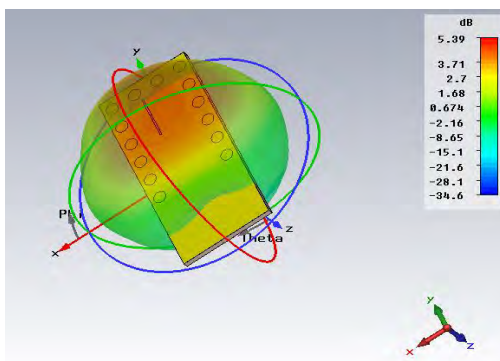


Fig.5. Simulated three-dimensional radiation patterns at 16 GHz

In this part, we simulated two arrays antennas composed of two and four elements. This array antenna is fed by a quarter-wave $\lambda/4$ T-power divider and 70.7Ω impedance was used between the 50Ω lines of the antennas to adapt the network [10]. The results are shown below.

C. Reflection Coefficient

Return loss characteristics of the SIW array antennas of two and four elements are given in Fig. 6. According to simulated results, the S_{11} is less than -10 dB over the whole band $[15.7, 16.22]$ GHz. with a relative bandwidth of 2.26% for two elements and 3.21% for four elements.

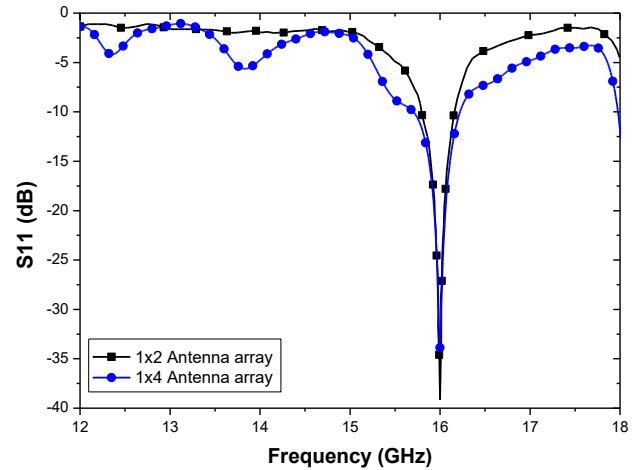


Fig. 6. Simulated reflection coefficient S_{11} vs frequency of two and four elements

D. Radiation Pattern

The Fig. 6 represents the antenna radiation pattern of four elements on the Cartesian plane, for $\Phi = 90^\circ$ we notice a main lobe with an opening angle at 3 dB equal to 86.7° while for $\Phi = 0^\circ$ the opening angle is 24.3° at 3 dB, and the radiation angle is 180° , which represents a directive radiation pattern. It is shown more properly in the 3D radiation pattern of polar gain in Fig. 8.

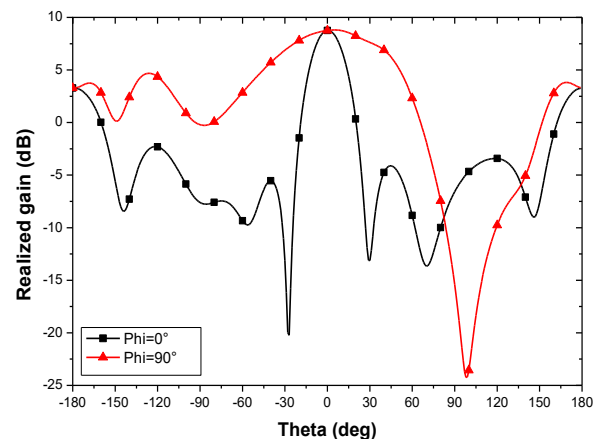


Fig. 7. Simulated radiation patterns at 16 GHz: $\Phi = 0^\circ$; $\Phi = 90^\circ$

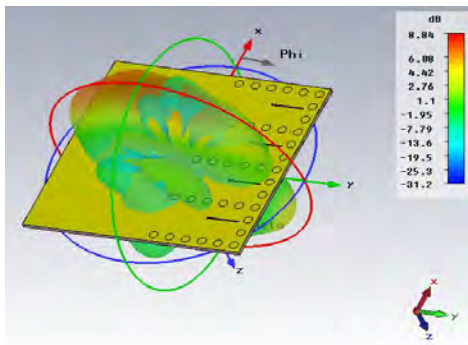


Fig. 8. Simulated three-dimensional radiation patterns at 16 GHz

E. Summary and comparison of antenna array

In Table 2, we present the simulated gain, the calculated directivity, Bandwidth and S11 parameter for the Array antennas at 16 GHz. These results show that the antenna arrays have as role to increase the performance like gain, Bandwidth and directivity.

TABLE II
Gain, Directivity, Bandwidth and S11 parameter

Topology of antenna array	Comparison criteria			
	Gain (dB)	directivity (dBi)	BW (%)	S11 (dB)
one Antenna	5.39	6.55	1.81	-45.14
(1x2) antenna Array	6.77	8.23	2.26	-43.39
(1x4) antenna Array	8.83	10.22	3.21	-33.87

Fig. 9 shows the variation of the gain vs frequency for the antenna and the antenna arrays of two and four elements. We notice that the value of the gain is maximum each time we increase the number of antennas.

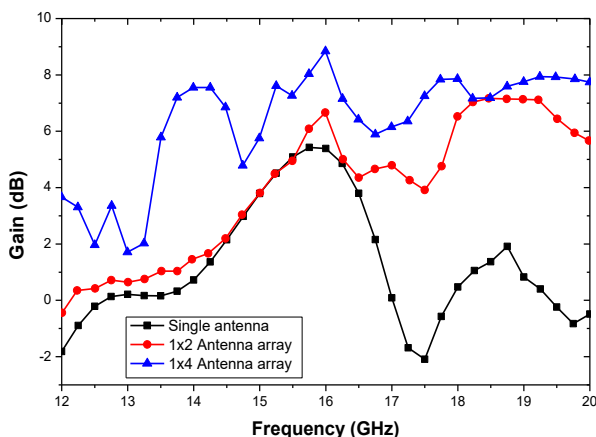


Fig. 9. Simulated gain vs frequency of one, two and four elements

4. CONCLUSION

In this paper, we have proposed a 1x2 and 1x4 antenna arrays based on SIW structure radiating slots at 16 GHz. The array was fed by T-power divider. A significant increase of gain and directivity parameters and bandwidth has been obtained with good results in terms of reflection coefficient. Compared with a single element SIW antenna, the 1x4 antenna array offers much.

REFERENCES

- [1] G. Q. Luo, T. Y. Wang, X. Hong Zhang, "Review of Low Profile Substrate Integrated Waveguide Cavity Backed Antennas", *International Journal of Antennas and Propagation*, vol. 2013, pp. 1, 2013.
- [2] J. Gao, K. Li, T. Sato, J. Wang, H. Harada, and S. Kato, "Implementation considerations of patch antenna array for 60 GHz beam steering system applications," *IEEE Radio and Wireless Symposium*, 2009. RWS '09, 2009, pp. 35–38.
- [3] X.-P. Chen, K. Wu, L. Han, and F. He, "Low-Cost High Gain Planar Antenna Array for 60-GHz Band Applications," *IEEE Transactions on Antennas and Propagation*, vol. 58, no. 6, pp. 2126–2129, Jun. 2010
- [4] J. E. Rayas-Sanchez, "An Improved EM-Based Design Procedure for Single-Layer Substrate Integrated Waveguide Interconnects with Microstrip Transitions," *IEEE MTT-S International Microwave Workshop*, vol., pp. - 30, 2009.
- [5] F. Taringou, D. Dousset, J. Bornemann and K. Wu, "Broadband CPW feed for millimeter-wave SIW-based antipodal linearly tapered slot antennas," *IEEE Trans. Antennas Propag.*, vol. 61, no. 4, pp. 1756–1762, 2013
- [6] Y. Cassivi, L. Perregrini, P. Arcioni, M. Bressan, K. Wu, and G. onciauro, "Dispersion characteristics of substrate integrated rectangular waveguide," *IEEE Microw. Wireless Compon. Lett.*, Vol. 12, pp.333–335, February 2002.
- [7] L. Yan, W. Hong, G. Hua, J. Chen, K. Wu and T. Cui, "Simulation and experiment on SIW slot array antennas," *IEEE, Microwave and Wireless Components Letters*, vol. 14, pp. 446- 448, 2004.
- [8] D. Deslandes, "Design equations for tapered microstrip-to-substrate integrated waveguide transitions," *Microwave Symposium Digest, IEEE MTT-S International*, pp. 704-707, 2010.
- [9] X. Xu, R. G. Bosisio and K. Wu, "A New Six-Port Junction Based on Substrate Integrated Waveguide Technology," *IEEE Transactions on Microwave Theory and Techniques*, Vol. 53, No. 7, July 2005.
- [10] N. Ashraf, H. Vettikalladi, and M.A.S. Alkanhal, "Substrate integrated waveguide antennas/array for 60 GHz wireless communication systems," *RF and Microwave Conference (RFM), 2013 IEEE International*, pp.56,61, 9-11 Dec. 2013.

VEHICLE MOTION PARAMETER ESTIMATION USING CLOSED-FORM SOLUTION BASED ON TIME-FREQUENCY ANALYSIS

Hakima TIMLELT¹, Adel BELOUHRANI², Youcef REMRAM¹

¹ Faculty of Electronics and Computers, PO.Box 32, Bab-Ezzouar, Algiers,
hakimatimlelt@gmail.com, yremram@gmail.com

² Ecole Nationale Polytechnique, LDCCP lab, Electrical Engineering Department
10 Avenue Hassen Badi El Harrach 16200, Algiers, ALGERIA adel.belouchrani@enp.edu.dz

ABSTRACT

A novel closed-form solution is used to estimate the motion parameters of a ground moving acoustic source. The Doppler shift of the source frequency is observed when a noise-emitting source travels at a constant speed and range along a straight trajectory. This solution is used to estimate the motion parameters such as the speed, the distance between the source and the sensor, the source frequency and the closest point of approach (CPA) time. This method has been compared to previously used ones. The effectiveness of this solution has been first validated on simulated data then on real life ground acoustic recorded data during the passage of a road vehicle.

Index Terms— Acoustic localization, Doppler effect, Road vehicle, Instantaneous frequency, Microphone.

I. INTRODUCTION

Acoustic source localization consists of determining the source motion parameters such as, the range, the speed, the altitude and other parameters. A road vehicle's acoustic signal consists of a combination of various noise signals generated by the engine, the tires, the exhaust system, and the aerodynamic and mechanical effects. Hence, the spectral content of a vehicles signal includes wide-band processes as well as harmonic components. The mixture weighting of these spectral components at any given location depends on the speed of the vehicle, whether it is accelerating, decelerating, turning, and whether it is in good mechanical condition. Different methods have been developed [1]–[12] depending on the acoustic sources type; which can be jet aircraft, propeller driven aircraft, helicopters or other types of vehicle [6], [10]–[12]. Ferguson *et al.* [6] propose a method for flight parameters estimation based on temporal evolution of the frequency relied on the Doppler shift of the emitted sound of the moving source using one microphone and a geometrical model is used to express the instantaneous frequency using the parameters to be estimated. They are the first who initiated the use of the instantaneous frequency to estimate the parameters of a moving acoustic

source exploiting the short time Fourier transform and the Wigner Ville distribution as an instantaneous frequency (IF) estimators. Quinn [13] proposes an improved algorithm which uses amplitude and frequency estimators to estimate speed and range of a ground moving acoustic source. The parameter estimation algorithm is directly affected by the IF estimation, therefore, many contributions in this area appeared in the literature and are primarily based on the time-frequency distribution [11], [12].

Most previous work proposed a numerical solution to solve the problem of parameter estimation by minimizing the sum of the squared deviations of the estimated frequency and predicted values [10], [11], [14]. Only few ones have given an analytical solution to solve the problem of parameter estimation, Webster in [1] proposes an exact trajectory estimation from Doppler shift measurement of an acoustic source. Dommermuth [15] also proposed a closed-form solution using four sensors on a plane (x-y geometry) utilizing the closest point of approach time of each sensor. These solutions need at least two sensors and the prior knowledge of one of the source parameter.

In this paper, an analytical solution [16], [17] is applied to estimate the motion parameters of a ground moving acoustic source traveling at a constant speed with straight trajectory. This solution has a great advantage compared to the existing methods, because it only needs one microphone and no prior knowledge on any parameter. The instantaneous frequency information obtained from the source frequency shift is used to estimate the speed, the sensor to microphone separation distance at the CPA time, the frequency and the closest point of approach time. In this work, the recursive least square method [18] is used to estimate the IF instead of time-frequency distributions. The paper is organized as follows: in the first section, the model descriptions and general assumptions of the time-frequency analysis used method are given in details; the second section gives simulations results and model evaluation; at the end, an experimental tests and discussions of the obtained results are presented.

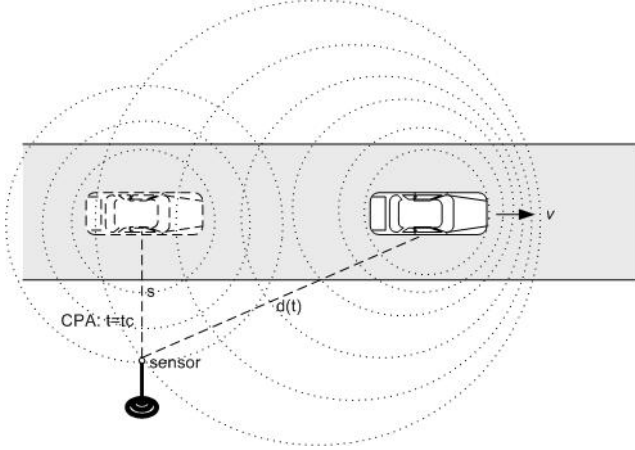


Fig. 1. Geometry of the road vehicle localization using a single microphone.

II. INSTANTANEOUS FREQUENCY MODEL

We consider an acoustic source emitting a constant frequency f_0 waves moving along a linear trajectory at a constant speed v and range s at the CPA time. These sounds are recorded by a microphone placed on the ground. The experimental setup is shown in Fig1. The sound emitted by the source at time τ is received by the microphone at time t , as mentioned in Eq.1, the time delay is equal to the ratio of the distance d and the sound speed in the air ($c = 1224$ km/h). In this model we assume that the sound speed is not affected by the atmospheric conditions (temperature, wind, humidity).

$$t = \tau + \frac{d}{c} \quad (1)$$

Then the separation distance can be derived as:

$$d = (t - \tau)c = (s^2 + v^2(\tau - t_c)^2)^{1/2} \quad (2)$$

Substituting Eq.(2) into Eq.(1) and solving for τ gives:

$$\tau = \frac{c^2 t - v^2 t_c - [s^2(c^2 - v^2) + v^2 c^2 (t - t_c)^2]^{1/2}}{c^2 - v^2} \quad (3)$$

The phase of the signal received at time t , denoted by $\theta(t)$, equals the phase of the signal emitted by the source at time τ plus a constant initial phase. It follows that the Instantaneous Frequency (IF) of the received signal at time t is given by:

$$f(t) = \frac{1}{2\pi} \frac{d\theta(t)}{dt} = f_0 \frac{d\tau}{dt} \quad (4)$$

Substituting Eq.(3) in Eq.(4), yields:

$$f(t) = f_0 \frac{c^2}{c^2 - v^2} \left(1 - \frac{v^2(t - t_c)}{[s^2(c^2 - v^2) + c^2 v^2 (t - t_c)^2]^{1/2}} \right) \quad (5)$$

Eq.(5) is function of the parameter to estimate $\theta = [v, s, f_0, t_c]^T$.

In [6], [10], [11] the parameters are obtained by minimizing

the sum of the squared deviations of the frequency estimates from their predicted values.

$$\sum_{j=1}^N (g_{t_j} - f_{t_j})^2 \quad (6)$$

Where g_{t_j} is the frequency estimate at time t_j obtained using time-frequency distributions, f_{t_j} is the predicted frequency given by Eq.(5) and N is the time record window.

In this work, we propose the use of a novel closed-form solution instead of the numerical method to estimate the parameters. This method is based on the use of the instantaneous frequency and its derivatives which gives a direct estimation with only a few mathematical equations. The steps of the motion parameter estimation of the source are expressed as follow:

from Eq.(5) and making $t = t_c$ the obtained equation is:

$$f(t_c) = f_0 \frac{c^2}{c^2 - v^2} \quad (7)$$

The ratio of instantaneous frequency at t and t_c is then given by:

$$\frac{f(t)}{f(t_c)} = 1 - \frac{v^2(t - t_c)}{[s^2(c^2 - v^2) + v^2 c^2 (t - t_c)^2]^{1/2}} \quad (8)$$

The derivative of the Eq.(8) gives:

$$\frac{f'(t)}{f(t_c)} = - \frac{v^2 s^2 (c^2 - v^2)}{[s^2(c^2 - v^2) + v^2 c^2 (t - t_c)^2]^{3/2}} \quad (9)$$

For $t = t_c$, Eq.(9) becomes:

$$\frac{f'(t_c)}{f(t_c)} = - \frac{v^2}{[s^2(c^2 - v^2)]^{1/2}} \quad (10)$$

After some workout, the parameters are expressed as follow: v is given by :

$$v^2 = \frac{c^2 [(t - t_c) f'(t_c)]^2 [f(t_c) - f(t)]^2}{[(t - t_c) f'(t_c)]^2 - [f(t_c) - f(t)]^2 f(t_c)^2} \quad (11)$$

The source's fundamental frequency is estimated from Eq.(7).

$$f_0 = f(t_c) \left(1 - \frac{v^2}{c^2} \right) \quad (12)$$

The range is estimated from Eq.(10) as follow:

$$s = - \frac{f'(t_c) v^2}{f'(t_c) (c^2 - v^2)^{1/2}} \quad (13)$$

This solution provides a faster and less complicated algorithm for a ground moving acoustic source motion parameter estimation [16]. Algorithm 1 summarizes the different steps of the proposed closed-form solution.

In order to estimate the performance of the proposed closed-form approach in term of computation time and simplicity, a comparison was fulfilled with the algorithm proposed by Ferguson et al. [6], this algorithm was implemented in MATLAB using *fminsearch* function for this purpose. The

- Signal record

- 1) Fix the time record window N
- 2) Noise suppression with a band pass filter of a cut off frequencies f_{c1} and f_{c2}

for $t \leftarrow 1$ **to** N **do**

- 1) Estimate of the instantaneous frequency $f(t)$ from the signal $y(t)$.
- 2) High frequency noise reduction using a low pass smooth filter with a cut off frequency $f_c = 1\text{Hz}$.
- 3) Numerical derivative $f'(t)$ computation of the IF $f(t)$.
- 4) CPA time t_c estimation from the peak of $f'(t)$.

end

- Motion parameter estimation

- 1) Estimation of v (see Eq.11)
- 2) Estimation of f_0 (see Eq.12)
- 3) Estimation of s (see Eq.13)

Algorithm 1: Summary of the algorithm [16].

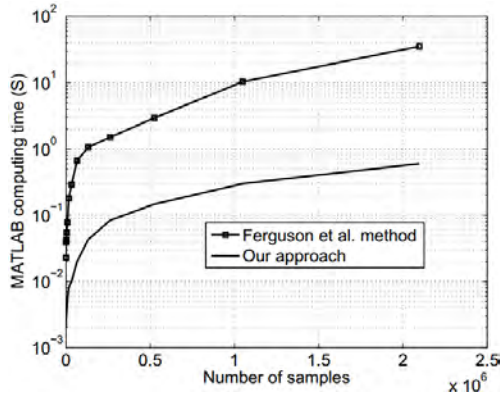


Fig. 2. Computation time by varying the signal size.

computation time of the motion parameter estimation for both approaches is computed by varying the signal size. Fig.2 gives the results of the computation time and shows that the closed- form solution yields the same results as those obtained using the numerical method with an optimal computation time and simplicity. The numerical method converges after 6 iterations from the initial estimate at signal-to-noise ratio of 30dB , which explains the important difference in the computation time between the two estimators for large signal size.

Table I. RMSs obtained using both methods for the estimation of the range, the speed and the source frequency.

RMSs	Range(m)	Frequency(Hz)	Speed(km/h)
Analytical solution	0.0699	0.9357	$1.10 \cdot 10^{-6}$
Ferguson <i>et al.</i> [6]	0.0790	0.9472	$0.924 \cdot 10^{-6}$

III. SIMULATION RESULTS

The closed-form solution in this application is validated using a computer simulations and real passive acoustic data. Numerical simulations are performed using 1024-point test signal $y(t)$, this signal is modelled as the sum of a tonal noise signal corrupted by additive white Gaussian noise with a maximum amplitude of 1 unit at signal to noise ratio of 10 dB . The motion parameter values in these simulations are, $f_0=125\text{Hz}$, $s = 70\text{ m}$. For the first generated signal (Fig.3.a), $v=54\text{ km/h}$ and for the second (Fig.3.b), $v= 108\text{ km/h}$. The data are sampled at 300Hz and the closest point of approach is situated in the middle of the acquisition time. A recursive least square (RLS) adaptive instantaneous frequency estimation method is used to extracted the IF of the signal. This method is based on extracting the peak of a short-time linear prediction based spectral estimate [18], [19].

The motion parameters are estimated using the procedure described in the algorithm 1. The results are given in the tables of Figures (3.a and 3.b), where the estimated values are compared to the actual ones. It can be seen that the motion parameters obtained from the estimation are in close agreement with those simulated.

Table I contains the root mean square error (RMSs) obtained from the closed- form solution and Ferguson *et al.* [6] method. The above studies shows that the two methods reach approximately the same results for the parameter estimation, and the novel closed-form solution can successfully be used for the motion parameter estimation of a ground moving source.

IV. REAL LIFE EXPERIMENTS

This experiment demonstrates the use of the novel analytical solution with a real passive acoustic signal. The experiment was conducted in free field where a vehicle traveling at a speed v in a direction nominally horizontal to the sensor. In order to overcome the reflections from the ground and the acquisition materials, a wireless microphone were used and positioned at a height of about 1 meter from the ground (see Fig.4). The background noise level and the wind were moderate. Various transits of the vehicle were carried out, in the following real passive acoustic signal, the nominal motion parameters values are $v = 39.6\text{ km/h}$, $s= 3\text{ m}$, t_c is in the middle of the acquisition window. The source frequency of the source is $f_0= 215.3\text{ Hz}$ (see Fig.5). The motion parameters estimated using the closed-form

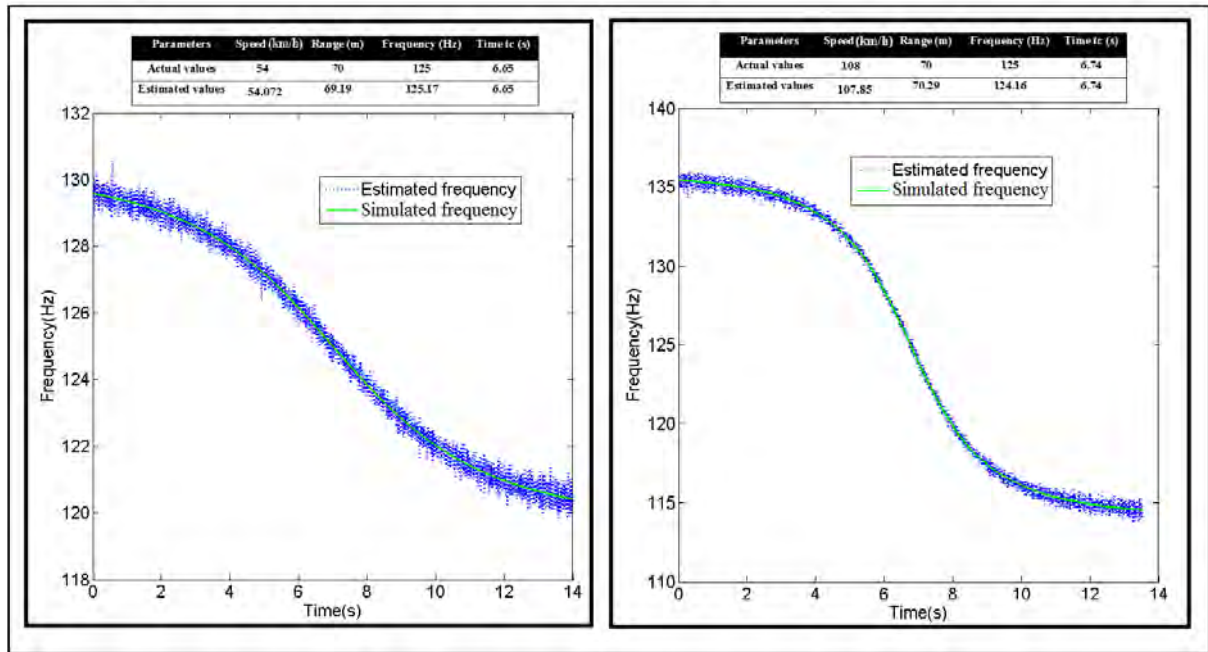


Fig. 3. In dotted (blue) line the estimated instantaneous frequency using the RLS method, in solid line (green) the real instantaneous frequency law. The two tables show the results of the parameter estimation using the analytical solution developed above for two simulated signals.

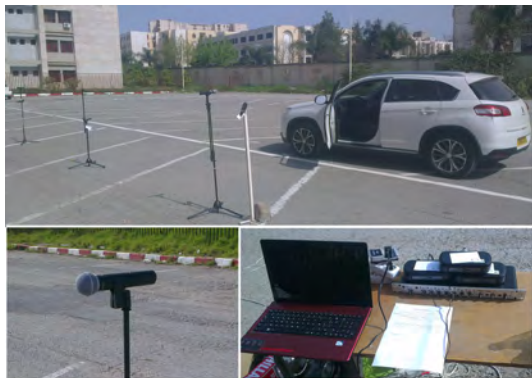


Fig. 4. Real life experiment.

Table II. The results of the motion parameter estimation for a real recorded signal.

	Frequency(Hz)	Speed(km/h)	Range(m)
Experimental values	215.3	39.6	3.5
Analytical solution	219.73	46.8	4.04

solution are shown in the table II, and are found to be in close agreement to measured experimental values.

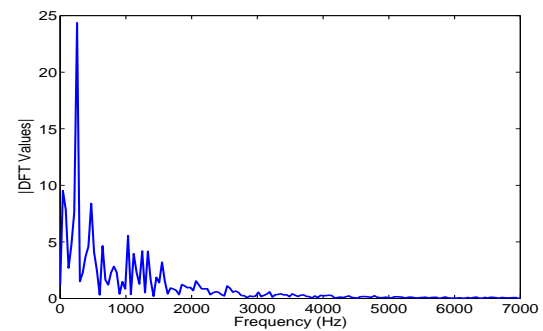


Fig. 5. Stationary Peugeot 4008 sound measurement set up is illustrated. In the measurements, the engine measurements were taken with a microphone approximately 1m away from the center of the engine. The strongest peak in the Fourier transform of the engine microphone data (the sampling frequency $F_s = 44100\text{Hz}$) is 215.3 Hz corresponding to f_0 . Harmonic components and additional peak due to the environmental noise are also present in the signal with weak energy.

V. CONCLUSION

A simple solution for estimating the motion parameters of a ground moving acoustic source using a single sensor is proposed. This method enables to eliminate the complex and time consuming numerical iterative methods, and simplifies

the localization algorithm to a few mathematical equations. The robustness of this solution was validated through numerical simulations and real recorded data. To evaluate the performance, results were compared to those obtained using Ferguson et al. [6] method and confirmed that the used closed-form solution performs well and as expected. The usefulness of this analytical solution is demonstrated using a real-life passive acoustic signal for which the motion parameters were accurately known.

REFERENCES

- [1] R.J. Webster, "An exact trajectory solution from doppler shift measurements," *Aerospace and Electronic Systems, IEEE Transactions on*, vol. AES-18, no. 2, pp. 249–252, March 1982.
- [2] F. Dommermuth and J. Schiller, "Estimating the trajectory of an accelerationless aircraft by means of a stationary acoustic sensor," *The Journal of the Acoustical Society of America*, vol. 76, no. 4, 1984.
- [3] J.I. Statman and Eugene R. Rodemich, "Parameter estimation based on doppler frequency shifts," *Aerospace and Electronic Systems, IEEE Transactions on*, vol. AES-23, no. 1, pp. 31–39, Jan 1987.
- [4] Yiu-Tong Chan and F.L. Jardine, "Target localization and tracking from doppler-shift measurements," *Oceanic Engineering, IEEE Journal of*, vol. 15, no. 3, pp. 251–257, Jul 1990.
- [5] Y.T. Chan and J. J. Towers, "Sequential localization of a radiating source by doppler-shifted frequency measurements," *Aerospace and Electronic Systems, IEEE Transactions on*, vol. 28, no. 4, pp. 1084–1090, Oct 1992.
- [6] Brian G. Ferguson and Barry G. Quinn, "Application of the short-time fourier transform and the wigner ville distribution to the acoustic localization of aircraft," *J. Acoust. Soc. Am*, vol. 94, pp. 821 – 827, 1992.
- [7] Brian G. Ferguson and Kam W. Lo, "Turboprop and rotary-wing aircraft flight parameter estimation using both narrow-band and broadband passive acoustic signal-processing methods," *J. Acoust. Soc. Am*, vol. 108, pp. 1763 – 1771, October 2000.
- [8] K.W. Lo and B.G. Ferguson, "Broadband passive acoustic technique for target motion parameter estimation," *Aerospace and Electronic Systems, IEEE Transactions on*, vol. 36, no. 1, pp. 163–175, Jan 2000.
- [9] D.C. Torney, "Localization and observability of aircraft via doppler shifts," *Aerospace and Electronic Systems, IEEE Transactions on*, vol. 43, no. 3, pp. 1163–1168, July 2007.
- [10] Kam W. Lo and Brian G. Ferguson, "Vehicle motion parameter estimation using a wide aperture acoustic sensor array of unknown shape," in *ACOUSTICS*, 23-25 November 2009.
- [11] D. Lindgren, M.B. Guldogan, F. Gustafsson, H. Habberstad, and G. Hendeby, "Acoustic source localization in a network of doppler shift sensors," in *Information Fusion (FUSION), 2013 16th International Conference on*, July 2013, pp. 1281–1288.
- [12] Sara R. Martn, Meritxell Genesc, Jordi Romeu, and Teresa Pmies, "Aircraft tracking by means of the acoustical doppler effect," *Aerospace Science and Technology*, vol. 28, no. 1, pp. 305 – 314, 2013.
- [13] B. G. Quinn, "Doppler speed and range estimation using frequency and amplitude estimates," *The Journal of the Acoustical Society of America*, vol. 98, no. 5, 1995.
- [14] Brian G. Ferguson, "A ground-based narrow-band passive acoustic technique of estimating altitude and speed of a propeller-driven aircraft," *J. Acoust. Soc. Am*, vol. 92, pp. 1403–1407, 1992.
- [15] F. M. Dommermuth, "The estimation of target motion parameters from cpa time measurements in a field of acoustic sensors," *The Journal of the Acoustical Society of America*, vol. 83, no. 4, 1988.
- [16] Hakima Timlelt, Youcef Remram, and Adel Belouchrani, "Closed-form solution to motion parameter estimation of an acoustic source exploiting doppler effect," *Digital Signal Processing*, vol. 63, pp. 35 – 43, 2017.
- [17] Y. Remram and H. Khelladi, "Construction of an inexpensive anechoic chamber for teaching aid," *proceedings of the 38th International Congress and Exposition on Noise Control Engineering INTER-NOISE 2009*, Ottawa, Canada, 23-26 August 2009.
- [18] Lloyd J. Griffiths, "Rapid measurement of digital instantaneous frequency," *Acoustics, Speech and Signal Processing, IEEE Transactions on*, vol. 23, no. 2, pp. 207–222, Apr 1975.
- [19] Simon Haykin, *Adaptive Filter Theory (2Nd Ed.)*, Prentice-Hall, Inc., Upper Saddle River, NJ, USA, 1991.

Wide range and high linearity CMOS temperature sensor core circuit for RFID applications.

Abdelhakim megueddem¹ and Khaled Bekhouche¹

¹ Mohamed Khider University, LMSM Lab, Faculty of electrical engineering, Biskra, Algiers. hakimmegueddem@gmail.com and khaledbekhouche@yahoo.com

ABSTRACT

In this article, we propose a new temperature sensor based on 6 MOSFETS transistors to minimize the surface, the characteristics of these transistors and the proposed architecture given to us a good result on the linearity dimension, the transistors are polarized in the sub-threshold area to reduce energy consumption.

the temperature range realized give us a space to use in different areas for radio frequency identification (RFID) applications. The sensor has a low power consumption of 38nW, a supply voltage of 1.4V and a sensibility of 0.5mV / ° C in the temperature range of -100 ° C to 100 ° C. The simulation is carried out with the OrCAD PSpice software.

Key Words: low power consumption, MOSFET, RFID, sub-threshold, temperature sensor.

1. INTRODUCTION

Over the last decades, the Radio Frequency Identification (RFID) tags have been used largely in our life, such inventory, manufacturing management,

monitoring the temperature of food and Substances [1,2], the human body and patient [3,4,5].

Two categories of RFID tags are used: passive and active. Passive tags do not incorporate power supply hence their size can be extremely reduced. Active tags supplied with a battery such the tag detection is possible from a hundred meters [6]. Our proposal is based on the active tag.

Temperature measurement is critical in many fields as it affects most physical, electronic, chemical, mechanical and biological systems. To measure the temperature there are many topologies that

use different electronic elements such as resistors, BJT transistors and/or MOSFET transistors [7,8].

The latter is almost the most used in RFID applications because of its features in the area of energy consumption [5,9].

Often the design methodology is based on power proportional to absolute temperature (VPTAT) and power complementary to absolute temperature (VCTAT) [10,11].

To convert the voltage produced by the sensor core to digital we use an analog to Digital Converter (ADC), it has the ability to be controlled according to RFID digital control, therefore it can be disabled to reduce power consumption when this is not necessary.

This work presents a temperature sensor core circuit based on MOSFET technology which can be used in active tags to achieve high linearity wide range temperature measurements.

2. ANALYTIC ANALYSIS OF THE PROPOSED SENSOR CORE CIRCUIT

The circuit is supplied with a low DC power and based on 6 MOSFET transistors functioning in the sub-threshold region.

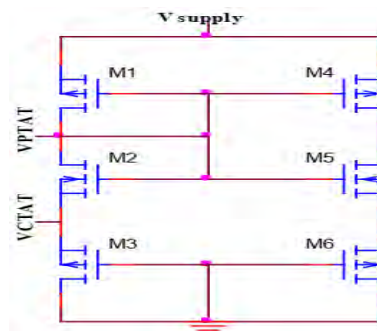


Figure. 1. VPTAT and VCTAT generator

The design of the sensor core is based on generating two voltages linearly related to the temperature: V_{PTAT} and V_{CTAT} as shown in Figure. 1. To simplify the analysis of the circuit, we will use the following approximate formula of the sub-threshold MOSFET drain current.

$$i_D = I_{S,s-t} \exp\left(\frac{v_{GS} - V_{th}}{\eta\phi_t}\right) \left(1 - \exp\left(-\frac{v_{DS}}{\phi_t}\right)\right) \quad (1)$$

Where:

$I_{S,s-t}$ is the sub-threshold saturation current, v_{GS} is the input gate-source voltage, V_{th} is the threshold voltage, η is sub-threshold swing parameter, v_{DS} is the drain-source voltage.

The thermal voltage is given by

$$\phi_t = \frac{kT}{Q} \quad (2)$$

Where k is the Boltzmann constant, T is the temperature, q is the elementary charge.

As v_{DS} is much larger than ϕ_t , the second term in the equation (1) can be neglected and the equation can be rewritten as

$$I_{sub} = k'_n \left(\frac{W}{L}\right) \phi_t^2 \exp\left(\frac{V_{gs} - V_{th}}{\eta\phi_t}\right) \quad (3)$$

Where $k'_n = \mu_n C_{ox}$ is called the process conduction parameter, W is the channel width and L is the channel length.

V_{PTAT} voltage is the voltage difference between the gate-source voltages of transistors M_2 and M_3 , hence

$$\begin{aligned} V_{PTAT} &= V_{gs2} - V_{gs3} \\ &= \eta\phi_t \ln\left(\frac{k'_{n3}}{k'_{n2}}\right) + (V_{th2} - V_{th3}) \end{aligned} \quad (4)$$

V_{CTAT} voltage is the complement to V_{DD} of the voltage difference between the gate-source voltages of transistors M_2 and M_1

$$\begin{aligned} V_{CTAT} &= V_{DD} + V_{gs1} - V_{gs2} \\ &= V_{DD} - \eta\phi_t \ln\left(\frac{k'_{n1}}{k'_{n2}}\right) + (V_{th1} - V_{th2}) \end{aligned} \quad (5)$$

In this paper, we focus on the linearity and the measurement range and we will give the difference voltage V_{diff} between V_{PTAT} and

V_{CTAT} as it will be used by the voltage-to-time converter not presented in this work.

$$V_{diff} = V_{ptat}(T) - V_{ctat}(T) \quad (6)$$

The x-coordinate of the intersection point between $V_{PTAT}(T)$ and $V_{CTAT}(T)$ is called the reference temperature T_0 . After reformulating equation (6) and using equation (2) we obtain

$$V_{diff} = a(T - T_0) \quad (7)$$

where a is the sensitivity or the slope of the voltage V_{diff} vs temperature.

3. SIMULATION RESULTS

The simulation tool used in this work is Orcad Pspice16.6. The main objectives are the design of a temperature sensor core with high linearity, large range temperature, low power supply and low energy consumption.

The output signals of the proposed temperature sensor core, V_{PTAT} and V_{CTAT} , are shown in Figure. 2.

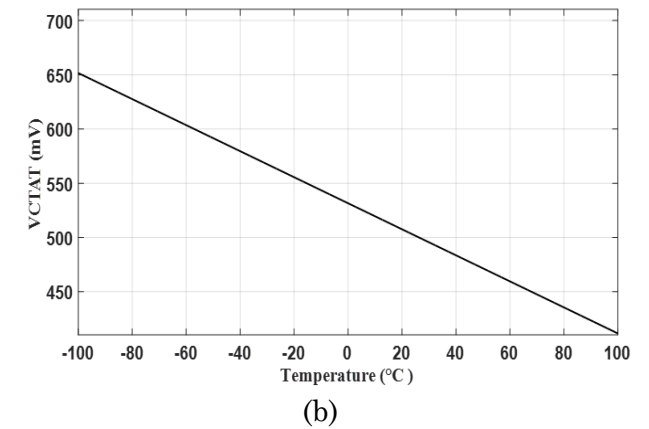
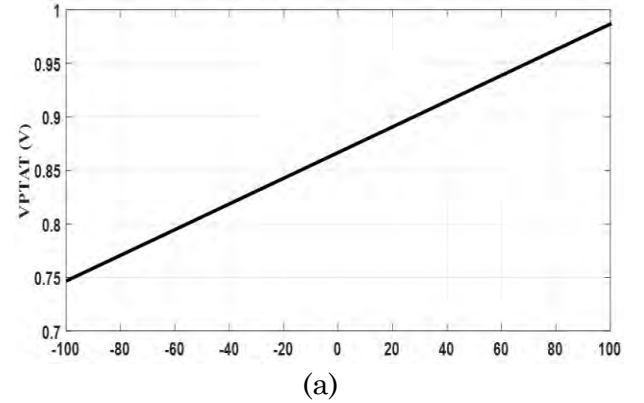


Figure.2. The simulation results for a temperature range from -100 °C to 100 °C, (a) V_{PTAT} , (b) V_{CTAT} .

For the temperature range from $-100\text{ }^{\circ}\text{C}$ to $100\text{ }^{\circ}\text{C}$, the output signal has a good linearity with a coefficient of determination $R^2 = 0.9994$ for V_{CTAT} and $R^2 = 0.9997$ for V_{PTAT} .

The slopes are slightly different in comparison to the expected theoretical values in equation (7).

The reason is that threshold voltages and other parameters in reality depends on temperature.

Figure. 3. a show the variation of the output voltages V_{PTAT} (a), V_{CTAT} (b) versus temperature in the interval from $-100\text{ }^{\circ}\text{C}$ to $100\text{ }^{\circ}\text{C}$.

In the studied temperature range, the V_{PTAT} voltage increases from 651 mV to 986 mV and the V_{CTAT} voltage decreases from 746 mV to 411 mV , Thus the sensibility is around 0.5 mV per degree Celsius for both voltages.

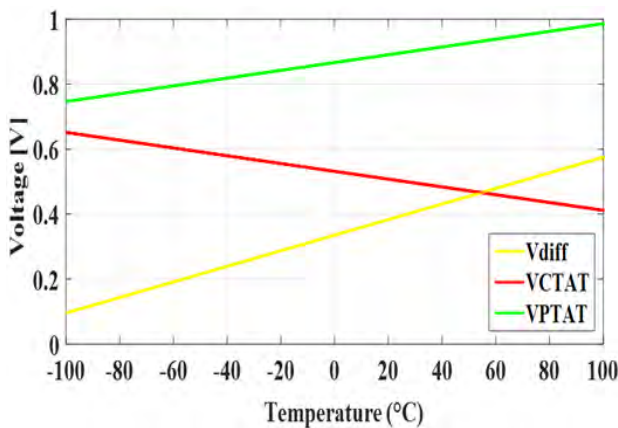
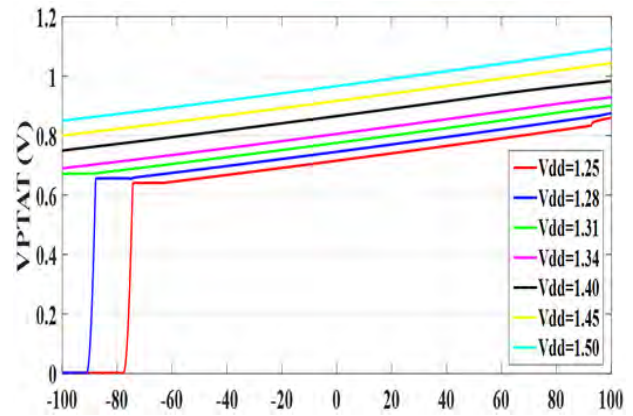


Figure. 3. The variation of V_{PTAT} , V_{CTAT} and difference voltage versus temperature.

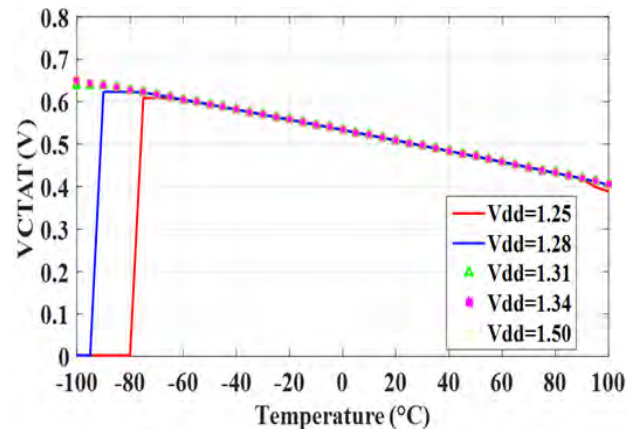
As the battery voltage of an RFID sensor decreases with time, it is important to study how this affects the long-term stability (linearity and range in our case) of the sensor.

Figure. 4 shows the effect of the power supply on both V_{PTAT} (c) and V_{CTAT} (d). We started with $V_{DD} = 1.50\text{ V}$ which is three times the threshold voltage (all transistors have the same threshold voltage), that is the limit of the sub-threshold region.

As we decrease V_{DD} we go towards the blocking region and the linearity interval is more and more reduced.



(c)



(d)

Figure. 4. The effect of supply power on V_{PTAT} (c) and V_{CTAT} (d)

4. CONCLUSION

This paper presents an analysis and topology of a low-power temperature sensor in CMOS technology, the core of the sensor is designed in the temperature range of $-100\text{ }^{\circ}\text{C}$ to $100\text{ }^{\circ}\text{C}$, for different application RFID. This temperature range is considered as wide in comparison to other works [1,12].

The simulation results have shown that good linearity and accuracy [13], for a low power all MOSFETS transistors of the sensor core work in the sub-threshold region, the measured data showed that the linearity Affected by the supply power V_{DD} and the characteristic of the transistor.

The consumption of the core sensor is 24 nW at $25\text{ }^{\circ}\text{C}$. with power supply of 1.4 V , the sensibility is around $0.5\text{ mV}/^{\circ}\text{C}$.

ACKNOWLEDGMENT

The authors would like to thank the Semiconductor and Metallic Materials

(LMSM) Laboratory of the University of Biskra.

REFERENCES

- [1] Dastanian. R, Abiri. E. and Ataiyan. M, "A 0.5 V, 112 nW CMOS temperature sensor for RFID food monitoring application,". in *Electrical Engineering (ICEE) 24th Iranian Conference on*. IEEE, 2016., p. 1433-1438.
- [2] Chen. Z, Deng. F, He. Y, Liang. Z, Fu. Z, and, Zhang. C, "A Self-Powered RFID Sensor Tag for Long-Term Temperature Monitoring in Substation," *Journal of Electrical Engineering & Technology*, 2018, vol. 13, no 1, p. 501-512.
- [3] Vaz. A , Ubarretxena. A , Zalbide. I, Pardo. D, Solar. H, Garcia-Alonso. A , , Berenguer. R, *and al*," Full passive UHF tag with a temperature sensor suitable for human body temperature monitoring,". *IEEE Transactions on Circuits and Systems II: Express Briefs*, 2010, vol. 57, no 2, p. 95-99.
- [4] Lim. C. L, Byrne. C, and Lee. J. K, "Human thermoregulation and measurement of body temperature in exercise and clinical settings,". *Annals Academy of Medicine Singapore*, 2008, vol. 37, no 4, p. 347.
- [5] Chowdhury. G. R, and Hassibi. A, "A 0.001 mm² 100 μ W on-chip temperature sensor with $\pm 1.95^\circ$ C (3 σ) Inaccuracy in 32nm SOI CMOS". In *Circuits and Systems (ISCAS), 2012 IEEE International Symposium.*, p. 1999-2002.
- [6] Zhao. Y, and Ye. Z. A, "low cost GSM/GPRS based wireless home security system,". *IEEE Transactions on Consumer Electronics*, 2008, vol. 54, no 2.
- [7] Park. H, and Kim. J. A., "0.8-V Resistor-Based Temperature Sensor in 65-nm CMOS With Supply Sensitivity of 0.28° C/V". *IEEE Journal of Solid-State Circuits*, 2018, vol. 53, no 3, p. 906-912
- [8] Yousefzadeh. B, Shalmany. S. H, and Makinwa. K. A., "A BJT-Based Temperature-to-Digital Converter With ± 60 mK ($3\text{-}\sigma$) Inaccuracy From -55° C to $+125^\circ$ C in 0.16- μ m CMOS". *IEEE Journal of Solid-State Circuits*, 2017, vol. 52, no 4, p. 1044-1052.
- [9] Shan. H, Peterson. J, Tsai. M. S, and Tang. Y, "Conrad, N. J., & Mohammadi, S.A "low power CMOS temperature sensor frontend for RFID tags," In *Silicon Monolithic Integrated Circuits in RF Systems (SiRF), 18th Topical Meeting on*. IEEE, 2018. p. 15-18.
- [10] Garulli. N, Boni. A, Caselli. M, Magnanini. A, and Tonelli. M," "A low power temperature sensor for IOT applications in CMOS 65nm technology," In *Consumer Electronics-Berlin (ICCE-Berlin), 7th International Conference on*. IEEE, 2017. p. 92-96.
- [11] Tewari. S, and Singh. K, "Intuitive design of PTAT and CTAT circuits for MOSFET based temperature sensor using Inversion Coefficient based approach,". In *VLSI Design and Test (VDAT), 19th International Symposium on*. IEEE, 2015. p. 1-6.
- [12] Gomes F. O, de Paula. L, Santos. J. C, Courcelle. L, Piovani. D, Viera. F, and Lubaszewski. M, "A low-power RFID enabled temperature sensor for cold chain management,". In *Circuits and Systems (ISCAS), International Symposium on IEEE*, May 2015. p. 2113-2116.
- [13] Brito. J. P. M., and Rabaeijs. A, "CMOS smart temperature sensors for RFID applications,". In *Integrated Circuits and Systems Design (SBCCI), 26th Symposium on*. IEEE, September 2013. p. 1-6.

WobbleBox, an adaptive instrument to quantify angles variations exercises on wobble boards

Anwar S. BENBAKHTI¹, Samir BOUKHENOUS¹ and Mokhtar ATTARI¹

¹ USTHB, LINS Lab, Faculty of Electronics and Computers, PO.Box 32, Bab-Ezzouar, Algiers
anwar.benbakhti@gmail.com, s.boukhenous@gmail.com and attari.mo@gmail.com

ABSTRACT

Home-based ankle exercises are often preconized by therapists to recover some ankle pathologies like ankle ligament sprain, or for proprioceptive enhancement for athletes. The traditional wobble board remains the principal passive tool preconized due to its simplicity, ease of access and cheap price, but it gives no information to either the clinician or the patient to analyze the exercises. In order to enhance wobble boards with the capability to quantify exercises, we present the “WobbleBox”, an instrument to use on any wobble board or unstable surface. The WobbleBox contains an accelerometer to record angles and sends data wirelessly via Bluetooth to dedicated software for the time spent calculation (?) and displays dots on various region of the wobble board in real time. The developed application offers to the clinician an access to the data and offers to the patient an interactive platform to effectively track his/her rehabilitation protocol or simple proprioceptive enhancement exercises.

Key Words: instrumented wobble board; ankle exercises, proprioceptive enhancement.

1. INTRODUCTION

The ankle sprain is one of the most common trauma diseases that affect different categories of people. Athletes who practice sports register the highest ankle injury [1] as running and jogging (25%), soccer (14%), racket sports (20%) and ball games (19%) due to the high solicitation of the ankle articulation during their movements such as landing on inverted foot. Inadequate rehabilitation can lead to chronic ankle

instability [2]. On the other hand, sportsmen need to enhance their stability capabilities to improve the proprioceptive ability and reduce the experience of ankle sprain. After an ankle sprain, the muscle retains a motor deficiency of muscle strength and damages to the mechanoreceptor of the ligament which results in a functional ankle instability that manifests as proprioceptive deficit, muscular weakness, loss of balance control, and abnormal ankle movements [3]. Hence the need for a functional and orthopaedic neuromuscular rehabilitation, adapted and controlled, is highly recommended to avoid these functional disorders.

The main objectives of rehabilitation are to treat disabilities caused by the stroke and to help the sprained subject in reintegrating society as much as possible by allowing him to regain his/her total joint mobility, correcting his/her walk, and recover his/her proprioceptive capability. This recovery is possible by developing muscular and joint strength for a total ankle flexibility. This neuromuscular proprioceptive reprogramming was introduced by Freeman et al. [4] who described the link between postural stability alterations and chronic ankle instability and the disorder caused to the mechanoreceptor residing in the ankle ligament after an ankle sprain injury [5].

This work led him to design a standing plate based on a hemisphere as a balance platform in order to reproduce a balance training that moves on two axes. The standing plate allows the restoration of the capability of the mechanoreceptor located in muscles and ligaments to retrieve their proprioceptive function by the

reprogramming of neuromuscular control. This platform, often called a Freeman plate, a balance board or a wobble board is nowadays the common tool used for the rehabilitation of the ankle. The literature review of Postle & al [6] shows the effectiveness of proprioceptive exercises for ankle injury. McGuine & al [7] showed the results of balance training to prevent ankle sprains. Verhagen & al [8] proves that the use of proprioceptive balance board program in a volleyball team is effective for prevention of ankle sprain recurrences.



Fig. 1. Examples of proprioceptive ankle exercises

Several wobble boards are embedded with sensors and enhanced with functionalities to increase the effectiveness of the exercises by offering to the user an interactive tool that assists him/her in the rehabilitation process and by offering to the patient more motivation to perform the preconized exercises. Karime & al [9] developed the E-Wobble, a board for the ankle and toe rehabilitation by using a sensitized wobble interface with a game to motivate the patient. Parameters such as Jerkiness and angular velocity [10] are extracted as benchmarks to examine healthy subjects' training performances and to make references by analysing how smooth the movements are.

The objective of this work is to transform any traditional wobble board into an ambulatory instrument to assist persons who want to increase their proprioceptive performances, or need rehabilitation exercises, to perform training interactively by following the evolution of the exercises through a real-time interface that shows the tilt angles of the platforms in three different regions. To do this, we have developed the "Wobble Box", an instrument that can be installed on any wobble board or unstable surface. The Wobble Box communicates with dedicated software to display data such as angles of variation, time spent on each region and percentage of time in real time.

Moreover, it provides the therapist with a database containing extracted parameters to evaluate the process and adapt the exercises.

2. SYSTEM DESCRIPTION

A. Angles measurements

In order to measure angles and detect impacts, we use an Invensens MPU6050 Inertial Measurement Unit (IMU) containing an accelerometer and gyroscope in order to perform a 6 Degree of freedom (DoF) measurement unit. This motion tracking sensor has a low power consumption (9.3uA) and contains an integrated built-in digital motion processor DMP. The system principle is presented in Fig.2.

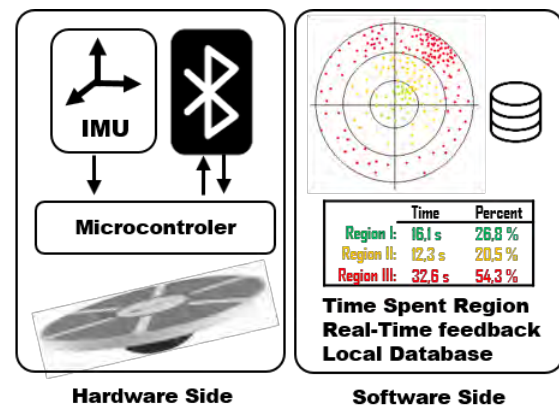


Fig. 2. System principle

B. The Wobble Board

A general-use wobble board (Domyos Balance board, Oxylane, Villeneuve d'Ascq, France) was used as the unstable surface. It is a common cost-effective, commercial wooden wobble board of the FREEMAN type used for muscle toning, balance and coordination. Its characteristics are 1.25kg in weight, 39.5 cm in circumference and 7.5 cm in height. The maximum tilt angle is 20.79°. Any Wobble board or unstable surface can be used with the instrument, one of conditions being that it has the same angle tilt range in all directions.

C. Instrumentation

To offer a full-duplex wireless communication between the wobble board and the software, we use a HC-06 bluetooth module. The module is powered by 3.3V directly from an integrated battery. The

current consumption during communication is 8mA.

The IMU sensor data are collected by an Atmega328p microcontroller via an I2C interface, and data are sent by HC-06 Bluetooth module through serial interface. The power is provided by a couple of batteries, regulated by a 5V regulator to power supply all the electronics. The batteries are charged by a TP4056 Lithium-ion charge driver.

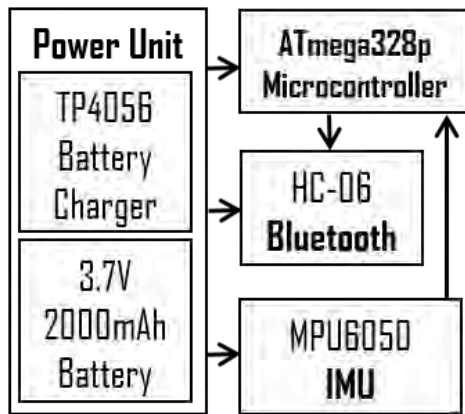


Fig. 3. Electronics architecture



Fig. 4. The Wobble Box disassembled. Left up is the HC-06 Bluetooth module. On the bottom left is the TP4056 Li-ion battery charger. In the middle is the Inertial Motion Unit MPU6050 and on the right the Arduino board. The batteries on the left gives an output of 7,4V.

D. The developed Software

The aims of our device being to be accessible by anyone and to offer a visual feedback to track balance exercises or an ankle sprain rehabilitation, we have developed a software that displays and records the user's performances and stores them on local database. First the connection link must be

achieved with the platform through serial com.

Predefined data for a general wobble board (Domyos) can be chosen on the interface. The angles are divided into 3 equal regions, but can be modified and adapted according to user choice. The maximum angle can also be chosen through a calibration function to estimate the maximum angle and stored. To do so, the user must click on the "calibrate" button and tilt the platform. The maximum angle will be automatically stored. The 3 regions will be automatically calculated and displayed. The user can still change the values at any time.

The default recording duration is 1 of minute, which can be adjusted. After hitting start to record, 10 seconds are left for the user to stand on the surface then the record starts for the specified duration.

The software displays dots that represent the tilt angle in pitch and roll in real-time. The dots are displayed in three different colours which represent the three different regions, green for the most difficult, yellow for the intermediate and red for the maximum angles which results in bad region.

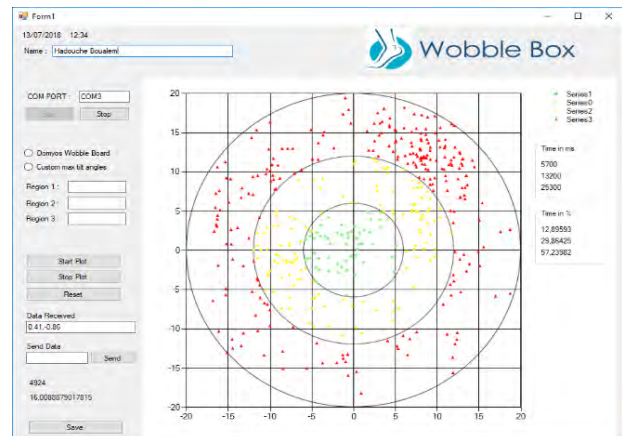


Fig. 5. WobbleBox software usage

3. METHODS

A. Region Time Spent

To analyze and quantify the performance of the ankle exercises, the system provides the time spent on three regions. The time spent is displayed in milliseconds and in percentage of total time.



Fig. 6. The 3 different ranges of tilt angles for the used wobble board.

As shown in Fig.6, the wobble board used has a maximum angle of 20.8°, so region I is limited to 6.5°, region II ranges from the latter up to 13°, and region III ranges from the latter up to 20.8°. This last region is larger than the two others by 0.2°. These values are automatically calculated by the software during calibration, and can be adjusted manually by the user.

B. Procedure

The dots are displayed at a rate of 20Hz. The time spent in each region (TR1, 2, 3) is displayed in second and the percentage of total exercise time (%R1, 2, 3) are displayed simultaneously. To display the feasibility and reliability of our system, we performed tests with 2 persons to give an example of the results of the system outputs. Each person performed 3 kinds of exercises, Eyes Opens on One Leg (EOOL), Eyes Opens on Two Legs (EOTL) and Eyes Closed on Two Legs (ECTL). Fig.7 shows a person with three kind of exercises.



Fig. 7. Person with three kind of exercises, from left to right EOTL, ECTL, EOOL. The Wobble box is positioned according to foot orientation

4. TEST AND RESULTS

At this stage, our goal is to demonstrate the capabilities of the wobble board connected to a dedicated application to record data for analysis, as well as the real-time feedback to the user. Fig.6 shows an example of a report

of data extracted from a healthy person (no ankle sprain or equilibrium disorder) who didn't experience an ankle injury or other lower limb musculoskeletal, neurological or any other disorder which can affect stability.

We conducted tests on two persons with no stability or musculoskeletal disease. These persons don't practice any sport that can increase their stability, however they were given an opportunity to familiarize themselves to the board before proceeding to the recordings.

Table 1

Time spent and percentage of time in second for each region. Three Exercises done by two persons

	TR1	TR2	TR3	% R1	%R2	%R3
P1 EOTL	29	32	11	40.27	44.4	15.1
EOOL	13	22	43	16.6	28.2	55.1
ECTL	5	12	56	6.8	16.6	76.7
P2 EOTL	21	19	32	29.1	26.3	44.4
EOOL	2	29	42	2.7	39.7	58.3
ECTL	4	18	50	5.5	25	69.4

The results show no important evolution in the performances between the two persons. As expected, the percentage of time spent in region 3 is high in all exercises only for person 1 in EOTL. The time spent in region three for eyes closed is greater than for EOTL. For person 2, in EOTL the results are stable between the two first regions compared to other exercises and the other person.

5. CONCLUSION

In this work we have presented the development of the "Wobble Box", an instrument which enhances any balance exercise on an unstable surface or wobble board to an interactive one with real-time feedback of the pitch and roll angles and display as dots on a dedicated software. The software divides the tilt angle ranges into three regions and gives the time spent on each one and percent time from total time. A test was realized with one person to demonstrate the feasibility of the device. More experience such as eyes open and with different legs must be done to investigate and compare the performances with different

persons profiles (older, sportive, person with ankle sprain disease) to evaluate the stability performances.

ACKNOWLEDGMENT

This work was supported by MESRS (Ministère de l'Enseignement Supérieure et de la Recherche Scientifique) under the supervising of the CNEPRU, www.cnepru-mesrs.dz.

REFERENCES

1. D. T. Fong, Y.-Y. Chan, K.-M. Mok, P. S. Yung, and K.-M. Chan, "Understanding acute ankle ligamentous sprain injury in sports.," *Sports Med. Arthrosc. Rehabil. Ther. Technol.*, vol. 1, p. 14, Jan. 2009.
2. B. M. Zouita, O. Majdoub, H. Ferchichi, K. Grandy, C. Dziri, and F. Z. Ben Salah, "The effect of 8-weeks proprioceptive exercise program in postural sway and isokinetic strength of ankle sprains of Tunisian athletes.," *Ann. Phys. Rehabil. Med.*, vol. 56, no. 9–10, pp. 634–43, Dec. 2013.
3. M. J. Santos and W. Liu, "Possible factors related to functional ankle instability.," *J. Orthop. Sports Phys. Ther.*, vol. 38, no. 3, pp. 150–7, Mar. 2008.
4. M. A. Freeman, M. R. Dean, and I. W. Hanham, "The etiology and prevention of functional instability of the foot.," *J. Bone Joint Surg. Br.*, vol. 47, no. 4, pp. 678–85, Nov. 1965.
5. M. A. Freeman and B. Wyke, "Articular contributions to limb muscle reflexes. The effects of partial neurectomy of the knee-joint on postural reflexes.," *Br. J. Surg.*, vol. 53, no. 1, pp. 61–8, Jan. 1966.
6. K. Postle, D. Pak, and T. O. Smith, "Effectiveness of proprioceptive exercises for ankle ligament injury in adults: a systematic literature and meta-analysis.," *Man. Ther.*, vol. 17, no. 4, pp. 285–91, Aug. 2012.
7. T. a McGuine and J. S. Keene, "The effect of a balance training program on the risk of ankle sprains in high school athletes.," *Am. J. Sports Med.*, vol. 34, no. 7, pp. 1103–11, Jul. 2006.
8. E. Verhagen, A. van der Beek, J. Twisk, L. Bouter, R. Bahr, and W. van Mechelen, "The effect of a proprioceptive balance board training program for the prevention of ankle sprains: a prospective controlled trial.," *Am. J. Sports Med.*, vol. 32, no. 6, pp. 1385–93, Sep. 2004.
9. A. Karime, H. Al-Osman, W. Gueaieb, J. Mohamad Alja'am, and A. El Saddik, "E-wobble: An electronic wobble board for ankle and toe rehabilitation," 2011 *IEEE Int. Symp. Med. Meas. Appl.*, pp. 366–369, May 2011.
10. A. Karime, H. Al Osman, M. Eid, W. Gueaieb, and A. El Saddik, "Capturing ankle benchmark kinematics using an interactive sensory wobble board," *Electron. Proc. 2013 IEEE Int. Conf. Multimed. Expo Work. ICMEW 2013*, pp. 1–6, 2013.
11. D. Fitzgerald, N. Trakarnratanakul, L. Dunne, B. Smyth, and B. Caulfield, "Development and user evaluation of a virtual rehabilitation system for wobble board balance training.," *Conf. Proc. IEEE Eng. Med. Biol. Soc.*, vol. 2008, pp. 4194–8, Jan. 2008

Thermal flow sensor used for thermal mass flowmeter

Amina BEKRAOUI^{1,2}, Ahmed HADJADJ³

¹Unité de Recherche en Energies Renouvelables en Milieu Saharien(URERMS), Centre de Développement des Energies Renouvelables, CDER, 01000, Adrar, Algeria,

²Research Unit Materials, Processes and Environment (UR/MPE), Boumerdes, Algeria, aminabekraoui@urerms.dz

³Laboratory of LFEPM, Hydrocarbons and Chemistry Faculty, Boumerdes, Algeria,

ABSTRACT

This work deals with thermal mass flowmeters. Thermal mass flowmeters fabricated by hot wire anemometers technology using the thermal domain for the measurement of fluid flow are discussed. Attention is paid to geometry of the sensors. Thermal anemometer flow sensor may comprise a heater and several temperature sensors. They convert the flow energy over heat transfer into electrical signals. The aim of this work is to propose thermal mass flowmeter for measuring natural gas in transaction operations, where it is unusually used. Basic type of thermal flow sensor anemometer is used and discussed.

Key Words: Flow sensor, hot wire anemometer, thermal flowmeter, flow rate.

1. INTRODUCTION

In natural gas industry, various type of instruments are used to calculate volume flow rate such as Orifice place, turbine and ultrasonic meters. The alternative of measuring mass flow rate is possible employing Coriolis and thermal mass flowmeters, but still now, none of these devices is used in natural gas fiscal metering plants [1, 2, and 3]. The measurement and control of gas flow rates is critical in many engineering applications [4]. Thermal flow sensors are widely used in various applications for both liquids and gases [5, 6]. They have great utility in a number of diverse applications requiring monitoring of gas or fluid flow including flow cytometry, cleanroom environmental monitoring, wind,

gas chromatography, wall shear stress, and viscosity measurements [6]. Flow rate determination is an important concern in many cases, including laboratory, industrial and medical applications. Thermal flow sensors have various advantages in comparison to other technologies, such as minimal flow restriction, absence of moving parts, low maintenance requirements, low cost [7]. Another reason for the large interest in thermal flow sensors is the advantages gained through miniaturization: low power consumption, higher sensitivity to low flow rates, and ease of use with different modes of operation [8]. A thermal flow sensor consists of a heater and one or more temperature sensors. The effects caused by heat transfer are evaluated in different ways, which correspond to the operating modes of a thermal flow sensor. Measuring the heating power or heater temperature and feeding back to heating current allow the heater to be controlled in two modes: constant power and constant temperature [9, 10]. We can classify thermal mass flow meters in function of three different principles: thermal anemometers, calorimetric flow sensors, and time-of-flight flow sensors. Figure.1 illustrates the principles [11]. Thermal mass flow meters that measure the effect of the flowing fluid on a hot body are called hot-wire or hot-film sensors. The displacement of temperature profile around the heater which is modulated by the fluid flow are calorimetric sensors. Thermal mass flowmeters based on a heat pulse created at the heater and fed to the fluid, and a temperature sensor located downstream to detects the time between the pulse and the response of the sensing element

determines the flow velocity are called time-of-flight sensors [12, 13]. Calorimetric flow sensors and time of flight sensors require two or more elements. By adding sensing elements, they can be made direction sensitive [11, 14]. The structural and electronic simplicity of thermal flow sensor make of them easily integrated into the micromachining fabrication process. They are the oldest type of micro machined flow sensors [11]. In this work, we present the design and characterization of thermal mass flow meters based on thermal anemometer flow sensor. Attention is paid to geometry of sensors. Data use for simulation are from a gas field situated in the south of Algeria.

2. THERMAL MASS FLOW METERS

The Full paper has to be submitted electronically via Easy Chair Platform. Thermal flow meters measure the mass flow rate directly, they are based on a variety of operating principles, but most involve heat dispersion. The associated physical quantity measured by the meter is the mass velocity or the mass flux that flows through a unit cross-section [15]. Figure 1 illustrates the complete transduction process for thermal flow sensor with a voltage output signal. As, it is shown two transduction processes take place, first, the mechanical signal (mass flow) is convert in to a thermal signal (heat transfer), the flow induces a temperature difference which is converted into an electrical output signal (current or voltage) [16, 17]. The principle of the gas mass-flow measurement is based on the fact that the output voltage of the sensor element is related to the rate of heat transfer deducted between the sensor and the gas. The rate of heat transfer depends mainly on the gas flow rate (or velocity), as a main effect, but also on the gas composition, which influences its thermo-physical properties, like the thermal conductivity and diffusivity [18]. The working range for any mass flow sensor dependent on the fluid properties, such as thermal conductivity, specific heat, and density [16]. The achievement of thermal mass flowmeters is attributed to L.V. King [19] who in 1914, published his famous King's Law revealing how a heated wire immersed in a fluid flow measures the mass velocity at a point in the flow. King called his instrument "hot-wire anemometer" [20]. Figure 2 shows

the two configurations of thermal mass flow meter and its major components. In-line flowmeters measure the total mass flow rate flowing through the pipe and insertion flow meters have the same major components as in-line flow meters, but not a flow body [20].

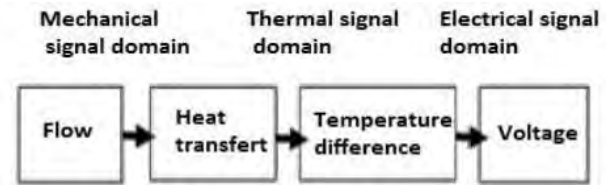


Figure. 1: The three signal domains and the signal transfer process of a thermal flow sensor [17].

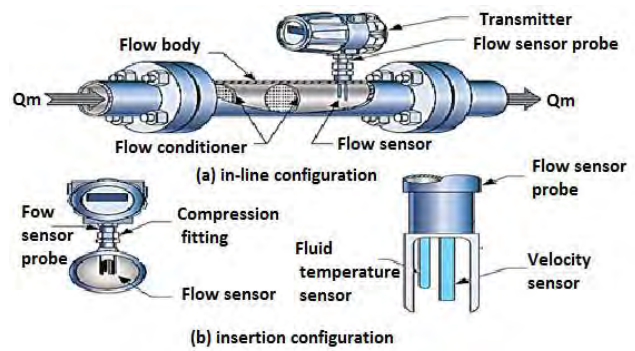


Figure. 2: The two configurations of thermal mass flow meter [3].

2.1. Thermal flow sensor

A thermal flow sensor generally consists of a heater and one or more temperature sensors. Depending on the heated element in a thermal anemometer, sensors of this type are called hot-wire, hot-chip, or hot-film anemometers [8, 11].

As shown in Figure.3 the flow sensor of both in-line and insertion configurations has an electrically heated velocity sensor and a fluid temperature sensor immersed in the flowing fluid. Figure.4 shows a typical thermal mass flow sensing element, it consists of two sensors: a mass flow sensor and a temperature sensor, which automatically corrects the changes in gas temperature, Both sensors are referenced grade platinum resistance temperature detectors (RTDs).The electrical resistance of RTDs increases as temperature increases [16]. The hot wire anemometer use a small electrically heated element to measure fluid flow velocities. Its principle is based on the

heat transfer convection from a heated element placed in the fluid flow, hence the changes in the fluid medium will cause an alteration in the sensor heat loss [21].

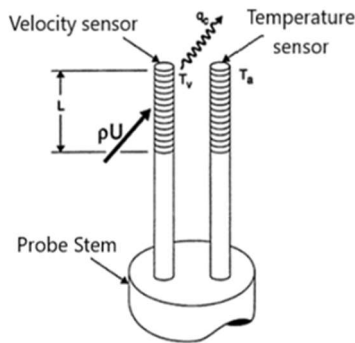


Figure. 3: Industrial thermal mass flow sensing element consists of two sensors [16].

In practice, the fluid temperature sensor measures the fluid temperature T_f . The sensor drive in the transmitter delivers an electrical power to the velocity sensor. This last is heated in return to an average temperature T higher than the fluid one. The heat transferred from the velocity sensor to the flowing fluid provide the desired measurement of the fluid mass flow rate Q_m .

The front end of the flow sensor drive is often an analog Wheatstone bridge circuit. The velocity and the fluid temperature sensors are located on opposite legs of the bridge. This provides analog compensation of changes in fluid temperature. The bridge voltage is a high-level output signal rounding several volts [20].

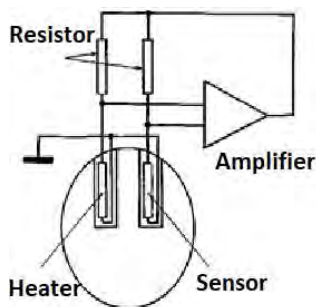


Figure. 4: Schematic of in-line thermal mass flowmeter with Wheatstone bridge arrangement [22].

2.2. Constant temperature anemometer architecture

Thermal anemometers can be run in several different modes. Constant temperature anemometer (CTA) and constant current anemometer (CCA) [11], the first one is considered here. The major advantage of maintaining hot-wire at a constant operational temperature (constant resistance) is that the thermal inertia of the sensing element is automatically adjusted when the fluid flow conditions change. The mode of operation is achieved by incorporating a feedback differential amplifier into the hot-wire anemometer circuit [23]. The mode of operation used here is Constant Temperature Anemometry (CTA); its bridge circuit is shown below in figure.5. Initially the bridge is balanced by adjusting the variable resistor R_3 while the rest of resistors are fixed. The flow velocity variation causes the change in the resistance R_1 and to keep this last constant, a power is needed to feed the sensor [21, 24].

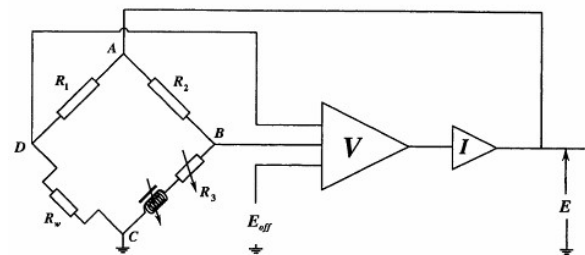


Figure. 5: Schematic of a constant temperature anemometer [17].

2.3. Hot wire equation

The equation which model the hot wire behaviour will be used to study its steady state response is given by:

$$w = I_w^2 R_w = h(v) \cdot A_s \cdot (T_w - T_f) \quad (1)$$

If current I is passed through a resistive element, the element is heated to a temperature T which is greater than T_f the fluid temperature. The temperature of resistive element T and resistance R_T harmony between electrical power $I^2 R_T$ and the rate of total convective heat transfer between element and fluid. The first law of thermodynamic experiment the equation of heat balance as:

$$w = I_w^2 R_w = h(v). A_s. (T_w - T_f) + mc \frac{dT_s}{dt} \quad (2)$$

With:

m: Wight of the wire [Kg];

c: calorific capacitor of wire [J/Kg.K];

If I_0, R_{T0}, T_0, v_0 represent steady equilibrium conditions then:

$$I_{w0}^2 R_{wT0} - h(v_0). A_s. (T_0 - T_f) = 0 \quad (3)$$

If $\Delta I, \Delta R, \Delta v$ and ΔT are the small deviations from the above equilibrium values, we have:

$$I_w = I_{w0} + \Delta I \quad ; \quad R_w = R_{wT0} + \Delta R_{wT}$$

$$T_w = T_0 + \Delta T \quad ; \quad h(v) = h(v_0) + \sigma \Delta v$$

$\sigma = \frac{\partial h}{\partial v}$ is the rate of change of h, calculated at equilibrium v_0 from (1) and (2), we have:

$$(I_{w0} + \Delta I)^2 (R_{wT} + \Delta R_{wT}) - (h(v_0) + \sigma \Delta v)(T_0 + \Delta T) A_s = mc \frac{d\Delta T}{dt} (T_0 + \Delta T) \quad (4)$$

Neglecting all the terms involving the multiplication of small quantities gives:

$$(I_{w0}^2 + 2I_0 \Delta I) R_{wT} + I_{w0}^2 \Delta R_{wT} - h(v_0)(T_0 - T_f) A_s - h(v_0) \Delta T. A_s - \sigma A_s (T_0 - T_f) \Delta v = mc \frac{d\Delta T}{dt} \quad (5)$$

Subtracting (3) from (5) gives:

$$2I_{w0} R_{wT0} \Delta I + I_{w0}^2 \Delta R_{wT} - h(v_0) \Delta T. A_s - \sigma (T_0 - T_f) \Delta v. A_s = mc \frac{d\Delta T}{dt} \quad (6)$$

Replacing ΔT by a can be eliminate by setting resistive coefficient of element, we found:

$$\left[\frac{h(v_0) A_s}{\alpha} - I_{w0}^2 \right] \Delta R + \frac{mc}{\alpha} \frac{d\Delta R_T}{dt} = 2I_{w0} R_{wT} \Delta I - \sigma A_s (T_0 - T_f) \Delta v \quad (7)$$

$$\Delta R_T + \tau_v \frac{d\Delta R_T}{dt} = K_I \Delta I - K_v \Delta v \quad (8)$$

Where:

$$\tau_v = \frac{mc}{[h(v_0) A_s - I_{w0}^2 \alpha]} \quad K_I = \frac{2\alpha I_{w0} R_{T0}}{[h(v_0) A_s - I_{w0}^2 \alpha]}$$

$$K_v = \frac{\alpha \sigma A_s (T_0 - T_f)}{[h(v_0) A_s - I_{w0}^2 \alpha]}$$

The Laplace transform of eqt. (8) gives:

$$(1 + \tau_v s) \Delta R_T = K_I \Delta I - K_v \Delta v \quad (9)$$

The transfer function of thermal velocity sensor:

$$\Delta R_T = \frac{K_I}{(1 + \tau_v s)} \Delta I - \frac{K_v}{(1 + \tau_v s)} \Delta v \quad (10)$$

The block diagram of thermal velocity sensor is below:

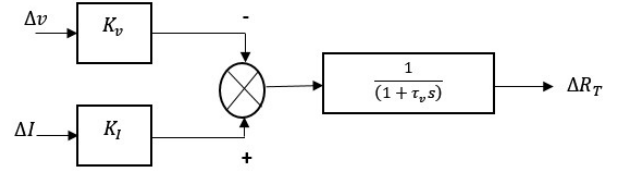


Figure. 6: Block diagram of thermal velocity sensor.

3. CONSTANT TEMPERATURE ANEMOMETER SYSTEM

The steady state equilibrium equation for a fluid velocity sensor with self-heating current is:

$$I_w^2 R_w = h(v). A_s (T_w - T_f) \quad (11)$$

In the operating mode of the CTA, resistance R_w and the temperature T_w of the sensor are maintained at constant values. From (11) we see that if the fluid velocity v increases, it will cause an increase in $h(v)$, the system must increase the current I through the sensor in order to restore balance. In the rest of our study, we will work with the universal correlation of Kramer proposed for flow sensors:

$$Nu = 0.42 Pr^{0.2} + 0.57 Pr^{0.33} Re^{0.5} \quad (12)$$

$$h = \frac{k}{d} \left[0.42 Pr^{0.2} + 0.57 Pr^{0.33} \left(\frac{\rho v d}{\mu} \right)^{0.5} \right] \quad (13)$$

So:

$$h = A_0 + B_0 \sqrt{v}$$

Where:

$$A_0 = \frac{k}{d} 0.42. Pr^{0.2} \quad , \quad B_0 = \frac{k}{d} 0.57 Pr^{0.33} \left(\frac{\rho d}{\mu} \right)^{0.5}$$

So:

$$\frac{I_w^2 R_w}{(R_w - R_0)} = A + B \sqrt{v} \quad (14)$$

With:

$$A = \frac{A_s}{\alpha R_0} A_0 \quad \text{and} \quad B = \frac{A_s}{\alpha R_0} B_0$$

$$E_{out} = I R_w$$

$$E_{out}^2 = R_w [(R_w - R_0) (A + B \sqrt{v})]$$

$$E_{out} = (E_0 + \gamma \sqrt{v})^{0.5} \quad (15)$$

$$E_0 = R_w (R_w - R_0) A \quad \text{and} \quad \gamma = R_w (R_w - R_0) B$$

3.1 Dynamic characteristics of CTA

The classic architecture of a CTA base on Wheatstone bridge is illustrated in figure.7. This architecture allows us to extract equations representing each block of CTA.

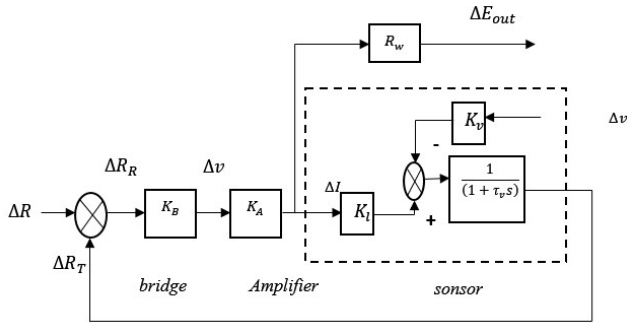


Figure. 7: Block diagram of CTA.

The characteristic equation of the sensor is:

$$\Delta R_T = \frac{K_I}{(1 + \tau_v s)} \Delta I - \frac{K_v}{(1 + \tau_v s)} \Delta v$$

The Wheatstone bridge provides a voltage in its output. It's characteristic equation is:

$$\Delta V = K_B \Delta R_R$$

Since the amplifier is used to make the balancing of the Wheatstone bridge, and it's the only parameter that can play the role of current controller, the output of the amplifier is the variation in current represented by the following equation:

$$\Delta I = K_A \Delta V$$

The output voltage equation is:

$$\Delta E_{out} = R_w \Delta I$$

The change in the resistance of the bridge is represented by the following equation:

$$\Delta R_R = \Delta R - \Delta R_T \text{ so } \Delta R_R = -\Delta R_T$$

From these equations, we found:

$$\frac{-1}{R_w K_B K_A} \Delta E_{out} = \frac{1}{(1 + \tau_v s)} \left[\frac{K_I}{R_w} \Delta E_{out} - K_v \Delta v \right]$$

So:

$$[(1 + K_I K_A K_B) + \tau_v s] \Delta E_{out} = K_v K_A K_B R_w \Delta v$$

The transfer function of CTA is:

$$\frac{\Delta E_{out}}{\Delta v}(s) = \frac{K_{CTA}}{1 + \tau_{CTA} s} \quad (16)$$

With:

$$K_{CTA} = \frac{K_v K_A K_B R_w}{1 + K_I K_A K_B} \quad \text{and} \quad \tau_{CTA} = \frac{\tau_v}{1 + K_I K_A K_B}$$

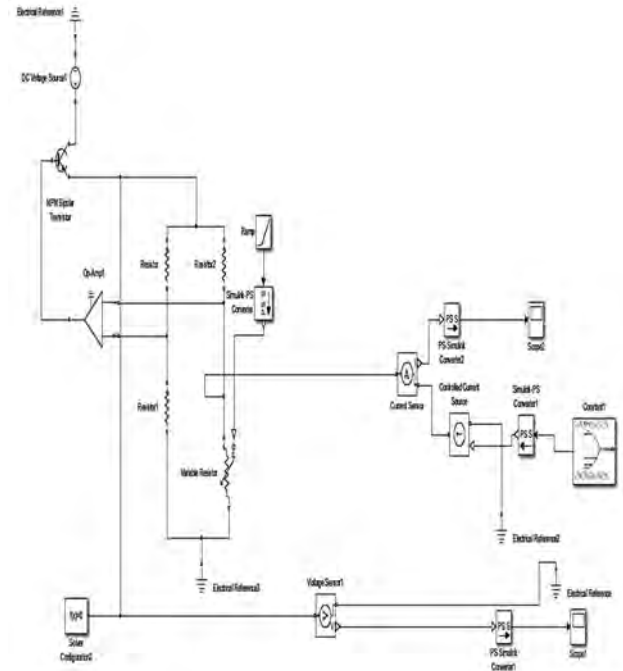


Figure. 8: Configuration of CTA electronic circuit in Simulink.

4. CALCULATION OF FLUID VELOCITY AND MASS FLOW RATE

The utility of all these calculations resides in the fact that the mass flow rate of natural gas can be extracted from the fluid velocity. The King's law relating the power and fluid velocity was simulated in Matlab / Simulink to get the fluid mass flow rate. A voltage variation range corresponding to the natural gas flow variation was used in the calculation.

We can derive the relationship that relates the velocity on the voltage in the following manner:

$$E_{out}^2 = R_w [(R_w - R_0)(A + B\sqrt{v})]$$

So:

$$v = \left[\frac{E_{out}^2 - A}{R_w \cdot (R_w - R_0) \cdot B} \right]^2 \quad (17)$$

Equation.17 shows the relation between the fluid velocity, the output voltage, coefficients A, B, resistances of the wire and the fluid. According to existing commercial thermal flowmeters, the voltage output variation is generally between 2 to 4 volts. Hence, the following graph of change of velocity v according to voltage variation is

obtained:

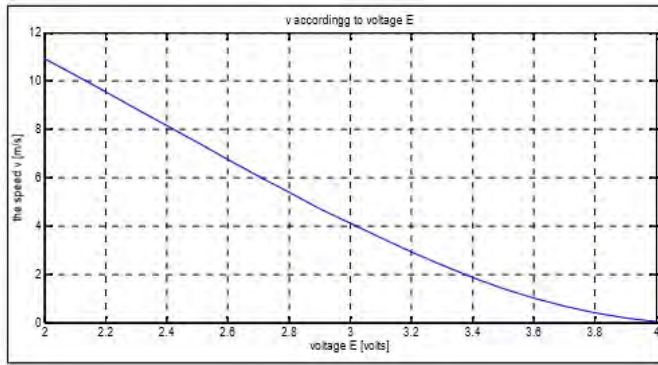


Figure. 9: The rate of velocity v change according to voltage E .

The velocity is inversely proportional to the voltage. Low increase voltage causes opposite changes in velocity. The next step is to calculate the mass flow rate from the previous result. The mass flow has no direct relationship with the fluid velocity; first, it should compute the flow volume then the mass flow. The volumetric flow equation is given by:

$$Q_v = S \cdot v \quad (18)$$

The mass flow rate is defined by:

$$Q_m = Q_v \cdot \rho \quad (19)$$

So:

$$Q_m = S \cdot v \cdot \rho \quad (20)$$

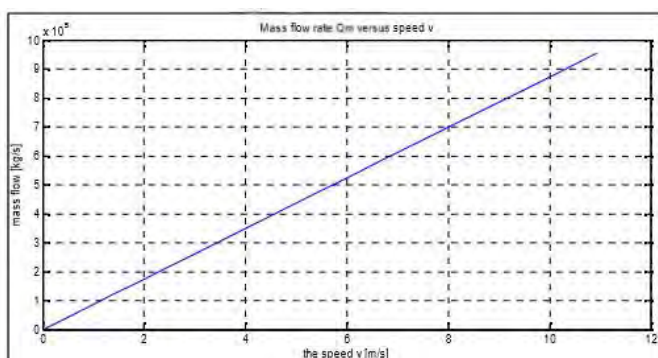


Figure. 10: Mass flow rate Q_m versus fluid velocity v .

The mass flow rate increases with the increase of fluid velocity. It has a linear relationship that validates the theoretical relationship found in equation.20.

5. CONCLUSION

The architecture of a hot wire anemometer with constant temperature was presented and simulated by Matlab/Simulink. Therefore, the numerical study is done using a natural gas process variation to study the performance of thermal flowmeters constructed from thermal hot wire anemometer. The results allowed us to conclude that hot wire constructed from thermal sensor can give meaningful results for the calculation of the mass flow rate according to the fluid velocity. The counting of flow rate using thermal mass flow meters has many advantages regarding its direct calculation law of flow velocity. The employ of some parameters such as fluid temperature, heat transfer and fluid physical properties is its strong advantage versus other flowmeters types. Following this work, we can say that the hot wire anemometer is a technique used to measure the turbulence of a fluid. The laws established by King facilitated tasks to go from velocity of a fluid to its mass flow rate.

REFERENCES

- [1] Parvizi S, Arabkoohsar A, and Farzaneh-Gord M, "Natural gas compositions variation effect on capillary tube thermal mass flow meter performance", *Flow Measurement and Instrumentation*, 50, pp.229-236, 2016.
- [2] Farzaneh-Gord M, Parvizi S, Arabkoohsar A, Machado L, Koury R.N.N, "Potential use of capillary tube thermal masse flow meters to measure residential natural gas consumption", *Journal of Natural Gas Science and Engineering*, 22, pp.540-550, 2015.
- [3] Bekraoui A, Hadjadj A, "An Overview of Thermal Mass Flowmeters Applicability in Oil and Gas Industry", *Energy Procedia* 141, pp.299-303, 2017.
- [4] Dong-Kwon Kim, Il Young Han and Sung Jin KimK, "Study on the steady-state characteristics of the sensor tube", *International Journal of Heat and Mass Transfer*, 50, pp. 1206-1211, 2007.
- [5] Ali Sukru Cubukcu, "A dynamic thermal flow sensor for simultaneous measurement of thermal conductivity and flow velocity of gases", *journal of sensor and actuators A* 208, pp.73-87, 2014.

- [6] C. Sosna et al, "Response time of thermal flow sensors with air asfluid", journal of Sensors and Actuators A 172, pp.15–20, 2011.
- [7] Anastasios Moschos et al, "Thermal flow measurements by a flexible sensor, implemented on the external surface of the flow channel", Procedia Engineering, 87, pp. 1366 – 1369, 2014.
- [8] N. T. Nguyen, Micromachined flow sensors—a review, Flow Meas. Instrum., Vol. 8, No. 1, (1997), pp. 7–16.
- [9] Num-Trung Nguyen : Nam-Trung Nguyen, Thermal mass flow sensors, chapter 28.9 in John G. Webster, Halit Eren, the Measurement, Instrumentation and Sensor Handbook, CRC Press 1999.
- [10] Nam-Trung Nguyen et Steven T. Wereley, Fundamentals and Applications of Microfluidics, Artech House, 2006.
- [11] Sjoerd Haasl and Göran Stemme, Flow Sensors, Comprehensive Microsystems, volume 2, Physical Sensing, 2008, p.209-272.
- [12] S. Moroe et al, "Thermal Conductivity Measurement of Gases by the Transient Short-Hot-Wire Method", Experimental Heat Transfer, 24, pp.168–178, 2011.
- [13] R. Vilares et al, "Fabrication and testing of a SU-8 thermal flow sensor", journal of Sensors and Actuators B 147, pp. 411–417, 2010.
- [14] M. Elwenspoek, Thermal flow micro sensors, mechanical micro-sensors, 1999, p.423-435.
- [15] Sriyanka Agrawal, "Calibration of capillary type thermal mass flowmeter", department of mechanical engineering, national institute of technology, Rourkela 2008-2009.
- [16] John G. Olin, Thermal anemometry, chapter 29.2 in John G. Webster, Halit Eren, the measurement, instrumentation and sensor handbook, CRC 2014.
- [17] Huibert-Jan Verhoeven, "Smart thermal flow sensors", Delft, 15Janvier 1996.
- [18] Manuel Arlindo Amador de Matos and Viviana da Silva Ferreira, "Gas mass-flow meters: Principles and applications", Journal of Flow Measurement and Instrumentation, 21, pp. 143-149, 2010.
- [19] L.V. King, "On the convection of heat from small cylinders in a stream of fluid", Philos. Trans. R. Soc. A 214 (1914) 373.
- [20] John G. Olin, "Thermal dispersion mass flow meters", Sierra press 2008.
- [21] Nirupa Majhi et Monalisha Topno, "Fluid flow measurement system using hot wire anemometer", department of electronics & communication engineering national institute of technology, Rourkela, 2012.
- [22] Roger C. Baker, "Flow measurement handbook", Cambridge University Press, Cambridge, 2000.
- [23] http://www.robots.ox.ac.uk/~sjp/publns/sjp_thesis_c4_chapter4.pdf.
- [24] P. Ligeza, "Constant-bandwidth constant-temperature hot-wire anemometer", review of scientific instruments 78, 2007.

Sensors networks for Platform radiotherapy services

Malika TIGHIDET¹, Abdelkrim ALLAM², Mokhtar ATTARI¹

¹USTHB, LINS Lab, Faculty of Electronics and Computers, PO.Box 32, Bab-Ezzouar, Algiers
mteghidet@gmail.com, attari.mo@gmail.com

²CDTA, Instrumentation and Quality Control Group, Baba-Hassen, Algiers
allam@cdta.dz

ABSTRACT

Given the number of patients coming from several regions of Algeria, the management of the radiotherapy department of the CPMC is overloaded therefore the process of treatment of the patients is disturbed. Faced with this situation, the head of the radiotherapy department decided to set up a platform for quality control and monitoring the radiotherapy department. Knowledge of the various indicators, such as the performance and condition of the simulation and treatment machines, the monitoring of the ignition system, the air conditioning, the generators or inverters installed in the event of a power failure, the measurement of the temperature and the humidity in the rooms etc., make it possible to improve the operating time and the efficiency of the machines and consequently the number of treated patients. In this article we realized a sensor network for the measurement of essential environmental parameters such as temperature and humidity in radiotherapy rooms. We have developed a user interface under LABVIEW for data traceability that we integrated into the control platform. Some results are obtained and described in this study. One special PC (the server) is used as a data server in order to store all data of the system like the check-list of the devices, the temperature and the humidity data and the physicians and patients' management.

Key Words: Sensors network, cancer,

temperature, humidity, medical procedures, radiotherapy treatment, client/server architecture, MySQL databas

1. INTRODUCTION

Radiation therapy (or radiation oncology) is used to treat cancer. The cure of cancer in radiotherapy services requires a lot of attention and rigor. Many people are involved (physicians, technicians, physicists and manipulators) to take care and to treat patients by using dangerous devices like linear accelerators. It is not easy to control all this persons and to check daily the quality of the apparatus (five devices in this example). For example, the medical, physicist and technical staff of the radiotherapy service of "Centre Pierre et Marie Curie hospital (CPMC)" is composed of fifty (50) persons.

The proposed system of this work permits to avoid some mistakes of manipulation and managements. It improves the quality of services and increases the medical care while applying some medical, technical and physical procedures. These procedures should be applied by the personnel of the radiotherapy service. The developed program permits the application of these procedures. The main purpose of this work is to avoid mistakes of manipulation that if they occur are deadly for patients. Accidents occur till now even in

developed countries (USA, France, England, etc) [1]-[2].

Currently the problem of the quality services and the accidents in radiotherapy services in the world is not solved [3]-[4]-[5]-[6]-[7]-[8]-[9]. The first version of this system proposed and described in this paper is implemented in the radiotherapy service of the hospital CPMC in Algiers.

2. COMPUTERS NETWORK PLATFORM

The block diagram of the control platform used in this study is shown in figure 1.

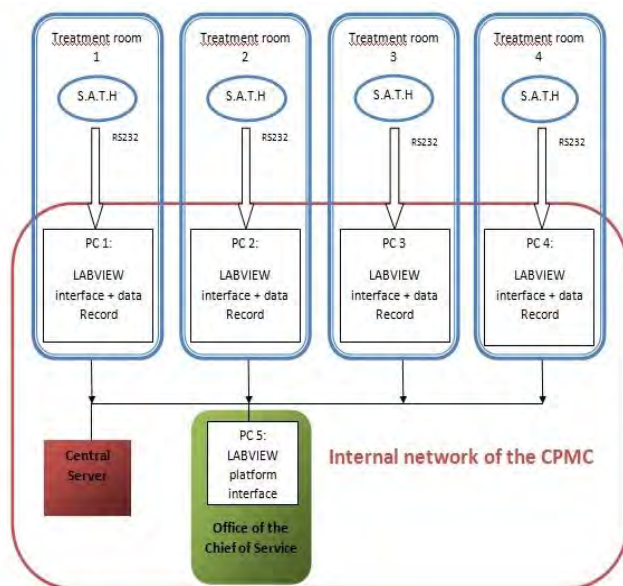


Figure 1. Local network platform of the radiotherapy service.

We realized a System of Acquisition Temperature and Humidity (S.A.T.H). The S.A.T.H system is placed in each of the treatment rooms in the radiotherapy service. The control platform supervises the four treatment rooms. The four rooms are connected to a central server. In the first step, the computer system consists of 4 personal computers (PC's), one PC server, 5 linear accelerators (VARIAN model) [10]-[11], 2 scanner simulators (VARIAN and General Electric), four sensors network of temperature and humidity for the four cure rooms. The PC's are put in a network and three of them are used to control the check list of the apparatus (linear accelerators). These 3 PC's are put outside the cure rooms.

The PC server is used as a data server in order to store all data of the system (the check list of the devices, the temperature

and the humidity data, physicians and patients' management). Four PC's are devoted to the manipulators (physicians, physicists and technicians) to enter their coordinates and all medical information related to patients during the sessions of the radiotherapy simulation and treatment.

One PC among the four is used to view all the screens of the four PC's linked to the four cure rooms in one big screen working in real time (active multiple windows). One PC is linked to the two simulation rooms. The head or the technical manager of the radiotherapy services could by this means controls and supervises all the machines in only one PC'screen.

Five temperature and humidity sensors are used with a serial RS232 port. The port RS232 is applied inside the 4 cure and simulation rooms with the 3 linear accelerators and the 2 scanner simulators.

This system is used in order to improve the quality of services and to increase the medical care.

3. MEDICAL PROCEDURE INTERFACE LABVIEW

The manager can better manage the staff and supervise the work thanks to the layout of a platform that allows him to visualize on the screen (figure 2):

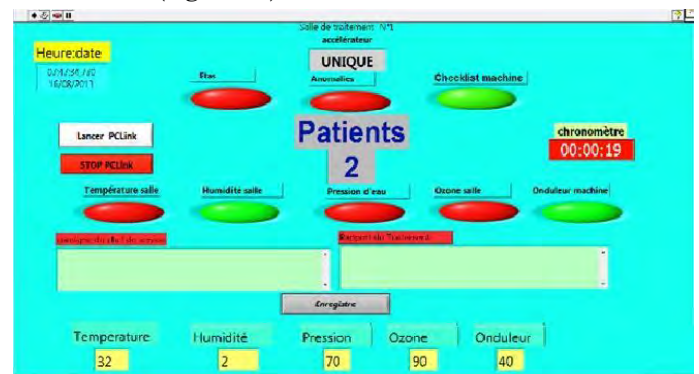


Figure 2: Control platform of the radiotherapy

- List of issues involved in CPMC services in real time.
- The types of anomalies.
- The number of patients per machine and per day.
- The duration of hardware activation per day.
- The values of the sensors.

The real time control of the 4 cure rooms and achieved by using LABVIEW software (version 7.0). The architecture

client/server is used by the personnel treating (technicians, physicists, physicians and the manipulators). The data are stored in MYSQL database located in the main server by the program [12]-[13]-[14]-[15]-[16]-[17]. The information about the checklist of the devices is got in by using a PHP sheet and stored in MYSQL database. This operation is made only one time a day for each machine. The result of the sensor information (temperature and humidity) and the device's checklist (physical and technical aspect of the machines) will be shown in real time on the PC server by a LABVIEW program.

4. APPLICATION RESULTS

The SATH acquisition card represented in figure 3 consists of a PIC microcontroller "16F88"; a temperature and humidity sensor and a display device.

To realize our sensor network, our choice fell on the sensor "DHT22". Its technical characteristics seem to meet our requirements. It has a very good precision (+/- 0.2 ° C and +/- 2% RH). It is a digital sensor (the analog / digital conversion is internal to the sensor) of both temperature and humidity. It has several advantages: a small footprint; a simplification of the electrical circuit as well as an economy of the inputs / outputs for our microcontroller. We have opted for a 7 segment display because this type of display allows clarity and legibility even at long distance, unlike an LCD display of the same size. Our display consists of two displays with three digits common anode, the one to display the temperature and the other the humidity. The microcontrollers read the temperature and humidity from the sensor and display them. Data is transmitted through RS232 serial port to the platform under LABVIEW.

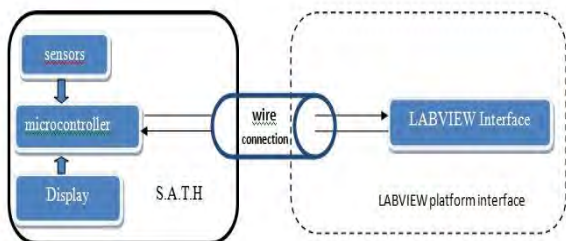


Figure 3: functional block of S.A.T.H with LABVIEW interface

Protocol of communication of the sensor: The "DHT22" is equipped with a point-to-point communication device using only one wire (DATA) (in addition to ground). The latter makes it possible to connect the internal circuit of the sensor to the microcontroller and thus transmits the temperature and humidity information by means of a communication protocol RS232 port.

With LABVIEW we have developed a VI (virtual instrument) that allows us to configure the RS232 serial port and receives the data from the sensor and we have integrated this code into the overall application of the platform.

Format of the transmitted frame:

@T	<signe>	<température>	<code Error>	F	<humidité>	<code error>	<numéro série>	<checksum>	<CR>	<LF>
----	---------	---------------	-----------------	---	------------	-----------------	-------------------	------------	------	------

Here is an example of the transmitted

frame: @T; + 021.37; A00; F; 038.92; A00; 00000121;
38 command character: "Carriage Return" command character
"Line Feed"

transmission start	end of transmission	separator
@	"CR" et "LF"	","

We have provided our S.A.T.H system an error code device to the manipulator in order to know the state of the S.A.T.H real-time system. The Error codes used are:

- A00: no error, no corrupted data
- A01: corrupted data.
- A02: no response from the sensor

The graphical interface to be realized with LabVIEW (Front- Face) of the CPMC room Supervision Platform is shown in Figure 4. It includes:

- Temperature and humidity curves.
- Date and time for recording data.
- Anomaly: if there are errors concerning the sensor or the data.
- Thermometer and temperature indicator.
- Hygrometer and humidity indicator.
- COM port that communicates with SATH acquisition card.

The realization of the SATH is shown in Figure 5.

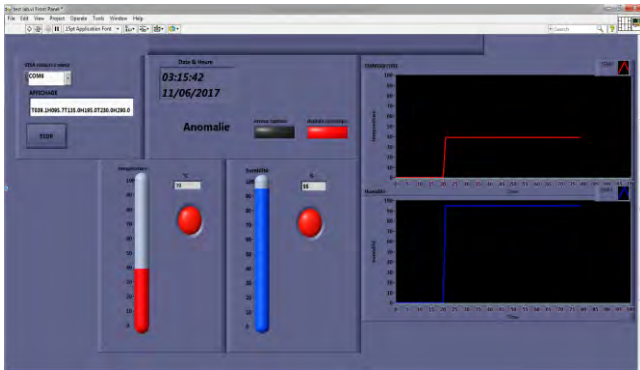


Figure 4: Control temperature and humidity with Labview interface

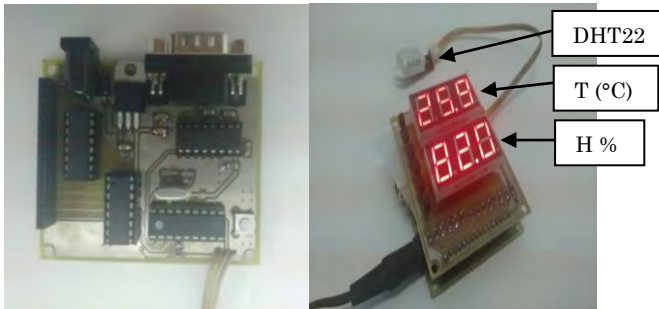


Figure 5: SATH acquisition card (Temperature and Humidity)

5. CONCLUSION

The Computers network platform dedicated to radiotherapy services is designed and implemented to improve quality service and treatment cure. We contributed to the measurement of two essential environmental parameters T and H (Temperature and Humidity) in the radiotherapy rooms. We have developed a user interface under LABVIEW for data traceability that we integrated it into the control platform. In our future work we plan to develop procedures and protocols linked to a cognitive system (expert system driven by machine learning) combined to a workflow process by using the collected data (T and H).

ACKNOWLEDGMENT

This work is part of a joint project between the CDTA (advanced technology development center) and the CPMC (Center Pierre and Marie Curie) of the CHU hospital Mustapha Bacha. We are grateful to the whole medical and technical staff of the radiotherapy service of Algiers CPMC hospital for their experimental help and useful discussions. We apologize about people that we have not named individually.

REFERENCES

- [1] O Holmberg, "Accident prevention in radiotherapy", *Biomedical Imaging and Intervention Journal*, 2007, 3(2):e27.
- [2] International Atomic Energy Agency. The over exposure of radiotherapy patients in San José, Costa Rica. Vienna, Austria:IAEA, 1999.
- [3] International Atomic Energy Agency. Investigation of an accidental exposure of radiotherapy patients in Panama. Vienna, Austria: IAEA, 2011.
- [4] International Atomic Energy Agency. The accidental over exposure of radiotherapy patients in Bialystok. Vienna, Austria: IAEA, 2002.
- [5] International Atomic Energy Agency. Lessons learned from accidents in radiotherapy. Vienna: IAEA, 2000. (Safety Reports Series; 17).
- [6] Prevention of accidental exposures to patients undergoing radiation therapy. A report of the International Commission on Radiological Protection. *Ann ICRP* 2000; 30(3):7-70.
- [7] Cohen L, Schultheiss TE, Kennaugh RC. A radiation overdose incident: initial data. *Int J Radiat Oncol Biol Phys* 1995; 33(1):217-24.
- [8] Ash D, Bates T. Report on the clinical effects of inadvertent radiation underdosage in 1045 patients. *Clin Oncol (R Coll Radiol)* 1994; 6(4):214-26.
- [9] The accident of the linear accelerator in the "Hospital Clínico de Zaragoza". *Spanish Society of Medical Physics*, 1991.
- [10] Report of an investigation by the Inspector appointed by the Scottish Ministers for The Ionising Radiation (Medical Exposures) Regulations 2000. Unintended overexposure of patient Lisa Norris during radiotherapy treatment at the Beatson Oncology Centre, Glasgow in January 2006.
- [11] Li Pengfei, Nie Luhua, « Remote Control Laboratory Based On LabVIEW », *icicta*, vol. 4, pp.84-87, 2009 Second International Conference on Intelligent Computation Technology and Automation, Changsha, Hunan, China, 2009.
- [12] Xiaoyan, C., Xiaodong, Z., Xi, C. "A Virtual Laboratory for Electrical and Electronics Teaching", *IEEE International Symposium on Microwave, Antenna, Propagation and EMC Technologies for Wireless Communications Proceedings*, pp.491-495, 2005.
- [13] A. Bhandari and M. Shor. Access to an instructional control laboratory experiment trough the world wide web. In *Proc. of IEEE American Control Conference*, pages 1319–1325, Philadelphia, June 1998.
- [14] P. Anhoury, D. Dejean, "bonnes pratiques organisationnelles observées", *Service de radiothérapie du CHU de Besançon, France*, 2004.
- [15] Niloy Ranjan Datta, David Rajasekar, « Improvement of radiotherapy facilities in developing countries: a three-tier system with a teleradiotherapy network », *The lancet oncology*

review, Volume 5, Issue 11, November 2004, Pages 695-698.

- [16] M. Bolla, B. Chauvet, G. Chantôme « Observatoire national de la radiothérapie », rapport d'enquête, collection Etudes & Expertises, institut national du cancer, Publication – Diffusion, 52, avenue André Morizet – 92100 Boulogne-Billancourt, France, 2008.
- [17] K.Lamamra, A.Allam, M.Afiame, “Artificial neural networks for acquisition and processing of sensors data in a radiotherapy application”, Inderscience journal, IJSPM International Journal of Simulation and Process Modelling, **2018** – Vol.13, No.1 pp. 15 –23. DOI: 10.1504/IJSPM.2018.10011346

Photonic Crystal Sensor Arrays Based on Side-Coupled Resonant Cavity Arrays

Chayma Mosbah¹, Ahlem Benmerkhi¹, Mohamed Bouchemat¹
and Touraya Bouchemat¹

¹ University of frères Mentouri, L.M.I Lab, Department of Electronics, Constantine1, ALGERIA
chayma.mosnah@gmail.com, ahlemelec@hotmail.fr, hm_bouchemat@yahoo.fr
and tboumaza2001@yahoo.fr

ABSTRACT

In this work, we presented a two-dimensional photonic crystal sensor, which the structure is based on photonic crystal micro-cavity coupled to a waveguide. The shape of the holes situated in the first row above and below line-defect was modified in order to improve transmission and quality factor. Then we infiltrated the holes nearby the resonant cavity being functionalized. We vary the number of holes ($N=6, 14, 18, 20, 24$ and 27 holes) to study the mass sensitivity ($\Delta\lambda/N$) of the device. In our sensor design, we determine that the functionalized hole number is $N=14$. After that, we filled the functionalized holes with a change in refractive index from $n=1.33$ to 1.338 with an interval $\Delta n=0.002$. The sensitivity can achieve $150 \text{ nm}/\text{RIU}$. All analyses are based on the finite difference time domain method (FDTD).

Key Words: Photonic Crystal, Sensor, Waveguide, Micro-cavity, Sensitivity.

1. INTRODUCTION

Photonic crystal (PhC) is a periodically arranged dielectric material. The periodic variation of the refractive index gives rise to a unique band structure, and may have a Photonic Band Gap [1, 2]. The adaptation of PhC to optoelectronics makes it possible to envisage new perspectives, such as the production of integrated optical components and devices with reduced dimensions and the integration of several functions on the same substrate. Among these components:

waveguides [3, 4, 5], lasers [6, 7], fibers [8], and sensors [9, 10]. The realization of this device is affected by creating a defect on the photonic crystal structure. The optical sensor is an analytical device which is used to convert the amount of analytes into a detectable signal. It is also employed for different sensing applications like industrial process control, military, environment monitoring and medical diagnostic [1]. The change of properties of the surrounding media lead to the variation of optical characters, and these changes determine the all-optical sensors principle of operation [11, 12]. There are various structures of optical sensor elements for RI measurements such as ring resonators [13, 14], surface Plasmon resonance [15, 16], microcavities coupled with waveguide [17], PhC microcavities [18, 9], waveguide [19]...

• The present work aims to investigate a novel design of PhC sensor based on a two-dimensional photonic crystal (2D-PhC) micro-cavity coupled to a waveguide. In Γ -K direction of our structure, we removed the central row of air holes to form the waveguide. Then we created a cavity by removing one hole. In this study, we are interested to realize a high sensitivity. For that we modified waveguide geometry, where the holes situated in the first row above and below line-defect are deformed to elliptical shape. Then by adjusting the number (N) of functionalized holes, we demonstrate that $N=14$ is the functionalized holes. After that, we filled the functionalized holes with a change in refractive index from $n=1.33$ to 1.338 with an interval $\Delta n=0.002$.

2. STRUCTURE DESIGN AND OPTIMIZATION

The structure consists of a 2D triangular PhC of periodic disposition of air holes ($n=1$) in a silicon substrate ($n=3.48$). The 2D finite difference time domain (FDTD) method is used in order to reduce the computer memory and simulation time for 3D calculation, using effective refractive index approximation method for the fundamental TE guided mode. The structure is simulated by plane wave expansion (PWE) of the RSoft (BandSOLVE) software. Two TE photonic band gaps (PBGs) are presented in the PhC structure see Fig. 1(a). The range frequency of first TE PBG is from 0.24529 to 0.32866, corresponding to the range wavelength between 1369 nm and 1834 nm. The second PBG is from 0.699 to 0.71984 for frequency corresponding to the range wavelength between 625 nm and 644 nm. The first TE PBG is considered for designing our sensor as it covers the second and third windows in optical region.

The proposed sensor shown in Fig. 1(b) is formed with one waveguide and one micro-cavity. A photonic waveguide and micro-cavity are obtained by eliminating central row of air holes in the Γ -K direction and removing one hole of our structure respectively. The microcavity is side-couples to a waveguide. For this structure, the resonant wavelength located at $\lambda = 1525$ nm with quality factor $Q = 5589$. For further improve the quality factor, we proposed a technique, where we deformed the holes situated in the first row above and below line-defect to elliptical shape (blue holes).

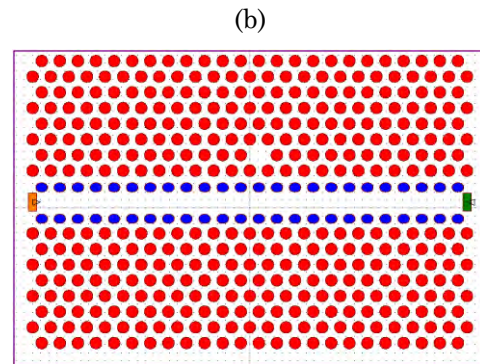
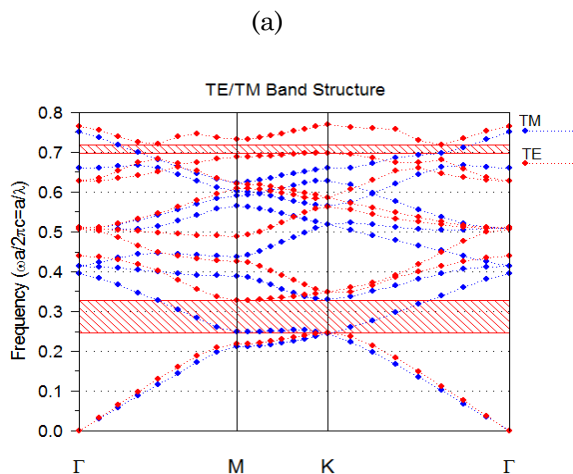


Figure.1: (a) Photonic crystal band gap, (b) Structure of the sensor based on photonic crystal waveguide coupled to a micro-cavity

3. SIMULATION RESULTS AND DISCUSSION

We begin our consideration by the study the influence of elliptical shape holes. Ellipse has the semi-major axis (R_x) and semi-major axis (R_y). We fixed the value of R_x at $0.32a$ and R_y is varied from $0.24a$ to $0.28a$ of the holes situated in the first row above and below line-defect (blue ellipse in Fig. 1). Fig. 2 shows the resonant wavelength and the quality factor as a function of change in the value of R_y . From this figure, it can be observed that, whereas the value of R_y increases, the resonant wavelength is pushed to lower wavelengths. Similarly the quality factor increases as the value of R_y increases from $0.24a$ to $0.28a$ and reaches its maxima of 15431 at the resonant wavelength located at 1579 nm for $R_y = 0.26a$, followed by a sharp decrease.

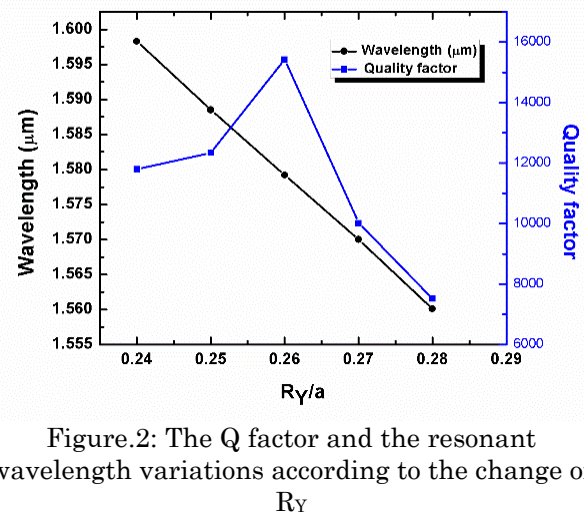


Figure.2: The Q factor and the resonant wavelength variations according to the change of R_y

3.1. Functionalized holes number discussion

Actually, for application such as biosensing or chemical detection, the magnitude of the resonant wavelength shift is dependent on the combination of many factors such as the number of functionalized holes and the effective refractive index change of targets. To study the sensitivity of this sensor design and determine how to achieve the lowest mass limit of detection using this architecture. We assume that the holes around the micro-cavity are completely filled with the analyte (DI-Water) ($n=1.33$). Therefore, we study the mass sensitivity which is defined as $(\Delta\lambda/N)$ of the device as a function of the number of functionalized holes. For that, we vary the number of holes around the micro-cavity being functionalized holes. We carried out the simulations for the cases with 6 holes, 14 holes, 18 holes, 20 holes, 24 holes and up to 27 holes illustrated in Fig. 3(b). For all these cases, we have calculated the mass sensitivity $\Delta\lambda/N$. Which $\Delta\lambda$ is the resonant wavelength shift as the RI changed. Fig. 3(a) shows the mass sensitivity $(\Delta\lambda/N)$ as a function of the number of functionalized holes (N). It can be seen that, when the number of the functionalized holes increased, the sensor mass sensitivity decreases. The highest mass sensitivity can be achieved for $N=6$. Fig. 4 shows the resonance shift $(\Delta\lambda)$ as a function of the number of functionalized holes (N). We observed that when the number of the functionalized holes increased, the sensor resonant wavelength shift increases. That means the RI-sensitivity $(\Delta\lambda/\Delta RI)$ increases as a function of the number of the functionalized holes increased. Thus, the resonant shift is larger for the greater number of functionalized holes.

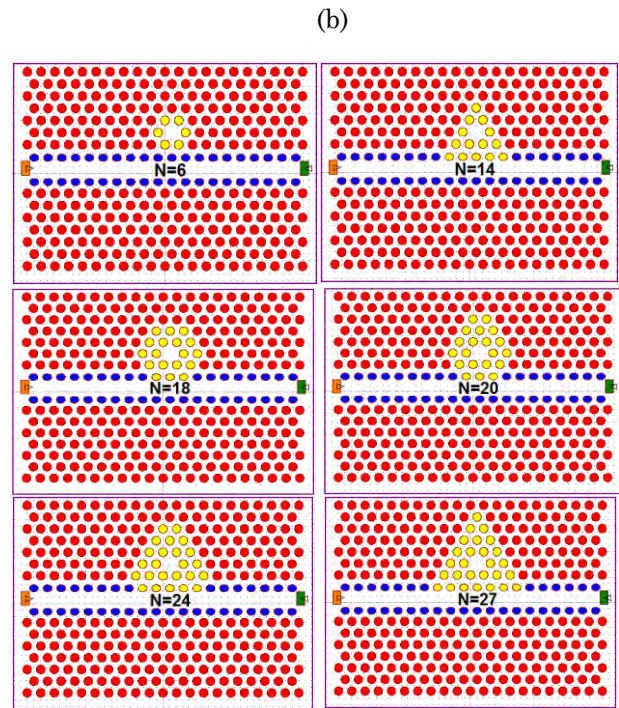
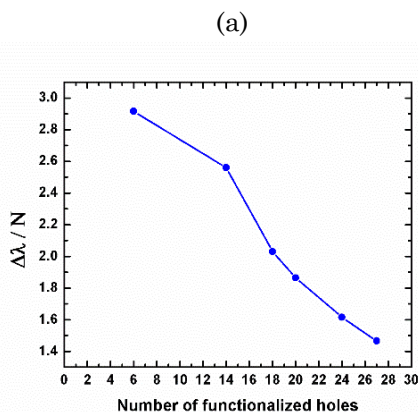


Figure.3: (a) The mass sensitivity as a function of the number of functionalized holes, (b) The schematic illustration of number of functionalized holes

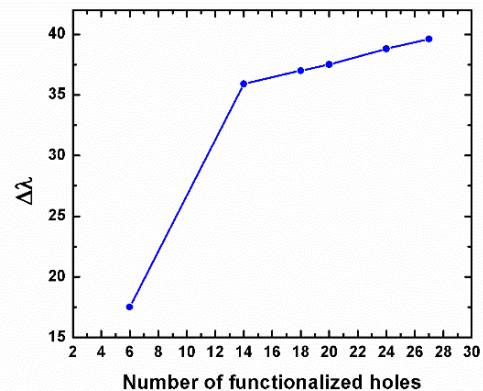


Figure.4: Dependence of the cavity resonance shift ($\Delta\lambda$) as the number of functionalized holes changed

Fig. 3 and Fig. 4 results indicated that in the left area of $N=14$, the sensing element can attain higher mass sensitivity, but the refractive index (RI) sensitivity is lower. In the right area of $N=14$ the sensing element can realize higher refractive index sensitivity, but the mass sensitivity is lower. Her, we fixed the functionalized holes number $N=14$ as the sensing element. This result is considered using a tradeoff between the mass sensitivity and the RI-sensitivity.

3.2. Sensitivity analysis

For estimate a sensitivity of our proposed sensor, the refractive index of functionalized holes (N=14) is changed. First, we supposed that the holes are filled with water (n = 1.33). Then the refractive index of analyte has been varied from 1.33 to 1.338 with increment of 0.002. Fig 5(a) shows the transmission spectrum of the PhC waveguide coupled to micro-cavity, when the refractive index of functionalized holes is changed. From this figure, we noted that when the refractive index increase the resonant wavelength shifts to a higher wavelength. The resonant wavelength shift as a function of the variations of refractive index is shown in Fig. 5(b). The sensitivity is expressed as follow:

$$S = \frac{\Delta\lambda}{\Delta n} \quad (1)$$

$\Delta\lambda$ is the resonance shift as the RI changed.
 Δn : RI variations.

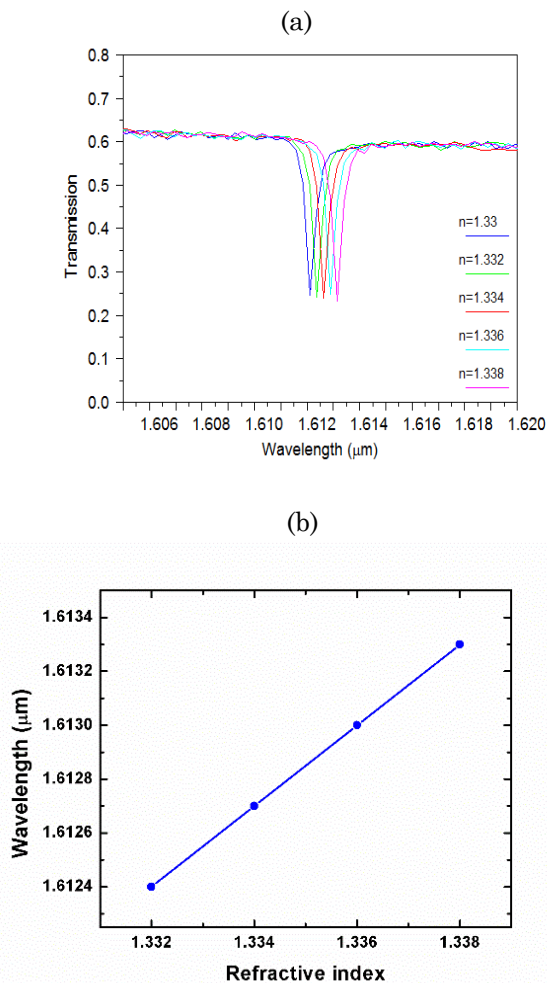


Figure.5: (a) Transmission spectrum as a function of change in RI,(b) Resonant wavelength shift as a function of the refractive index change

From the simulation results shown in Fig. 5, the resonance wavelength for sensor structure shifts up by 0.300 μm for $\Delta n = 0.002$. So the sensor's sensitivity of the proposed PhC sensor is $S = 150 \text{ nm/RIU}$.

4. CONCLUSION

In this paper we have proposed a novel photonic crystal for refractive index sensing. The PhC RI sensor arrays consist of a PhC micro-cavity side-coupled to a waveguide. High quality factor and sensitivity are obtained by adjusting the shape of holes and number of functionalized holes around the micro-cavity. By deforming the shape of holes situated in the first row above and below line-defect to elliptical shape, the quality factor is improved to 15413. Then, we infiltrated the holes around the resonant cavity being functionalized. We vary the number of holes (N= 10, 16, 26, 34, 40 holes) to study the mass sensitivity ($\Delta\lambda/N$) of the device as a function of the number of functionalized holes. We determine that the functionalized hole number is N=14. After that we filled the functionalized holes with a change in refractive index from n=1.33 to 1.338 with an interval $\Delta n=0.002$. The sensitivity can achieve 150 nm/RIU. All analyses are based on the finite difference time domain method (FDTD).

REFERENCES

- [1] Joannopoulos. J. D, Johnson. S. G, Winn. J. N and Meade. R. D, "Photonic Crystals : Molding the Flow of Light (Second Edition)," *Princeton: Princeton University Press*, 2008.
- [2] John. S, "Photonic band gap materials: a semiconductor for light," 4th Pacific Rim Conf, *Lasers Electro-Optics*, vol. 1, pp. 1–23, 2001.
- [3] Mekis. A, Chen. J. C, Kurland. I, Fan. S, Villeneuve. P. R and Joannopoulos. J. D, "High transmission through sharp bends in photonic crystal waveguides," 1996 *Phys. Rev. Lett*, pp. 3787–3790, 1996.
- [4] Mehmet. B, Temelkuran. B and Ozbay. E, "Propagation of photons by hopping: A waveguiding mechanism through localized coupled cavities in three-dimensional photonic crystals," 2000 *Phys. Rev. B* , pp. 11855–11858, 2000.

- [5] Lončar. M, Nedeljković. D, Doll. T, Vučković. J, Scherer. A and Pearsall. T. P, "Waveguiding in planar photonic crystals," *Appl. Phys. Lett.*, vol. 77, no. 13, pp. 1937–1939, 2000.
- [6] Painter. O *et al*, "Two-dimensional photonic band-gap defect mode laser," *Science*, vol. 284, no. 5421, pp. 1819–1821, 1999.
- [7] Noda. S, Yokoyama. M, Imada. M, Chutinan. A and Mochizuki. M, "Polarization mode control of two-dimensional photonic crystal laser by unit cell structure design," *Science (80-.)*, vol. 293, no. 5532, pp. 1123–1125, 2001.
- [8] Lebbal, M. R, Boumaza. T and Bouchemat. M, "Structural study of the single-mode photonic crystal fiber," *Optik (Stuttg)*, vol. 124, no. 20, pp. 4610–4613, 2013.
- [9] Benmerkhi. A, Bouchemat. M and Bouchemat. T, "Influence of elliptical shaped holes on the sensitivity and Q factor in 2D photonic crystals sensor," *Photonics Nanostructures - Fundam. Appl*, vol. 20, pp. 7–17, 2016.
- [10] Bougriou. F, Bouchemat. T, Bouchemat. M and Paraire. N, "Optofluidic sensor using two-dimensional photonic crystal waveguides," *Eur*, pp. 1–5, 2013.
- [11] Levi. O *et al* "Sensitivity analysis of a photonic crystal structure for index-of-refraction sensing." *Proc. SPIE*, vol. 6447, no. 64, pp. 1–9, 2007.
- [12] Adams. M, Derosé. G. A, Loncar. M, Scherer. A and Scherer. A, "Lithographically fabricated optical cavities for refractive index sensing," *J. Vac. Sci. Technol. B*, vol. 23, no. 6, pp. 3168–3173, 2005.
- [13] White. I. M, Oveys. H and Fan. X, "Liquid-core optical ring-resonator sensors," *Opt. Lett.*, vol. 31, no. 9, pp. 1319–1321, 2006.
- [14] Zhang. W, Serna. S, Le Roux. X, Vivien. L and Cassan. E, "Highly sensitive refractive index sensing by fast detuning the critical coupling condition of slot waveguide ring resonators," *Opt. Lett.*, vol. 41, no. 3, pp. 532–535, 2016.
- [15] Homola. J *et al*, "Surface plasmon resonance sensors: review," *Sensors Actuators B*, vol. 54, pp. 3–15, 1999.
- [16] Fan. Z *et al*, "High sensitivity of refractive index sensor based on analyte-filled photonic crystal fiber with surface plasmon resonance," *IEEE Photonics J*, vol. 7, no. 3, pp. 1–9, 2015.
- [17] Benelarbi. D, Bouchemat. T and Bouchemat. M, "Study of photonic crystal microcavities coupled with waveguide for biosensing applications," *Opt. Quantum Electron*, vol. 49, no. 11, pp. 1–16, 2017.
- [18] Chow. E, Grot. a, Mirkarimi. L. W, Sigalas. M, and Girolami. G, "Ultracompact biochemical sensor built with two-dimensional photonic crystal microcavity," *Opt. Lett.*, vol. 29, no. 10, pp. 1093–1095, 2004.
- [19] Dutta. H. S and Pal. S, "Design of a highly sensitive photonic crystal waveguide platform for refractive index based biosensing," *Opt. Quantum Electron*, vol. 45, no. 9, pp. 907–917, 2013.
- [20] Yang. D, Tian. H and Ji. Y, "Nanoscale Low Crosstalk Photonic Crystal Integrated Sensor Array," *IEEE Photonics J*, vol. 6, no. 1, 2014.
- [21] Yang. D, Tian. H, and Ji. Y, "Nanoscale photonic crystal sensor arrays on monolithic substrates using side-coupled resonant cavity arrays," vol. 19, no. 21, pp. 11709–11717, 2011.
- [22] Zhou. J, Tian. H, Yang. D, Liu. Q, and Ji. Y, "Integration of high transmittance photonic crystal H2 nanocavity and broadband W1 waveguide for biosensing applications based on Silicon-on-Insulator substrate," *Opt. Commun.*, pp. 1–9, 2014.

Vector control of a shunt active power filter based on synchronous reference frame identification method

Yassine SADKI¹, Abdellah KOUZOU¹ and Ahmed HAFAIFA¹

¹ Applied Automation and industrial diagnostics laboratory, Sciences and technology faculty, University of Djelfa, Algeria
yacineosadki@gmail.com, kouzouabdellah@ieee.org and hafaifa@hotmail.com

ABSTRACT

Recently, the increasing use of power electronics converter-based equipment has been an important contributor to the degradation of power quality in the power grid, especially the low-voltage grid. Active shunt power filtering can be a curative solution against different disturbances. In this paper we present the vector control of an active shunt filter controlled by the reference current identification method and we will study the performance of this method in the different voltage source cases in a three-phase electrical network; Balanced unpolluted voltage source, unbalanced voltage source, balanced and polluted voltage source, unbalanced and polluted voltage source.

Key Words: Active power filter, harmonics, synchronous reference frame (SRF), SVM control technique, THD.

1. INTRODUCTION

Current and voltage disturbances in power distribution networks are caused by the proliferation of non-linear loads, such as converters, computer hardware, fluorescent tube lighting, etc. These devices absorb non-sinusoidal currents and thus introduce harmonic pollution. Parallel active filters (FAP) are to day the most advanced solutions of the most adequate depollutions. Their answer is instantaneous and they adapt automatically to the evolutions of disturbances introduced by the loads of the electrical network.

Since the 1970s, these have been studied for the compensation of reactive energy, the negative sequence of currents and harmonics in industrial power systems. Active Shunt filters were originally proposed in 1971 by Sasaki and Machida [1] as a way of eliminating current harmonics.

In 1976, Gyugyi and Strycula [4] used the term "active AC power filter" for the first time, introduced a family of parallel and series active filters, and established the concept of active filters. PWM inverters consisting of power transistors.

An active filter essentially consists of an inverter. The correct choice of the method of identification of the reference quantities, as well as the control technique, is essential so that the active filter can fulfill the tasks for which it is intended.

Several algorithms for identifying harmonic reference quantities and many control and regulation techniques have been developed since the introduction of the first active filters. The so-called synchronous reference frame (SRF) method is one of the most efficient methods for the identification of harmonic currents; this method was introduced in 1991 by Bhattacharya [8]

2. PRINCIPLE OF SHUNT ACTIVE FILTER

The active parallel filter injects into the grid the current harmonics consumed by the load so that the network no longer provide the fundamental current. The purpose of this type of filter is to cancel the current harmonics that provides the load to the source. It can also contribute to the

compensation of reactive power balance and the 3-phases current. Active parallel filters have the advantage of providing only the compensation current and some of the fundamental of current supplied to compensate for system losses. It is also possible to connect multiple filters in parallel to supply large currents, which makes this type of circuit suitable for a wide range of power. The Fig.1 shows a voltage inverter with three arms used in an APF voltage structure connected to an electrical network with three phases, this filter class is the most widespread configuration in industrial processes.

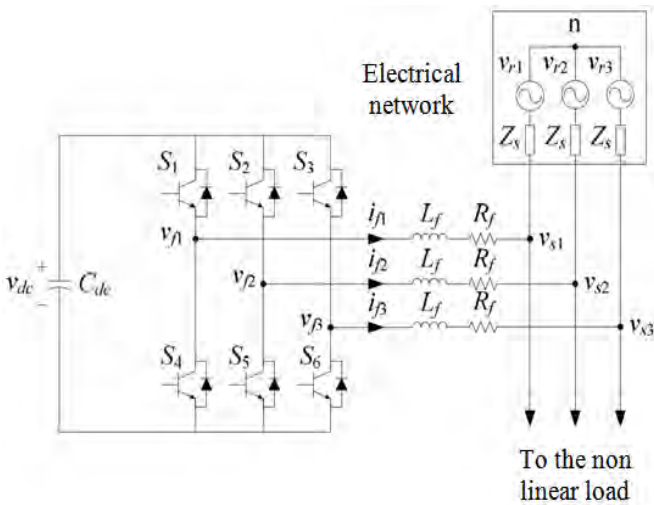


Figure.1: Shunt active power filter

3. IDENTIFICATION OF HARMONIC CURRENTS

The Synchronous Reference Frame (SRF) method exploits the Concordia transformation but is applied only to load currents i_{c1} , i_{c2} and i_{c3} . A second transformation is then performed to switch to line currents along the axes dq. This makes it possible to transform the fundamental component of the current into a continuous component and the harmonic components of the current into alternative components. The DC component of the charging current can then be eliminated using a simple LPF or HPF. The major advantage of this method lies in the fact that any harmonic voltages have no influence on the currents identified. The following steps detail the calculation of references.

In the case of a three-phase system without homopolar component, notes i_{c1} , i_{c2} , i_{c3} . Concordia's transformation makes it possible to reduce this balanced three-phase

system to a two-phase system of current, by the following relation:

$$\begin{bmatrix} i_\alpha \\ i_\beta \end{bmatrix} = \sqrt{\frac{2}{3}} \begin{bmatrix} 1 & -\frac{1}{2} & -\frac{1}{2} \\ 0 & \frac{\sqrt{3}}{2} & -\frac{\sqrt{3}}{2} \end{bmatrix} \begin{bmatrix} i_{c1} \\ i_{c2} \\ i_{c3} \end{bmatrix} \quad (1)$$

By generating the signals from a PLL $\cos(\hat{\theta})$ and $\sin(\hat{\theta})$ from the "fundamental" voltage of the network, we obtain the following matrix expression for the currents in the system dq:

$$\begin{bmatrix} i_d \\ i_q \end{bmatrix} = \begin{bmatrix} \sin(\hat{\theta}) & -\cos(\hat{\theta}) \\ \cos(\hat{\theta}) & \sin(\hat{\theta}) \end{bmatrix} \begin{bmatrix} i_\alpha \\ i_\beta \end{bmatrix} \quad (2)$$

With $\hat{\theta}$ the angular position of the fundamental network voltage, estimated by the PLL.

These components can then be expressed as the sum of a DC component and an AC component:

$$\begin{bmatrix} i_d \\ i_q \end{bmatrix} = \begin{bmatrix} \bar{i}_d + \tilde{i}_d \\ \bar{i}_q + \tilde{i}_q \end{bmatrix} \quad (3)$$

With \bar{i}_d, \bar{i}_q are the continuous components of i_d and i_q , \tilde{i}_d, \tilde{i}_q are the alternative components of i_d and i_q .

From equation (2), we can express the components of the current according to the axes $\alpha\beta$ by:

$$\begin{bmatrix} i_\alpha \\ i_\beta \end{bmatrix} = \begin{bmatrix} \sin(\hat{\theta}) & -\cos(\hat{\theta}) \\ \cos(\hat{\theta}) & \sin(\hat{\theta}) \end{bmatrix}^{-1} \begin{bmatrix} i_d \\ i_q \end{bmatrix} = \begin{bmatrix} \sin(\hat{\theta}) & \cos(\hat{\theta}) \\ -\cos(\hat{\theta}) & \sin(\hat{\theta}) \end{bmatrix} \begin{bmatrix} i_d \\ i_q \end{bmatrix} \quad (4)$$

$$\begin{bmatrix} i_\alpha \\ i_\beta \end{bmatrix} = \begin{bmatrix} \sin(\hat{\theta}) & \cos(\hat{\theta}) \\ -\cos(\hat{\theta}) & \sin(\hat{\theta}) \end{bmatrix} \begin{bmatrix} \bar{i}_d \\ \bar{i}_q \end{bmatrix} + \begin{bmatrix} \sin(\hat{\theta}) & \cos(\hat{\theta}) \\ -\cos(\hat{\theta}) & \sin(\hat{\theta}) \end{bmatrix} \begin{bmatrix} \tilde{i}_d \\ \tilde{i}_q \end{bmatrix} \quad (5)$$

Depending on the function we give to the active power filter, we can simultaneously compensate the harmonics of the load current and the reactive energy or only one of them. If we want to compensate only the current harmonics and after adding to the AC component \tilde{i}_d the current i_c necessary for the regulation of the DC voltage v_{dc} , the equation (6) is given by :

$$\begin{bmatrix} i_{ref\alpha} \\ i_{ref\beta} \end{bmatrix} = \begin{bmatrix} \sin(\hat{\theta}) & \cos(\hat{\theta}) \\ -\cos(\hat{\theta}) & \sin(\hat{\theta}) \end{bmatrix} \begin{bmatrix} \tilde{i}_d + i_c \\ \tilde{i}_q \end{bmatrix} \quad (6)$$

Then, the inverse transformation of Concordia makes it possible to obtain the reference currents, along the axes abc.

$$\begin{bmatrix} i_{f1}^{ref} \\ i_{f2}^{ref} \\ i_{f3}^{ref} \end{bmatrix} = \sqrt{\frac{2}{3}} \begin{bmatrix} 1 & 0 \\ -\frac{1}{2} & \frac{\sqrt{3}}{2} \\ -\frac{1}{2} & -\frac{\sqrt{3}}{2} \end{bmatrix} \begin{bmatrix} i_{ref\alpha} \\ i_{ref\beta} \end{bmatrix} \quad (7)$$

Figure 2 illustrates the identification of reference currents for compensation of current harmonics by the so-called SRF method

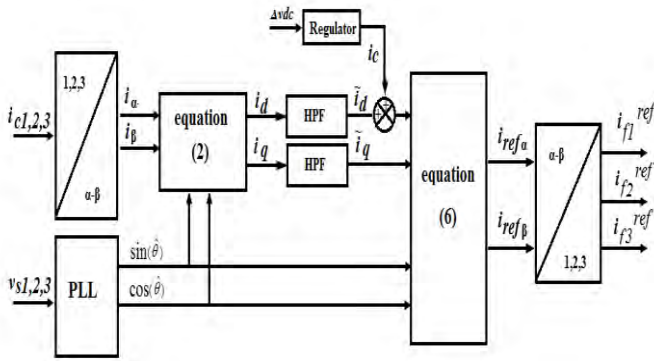


Figure.2: Determination of reference currents by the SRF method

4. THE APF CONTROL

4.1. Voltage supplied by the inverter

The two semiconductors of the same arm are controlled in a complementary manner; the conduction of one implies that the other is blocked. The opening and closing of the switches of the inverter of the Fig.1 depend on the state of control signals (S_1, S_2, S_3), as defined below:

$$s_a = \begin{cases} 1 & s_1 \text{ closed and } s_4 \text{ open} \\ 0 & s_1 \text{ open and } s_4 \text{ closed} \end{cases} \quad (8)$$

$$s_b = \begin{cases} 1 & s_2 \text{ closed and } s_5 \text{ open} \\ 0 & s_2 \text{ open and } s_5 \text{ closed} \end{cases} \quad (9)$$

$$s_c = \begin{cases} 1 & s_3 \text{ closed and } s_6 \text{ open} \\ 0 & s_3 \text{ open and } s_6 \text{ closed} \end{cases} \quad (10)$$

The line voltages imposed by the inverter, are then defined by:

$$\begin{bmatrix} v_{f1} - v_{f2} \\ v_{f2} - v_{f3} \\ v_{f3} - v_{f1} \end{bmatrix} = \begin{bmatrix} s_a - s_b \\ s_b - s_c \\ s_c - s_a \end{bmatrix} v_{dc} \quad (11)$$

The inverter output voltages, denoted v_{fk} with ($k = \{1, 2, 3\}$), are referenced to the neutral of the network and verify the following equations:

$$v_{fk} = v_{sk} + L_f \frac{di_{fk}}{dt} + R_f i_{fk} \quad (12)$$

The network voltages are supposed equilibrated, and knowing that the sum of currents injected by the inverter is zero, we can write:

$$\begin{cases} v_{s1} + v_{s2} + v_{s3} = 0 \\ i_{f1} + i_{f2} + i_{f3} = 0 \end{cases} \quad (13)$$

We can deduce from equations (12) and (13) the following relationship:

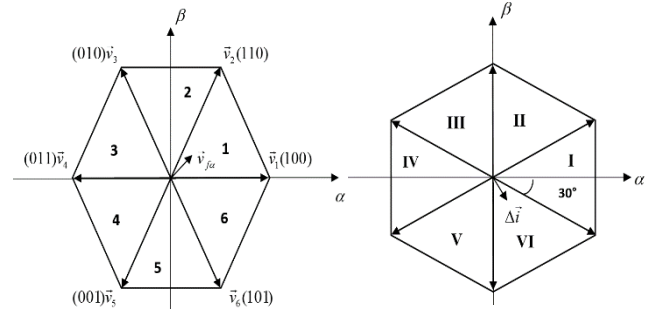
$$v_{f1} + v_{f2} + v_{f3} = 0 \quad (14)$$

From equations (11) and (14) we get:

$$\begin{bmatrix} v_{f1} \\ v_{f2} \\ v_{f3} \end{bmatrix} = \begin{bmatrix} 2s_a - s_b - s_c \\ -s_a + 2s_b - s_c \\ -s_a - s_b + 2s_c \end{bmatrix} \frac{v_{dc}}{3} \quad (15)$$

4.2. SVM Control of FAP based on a two-level inverter

This control technique divides the referential α - β of currents and voltages into six regions with a current / voltage offset of 30° as illustrated in Figure 3. [11],[5].



(a) Hexagons of voltages (b) Hexagons of currents

Figure.3: Hexagons of the voltages and currents defined in the plane α - β

The tension of Figure 3.(a) is the vector representation of the non-zero vectors \vec{v}_1 to \vec{v}_6 which the modulus is $\sqrt{2/3}v_{dc}$, (\vec{v}_0 and \vec{v}_7 being the null vectors corresponding to states 000 and 111 respectively). Then, the control algorithm must identify the region, among the six regions of the current hex or the current error Δi is located and then select the output voltage vector of the active filter v_{fa} belonging to the voltage hexagon this its role

is to force the error Δi to vary in the opposite direction, in order to keep the output current close to its set point.

5. CURRENT REGULATION OF PARALLEL ACTIVE FILTER

A regulator must satisfy the general objectives of the regulation and the constraints disturbance rejection. In the case of a simple controller like the PI controller, and due to lack of degree of freedom that it imposes only further references for a fixed operating point can be considered. Add to this the problem of trade-off in the case of an active filter structure parallel with an output filter of the first order (choice of inductance). Indeed, a PI controller can not ensure with only KP and KI correction parameters, the regulatory objectives in a closed loop system for a higher order than one [7]. The structure of the current control loop of A.P.F is illustrated in Figure 4.

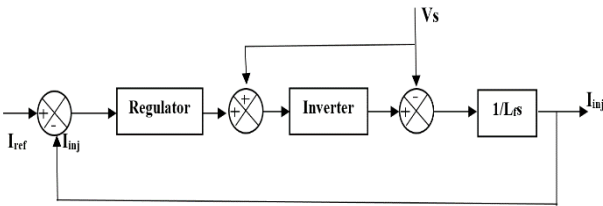


Figure.4: Scheme for A.P.F regulation current

6. REGULATION OF THE CONTINUOUS VOLTAGE

The variation of the continuous voltage V_{dc} is essentially caused by the losses in the active filter particularly in the semi-conductors and output filter. The regulation of this voltage is done by adding to the power \tilde{p} another power P_c for the compensation of losses.

The regulator used here is a simple proportional regulator with a filtering action beforehand to the measured voltage V_{dc} realized with a second order low pass filter in a way to attenuate the fluctuations to 300 Hz. The regulator transfer function is:

$$K_s = \frac{K_c}{1 + \tau_c s} \quad (16)$$

The relation between the absorbed power by the active filter and capacitor voltage can be written in the following form:

$$P_c = \frac{d}{dt} \left(\frac{1}{2} C_{dc} V_{dc}^2 \right) \quad (17)$$

From the equations (16) and (17), the regulation loop of the continuous voltage can be represented by the scheme of the figure 5.

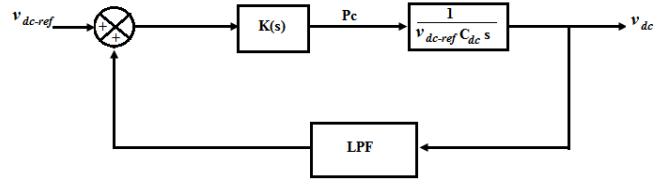


Figure.5: The regulation loop of the continuous voltage

7. SIMULATION RESULTS

The network simulation parameters is:

- Line resistance $R_s = 0.25 \text{ m}\Omega$
- Line inductance $L_s = 19.4 \text{ }\mu\text{H}$
- Load simulation parameters

The pollutant load consists of a three-phase diode rectifier bridge with a capacitor for storing the DC voltage and feeds a load RL;

- The DC load resistance $R_c = 6.7 \text{ }\Omega$
- DC load inductance $L_c = 25 \text{ mh}$
- DC load capacitor $C_c = 1000 \text{ }\mu\text{F}$

The APF simulation parameters is :

- The output filter $L_f = 0.5 \text{ mh}$
- DC voltage $v_{dc} = 840 \text{ V}$
- Storage capacity $C_{dc} = 2350 \text{ Mf}$

7.1 Case of an unpolluted balanced voltage source

The Figure 6 presents the simulation results obtained when the source voltages are balanced three-phase and contain no harmonic. For this simulation, the voltages of the source are as follows:

- $v_{s1} = 230\sqrt{2} \sin(\omega t) ;$
- $v_{s2} = 230\sqrt{2} \sin\left(\omega t - \frac{2\Pi}{3}\right) ;$
- $v_{s3} = 230\sqrt{2} \sin\left(\omega t + \frac{2\Pi}{3}\right).$

- The frequency $f = 50$ Hz.

In this case, the THD of source current i_{s1} before filtering is 51.15%, this THD becomes equal to 1.07% after filtering. The frequency spectra of the source current before and after filtering are shown respectively in Figure 7 and Figure 8.

7.2 Case of an unpolluted unbalanced voltage source

The Figure 9 presents the simulation results obtained when the source voltages are unbalanced. For this simulation, the voltages of the source are as follows:

- $v_{s1} = 230\sqrt{2} \sin(\omega t)$;
- $v_{s2} = 253\sqrt{2} \sin\left(\omega t - \frac{2\Pi}{3}\right)$;
- $v_{s3} = 207\sqrt{2} \sin\left(\omega t + \frac{2\Pi}{3}\right)$.
- The frequency $f = 50$ Hz.

In this case, the THD of source current i_{s1} before filtering is 63.97%. This THD become equal to 1.97% after filtering. The frequency spectra of the source current before and after filtering are presented respectively in Figure 10 and Figure 11.

Figure.6: Simulation result for an balanced and unpolluted voltage source

Figure.7: i_{s1} frequency spectrum before filtering

Figure.9: Simulation result for an unbalanced and unpolluted voltage source

Figure.8: i_{s1} frequency spectrum after filtering

Figure.10: i_{s1} frequency spectrum before filtering

Figure.11: i_{s1} frequency spectrum after filtering

7.3 Case of a balanced and polluted source of tension

The Figure 12. Presents the simulation results obtained when the source voltages are balanced and polluted (contain the harmonic of order 5). For this simulation, the voltages of the source are as follows:

- $v_{s1} = 230\sqrt{2} \sin(\omega t) + \frac{230\sqrt{2}}{5} \sin(5\omega t) ;$
- $v_{s2} = 230\sqrt{2} \sin\left(\omega t - \frac{2\Pi}{3}\right) + \frac{230\sqrt{2}}{5} \sin\left(5 * \left(\omega t - \frac{2\Pi}{3}\right)\right);$
- $v_{s3} = 230\sqrt{2} \sin\left(\omega t + \frac{2\Pi}{3}\right) + \frac{230\sqrt{2}}{5} \sin\left(5 * \left(\omega t + \frac{2\Pi}{3}\right)\right).$
- The frequency of the fundamental $f = 50$ Hz; and the frequency of the harmonic of rank '5' $f_5 = 250$ Hz.

In this case, the THD of source current i_{s1} before filtering is 55.80%. This THD become equal to 1.46% after filtering. The frequency spectra of the source current before and after filtering are shown respectively in Figure 13 and Figure 14.

Figure.12: Simulation result for an balanced and polluted voltage source

Figure.13: i_{s1} frequency spectrum before filtering

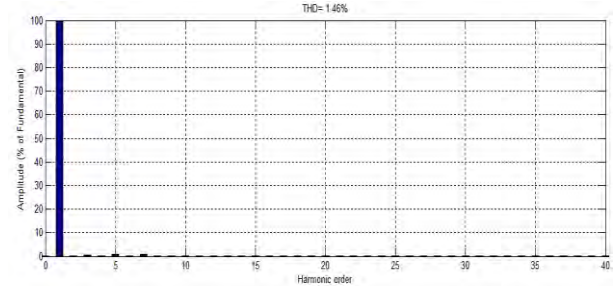


Figure.14: i_{s1} frequency spectrum after filtering

7.4 Case of an unbalanced and polluted source of tension

The Figure 15 presents the simulation results obtained when the source voltages are unbalanced and polluted (contain the harmonic of order 5). For this simulation, the voltages of the source are as follows:

- $v_{s1} = 230\sqrt{2} \sin(\omega t) + \frac{230\sqrt{2}}{5} \sin(5\omega t) ;$
- $v_{s2} = 253\sqrt{2} \sin\left(\omega t - \frac{2\Pi}{3}\right) + \frac{230\sqrt{2}}{5} \sin\left(5 * \left(\omega t - \frac{2\Pi}{3}\right)\right);$
- $v_{s3} = 207\sqrt{2} \sin\left(\omega t + \frac{2\Pi}{3}\right) + \frac{230\sqrt{2}}{5} \sin\left(5 * \left(\omega t + \frac{2\Pi}{3}\right)\right).$
- The frequency of the fundamental $f = 50$ Hz; and the frequency of the harmonic of rank '5' $f_5 = 250$ Hz.

In this case, the current source THD i_{s1} before filtering is 68.92%, this THD become equal to 1.95% after filtering. The frequency spectra of the source current before and after filtering are presented respectively in Figure 16 and Figure 17.

Figure.15: Simulation result for an unbalanced and polluted voltage source

Figure.16: i_{s1} frequency spectrum before filtering

Figure.17: i_{s1} frequency spectrum after filtering

8. CONCLUSION

In this study, we presented a shunt active power filter controlled by the SRF identification method to eliminate the harmonics generated by nonlinear loads in the electrical network. After application of the filtering operation, we found an excellent improvement in the current rate and the THD value for the different cases studied, which confirms the efficiency of this method in any form of voltage (balanced-unpolluted, unbalanced-unpolluted, balanced-polluted, unbalanced-polluted).

REFERENCES

- [1] H. Sasaki & T. Machida, "A new method to eliminate AC harmonic currents by magnetic flux compensation-considerations on basic design", IEEE Trans. Power Appl. Syst., vol. PAS-90, No. 5, pp. 2009–2019, Jan. 1971.
- [2] L. Gyugyi and B. R. Pelly, "Static Power Frequency Changers: Theory, Performance and Application", Wiley, 1976.
- [3] F. Harashima, H. Inaba, and K. Tsuboi, "A Closed-loop Control System for the Reduction of Reactive Power Required by Electronic Converters," IEEE Transactions on IECEI, vol. 23, no. 2, May 1976, pp. 162–166.
- [4] L. Gyugyi and E. C. Strycula, "Active ac Power Filters," in Proceedings of IEEE Industry Application Annual Meeting, vol. 19-C, 1976, pp. 529–535.
- [5] Hind Djeghloud "Filtrage Actif De Puissance" .Phd theses of Mantouri University– Constantine 2007.
- [6] I. Takahashi, K. Fujiwara, and A. Nabae, "Distorted Current Compensation System Using Thyristor Based Line Commutated Converters," Transactions of the IEE-Japan, Part B, vol. 101, no.3, 1981, pp. 121–128 (in Japanese).
- [7] M.A.E Alali "Contribution à l'Etude des Compensateurs Actifs des Réseaux Electriques Basse Tension" .Phd theses of the Louis .Pasteur University– Strasbourg – Electrical engineering, 2002 .
- [8] S. Bhattacharya, D. M. Divan, B. Banerjee, "Synchronous frame harmonic isolator using active series filter", EPE'91, pp. 30-35, 1991.
- [9] M. Takeda, K. Ikeda, & Y. Tominaga, "Harmonic current and reactive power compensation with an active filter," in Conf. Rec. IEEE-PESC 1988, pp. 1174–1179.
- [10] S. Moran, "A line voltage regulator / conditioner for harmonic-sensitive load isolation", Conf. Rec. IEEE Ind. Appl. Soc. Ann. Meet., vol. 1, pp. 947 – 951, 1-5 October 1989.
- [11] A.Nabae, S. Ogasawara, & H. Akagi, "A novel control scheme for current controlled PWM inverters", IEEE Trans. Ind. Applicat., vol. 22, No. 4, pp. 312-323, July/August 1986.

Direct Torque Control of PMSM Supplied By Photovoltaic Source

S. Boukhalfa, I. Hamzaoui and F. Bouchafaa

Abstract — The Permanent Magnet Synchronous Motor (PMSM) is suitable for many applications, such as traction, aerospace and generally automated process industry. In our work, we will study the application of the PMSM in renewable energies. Our objective is to model the complete system, including the photovoltaic inverter, PMSM under Matlab/Simulink environment. Solar panels generate DC power by direct conversion of solar radiation using. The energy received depends on the radiation and the ambient temperature. The permanent magnet synchronous motor (PMSM) is not stable in an open loop. To control the PMSM in terms of speed, torque or position, we need to implement direct torque control. We will establish the oriented control field of a PMSM powered by a photovoltaic source with focus on their applications in the field of variable speed

Index Terms — PVG, MPPT, P&O, PMSM, DTC.

I. INTRODUCTION

For many years, the industry has used the DC motor with the main advantage of being easily controllable by the natural decoupling of flux and torque. However, the presence of the collector brush system has always been a major disadvantage of the motor among others which limits its use more and more. It is for this reason that AC electric motors are used in order to avoid this inconvenience and to take advantage of their advantages such as the flexibility of variation of speed and the stability of operation. Among the AC electric motors used in drives, the Permanent Magnet Synchronous Motor (PMSM).

The synchronous motor is strongly penalized by the absence of the torque out of synchronism. Powered by fixed frequency networks, it must be launched at synchronous speed to provide electromagnetic torque. To overcome these difficulties, it must be equipped with a variable frequency power supply. The variable frequency power supply of the machine is done by means of a generally DC-AC converter (inverter) [1, 2].

Many control strategies have been developed to make it an actuator that overrides all other machines. The

Manuscript received August 08, 2018. This work was supported in part by the MESRS Ministry under Grant J0200220090020. S. Boukhalfa is with the Laboratory of Instrumentation, USTHB, PO.Box. 32, Bab-Ezzouar, Algies, Email : saidaboukhalfa@yahoo.fr. I.Hamzaoui is with the Faculty of Science and Technology University of Khemis Miliana UDBKM , Algeria , Email: hamzaoui_ihssen2000@yahoo.fr. F. Bouchafaa is also with the Laboratory of Instrumentation, USTHB , PO.Box. 32, Bab-Ezzouar, Algies, Phone: 213-24217912 (Ext. 804), Fax: 213-21207664, URL: <http://www.lins.usthb.dz>, Email : fbouchafa@gmail.com.

development of increasingly efficient digital signal processors has made possible the implementation of sophisticated control laws at low cost (vector control, DTC control, etc.) [3].

The direct torque control method has been proposed by DEPENBROCK and TAKAHASHI for the operation of asynchronous machines [4]. Subsequently, numerous research studies have been developed in this field [5,6] to improve the performances of this technique and to compete with vector control [7]. The current trend is to replace the asynchronous motor with the permanent magnet synchronous motor which is of low cost and much higher inertia torque ratio [8].

The use of photovoltaic (PV) modules as a source of renewable energy is attracting more and more attention today. PV modules can be used as an isolated system (stand-alone system) or connected to the network. In both cases, they must be connected to an inverter to convert the continuous energy generated into alternating current. The PV direct voltage is low, which requires a DC-DC boost converter to generate an appropriate high input voltage for the inverter, the PV can be used to power the permanent magnet synchronous motor.

Our main goal is to improve the performance of the conventional DTC control to permanent magnet synchronous machine powered by photovoltaic source. This objective includes an improvement in the dynamic response of the system, as well as performance in the statistical regime.

II. MODELING OF THE PV GENERATOR

The photovoltaic cell is characterized by its equivalent circuit diagram (Fig.2) which consists of a current source which models the luminous flux conversion into electrical energy, a shunt resistor R_p modeling the leakage current at the junction, a series resistor R_s representing the various resistances of contacts and connections and a bypass diode which models the PN junction [9][10].

The current generated by the module is given by the following equation:

$$I = I_{ph} - I_s \left(\exp \left(\frac{q(V + I.R_s)}{nkT} \right) - 1 \right) - \frac{(V + I.R_s)}{R_p} \quad (1)$$

With

I : current provided by the PV cell;

I_{ph} : Current photogénére;

I_d : current through the diode;

I_s : Saturation current of the diode;
 V : output voltage;
 q : Electron charge ($1.6 \cdot 10^{-19}$ C);
 K : Boltzmann's constant ($1.38 \cdot 10^{-23}$ J / K);
 n : quality factor of the solar cell ($1 < n < 2$);
 T : temperature of the junction of K;
 R_p : shunt resistor;
 R_s : series Resistor.

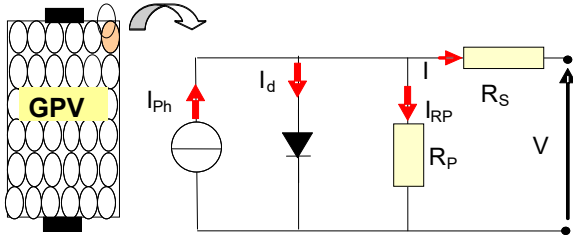


Fig 2: Equivalent circuit of a photovoltaic cell

The photogenerated current I_{ph} is expressed as follows:

$$I_{ph} = I_{ccref} \times \frac{E}{E_{ref}} \quad (2)$$

The saturation current is expressed as follows

$$I_s = \frac{I_{ccref}}{\exp\left(\frac{V_{oc}}{V_t}\right) - 1} \times \left[\frac{T}{T_0}\right]^3 \times \exp\left(\frac{-qE_g}{KT}\right) \quad (3)$$

The term of the current-voltage characteristic of a PVG for a given temperature and illumination can be written as follows:

$$I = N_p \cdot I_{ph} - N_p \cdot I_0 \left(\exp\left(\frac{q(V + I R_s)}{N_s n K T}\right) - 1 \right) - \frac{(V + I R_s)}{R_p} \quad (4)$$

Figure 3 shows the characteristics (I-V) and (P-V) of a photovoltaic panel under constant conditions of temperature and radiation.

It is noted that the current-voltage (I-V) we provided the maximum current (short circuit current I_{sc}) and the maximum voltage V_{oc} (open circuit voltage) characteristics and the power-voltage (PV) we provided the maximum power point the PV generator (MPP) (Fig.3).

The electrical characteristics of a PV generator vary depending on the temperature and lighting. We simulated the behavior of the generator subject to various constraints. These notions are indeed necessary to understand the behavior of a PV generator to optimize the operation of a PVG.

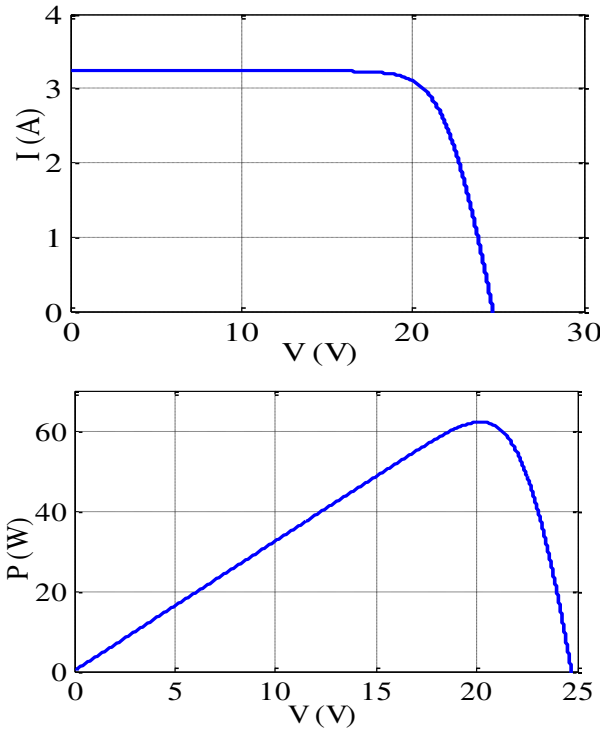


Fig.3. Characteristics (I-V) and (P-V) of a photovoltaic generator

The influence of the illumination and temperature on the characteristic $P = f(V)$ are shown in figure 4 and 5.

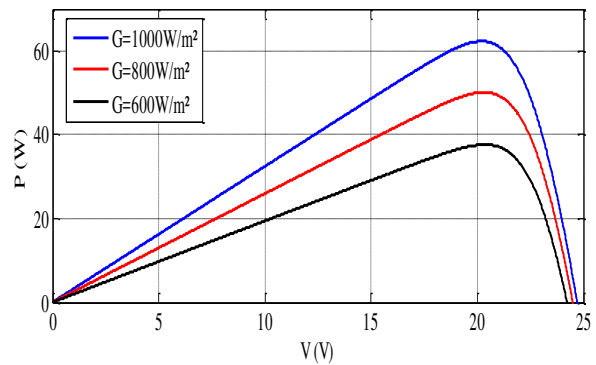


Fig.4. Influence of illumination on the Characteristic (P-V) of PVG

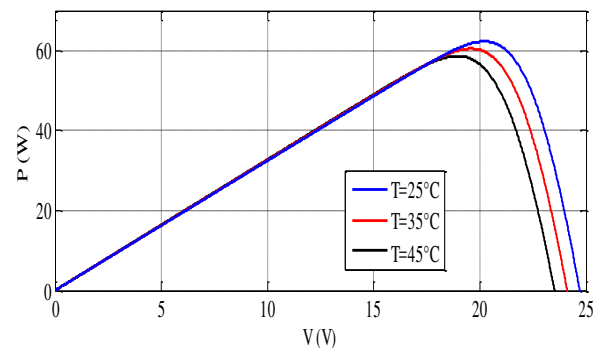


Fig.5. Influence of temperature on the characteristic (P-V) of PVG

Note that the open circuit voltage decreases slightly with illumination. This implies that the optimum power photovoltaic generator is substantially proportional to the

illumination and the points of maximum power are at about the same voltage.

The maximum power decreases with increasing temperature as shown in figure 5. The increase in temperature implies a significant decrease in open circuit voltage; hence the temperature affects the open circuit voltage.

III. THE SEARCH FOR THE MAXIMUM POWER POINT

The power of a chain in which a load PVG is powered by a DC generator through a static converter controlled by a control MPPT whose role is to vary the duty cycle of static converter so that the power supplied by PVG is the P_{MAX} (maximum power) available at its terminals. The MPPT algorithm can be more or less complicated to find the MPP and usually is based on the variation of the duty cycle of the chopper with the aim of reaching the MPP according to changes of input parameters of the static converter (I_{PV} and V_{PV}) [10].

IV. PERTURBATION AND OBSERVATION ALGORITHM

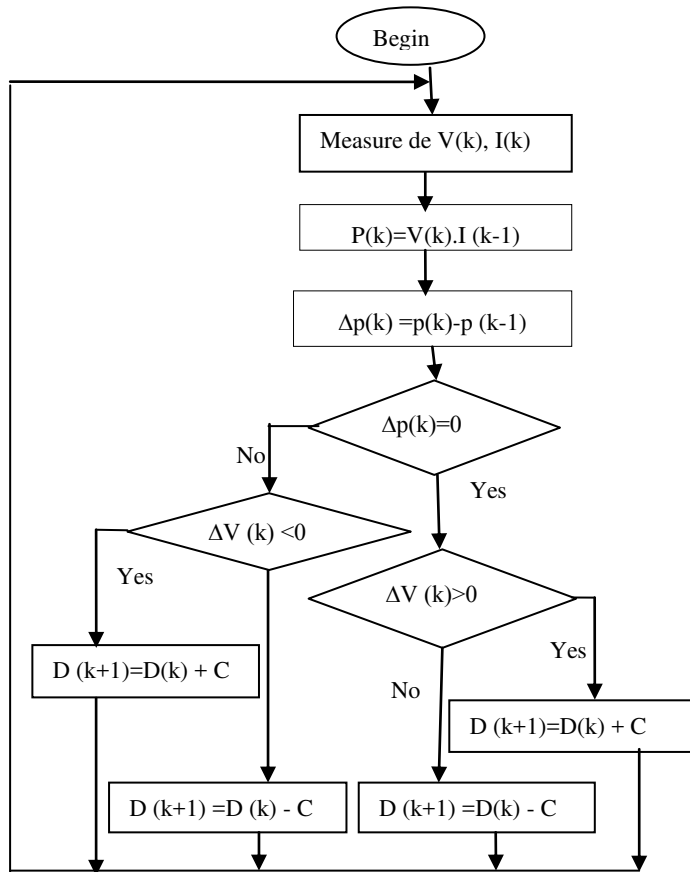


Fig.6. P&O method flow chart

This algorithm is designed so that it runs on a computer and thus each cycle of the algorithm, V and I are measured to calculate P(k). This value P(k) is compared with that of P(k-1). If the output power has increased since the last measurement, the disturbance of the output voltage will continue in the same direction as that taken in the last cycle. If the output power has decreased since the last measurement, the voltage V of PVG is perturbed in the direction opposite to that of the previous iteration [11]. Figure 6 shows the flowchart of this algorithm.

Figure 7 shows the response of the algorithm P & O in the case of operation of the PVG under standard atmospheric conditions ($G=1000W/m^2$, $T = 25^{\circ}C$).

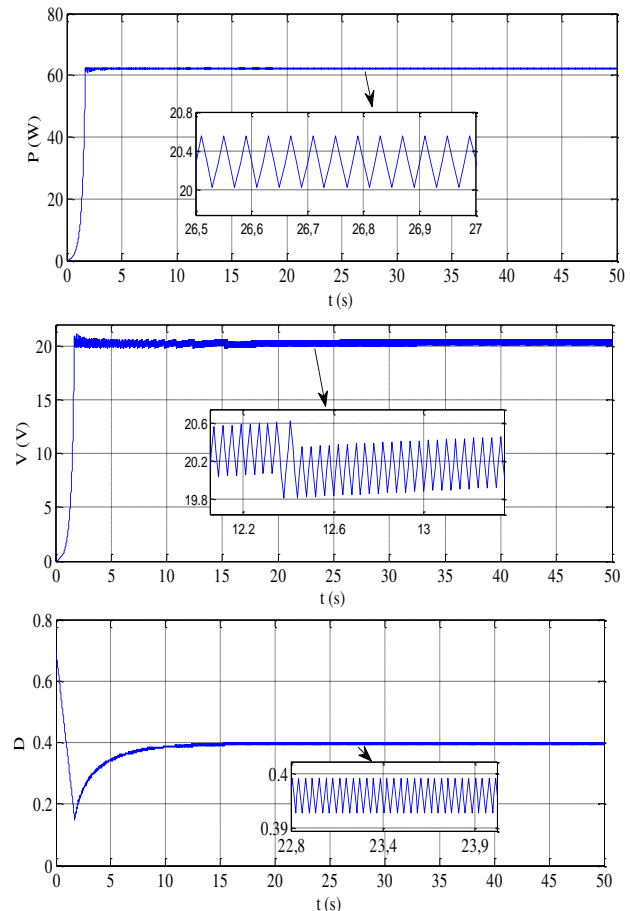


Fig.7. MPPT control behavior (P & O) in the standard conditions

This feature produced under standard climatic conditions, not allowed to see that the MPPT control introduced in the PV generator, the forced to keep almost the same value of PPM after he has waiting.

V. MODELING OF PMSM

The electrical equations of the synchronous machine in the frame d, q are expressed as follows [12, 13].

$$\begin{cases} V_{ds} = R_s i_{ds} + L_d \frac{di_{ds}}{dt} - L_q i_{qs} \omega_s \\ V_{qs} = R_s i_{qs} + L_q \frac{di_{qs}}{dt} + L_d i_{ds} \omega_s + \Phi_r \omega_s \end{cases} \quad (7)$$

V. PRINCIPLE OF DIRECT TORQUE CONTROL

The objective of the DTC direct torque control of the machine, by applying different voltages vectors of the inverter, which determines its state. Controlled variables are: The stator flux and electromagnetic torque which are usually ordered by regulators to hysteresis. This is to keep the magnitudes of stator flux and electromagnetic torque within the hysteresis bands. The output of these regulators determines the voltage vector of the inverter to apply to

each optimal switching instant. The order by the DTC PMSM, can be outlined in figure 10:

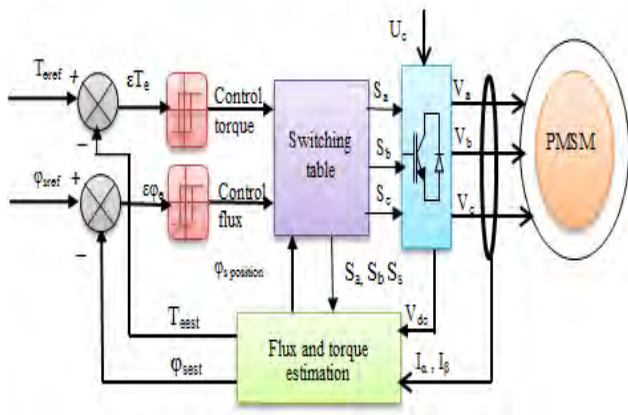


Fig.10. The general structure of DTC applied to a PMSM

It develops the truth table based on errors of flux and torque, depending on the position of the stator flux vector. The sharing of the complex plane into six angular sectors to determine, for each sector, the sequence of the switches of the inverter states corresponding to different magnitudes of control following the logic of the flow behavior and torque screws to -vis the application of a stator voltage vector [14, 15].

TABLE.I.

Generalized table of voltage vectors of an order by DTC

	Increase	Decrease
ϕ_s	V_{i-1} and V_{i+1}	V_{i-2}, V_{i+2} and V_{i+3}
T_{em}	V_{i+1} and V_{i+2}	V_2 and V_{i-1}

When the flow vector is in a zone numbered 'i', the flow and torque control is ensured by selecting one of the four non-zero vectors or one of the two zero vectors [14]. The role of the selected voltage vector is described in figure 11.

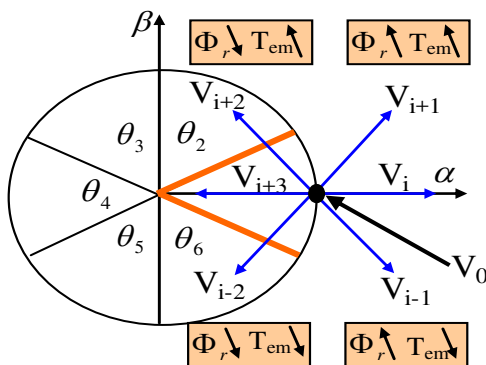


Fig.11. Effects of different voltage vectors in the first sector

From the simplified model of the PMSM in a frame (α, β) linked to the stator, the stator flux is defined by the following equation [16,17]:

$$\phi_s = \int_0^t (V_s - R_s I_s) dt + \phi_{s0} \quad (8)$$

The stator flux, in a reference frame linked to the stator [16, 17], is given by:

$$\phi_s = \int_0^t (V_s - R_s I_s) dt + \phi_{s0} \quad (9)$$

With ϕ_{s0} the flux at $(t_0 = 0)$.

By neglecting the term "Rs.Is", a hypothesis valid for high speeds, we will have:

$$\phi_s = \int_0^t V_s dt + \phi_{s0} \quad (10)$$

An equation of the electromagnetic torque can be established as a function of the rotor and stator flux, namely [17]:

$$C_e = p \frac{M}{\sigma L_r L_s} \phi_r \phi_s \sin \theta_{sr} \quad (11)$$

or:

θ_{sr} : The angle between the stator and rotor flux vectors

The table of the control structure is developed according to flow hysteresis controller outputs (Table.II).

Table.II.

DTC table defining the sequences of a two-level inverter

The zero sequence V_0 and V_i , are independent of the flow state, they are related only to the gap Δcem . These sequences are applied when the couple wants to keep his

torque	flow	N=1	N=2	N=3	N=4	N=5	N=6
$K_\phi=1$	$K_T=1$	V_2	V_3	V_4	V_5	V_6	V_1
	$K_T=0$	V_7	V_0	V_7	V_0	V_7	V_0
$K_\phi=0$	$K_T=1$	V_3	V_4	V_5	V_6	V_1	V_2
	$K_T=0$	V_0	V_7	V_0	V_7	V_0	V_7

band:

$$-\varepsilon_{cem} \leq \Delta cem \leq \varepsilon_{cem}$$

VI. SIMULATION RESULTS

The following figures show the performance of the chain of photovoltaic using voltage inverter with two levels is controlled by direct torque control. The PVG supplies a voltage of 750V in steady state and applying a load torque resistant positive $C_r = 2N.m$ between two instants 0.5 s and 0.7 s, $T = 25^\circ C$ and $G = 1000 W/m^2$. Figure 12 shows the performance of the PMSM supplied by a two-level controlled by the direct torque control, in the case where the latter is powered by a photovoltaic source.

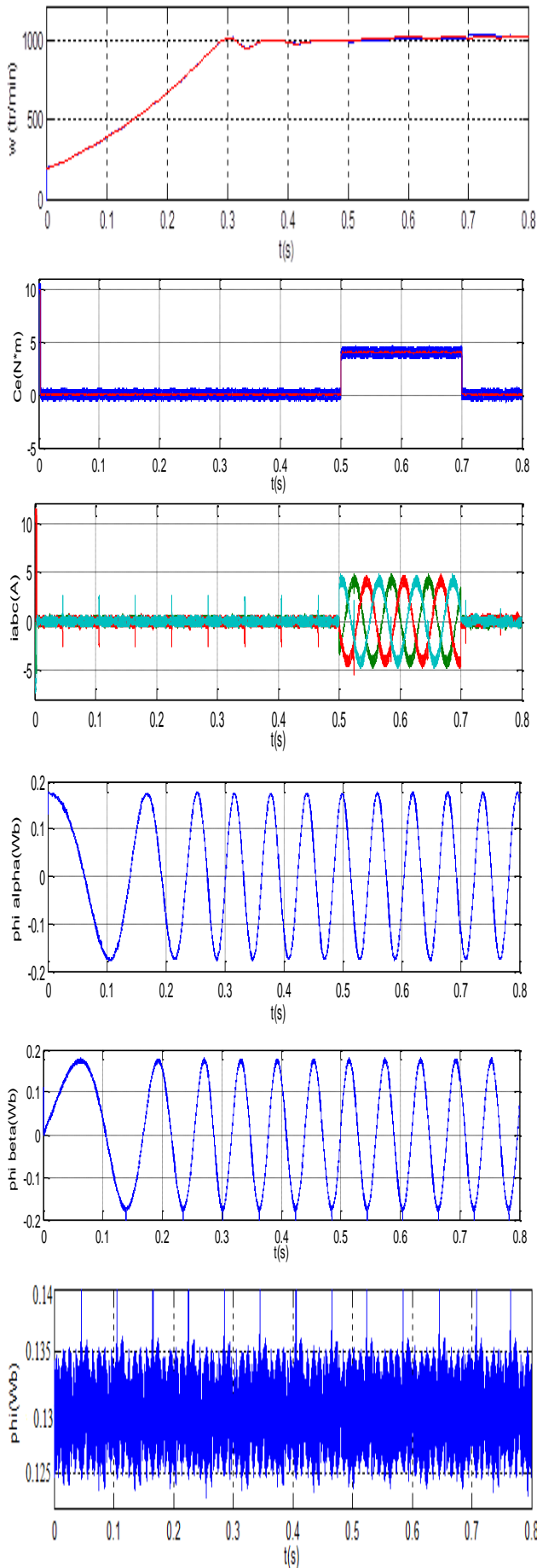


Fig.12. Performance of the PMSM with applying a torque in standard conditions

It is noted that following the reference torque from the reference speed control, the currents of sinusoidal shapes at the moment when the resisting torque is applied.

The disturbance torque, speed and currents (i_a , i_b , i_c) are due to the variation of the supply voltage of the inverter and the power supplied U_{dc} of the photovoltaic panel because of the variation of temperature and illumination.

And it is clear that the couple perfectly follows the set point value, the current follows the load variation and the response speed shows that the DTC has a high dynamic performance at startup.

VII. CONCLUSION

In this paper, we studied the performance of a photovoltaic system using a two-level inverter. Thus, we performed modeling of a photovoltaic generator using an exponential model and studied the influence of meteorological parameters (temperature and irradiance and internal parameters on the electrical characteristics of the latter.

The technique of optimization algorithm of the solar generator, which has been studied, is the perturbation and observation (P & O), it is generally used by designers to tracking the maximum power point tracking (MPPT), but it suffers from some disadvantages, in terms of execution or in the prosecution process.

The introduction of the direct control of torque in the plane of Park allowed us to decouple the magnitudes of the machine and make the mathematical model of it equivalent to a DC machine with separate excitation.

The robustness of the DTC control has been proven, whether for a load change of speed reference. The use of a hysteresis controller at three levels for the torque reduces torque ripple and the frequency switching of the switches of the inverter.

REFERENCES

1. A. BOUREK, "Commande sans capteur de vitesse d'un moteur synchrone à aimants permanents par l'utilisation de la commande directe du couple et d'un observateur de vitesse à mode glissant", Thèse de Magister, Université Mohamed Khider-Biskra.
2. H. BENALLA, "Stratégies de commande et techniques intelligentes appliquées aux machines de type synchrone", Thèse de Magister, Université Mentouri Constantine, 2010.
3. N. Benharir, M. Zerikat, S. Chekroun, A. Mechernene, "Approche adaptative d'une commande neuronale sans capteur d'un moteur asynchrone associée à un observateur par mode glissant", Communication Science & Technology, Cost, no.14, Januray 2014.
4. M.Dепенbrock, "Direct self control DSC of divert fed induction machine", IEEE Trans. Power electronics, Vol 3, no.4, pp.420-429, october 1988.
5. Cristian Iascu, Ion Boldea and Fede Blaabjerg, "A modified Direct Torque Control for induction motors sensorless drive", IEEE Trans, Ind Applicat, Vol 26, no.1, pp.112-130, January /February/2000.
6. Manuele Bertoluzzo, Giuseppe Buja and Roberto Menis, "Direct Torque Control of an induction motor using a single current sensor," IEEE Trans, Ind., Electronics, Vol 55, no.3, pp.778-784, jun 2006.
7. D. CASADEI, G. SERRA, A. TANI, and L. ZARRI ZARRI, "Assessment of direct torque control for induction motor

- drives", bulletin of the polish academy of sciences technical sciences Vol.54, no.3, 2006.
8. L.Zhono, M.F, Rahman, W.Y .Hu and K.W. Lin , "Analysis of Direct Torque Control in permanent magnet synchronous motor drivers", IEEE Trans, on Power Electronic, Vol.12, pp.528-536, May 1997.
 9. H. Mabrouk, S. Mebrouk, A.B.H. Adamou-Mitiche,M. Saraoui, "Etude de la technique d'optimisation sur le système de pompage photovoltaïque au fil de soleil", Revue des Energies Renouvelables Vol. 17 no.4, 579-588. 2014.
 10. M. Ouada, A.Tarfaya, M.S. Meridjet, Dib Djalel, "Etude et Caractérisation sous Matlab/Simulink d'un Générateur Photovoltaïque", The 2nd International Seminar on New and Renewable Energies, Ghardaïa-Algérie 15, 16 et 17 Octobre 2012.
 11. F. Belhachat, C. Larbes, L. Barazane, S. Kharzi, "Commande neuro-floue d'un hacheur MPPT", 4th international conference on computer integrated manufacturing CIP'2007.
 12. A. Guen, "Contribution à l'étude des systèmes de télécommunications mobiles", Mémoire de Magister, Université de Tlemcen, Février 1992.
 13. M. Malek, "Forced Dynamic Position Control of PMSM with DTC Utilization", Journal of Electrical Engineering, Vol.63, no.5, pp.328-332, 2012.
 14. C. Ogbuka , C. Nwosu , M. Agu, "A fast hysteresis current–controlled permanent magnet synchronous motor drive based on field orientation", Journal Of Electrical Engineering, Vol.67, no.2, PP.69-77, 2016.
 15. M.Kadjoudj, C.Ghennai, C.Boucharab and N.Golea, "variable band hysteresis controller for direct torque of PMSMN drive", in pricceedings of the thirty sixth IEEE-LAS annual meeting,Chicago, Septembre /Octobre 2001.
 16. P.A.Arias, "Improvement in direct torque control of induction motos", PhD thesis, University of Catalunya, Espagne, 2000.
 17. M. F. Rahman, L. Zhong, E. Haque, and M. A. Rahman, "A Direct Torque-Controlled Interior Permanent-Magnet Synchronous Motor Drive Without a Speed Sensor", IEEE Trans. Energy conversion, Vol.18, no.1, Mar. 2003.
 18. M. S. Merzoug, and F. Naceri, "Comparison of Field-Oriented Control and Direct Torque Control for Permanent Magnet Synchronous Motor (PMSM)", World Academy of Science, Engineering and Technology 45, 2008.

Photovoltaic generator characteristics

Number of cells in series n_s	36,
Maximum power P_{max}	83W,
Short circuit current I_{sc}	3.25A,
Open circuit voltage V_{oc}	21.2V,
series Resistor of photovoltaic cell R_s	0.099 Ω ,
Shunt resistor of the photovoltaic cell R_P	200 Ω ,

The parameters of the PMSM

$R_s = 1 \Omega$,
 $L_d = L_q = 0.0032H$,
 $J = 0.0006 \text{ Kg.m}^2$,
 $f = 0.000095 \text{ Kg.m}^2/s$,
 $C_r = 5N.m$,
 $\phi_r = 0.13 \text{ Wb}$,
 $p = 3$,
 $P_n = 4 \text{ kW}$,
 $V_n = 220 / 380 \text{ V}$,
 $f = 50 \text{ Hz}$,
 $\Omega_r = 1420 \text{ tr / min}$,

Fuzzy Backstepping Control of Double Star Induction Machine for Driving HEV at Low Speed

Noureddine LAYADI¹, Ali DJERIOUI¹, Samir ZEGHLACHE², Azeddine HOUARI³, Mohamed Fouad BENKHORIS³ and Fouad BERRABAH¹

¹University Mohamed Boudiaf of M'Sila, Laboratoire de Génie Electrique, Department of Electrical Engineering, Faculty of technology, BP 166, Ichbilia, M'Sila, 28000, Algeria
layadinoureddine1@gmail.com, alidjerioui@yahoo.fr and Fouadberrabah1@gmail.com

²University Mohamed Boudiaf of M'Sila, Laboratoire d'Analyse des Signaux et Systèmes, Department of Electronics, Faculty of technology, BP 166, Ichbilia, M'Sila, 28000, Algeria
zagsam5@gmail.com

³University of Nantes, IREENA Laboratory, Saint-Nazaire, France
Azeddine.Houari@univ-nantes.fr, Mohamed-Fouad.Benkhoris@univ-nantes.fr

ABSTRACT

This paper presents a combination of control based on the robustness of the backstepping control (BSC) and the smoothness of the fuzzy Logic controller (FLC) of a double star induction machine (DSIM) in order to improve the dynamic response and efficiency of a hybrid electric vehicle (HEV) system in low speed operation. In the proposed control scheme, the backstepping gain of speed is replaced by a fuzzy inference to smooth the classic backstepping control action. The FLC is proposed for speed regulation because it does not depend on the machine parameters. Simulation results clearly show that the proposed control improves the robustness of the system against low speed variations and load disturbances with a high accuracy and superiority over the backstepping classic.

Key Words: Double star induction machine, Hybrid electric vehicle, Backstepping control, Fuzzy logic controller, Low speed.

1. INTRODUCTION

The double star induction machine (DSIM) belongs to the multiphase machines category. It has been proposed for different fields of industry that need high power such as electric hybrid vehicles, locomotive traction and ship propulsion. DISM not only

guarantees a decrease in rotor harmonic currents and torque pulsations but also has many others advantages such as: reliability, power segmentation and higher efficiency [1, 2].

The pollution caused by greenhouse gas emissions is mainly due to incomplete combustion. Usually this chemical phenomenon occurs in thermal vehicles, for this reason, the electric vehicle (EV) is the best alternative to ameliorate air quality and safeguarding the environment [3-5]. Induction motor is widely used in the driving system of HEV than another electrical machine such as the permanent magnet synchronous machine (PMSM).

Backstepping control (BSC) is able to stabilize system states through a step-by-step recursive process that mitigates the complexity of the control scheme and ensures the stability of the closed-loop system according to Lyapunov's theory [6]. BSC not only guarantees high performance in both dynamic and steady mode, but also offers excellent closed-loop stability and good tracking, even in a critical operating state. Low speed operation is a challenge for high power multiphase induction machines. In [7], at low speed, very high torque and currents are observed with a high noise level in a five-phase induction motor where torque and flux control dynamics become difficult to achieve. To overcome these abnormal

operating conditions, [7] proposes a nonlinear backstepping controller to make the system asymptotically stable and the error converge to zero. The only difficulty of the backstepping controller is to develop an appropriate Lyapunov function adequate to the system.

FLC is a smart controller. Recently, it has been applied successfully on a double star induction machine [2, 8-9]. FLC is based on an orderly method in order to integrate human experience and to achieve nonlinear algorithms. The main advantage of FLC is its autonomy over the mathematical model, it does not need a precise knowledge of the system and does not depend on the machine parameters, and therefore, it can master almost any complex nonlinear system. Applying a fuzzy controller to a multiphase induction machine reduces non-sequential currents and improves the quality of the energy transported inside the machine, which leads to a reduction in mechanical vibrations [3]. FLC is a robust control, able to adapt to the variation of parameters because it does not require precise mathematical model [10].

This paper presents a comparative study between the fuzzy backstepping control (FBSC) and the classical BSC, along with simulation results and analyzes to prove the effectiveness of the proposed control. Compared to existing work published in the literature, the main contributions of this paper can be summarized as follows:

- In this paper, the application of speed fuzzy control based on the backstepping strategy of a double-star induction machine running at very low speed is performed for the first time.

- The proposed control has improved the control strategy presented in [1] by increasing its dynamic performance, especially in low speed operation.

- Compared to [8], the BSC-associated FLC gives a fast dynamic response and better steady-state stability than the FLC combination with indirect field oriented control (IFOC).

This paper is organized as follows: In section 2, the modeling of the DSIM is given. Section 3 describes the hybrid power system. The speed fuzzy logic controller is designed in section 4. Section 5 presents the BSC strategy. Simulation results are shown and

analyzed in section 6. Finally, the conclusion is given in section 7.

2. DSIM MODELING

The d-q dynamic healthy model of squirrel cage double star induction machine with a reference frame fixed to the rotor is given by:

$$\dot{x} = f(x) + Bv + DT_L \quad (1)$$

Where x is the state vector given by:

$$x = [x_1 \ x_2 \ x_3 \ x_4 \ x_5 \ x_6]^T \\ = [i_{sd1} \ i_{sq1} \ i_{sd2} \ i_{sq2} \ \omega_r \ \varphi_r]^T,$$

$$v = [v_{sd1} \ v_{sq1} \ v_{sd2} \ v_{sq2}]^T \text{ is the vector}$$

control and $[\omega_r \ \varphi_r]^T$ is the system output.

$$B = \begin{bmatrix} b_1 & 0 & 0 & 0 & 0 & 0 \\ 0 & b_1 & 0 & 0 & 0 & 0 \\ 0 & 0 & b_2 & 0 & 0 & 0 \\ 0 & 0 & 0 & b_2 & 0 & 0 \\ 0 & 0 & 0 & 0 & 0 & 0 \\ 0 & 0 & 0 & 0 & 0 & 0 \end{bmatrix}; \quad b_1 = \frac{1}{L_{s1}}; b_2 = \frac{1}{L_{s2}};$$

$$D = [0 \ 0 \ 0 \ d \ 0 \ 0]^T; \quad d = -\frac{p}{J}.$$

$f(x)$ is a vector which given by the following system of equations :

$$\begin{cases} f_1(x) = a_1x_1 + a_2x_2 + a_3 \\ f_2(x) = a_4x_1 + a_1x_2 + a_5 \\ f_3(x) = a_6x_3 + a_2x_4 + a_7 \\ f_4(x) = a_4x_3 + a_6x_4 + a_8 \\ f_5(x) = a_9(x_2 + x_4) + a_{10}x_5 \\ f_6(x) = a_{11}(x_1 + x_3) + a_{12}x_6 \end{cases} \quad (2)$$

$$a_1 = -\frac{R_{s1}}{L_{s1}}; \quad a_2 = \omega_s; \quad a_3 = -\frac{\omega_s T_r \varphi_r \omega_{gl}}{L_{s1}};$$

$$a_4 = -\omega_s; \quad a_5 = -\frac{\omega_s \varphi_r}{L_{s1}}; \quad a_6 = -\frac{R_{s2}}{L_{s2}};$$

$$a_7 = \frac{\omega_s T_r \varphi_r \omega_{gl}}{L_{s2}}; \quad a_8 = -\frac{\omega_s \varphi_r}{L_{s2}}; \quad a_9 = \frac{p^2 L_m \varphi_r}{J(L_m + L_r)};$$

$$a_{10} = -\frac{K_f}{J}; \quad a_{11} = \frac{L_m R_r}{L_m + L_r}; \quad a_{12} = -\frac{R_r}{L_m + L_r}.$$

Where: v_{sd1} , v_{sq1} are stator1 voltages components. v_{sd2} , v_{sq2} are stator2 voltages components. i_{sd1} , i_{sq1} are stator1 currents components. i_{sd2} , i_{sq2} are stator2 currents components. L_{s1} , L_{s2} , L_r and L_m are stator1, stator2, rotor and mutual inductance, respectively. R_{s1} , R_{s2} and R_r are respectively stator1, stator2 and rotor resistance. $T_r = L_r / R_r$ is the rotor time constant. T_L is the applied load torque. ω_r is the rotor speed. J , K_f denote the rotor inertia and friction coefficient. ω_s is the stator pulsation. ω_{gl} is the slip pulsation. ϕ_r is the rotor flux. p denotes the number of pole pairs. The subscripts d and q designate direct and quadrature indices according to the usual d-q axis components in the synchronous rotating frame.

3. HYBRID POWER SYSTEM

The hybrid power system (HPS) consists of a fuel cell as the main source and storage device (SC) as an auxiliary source. The role of the fuel cell is to convert the chemical energy of reactant into electricity [11]. In this paper, PEMFC is the main source of energy for HEV, its dynamics (cell voltage/current) and (total power/current) are given in Fig. 1.a and Fig. 1.b, respectively. SC is a new kind of energy storage element between conventional electrolytic capacitor and electrochemical battery. SC is widely used in electric vehicles; its advantage over the battery is that the SC allows the voltage change at the terminal even with a different current discharge rate [12]. The dynamics of the electric potential of SC is given by the following equation.

$$\frac{dV_c}{dt} = -\left(\frac{i+i_L}{C}\right) = \frac{V_c}{CR_L} + \frac{i}{C} \quad (3)$$

Where: i is the discharging current, i_L is the leakage current, C is the capacitance and R_L is the insulating leakage resistance.

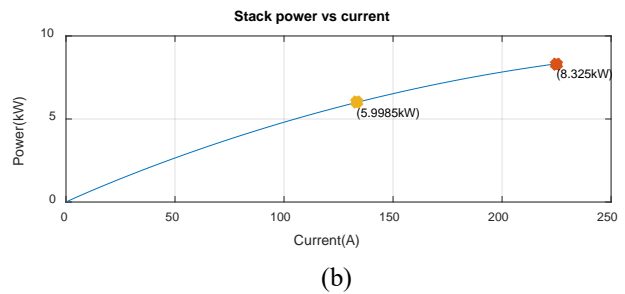
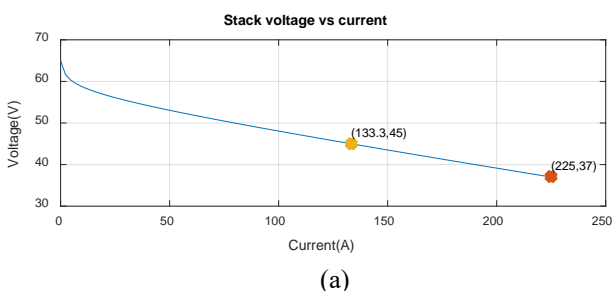


Figure.1: Characteristic of fuel cell (PEMFC)

4. SPEED FUZZY LOGIC CONTROLLER

FLC is a control algorithm based on the knowledge and experience of human experts such as intuition, experience and heuristics, its theory is an artificial intelligence discipline founded by Zadeh. FLC establishes the control law from the human expertise after having made linguistic rules (if / then) which concern the dynamic behavior of the system [9]. The main advantage of FLC is its independence from the mathematical model of the system and its flexibility. The FLC design is similar to that of a conventional PI controller. The only difference is that the speed error (e) and its variation (de) are given as input linguistic variables and the variation of the quadratic reference current Δi_{sq}^* as the output linguistic variable. The main blocks constituting the fuzzy control are: fuzzification, knowledge base (database), Inference engine, defuzzification, membership functions, input and output normalization scale factors that adjust the dynamic and steady-state of the closed-loop system. In this work, they are taken as constant positive values. The fuzzy logic diagram is shown in Fig. 2.

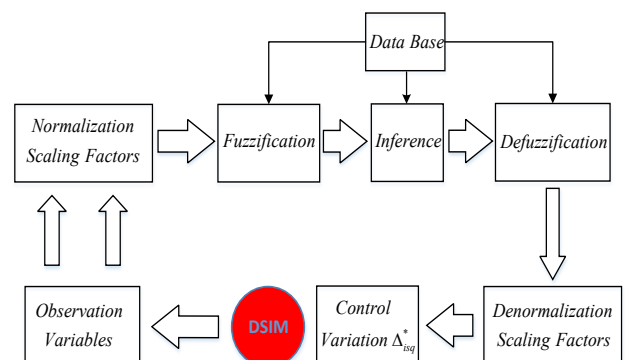


Figure.2: Speed fuzzy logic controller basic diagram

Two membership functions of triangular shape and equal size specify each input. For the output, three membership functions are defined. The membership functions relating to the inputs and the output of the fuzzy controller are shown in Fig. 3 and Fig. 4, respectively [8]. The 3D Control surface of FLC is presented in Fig. 5. The speed error “e” and its variation “de” are represented by the following equations:

$$e_x(k) = x^*(k) - x(k) \quad (4)$$

$$de_x(k) = e^*(k) - e(k-1) \quad (5)$$

Where: x presents the rotor speed ω_r .

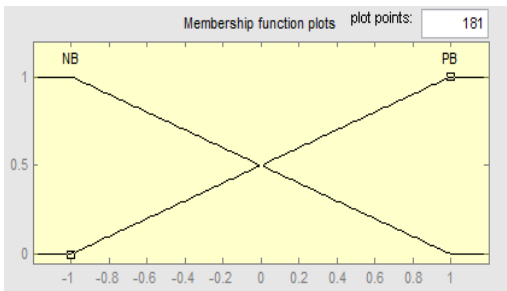


Figure.3: Membership functions for inputs “e” and “de”

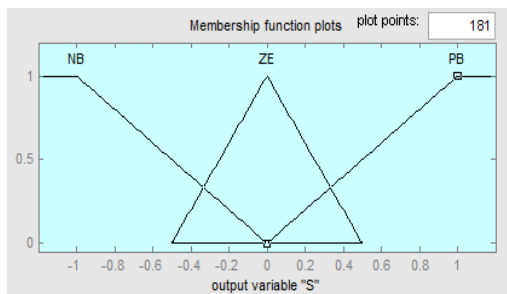


Figure.4: Membership functions for output Δi_{sq}^*

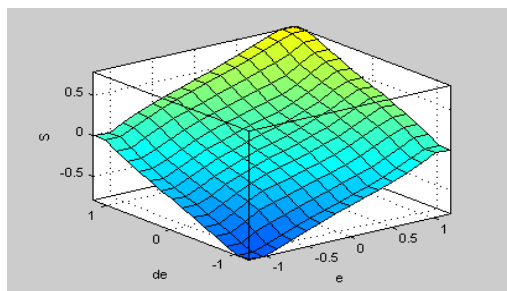


Figure.5: Control surface of FLC

• **Rules:**

According to [8], the fuzzy rules define the inputs and the outputs of the FLC are given in table1.

Table.1 Rules base for FLC

e/de	B	PB
B	B	ZE
PB	E	PB

Where: (NB) is negative big, (PB) is positive big and (ZE) is approximately Zero.

• **Defuzzification:**

The purpose of this step is to obtain a clear output from a fuzzy logic system. The widely used method is the center of gravity (COG), represented by the following equation:

$$S_{out}(x) = \frac{\sum S_i \mu(S_i)}{\sum \mu(S_i)} \quad (6)$$

Where: μ is a membership function, its surface is represented by the real value S_i .

5. BACKSTEPPING CONTROL

The dynamic equations of DSIM are non-linear. However, using the backstepping strategy, the system is progressively controlled step by step from "virtual controls" (stator currents) to real controls (stator voltages). The state equation (1) clearly shows that the rotor flux φ_r can be controlled by the sum of the components of the stator currents i_{sd1} and i_{sd2} . The speed ω_r is adjusted by the sum of i_{sq1} and i_{sq2} . On the other hand, the currents are in turn controlled by the stator voltages v_{sd1} , v_{sq1} , v_{sd2} and v_{sq2} . Therefore, backstepping control design requires two steps [1]:

5.1. Step N°01: Speed and flux control

The aim of this step is to lead the flux φ_r and the speed ω_r to their desired references φ_r^* and ω_r^* , respectively. Speed and flux tracking errors are given by:

$$\begin{cases} e_\omega = x_5^* - x_5 \\ e_\varphi = x_6^* - x_6 \end{cases} \quad (7)$$

The time derivative of (7) is given by:

$$\begin{cases} \dot{e}_\omega = \dot{x}_5^* - \dot{x}_5 \\ \dot{e}_\varphi = \dot{x}_6^* - \dot{x}_6 \end{cases} \quad (8)$$

Using (1), (2) and (8) we obtain:

$$\begin{cases} \dot{e}_\omega = \dot{x}_5^* - a_9(x_2 + x_4) - a_{10}x_5 \\ \dot{e}_\varphi = \dot{x}_6^* - a_{11}(x_1 + x_3) - a_{12}x_6 \end{cases} \quad (9)$$

The first Lyapunov function candidate is defined by:

$$V_1 = \frac{1}{2}e_\omega^2 + \frac{1}{2}e_\varphi^2 \quad (10)$$

The derivative of (10) is given by:

$$\dot{V}_1 = \dot{e}_\omega e_\omega + \dot{e}_\varphi e_\varphi \quad (11)$$

In order to have the derivative of Lyapunov function negative definite, we pose:

$$\begin{cases} \dot{e}_\omega = -K_\omega e_\omega \\ \dot{e}_\varphi = -K_\varphi e_\varphi \end{cases} \quad (12)$$

This choice is correct since we have:

$$\dot{V}_1 = -K_\omega e_\omega^2 - K_\varphi e_\varphi^2 < 0 \quad (13)$$

Where: K_ω and K_φ are positive gains. From (9) and (12), we obtain:

$$\begin{cases} \dot{x}_5^* - a_9(x_2 + x_4) - a_{10}x_5 = -K_\omega e_\omega \\ \dot{x}_6^* - a_{11}(x_1 + x_3) - a_{12}x_6 = -K_\varphi e_\varphi \end{cases} \quad (14)$$

We suppose that:

$$\begin{cases} x_2 + x_4 = i_{sq}^* \\ x_1 + x_3 = i_{sd}^* \end{cases} \quad (15)$$

And

$$\begin{cases} i_{sq1}^* = i_{sq2}^* = \frac{i_{sq}^*}{2} \\ i_{sd1}^* = i_{sd2}^* = \frac{i_{sd}^*}{2} \end{cases} \quad (16)$$

By substituting (15) into (14), we get the virtual control represented by the following equations:

$$i_{sq}^* = \frac{1}{a_9} \left[\dot{x}_5^* - a_{10}x_5 + K_\omega e_\omega \right] \quad (17)$$

$$i_{sd}^* = \frac{1}{a_{11}} \left[\dot{x}_6^* - a_{12}x_6 + K_\varphi e_\varphi \right] \quad (18)$$

5.2. Step N°02: Currents control

In this step the control law will be established by adjusting the four stator currents: i_{sd1} , i_{sq1} , i_{sd2} , i_{sq2} generated by the first step, we also specify their error signals:

$$e_i = x_i^* - x_i \quad i = \{1, 2, 3, 4\} \quad (19)$$

The time derivative of (19) gives:

$$\dot{e}_i = \dot{x}_i^* - \dot{x}_i \quad i = \{1, 2, 3, 4\} \quad (20)$$

From equations (1) and (2), (20) can be written as follows:

$$\begin{bmatrix} \dot{e}_1 \\ \dot{e}_2 \\ \dot{e}_3 \\ \dot{e}_4 \end{bmatrix} = \begin{bmatrix} \dot{x}_1^* - a_1x_1 - a_2x_2 - a_3 - b_1v_{sd1} \\ \dot{x}_2^* - a_4x_1 - a_2x_2 - a_5 - b_1v_{sq1} \\ \dot{x}_3^* - a_6x_3 - a_2x_4 - a_7 - b_2v_{sd2} \\ \dot{x}_4^* - a_4x_3 - a_6x_4 - a_8 - b_2v_{sq2} \end{bmatrix} \quad (21)$$

The increasing function of Lyapunov which analyzes the stability of the system is defined by:

$$V_2 = \frac{1}{2} \left[V_1 + (e_1^2 + e_2^2 + e_3^2 + e_4^2) \right] \quad (22)$$

Its time derivative is:

$$\dot{V}_2 = \dot{V}_1 + \dot{e}_1 e_1 + \dot{e}_2 e_2 + \dot{e}_3 e_3 + \dot{e}_4 e_4 \quad (23)$$

The overall stability of the system is obtained if only \dot{V}_2 is definite negative therefore \dot{e}_1 , \dot{e}_2 , \dot{e}_3 , \dot{e}_4 are chosen as in the first step:

$$\begin{cases} \dot{e}_1 = -K_1 e_1 \\ \dot{e}_2 = -K_2 e_2 \\ \dot{e}_3 = -K_3 e_3 \\ \dot{e}_4 = -K_4 e_4 \end{cases} \quad (24)$$

Where: K_1 , K_2 , K_3 and K_4 are positive constants. The machine stability according to the Lyapunov stability theory is proved by the following inequality:

$$\dot{V}_2 = \dot{V}_1 - K_1 e_1^2 - K_2 e_2^2 - K_3 e_3^2 - K_4 e_4^2 < 0 \quad (25)$$

Finally the actual control is represented by the following components of stator voltages:

$$v_{sd1} = \frac{1}{b_1} \left[\dot{x}_1^* - a_1 x_1 - a_2 x_2 - a_3 + K_1 e_1 \right] \quad (26)$$

$$v_{sq1} = \frac{1}{b_1} \left[\dot{x}_2^* - a_4 x_1 - a_2 x_2 - a_5 + K_2 e_2 \right] \quad (27)$$

$$v_{sd2} = \frac{1}{b_2} \left[\dot{x}_3^* - a_6 x_3 - a_2 x_4 - a_7 + K_3 e_3 \right] \quad (28)$$

$$v_{sq2} = \frac{1}{b_2} \left[\dot{x}_4^* - a_4 x_3 - a_6 x_4 - a_5 + K_4 e_4 \right] \quad (29)$$

The global control scheme of the HEV system is illustrated in Fig. 6, the scaling factors K_e and K_{de} are used to normalize the error "e" and error variation "de", respectively while α is for the output.

6. SIMULATION RESULTS AND INTERPRETATION

The DSIM studied in this paper is powered by two voltage source inverters with a pulse width modulation (PWM) control strategy. Its nominal electrical and mechanical parameters are as follows: $P_n=4.5\text{kw}$, $R_{s1,s2}=3.72\Omega$, $R_r=2.12\Omega$, $L_m=0.3672\text{H}$, $L_{s1,s2}=0.022\text{H}$, $L_r=0.006\text{H}$, $J=0.0625\text{Kg.m}^2$, $p=1$ and $K_f=0.001\text{Nm.}(\text{rd/s})^{-1}$. The reference speed is set to $+4\text{rd/s}$ and -4rd/s in low speed inversion mode. Throughout the simulation, the value of the reference flux is maintained at 1Wb thanks to a weakening block.

Some tests using the MATLAB/SIMULINK environment are performed to show the performance of the fuzzy backstepping control in the transient and permanent regime for a healthy DSIM. The machine is only under the load torque (equal to the nominal value of 15N.m) which is applied at $t=1\text{sec}$, followed by a speed reversal at $t=1.5\text{sec}$. Fig. 7.a presents the simulation results of the rotor speed signal. With FBSC, the speed follows its reference value (4rd/s) without overtake, imposing the smallest average static error, while BSC imposes a fast dynamic, but with an overtaking of 10% , the static error is large at steady-state. No oscillations in speed response after $t=1\text{sec}$ for both control strategies, which explains the rejection of the load torque effect. When the DSIM operates in speed reversal at $t=1.5\text{sec}$, the FBSC ensures a smooth and precise speed reversal with a good reference tracking (-4rd/s). Fig. 7.b illustrates a good electromagnetic response with a nominal load application, but with the BSC, at start-up and speed reversal, the electromagnetic torque has the highest peaks of 60N.m and -60N.m respectively, after a fast dynamic, the torque compensates the friction losses and the load torque. No ripples in the steady-state electromagnetic signal proving that the FBSC scheme is able to compensate for external load torque.

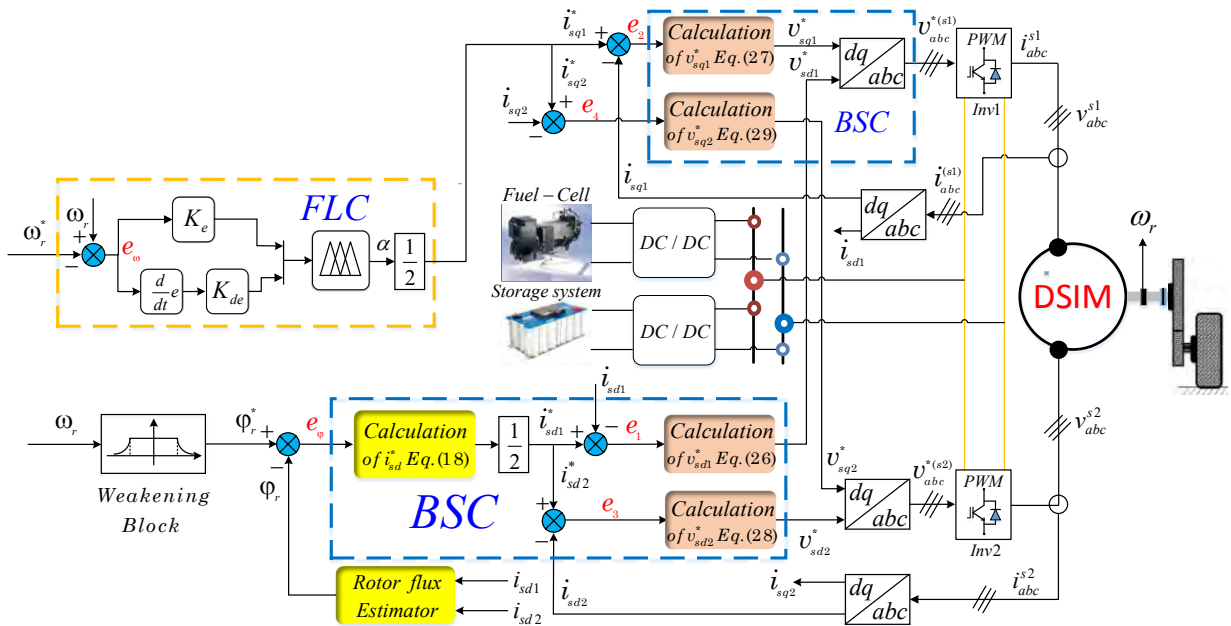
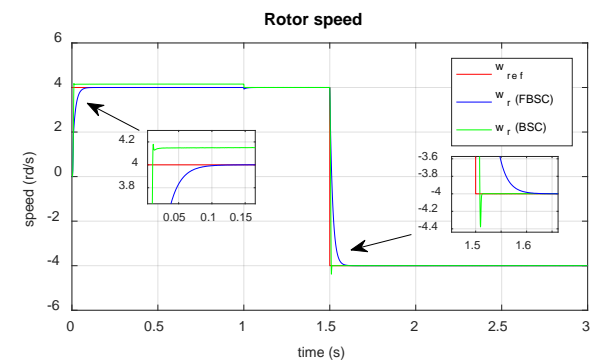
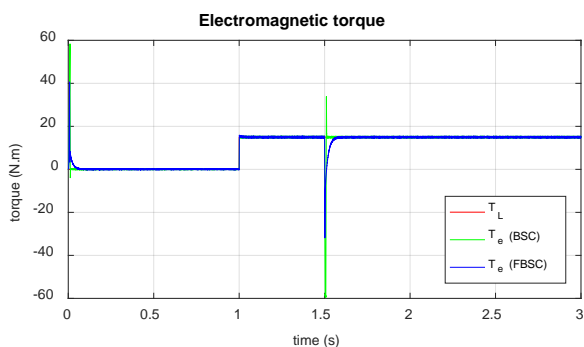


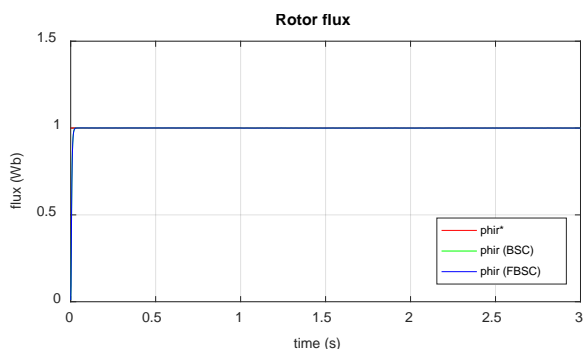
Figure.6: Global FBSC scheme of HEV system



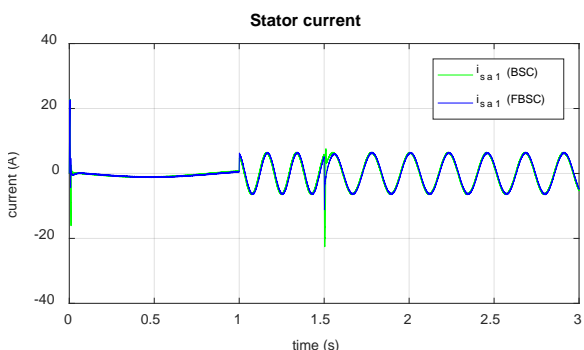
(a)



(b)



(c)



(d)

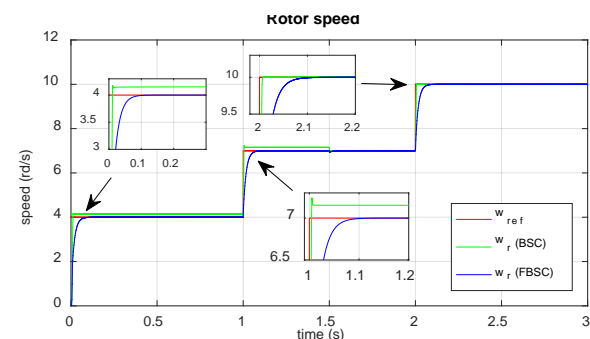
Figure.7: Simulation results of BSC and FBSC

Fig. 7.c proves that the FBSC is able to correctly lead the flux to its desired reference (1Wb), even under load torque disturbances and speed reversal. Fig. 7.d

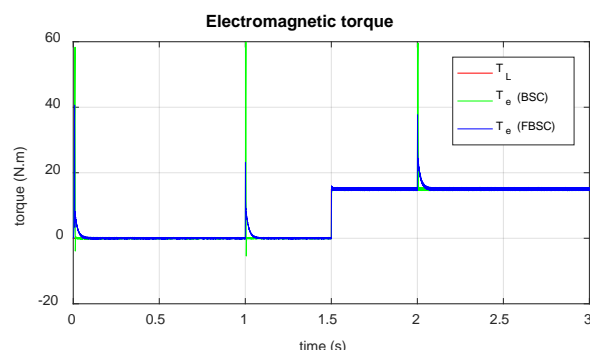
shows the behavior of the line current i_{sa1} of the first stator which has a steady-state sinusoidal waveform, slightly affected by the switching frequency generated by the inverters. During the dynamic states (start-up and speed reversal), the DSIM consumes very important currents, with the BSC, there are three peaks of current: 22A, -16A and -22A, the amplitudes of these peaks decreased when using FBSC: 22A, -4A and -11A. When inserting the load, the amplitude of currents reaches 6.5A for both control methods. The obtained results summarize and reflect the improvement in the dynamic and steady-state of DSIM in low speed operation when controlled by the FBSC.

Test of robustness

Influence of the speed variation on the electromagnetic torque response is shown in Fig. 8.



(a)



(b)

Figure.8: Simulation response to a stair of reference speed (4rd/s, 7rd/s and 10rd/s) with rated load at $t=1,5s$

The change of the reference speed is chosen as follows: ($0s < t < 1s$: $\omega_{ref}=4rd/s$), ($1s < t < 2s$: $\omega_{ref}=7rd/s$) and ($2s < t < 3s$: $\omega_{ref}=10rd/s$). It can be seen that the amplitude of the transient

peaks is reduced with FBSC due to its better perturbations rejection. The DSIM using the FBSC offers good performance and better stability at variable low speed.

7. CONCLUSION

In this paper, a fuzzy backstepping control applied to the low speed regulation of a double star induction machine driving an HEV has been presented. The proposed control uses the robustness of the BSC and the smoothness of the FLC. The validity of the proposed control is confirmed via MATLAB/SIMULINK. Obtained results assert that the combination of FLC-BSC improves the dynamic performance of the HEV in lower speed operation, where the speed tracks the desired reference without overshoot or static error. In addition, the robustness test shows that the proposed control is insensitive to low speed variation and external disturbances. The proposed control can replace the classic backstepping control, especially in critical operations. As future work, the proposed control will be injected into a fault-tolerant control system for a HEV driven by DSIM with a new version without a speed sensor.

REFERENCES

- [1] Layadi. N, Zeglache. S, Benslimane. T and Berrabah. F, "Comparative Analysis between the Rotor Flux Oriented Control and Backstepping Control of a Double Star Induction Machine (DSIM) under Open-Phase Fault," *AMSE Journals, Series Advances C*, Vol. 72, No. 4, pp. 292-311, 2017.
- [2] Youb. L, Belkacem. S, Naceri. F, Cernat. M and Pesquer. L, "Design of an Adaptive Fuzzy Control System for Dual Star Induction Motor Drives," *Advances in Electrical and Computer Engineering*, Vol. 18, No. 3, pp. 37-44, 2018.
- [3] Iffouzar. K, Amrouche. B, Cherif. T.O, Benkhoris. M.F, Aouzellag. D and Ghedamsi. K, "Improved direct field oriented control of multiphase induction motor used in hybrid electric vehicle application," *International Journal of Hydrogen Energy*, Vol. 42, No. 30, pp. 19296-19308, 2017.
- [4] Wang. M, Tong. C, Song. Z, Liu. J and Zheng. P, "Performance Analysis of an Axial Magnetic-Field-Modulated Brushless Double-Rotor Machine for Hybrid Electric Vehicles," *IEEE Transactions on Industrial Electronics*, Vol. 66, No. 1, pp. 806-817, 2019.
- [5] Ma. G, Ghasemi. M and Song. X, "Integrated Powertrain Energy Management and Vehicle Coordination for Multiple Connected Hybrid Electric Vehicles," *IEEE Transactions on Vehicular Technology*, Vol. 67, No. 4, pp. 2893-2899, 2018.
- [6] Yang. Y and Yan. Y, "Backstepping sliding mode control for uncertain strict-feedback nonlinear systems using neural-network-based adaptive gain scheduling," *Journal of Systems Engineering and Electronics*, Vol. 29, No. 3, pp. 580-586, 2018.
- [7] Echeikh. H, Trabelsi. R, Iqbal. A, Bianchi. N and Mimouni. M.F, "Non-linear backstepping control of five-phase IM drive at low speed conditions—experimental implementation," *ISA transactions*, Vol. 65, pp. 244-253, 2016.
- [8] Tir. Z, Soufi. Y, Hashemnia. M.N, Malik. O.P. and Marouani. K, "Fuzzy Logic Field Oriented Control of Double Star Induction Motor Drive," *Electrical Engineering*, Vol. 99, No. 2, pp. 495-503, 2017.
- [9] Lekhchine. S, Bahi. T and Soufi. Y, "Indirect rotor field oriented control based on fuzzy logic controlled double star induction machine," *International Journal of Electrical Power & Energy Systems*, Vol. 57, pp. 206-211, 2014.
- [10] Liu. Z, Zheng. Z and Li. Y, "Enhancing fault-tolerant ability of a nine-phase induction motor drive system using fuzzy logic current controllers," *IEEE Transactions on Energy Conversion*, Vol. 32, No. 2, pp. 759-769, 2017.
- [11] El-Fergany. A.A, "Electrical characterisation of proton exchange membrane fuel cells stack using grasshopper optimiser", *IET Renewable Power Generation*, Vol. 12, No. 1, pp. 9-17, 2017.
- [12] Zuo. W, Li. R, Zhou. C, Li. Y, Xia. J and Liu. J, "Battery-Supercapacitor Hybrid Devices: Recent Progress and Future Prospects," *Advanced Science*, Vol. 4, No. 7, pp.1600539, <https://doi.org/10.1002/advs.201600539>, 2017.

Temperature Effects on the Structure InP/InGaP IBQD for Solar Cell

Nabila HARCHOUCH¹, Abdelkader AISSAT^{1,2,*} and Jean Pierre VILCOT²

¹Faculty of Technology University of Blida.1 09000, Blida, Algeria

²Institut d'Electronique, de Microélectronique et de Nanotechnologie, UMR CNRS 8520, Université des Sciences et Technologies de Lille1, Avenue Poincaré, CS 60069, 59652 Villeneuve d'Ascq, France
sakre23@yahoo.fr

ABSTRACT

In this work, we are interested in modeling and simulation of InP/InGaP quantum dot solar cell, two parameters were investigated the number of quantum dots embedded in the solar cell's structure and the thermal effect on their parameter characteristics, first we have studied the effect of number of quantum dot layers inserted, the insertion of 30 quantum dot layers gives better results, then we have studied the effect of the temperature on the parameter characteristics of InP/InGaP solar cell with 30 quantum dot layers, like all other semiconductor devices solar cells are sensitive to temperature the most parameter affected by the temperature rising is the open circuit voltage, the increase of temperature from 260 to 400K leads to the decrease of V_{oc} from 0.67V to 0.48V and, in turn, the conversion efficiency from 17.26% to 12.20%, however the J_{sc} increases slightly from 31.64 Am/cm² for 260 K to 32.02 Am/cm² for 400K .

Keywords: Quantum Dot, Solar Cell, Temperature, Thermal Effect.

1. INTRODUCTION

Several external factors degrade the performance of solar cells the most important factor is the temperature. Temperature rising is a negative factor in almost all systems, high operating temperatures tend to cause performance degradation or even malfunctioning of circuits and components, thus reducing the reliability of all system. In solar photovoltaic cells this temperature rising affects on the behavior of cells and therefore the electrical properties of solar cells such as short circuit current, open

circuit voltage, the fill factor and conversion efficiency [1-2]. The quantum dots is one of the indispensable technology for realizing photovoltaic devices with high efficiency, they allow the tuning of the effective band gap which lead to the tuning of the optical properties to correspond to the desired wavelength. For photovoltaic applications, such as quantum dot solar cells (QDSCs) which are known as third generation solar cells, the quantum dot structure have been demonstrated an improvement in the solar cells characteristics such as short circuit current, open circuit voltage and conversion efficiency [3-4], this due to the absorption of sub-band gap photons. III-V QDs solar cells are one of the most active research fields, among them the InAs/GaAs, GaSb/GaAs, InGaAs/GaAs, AlGaAs/GaAs; their physical and optical properties have enhanced the solar cell's efficiency [5-6]. Recently a lot of works concentrate on novel structure to boost the photovoltaic conversion efficiency like the InGaP which was integrated in GaAs quantum dot structures, previously works have been used the InGaP for double and triple junction photovoltaic also for tandem solar cells [7-9].

In the present paper we are interested in modeling and simulation of InP/InGaP quantum dots solar cell to show the effect of the insertion of quantum dot layers and the temperature on the characteristic parameters of the studied solar cell. The schematic diagram of the present InP/InGaP Quantum Dot Solar Cell is shown in fig.1.



Figure.1: Structure of InP/InGaP quantum dots solar cell.

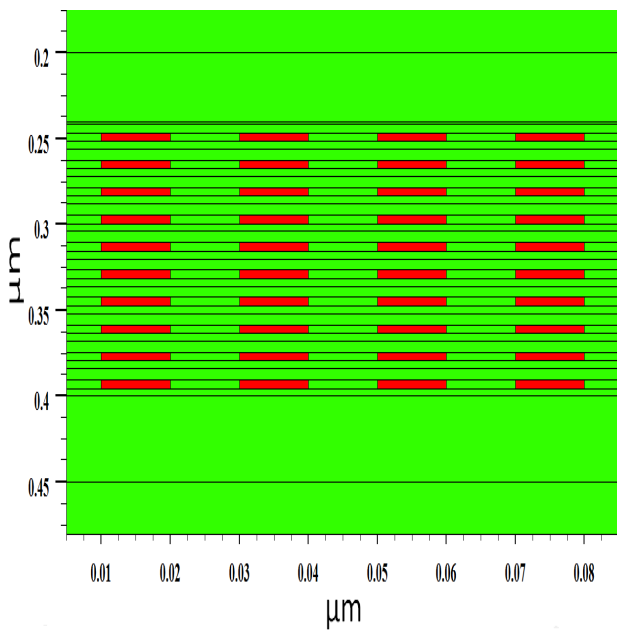


Figure.2: Zoom of the quantum dots region within the InP/InGaP quantum dots solar cell structure.

All the quantum dot solar cells have a p-i-n structure consisting of 50 nm GaAs contact layer with Be doping density of 1×10^{19} , 30 nm $\text{Al}_{0.75}\text{Ga}_{0.25}\text{As}$ window layer with Be doping of $2 \times 10^{18} \text{ cm}^{-3}$, 200 nm GaAs emitter layer with

Be doping density of $2 \times 10^{18} \text{ cm}^{-3}$, intrinsic region which contains a different number of InP/In $_{0.5}$ Ga $_{0.5}$ P quantum dot layers (see zoom in fig. 2), the quantum dots are capped by 15 nm i - GaAs which separates the quantum dot layers, 300 nm GaAs base layer with Si doping density of $1 \times 10^{17} \text{ cm}^{-3}$, and 200 nm GaAs buffer layer with Si doping density of $1 \times 10^{18} \text{ cm}^{-3}$, the structure is deposited on GaAs substrate.

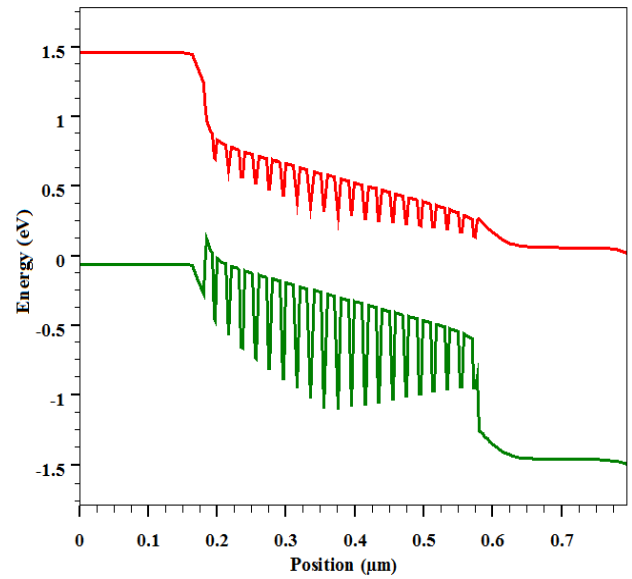


Figure.3: Simulated band diagram of InGaP/InP quantum dots solar cell structure.

All the quantum dot solar cells have a p-i-n structure consisting of 50 nm GaAs contact layer with Be doping density of 1×10^{19} , 30 nm $\text{Al}_{0.75}\text{Ga}_{0.25}\text{As}$ window layer with Be doping of $2 \times 10^{18} \text{ cm}^{-3}$, 200 nm GaAs emitter layer with Be doping density of $2 \times 10^{18} \text{ cm}^{-3}$, intrinsic region which contains a different number of InP/In $_{0.5}$ Ga $_{0.5}$ P quantum dot layers (see zoom in fig. 2), the quantum dots are capped by 15 nm i - GaAs which separates the quantum dot layers, 300 nm GaAs base layer with Si doping density of $1 \times 10^{17} \text{ cm}^{-3}$, and 200 nm GaAs buffer layer with Si doping density of $1 \times 10^{18} \text{ cm}^{-3}$, the structure is deposited on GaAs substrate. Fig.3 shows the simulated band diagram of quantum dots solar cell structure under the AM 1.5G illumination where quantum dots are inserted inside the intrinsic region of a p-i-n solar cell structure. The

concept of quantum dots create a sub-bandgap photons which contribute to the device current, whereas the carriers confined in the intrinsic region will be pumped to the emitter and base region, and therefore enhances the photocurrent of the solar cell.

2. THEROTICAL MODEL

In this section we will see the equations used in the modeling and simulation of this structure and the relation between the main parameters of solar cells and the temperature of an idealized single-junction PV cell.

Poisson's Equation relates the electrostatic potential ψ to the space charge density [10].

The current densities in the continuity equations may be approximated by a drift-diffusion model [11].

The solution of Schrodinger's equation gives a quantized description of the density of states in the presence of quantum mechanical confining potential variations [12].

The Capture-Escape Model treats the dynamics of bound carriers by breaking carriers into bulk and bound subsystems coupled to each other by a capture-escape rate [12,13].

- The lattice constant of $\text{In}_{1-x}\text{Ga}_x\text{P}$ material system with composition dependent is given by the Vegard's law:

$$a_{\text{In}_{1-x}\text{Ga}_x\text{P}} = (1-x)a_{\text{InP}} + xa_{\text{GaP}} \quad (1)$$

Where a_{InP} is the lattice constant of InP , a_{GaP} is the lattice constant of GaP there values are 5.87\AA , 5.45\AA respectively.

- The composition dependent of energy band gap is given by [14]:

$$E_{\text{In}_{1-x}\text{Ga}_x\text{P}} = 1.35 + 0.73x + 0.7x^2 \quad (2)$$

- The strain produced between $\text{In}_{1-x}\text{Ga}_x\text{P}$ and InP is given as follows:

$$\varepsilon = \frac{a_{\text{InP}} - a_{\text{In}_{1-x}\text{Ga}_x\text{P}}}{a_{\text{In}_{1-x}\text{Ga}_x\text{P}}} \quad (3)$$

- The strain produced between $\text{In}_{1-x}\text{Ga}_x\text{P}$ and GaAs is given as follows:

$$\varepsilon = \frac{a_{\text{GaAs}} - a_{\text{In}_{1-x}\text{Ga}_x\text{P}}}{a_{\text{In}_{1-x}\text{Ga}_x\text{P}}} \quad (4)$$

- The open-circuit voltage is the maximum voltage available from a solar cell; V_{oc} is strongly dependent on temperature. For an ideal p-n junction, V_{oc} can be given as [1]:

$$V_{oc} = \frac{KT}{q} + \ln\left[\left(\frac{I_{ph}}{I_s}\right) + 1\right] \quad (5)$$

Where, K is Boltzmann constant, T is the temperature, q is the electronic charge, I_{ph} is the photocurrent, and I_s , is the diode saturation current.

- The short circuit current (I_{sc}) increases slightly with temperature, for an ideal p-n junction, I_{sc} can be given as [15]:

$$I_{sc} = I_s \left[\exp\left(\frac{qV}{KT}\right) - 1 \right] - I_{ph} \quad (6)$$

- Fill factor is defined as the ratio of the maximum power output (P_{max}) at the maximum power point to the product of I_{sc} and V_{oc} . The fill factor can be given as [2]:

$$FF = \frac{I_m \times V_m}{I_{sc} \times V_{oc}} \quad (7)$$

Where I_m is the maximum current and V_m is the maximum voltage:

- The efficiency of a solar cell is the ratio of the power output corresponding to the maximum power point to the power input the efficiency (η) can be given as [2]:

$$\eta = \frac{I_{sc} \times V_{oc} \times FF}{P_{in}} \quad (8)$$

Where P_{in} is the power input.

3. RESULTS AND DISCUSSION

In this work, we are interested in modeling and simulation of InP/In_{0.5}Ga_{0.5}P quantum dots solar cell in goal to enhance the standard solar cell performances. Along the first part of this work, all simulations were performed at room temperature using AM1.5 of one sun. The composition fraction of In_{1-x}Ga_xP used in solar cells grown on GaAs is around 0.5 Ga_{0.5}In_{0.5}P that is lattice matched to GaAs. The simulation of InP/In_{0.5}Ga_{0.5}P quantum dots solar cells for different number of quantum dots layers 10, 20, and 30, respectively is done to indicate the influence of the quantum dots on spectral response and the current-voltage characteristics.

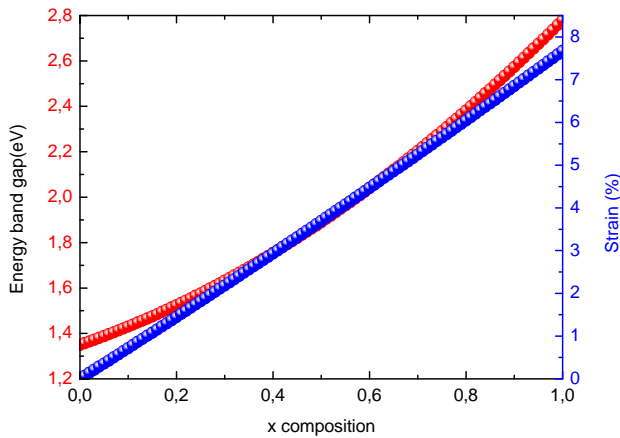


Figure.4: Simulated strain of In_{1-x}Ga_xP /InP material composition dependence

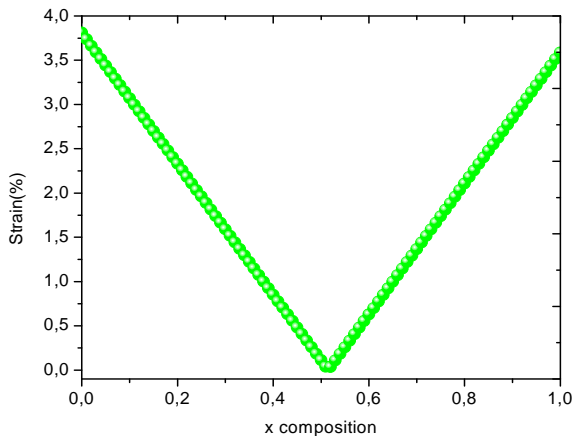


Figure.5: Simulated strain of In_{1-x}Ga_xP /GaAs material composition dependence

Fig.7 presents the simulated EQE values as a function of wavelength. The External Quantum Efficiency EQE is the ratio of the number of photo generated electron-hole pairs collected at the electrodes to the number of incident photons. As we can see in this figure the EQE gradually increases with inserting the quantum dot layers, there is a clear enhancement of EQE in the wide range of 500-800 nm for all the solar cell devices [21-22]. The EQE of a reference GaAs cell turn to zero around the wavelength of 900 nm this wavelength is extending to 1020 nm by adding the quantum dot layers ,this enhancement is related to the increase of number of quantum dots, In the range of 900-1020 nm there is an enhancement of EQE for devices with 30 quantum dots. These results confirm what we have obtained and presented previously in fig.6.

The increase of quantum dot layers improves the absorption of light, it leads to have more and more sub-band photons, which enhance the creation of electron-hole pairs therefore, contribute to the additional photocurrent [23-24].

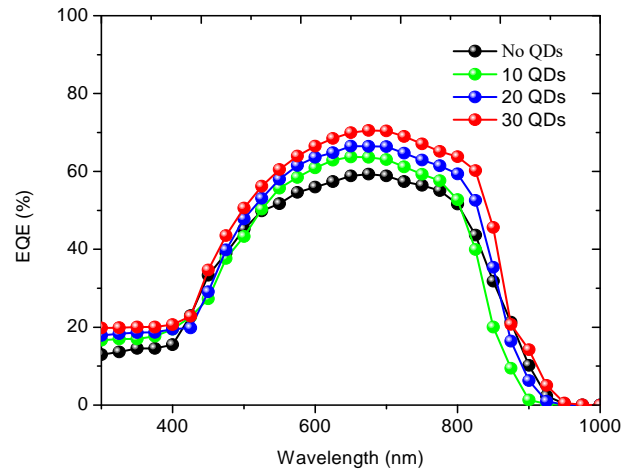


Figure.7: External Quantum Efficiency versus the wavelength for InP/InGaP QDSCs.

The current density–voltage characteristics for these devices for different number of quantum dots are presented in fig. 6 and summarized in table I.

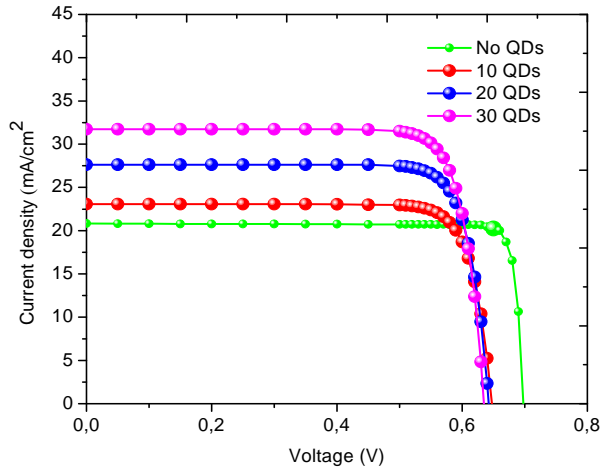


Figure.8: J (V) of InP/InGaP for different number of quantum dot layers.

Compared to the reference cell, all the quantum dot solar cells have a high short circuit current density J_{sc} and low open circuit voltage V_{oc} , due to the effect of quantum dot embedded in the intrinsic region. Also as we can see in fig. 6 there is a clear enhancement of the short circuit current density J_{sc} with increasing number of quantum dots introduced in the intrinsic region, the short circuit current density increases from 23.07 mA/cm² for 10 QDs to 31.73 mA/cm² for 30 QDs this enhancement could be explained by the improvement of the additional sub-band gap absorption from QDs.

TABLE 1. The important parameters of InP/InGaP quantum dot solar cell for different number of qds layers

QDs	J_{sc} (mA/cm ²)	V_{oc} (V)	FF(%)	η (%)
No QDs	20.82	0.7	79.93	11.65
10	23.07	0.657	83	12.58
20	27.64	0.644	82.36	14.66
30	31.73	0.635	82.33	16.59

However, the increase of number of quantum dots stacked into the intrinsic region leads to a degradation of the open circuit voltage V_{oc} from 0.657 V for 10 QDs to 0.635 V for 30 QDs [16-17].The reduction in the open circuit voltage may

have resulted by the thickness of the active region. When the number of quantum dots inserted in the intrinsic region becomes very high, this leads to have a large lattice mismatch. The strain induced defects act as a non radiative recombination [18-20]. In this second part; we have studied the effect of the temperature on the InP/In_{0.5}Ga_{0.5}P -30 QDSC to show the effect of the temperature on the characteristics parameters of the studied solar cell.

TABLE 2. The important parameters of inp/ingap -30 quantum dots solar cell with different temperature.

Temperature (K)	J_{sc} (mA/cm ²)	V_{oc} (V)	FF (%)	η (%)
260	31.64	0.675	80.81	17.26
280	31.72	0.652	81.18	16.79
300	31.73	0.635	82.33	16.59
320	31.81	0.604	80.81	15.56
340	31.85	0.58	80.65	14.9
360	31.87	0.556	78.44	13.9
380	31.91	0.53	77.87	13.17
400	32.02	0.482	79.04	12.2

The current density–voltage characteristics for different values of temperature are shown in fig. 8. The temperature dependences of the short circuit current, open circuit voltage and conversion efficiency of InP/InGaP QDSC are calculated and shown in table II, fig. 9 and fig. 10. As we can see in fig.8 and fig.9 the open circuit voltage decreases with increasing temperature. From 0.675 V for 260 K to 0.482 V for 400 K due to the decrease in the band gap. However, the short circuit current density increases with increasing temperature from 31.64 mA/cm² for 260 K to 32.02 mA/cm² for 400 K as shown in fig.9. This increasing could be well explained by the decrease in the band gap with temperature for most semiconductors. As the temperature increases the band gap decreases. The solar cell responds to longer wavelength in the solar spectrum so more photons have enough energy to create electrons holes pairs and therefore J_{sc} increases.

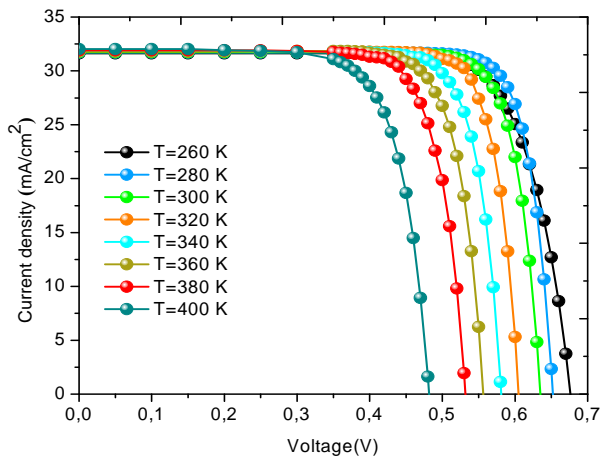


Figure.8: J (V) of InP/InGaP characteristics for different values of Temperature.

Fig.10 shows the change in conversion efficiency with temperature. The fill factor and conversion efficiency decrease with increasing the temperature, as it is shown in table II. The decrease in fill factor and the conversion efficiency is mainly due to the decrease in the open circuit voltage. Whereas, the increase in the short circuit current with temperature it will not significantly affect the fill factor and the conversion efficiency [25-27].

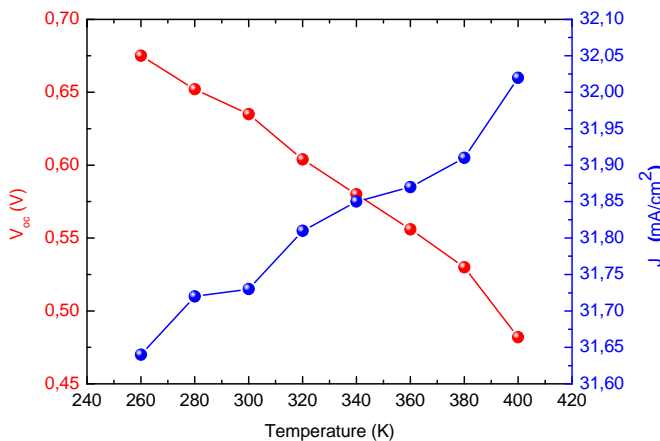


Figure.9: Short-circuit current density (J_{sc}) and open circuit voltage (V_{oc}) versus Temperature for InP/InGaP -30 QDSC.

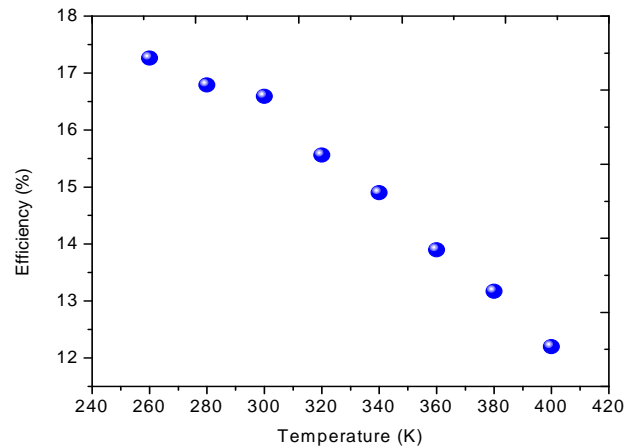


Figure.10: Conversion Efficiency (η) versus Temperature for InP/InGaP-30 QD.

4. CONCLUSION

In this work, the structure InP/In_{0.5}Ga_{0.5}P solar cell with quantum dot structure showed an enhancement of conversion efficiency compared with reference GaAs solar cell. The maximum value of conversion efficiency of 16.59 % is obtained under 1 Sun AM1.5G with 30 QDs. The values of the short circuit current and open circuit voltage have been changed with the number of quantum dot layers inserted from 10 QDs to 30 QDs. The analysis of the temperature dependence electrical properties showed a slight increasing of the short circuit current and degradation in the open circuit voltage with increasing the temperature leading to the degradation in fill factor and conversion efficiency.

REFERENCES

- [1]. E. Skoplaki, JA. Palyvos, "Operating temperature of photovoltaic modules: a survey of pertinent correlations," *Renew Energ* 2009; 34:23e9.
- [2]. G. Landis, R. Raffaele, D. Merritt, "High temperature solar cell development", 19th European Photovoltaic Science and Engineering Conference, Paris, France, June 7-11, 2004.

- [3]. K. Yoshida, Y. Okada, and N. Sano, "Device simulation of intermediate band solar cells: Effects of doping and concentration," *J. Appl. Phys.* 112, 084510 (2012).
- [4]. A. Luque and A. Marti, "The intermediate band solar cell: progress toward the realization of an attractive concept", *Advanced Materials* 2010, 22, (2), pp 160-174.
- [5]. F.K. Tutu, I.R. Sellers, M.G. Peinado, C. E. Pastore, S. M. Willis, A. R. Watt, T. Wang, and H. Y. Liu, "Improved performance of multilayer InAs/GaAs quantum-dot solar cells using a high-growth-temperature GaAs spacer layer on Electricity and Magnetism," *J. Appl. Phys.* 111(4), 046101 (2012).
- [6]. C. Vurgaftman, I., J.R. Meyer, L. R. Ram-Mohan, "Band Parameters for III-V Compound Semiconductors and their Alloys", *Journal of Applied Physics* Vol. 89, No. 11 (June 2001): 5815-5875.
- [7]. K.Sasaki, T. Agui, K. Nakaido, N. Takahashi, R. Onitsuka, and T. Takamoto, "Development Of InGaP/GaAs/InGaAs Inverted Triple Junction Concentrator Solar Cells," *AIP Conference Proceedings* 1556, 22 (2013); doi: 10.1063/1.4822190
- [8]. A.S. Gudovskikh , J.P.Kleider, N.A.Kalyuzhnyy , V.M.Lantratov , S.A.Mintairov, "Band structure at heterojunction interfaces of GaInP solar cells," *Solar Energy Materials & Solar Cells* 94 (2010) 1953–1958
- [9]. D. Shahrjerdi, S. Bedell, C. Ebert, C. Bayram, B. Hekmatshoar, K.Fogel, P.Lauro, M.Gaynes, T.G okmen, J.Ott, and D.Sadana, "High-efficiency thin-film InGaP/InGaAs/Ge tandem solar cells enabled by controlled spalling technology , " *Appl. Phys. Lett.* 100, 053901 (2012).
- [10]. Pinto M.R., Conor S. Rafferty, and Robert W. Dutton, "PISCES2 - Poisson and Continuity Equation Solver", *Stanford Electronics Laboratory Technical Report, Stanford University, September 1984.*
- [11]. S.Selberherr, *Analysis and Simulation of Semiconductor Devices.* Wien, New York: Springer-Verlag, 1984.
- [12]. R.Mahapatra, R.Melnik, M.Willatzen, B.Lassen and L.Voon, "Poisson-Schrodinger Model in the Analysis of Coupled Effects in Quantum Well Nanostructures," 2006 Conference on Optoelectronic and Microelectronic Materials and Devices, Perth, WA, 2006, pp. 280-282.
- [13]. S. M. Ramey and R. Khoie, "Modeling of multiple-quantum-well solar cells including capture, escape and recombination of photo excited carriers in quantum wells," *IEEE Trans. Electron. Devices*, vol. 50, no. 5, pp. 1179– 1188, 2003.
- [14]. Martinez, O., et. al., "InGaP Layers Grown on Different GaAs Surfaces for High Efficiency Solar Cells", *Mater. Res. Soc. Symp. Vol. 1167, Materials Research Society, (2009): Paper 1167-003-04.*
- [15]. B. U. Mustapha., M. K. Musa1. Dikwa and M. Abbagana, "Electrical Parameters Estimation of Solar Photovoltaic Module," *Journal of Engineering and Applied Science*, vol. 4, 28-37(2012).
- [16]. T. Sugaya, R. Oshima, K. Matsubara, and S. Niki, "InGaAs quantum dots on InGaP layers grown by solid-source molecular beam epitaxy," *J. Cryst. Growth*, vol. 378, pp. 430–434, 2013.
- [17]. H.Yoshikawa, T.Kotani, Y.Kuzumoto, M.Izumi, Y.Tomomura, C.Hamaguchi, "Proposal of high efficiency solar cells with closely stacked InAs/In_{0.48}Ga_{0.52}P quantum dot superlattices: analysis of polarized absorption characteristics via intermediate-band," *Appl.Phys.Lett.* 105(2014)011120.
- [18]. K. Sablon, J. Little, N. Vagidov, Y. Li, V. Mitin, and A. Sergeev, "Conversion of above- and below-bandgap photons via InAs quantum dot media embedded into GaAs solar cell, " *APPLIED PHYSICS LETTERS* 104, 253904 (2014).
- [19]. Yeongho Kim, Keun-Yong Ban, and Christiana B. Honsberg, "Multi-stacked InAs/GaAs quantum dots grown with different growth modes for quantum dot solar cells, " *Applied Physics Letters* 106, 222104 (2015).
- [20]. P.Lam, J.Wu, S.Hatch, D.Kim, M.Tang, H.Liu, "The Effect of Rapid Thermal Annealing on InAs/GaAs Quantum Dot Solar Cells," *IET Optoelectron.*, vol. 9, iss. 2, pp. 65-68, 2014.
- [21]. P.Lam, J.Wu, M.Tang, D.Kim, S.Hatch, I.Ramiro, V.G.Dorogan, M.Benamara, Y.I.Mazur, G.J.Salamo, J.Wilson, R.Allison, H.Liu, "InAs/InGaP quantum dot solar cells with an AlGaAs interlayer," *Solar Energy Materials & Solar Cells* 144(2016)96–101.

- [22]. T. Aihara, T. Tayagaki, Y. Nagato, Y. Okano, and T. Sugaya, "InGaP-based InP quantum dot solar cells with extended optical absorption range," *Jpn. J. Appl. Phys.* 56, 04CS06 (2017).
- [23]. P.Lam, J.Wu, M.Tang, Q.Jiang, S.Hatch, R.Beanland, J.Wilson, R.Allison, H.Liu, "Submonolayer InGaAs/GaAs quantum dot solar cells," *Solar Energy Materials & Solar Cells* 126 (2014)83–87.
- [24]. D. Alonso-Alvarez, A. G. Taboada, J. M. Ripalda, B. Alen, Y. Gonzalez, L. Gonzalez, J. M. García, F. Briones, A. Martí, A. Luque, A. M. Sanchez, and S. I. Molina, "Carrier recombination effects in strain compensated quantum dot stacks embedded in solar cells," *APPLIED PHYSICS LETTERS* 93, 123114 (2008).
- [25]. J.Jiang, J.Wang, K.Kuo, Y.Su, J.Shieh, J.Chou, "Analysis of the junction temperature and thermal characteristics of photovoltaic modules under various operation conditions," *Energy* 44 (2012) 292e301.
- [26]. P. Loper, D. Pysch, A. Richter, M. Hermle, S. Janz, M. Zacharias, S.W. Glunz, "Analysis of the Temperature Dependence of the Open-Circuit Voltage," *Energy Procedia* 27 (2012) 135 – 142.
- [27]. A. Elnozahy, Ali K. Abdel Rahman, Ahmed Hamza H. Ali, Mazen Abdel-Salam, and S. Ookawara, "Thermal/Electrical Modeling of a PV Module as Enhanced by Surface Cooling," *Journal of Clean Energy Technologies*, Vol. 4, No. 1, January 2016.

Exploitation of the XGS in the FPGA Hardware Implementation of a medical Image Signal Processing

Saliha OULD SLIMANE¹, Fouad BELALEM¹, Malika-D. KEDIR-TALHA ¹
and Karim MEDDAH¹

¹ USTHB, LINS Lab, Faculty of Electronics and Computers, PO.Box 32, Bab-Ezzouar, Algiers
ouldelhadjsaliha@gmail.com, fouadrm93@gmail.com, malikakedir@gmail.com, ka.meddah@gmail.com

ABSTRACT

This article presents the realization of an embedded system under FPGA in image signal digital processing for noise suppression and edge detection. The implementation was carried out using the advanced Xilinx System Generator (XSG) language and associating it with a high-level graphical interface under Matlab based on Simulink blocks. We validated this system by functional tests on many images under Matlab then under VHDL generated by XSG. The results obtained allowed us to appreciate the functionality and the performances of our system implemented under FPGA Nexys2.

Key Words: FPGA, Edge detection, VHDL, XSG.

1. INTRODUCTION

At present, there is a growing interest in the development and use of programmable logic circuits, such as FPGAs, in multidimensional applications of processing such as biomedical imaging and robotic vision that require high speed and flows. The capacity and performance of FPGAs have been improved to such an extent that these circuits have become a reconfigurable hardware platform of prototyping for the implementation of high performance image processing algorithms. They are now widely used in high performance filtering applications such as medical imaging, portable image, mobile video applications, satellite data, weather forecasts and seismic

data. The industrial goal in this case is to reduce the cost of these equipments by implementing them on programmable logic devices such as the FPGAs. As the complexity of FPGAs has increased, several tools and software have been associated with FPGA realizations to facilitate the algorithms implementation. The Xilinx Generator System is a Xilinx design tool that allows us to use Math Works design environment based on Simulink model for FPGA design. A design is modeled using the intuitive visual environment within Simulink that uses multiple sets of specific blocks to accelerate development.

In addition, the system can perform the FPGA implementation steps such as synthesis, mapping, and generation of FPGA executable files (.lib).

Integrating of embedded processing functionalities on an FPGA provides several benefits. There is no fixed architecture implementation and therefore no requirement that the functions be performed by hardware rather than software. There is therefore a vast choice of possible solutions for each application, ranging from more general to more specific. FPGAs provide very high performances of hardware with simple and fast use of software configuration.

Our work is to establish how convolution and multi-dimensional digital correlation operations are used for image digital processing applications such as image filtering, enhancement, and recognition, to

realize an embedded system under FPGA, [1].

2. PRETREATMENT OF IMAGES

To import data into the MATLAB workspace from a graphics file, we use the (Image from file) block. With this block, we can import file data in many formats of standard files, including the format (TIFF, GIF, JPEG, and PNG).

The Video Viewer block allows us to view a binary file, the intensity, an RGB image or a video stream. The block provides simulator controls for the game, pause, and stage of the model's execution.

The Resize block enlarges or shrinks an image by resizing the image along a dimension (row or column). Then, it resizes the image along the other dimension (column or row). This block supports intensity and color images on its ports. When we enter a floating point data type signal, the block issues the same data type.

The color space conversion block converts color information between color spaces. We use the conversion parameter to specify the color spaces. In our case we have chosen a transformation (R'G'B 'to intensity) to have a 2D gray image in order to be able to introduce the image into the next dimension conversion block.

The 2-D convector at 1-D block reshapes an M-by-N input matrix to a 1-D vector with a length $M * N$. The input is remodeled, as shown in Fig.1 for a 3-by-2 matrix. The frame block passes the input to the output by setting the output sample mode. The latter selected may at the base of samples or frames.

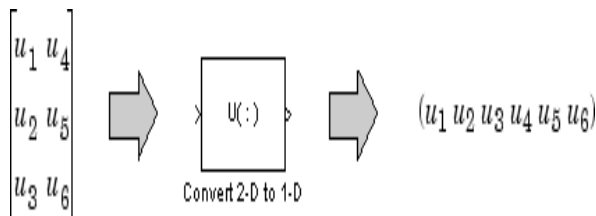


Fig. 1. Operating principle of a converter

The frame conversion block makes changes only on the sampling mode of the input signal. This block can not resize 2D inputs because 1-D vectors can not be sampled in

frame mode. When the input is a 1-D vector of length M and the conversion block is in frame mode, the output is an M-by-1 matrix or a single channel.

The Unbuffer block transforms an entry M_i by N, into a 1-by-N output. In other words, the inputs are arranged so that each row of the matrix becomes an independent sample time at the output. The rate at which the block receives inputs is generally less than the rate at which the block produces outputs, [2].

3. REALIZATION OF MEDIAN FILTER WITH THE XSG

The realization of a median filter requires the following blocks:

A. Window block

The pixel values of the input image are imported into this module in series. In order to obtain an NxN window, a number N of delay blocks are necessary where the first block has a zero delay and the others have a delay of 1. A window creation module 5x5 is represented in figure 2.

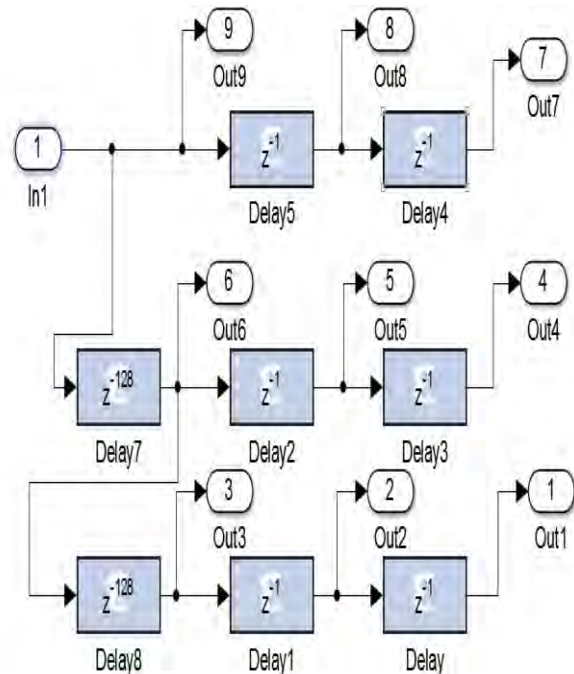


Fig. 2. windowing module

B. Calculation block

In this step, the calculation of the median value is done from the image where each

value window is divided into three parts. The median value for each part is then calculated to have the final median value. Figure 3 shows the block diagram used in the calculation of the median value.

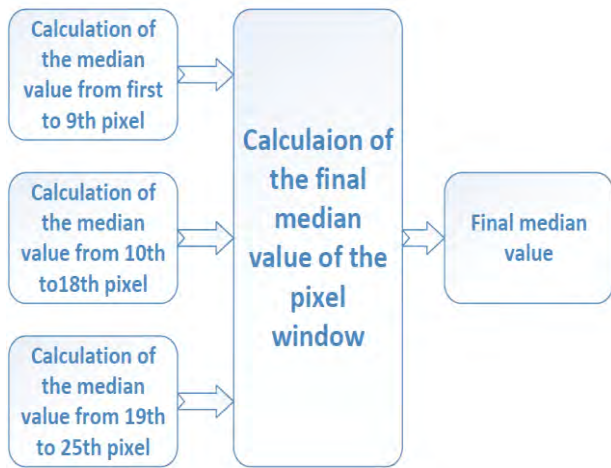


Fig. 3. Block diagram showing the calculation method used

To better detail the calculation method used, Figure 4 below shows the contents of a calculation block, this block calculates the maximum, minimum and median value of each of the three values separately in order to have the median value of the pixels introduced at the entrance of the block.

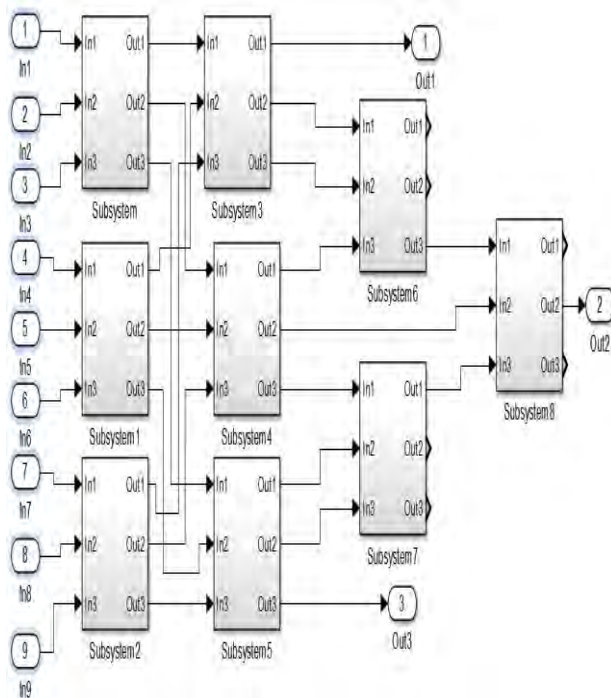


Fig. 4. Detailed calculation block

To obtain the three values mentioned above, multiplexers are used. They are connected to comparators. The value of one of the two inputs (a and b) will be propagated on the output of the multiplexer according to the value of sel (called selection): if sel = 0, the propagated value will be d0 and in the opposite case the propagated value will be d1. And figure5 below shows the internal calculation circuit.

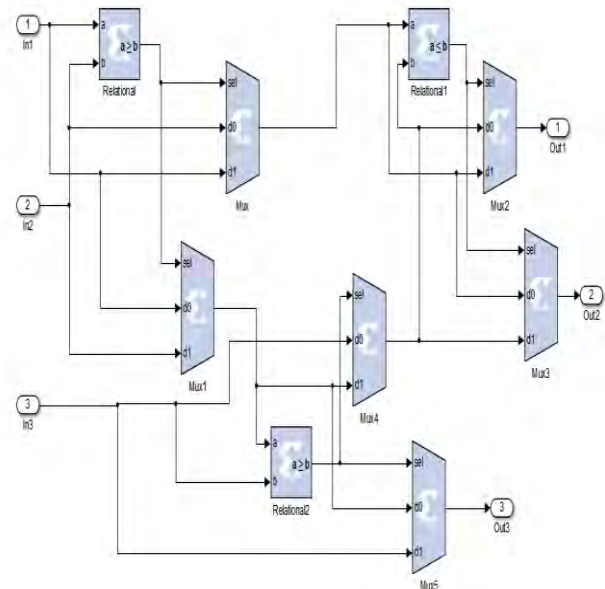


Fig. 5. Internal calculation circuit.

In the complete diagrams illustrated in Figures 6 and 7, we have a windowing block and a calculation block of the median value plus a selection block that does not replace the value of the central pixel by the median value of its neighborhood.

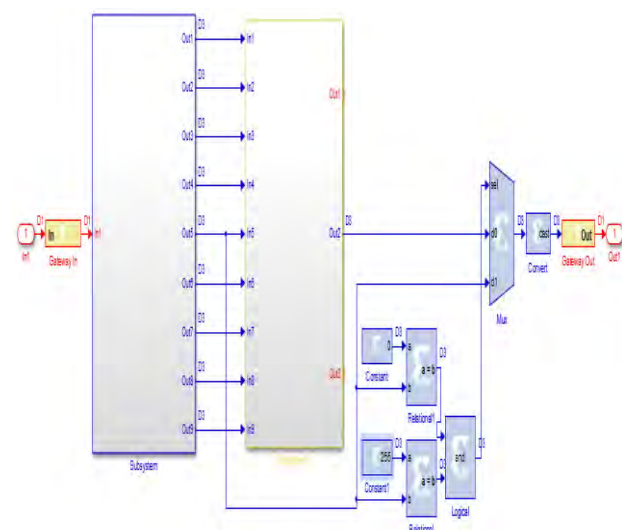


Fig. 6. Complete Block diagram of a 3x3 median filter.

Before simulating, we must add a noise: pepper and salt to compare our results with those obtained by matlab programming.

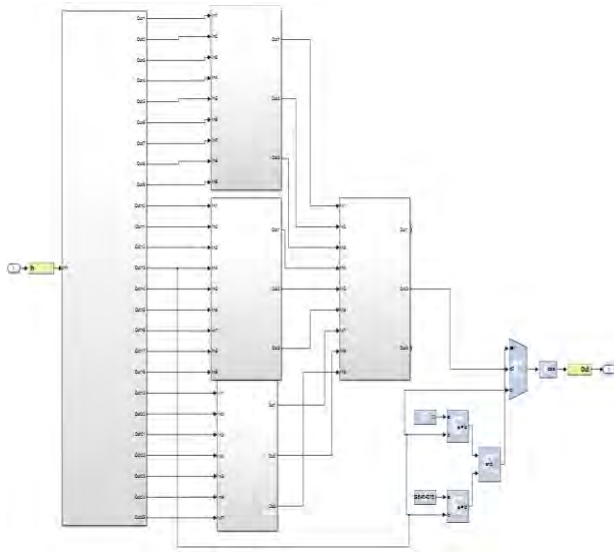


Fig. 7. Complete Block diagram of a 5x5 median filter.

For that we use the block (interpret matlab function) which allows us to add functions to the simulink block, [3-7].

C. Results

In this part we are interested in the design in VHDL language of digital filters mentioned before. For that, we used the software of Xilinx ISE 14.7 as well as Matlab 2011.

For the hardware implementation, we consider the performances of the FPGA card, especially the required memory space. The advantage of FPGAs is that make it possible to realize high performance filters in terms of speed.

However, the major difficulty is having the input and output image without any offset or loss of data.

After realizing the complete schema, we implemented it on the FPGA. The FPGA implementation consists of several steps namely: translation, mapping, placement, routing and finally the generation of the ".bit" configuration file in order to program the FPGA. To accomplish these steps, we used the ISE Xilinx 14.7 software where all the implementation tools are integrated into the ISE Navigator. To check the syntax problems of the program, we click on the item 'check syntax' then on the item

"Implement Design", which consists in translating the coded instructions of the program to the Hardware and make the location and the routing between logical blocks. The last step is the generation of the program in order to implement it on the card. To do this, we click on the item "Generate Programming File". At the end of this step, a 'JTAG' file is generated and we can load our design into the FPGA card.

▪ Stream Bit Generation

After generating the global system in VHDL under XSG, the next step is to generate the Bitstream file.

After BitStream generation, the JTAG file containing the VHDL program is generated. We obtain the figure 8.

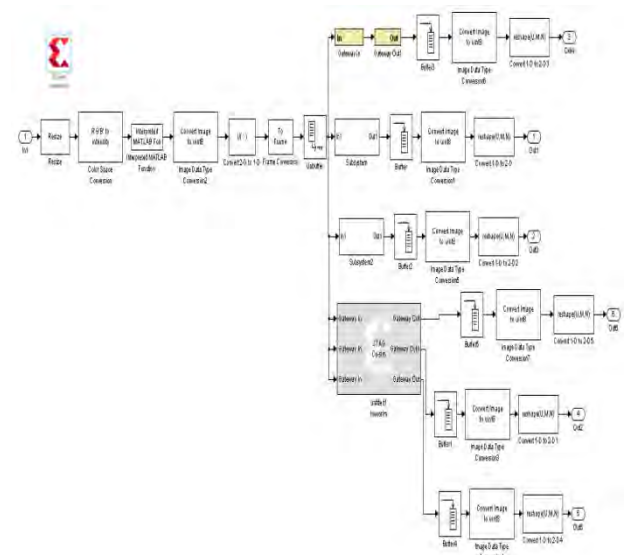


Fig. 8. Complete schema with the JTAG block.

The results obtained by simulation using the xilinx generator system, will be compared to the results obtained by Matlab programming . Figures 9 and 10 below illustrate the results obtained after simulation of median filters 3x3 and 5x5.

Comparing Fig.9(a) and Fig.9 (b) which represent the results obtained for the 3x3 median filter, under Matlab and the Xilinx generator system respectively, it is noted that the image obtained using XSG is identical to that obtained by Matlab programming.

Through the flexibility of programming the FPGA card, the size of the filter can be increased from 3x3 filter to 5x5 filter. Note that the results obtained with the 5x5 filter by Matlab programming are better than

those obtained with the Xilinx generator system. Indeed we see a loss in details and a decrease in the quality of the image.

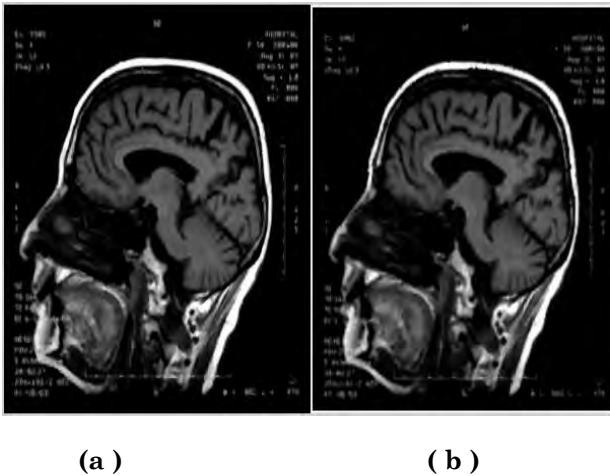


Fig. 9. Comparison of obtained results with the 3x3 median filter.

3x3 filtering is therefore better suited by using Xilinx generator system.

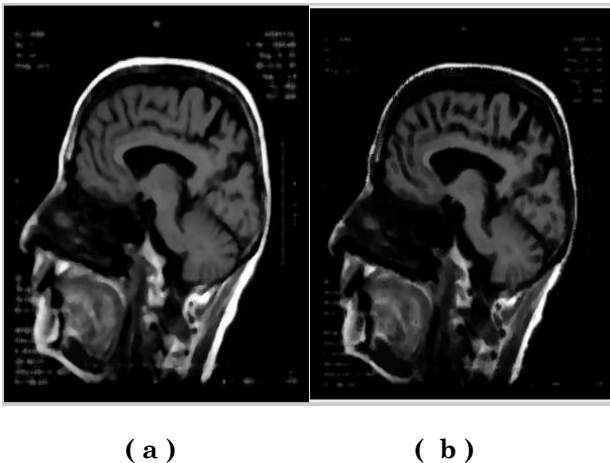


Fig. 10. Comparison of obtained results with the 5x5 median filter.

After the implementations of the median filters, we were interested in the detection of contours in an image by a particular type of filter which is the Sobel filter.

4. EDGE DETECTION

Edge detection includes a variety of mathematical methods that aim at identifying points in a digital image at which the image brightness changes sharply or, more formally, has discontinuities. The purpose of detecting sharp changes in image brightness is to capture important events

and changes in properties of the considered image. It includes discontinuities in the depth, in the orientation of a surface, in the properties of a material etc ... Edge detection is a fundamental tool in image processing, machine vision and computer vision, particularly in the areas of feature detection and feature extraction.

Applying an edge detection algorithm to an image may significantly reduce the amount of data to be processed and may therefore filter out information that may be regarded as less relevant, while preserving the important structural properties of an image. In an image with gray levels, a sharp change in the value characterizes an edge. The purpose of the operation is to transform this image into another one of the same dimensions in which the edges appear by convention in white on a black background, [8,9].

A. Sobel edge detection

The Sobel filter is an operator used in image processing for edge detection. It is one of the simplest operators, but gives correct results.

Technically, it is a discrete differentiation operator, computing an approximation of the gradient of the image intensity function. The gradient calculation is conducted through two masks, the first performing a horizontal gradient, the second a vertical gradient. The second mask is deduced from the first by a rotation of $\Pi / 2$. The masks are given below for horizontal and then vertical edges.

When $c = 1$, it is the operators of Prewitt, when $c = 2$, of those of Sobel.

1	c	1
0	0	0
-1	-c	-1

-1	0	1
-c	0	c
-1	0	1

Compared to the previous ones, these masks have the advantage of producing two effects. In addition to calculating the gradient in one direction, these masks perform smoothing in the orthogonal direction. This smoothing makes these masks a little less sensitive to noise than the previous ones, [10, 11].

B. Realization of a Sobel filter with the XSG

The block diagram in Fig. 11 below shows the principle of a Sobel filters which makes horizontal and vertical edges detection of the X and Y gradient. There are two detection blocks: vertical and horizontal plus a binarization block that cancels values below the threshold and sets a value of 255 to the higher value to have a white edge on a black background.

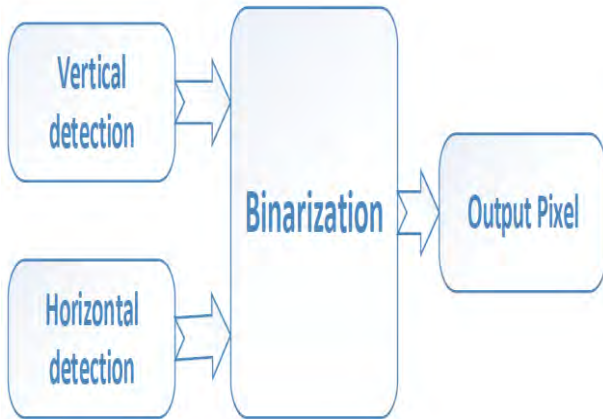


Fig. 11. Operating principle of a Sobel filter

The filter coefficients are displayed above each FIR block in Fig. 12.

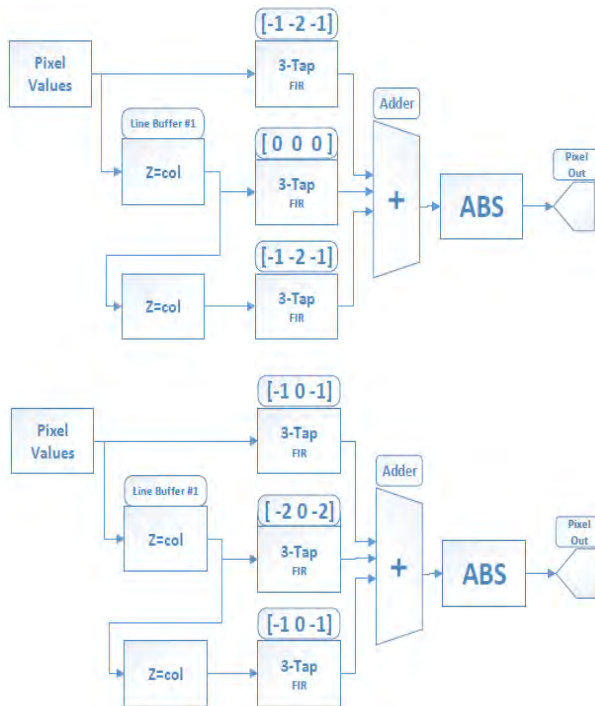


Fig. 12. Functional diagram of the Sobel filter

Fig. 13 shows the schematic of the Sobel filter obtained with the Xilinx generator system.

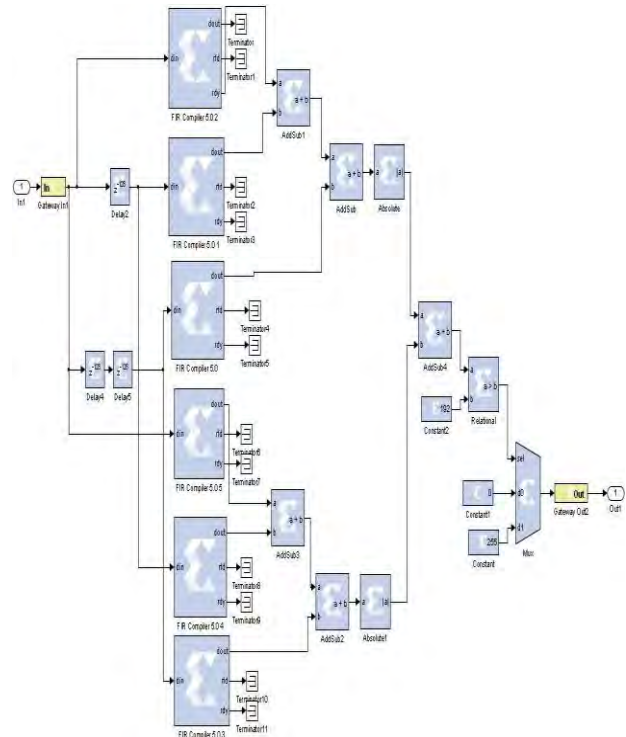


Fig. 13. Block diagram of the Sobel filter using XGS.

The next step is to generate the Bitstream file.

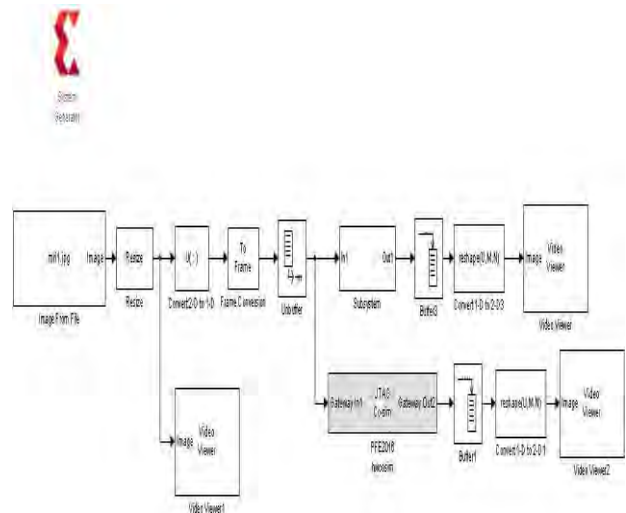


Fig. 14. Complete diagram with the JTAG block.

C. RESULTS

After realizing the simulation, the results obtained are displayed using one of the applications that uses edge detection based on a segmentation method used in medical imaging, for the detection of tumors in

cervical scanners in order to have maximum accuracy the contour of the tumor, [12]. The results are shown in Fig. 15. We see that the purpose of detecting sharp changes in image brightness is to capture important events and changes in properties of the considered image.

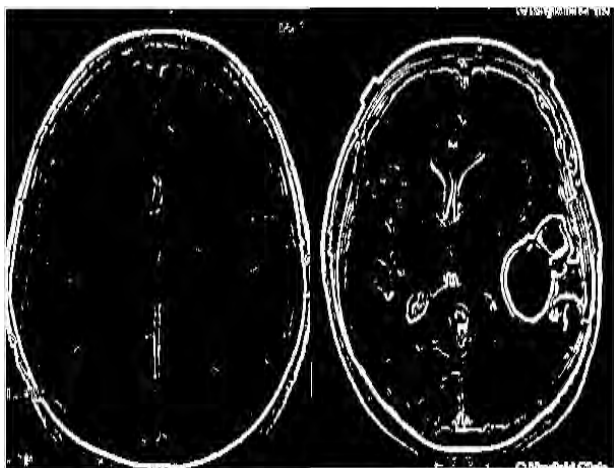


Fig. 15. Tumor detection

In this part we realized the different phases of implementation under FPGA for the various treatments of the biomedical image. Thus we have validated by functional tests the implementation of the preprocessing of the image signal, by the median filter in the case of image denoising and Sobel filter for the detection of the edges. FPGA hardware implementations of all these applications have been successfully realized.

5. CONCLUSION

In order to achieve a hardware implementation on the Nexys2 FPGA card, we proposed a global design of a VHDL embedded expert system.

The hardware implementation on FPGA Nexys2, was carried out using the advanced language XSG. This required the translation of the different phases of the filtering and edge detection system, into mathematical equations that can be implemented in a hardware way.

Taking into account the hardware constraints of the FPGA, we were able to acquire and condition the image signal so that it could be processed in real time on the Nexys2 card.

We validated our system by functional tests of our algorithm on many images under Matlab then under VHDL generated by

XSG. The results obtained allowed us to appreciate the functionality and performance of our implemented system.

We can conclude that the Xilinx Generator System (XSG), which uses Matlab's two Simulink interfaces and Xilinx XSG softwares, is the future of algorithmic model design and simulation applications. It provides fast ways to make the implementation of complex techniques used in image processing. The main application of XSG is its response to time and fast start constraints by producing all the files required for hardware co-simulation automatically.

In addition, the intrinsic FPGA structure lends itself to parallel processing, which is advantageous for imaging algorithms dedicated to very specialized applications in the medical domain.

REFERENCES

- [1] H.Yang, J.Zhang, J.Sun, and L.Yu, "Review of advanced FPGA architectures and technologies," *J. Electron.* **31**(5), 371–393 (2014)
- [2] A.C.Suthar, M.Vayada, C.B.Patel, and G.R.Kulkarni, "Hardware Software Co-simulation for Image Processing Applications," IJCSI Press, 2012.
- [3] M.Kazmi, A. Aziz, P.Akhtar and N. Ikram, "A low cost structurally optimized design for diverse filter types," *PLoS ONE* **11**(11), e0166,056 (2016)
- [4] D.G .Bailey, "Design for Embedded Image Processing on FPGAs," Wiley, New York (2011)
- [5] K. Anil Kumar and M. Vijay Kumar, "Implementation of image processing lab using Xilinx System Generator," *AIVP*, vol.2, n°5, 2014.
- [6] S.Munawar Ali and S. Naveen Kumar, "FPGA based design and implementation of image architecture using Xilinx system generator," *IJCAE*, Vol. No. 3 Issue 1, July 2012, pp132- 138.
- [7] K.Wiatr and E.Jamro, "Implementation image data convolutions operations in FPGA reconfigurable structures for real-time vision systems," *International Conference on Information Technology: Coding and Computing*, 2000. Proceedings. IEEE, pp. 152–157.
- [8] J. Canny, "A computational approach to edge detection," *IEEE Transactions on Pattern Analysis and Machine Intelligence*, vol.8, n°6, novembre 1986, p. 679–714.

- [9] R.Obili, P.V.Krishna and M. Gupta, "A real time hardware and software co-simulation of edge detection for image processing system," International Journal on Engineering and Research Trends(IJERT), vol.2, issue.8, PP.1695-1701, aug-2013.
- [10] Moore, C.T., Devos, H., Stroobandt, D.: Optimizing the FPGA memory design for a sobel edge detector. In: 20th Annual Workshop on Circuits, Systems and Signal Processing (ProRISC 2009), STW Technology Foundation, pp. 496–499 (2009)
- [11] S.Halder, D. Bhattacharjee, M. Nasipuri and Di. Kumar Basu, "A Fast FPGA Based Architecture for Sobel Edge Detection," Progress in VLSI Design and Test - 16th International Symposium, VDAT 2012, Shibpur, India, July 1-4, 2012. Proceedings (pp.300-306).
- [12] F. Hamdaoui, A. Ladgham, A. Saklyand A. Mtibaa," Real Time Implementation of Medical Images Segmentation Using Xilinx System Generator," International Review on Computers and Software IRECOS, Praise Worthy Prize, 7 (6) (2012).

Antenna Powered by a Coplanar Waveguide CPW for Wi-Fi and WLAN Mobile Phone Applications

Nassima BELGACEM¹, Mehadji ABRI²

¹Laboratory of Telecommunication, Faculty of Technology, University of Tlemcen, Algiers
belgacem_nassima@yahoo.fr

²Stic laboratory, Faculty of Technology, University of Tlemcen, Algiers
abrim2002@yahoo.fr

ABSTRACT

The wireless local area networks, WLAN, Wi-Fi are generally a dual band or multiband wireless standard communication devices. Due to the gradual development of electronics and wireless communications, the requirement for mobile devices operating at different standards or for different applications is extending. So, on the other hand, wireless communication systems are developing toward biband functional devices. Several researchers have devoted large efforts to improve performance of antennas that satisfy the above demands. The antenna is designed using coplanar waveguide CPW and is suitable to be embedded inside the casing of mobile phone applications. Two operating bands covering 2.47 for Wi-Fi and 5.32 GHz for WLAN systems are achieved with good radiation efficiencies.

Key Words: CST; CPW, Dual band, Antenna WLAN/Wi-Fi applications.

1. INTRODUCTION

The modern wireless communication systems have a great demand for compact designs, dual band and low-cost antennas that can operate at various communication standards simultaneously. These antennas can allow the designer to integrate wireless local area network (WLAN) and worldwide interoperability for microwave access (WIMAX) into one single system. Since the WLAN standards are ranges from WLAN in

USA [5.15 - 5.35 GHz, 5.725 - 5.875 GHz] and the Wi-Fi standards ranges from [2.4 - 2.48 GHz] [1].

The coplanar transmission line, also called coplanar guide and CPW (Coplanar Waveguide), is a key element in the design of integrated circuits. It was proposed for the first time as an alternative to the micro strip line by Wen [2-3]. The coplanar transmission line has several advantages over the micro strip line. It makes it possible to dispense with the back-end technological processes used for the production of micro strip lines and thus to reduce the cost of manufacture. It also presents a flexibility of design and realization. It also shows ease of integration with other circuits without the use of metal was due to its uniplanar nature. In addition, it facilitates the realization of complex circuits such as filters and insulators. It is for these reasons that we chose to use coplanar interconnections [4-8].

These antennas have the advantage of having a dual bandwidth and allow easy integration with the active devices. The CPW feed mechanism offers several advantages over the micro strip feed because it has less dispersion and low radiation loss. As a result, CPW powered antennas are good candidates for antenna design short [9-11]. The supply line, the ground plane and the radiating element are on the same face of the substrate. In addition, the characteristic impedance of a CPW line depends little on the substrate height and depends on the dimensions of the conductive surface [12-14].

In this paper, we propose a new promising design of bi-band antenna with coplanar waveguide (CPW) for Wi-Fi and WLAN band operations. This antenna meets the simple structure, easy production, low cost and the bandwidth requirements in the required frequency bands.

2. ANTENNA DESIGN

The geometry of the proposed configuration consists of a patch powered by a CPW feed line antenna, shown in Figure.1. The proposed antenna is designed using CST software based on FIT method and constructed on a FR-4 substrate $h=1.6$ mm. The dimensions of the substrate are $W \times L = (47 \times 25)$ mm² and having a CPW ground of size $L_1 \times W_1$, a relative permittivity of $\epsilon_r = 4.3$ and a dielectric loss tangent of 0.018.

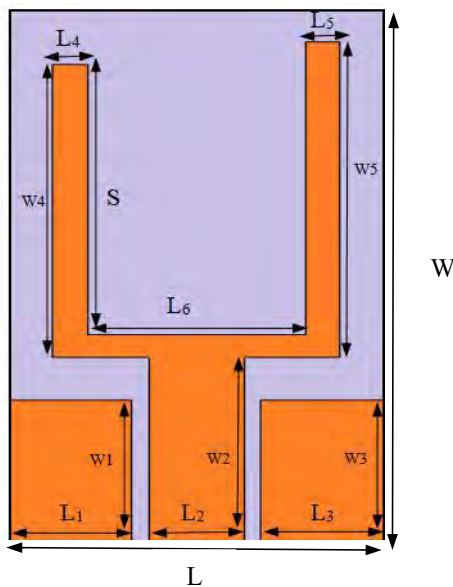


Figure.1: Basic printed antenna prototype.

The geometric parameters of the antenna Figure.1 are shown in the following Table.1.

Table.1 Basic Antenna Geometrical Parameters.

Parameters	Value (mm)
L	25
L ₁	8.27
L ₂	6.26
L ₃	8.27
L ₄	2.25
L ₅	2.25
L ₆	14.3
W	47
W ₁	12.6
W ₂	18.32
W ₃	12.6
W ₄	24
W ₅	26

3. PARAMETRIC STUDY

To improve the performance of the antenna, we performed a parametric study at certain parameters S. This parametric study showed us how these parameters can modify the antenna performance and mainly their effect on the two frequency bands (bandwidth) as well as the effect on the adaptation of the antenna. These properties make the antenna suitable for Wi-Fi/WLAN applications.

Table.2 The results of the simulated antenna for different values.

Width S (mm)	Frequency (GHz)		Amplitude (dB)	
19	2.66	5.14	-27	-19
20	2.61	5.89	-28	-53
21	2.57	5.74	-30	-40
22	2.53	5.58	-29	-36
23	2.50	5.41	-28	-42

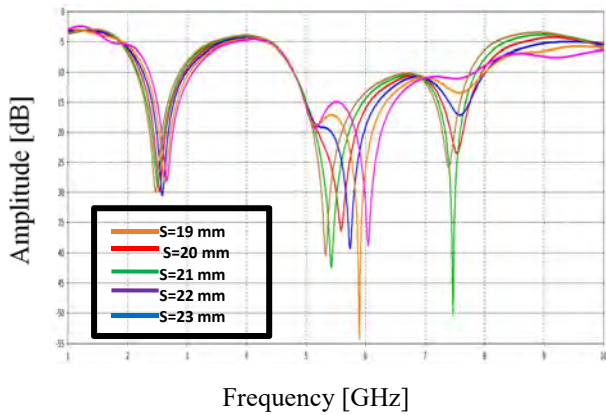


Figure.2: Simulated return losses for different values.

4. SIMULATION AND RESULT

We have simulated a printed antenna powered by a coplanar waveguide CPW for mobile application, which is a specific type of miniature antenna intended for Wi-Fi and WLAN standards operating at 2.47 GHz and 5.32 GHz respectively. The simulation result obtained for the return loss S11 as a function of the frequency (GHz). Fig. 3 represented in the frequency range [1-10 GHz] under the simulation tool CST.

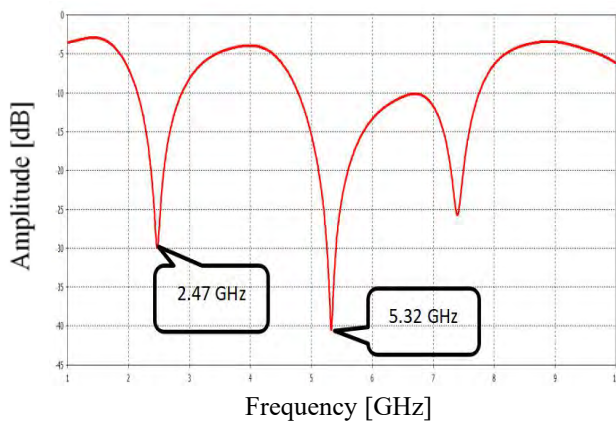


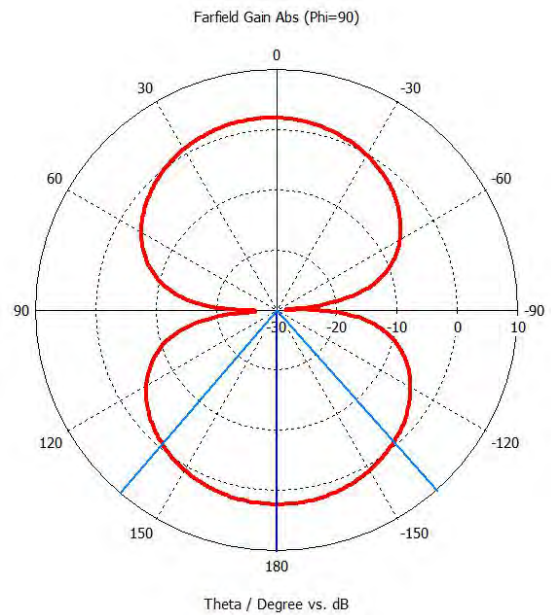
Figure.3: Bi- band antenna computed return loss.

The Figure.3 shows that there are two frequency bands of resonances in the frequency range from 1 to 10 GHz. A good adaptation is observed at the frequency 5.32 GHz. The reflected powers are -41 dB and for the second frequency 2.47 GHz equal to -30 dB.

Figure.4 shows the radiation patterns in the H- and E-planes at resonance frequencies of 2.47 and 5.32 GHz, respectively. It is found that the antenna has

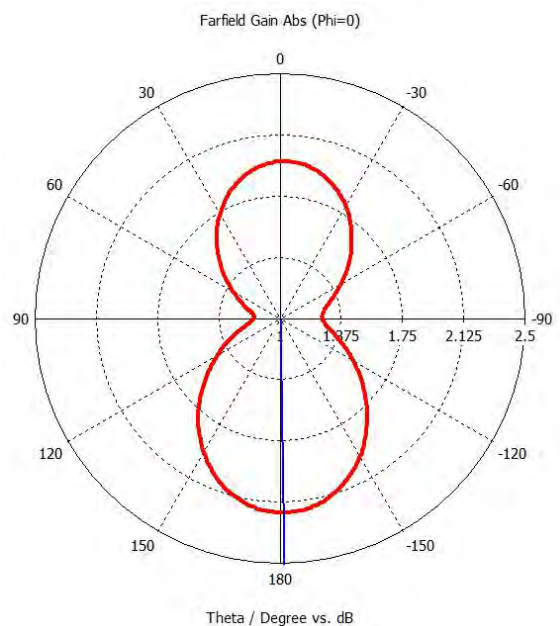
good radiation patterns at all frequencies in the E-plane and the H-plane.

From Figure.4 we observe the gain equal to 2.18 dB for the frequency 2.47 GHz. With an opening angle of 3 dB corresponds to 180 ° the and the main lobe angle equal to 177 °, for the frequency 5.32 GHz the value of the equal gain of 4.45 dB, with an opening angle of 3 dB corresponding to 47.1 ° and the back lobe is of the order of -3.4 dB.



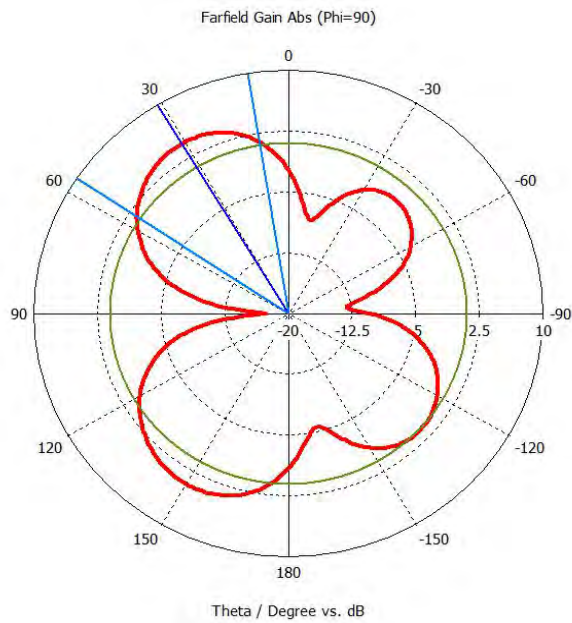
(a)

f=2.47 GHz.

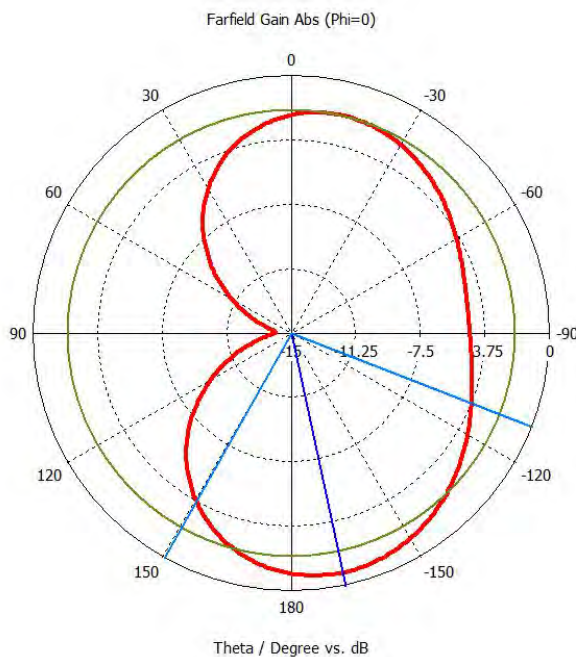


(a)

f=2.47 GHz.



(c)
f=5.32 GHz.



(d)
f=5.32 GHz.

Figure.4: Simulated radiation patterns for Bi-band antenna at 2.47 GHz, 5.32 GHz for E-plane (Phi=0) and H-plane (Phi=90).

Figure.5 shows the gain variation as a function of the frequency of the structure. It can be seen that the proposed antenna has a minimum gain of 2 dB and maximum gain of 5 dB. The gain of the proposed antenna satisfies the requirement of some Wi-Fi/WLAN applications. We notice that the

gain is positive and increasing with the frequency.

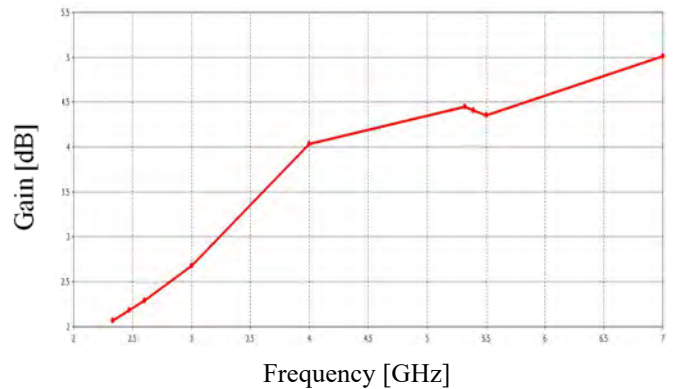


Figure.5: The gain as a function of frequency.

The following Table 3 shows the gain variation as a function of the resonant frequency of different values. The peak gain was calculated using CST software.

Table.3 Variation of simulated antenna gain.

Frequency (GHz)	Peak Gain (dB)
2.33	2
2.47	2.18
2.6	2.3
3	2.6
4	4
5.32	4.45
5.4	4.1
5.5	4.35
7	5

5. CURRENT DISTRIBUTION

Figures. (6-7-8-9) illustrates the current distribution for $f_1=2.47$ GHz and $f_2=5.32$ GHz, the electric current distribution was chosen because it facilitated identifying the distribution characteristics of bi-band antenna. We can observe that the current distribution is concentrated at the CPW feed line and in the surface of a patch antenna proposed. The simulated surface current distribution at different frequencies 2.47 and 5.32 GHz as shown in Figures. (6-7-8-9).

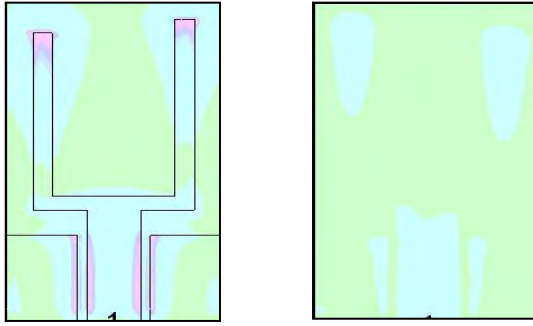


Figure.6: Current distributions of the proposed antenna at 2.47GHz.

The first resonant frequency occurs at 2.47 GHz and the maximum value of the continuous current path is 80.1 A/m^2 .

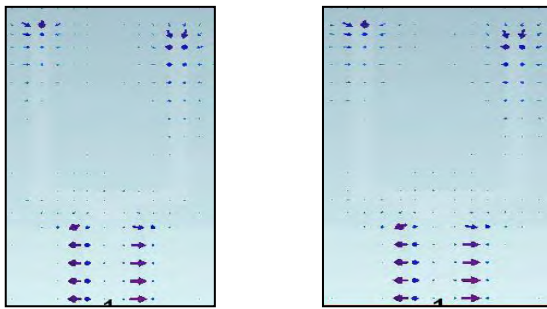


Figure.7: Surface current distribution of the proposed antenna at 2.47 GHz.

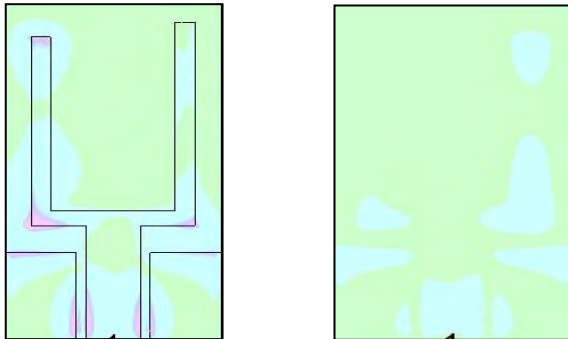


Figure.8: Current distributions of the proposed antenna at 5.32 GHz.

The second resonant frequency occurs at 5.32 GHz and the maximum value of the continuous current path is 181 A/m^2 .

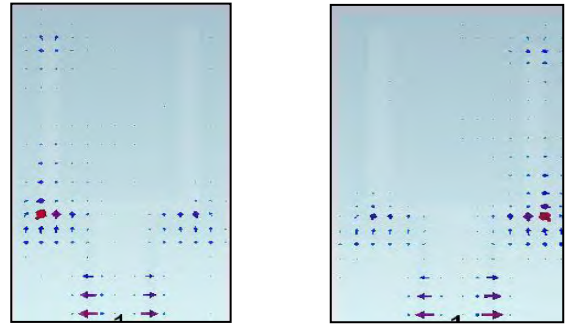


Figure.9: Surface current distribution of the proposed antenna at 5.32 GHz.

6. CONCLUSION

The bi-band antenna with coplanar waveguide (CPW) for operating in the 2.47GHz and 5.32 GHz bands has been proposed and successfully designed. The proposed antenna has several advantages, such as small size, excellent radiation patterns, and high gain which meets the requirements of Wi-Fi/WLAN applications. This antenna was designed in the CST microwave studio software.

REFERENCES

- [1] Wolff. I, "Coplanar Microwave Integrated Circuit", John Wiley & Sons, INC,2006.
- [2] Dib. N, "Comprehensive study of CAD models of several coplanar waveguide(CPW) discontinuities", IEE Proc Microwave Antennas Propagation, Vol. 152,N°. 2,pp. 69-76, April 2005.
- [3] Gautam. K, Aditi Bisht, Binod Kr Kanaujia "A wideband antenna with defected ground plane for WLAN/WiMAXapplications"International Journal of Electronics and Communications (AEÜ) ,Int. J. Electron. Commun. N°.5 ,(AEÜ) 70 (2016) 354–358,Elsevier GmbH. All rights reserved. .
- [4] Yingsong. Li,Wenhua. Yu"A Miniaturized Triple Band Monopole Antenna for WLAN andWiMAX Applications"Hindawi Publishing Corporation International Journal of Antennas and Propagation Vol. 2 ,2015, Article ID 146780.
- [5] Abri. M,Belgacem. N andBelgacem. W "New GSM, DCS and GSM/DCS PIFA AntennasDesigns for Wireless Networks applications", International Journal of Information & Network Security (IJINS), Vol. 2, N°.4, August 2013, pp. 305-310, 2013.

- [6] Abri. M, Boukli-hacene. N, Bendimerad. F. T, Cambiaggio. E "Design of a Dual Band Ring Printed Antennas Array" Microwave journal., Vol. 49, N°. 5, pp. 228-232, 2006.
- [7] Freytag, "Design, Realization and Characterization of Antennas for Base Stations of Wireless Telecommunication Networks", Doctoral Thesis University of Limoges, 18 November, 2004.
- [8] Abri. M., Bendimerad. F. T., Boukli-hacene. N and Bousahla. M "Log Periodic Series-Fed Antennas Array Design Using a Simple Transmission Line Model"., International Journal of Communication Engineering Vol. 2, N°. 3, pp. 161-169, 2009.
- [9] Abri. M, Abri Badaoui. H, Didouh. S and Bahloul. S.M, "Seven Bow-Tie Antennas Array Design For C Band Applications", congres mediterraneen des telecommunications et exposition, 22, 23 & 24 Mars 2012, Fes, Maroc.
- [10] Didouh. S, Abri. M and Bendimerad F. T „Multilayered Bow-tie Antennas Design for RFID and Radar Applications Using a Simple Equivalent Transmission Line Model", International Journal of Computer Networks & Communications (IJCNC), Vol. 4, N°.3, pp. 121-131, May-June 2012.
- [11] Tawk. Y, Kabalan. K, El Haj. A, Sadek. S, Al-Husseini. M "A Modified Bowtie Antenna Design For Wi-Fi and WiMAX Applications", 978-1-4244-2202, 2008 IEEE.
- [12] Wong, K.-L, W.-Y. Chen, and T.-W. Kang, "On-board printed coupled-fed loop antenna in close proximity to the surrounding ground plane for penta-band WWAN mobile phone," IEEE Trans. Antennas Propag., Vol. 59, N°. 3, 751757, Mar. 2011.
- [13] Shynu, S. V, G. Augustin, C. K. Aanandan, P. Mohanan, and K. Vasudevan, "Design of compact reconfigurable dual frequency microstrip antennas using varactor diodes," Progress In Electromagnetics Research, Vol. 60, 197205, 197.
- [14] Azremi. A.A.H, Saidatul. N.A, Ahmad. R.B, Soh. P.J "A Parametric Study of roadband Planar Inverted F Antenna (PIFA) for WLAN Application ", International Conference on Electronic Design, December 1-3, 2008, Penang, Malaysia.

Flattened chromatic dispersion controllability in nonlinear liquid photonic bandgap fibers

Meriem BENLACHEHEB¹, Lynda BAZI-CHERBI¹, and Mohamed Lamine FERHAT¹

¹USTHB, LINS Lab, Faculty of Electronics and Computers, PO. Box 32, Bab-Ezzouar, Algiers
mbenlacheheb@usthb.com, cherbi_lynda@hotmail.com,

ABSTRACT

This work involves studying Hollow-core Photonic Bandgap Fiber with highly nonlinear medium to generate an ultra-broadband signal supercontinuum in the near infrared region. The purpose of this study is to control dispersion in PBG photonic crystal fibers (PCFs) by choosing the geometry and materials of these fibers to minimize and flatten the dispersion. This work will enable nonlinear effects to be predominate, which will help to generate ultra-short signals, supercontinuum (SC) light, that can be applied in many fields such as medical imaging and WDM. The optimized design offers an ultra-flattened dispersion of 300 ps / nm.km in the wavelengths range [1460 nm-1665 nm].

Key Words: Fiber optics, photonic crystal, photonic band gap, fiber nonlinear optics, optical imaging.

1. INTRODUCTION

Hollow-core photonic Bandgap fibers (HC-PBGFs) possess interesting guidance mechanism. A major characteristic imposed by the photonic bandgap effect is that their linear properties are strongly dependant of the wavelength, which makes them a good choice for investigating nonlinear effects [1]. Indeed, the generation of broadband flattened supercontinuum spectra has attracted much interest over the last decade

since the advent of photonic crystal fiber (PCF) [2]. Taking advantage of the dispersive and nonlinear properties, the generation of new frequencies through supercontinuum generation in PCF has found many applications in source development, optical coherence tomography (OCT), optical frequency metrology, optical code division multiple access (CDMA) systems, and dense wavelength division multiplexing (DWDM) optical communication systems [3].

Photonic crystal fibers, with their large degrees of freedom which offer a variety of possible geometries, allow a better control of the dispersion curve. Several geometries have been obtained by exploiting many complicated design methods, such as varying the diameter of the air holes of the PCF, modifying the shape of the air holes, filling the air with liquids and many others methods [4]. The type of PBG-guiding fiber has several advantages, such as the ability to propagate light in a low-index core. The cladding microstructure can both confine light to wavelength-scale cores and substantially control chromatic dispersion [5]. The inclusion of the air holes allows lowering the refractive index locally, which makes it possible to confine the light within the waveguide. The spectral width of the photonic bandgaps strongly depends on the difference index between the media that make up the crystal. The larger the index difference, the larger the bandgap range and hence the larger the transmission band of the PCF. In addition, the fiber makes it possible to achieve a better non-linear

efficiency, for example the phase auto-modulation generated by the Kerr effect is exploited in a useful way to compensate the chromatic dispersion of the fiber.

The interplay between nonlinear effects, such as Kerr and Raman Effect and a flat dispersion is used for supercontinuum generation to broaden the bandwidth of the initial injected pulses [4].

In this work we model with full-vectorial finite element method (*V-FEM*) many geometries of (HC-PBGFs) which the core is filled with water to minimize and flatten the chromatic dispersion in visible and near infrared. We show here that there is interesting spectral range where the chromatic dispersion is minimized and flattened and in other hand the nonlinear coefficient is very high; these results could be applied in supercontinuum generation, multiplexing systems, optical sources in biomedical imaging systems.

2. DESIGN PROCEDURES OF HC-PBGF

A triangular hexagon air-hole of refractive index $n_{air} = 1$, included in a silica lattice of refractive index $n_{silica} = 1.45$ is modeled. The hollow core is formed by 7 missing holes, which helps to reduce dispersion and surface modes number [5]. The air-holes diameter and pitch are changed to shape the desired dispersion curve. By keeping the air-filling fraction $d/\Lambda = 0.98$ we concentrate on modifying the geometry parameters to reduce and flatten the chromatic dispersion as much as possible. We successfully designed this highly nonlinear HC-PBGF by filling the core with water of refractive index $n_{water} = 1.33$ which is highly nonlinear. Fig. 1, shows the geometry of the proposed HC-PBGF with the air hole diameter d and pitch Λ .

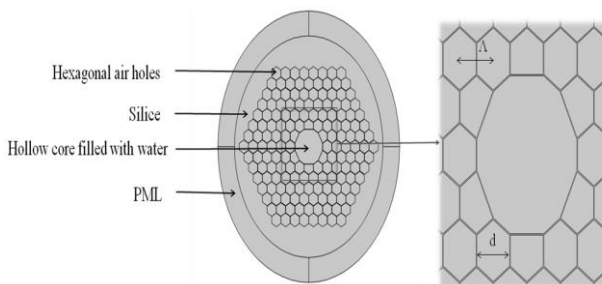


Figure.1 : A cross-section of the modeled 7-cell hollow-core fiber, surrounded by PML.
ISBN: 978 9931 9548 04/\$00.0 © 2018

(FVFEM) is used to determine dispersion properties of fundamental mode in the proposed HC-PBGF with taking in consideration the dispersion of each material by using the Sellmeier equation [7]:

$$n^2(\lambda) = 1 + \frac{B_1\lambda^2}{\lambda^2 - C_1} + \frac{B_2\lambda^2}{\lambda^2 - C_2} + \frac{B_3\lambda^2}{\lambda^2 - C_3} \quad (1)$$

To damp backscattering at the boundaries of simulation area, a circular PML is imposed inside the simulation domain [6].

Once the electric field $E(x, y)$ and the effective index n_{eff} are obtained by FEM, the chromatic dispersion $D(\lambda)$, β_2 and the effective area A_{eff} can be obtained by the following equations:

$$D(\lambda) = -\frac{\lambda}{c} \frac{d^2 \text{Re}[n_{eff}]}{d\lambda^2}, \quad (2)$$

$$\beta_2 = -\frac{\lambda^2}{2\pi c} D(\lambda), \quad (3)$$

$$A_{eff} = \frac{\left(\int_{-\infty}^{\infty} \int_{-\infty}^{\infty} |E_t(x,y)|^2 dx dy\right)^2}{\int_{-\infty}^{\infty} \int_{-\infty}^{\infty} |E_t(x,y)|^4 dx dy} \quad (4)$$

Where $\text{Re}[n_{eff}]$ is the real part of n_{eff} , c is the velocity of light vacuum and λ is the wavelength.

After optimizing the chromatic dispersion of the proposed HC-PBGF, we calculate the nonlinear coefficient of this fiber using the following equation:

$$\gamma = \left(\frac{2\pi}{\lambda}\right) \left(\frac{n_2}{A_{eff}}\right) \quad (5)$$

$$\gamma = \frac{2\pi}{\lambda} \left[\left(\epsilon_p(air) \times \frac{n_2(air)}{A_{eff}(air)} \right) + \left(\epsilon_p(silica) \times \frac{n_2(silica)}{A_{eff}(silica)} \right) + \left(\epsilon_p(water) \times \frac{n_2(water)}{A_{eff}(water)} \right) \right] \quad (6)$$

Here, $n_2(air)$, $n_2(silica)$ and $n_2(water)$ are respectively the nonlinear refractive index of air, silica and water, and $A_{eff}(air/silica/water)$ is the effective area of the fundamental mode in each media. $\epsilon_p(air)$, $\epsilon_p(silica)$ and

ϵ_p (water) are respectively the energy distribution of air-hole, silica and the core of water. The numerical value of the nonlinear refractive index of air, pure silica and water is reported to be $2.9 \times 10^{-23} \text{ m}^2/\text{W}$, $2.6 \times 10^{-20} \text{ m}^2/\text{W}$ and $2.7 \times 10^{-20} \text{ m}^2/\text{W}$ respectively [8][9].

3. SIMULATION RESULTS AND DISCUSSION

In order to calculate chromatic dispersion of the proposed HC-PBGF, we compute first the mode field profile and effective index of fundamental mode (HE_{11}) using the V-FEM. Fig 2 shows the distribution of the electric field of the fundamental mode HE_{11} of the proposed PCF.

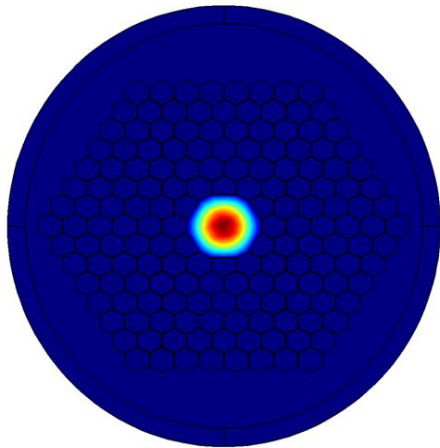


Figure.2 : The fundamental mode field confinement HE_{11} of the HC-PBGF, $d=11.76 \mu\text{m}$ et $d/\Lambda = 0.98$.

Table.1 Geometrical parameters of different simulated PCFs

Geometrical parameters	PCF1	PCF2	PCF3
$d (\mu\text{m})$	4.361	11.76	10.8976
$\Lambda (\mu\text{m})$	4.45	12	11.12
d/Λ	0.98	0.98	0.98

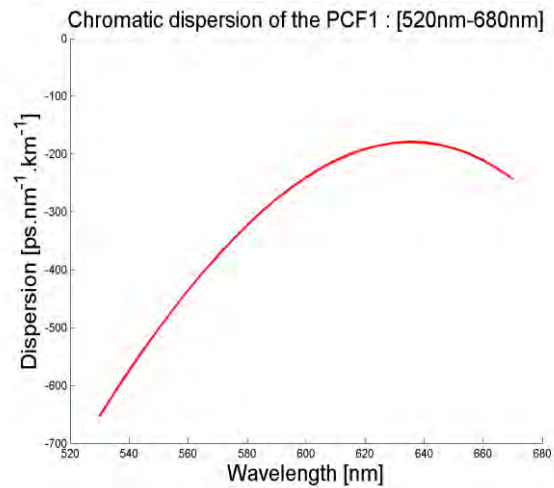


Figure.3 : Chromatic dispersion of the PCF1 $d=0.98 \Lambda$ and $\Lambda=4.45 \mu\text{m}$.

Our subject is to minimize and flatten dispersion in a large band wavelength and to make the nonlinear effects preponderant in the working band. In hence, we have simulated several geometries by changing d and Λ , and keeping the same air-filling fraction d/Λ . Table 1 gives the geometrical parameters of three simulated PCFs.

Fig 3 shows the chromatic dispersion of PCF1 in a spectral range extending from 530 nm to 670 nm. It presents very high all-normal dispersion which is decreasing toward long wavelength. The small dispersion value reached is around $-170 \text{ ps} / \text{nm.km}$. We can deduce that water is very dispersive at long wavelength.

In order to reduce this value of dispersion we change the pitch to $12 \mu\text{m}$ by keeping $d = 0.98 \Lambda$ (PCF2). Note that the electric field is mostly confined inside the core of the fiber (PCF2), because we increased the index contrast between the core and the optical cladding. We distinguee three photonic band gaps (PBG). The first is extending from 1300 nm to 1396 nm, the second from 1419 nm to 1442 nm, the third from 1460 to 1665.

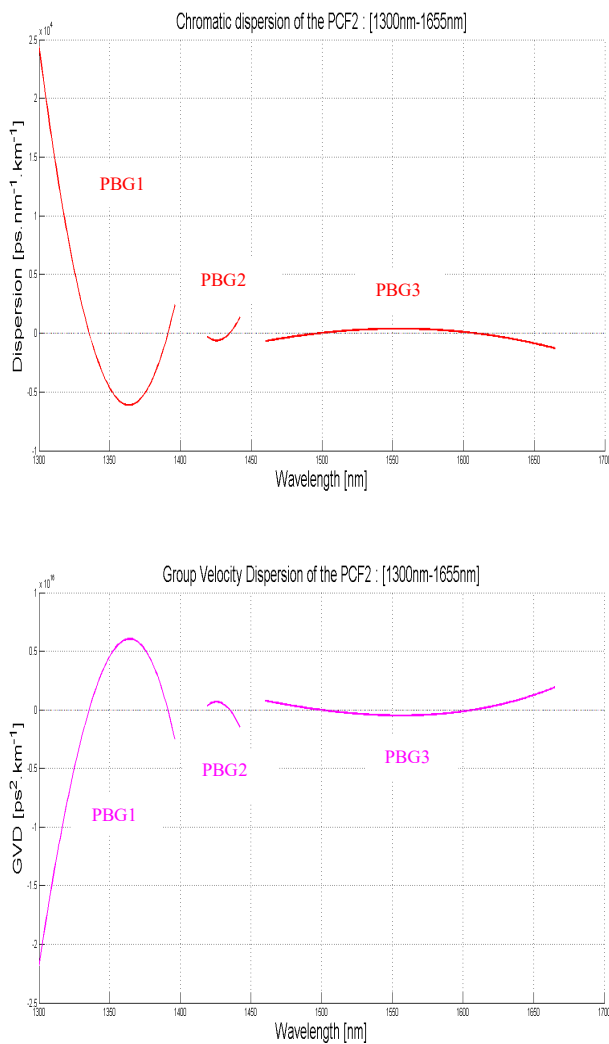


Figure.4 : Chromatic dispersion and the GVD of the PCF2 $d = 0.98 \Lambda$ and $\Lambda = 12 \mu m$.

Fig 4 shows the chromatic dispersion and GVD of these three transmission bands of PCF2. The variation of chromatic dispersion takes very high values in short wavelengths, although PBG1 has two zeros (ZDW) at 1336 nm and 1391 nm wavelengths that can be used for specific applications. The second PBG [1429 nm – 1435] has one ZDW at 1436 nm, and very low dispersion as well as the distribution of the electric field of the fundamental mode that is less intense and tends to cancel out (fig 5). The third PBG, the most interesting, presents two ZDWs at 1500 nm and 1600 nm. A normal dispersion regime for wavelengths lower than 1500 nm and higher

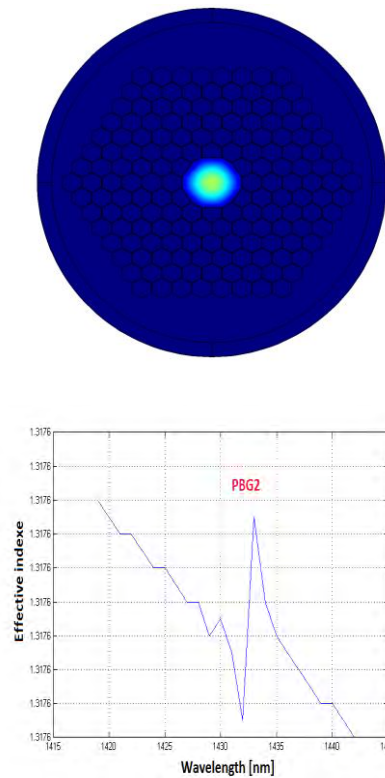


Fig. 5. The fundamental mode field confinement of PCF2 at the PBG2 and its effective index variations.

than 1600nm, and anomalous dispersion regime flattened around a value of 300 ps / nm.km in [1500nm -1600nm]. Indeed, although the dispersion value is around -100 ps / nm.km in visible, while in near infrared it's around 300 ps / nm.km, going towards the long wavelengths allowed us to flatten the dispersion curve obtaining two ZDWs.

In fig 6, we arrive to the optimized HC-PBGF (PCF3), which gives us the desired flattened dispersion over a larger frequency range. We distinguish two PBG, one extends from 1305 nm to 1328 nm, and the second more larger and interesting from 1350 nm 1665 nm. The PCF3 presents an anomalous dispersion regime flattened and has the minimum value of dispersion reached is 33 ps / nm.km in [1450 nm -1550 nm]. We can also see that this proposed fiber has two ZDWs at 1308 nm and 1320 nm in the first PBG.

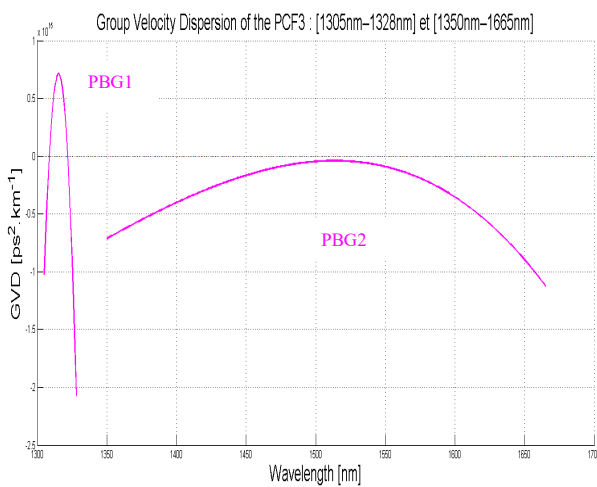
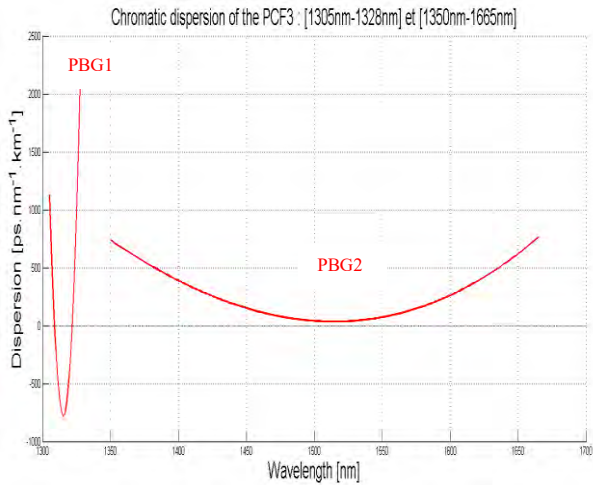


Figure.6 : Wavelength response of chromatic dispersion and the GVD of the PCF3 $d = 0.98 \Lambda$ and $\Lambda=11.12 \mu\text{m}$

Varying the different geometrical parameters of the PCFs has allowed the optimization of the dispersion shape as it is obtained with the PCF2 where the dispersion is more flattened than the others and it contains two ZDWs.

In the fig7 we represent the evolution of the nonlinear coefficient of the PCF2 filled with water that has a high nonlinear coefficient of the order of $10^4 \text{ W}^{-1}.\text{km}^{-1}$ and decreases at long wavelengths.

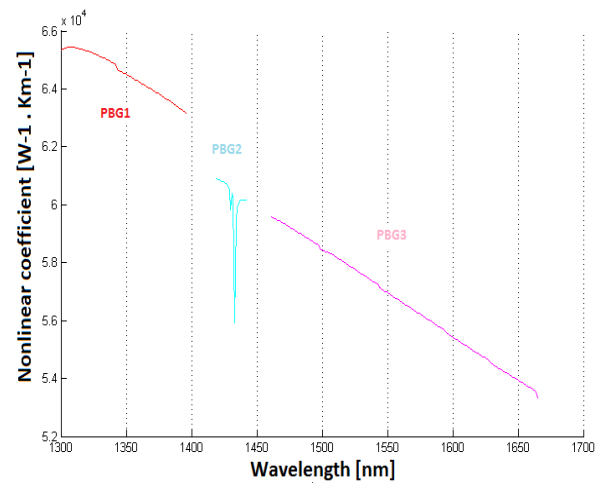
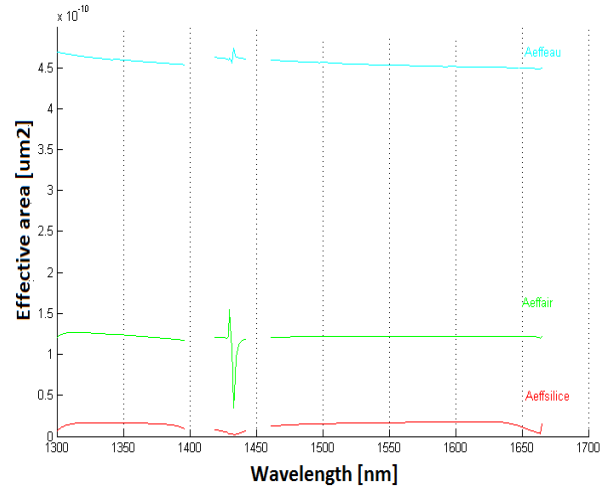


Figure.7 : Wavelength response of effective area A_{eff} and nonlinear coefficient of the proposed HC-PBGF (PCF2) at spectral ranges of [1300-1396], [1419-1442] and [1460-1665].

4. CONCLUSION

A design of Water HC-PBGF with flatten dispersion is presented. It has been shown that we can arrive to the desired shape of chromatic dispersion curve by modifying the opto-geometrical parameters of the PCF. We conclude that the proposed optimized fiber presents interesting applications in two spectral ranges. In the first spectral range extending from 1300 nm to 1396 nm the nonlinear effects are of the same order of the dispersion, where this fiber can be applied in soliton generation.

The second transmission band which is very interesting for our subject is extending from 1460 nm to 1665 nm. This band presents a minimized and flattened chromatic dispersion at 300 ps / nm.km in a large band of wavelength to make the nonlinear effects preponderant with a value that varies around $5.5 \times 10^4 \text{ W}^{-1} \cdot \text{km}^{-1}$ which makes it a very good candidate for the generation of supercontinuum which can be applied in medical imaging, such as OCT.

ACKNOWLEDGEMENTS

This work was supported by the PNR Project entitled : *Développement d'une Instrumentation pour le Diagnostic et la Prévention du Mal Perforant Plantaire chez le Diabétique* under the supervision of ATRSS (*Agence Thématique de Recherche en Sciences de la Santé*, <https://www.atrss.dz>). Also, many thanks to the DGRSDT (*Direction Générale de la Recherche Scientifique et du Développement Technologique*, <http://www.nasr.dz>) for their supports and funding the INSEM team.

REFERENCES

- [1] A. Bétourné, A. Kudlinski, G. Bouwmans, O. Vanvincq, A. Mussot, and Y. Quiquempois, "Control of supercontinuum generation and soliton self-frequency shift in solid-core photonic bandgap fibers", OSA, October 15, 2009 / Vol. 34, No. 20 / OPTICS LETTERS 3083.
- [2] Vincent Pureur and John M. Dudley, "Design of solid core photonic bandgap fibers for visible supercontinuum generation", ELSEVIER, Optics Communications 284 (2011) 1661–1668
- [3] Md. A. Hossain and Y. Namihira, "Center Wavelength Adoption Techniques for Supercontinuum Generating Highly Nonlinear Noncircular Core Photonic Crystal Fiber", Jpn. J. Appl. Phys. 52 (2013) 052502.
- [4] Mohamed Lamine Ferhat, Lynda Cherbi, Issam Haddouche, "Supercontinuum Generation in Silica Photonic Crystal Fiber at 1.3 μm and 1.65 μm Wavelengths for Optical Coherence Tomography", Optik - International Journal for Light and Electron

Optics

<https://doi.org/10.1016/j.ijleo.2017.09.1>.

- [5] P. St. J. Russel, "photonic-crystal fibers," J. Lightwave technol.12, 4729-4749(2006)
- [6] Rodrigo Amezcua Correa, "Development of Hollow-core Photonic Bandgap Fibers free of surface modes, a thesis of University of Southampton", March 2009.
- [7] Linear Pierre Viale, Sébastien Février, Frédéric Gérôme, Hervé Vilard, Confinement Loss Computation in Photonic Crystal Fibers using a novel Perfectly Matched Layer Design, Expert from proceeding of the COMSOL Multiphysics User's Conference2005 Paris.
- [8] Linear refractive index and absorption measurements of nonlinear optical liquids in the visible and near-infrared spectral region, OSA 1 November 2012/ Vol. 2, No. 11 /OPTICAL MATERIAL EXPRESS 1588
- [9] Agrawal, G. P. [Nonlinear Fiber Optics], 5th ed. Academic Press, 2013.
- [10] D. N. Nikogosyan, Properties of Optical and Laser Related Materials Wiley, New York, 1997.
- [11] G. Humbert, W. J. Wadsworth, S. G. Leon-Saval, J. C. Knight, T. A. Birks, P. St. J. Russell, M. J. Laderer, D. Kopf, K. Wiesauer, E. I. Breuer, and D. Stifter, "Supercontinuum generation system for optical coherence tomography based on tapered photonic crystal fibre," Opt. Express 14, 1596-1603 (2006).

Direct torque control strategies combined with space vector modulation applied to the monitoring of doubly fed induction generator

Habib Chaouki Ben Djoudi ⁽¹⁾, Mouloud Guemana ⁽²⁾ and Ahmed Hafaifa ⁽¹⁾

Abstract-- This work deals with the control of a system of conversion of wind energy to the basis of a doubly fed induction generator (DFIG) connected to the electrical network. A control strategy of maximizing power (MPPT) was proposed to apply to the wind turbine to generate the references (torque, power), to carry out this study. We will use two distinct methods for the control of the converter side machine (CCM). The first method is based on the vector control direct and indirect (with and without power loop) and whose main purpose is the control of powers and the second method is based on the control (DTC) that has for objective the direct control of the torque, but this method and classic then we propose to add the algorithm of the vector modulation (SVM) in order to improve the obtained results.

Index Terms-- Wind energy, Doubly Fed Induction Generator (DFIG), Direct Torque Control (DTC), Space Vector Modulation (SVM), Maximum Power Point Tracking (MPPT).

I. INTRODUCTION

After the 1973 oil crisis that alerted states producing fossil fuels and rising oil prices with increasing global energy requirements, the world is turning its attention to nuclear centers, but the risk is growing. Faced with these various problems, and in order to limit the use of nuclear energy (the use of nuclear power plants), countries are increasingly turning to the use of clean and renewable energy sources. Among these sources of renewable energy, wind energy is the one with the greatest energy potential. It was in 1891 that the Danish hen The Court built for the first time a wind turbine generating electricity [1-4].

In this context, we base ourselves on the objective of designing the control laws of wind turbines using the doubly fed induction generator (DFIG). The control strategies of these machines and their possible network connection interfaces must make it possible to capture as much energy as possible over the widest range of wind speed variation possible in order to improve the profitability of the wind power plants. We must know that the overall goal of this thesis is how to order a wind energy production system? And what are the most ideal strategies used on the system studied?

^(a) Applied Automation and Industrial Diagnostics Laboratory, Faculty of Science and Technology, University of Djelfa 17000 DZ, Algeria

Emails : HC.Bendjoudi@univ-djelfa.dz, hafaifa.ahmed.dz@ieee.org

^(b) Science and Technology Faculty, Médéa University, Algeria.

Email: guemana.mouloud@univ-medea.dz

II. GENERAL STRUCTURE OF THE STUDIED TURBINE

The production of energy to grow over time in the face of increasing people in the world, because of this reason the world turned to renewable energy “wind systems” to meet the needs.

The conversion of wind energy into electrical energy takes a lot of research and studies in the 21 st century, this research is based on the electromechanical side of the system as this part has been essential to produce.

Several studies based on the doubly fed induction generator. The latter was attacked by different control strategies to improve the wind system. We have taken these studies as a reference to our work.

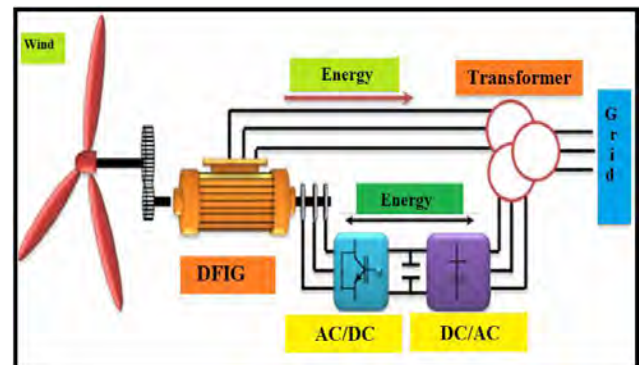


Fig. 1. Wind system based on the DFIG

The turbine captures the kinetic energy of the wind and converts it to a couple who is turning the rotor blades. Three factors determine the ratio between the energy of the wind and the mechanical energy recovered by the rotor: the density of the air, the surface area swept by the rotor and the speed of the wind [7].

The density of the air and the speed of the wind are of climatological parameters which are dependent on the site [3], [9].

$$P_w = \frac{1}{2} \rho \pi R^2 v_i^3 C_p(\lambda, \beta) \quad (1)$$

$$\lambda = \frac{\omega_r R}{v_i} \quad (2)$$

$$T_w = \frac{1}{2} \frac{\rho \pi R^3 v_i^2 C_p(\lambda, \beta)}{\lambda} \quad (3)$$

$$C_p(\lambda, \beta) = C_1 \left(C_2 \frac{1}{\lambda} - C_3 \beta - C_4 \right) e^{\frac{C_5}{\lambda}} + C_6 \lambda \quad (4)$$

$$\frac{1}{\lambda_i} = \frac{1}{\lambda + 0.08 \beta} - \frac{0.035}{\beta^3 + 1} \quad (5)$$

The presentation of the asynchronous machine this made by the following model:

The machine is represented by its model of Park. [5]

The eight equations are in function of the stator flux rotor and, the stator currents and rotorique ET the speed according to the mark (d, q) [2], [3].

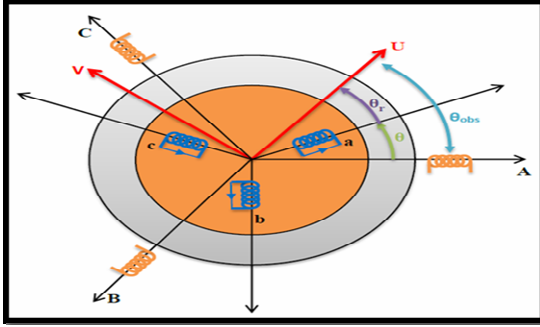


Fig. 2. Representation of the model of park.

$$\begin{cases} V_{ds} = R_s I_{ds} + \frac{d\varphi_{ds}}{dt} - \omega_s \varphi_{qs} \\ V_{qs} = R_s I_{qs} + \frac{d\varphi_{qs}}{dt} - \omega_s \varphi_{ds} \\ V_{dr} = R_r I_{dr} + \frac{d\varphi_{dr}}{dt} - (\omega_s - \omega_r) \varphi_{qr} \\ V_{qr} = R_r I_{qr} + \frac{d\varphi_{qr}}{dt} - (\omega_s - \omega_r) \varphi_{dr} \end{cases} \quad (6)$$

The flow:

$$\begin{cases} \varphi_{ds} = L_s I_{ds} + L_m I_{dr} \\ \varphi_{qs} = L_s I_{qs} + L_m I_{qr} \\ \varphi_{dr} = L_r I_{dr} + L_m I_{ds} \\ \varphi_{qr} = L_r I_{qr} + L_m I_{qs} \end{cases} \quad (7)$$

The powers:

$$\begin{cases} P_s = V_{ds} I_{ds} + V_{qs} I_{qs} \\ Q_s = V_{qs} I_{ds} - V_{ds} I_{qs} \\ P_r = V_{dr} I_{dr} + V_{qr} I_{qr} \\ Q_r = V_{qr} I_{dr} - V_{dr} I_{qr} \end{cases} \quad (8)$$

The electromagnetic torque:

$$T_{em} = P(\varphi_{ds} I_{qs} - \varphi_{qs} I_{ds}) \quad (9)$$

$$\begin{cases} \varphi_{qs} = \frac{d\varphi_{qs}}{dt} = 0 \\ \varphi_{ds} = \varphi_s \end{cases} \quad (10)$$

III. PROPOSED CONTROL SYSTEM

The objective of the order is to find the right combination of control switches in the control of the converter rotor rating, way to reconstruct the form of three sinusoidal signals. Either, $S_a S_b S_c$ the control signals of the arms of the UPS [4], [5], [13].

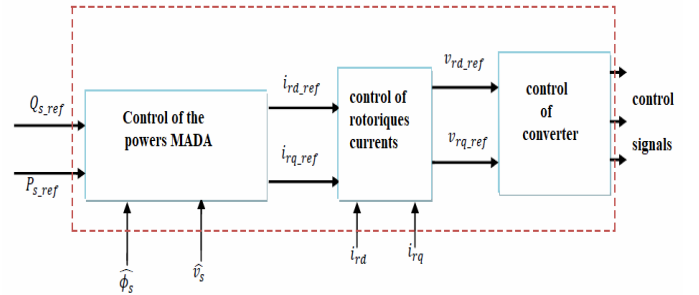


Fig. 3. Simplified diagram of the control of the converter side DFIG.

The principle of MLI vector consists in projecting the vector of rotor voltage desired on the two vectors of adjacent voltage corresponding to two switching states of converter rotor side, the values of these projections ensuring the calculation of the time of the desired switching corresponds to two States not void of switching of the converter. If we note and these two time, their sum must be less than the period of the switching of the converter. To maintain the switching frequency constant, a null state of the converter CCM is applied during duration complementary to T [5], [8].

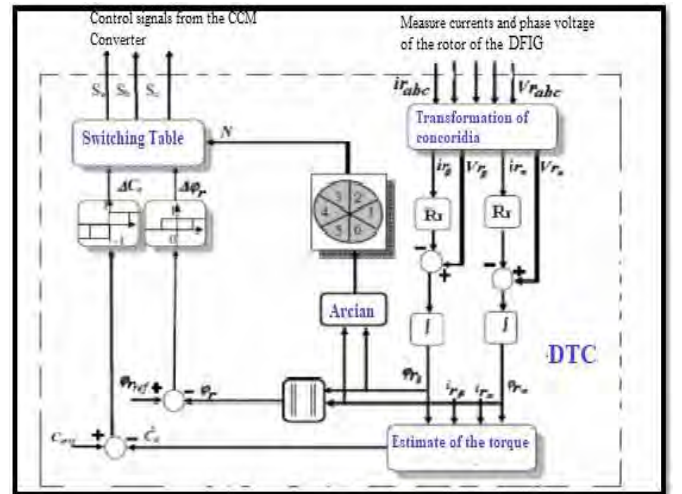


Fig. 4. Schematic diagram of the DTC applied to the DFIG.

IV. STRATEGY OF THE CONTROL DTC-SVM

The principle in the DTC Control is the direct regulation of the torque of the asynchronous machine to the dual power supply by the application of the different vectors of the voltage from the inverter, which determines its state. The two variables monitored are the Rotor flow and the electromagnetic torque which are controlled by the regulators to Hysteresis, in a command DTC it is preferable to work with a frequency of calculation high in order to reduce the torque oscillations caused by regulators [6], [10].

This technique that we called DTC to the frequency of constant modulation DTC-SVM (space vector Modulation).The control DTC-SVM proposed retains the basic idea of the control DTC Classic and the technique of orientation of the Rotor flux is used. In this work, the switching table is replaced by two regulators PI, one for the torque and the other for the flow in order to generate the tensions of control. It was an employee. This control structure because it has the advantages of the vector control and the direct control of the torque and allows you to surpass the problems of the DTC Classic [11], [12].

TABLE 1
PARAMETERS SYSTEM MECHANICAL AND ELECTRICAL SYSTEM OF WIND ENERGY

System	Parameters
Turbine	Number of blades: 3 Radius R=3m Inertia JT =0.3126 Kg. m2 Coefficient of Friction Kf=0.00681 Nominal wind speed Vn=12m/s
Multiplier	5.4m
DFIG	Us=380 V, f=50 Hz, n=1440tr/min Pn=10KW, p=2, Rs=1.2 Ω, Rr=1.8 Ω Ls=0.1554 H, Lr=0.1568 H, Lm=0.15 H
Continuos bus	C=4700μF, Vdc=620v
RL filter	Rf=0.2 Ω, Lf= 11.5 mH
Electrical network	V=380V, 50Hz

TABLE 2

Control	Parameters
Control for MPPT	$\lambda_{opt}=8.7, C_{pmax}=0.477$
Earnings of PI regulators of rotor currents	$K_{p_c}=(L_r - ((M_{sr}^2)/L_s))/\tau_1$; $K_{i_c}=10 * R_r / \tau_1$; Avec $\tau_1=10-5$.
Earnings of PI regulators of the powers	$K_{p_p}=\tau_1 / \tau_2$; $K_{i_p}=1 / \tau_1$; Avec $\tau_2=10-2$.
Control of the voltage of the continuous bus	$K_{p_vc}=0.25$; $K_{i_vc}=0.4$;

V. RESULTING FROM SIMULATION

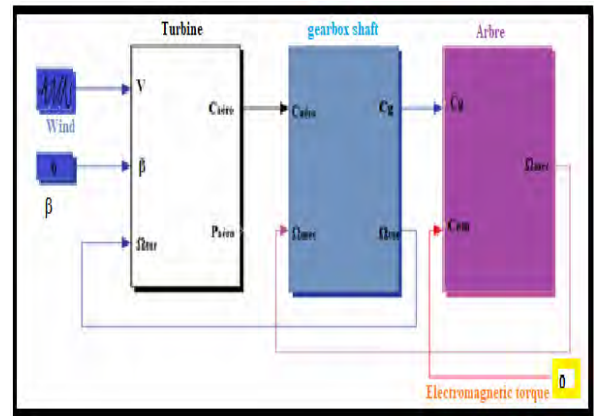


Fig. 5. Principle of the sinusoidal PWM control.

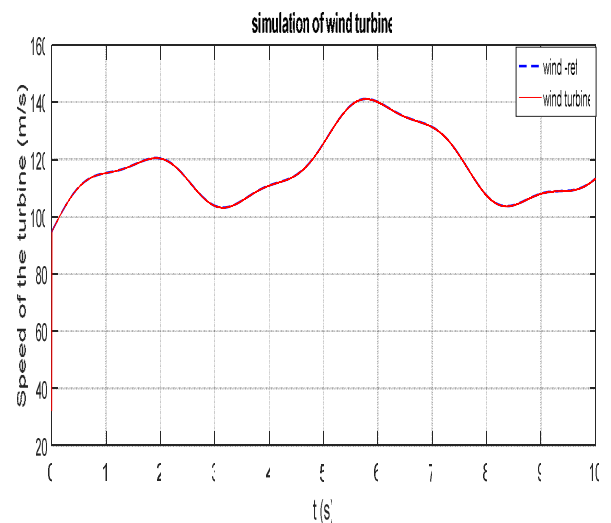


Fig. 6. Principles of the sinusoidal PWM control.

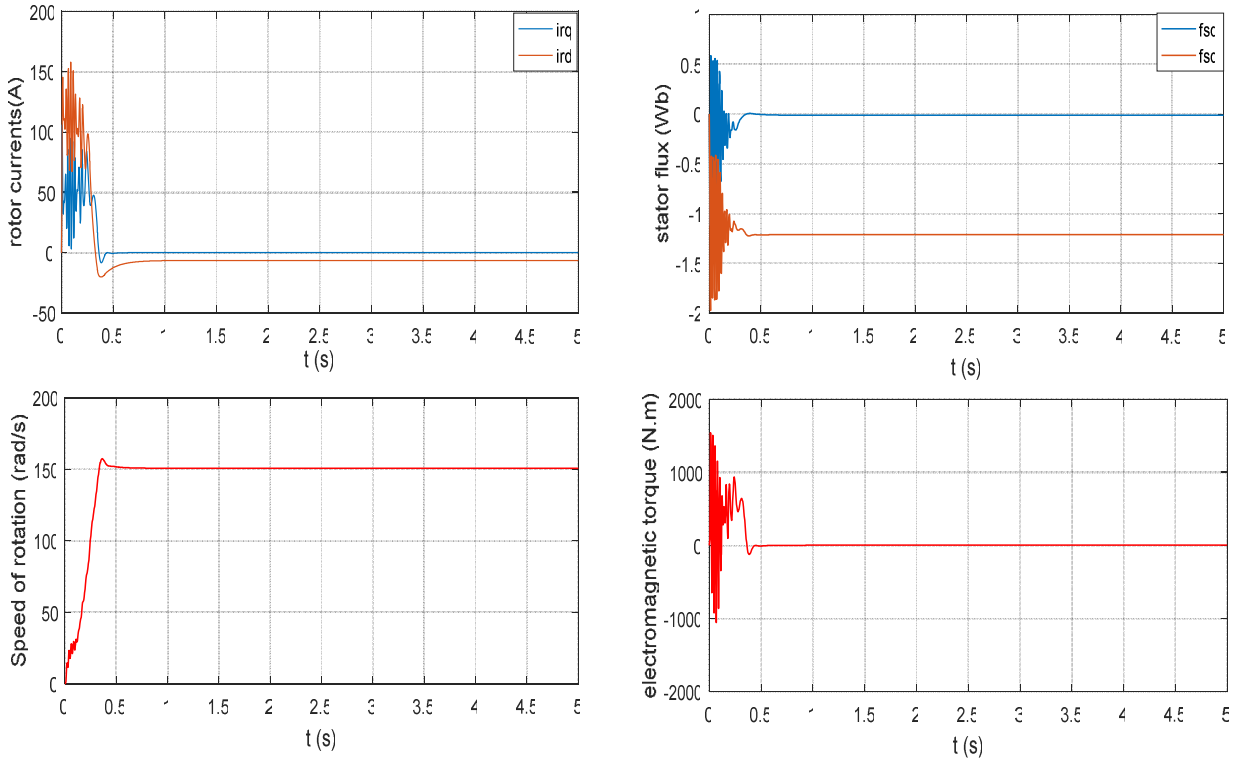


Fig. 7. Behavior of the DFIG in generator mode

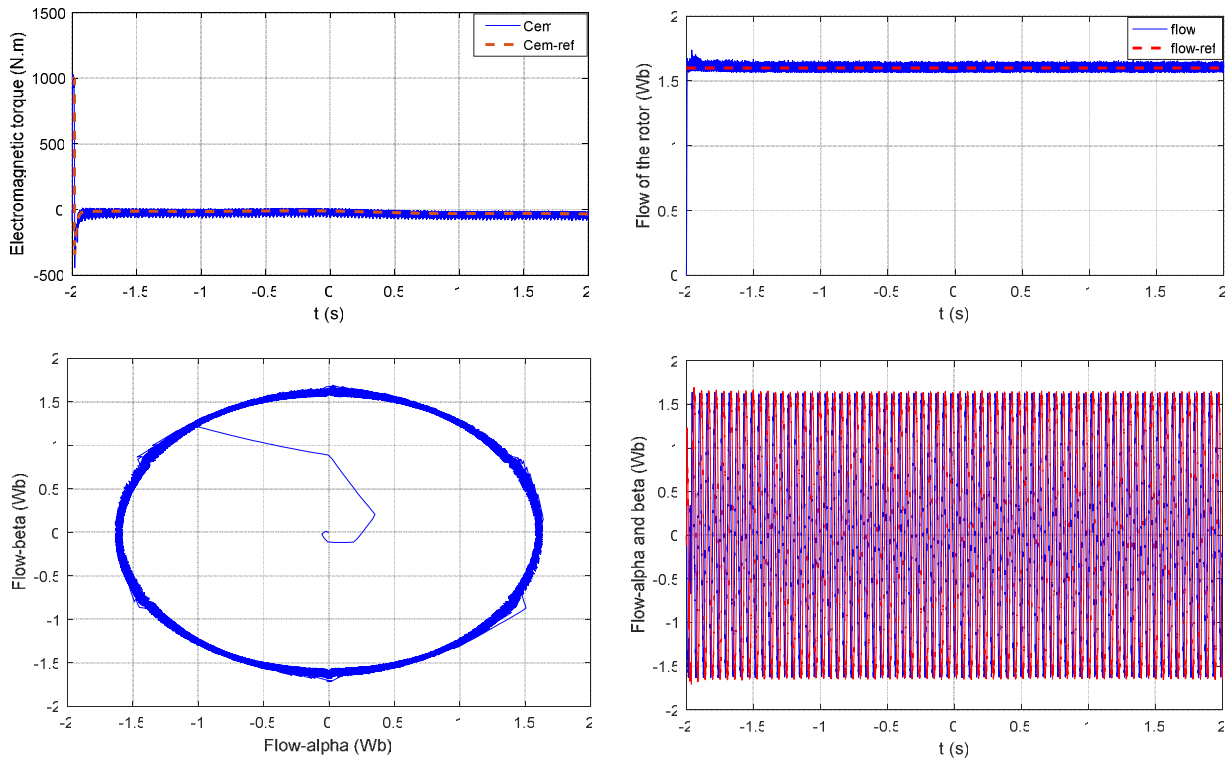


Fig. 8. Simulation the principle result of DTC

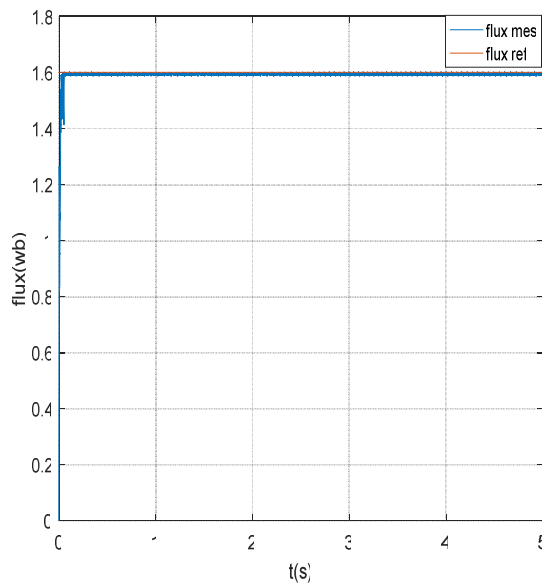


Fig. 9. Simulation the main results flow of the control DTC-SVM.

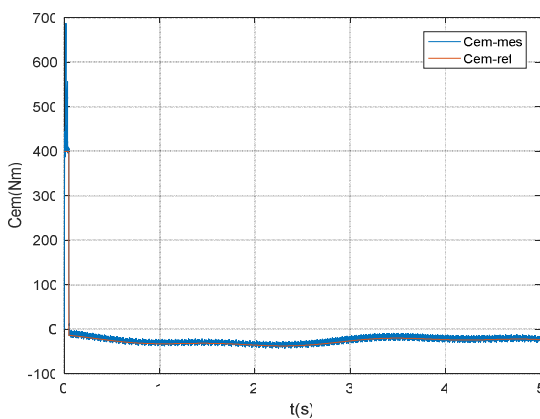


Fig. 10. Simulation the main results torque of the control DTC-SVM.

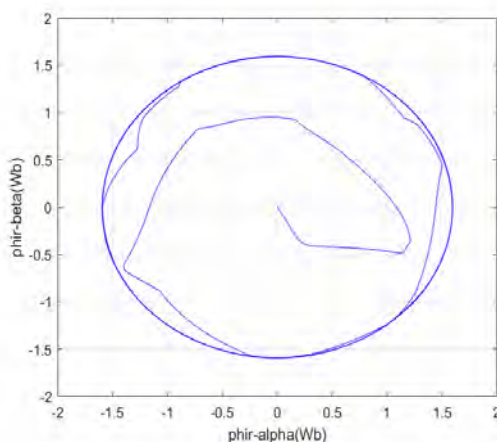


Fig. 11. Simulation the main results flow of the control DTC-SVM

VI. INTERPRETATION

This control is very dynamic and the aerodynamic power by the figures (Fig.6), Obtained in a transitional regime is, therefore, more important. The power coefficient and the report of speed are adjusted to their optimal values. The results obtained show the best static and dynamic performance, best continuation of the seven-point controlled (speed) and a desirable response time offered by the two regulators.

Through the simulation results illustrated by the figures (Fig.7), we find that all quantities of the machine at the start have a transitional regime oscillating with high values; they do stabilize that after 0.5s and present the sine-wave form. We note that the flows studied previously are well illustrated by the simulation.

Figure (Fig.8), illustrates the responses of the system and show the high dynamic of the couple, one finds that the controller at three levels allows the control of the machine in the two directions of rotation. The simulation results show the reliability and performance of the configuration of the control DTC studied, but with a number of commutations higher which increases the losses by switching of switches. On the other hand, we confirm the disadvantage of the DTC by the presence of large oscillations of the couple and of the flow. This phenomenon of oscillation will decrease the life of the machine.

Figure (Fig.9),(Fig.10),(Fig.11) Represents respectively the temporal evolution of the electromagnetic torque, voltage and flows, it has allows you to say after a short transitional regime, the electromagnetic torque follows its reference generate by the MPPT block with a dynamic very fast and fewer harmonics by report to the DTC classic. A decrease in the rate of TR harmonic to pin of flow and rotor voltage issue by the two correctors PI to the presence of the converter CCM, The simulation results show the high performance of the DTC-SVM developed by the report to the command DTC classic.

VII. CONCLUSION

In This work we have studied the control of the wind system (turbine more DFIG), by two different approaches, it was a question in the first place of introduced the principle of control classic DTC as well its application on our model. The latter is based on a regulator to the hysteresis of electromagnetic torque and the Rotor flux. It can be concluded that the whole of the six vectors active voltage provided by the converter to two-levels is sufficient to ensure the stability of the decoupled regulation of the torque and the Rotor flux, but unfortunately, it presents large oscillations at the level of these two quantities to cause of variation of the switching frequency. In the face of this problem, we have attacked the classic DTC by a vector command SVM in the third part of this chapter. This method allows to reduce the oscillations of torque is of flows.

This technique is known by the name DTC-SVM. A PI controller and a switching table are adopted to achieve this command. Finally according to the resulting from the simulation of the two approaches, it was noticed that the

command DTC-SVM gives more precise results compared to the command DTC.

VIII. REFERENCES

- [1] T. Ghennam, « Supervision of a wind farm for its integration in the management of a grid, contributions of the converters multi levels to the setting of the turbines at base of asynchronous machine with double power supply', school Centrale of Lille; Military school polytechnique Algiers, 2011.
- [2] A.Moualdia, MO.Mahmoudi, L.Nezli, "Commande DTC et DPC d'un Eolienne à Vitesse Variable Basée sur la MADA", International Conférence on Energie Renewable, (ICRE'12), Université A.Mira, Bejaia, Algeria, Avril-15- 16, 2012.
- [3] D. Swierczynski, Direct Torque Control with Space Vector Modulation (DTCSVM) of Inverter-Fed Permanent Magnet Synchronous Motor Drive, Warsaw University of Technology, Ph.D. Thesis, Warsaw, Poland, 2005.
- [4] R. D. Fernandez, P. E. Bataiot, R. J. Mantz "Wind Farm Control Based on Passivity", IEEE International Conference on Industrial Technology (ICIT), pp. 1000-1005, 2010.
- [5] A. MOUALDIA, « Control strategies DTC-SVM and DPC applied to a MADA used for the production of énergie éolienne», Doctoral thesis Ecole National Polytechnique, 2014.
- [6] S. Tamalouzt, T. Rekioua, et R. Abdessemed, « Direct torque and reactive power control of Grid Connected Doubly Fed Induction Generator for the wind energy conversion », in 2014 International Conference on Electrical Sciences and Technologies in Maghreb (CISTEM), 2014, p. 1-7.
- [7] M. Zelechowski, "Space Vector Modulated – Direct Torque Controlled (DTC-SVM) Inverter- Fed Induction Motor Drive", Ph.D Thesis, Warsaw University of Technology, 2005.
- [8] A. Boyette, « The control of a double fed asynchronous generator with storage system for the Wind Power Production », University Henri Poincaré-Nancy I, 2006
- [9] A. Mehdi, A. Reama, H. E. Medouce, S. E. Rezgui, et H. Benalla, « Direct active and reactive power control of DFIG based wind energy conversion system », in 2014 International Symposium on Power Electronics, Electrical Drives, Automation and Motion (SPEEDAM), 2014, p. 1128-1133.
- [10] [S. V. Paturca, M. Covrig, et L. Melcescu, « Direct Torque Control of Permanent Magnet Synchronous Motor (PMSM)-an approach by using Space Vector Modulation (SVM) », in Proceedings of the 6th WSEAS/IASME Int. Conf. on Electric Power Systems, High Voltages, Electric Machines, 2006.
- [11] G. Abad, J. López, M. Rodríguez, L. Marroyo, and G. Iwanski, "Doubly Fed Induction Machine: Modeling and Control for Wind Energy Generation". John Wiley & Sons, 2011.
- [12] M. Abdellatif, "Continuity of service of electrical drives for induction machine supplied by the stator and the rotor in the presence of faults Sensors", Doctoral thesis, Institut National Polytechnique de Toulouse (INP Toulouse), 2010.
- [13] F. Poitiers, « Study and control of asynchronous generators for the use of wind energy-Asynchronous machine to autonomous cage-Asynchronous machine to dual power supply connected to the network », University of Nantes, 2003.



Diagnostics Laboratory at Djelfa University.

Mr Habib Chaouki Ben Djoudi, was born in Setif, Algeria in 1992. He received the state of Master in automation and control of industrial systems in 2016 and Licence in electrical engineering and industrial computing in 2014 from Tiaret University and his obtained the diploma of Bachelor in Mathematics in 2011. Now he preparing his PhD degree on the study of stability problems at fault-tolerant control limits: Application to a wind energy system in the Applied Automation and Industrial



Dr. Guemana Mouloud, He was born in Medea, Algeria in 1975. He received the state engineer degree of the national institute of hydrocarbons and chemistry INH on Mechanical Engineering from the University of Boumerdes, Algeria, in 1998. From May 1999 to January 2003, He was associated researcher and associated lecturer. He received his Magister at the University of Boumerdes, Algeria in 2003. He received the Ph.D degree in Industrial Maintenance in 2012.

Currently he is an associate Professor at the University of Medea, Algeria. He is the head of the reliability in industrial systems group at the Applied Automation and Industrial Diagnostic Laboratory. He is the author and co-author of many scientific papers and research projects. His research interests include industrial maintenance, reliability system, dynamical systems, and diagnostic and reliability optimisation.



Pr Ahmed HAFIFA was born in Algeria in 1974, he received the State Engineer degree in 2000 on Applied Automation, the Magister degree in 2004 on Applied Automation and control systems and the PhD on Applied Automation and Signal Processing in 2010 from the UMBB Boumerdes University. He received the Habilitation from the University of Sciences and Technology Houari Boumediene

- USTHB - Faculty of Electronics and Computer Science, Department of Instrumentation and Automation on 2012. He is a PhD and Full Professor in Industrial Process: Automation / Diagnosis and Reliability Engineering at the Science and Technology Faculty of the University of Djelfa, Algeria, where He is actually the president of the scientific committee of Technical Sciences Department (CSD) since 2014 and he is pursuing his researches as a researcher at the Applied Automation and Industrial Diagnostic Laboratory of the University of Djelfa. Professor Ahmed HAFIFA has participated in several international research projects and has led several national research projects. Currently he is the Director of the Applied Automation and Industrial Diagnostic Laboratory of the University of Djelfa..

Commande Découplée du Système Multi-machines Connectées en Série

Taieb BESSAAD*, Rachid TALEB, M'hamed HELAIMI,
Abderrahmen BENBOUALI and Fayçal CHABNI

Electrical Engineering Department, Hassiba Benbouali University, Chlef, Algeria
Laboratoire Génie Electrique et Energies Renouvelables (LGEER)

*E-mail: t.bessaad@univ-chlef.dz

ABSTRACT

Ce travail s'intéresse à la commande d'un système d'entraînement multi-machines mono-convertisseur (SMMC). La commande découplée du système global est réalisée selon un modèle mathématique décrivant son comportement. Grâce à ce modèle, il devient possible de commander indépendamment deux types de machines connectées en série à savoir : la machine hexaphasée et la machine triphasée à travers leurs courants statoriques. Parmi les techniques de commande basées sur le contrôle du courant, on trouve la commande vectorielle qui est largement développée et testée sur des processus industriels de différentes puissances. Ainsi, la commande appliquée, dans ce travail, est basée sur le principe de la commande vectorielle développée pour les machines à courant alternatif.

Key Words: Multiphase machines, Vector control, Hexa-phase inverter.s.

1. INTRODUCTION

Les machines à courant alternatif, asynchrone en particulier, ont largement dominé le domaine des machines électriques. Cependant, récemment, les chercheurs s'intéressent aux machines ayant un nombre de phases supérieur à trois. Ces machines sont souvent appelées «machines à grand nombre de phases» ou «machines multi-phasées». Il est possible de connecter en série plusieurs machines alimentées par un seul convertisseur statique et que chaque machine du groupe avoir un contrôle de

vitesse indépendant. Cependant, l'emploi des convertisseurs polyphasés associés aux machines polyphasées, génère des degrés de libertés additionnels. Grâce à ces derniers, plusieurs machines polyphasées peuvent être connectées en série selon une transposition des phases appropriées [1, 4].

La mise en série des machines asynchrones polyphasées peut être une solution très intéressante pour certaines applications, telle que la traction électrique. Le système global est alors défini par la dénomination système multi-machines mono-convertisseur connectées en série (SMMC). Ce système est composé de plusieurs machines connectées en série selon une transposition des phases appropriée. L'ensemble est alimenté par un seul convertisseur via la première machine. La commande de chaque machine du groupe multi-machines doit être indépendante des autres [5, 8].

2. MODELISATION DU SYSTEME MULTIMACHINES

Le système d'entraînement électrique est composé de deux machines asynchrones. Un moteur asynchrone hexaphasé M(1) symétrique dont les enroulements sont montés en série avec ceux d'un second moteur asynchrone triphasé M(2). Les deux moteurs sont alimentés par un seul onduleur de tension hexaphasé.

La Fig. 1 présente le diagramme de connexion et d'alimentation des deux moteurs [9, 11]. Le stator de la machine hexaphasée est constitué de six

enroulements identiques et décalés d'un angle électrique ($\alpha = 2\pi/6$).

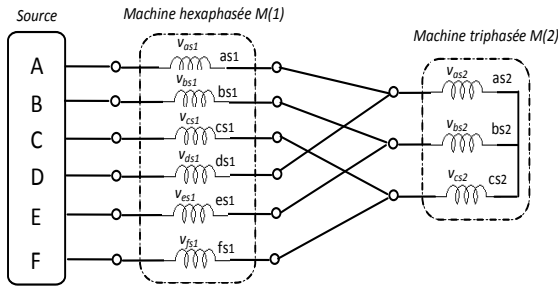


Figure.1: Schéma de connexion en série d'une machine hexaphasée avec une machine triphasée.

Notons qu'une simple connexion en série des enroulements statoriques n'aboutit pas au résultat désiré. Une transposition adéquate des phases statoriques est une solution à cette contrainte [12, 13]. En effet, les sorties de chaque deux enroulements, appartenant à la machine hexaphasée décalée d'un angle égal à π , sont connectés au même point et mises, par la suite, en série avec un enroulement de la machine triphasée [14, 15]. De cette façon, les courants traversant les enroulements de la machine hexaphasée vont se neutraliser aux points de connexions. De la même manière, chaque courant traversant un enroulement de la machine triphasée se divise par deux en traversant les deux enroulements, de la machine hexaphasée, connectés au même point. Ceci produira des ondes de forces magnétomotrices égales et en opposition de phases alors la résultante sera nulle au niveau de l'entrefer de la machine hexaphasée. Par conséquent, un découplage naturel des deux moteurs sera possible en adoptant le diagramme de connexion présenté par la Fig. 1.

D'après la Fig. 1, les tensions statoriques et rotoriques des deux machines peuvent s'écrire comme suit [1, 4] :

$$[V_s] = \begin{bmatrix} V_A \\ V_B \\ V_C \\ V_D \\ V_E \\ V_F \end{bmatrix} = \begin{bmatrix} v_{as1} + v_{as2} \\ v_{bs1} + v_{bs2} \\ v_{cs1} + v_{cs2} \\ v_{ds1} + v_{as2} \\ v_{es1} + v_{bs2} \\ v_{fs1} + v_{cs2} \end{bmatrix} \quad (1)$$

La relation entre les courants de source et les courants statoriques de chaque machine sont donnés comme suit :

$$\begin{aligned} [i_s] &= [I_A \ I_B \ I_C \ I_D \ I_E \ I_F]^T \\ &= [i_{as} \ i_{bs1} \ i_{cs1} \ i_{ds1} \ i_{es1} \ i_{fs1}]^T \\ &= [i_{s1}] \end{aligned} \quad (2)$$

$$[i_{s2}] = \begin{bmatrix} i_{as2} \\ i_{bs2} \\ i_{cs2} \end{bmatrix} = \begin{bmatrix} I_A + I_D \\ I_B + I_E \\ I_C + I_F \end{bmatrix} \quad (3)$$

Equations électriques :

$$\begin{cases} [v_{sk}] = [R_{sk}] \cdot [i_{sk}] + \frac{d}{dt} [\varphi_{sk}] \\ [0] = [R_{rk}] \cdot [i_{rk}] + \frac{d}{dt} [\varphi_{rk}] \end{cases} \quad (4)$$

où

$$\begin{cases} [\varphi_{sk}] = [L_{ssk}] \cdot [i_{sk}] + [M_{srk}] \cdot [i_{rk}] \\ [\varphi_{rk}] = [L_{rrk}] \cdot [i_{rk}] + [M_{rsk}] \cdot [i_{sk}] \end{cases} \quad (5)$$

Sachant que $k = 1$ pour la machine hexaphasée et $k = 2$ pour la machine triphasée.

avec :

$$[R_{seq}] = [R_{s1}] + \begin{bmatrix} [R_{s2}] & [R_{s2}] \\ [R_{s2}] & [R_{s2}] \end{bmatrix}$$

$$[L_{seq}] = [L_{s1}] + \begin{bmatrix} [L_{s2}] & [L_{s2}] \\ [L_{s2}] & [L_{s2}] \end{bmatrix}$$

3. MODELE DU SMMC DANS LE REPERE (α, β) , (X, Y) , $(O+, O-)$

Le SMMC peut être représenté par les sous-systèmes (α, β) (X, Y) $(o+, o-)$ à l'aide de la transformation suivante : $X_{\alpha\beta o} = [T_6(\theta)]^{-1} \cdot X_{abc}$ et $X_{dqo} = [T_6(\theta)]^{-1} \cdot X_{\alpha\beta o}$

où X peut représenter le courant, la tension ou le flux dans le SMMC.

$$[T_6] = \frac{1}{\sqrt{3}} \begin{bmatrix} 1 & \cos(\alpha) & \cos(2\alpha) & \cos(3\alpha) & \cos(4\alpha) & \cos(5\alpha) \\ 0 & \sin(\alpha) & \sin(2\alpha) & \sin(3\alpha) & \sin(4\alpha) & \sin(5\alpha) \\ 1 & \cos(2\alpha) & \cos(4\alpha) & \cos(6\alpha) & \cos(8\alpha) & \cos(10\alpha) \\ 0 & \sin(2\alpha) & \sin(4\alpha) & \sin(6\alpha) & \sin(8\alpha) & \sin(10\alpha) \\ \frac{1}{\sqrt{2}} & \frac{1}{\sqrt{2}} & \frac{1}{\sqrt{2}} & \frac{1}{\sqrt{2}} & \frac{1}{\sqrt{2}} & \frac{1}{\sqrt{2}} \\ \frac{1}{\sqrt{2}} & -\frac{1}{\sqrt{2}} & \frac{1}{\sqrt{2}} & -\frac{1}{\sqrt{2}} & \frac{1}{\sqrt{2}} & -\frac{1}{\sqrt{2}} \end{bmatrix} \quad (6)$$

$$[T_3] = \sqrt{\frac{2}{3}} \begin{bmatrix} 1 & \cos(2\alpha) & \cos(4\alpha) \\ 0 & \sin(2\alpha) & \sin(4\alpha) \\ \frac{1}{\sqrt{2}} & \frac{1}{\sqrt{2}} & \frac{1}{\sqrt{2}} \end{bmatrix} \quad (7)$$

$$[\rho(\theta)] = \begin{bmatrix} \begin{bmatrix} \cos(\theta) & -\sin(\theta) \\ -\sin(\theta) & \cos(\theta) \end{bmatrix} & [0]_{2 \times 4} \\ [0]_{4 \times 2} & [I]_{4 \times 4} \end{bmatrix} \quad (8)$$

Alors ces modèles sont :

$$\begin{cases} [T_6]^{-1}[\varphi_{s,abcdef}] = [\varphi_{s\alpha} \ \varphi_{s\beta} \ \varphi_{sx} \ \varphi_{sy} \ \varphi_{so+} \ \varphi_{so-}]^T \\ [T_6]^{-1}[i_{s,abcdef}] = [i_{s\alpha} \ i_{s\beta} \ i_{sx} \ i_{sy} \ i_{so+} \ i_{so-}]^T \end{cases} \quad (9)$$

$$\begin{cases} [T_6]^{-1}[\varphi_r] = [0 \ 0 \ 0]^T \\ [T_6]^{-1}[i_r] = [i_{r\alpha} \ i_{r\beta} \ i_{ro+}]^T \end{cases}$$

En appliquant la matrice de transformation (6) et (7) aux équations des flux et des tensions, le système réel d'équations statoriques, de dimension six, sera décomposé en trois sous-systèmes découplés de dimension deux : les systèmes (α , β), (x , y) et ($0+$, $0-$).

Géométriquement, les variables statoriques projetées sur trois "plans" orthogonaux. Le système global dans le repère (α , β), (x , y) et ($0+$, $0-$) est écrit :

$$\begin{cases} V_{s\alpha} = R_{s1}i_{s\alpha1} + L_{s1} \frac{di_{s\alpha1}}{dt} + M_1 \frac{di_{r\alpha1}}{dt} \\ V_{s\beta} = R_{s1}i_{s\beta1} + L_{s1} \frac{di_{s\beta1}}{dt} + M_1 \frac{di_{r\beta1}}{dt} \end{cases} \quad (10)$$

$$\begin{cases} V_{sx} = R_{seq} i_{sx1} + (L_{s1} + 2L_{s2}) \frac{di_{sx1}}{dt} + \sqrt{2}M_2 \frac{di_{r\alpha2}}{dt} \\ V_{sy} = R_{seq} i_{sy1} + (L_{s1} + 2L_{s2}) \frac{di_{sy1}}{dt} + \sqrt{2}M_2 \frac{di_{r\beta2}}{dt} \end{cases} \quad (11)$$

$$\begin{cases} V_{so+} = R_{seq} i_{so+} + (L_{s1} + 2L_{s2}) \frac{di_{so+}}{dt} \\ V_{so-} = R_{seq} i_{so-} + L_{s1} \frac{di_{so-}}{dt} \end{cases} \quad (12)$$

Equations rotoriques des tensions:

$$\begin{cases} 0 = R_{r1}i_{r\alpha1} + L_{m1} \frac{di_{s\alpha1}}{dt} + L_{r1} \frac{di_{r\alpha1}}{dt} + \omega_{r1}(L_{m1}i_{s\beta1} + L_{r1}i_{r\beta1}) \\ 0 = R_{r1}i_{r\beta1} + L_{m1} \frac{di_{s\beta1}}{dt} + L_{r1} \frac{di_{r\beta1}}{dt} + \omega_{r1}(L_{m1}i_{s\alpha1} + L_{r1}i_{r\alpha1}) \end{cases} \quad (13)$$

$$\begin{cases} 0 = R_{r2}i_{r\alpha2} + \sqrt{2}L_{m2} \frac{di_{sx1}}{dt} + L_{r2} \frac{di_{r\alpha2}}{dt} + \omega_{r2}(\sqrt{2}L_{m2}i_{sy1} + L_{r2}i_{r\beta2}) \\ 0 = R_{r2}i_{r\beta2} + \sqrt{2}L_{m2} \frac{di_{sy1}}{dt} + L_{r2} \frac{di_{r\beta2}}{dt} - \omega_{r2}(\sqrt{2}L_{m2}i_{sx1} + L_{r2}i_{r\alpha2}) \end{cases} \quad (14)$$

avec

$$\begin{cases} L_{s1} = l_{s1} + \frac{3}{2} L_{ms1} \\ M_1 = \frac{3}{\sqrt{2}} L_{sr1} \\ L_{r1} = l_{r1} + \frac{3}{2} L_{ms1} \end{cases} ; \begin{cases} L_{s2} = l_{s2} + \frac{3}{2} \\ M_2 = \frac{3}{\sqrt{2}} L_{sr2} \\ L_{r2} = l_{r2} + \frac{3}{2} L_{mr2} \end{cases} \quad (15)$$

$$\begin{bmatrix} v_{s\alpha} \\ v_{s\beta} \\ v_{sx} \\ v_{sy} \\ v_{so+} \\ v_{so-} \end{bmatrix} = [T_6] \begin{bmatrix} v_{sa1} + v_{sa2} \\ v_{sb1} + v_{sb2} \\ v_{sc1} + v_{sc2} \\ v_{sd1} + v_{sd2} \\ v_{se1} + v_{se2} \\ v_{sf1} + v_{sf2} \end{bmatrix}$$

$$= \begin{bmatrix} v_{s\alpha} \\ v_{s\beta} \\ v_{sx1} + \sqrt{2}v_{s\alpha2} \\ v_{sy1} + \sqrt{2}v_{s\beta2} \\ v_{so+} \\ v_{so-} \end{bmatrix} \quad (16)$$

$$\begin{cases} i_{s\alpha} = i_{s\alpha1} \\ i_{s\beta} = i_{s\beta1} \end{cases} ; \begin{cases} i_x = i_{sx1} = \frac{i_{s\alpha2}}{\sqrt{2}} \\ i_y = i_{sy1} = \frac{i_{s\beta2}}{\sqrt{2}} \end{cases} ; \begin{cases} i_{o+} = i_{so+1} \\ i_{o-} = i_{so-1} \end{cases} \quad (17)$$

L'application de (18), le couple électromagnétique fourni par chacune de ces deux machines est donné par :

$$\begin{cases} T_{em1} = P_1 M_1 (i_{rd1} i_{sq1} - i_{sd1} i_{rq1}) \\ T_{em2} = \sqrt{2} P_2 M_2 (i_{rd2} i_{sy1} - i_{sx1} i_{rq2}) \end{cases} \quad (18)$$

Les équations différentielles 10, 11, 12 et 13 montrent que les systèmes d'axes (α , β) et (x , y) sont complètement découplés l'un de l'autre. Les courants d'onduleur $i_{s\alpha}$ et $i_{s\beta}$ sont couplés, seulement, aux courants rotoriques $i_{r\alpha1}$ et $i_{r\beta1}$ de la machine hexaphasée. A l'inverse, les courants d'onduleur $i_{s\alpha2}$ et $i_{s\beta2}$ sont couplés, seulement, aux courants rotoriques $i_{r\alpha2}$ et $i_{r\beta2}$ de la machine triphasée.

Le système différentiel 10, qui fait intervenir les tensions d'onduleur v_{sa} et v_{sb} , décrit les équations de la machine hexaphasée; alors que le système différentiel 11, qui fait intervenir les tensions d'onduleur v_{sx} et v_{sy} , décrit les équations de Concordia de la machine triphasée.

4. COMMANDE VECTORIELLE DE DEUX MACHINES ELECTRIQUES

Seules les phases 1,3 et 5 sont utilisées par la deuxième machine, elles sont déphasées par un angle de $2\pi/3$. Cette machine possède alors trois phases. La Fig. 2, représente le diagramme de connexion de ce système multi-machines.

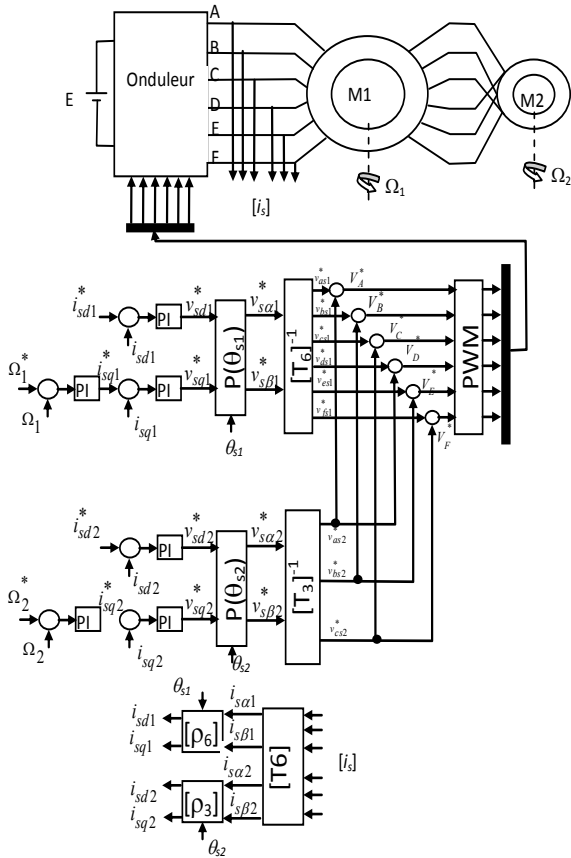


Figure. 2 : Régulation de courants et de vitesses d'un SMMC commandé par la méthode du flux orienté (IFOC).

5. MODELE SIMPLIFIE DU SMMC

Si le repère (d, q) est parfaitement orienté, on peut supposer que la composante $\varphi_{rq,k} = 0$. Ceci simplifie le modèle du SMMC comme suit :

$$\begin{cases} \frac{d\varphi_{ra1}}{dt} = \frac{M_k}{T_{r1}} i_{sa1} - \frac{1}{T_{r1}} \varphi_{ra1} \\ \frac{d\varphi_{r\beta1}}{dt} = \frac{M_1}{T_{r1}} i_{s\beta1} - (\omega_{s1} - P_1 \Omega_{m1}) \varphi_{ra1} \\ \frac{d\Omega_{m1}}{dt} = \frac{P_1 M_1}{J_1 L_{r1}} \varphi_{ra1} i_{sa1} - \frac{1}{J_1} C_{r1} \end{cases} \quad (19)$$

$$\begin{cases} \frac{d\varphi_{ra2}}{dt} = \sqrt{2} \frac{M_2}{T_{r2}} i_{sx} - \frac{1}{T_{r1}} \varphi_{ra2} \\ \frac{d\varphi_{r\beta2}}{dt} = \sqrt{2} \frac{M_2}{T_{r2}} i_{sy} - (\omega_{s2} - P_2 \Omega_{m2}) \varphi_{ra2} \\ \frac{d\Omega_{m2}}{dt} = \frac{P_2 M_2}{J_2 L_{r1}} \varphi_{ra2} i_{sa2} - \frac{1}{J_2} C_{r2} \end{cases} \quad (20)$$

En introduisant les vitesses angulaires de glissement, l'équation obtenue est de la forme suivante :

$$\begin{aligned} \frac{d\theta_{sl,k}}{dt} &= \omega_{sl,k} = (\omega_{s,k} - P_k \Omega_{m,k}) \\ &= \frac{M_k}{T_{r,k}} \cdot \frac{i_{sq,k}}{\varphi_{rd,k}} \end{aligned} \quad (21)$$

$$i^s = \begin{cases} i_{s\beta} & \text{for } k = 1 \\ \sqrt{2} i_{sy} & \text{for } k = 2 \end{cases}$$

Selon cette condition, les flux et les couples du SMMC sont alors :

$$\begin{cases} \varphi_{ra1} = \frac{M_1}{1+T_{r1}S} i_{sa1} \\ T_{em1} = \frac{P_1 M_1}{L_{r1}} \varphi_{ra1} i_{s\beta1} \end{cases} \quad (22)$$

$$\begin{cases} \varphi_{ra2} = \sqrt{2} \frac{M_2}{1+T_{r2}S} i_{sx} \\ T_{em2} = \sqrt{2} \frac{P_2 M_2}{L_{r2}} \varphi_{ra2} i_{sy} \end{cases} \quad (23)$$

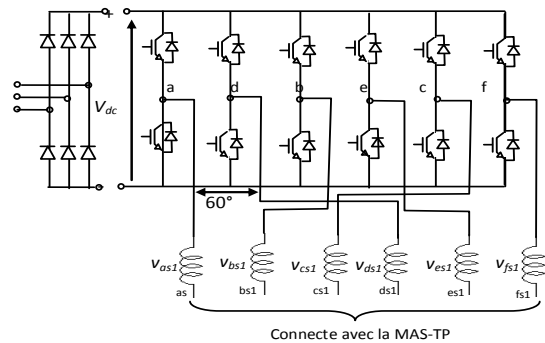


Figure. 3 : Représentation d'un onduleur hexaphasé

6. SIMULATION NUMERIQUE

Les résultats de simulation sont illustrés dans le but de prouver le découplage du contrôle des deux machines du SMMC. La première étape est réservée à la simulation de démarrage à vide, suivi de l'application d'un couple de charge égal à 39N.m, entre les deux instants $t=1s$ et $t=1.5s$, pour M(1) et un couple de charge égal à 4N.m, entre les deux instants $t=2s$ et $t=2.5s$, pour M(2).

La Fig.4. illustre les réponses en vitesses, couples et courants statoriques. Il est clair que le démarrage de MAS-HP (M1) n'a pas un impact ni sur la vitesse de la MAS-TP (M2) ni sur son couple électromagnétique.

Le second test concerne le comportement vis-à-vis des changements de sens de rotation des deux machines. En effet, la Fig.5 et Fig.6 montrent les résultats obtenus dans le cas où la M(1) tourne à 50 rad/s et $\Omega_2 = 100\text{rad/s}$ pour M(2) avec une inversion de sens de rotation à l'instant $t = 1.5s$. Il est remarquable que le contrôle découplé ait toujours conservé, aucune influence sur les caractéristiques des deux machines n'a été constatée. La même remarque est déduite lorsque la vitesse de la M(2) est inversé de $+100\text{rad/s}$ à -100 rad/s sous une vitesse $\Omega_1 = 50\text{ rad/s}$ (M1).

La Fig.7 montre le zoom des courants statoriques de deux machines M(1) et M(2) pour les trois cas précédents. (A) représente le premier teste et (B) deuxième teste.

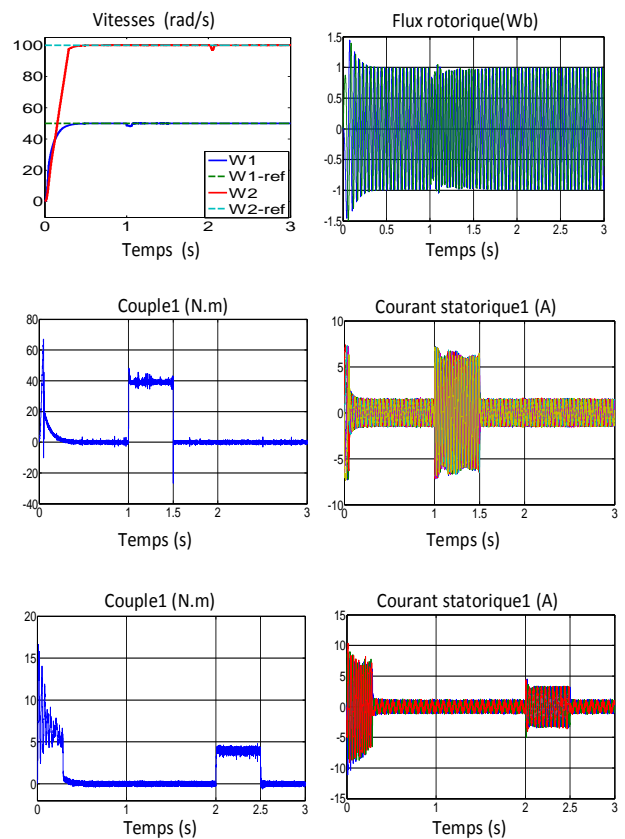
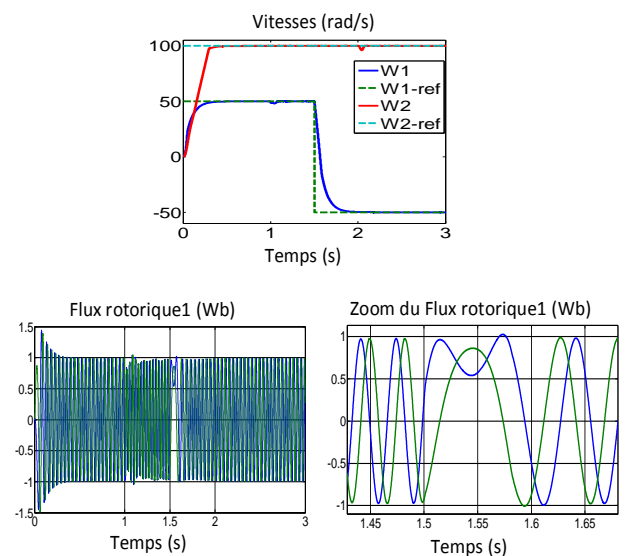


Figure. 4. Performance de la commande vectorielle indirecte du SMMC démarrage à vide et application une charge à M(1) et M(2)



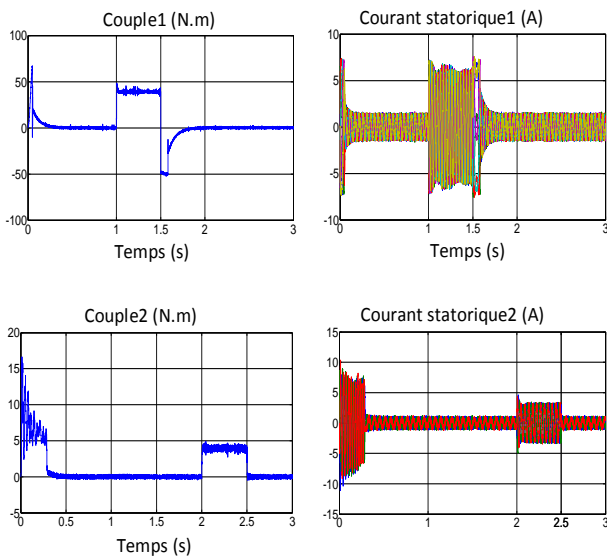


Figure. 5 : Performance de la commande vectorielle indirecte du SMMC Inversion de vitesse de MAS-HP $\Omega_1 = -50\text{rd/s}$

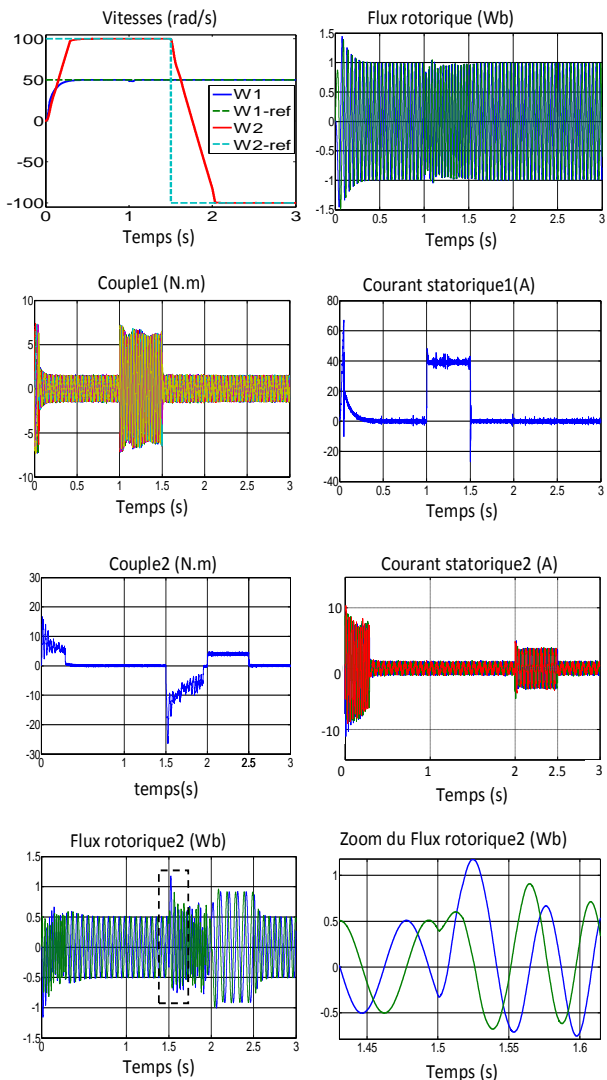


Fig. 6. Performance de la commande vectorielle indirecte du SMMC Inversion de vitesse de MAS-TP $\Omega_2 = -100\text{rd/s}$

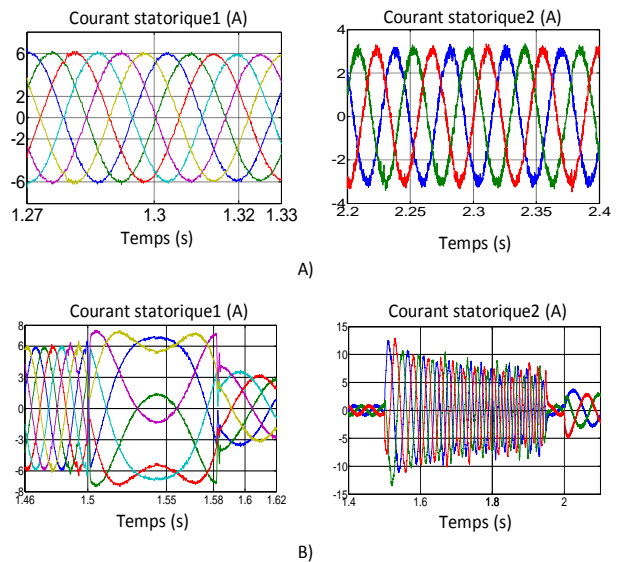


Figure.7 : Zoom des courants statoriques de M(1) et M(2) pour les testes précédant.

7. CONCLUSION

Dans ce travail, la modélisation du système multi-machine en vue d'une alimentation par convertisseur statique a été étudiée. De plus, plusieurs transformations ont été introduites afin de simplifier le modèle mathématique décrivant le comportement du système global. Le modèle est représenté par les sous-systèmes (α, β) (x, y) (o^+, o^-) à l'aide de ces transformations.

La dernière étape était d'élaborer la commande à flux orienté, en boucle fermée à ce système. Les résultats de simulations montrent clairement qu'on peut commander d'une façon indépendante les deux machines connectées en série.

Le traitement numérique de ce système multi-machines nous a conclu qu'il est possible pour certaine application industrielle de forte puissance de réaliser des actionneurs asynchrones formés par plusieurs moteurs connectés en série et alimentés par un seul convertisseur statique.

Les deux moteurs électriques entraînant deux charges mécaniques différentes. Cette configuration est très intéressante dans un système embarqué, en vu de la réduction du poids, de l'encombrement et de l'optimisation de la consommation de l'énergie électrique.

Le principal avantage de ce type de système multi-machines réside dans sa commande. En disposant d'une seule carte

de commande, on peut commander chaque moteur indépendamment des autres.

REFERENCES

- [1] M.Jones, S.N Vukosavic, E.Levi, "Independent vector control of a six-phase seriesconnected two-motor drive," *2nd IEE Int. Conf.Power Electronics, Machines and Drives PEMD, Edinburgh, UK*, pp. 879-884 (CD-ROM Paper No.157), 2004.
- [2] A.Iqbal, E.Levi, M.Jones, S.N.Vukosavic, "Dynamics of a series connected two-motor five-phase drive system with a single-inverter supply", *IEEE Industry Application Society Annual Meeting IAS, Hong Kong*, Oct.2005.
- [3] Y. Cui, R. Kavasseri, "A Particle Filter for Dynamic State Estimation in Multi-Machine Systems With Detailed Models", *IEEE Transactions on Power Systems*, vol. PP, no. 99, pp. 1-9, 2015.
- [4] S. Sachin, K. George, M. Mahesh, C. Vladimir, "Comparison of full and reduced scale solar PV plant models in multi-machine power systems", *IEEE PES T & D Conference and Exposition*, pp. 1-5, Chicago, USA, 14-17 April 2014.
- [5] Z. Hongshan, L. Xiaoming , "Excitation prediction control of multi-machine power systems using balanced reduced model", *IEEE Power and Energy Society General Meeting (PES)*, pp. 1-5, Vancouver, BC, 21-25 July 2013.
- [6] C. E. Ugalde-Loo, E. Acha, E. Licéaga-Castro, "Multi-machine power system state-space modelling for small-signal stability assessments", *Applied Mathematical Modelling*, vol. 37, no. 24, pp. 10141-10161, 15 December 2013.
- [7] I. Zubia, J.X. Ostolaza, A. Susperregui, J.J. Ugartemendia, "Multi-machine transient modelling of wind farms: An essential approach to the study of fault conditions in the distribution network", *Applied Energy*, vol. 89, no. 1, pp. 421-429, January 2012.
- [8] R. Saluja, S. Ghosh, M. H. Ali, "Transient stability enhancement of multi-machine power system by novel braking resistor models", *Proceedings of IEEE Southeastcon*, pp. 1-6, Jacksonville, FL, 4-7 April 2013.
- [9] E. Levi, M. Jones, S.N. Vukosavic, "Even-phasemulti-motor vector controlled drive with single inverter supply and series connection of stator windings", *IEEE Proc. Electric Power Applications*, vol. 150, no. 5, pp. 580-590, 2003.
- [10] D. Hadiouche, "Contribution à l'étude de la machine asynchrone double étoiles: modélisation, alimentation et structure", *Thèse de doctorat, UHP Nancy-1*, 2001.
- [11] J. P. Therattil, P. C. Panda, "Modeling and control of a multi-machine power system with FACTS controller", *International Conference on Power and Energy Systems (ICPS)*, pp. 1-6, Chennai, 22-24 Dec. 2011.
- [12] S. Mahapatra, A. N. Jha, "Modeling and simulation of TCSC based controller in a multi machine power system", *Students Conference on Engineering and Systems (SCES)*, pp. 1-6, Allahabad, 28-30 May 2014.
- [13] S. Kim, Y. Lee, H. Song, J. S. Kim, "Model based PID control design for bus voltage regulation in multi-machine power systems", *12th International Conference on Control, Automation and Systems (ICCAS)*, pp. 1796-1799, JeJu Island, 17-21 Oct. 2012.
- [14] H. Zhao, X. Lan, N. Xue, B. Wang, "Excitation prediction control of multi-machine power systems using balanced reduced model", *IET Generation, Transmission & Distribution*, pp. 1075-1081, June 2014.
- [15] Z. Ni, Y. Tang, H. He, J. Wen, "Multi-machine power system control based on dual heuristic dynamic programming", *IEEE Symposium on Computational Intelligence Applications in Smart Grid (CIASG)*, pp. 1-7, Orlando, FL , 9-12 Dec. 2014.
- [16] C. B. Jacobina, V. F .M. B. Melo, N. Rocha, E.R.C. da Silva, "Six-phase machine conversion system with three-phase and single-phase series converters", *IEEE Energy Conversion Congress and Exposition (ECCE)*, pp. 3896-3903, Denver, CO, 15-19 Sept. 2013.
- [17] C. H. Seng, E. Levi, M. Jones, M. J. Duran, "Operation of a Six-Phase Induction Machine Using Series-Connected Machine-Side Converters", *IEEE Transactions on Industrial Electronics*, vol. 61, no. 1, pp. 164-176, 2013.

An Improved Chaos Controller for Genesio-Tesi Chaotic System Based on Sliding Mode

Abdelilah CHIBANI *¹, Bachir DAAOU ² Abdelmadjid GOUICHICHE ¹
Ahmed SAFA ¹ Youcef MESSLEM ¹

¹ Laboratoire de Génie électrique et de plasmas, LGEP, Université Ibn Khaldoun, Tiaret. Algeria

² Laboratoire AVCIS, Université des Sciences et de la Technologie d'Oran -Mohamed Boudiaf, Algeria

*abdelilah.chibani@gmail.com

ABSTRACT

In this paper, we will focus on the development of a control strategy for a chaotic system. The aim of this work is to develop an algorithm that can drive the state of Genesio-Tesi to track and regulate the desired state. The designed scheme can control the uncertain chaotic behaviors to a desired state without oscillating very fast and guarantee the property of an asymptotical stability. First, we have designed a simple sliding mode (SMC) surface based on sliding mode control technique, for developing a chaos controller scheme. However, the SMC does not provide desired performances such as the chattering and slow dynamic response. Therefore, in order to obtain a better performance, we developed a higher order sliding mode controller (HOSMC). The effectiveness of the proposed algorithm is verified by simulation results.

Key Words: Chaotic system; Chaos control; Sliding mode control; Higher order sliding mode.

1. INTRODUCTION

The problem of chaos control attracts the attention of the researchers and engineers since the early 1990s [1] and over the last decades, much effort has been devoted to the research of chaotic systems [2]. Chaos theory and chaotic property have many useful applications in many engineering areas, such as secure communication, digital communication, power electronic devices, power quality, biological systems, chemical

reaction analysis, design, and information processing [3][4]. Many approaches and techniques have been proposed for controlling the chaotic system such as OGY method [5], variable structure control [9], nonlinear feedback control [6], and some other methods [7] have been successfully applied to chaotic systems.

Sliding-mode control (SMC) theory has made great progress in recent decades [8]. However, there are plenty of literature concerning control of the chaotic system via SMC [9] [10] [11]. In [12] authors investigated a robust adaptive PID controller design for a class of uncertain chaotic systems, which is motivated by the sliding mode control. In [13] based on the Lyapunov stability theorem, an adaptive control scheme is proposed for stabilizing the unstable periodic orbits of chaotic systems. In [14] adaptive synchronization of chaotic systems with fully unknown parameters is investigated. In [15] Chaos induced in Brushless DC Motor via current time-delayed feedback.

The purpose of this work is consisted to design two robust controllers a sliding mode controller (SMC) and an improved sliding mode controller (higher order (HOSMC)) for regulating the state trajectories of a chaotic dynamical Genesio-Tesi system. This present research work is structured as follows. First, the mathematical model of Genesio-Tesi is presented in Section 2. In order to eliminate the chaotic phenomenon, two robust control are developed sliding mode control (SMC) and improved sliding mode (HOSMC) in Section

3. Simulations results are presented in Section 4. Finally, some concluding remarks and conclusions are given in Section 5

2. SYSTEM DESCRIPTION

The chaotic Genesio–Tesi system, proposed by Genesio and Tesi [17], is one of a typical example of chaos. It includes a simple square part and three simple ordinary differential equations that depend on three positive real parameters [18]. The mathematical model of Genesio–Tesi is given by:

$$\begin{cases} \frac{dx_1}{dt} = x_2 \\ \frac{dx_2}{dt} = x_3 \\ \frac{dx_3}{dt} = -cx_1 - bx_2 - ax_3 + \gamma x_1^2 \end{cases} \quad (1)$$

Where x_1, x_2, x_3 represents the state variables of the system and $a, b,$ and $c,$ are the positive real constants. The dynamical Genesio–Tesi system has a rich chaotic phenomenon that can show in Fig.1. We consider the system (1) is perturbed by a disturbance term added to the equation. The uncertain Genesio–Tesi system can be written as

$$\begin{cases} \frac{dx_1}{dt} = x_2 + \varphi_1(t) \\ \frac{dx_2}{dt} = x_3 + \varphi_2(t) \\ \frac{dx_3}{dt} = -cx_1 - bx_2 - ax_3 + \gamma x_1^2 + \varphi_3(t) + u(t) \end{cases} \quad (2)$$

Where $\varphi_1 = 0.1 \cos(2t), \varphi_2 = 0.15 \cos(3t), \varphi_3 = 0.2 \cos(4t),$ are the disturbance term and $u(t)$ is the control input.

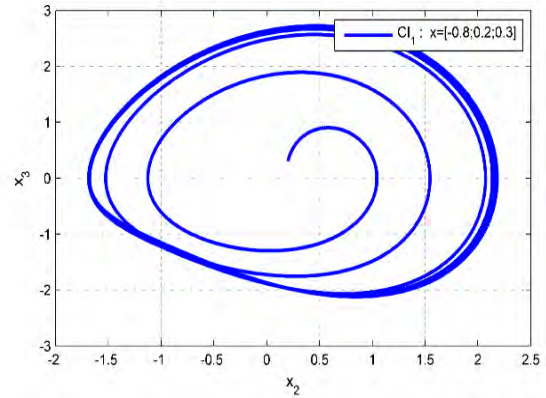
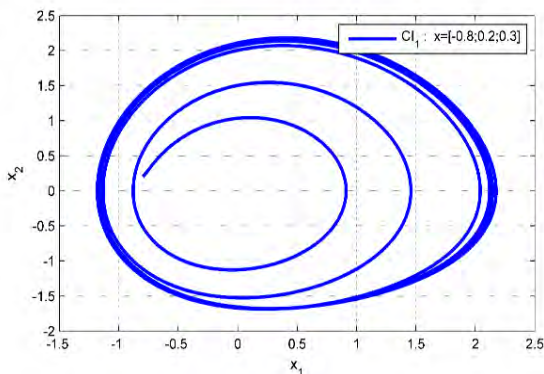


Figure.1: The Chaotic Trajectories of Uncertain Genesio–Tesi System.

3. ROBUST CONTROLLER FOR GENESIO-TESI CHAOTIC SYSTEM

The control objective aims to remove or synchronize the chaotic phenomenon. Therefore, in this section, two robust control laws are described: sliding mode control presented in [19] and an improved sliding mode control (higher order sliding mode control (HOSMC)).

Assumption 1.

The control problem is to get the system to track and regulate the reference state x^{ref} the control objective considered in this paper is that for any given target orbit $x^{ref} = 0$. A control scheme is designed, such that the resulting state response of tracking error vector satisfies

$$\lim_{t \rightarrow \infty} e_n(t) = \lim_{t \rightarrow \infty} x_n(t) - x_n^{ref}(t) \rightarrow 0$$

3.1. Sliding mode controller (SMC)

SMC is an effective methodology for controlling systems with variable structures and provides a systematic approach to the problem of maintaining stability and consistent performance in the face of modeling imprecision [10–12]

Let the dynamic errors are defined as:

$$e = [e_1 \ e_2 \ e_3]^T \quad (3)$$

When

$$\begin{cases} e_1 = x_1 - x^{ref} \\ e_2 = \dot{e}_1 = \dot{x}_1 - \dot{x}^{ref} = x_2 - x^{ref} \\ e_3 = \dot{e}_2 = \ddot{e}_1 = \ddot{x}_1 - \ddot{x}^{ref} = x_3 - x^{ref} \end{cases} \quad (4)$$

$$\begin{cases} e_1 = x_1 - x^{ref} \\ e_2 = x_2 - x^{ref} \\ e_3 = x_3 - x^{ref} \end{cases} \quad (5)$$

The dynamical system error can be expressed as flow:

$$\begin{cases} \dot{e}_1 = x_2 + \varphi_1(t) - x^{ref} \\ \dot{e}_2 = x_3 + \varphi_2(t) - x^{ref} \\ \dot{e}_3 = -cx_1 - bx_2 - ax_3 + \gamma x_1^2 + \varphi_3(t) + u(t) - x^{ref} \end{cases} \quad (6)$$

For designing the SMC, there are two basic steps. Firstly, we should define a sliding surface and secondly, we determine the control law [20]. In the first step, we should define the sliding surface. Therefore, we should use the general equation proposed by JJ Slotine [21], to determine the sliding surface given by

$$s(x,t) = \left(\frac{d}{dt} + \lambda \right)^{n-1} e \quad (7)$$

When λ is a positive coefficient, n is the degree relative and e is the tracking error vector that shown in (4).

We define the sliding surface

$$S = (e_3 + 2\lambda e_2 + \lambda^2 e_1) \quad (8)$$

Substituting (4) into (8) gives:

$$S = (x_3 + 2\lambda x_2 + \lambda^2 x_1) \quad (9)$$

The time derivative of S is:

$$\dot{S} = (\dot{x}_3 + 2\lambda \dot{x}_2 + \lambda^2 \dot{x}_1) \quad (10)$$

Let, $\dot{S} = 0$ we can get the equivalent control The sliding mode controller include the equivalent control and switching control, then we have

$$u = u_{eq} - k \text{sign}(s) \quad (11)$$

3.2. Higher order sliding mode control (HOSMC)

One particular approach to the robust controller is the sliding mode methodology [15]. In this section, we develop an improved higher order controller based on the use of sliding mode approaches. This technique has been chosen for the following reason: for its disturbance rejection, and strong robustness.

Therefore, we use this technique in order to remove the chaotic phenomenon.

Let the dynamic error $e_n = x_n - x_n^{ref}$ be as :

$$\begin{cases} e_1 = x_1 - x^{ref} \\ e_2 = x_2 - x^{ref} \\ e_3 = x_3 - x^{ref} \end{cases} \quad (12)$$

The sliding surface is selected as:

$$S = (e_3 + 2\lambda e_2 + \lambda^2 e_1) \quad (13)$$

Substituting (12) into (13) gives:

$$S = (x_3 + 2\lambda x_2 + \lambda^2 x_1) \quad (14)$$

The equivalent control is given by

$$u_{eq} = cx_1 + bx_2 + ax_3 - dx_1^2 - 2\lambda x_3 - \lambda^2 x_2 \quad (15)$$

The expiration of the control scheme is defined as:

$$u = u_{eq} + k\eta \text{sign}(s) \quad (16)$$

Where $\eta = \|s\|^{\frac{1}{p}}$ when p is a prime number.

The global higher order sliding mode controller HOSMC is described by

$$u = cx_1 + bx_2 + ax_3 - dx_1^2 - 2\lambda x_3 - \lambda^2 x_2 + k\eta \text{sign}(s) \quad (17)$$

Where k is a positive constant

4. SIMULATIONS RESULTS

In this section, simulation results are provided to verify the effectiveness of the proposed control schemes. Two control low (sliding mode control (SMC) and higher order sliding mode (HOSMC)) have been developed and applied to Genesisio-Tesi chaotic system with comparison study.

It can be clearly seen from the Fig.2 that the state of Genesisio-Tesi follow their reference $x^{ref} = 0$ even in transit state in each case. However, we note that in SMC controller we have a good steady. Therefore, The SMC controller has good performance tracking without overshooting and steady error of zero. Nevertheless, it has a slow dynamic response than the improved sliding mode controller (higher order sliding mode controller (HOSMC))

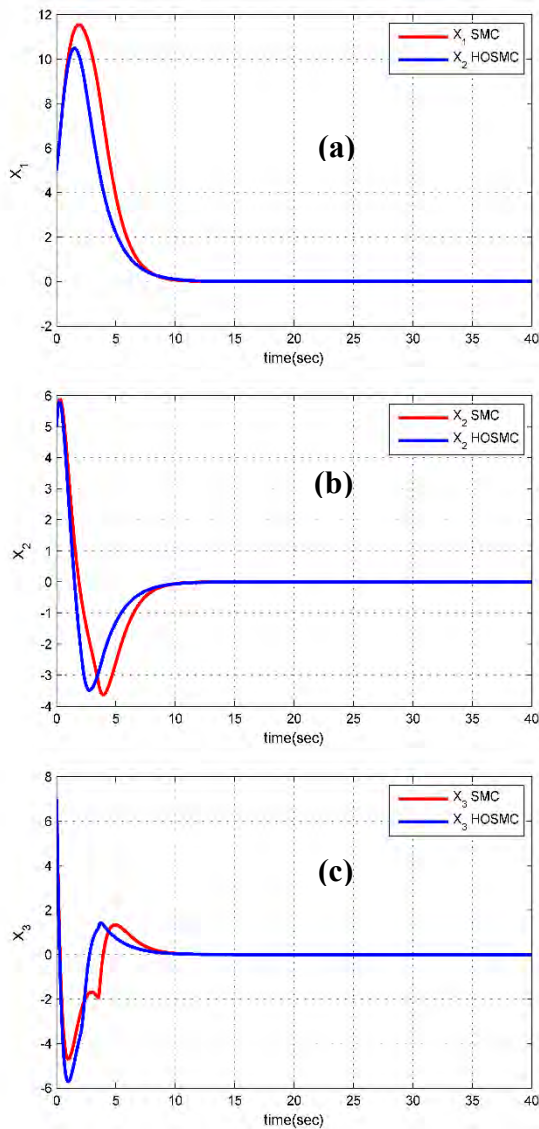


Figure.2 System responses with the chaos controller (SMC) and HOSMC without perturbation

To investigate the effectiveness of our proposed control law a perturbation parametric and external disturbances are introduced in the model of Genesio-Tesi. Fig 3. (a), (b), and (c) indicate the time response of the controller under perturbation.

Fig.3.a-c indicate the time responses of the states of Genesio-Tesi.

Fig.3.a show the variation of x_1 under perturbation parametric and external disturbances in both cases (Sliding mode (SMC)) and improved sliding mode (Higher order sliding mode control (HOSMC)).

In Figs., 3.b and 3.c respectively can demonstrate that the proposed HOSMC controller is more effective than the SMC.

Fig.4 illustrates the time response of

control input for the sliding mode control (SMC) and improved sliding mode control (higher order sliding mode (HOSMC))

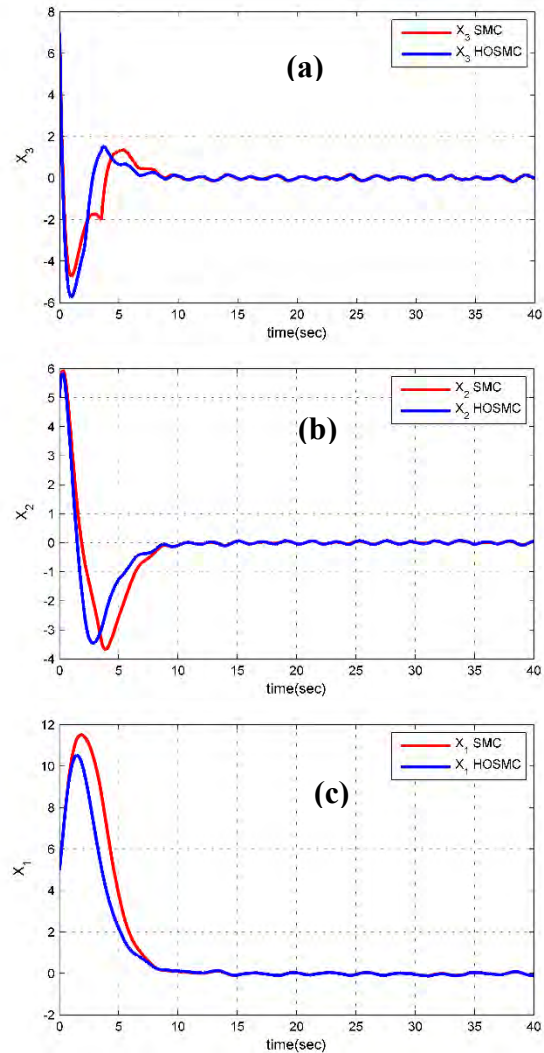


Figure.3 System responses with the chaos controller (SMC) and (HOSMC) with perturbation

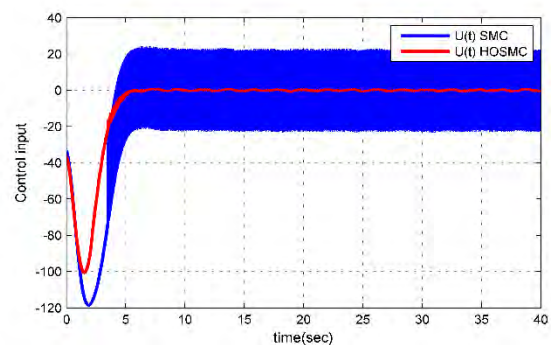


Figure.4 The time response of the controller's lows

To conclude this section, it is important to note that the proposed higher order sliding mode control HOSMC is able to achieve the proposed control objectives and to guarantee better tracking performances under nominal conditions and in presence.

5.CONCLUSION

A chaos controller algorithms based on the use of sliding mode controller for Genesis–Tesi was developed. The proposed control scheme aims to make the states of Genesis–Tesi to the desired states. In order to achieve a good performance, two robust controllers were developed: sliding mode and an improved sliding mode controller (higher order (HOSMC). The higher order sliding mode controller (HOSMC) was more interesting on maintaining control performance and equilibrium of Genesis–Tesi. The simulation results show the effectiveness of the proposed schemes

REFERENCES

- [1] Z.-L. Wang et H.-G. Zhang, «Adaptive synchronization of discrete chaotic systems», in 2002 International Conference on Machine Learning and Cybernetics, 2002. Proceedings, 2002, vol. 1, p. 336-339 vol.1.
- [2] B. R. Andrievskii et A. L. Fradkov, «Control of Chaos: Methods and Applications. I. Methods», Autom. Remote Control, vol. 64, no 5, p. 673-713, may 2003.
- [3] J.-J. Yan, «Design of robust controllers for uncertain chaotic systems with nonlinear inputs», Chaos Solitons Fractals, vol. 19, no 3, p. 541-547, févr. 2004.
- [4] M. Haeri, M. S. Tavazoei, et M. R. Naseh, «Synchronization of uncertain chaotic systems using active sliding mode control», Chaos Solitons Fractals, vol. 33, no 4, p. 1230-1239, août 2007.
- [5] C.-C. Peng et C.-L. Chen, «Robust chaotic control of Lorenz system by backstepping design», Chaos Solitons Fractals, vol. 37, no 2, p. 598-608, Jul. 2008.
- [6] J. Alvarez-Gallegos, «Nonlinear regulation of a Lorenz system by feedback linearization techniques», Dyn. Control, vol. 4, no 3, p. 277-298, Jul. 1994.
- [7] C.-C. Fuh et P.-C. Tung, «Controlling Chaos using Differential Geometric Method », Phys. Rev. Lett., vol. 75, no 16, p. 2952-2955, oct. 1995.
- [8] C. Edwards et S. Spurgeon, Sliding Mode Control: Theory And Applications. CRC Press, 1998.
- [9] S. Dadras et H. R. Momeni, «Fractional-Order Dynamic Output Feedback Sliding Mode Control Design for Robust Stabilization of Uncertain Fractional-Order Nonlinear Systems», Asian J. Control, vol. 16, no 2, p. 489-497, mars 2014.
- [10] A. Si-Ammour, S. Djennoune, et M. Bettayeb, «A sliding mode control for linear fractional systems with input and state delays», Commun. Nonlinear Sci. Numer. Simul., vol. 14, no 5, p. 2310-2318, may 2009.
- [11] A. Pisano, M. R. Rapaić, Z. D. Jeličić, et E. Usai, «Sliding mode control approaches to the robust regulation of linear multivariable fractional-order dynamics», Int. J. Robust Nonlinear Control, vol. 20, no 18, p. 2045-2056, déc. 2010.
- [12] W.-D. Chang et J.-J. Yan, «Adaptive robust PID controller design based on a sliding mode for uncertain chaotic systems», Chaos Solitons Fractals, vol. 26, no 1, p. 167-175, oct. 2005.
- [13] H. Salarieh et A. Alasty, «Adaptive control of chaotic systems with stochastic time-varying unknown parameters», Chaos Solitons Fractals, vol. 38, no 1, p. 168-177, oct. 2008.
- [14] J. Huang, «Adaptive synchronization between different hyperchaotic systems with fully uncertain parameters», Phys. Lett. A, vol. 372, no 27-28, p. 4799-4804, juin 2008.
- [15] C.-L. Li, W. Li, et F.-D. Li, «Chaos induced in Brushless DC Motor via current time-delayed feedback», Opt. - Int. J. Light Electron Opt., vol. 125, no 21, p. 6589-6593, nov. 2014.
- [16] Genesis R, Tesi A. A harmonic balance methods for the analysis of chaotic dynamics in nonlinear systems. Automatica 1992;28:531–48
- [17] Genesis R, Tesi A. A harmonic balance methods for the analysis of chaotic dynamics in nonlinear systems. Automatica 1992;28:531–48
- [18] Park JH. Adaptive controller design for modified projective synchronization of Genesis–Tesi chaotic system with uncertain parameters. Chaos, Solitons & Fractals 2007;34:1154–9.
- [19] A. Chibani, B. Daaou, A. Gouichiche, et A. Safa, «Nonlinear control applied to chaotic system using sliding mode », in 2014 International Conference on Electrical Sciences and Technologies in Maghreb (CISTEM), 2014, p. 1-5.
- [20] S. Dadras, H. R. Momeni, et V. J. Majd, «Sliding mode control for uncertain new chaotic dynamical system », Chaos, Solitons & Fractals, vol. 41, no 4, p. 1857-1862, août 2009
- [21] J.-J. Slotine et W. Li, Applied Nonlinear Control. Englewood Cliffs, N.J: Prentice Hall.

Author Index

Ababou, Amina	83, 98
Ababou, Nouredine	83, 98
Abdel Hafid, Hariz	92
Abdelaziz, Talha	143
Abdelilah, Chibani	330
Abdelmadjid, Gouichiche	330
Abidat, Redouane	195
Ahmed, Safa	330
Aissat, Abdelkader	137, 289
Aissou, Said	31
Allam, Abdelkrim	258
Amar, Guichi	143
Amrani, Faycal	1
Attari, Mokhtar	118, 128, 227, 246, 258
Bacha, Seddik	31
Bachir, Daaou	330
Badidi Bouda, Ali	112
Bahloul, Lyes	75
Barkat, Hamza	107, 112
Baudrand, Henri	215
Bekhouche, Khaled	242
Bekraoui, Amina	251
Belalem, Fouad	297
Belasri, Ahmde	201
Belboula, Abdelkader	23
Belouchrani, Adel	237
Ben Djoudi, Habib Chaouki	317
Benaicha, Samira	151
Benayad, Ali	64
Benbakhti, Anwar	246
Benbouali, Abderrahmen	323
Benkhoris, Mohamed-Fouad	281
Benlacheheb, Meriem	311
Benmerabet, Mohammed Salim	13
Benmerkhi, Ahlem	263
Benouar, Sara	227
Benrekaa, Kahina	98
Bensisaid, Karim	83, 98
Benstaali, Wafà	201
Benyamina, Faycal	6
BENYETTOU, Fethi	137
Benyoucef, Djilali	23
Berbezier, Isabelle	137

Berkani, Samir	58, 223
Berkouk, El Madjid	158
Berrabah, Fouad	281
Bessaad, Taieb	323
Bouchafaa, Farid	163, 183, 275
Bouchemat, Mohamed	69, 263
Bouchemat, Touraya	69, 263
Boudissa, El Ghalia	169
Boukazouha, Faiza	107
Boukhalifa, Saida	163, 275
Boukhelifa, Akila	195
Boukhelifa, Akkila	207
Boukhenous, Samir	118, 128, 246
Boulaam, Karima	207
Bounekhla, Mhamed	169
Bouraiou, Ahmed	183
Chabni, Fayçal	23, 323
Cherbi-Bazi, Lynda	75, 311
Chikh, Madjid	39
Dabou, Rachid	183
Degla, Aicha	39
Djail, Farid	98
Djerioui, Ali	281
El Madjid, Berkouk	13
Elmadjid, Berkouk	143
Farid, Bettine	132
Farouk, Laidoudi	132
Fayçal, Medjili	132
Feddal, Haroune	19
Ferhat, Mohamed Lamine	311
Fouad, Boubenider	132
Gabour, Nour El Houda	169
Ghoggal, Adel	176
Ghoumazi, Mehdi	188
Guemana, Mouloud	317
Guesmi, Houcine	137
Guessoum, Monia	107
Hadj Sadok, Mustapha	58, 223
Hadri Hamida, Amel	176
Hafaifa, Ahmed	268, 317
Hafid, Abdel Akram	227
Halimi, Rafik	112

Hamzaoui, Ihssen	163, 275
Harchouch, Nabila	289
Helaïmi, M'hamed	323
Herbadji, Abderahim	107
Herbadji, Abderrahim	112
Hocini, Abdesselam	188
Houari, Azeddine	281
Kahlouche, Marouane	52
Kedir, Malika	227
Kedir-Talha, Malika	52
Kedir-Talha, Malika D	297
Khaoula, Talbi	123
Khelili, Fatiha	176
Khlifi, Seyfallah	183
Khodja, Abdelhamid	215
Khoucha, Farid	6
Korchi, Narimane	46
Kouzou, Abdellah	268
Lahoubi, Mahieddine	69
Lamhene, Youssef	58, 223
Layadi, Noureddine	281
Lies, Bahloul	92
Lynda, Cherbi	92
Mahfoudi, Hichem	233
Mahrane, Achour	39
Meddah, Karim	297
Megueddem, Abdelhakim	242
Mehadji, Abri	305
Merabet, Nedjmeddine Ammar	75
Mosbah, Chayma	263
Nadji, Salah	151
Nassima, Belgacem	305
Necaïbia, Ammar	183
Ould Slimane, Saliha	52, 297
Oussaid, Rachid	46
Rekioua, Djamila	31
Remram, Youcef	237
Rouabha, Abdeslem	112
Rouabha, Abdesselam	107
Rouabha, Abdelkarim	183
Saadia, Nadia	98

Sadki, Yassine	268
SAFI, Meriem	137
Sahouane, Nordine	183
Saker, Khadidja	69
Samia, Harrouni	123
Sedda, Kamel	107
Seoane, Fernando	227
Taleb, Rachid	23, 323
Talha,	13
Talha, Abdelaziz	158
Tao, Junwu	19
Tellache, Mohamed	19, 64, 233
Tighidet, Malika	258
Timlelt, Hakima	237
Toubal Maamar, Alla Eddine	23
Touchen, Adel	118, 128
Touhami, Rachida	1, 215
Trabelsi, Mohamed	1
Vilcot, Jean Pierre	289
Yagoub, Mustapha Cherif-Eddine	215
Youcef, Messlem	330
Zabat, Mahdi	83
Zairi, Hadjar	52
Zaouche, Faika	31
Zaouche, Khelil	158
Zeghlache, Samir	281
Zerfaine, Abdelkader	233
Zerouali, Sakina	176
Ziane, Abderrezzaq	183
Zizoua, Cherif	118

Keyword Index

Acoustic localization	237
Acoustic wave	107
Active power filter	268
Admittance operator	215
Analysis	128
Ankle exercises	246
Antenna array	233
antenna WLAN/WiFi applications	305
Antenne planaire	58
Artificial neural network	195
Asymmetrical source configuration	13
Backstepping	151
Backstepping control	281
Bandwidth	1
Bandwith	46
Batteries	31
Battery storage	207
BIE 3D	58
Bifurcations	176
Bioimpedance	227
Biomedical Instrumentation	227
Cancer	258
Capderou	123
Cascaded Asymmetric H-bridge inverter	158
Center of gravity	118
Center of pressure	118
Ceramic Inspection	19
Chaos control	330
Chaotic system	330
Characteristic ICG points	227
Chebyshev polynomial	1
Client	258
Complementary filter	83
CPW	305
Crack Detection	19
CSRR	19
CST	305
CST Microwave Studio	58
Detection	137
DFIG	207
Dielectric Barrier discharge	201

Diesel generator	143
Diffuse	123
Digital capacitance	223
Direct	123
Direct power control	163
Direct torque control	163
Direct Torque Control (DTC)	317
Directivity Air holes	46
Dispersion flowmeter	251
Distributed amplifiers	1
Doppler effect	237
Double star induction machine	281
Doubly Fed Induction Generator (DFIG)	317
Dual band	305
Dynamic surface control (DSC)	151
EBG structures	223
ECG	227
Edge detection	297
Efficiency	201
Elbow flexion-extension	83
Electrolyzer	6
Embedded system	83, 98
EN 12668-1:2010 standard	112
Energy harvesting	64
Energy management	31, 39
Equivalent circuit	107
Excitation	201
Faraday Rotation	69
Fiber nonlinear optics	311
Fiber optics	311
Finite Element Analysis	132
Flow rate	251
Flow sensor	251
Foot	128
FPGA	52, 297
Fuzzy logic controller	281
Gain	1
Gas sensor	132
Generation of a high repetition rate pulse train	75
Genesio tesi chaotic system	330
Genetic Algorithm	169
Global maximum	195
Global solar radiation	123
Gyrotropy	69

Hardware	52
Harmonics	268
Harmonics compensation	158
Hexa-phase inverter	323
High order of dispersion.	75
Higher order sliding mod	330
Hot desert climate	183
Hot wire anemometer	251
Humidity	258
Hybrid electric vehicle	281
Hybrid mode	215
Hybrid system	143
Hydrogen liquids	188
Hydrogen production	6
ICG	227
Image processing	52
Impedance cardiography	227
Implementation	52
Inertial sensors	83
Inertial station	98
Instantaneous frequency	237
Instrumented handrim	98
Instrumented wobble board	246
Interconnection and Damping Assignment Passivity-Based Control (IDA-PBC)	23
Interior permanent magnet synchronous motor (IPMSM)	151
Intermediate power	143
Ku-band	233
Lamb acoustic waves	132
Lamps	201
Lead acid battery	39
Linear extended state observer (LESO)	151
Linear stability study.	75
Load cell	98
Local maximum	195
Localizd structures.	92
Low cost	98
Low power consumption	242
Low speed	281
Lyapunov theorem.	151
Magneto Optical	69
Manual wheelchair	98
Materials	137
MATLAB Toolbox	281
Maximum Power Point Tracking	163

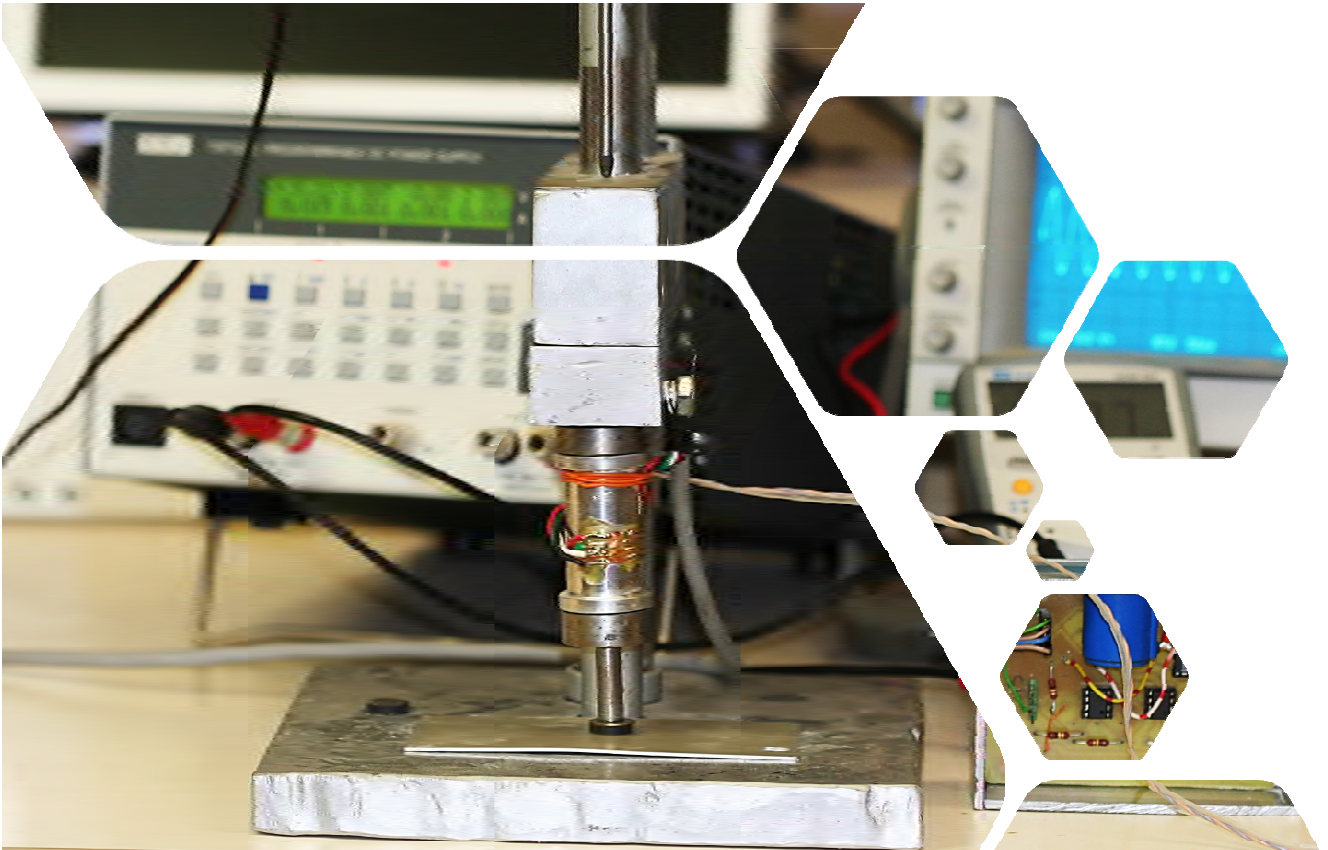
Maximum power point tracking	195
Maximum Power Point Tracking (MPPT)	23, 317
Mean bias error (MBE)	123
Measurement	251
Measurement uncertainty	112
Measurements	107
Mechanical characterization	132
Medical procedures	258
Metamaterials	223
Micro-cavity	263
Microphone	237
Microstrip patch antenna SINRD DSRC Gain	46
Microstructured fibers.	92
Microwaves	19
Mode Conversion TE-TM	69
Modified Coppetti model	39
Modulation instability.	75
MOSFET	242
MPPT	143, 275
Multi-band	64
Multilevel Inverter	163
Multilevel inverters	13
Multiphase machines	323
MySQL	258
Métamateriaux	58
Negative index materials	223
Neutral-Point Clamped Multilevel Inverters Objective Function	169
Non destructive test	19
Non linear optics.	92
Non-linear load	158
Nonlinear Schrödinger equation.	75
Normalized error	112
Operating temperature	183
Optical Fiber	69
Optical fiber.	75
Optical imaging	311
Optical Isolators	69
Optical Kerr effect.	75
Optimization	169
Optimized hybrid junction	64
P&O	275
Permanent-magnet synchronous generator	163
Perrin de Brichambaut	123
Pertub and observe	195
Photonic band gap	311

Photonic Crystal	263
Photonic crystal	311
Photonic crystal fiber	75
Photonic crystals	188
Photovoltaic	158
Photovoltaic systems	31
Piezoelectric thin films	132
Piezoelectroic transformer	107
Platform	128
PMSM	275
Power divider	233
Power management	143
Power storage management	207
Pressure	128
Proprioceptive enhancement	246
Propulsion force	98
Pulse measurement	112
PV module	183
PV system	39
PVG	275
Quality Factor	263
Quantum Dot	289
Quantum Dots	137
Radiation Structure	19
Radiofrequency	64
Radiotherapy treatment	258
Rehabilitation force sensor	118
Resonator	19
RFID	242
Ring resonators	188
Road vehicle	237
Robust controller system	23
Root mean square error (RMSE)	123
Scattering matrix	215
Selective Harmonic Elimination	169
Sensitivity	263
Sensor	263
Sensor nodes	83
Sensors network	258
Server architecture	258
Simulation	39
Simulation and prediction	183
Sliding mode control	330
SMC	176
Solar Cell	137, 289

Solar power system	23
Space Vector Modulation (SVM)	317
Split step Fourier method SSFM.	75
Stability	176
Standalone	143
Sub-threshold	242
Substrate integrated waveguide (SIW)	233
SVM control technique	268
Switched series/parallel inverter.	13
Temperature	258, 289
Temperature sensor.	242
THD	268
Thermal Effect	289
Thermal flowmeter	251
Total Harmonic Distortion	169
Trial functions	215
Ultrasonic instruments	112
Validation	183
Vector control	323
Velocity	251
VHDL	52, 297
Via holes	233
Vienna rectifier	6
Voltage doubler.	64
Voltage gain	107
Waveguide	263
Wind energy	317
Wind power	207
Wire antenna	223
Wireless communication	98
Wireless sensor	83
Xenon	201
XSG	297
Yttrium Iron Garnet	69
Z-RPI	227

Open Access Proceedings

Copyright © 2018 by the Laboratory of Instrumentation,
Publishing in Open Access, *All Right Reserved*



Legal Deposit in the Algerian Library

\$00.00

ISBN 978 9931 9548 04

<https://ic2em-2018.sciencesconf.org>